U.S. Department of Commerce
National Technical Information Service

N74-29885

PROCEEDINGS THIRD SPACE PROCESSING SYMPOSIUM SKYLAB RESULTS VOLUME 1

NATIONAL AERONAUTICS & SPACE ADMINISTRATION
WASHINGTON, DC

JUNE 74

June 1974

PROCEEDINGS

M-74-5

THIRD SPACE PROCESSING SYMPOSIUM

SKYLAB RESULTS

VOLUME I

APRIL 30-MAY 1-1974
MORRIS AUDITORIUM BLDG. 4200
MARSHALL SPACE FLIGHT CENTER
ALABAMA 35812

TECHNICAL REPORT STANDARD TITLE PAGE

1. REPORT NO.	2. GOVERNMENT ACCESSION NO.	3. RECIPIENT'S CATALOG NO.
M-74-5		

4. TITLE AND SUBTITLE
PROCEEDINGS THIRD SPACE PROCESSING SYMPOSIUM
SKYLAB RESULTS : Vol. I

5. REPORT DATE
June 1974

6. PERFORMING ORGANIZATION CODE

7. AUTHOR(S)

8. PERFORMING ORGANIZATION REPORT #

9. PERFORMING ORGANIZATION NAME AND ADDRESS
George C. Marshall Space Flight Center
Marshall Space Flight Center, Alabama 35812

10. WORK UNIT NO.

11. CONTRACT OR GRANT NO.

12. SPONSORING AGENCY NAME AND ADDRESS
National Aeronautics and Space Administration
Washington, D. C. 20546

13. TYPE OF REPORT & PERIOD COVERED
Miscellaneous

14. SPONSORING AGENCY CODE

15. SUPPLEMENTARY NOTES

16. ABSTRACT

This publication contains the presentations from the Third Space Processing Symposium. These papers cover the results of Materials Processing Experiments conducted on NASA's SKYLAB flights and several related research activities for Materials Processing in Space beyond SKYLAB.

Contents consist of the Welcoming Address by Dr. Rocco Petrone, Director, Marshall Space Flight Center; Introduction to Space Processing by Dr. Mathias P. Siebel, Director, Process Engineering Laboratory, Marshall Space Flight Center; thirty-eight papers; and the closing presentation titled Projected Future Space Processing Activities by Dr. James H. Bredt, Office of Applications, National Aeronautics and Space Administration.

The Keynote Address was presented by Mr. Charles W. Mathews, Office of Applications, National Aeronautics and Space Administration.

17. KEY WORDS	18. DISTRIBUTION STATEMENT
	Unclassified-unlimited W. K. Vandaman

19. SECURITY CLASSIF. (of this report)	20. SECURITY CLASSIF. (of this page)	21. NO. OF PAGES	22. PRICE
Unclassified	Unclassified	531	[redacted]

For sale by National Technical Information Service, Springfield, Virginia 22151

TABLE OF CONTENTS

TABLE OF CONTENTS (Continued)

TABLE OF CONTENTS (Continued)

TABLE OF CONTENTS (Continued)

WELCOMING ADDRESS
SPACE PROCESSING SYMPOSIUM

By

Dr. Rocco A. Petrone, Direcor
George C. Marshall Space Flight Center
Marshall Space Flight Center, Alabama 35812

Ladies and gentlemen I want to welcome you to the Marshall Space Flight Center. For the next two days we ask you to share our facilities and to accept our hospitality.

Today we want to reveal to you some of the unique experiences in materials science which were achieved through Skylab. Each of the principal investigators will discuss his technical findings and I know that is what you really came to hear.

However, this is not just a routine review of what was learned as a result of these very few experiments. The objective of the Symposium reaches beyond those experiments. Perhaps it might be better described as a look into the future.

As you know, there are many processes in materials science which are hampered here on Earth by the effects of gravity. Prior to the space program we did not have a really useful means to look in depth at the effects which we could expect through the removal of the gravity term in our equations. Even now these effects are not easy to analyze or to accept. Nor are they yet clearly understood.

Many postulations of the effects of zero gravity have been made. If only a few of the improvements foreseen can actually be achieved we can expect some dramatic and beneficial changes in materials science. There appears to be no new engineering technology needed to achieve these benefits. Manufacturing in space may become more than a catchword. We can readily foresee that it will become a field which industry will expand and exploit. It will become a routine profit-making venture. If the promise shown by Skylab experiments is an indicator, then the possibility of manufacturing more highly purified material for making more efficient semiconductors for use in the field of communications, and materials which will make better superconductors for the control and distribution of electrical energy, awaits only the availability of Shuttle and Spacelab. Of course we are looking into many other materials. We believe that biological materials can be purified to a much higher degree than is possible on Earth. Perhaps some particles can be separated and cultured on Earth for use by medical doctors for treating or preventing disease. We will study some of these separation processes on the Apollo/Soyuz mission. We are also interested in new glass compositions to meet the extremely complex

demands of the growing Laser technology. We need to learn how to process materials without containers and the resulting contamination from their walls. The list is almost endless. We have barely scratched the surface. The immediate need is to improve our knowledge of basic phenomena in a state of equilibrium and to prioritize the materials of interest.

We believe that we are opening for you today at Marshall a vista of new opportunities which will excite and challenge scientists and engineers far beyond this decade and the next. We are pioneering in an area which shows such high economic potential that I must admit to being very proud to be involved in these first steps.

I hope that your visit will be a profitable one and that you will enjoy the program which has been prepared for you.

INTRODUCTION TO SPACE PROCESSING

By

M.P.L. Siebel
Process Engineering Laboratory
Marshall Space Flight Center
Alabama 35812

In organizing this symposium we had two purposes in mind: one is to present to you experiment results: that is the results of Skylab and of other experiments; the other purpose which may be even more important is to show you opportunities for building on the existing basis of experience for the profitable exploitation of the space environment.

We held Space Processing Symposia in 1968 and 1969. We said then that space processing would yield scientifically useful knowledge and commercially useful products. We also invited broad participation in the program. By necessity, the papers presented contained mainly projections on the advantages of processing in space new or improved materials for use on earth. For processing materials the unique and most important aspect of space flight is that it provides an environment effectively free from the influence of gravity. We postulated that in the absence of gravity effects the theoretical properties of materials could be more nearly approached because thermal convection would not disturb the even progression of solidification in crystals and eutectics, because immiscible components or phases of differing densities would not separate, and because, by containerless processing, contamination of a molten material by the crucible would be prevented; we speculated on many other promising areas of endeavor, including the purification and separation of biologicals.

Since these early days of brain storming we have made progress. By progress I mean that we are in a position to continue accelerating our efforts from a now existing foundation of experimental knowledge and of world-wide participation.

At the time of our early symposia we could predict no specific space flight opportunities. But now we have assurance of flight opportunities because the Space Shuttle program has become a reality. The thrust to avail ourselves of the payload capability of the Shuttle lends urgency,

direction and purpose to our endeavors. The Shuttle will fly in five to six years and before then we have to develop the technologies and perform precursor tests so that we will be able to take every advantage of the Space Shuttle capabilities for commercial and scientific goals.

In my talk, I want to give you an overview of the activities during the past few years. Many details will be filled in by the papers to be given in this symposium. It will become apparent that the materials and apparatus technologies have grown step by step: indeed in most instances it is possible to trace the development of today's most advanced concepts to early experiments. I will conclude by describing the Skylab materials processing facility in which the Skylab experiments were performed. This description will lead into the subject for today -- Skylab Results.

Figure 1 shows the accelerating pace of space processing activities. You will note that the number of planned studies has been increasing year by year; this means that the program has broadened not only in technical content but also in participation by industry, universities and government. Five Scientific Advisory Groups in various disciplines have been established; further groups in other discipline areas will be established as necessary. The advisory groups have been and continue to be most helpful in defining the study efforts necessary to advance the scientific disciplines, and in the evaluation of the results.

The technical studies which were performed both by universities and industry have had various objectives -- first of all to provide a theoretical base for the understanding of the behavior of materials and the interaction of solids, liquids and gases with each other and with their environment when the effective gravity level is reduced by several orders of magnitude. Then other studies were to provide theoretical data on materials of industrial or scientific interest and finally the studies were to provide the design of ground based tests to validate certain assumptions or to verify study results. While laboratory one 'g' tests were sometimes helpful, in general low 'g' tests were required for this purpose.

LOW 'G' TEST CAPABILITIES

We have developed several methods of low 'g' testing. The most accessible tests are laboratory tests where under certain circumstances low 'g' times of the order of one second may be attained. The next most accessible facility is the drop tower (Figure 2). A free-fall time of about four seconds is attainable and otherwise this device has few limitations. A surprising amount of data can be obtained in this apparently short period.

The experimental KC-135 aircraft flying Keplerian trajectories provides 10 - 20 seconds of low 'g'. It was used to verify the functioning of two of the Skylab experiments: Metals Melting (M551) and Sphere Forming (M553). This however within the limitation of the prevailing 'g' levels which were fluctuating and of the order of 0.01 'g'. Because of these unacceptable fluctuations, this method of operation for low 'g' experimentation has been abandoned.

Another method of obtaining a low 'g' environment is to use the free coast phase of a sounding rocket flight; i.e., the time when the rocket is above the atmosphere and no propulsion is applied. Typically four to seven minutes of low 'g' time is attainable. A beginning has been made toward a test program using such rockets.

These ground based tests of course are quite limited in duration and are regarded as precursors to more elaborate space flight experiments.

In space flight we have flown demonstrations on Apollo 14, 16, and 17, and of course experiments on Skylab. On these flights, experiment times were long and the 'g' levels were generally very low, although as you will hear, attitude control thrusters, equipment operation, gravity gradient and crew movements sometimes have a noticeable influence.

Figure 3 shows a summary chart of tests performed. I will take a few examples in each category to illustrate the importance of this test effort.

MATERIALS

In the field of immiscibles, that is, compositions of materials having a miscibility gap in the liquid phase, the first demonstration of the existence of a stable dispersion in bulk samples was performed on Apollo 14 with Paraffin and Sodium Acetate (Figure 4); subsequent tests with a variety of metallic mixtures were performed on aircraft and in the drop tower. From these tests bulk samples with novel structures and properties were obtained. A single Ga-Bi sample (Figure 5) processed in the drop tower, for example, showed semi-conducting, conducting, and super-conducting properties. The results obtained led to the Skylab experiments which you will hear described later. In the case of immiscibles the progression from model materials to useful materials is well along; however, many new compositions and variations of processing parameters remain to be studied and tried. Over 500 materials compositions in this category have been identified many of which will need to be studied by processing in low 'g'.

For the growth of single crystals and eutectics relatively much longer processing times are needed. InBi cyrstals and eutectics were to be grown on Apollo 14 (Figure 6); however, crew time did not permit the performance of these particular experiments. Nonetheless, the experience gained from development and one 'g' ground testing contributed to the success of several Skylab crystal growth experiments.

The eleven materials samples that were processed on Apollo 14 included fiber and particle reinforced composites. These demonstrations indicated that homogeneous distributions of reinforcements can be attained and that wetting of the reinforcement by the matrix material is an important factor. Substantial differences in density between the matrix and the reinforcements had no effect on the distribution. This conclusion appears to be confirmed by one Skylab experiment, Whisker Reinforced Composites (M561).

PROCESS ELEMENTS

In order to produce materials the individual factors influencing the processes in the absence of gravity forces have to be understood. For this reason, experimental studies on heat flow and convection in a low gravity environment were performed on Apollo 14 and 17. It had been postulated that in such an environment, thermal convection currents would not occur; heat transfer would occur only by conduction, radiation, and by surface tension driven convection. Figure 7 shows the apparatus. In these Apollo demonstrations, a liquid having a free surface did in fact exhibit the predicted surface tension driven convection seen as Benard cells (Figure 8). On Apollo 14, the contained liquids and gases exhibited small though significant amounts of steady state as well as oscillating convection. On Apollo 17, these demonstrations with slight modifications were repeated. From studies of the data from both flights, it was concluded that the convection observed on Apollo 14 resulted from accelerations exceeding 10^{-4} 'g' caused by spacecraft or apparatus movement; on Apollo 17, because of appropriate precautions, accelerations were reduced to below 10^{-6} 'g' and similar effects were not observed. An important conclusion is that under low 'g' conditions in space thermal convection effects can be eliminated or controlled. The results of these preliminary tests appear to be confirmed by the Skylab experiments; particularly by the Radioactive Tracer Diffusion experiment (M558) and by several crystal growth experiments.

Another factor influencing the behavior of materials is wetting, for example wetting of the container by the contained material. One important discovery was made during the evaluation of a short duration rocket flight: on earth, contact is made between a fluid and its container by gravity; consequently,

heat can be readily extracted through the container whether the fluid wets the container or not. In the rocket flight we discovered the cooling and solidification of a molten InBi alloy contained in an aluminum cartridge did not proceed as fast as predicted from ground tests and some material remained molten on re-entry. In the Apollo 14 InBi samples unusual solidification patterns were observed. Both effects were attributed to the fact that the melt did not wet the cartridge wall and only touched it at random spots. The melt, in effect, floated free within the cartridge.

The influence of contact with the container wall on the solidification characteristics of the molten material still has many unknowns particularly during processes as sensitive as the growth of crystals.

Another wetting effect was observed where a mixture of molten materials present: preferential wetting of the wall by one material was a mechanism for segregation (Figure 4).

PROCESSING SYSTEMS

Various systems have been developed for processing materials in low 'g'. I want first to mention electrophoretic separation devices.

Electrophoresis in a free solution was first demonstrated on Apollo 14. While problems to do with apparatus design and sample materials were encountered, the results in a cell containing two different dyes indicated that the effort was worth pursuing. For Apollo 16, the mechanical equipment problems were solved and different model materials for separation were chosen. The apparatus is shown in Figure 9. During performance of the demonstration, back flow along the walls occurred owing to electro-osmosis. This distorted the separation fronts (Figure 10). However, the space demonstration showed that the deleterious effects due to gravity induced sedimentation and thermal convection were eliminated in low 'g'. The next experiments in this field are planned for the Apollo Soyuz mission (ASTP).

Systems for the containerless positioning of materials may be based for example on acoustic or on electromagnetic principles. For laboratory tests on glasses levitation in an airstream and location of the specimen on a sting have been used.

The value of drop tower tests was shown again during the development of an electromagnetic positioning system. Initial tests were performed on the ground: a test mass was suspended within the working volume of the system

SKYLAB EXPERIMENT FACILITY AND MODULES

Finally, I want to describe the M512 processing facility in which all Skylab space processing experiments were performed. It was mounted in the Multiple Docking Adapter of the Skylab (Figure 15). The facility itself is shown in the next slide (Figure 16).

The M512 facility provided the capability of performing the experiments by the use of individual experiment modules.

The facility was mounted on a honeycomb panel which in turn was attached to the MDA structure by shock mounts. The panel also served as a radiator of heat.

The facility was made up of the following main parts:

- Work chamber
- Control panel
- Electron beam gun and batteries
- Storage boxes for experiment modules and ancillary equipment

The work chamber incorporated a mount to accommodate each experiment module in turn; the mount doubled as a heat sink with a predetermined and calibrated thermal impedance. Near the mount and inside the chamber was located an electrical connector through which power and signals were provided to all the experiment modules except the Multipurpose Furnace, which was a late addition and used only the heat sink/mount and the vacuum capability of the chamber.

The work chamber could be vented to space and thus provide an evacuated environment for the experiments when desired. Windows and illumination within the work chamber permitted viewing of the experiments in progress and also photography by a fixed camera. Gages on the control panel (Figure 17) served to monitor the pressure in the chamber, certain temperatures and the beam current and voltage of the electron beam gun. In addition, switches and potentiometers served to operate and control the individual experiments.

The Metals Melting (M551) and Sphere Forming (M553) experiments used the electron beam gun to melt the specimens. It was a most compact gun for its 2 KW output (100mA at 20,000 V). The power supply package was contained in a canister pressurized with an insulating gas: perfluoropropane (C_3F_8). The filament and focusing devices were exposed to the vacuum of the work chamber.

The gun was powered by batteries and thus was independent of the spacecraft power bus. Incidentally, the M552 Exothermic Heating experiment also derived its igniter power from these same batteries. All other experiments operated on spacecraft power.

Most of the experiment modules and their accessories were stored in the storage container (Figure 18). To perform an experiment the appropriate module with its accessories was mounted in the chamber.

For the performance of the Metals Melting (M551) experiment the discs (Figure 19) were driven by a motor. The electron beam was focused on a tungsten target incorporated in each disc; the disc was then rotated at constant speed to make a weld bead and finally was stopped to melt a puddle. Three discs of different materials were provided for this experiment. They were processed successively.

The sphere forming specimens (M553) were carried on two wheels which were successively mounted on an indexing motor, each wheel carried a tungsten focusing target and 14 specimens. After each specimen was melted by the electron beam, a new specimen was indexed into position.

The Exothermic Brazing experiment container (M552) (Figure 20) held four exotherm packages. After the chamber was evacuated the exotherm packages were fired one at a time at about two hour intervals. The long intervals were necessary to allow for cooling between operations.

A set of experiments on Flammability (M479) was also performed in the chamber. To perform these experiments, an adapter was mounted in the chamber on the experiment connector; each specimen in turn was mounted in the adapter and ignited. The specimens could be burnt freely, or the combustion could be quenched by evacuating the chamber. Another quench system, by water spray, was also provided.

The Multipurpose Furnace System (M518) (Figure 21) consisted of the furnace, a control package and interconnecting cabling.

To perform the eleven experiments (M556 through M566), the furnace was installed in the work chamber, the control package was mounted on its special adapter and interconnections were made from the controls to the furnace, to the Skylab power receptacle and to the Skylab telemetry system. After the insertion of each set of three cartridges for an experiment, the work chamber was evacuated and the experiment was initiated after setting the appropriate peak temperature, soak time and cool-down rate. Lights indicated

what particular period of the total cycle had been reached. Thermocouples at the "hot" and "cold" ends of the cartridges provided outputs which were telemetered to the ground for real time evaluation of the progress of the experiments.

CONCLUSION

In this talk I have shown with a few examples that the space processing program is structured to allow progress from studies through ground based low 'g' tests to space flight experiments. This progression should and will go further. It is in this sense that our symposium is intended not as a monument to past achievements but as a stepping stone to future applications and benefits.

BIBLIOGRAPHY

GENERAL

Wuenscher, H. F., Low and Zero-g Manufacturing in Orbit, AIAA Paper 67-842, October 1967

Wheaton,E. P., Space Commerce. In Sci. and Technol. Ser., Vol. 10, Space Age in Fiscal Year 2001. Am. Astronaut. Soc., 1967, pp. 340-358.

Stanton, A. N., Commercial Development of the Resources of Space. In Advances in the Astronaut. Sci. Ser., Vol. 21 - Practical Space Applications. Am. Astronaut. Soc., 1967, pp. 361-374.

Mettler, R. F., Space Manufacturing. In Advances in the Astronaut. Sci. Ser., Vol. 23 - Commercial Utilization of Space. Am. Astronaut. Soc., 1968, pp. 295-306.

Manufacturing Technology Unique to Zero Gravity Environment, Presentations at Marshall Space Flight Center, November 1968.

Proceedings of Winter Study on Uses of Manned Space Flight, 1975-1985. National Aeronautics & Space Administration, NASA SP-196 Vol. II App. 1969.

Wuenscher, H. F., Space Manufacturing Unique to Zero Gravity Environment, Marshall Space Flight Center, NASA Technical Memorandum 53851, July 11, 1969.

Bannister, T. C., The Space Sciences Laboratory Ground-Based Research Program for Manufacturing in Space, Marshall Space Flight Center, Report MISC-SSL-69-2, July 29, 1969.

STARLAB, An Orbiting Space Technology and Applications Laboratory, Auburn, NASA CR-61296, August 1969.

Space Processing and Manufacturing Symposium, Presentations at Marshall Space Flight Center, October 1969.

Unique Manufacturing Processes in Space Environment, Papers Presented at Seventh Space Congress, April 23, 1970. ME-70-1

Boyton, Richard D., Duckworth, W. J., et al, Manufacturing in Outer Space, Carnegie-Mellon University, Contract NASA-25202, Senior Project Presentations, May 8, 1970.

Steurer, W. H., and Gorham, D. J., Processes for Space Manufacturing - Definition of Criteria for Process Feasibility and Effectiveness, General Dynamics/Convair, Contract NAS8-24979, Final Report, June 1970.

Wuenscher, H. F., Manufacturing in Space, New Scientist, Sept. 10, 1970.

Reference Earth Orbital Research and Applications Investigations (Blue Book), General Dynamics/Convair and TRW contracts, January 15, 1971.

Wuenscher, H. F., Materials Processing in Zero Gravity - An Overview, Report No. PE 72-1, Marshall Space Flight Center.

Ulrich, D. R., et al, Economic Analysis of Crystal Growth in Space, General Electric Company, Contract NAS8-27942, Final Report, July 1972.

Sinskey, A. J., Growth of Micro-organisms in Space, August 1972.

Wuenscher, H. F., Manufacturing in Space, Astronautics & Aeronautics, Sept. 1972.

Wuenscher, H. F., Materials Processing in Zero Gravity, Proceedings of XXIIIrd International Astronautical Congress 8-15 October 1972, Vienna, Austria.

Bloom, H. L., Identification of Beneficial Uses of Space, General Electric Contract NAS8-28179, Final Report, December 1972.

Bredt, J. H., The NASA Space Processing Program, AIAA 12th Aerospace Sciences Meeting, (74-152), February 1974.

Hammel, R. L., and Taylor, K. R., Space Processing Payloads for Space Shuttle Era, AIAA 12th Aerospace Sciences Meeting (74-153), February 1974.

MATERIALS

Wechsler, A., et al, Sphere Forming and Composite Casting in Zero-g, Arthur D. Little, Inc., Contract NAS8-21402, Final Report, January 7, 1970.

McCreight, L. R., et al, Investigation of the Preparation of Materials in Space, General Electric Company, Contract NAS8-24683, Final Report, March 1970.

Fabiniak, T. J., Investigation of Zero Gravity Effects on Material Properties, Cornell Aeronautical Laboratory, Inc., Contract NAS8-24952, Final Report, April 1970.

BIBLIOGRAPHY (continued)

Rubenstein, R. M., Zero Gravity Crystal Growth, Westinghouse, Contract NAS8-24509, Final Report, April 29, 1970.

Seidensticker, R. G., A Preliminary Analysis of the Solution Growth of GaAs in Zero-g, Westinghouse, Research Report 70-9J8-OGXTL-Rl, May 4, 1970

Jain, V. K., Utilization of Space Environments for Preparing Highly Perfect Crystals, NASA TMX-64564, December 1970.

Research Study on Composite Castings, Arthur D. Little, Inc., Contract NAS8-25709, Final Report, May 1971

Steurer, W. H., and S. Kaye, Preparation and Evaluation of Apollo 14 Composite Experiments, General Dynamics/Convair, Contract NAS8-24979, Report GDCA-DBG71-009, August 1971. NASA CR-61368

Wechsler, A., Berkowitz, J., et al, Apollo 14 Composite Casting Demonstration, Arthur D. Little, Inc., Contract NAS8-26687, Final Report, August 20, 1971. NASA CR-61369.

Jain, V. K., and J. C. Horton, Evaluation of Structural Defects in Crystals - A Prerequisite to Crystal Growth in Space, Marshall Space Flight Center, Astronautics Laboratory, Technical Note, September 1971.

Fabiniak, T. J. and Fabiniak, R. C., Test and Evaluation of Apollo 14 Composite Casting Demonstration Specimens, Cornell Aeronautical Laboratory, September 1971, NASA CR-61366.

Reger, J. L., Test and Evaluation of Apollo 14 Composite Casting Demonstration Specimens 6, 9 and 12, TRW Systems Group, Contract NAS8-27085, Final Report, Phase I, September 1971. NASA CR-61367.

Yates, I. C., Apollo 14 Composite Casting Demonstration, Marshall Space Flight Center, Final Report, NASA TMX 64641, October 1971.

Reger, J. L., Apollo Experiment Definition Study, TRW Systems Group, Contract NAS8-27085, Final Report, Phase II, November 1971

Characterization of Thermal Convection and Crystal Perfection in Metals Grown from the Melt, National Bureau of Standards, Contract H-84832A, Annual Report, June 1972.

Happe, R., Production of Unique New Glasses, North American-Rockwell, Contract NAS8-28014, Final Report, June 1972.

Davis, J., Walter, H., et al, Investigation of Crystal Growth in Zero-g and Investigation of Metallic Whiskers, University of Alabama in Huntsville, Contracts NAS8-24612 and 26793, Final Report, December 1972.

Li, C. H., Investigation of KC-135 Flight Samples, Grumman Aerospace Corp., Contract NAS8-28728, Interim Report, January 1973.

Walter, H., Investigation of Crystal Growth from Solution, University of Alabama in Huntsville, Contract NAS8-28098, Technical Summary Report, January 1973.

Doty, J. P. & Reising, J. A., Study of Single Crystals of Metal Solid Solution, Eagle-Picher Industries, Contract NAS8-29077, Final Report, May 1973.

Ulrich, D. R., et al, Crystal Growth in Fused Solvent Systems, General Electric Company, Contract NAS8-28114, Final Report, June 1973.

Happe, R. A., and Topol, L. E., Experiments Leading to Production of New Glasses in Space, AIAA 12th Aerospace Sciences Meeting (74-159) February 1974.

Reger, J. L., and Yates, I. C., Preparation and Metallurgical Properties of Low-Gravity Processed Immiscible Materials, AIAA 12th Aerospace Sciences Meeting (74-207), February 1974.

Lacy, L. L., and Otto, G. H., The Electrical Properties of Zero-Gravity Processed Immiscibles, AIAA 12th Aerospace Sciences Meeting (74-208) February 1974.

PROCESS FUNDAMENTALS

Zero-g Solidification, Lockheed Missiles & Space Co., Contract NAS8-21123 Final Report, March 1970.

Bauer, Helmut F., Theoretical Investigation of Gas Management in Zero Gravity Space Manufacturing, Georgia Institute of Technology, Contract NAS8-25179, Final Report, 30 October 1970.

Bannister, T. C., Heat Flow and Convection Demonstration (Apollo 14); Part I: The Data; Part II: Analysis and Results, Marshall Space Flight Center, SSL, Summary Report, July 14, 1971.

Benefield, John W., Heat Flow and Convection Demonstration, Lockheed Missiles and Space Company, Contract NAS8-25577, Final Report, August 1971.

Grodzka, P. G., Fan, C., and R. O. Hedden, The Apollo 14 Heat Flow and Convection Demonstration Experiments, Final Results of Data Analyses, Lockheed Missiles and Space Company, Contract NAS8-25577, September 1971.

Fan, C., Convection Phenomena in Electrophoresis Separation, Lockheed Missiles & Space Company, Contract NAS8-27015, December 1972.

Grodzka, P. G., and Bourgeois, S. V., Fluid & Particle Dynamic Effects in Low-g Composite Casting, Lockheed, Contract NAS8-27015, Summary Report, January 1973.

Miller, R. I., Analysis of Field Effects on Dense Liquid Materials, Boeing Company, Contract NAS8-28664, Final Report, May 1973.

Li, C., et al, Research of Metal Solidification in Zero-g, Grumman, Contract NAS8-28604, Final Report, May 1973.

Li, C., et al, Segregation Effects during Solidification in Weightless Melts, Grumman, Contract NAS8-27891, Final Report, June 1973.

Spradley, L. W., et al, Numerical Solution for Thermoacoustic Convection of Fluids in Low-g, Lockheed, Contract NAS8-27015, Summary Report, June 1973.

Bannister, T. C., et al, Final Results, Apollo 17 Heat Flow and Convection Experiment, NASA TMX-64772, July 1973.

Bhat, B. N., Thermotransport in Liquid Aluminum-Copper Alloys, NASA Technical Report NASA TR R-415, September 1973.

Bhat, B. N., Solute Diffusion in Liquid Metals, NASA Technical Report TR R-417, October 1973.

Grodzka, P. G., and Bannister, T. C., Natural Convection in Low-g Environments, AIAA 12th Aerospace Sciences Meeting (74-156), February 1974.

Carruthers, J. R., Studies of Liquid Drops in Simulated Zero Gravity, AIAA 12th Aerospace Sciences Meeting (74-158), February 1974.

Kuriyama, M., et al, Fluid Flow Effects on Crystalline Perfection, AIAA 12th Aerospace Sciences Meeting (74-204), February 1974.

Bourgeois, S. V., and Brashears, M. R., Fluid Dynamics and Kinematics of Molten Metals in the Low-Gravity Environment of Skylab II, AIAA 12th Aerospace Sciences Meeting (74-205), February 1974.

Larson, D., et al, Melting and Solidification of Metals in Zero-Gravity, AIAA 12th Aerospace Sciences Meeting (74-206), February 1974.

Dragoo, A. L., and Paule, R. C., Production of Ultrapure Materials: Containerless Evaporation and the Roles of Diffusion and Marangoni Convection, AIAA 12th Aerospace Sciences Meeting (74-209), February 1974.

PROCESSING SYSTEMS

Pfann, W. G., Zone Melting, First ed., John Wiley & Sons, 1958, p. 93.

Kober, C. L., and Goel, V.S., Zero-g Space Experiments, Isotope Separation, Martin Marietta Corporation, Research Report R-69-13, June 30, 1969.

Sparks, V. W., Preliminary Design of a High Temperature Space Manufacturing Furnace, Locheed Missiles & Space Company, Contract NAS8-21347, January 1970.

Frost, R. T., et al, Field Management for Positioning and Processing of Free Suspended Liquid Materials, General Electric Company, Contract NAS8-24683, Modification No. 2, Task IV, Final Report, May 15, 1970.

Preliminary Design, with Design Parameters of a Microminiaturized Microbiology Laboratory, Fairchild Hiller, Republic Aviation Division, Contract NAS8-26552, Final Report Vol. I & II, January 1971.

Seidensticker, R. G., Duncan, C. S., et al, Optimization of a Solution Growth Experiment for Zero Gravity and Development of Apparatus for a Melt Growth Experiment, Westinghouse, Contract NAS8-26122, Final Report, February 1971.

Frost, R. T., et al, Free Suspension Processing Systems for Space Manufacturing, General Electric, Contract NAS8-26157, June 1971.

Seidensticker, R. G., et al, Single Crystal Growth Flight Rated Experiment Packages, Westinghouse, Contract NAS8-26158, Final Report, August 1971.

McKannan, E. C., et al, Electrophoresis Separation in Space - Apollo 14, Marshall Space Flight Center, NASA TMX-64611, August 29, 1971

Reger, J. L., Study on Processing Immiscible Materials in Zero Gravity, TRW Systems Group, Technical Volume 14725.000, 9 February 1972.

Yates, I. C., and Yost, V. H., Research Rocket Tests RR 1 & 2, NASA TMX-64665, April 1972.

Griffin, R. N. and McCreight, L. R., Convectionless Electrophoretic Separation of Biological Preparations, General Electric Company, NAS8-27797, Final Report, June 1972.

Biogrowth Processing, Battelle, Contract NAS8-28085, Final Report, October 1972.

Snyder, R. S., Electrophoresis Separation in Space - Apollo 16, NASA TMX-64724, November 1972.

Reger, J. L., Experimental Development of Processes to Produce Homogenized Alloys of Immiscible Metals, TRW, Contract NAS8-27805, Final Report Phase III, December 1972.

Frost, R. T. et al, Electromagnetic Free Suspension System for Space Manufacturing, General Electric Company, Contract NAS8-27228, Final Report, December 1972.

Steurer, W. H., and S. Kaye, Preparation of Composite Materials in Space, General Dynamics Convair, Contract NAS8-27806, Final Report, January 1973.

Eiss, A., et al, High Temperature Radiation Furnace, Weiner Associates, Contract NAS8-28050, Final Report, April 1973.

Reger, J. L., Processing Immiscible Materials in Zero Gravity, TRW, Contract NAS8-28267, Interim (Annual) Report, May 1973.

Steurer, W. H. et al, Space Processes for Extended Zero-g Testing, General Dynamics Convair, Contract NAS8-28615, Final Report, NAS8-28615, June 1973.

Whymark, R., Acoustic Processing Methods for Space Processing, Interand Corp., NAS8-29030, Final Report, June 1973.

Halbach, C. R. and Page, R. J., 2200°C. Oxidizing Atmosphere Furnace for Space Manufacturing, AIAA 12th Aerospace Sciences Meeting (74-154), February 1974.

Wang, T. C., et al, Acoustic Chamber for Weightless Positioning, AIAA 12th Aerospace Sciences Meeting (74-155), February 1974.

Krupnick, A. C., Development of Coatings to Control Electro-osmosis in Zero Gravity Electrophoresis, AIAA 12th Aerospace Sciences Meeting (74-157), February 1974.

Krupnick, A. C., Development of Coatings to Control Electro-osmosis in Zero Gravity Electrophoresis, NASA TMX-64807, February 1974.

Bier, M. and Snyder, R. S., Electrophoresis in Space at Zero Gravity, AIAA 12th Aerospace Sciences Meeting (74-210), February 1974.

Van Oss, C. J., et al, Preparative Liquid Column Electrophoresis of T and B Lymphocytes at Gravity = 1, AIAA 12th Aerospace Sciences Meeting (74-211), February 1974.

FISCAL YEAR	1969	1970	1971	1972	1973	1974
STUDIES PLANNED	9	12	20	25	47	68
LOW 'G' TESTS						
DROP TOWER	-	1	9	64	70	144
RESEARCH AIRCRAFT			3	2	10	
ROCKET FLIGHTS			▲	▲		▲
APOLLO			▲ 14	▲ 16	▲ 17	
SKYLAB						▬

FIGURE 1. SPACE PROCESSING ACTIVITIES

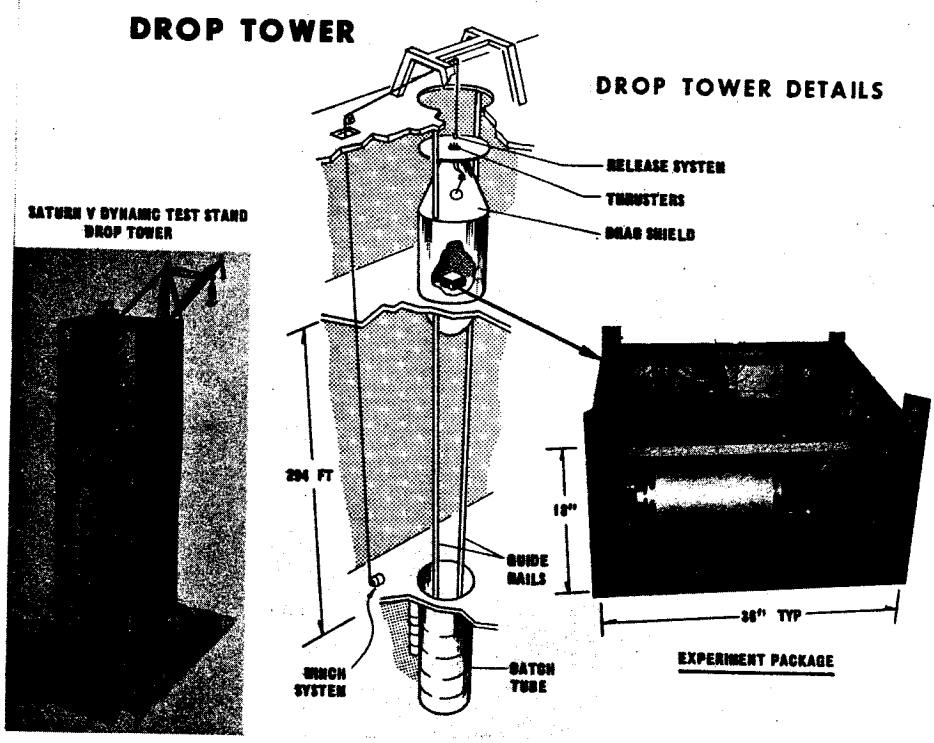

FIGURE 2. LOW "G" DROP TOWER FACILITY

MATERIAL	LABORATORY ONE 'G'	LABORATORY LOW 'G'	DROP TOWER	AIRCRAFT	APOLLO 14	APOLLO 16	APOLLO 17	ROCKET	SKYLAB	ASTP
CRYSTALS	▲				●				▲	■
IMMISCIBLES	▲		▲	▲	▲				▲	■
COMPOSITES	▲				▲			▲	▲	
EUTECTICS	▲				●				▲	
GLASSES	▲	▲								
BIOLOGICALS	▲				▲					■
PROCESS ELEMENTS										
HEAT FLOW/CONNECTION	▲				▲		▲			■
DIFFUSION	▲								▲	
WETTING	▲		▲	▲	▲			▲	▲	
PROCESSING SYSTEMS										
HEATING/COOLING	▲		▲	▲	▲			▲	▲	■
CONTAINERLESS POSITIONING	▲		▲	▲	●				▲	
HOMOGENIZATION/DISPERSION	▲			▲	▲				▲	
SEPARATION/PURFICATION	▲				▲	▲				■

▲ TESTS PERFORMED
● TESTS FLOWN BUT NOT PERFORMED
■ ASTP PLANNED

FIGURE 3. SPACE PROCESSING - TESTS AND EXPERIMENTS

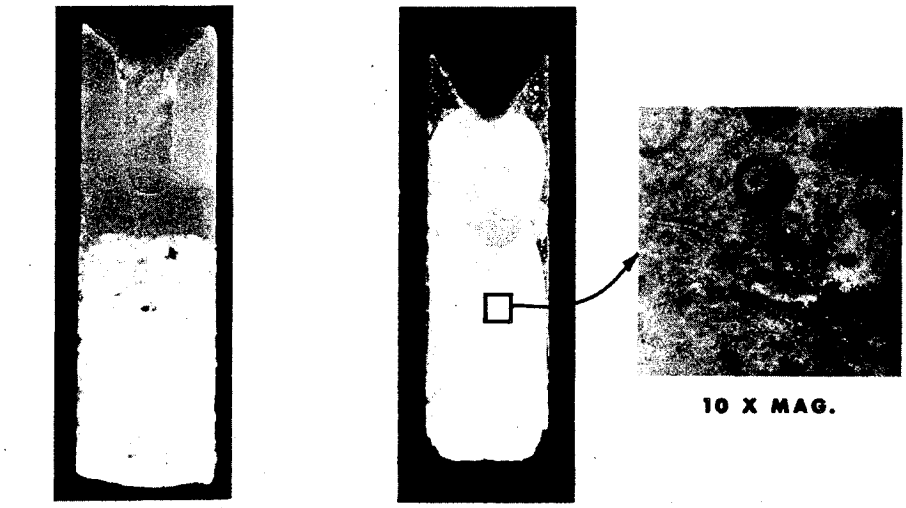

FIGURE 4. APOLLO 14 - IMMISCIBLE MATERIALS PROCESSING, SODIUM ACETATE - PARAFFIN

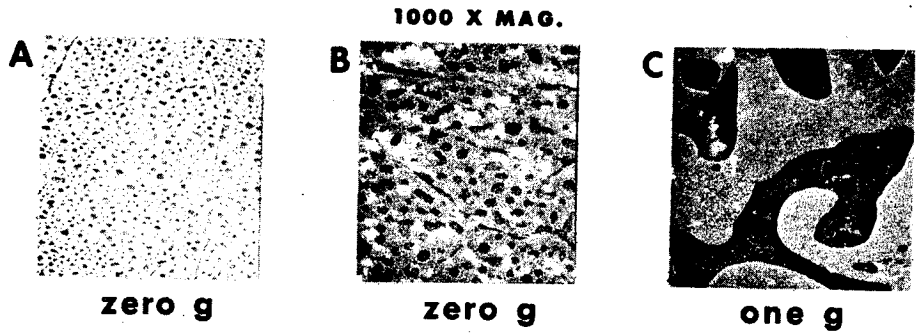

TYPICAL SAMPLES OF IMMISCIBLES Ga-Bi

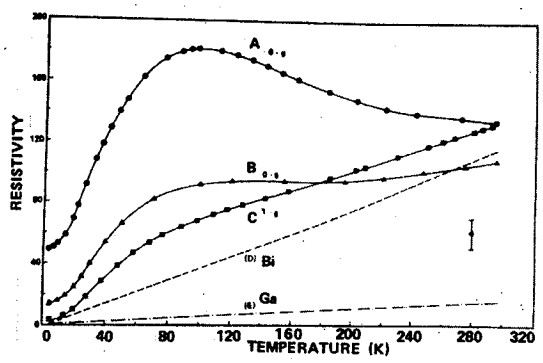

ELECTRICAL RESISTIVITY OF SAMPLES

FIGURE 5. TYPICAL RESULTS OF IMMESCIBLES Ga-Bi PROCESSED IN THE DROP TOWER

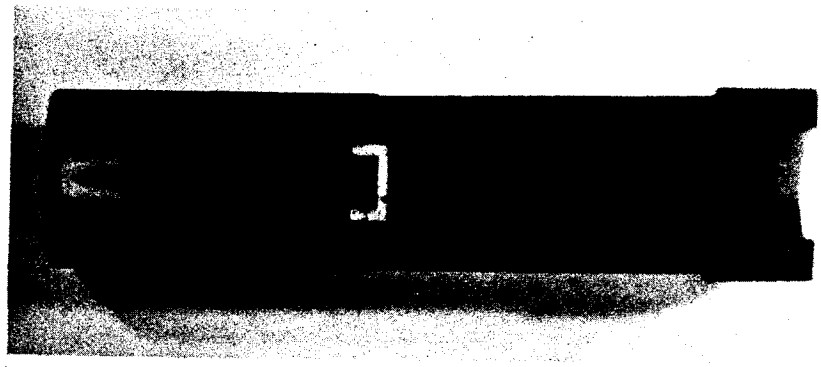

FIGURE 6. BRIDGEMAN CRYSTAL CARTRIDGE

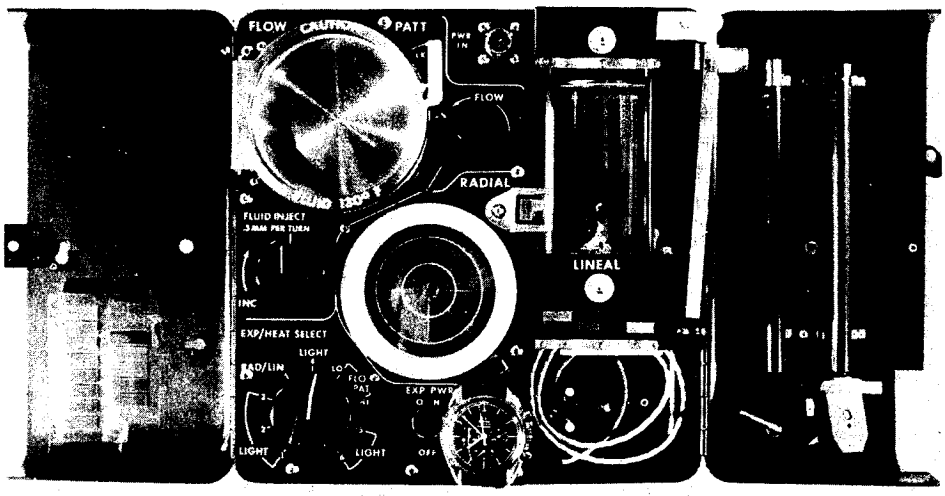

FIGURE 7. APOLLO 17 HEAT FLOW AND CONVECTION DEMONSTRATION (RECORDING CAMERA OMITTED)

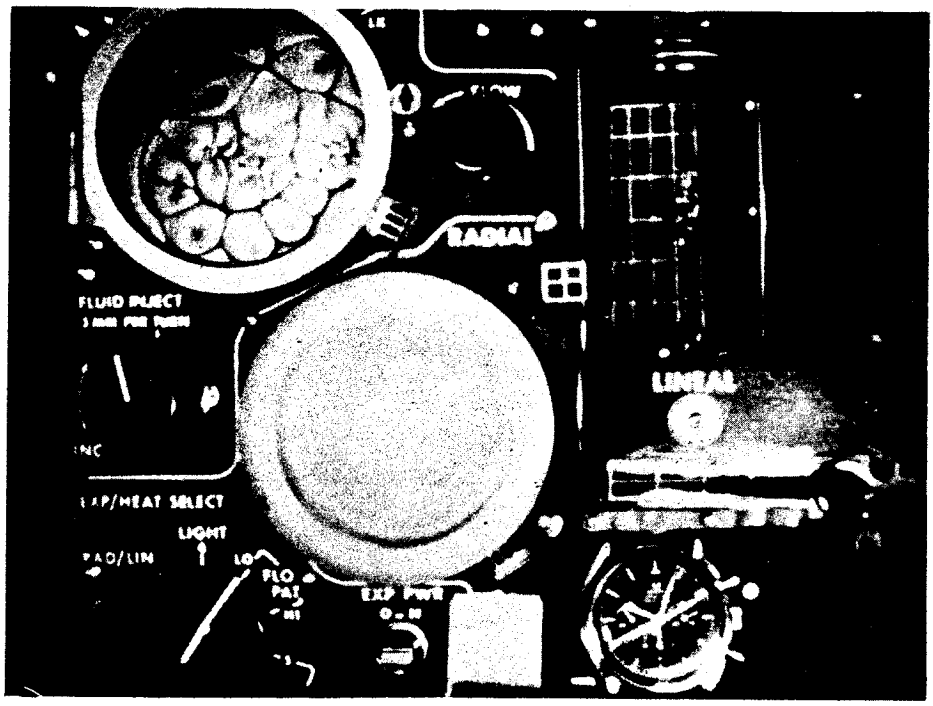

FIGURE 8. APOLLO 17 HEAT FLOW AND CONVECTION DEMONSTRATION: SURFACE TENSION DRIVEN CONVECTION IN LOW-G (BENARD CELL)

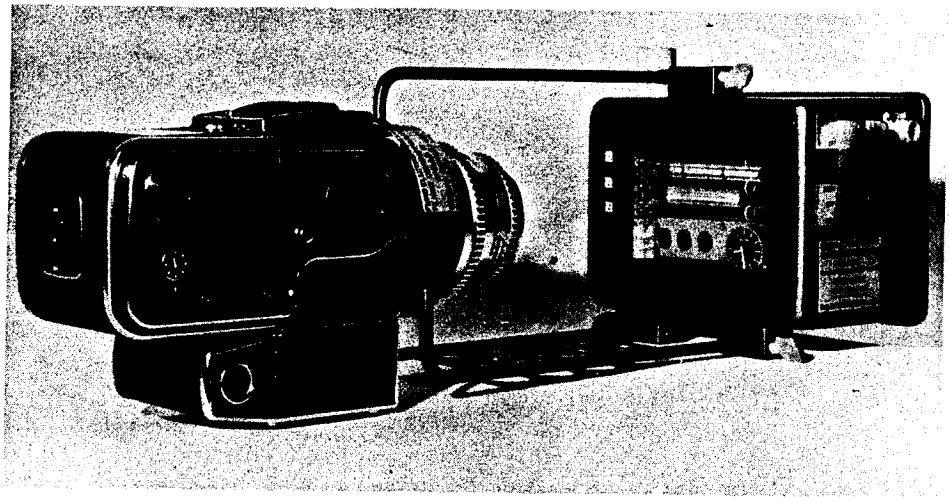

FIGURE 9. APOLLO 16 ELECTROPHORESIS DEMONSTRATION

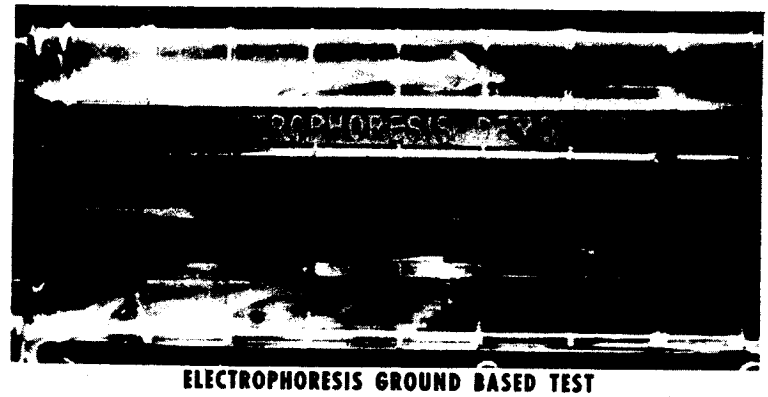

ELECTROPHORESIS GROUND BASED TEST

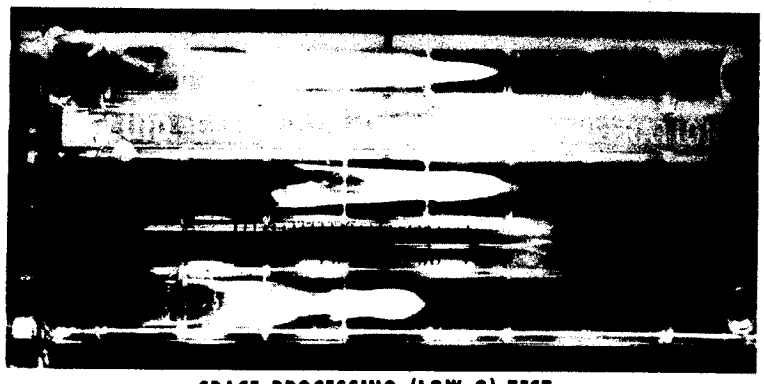

SPACE PROCESSING (LOW G) TEST

FIGURE 10. COMPARISON OF RESULTS OF GROUND BASED AND APOLLO 16 ELECTROPHORESIS DEMONSTRATION

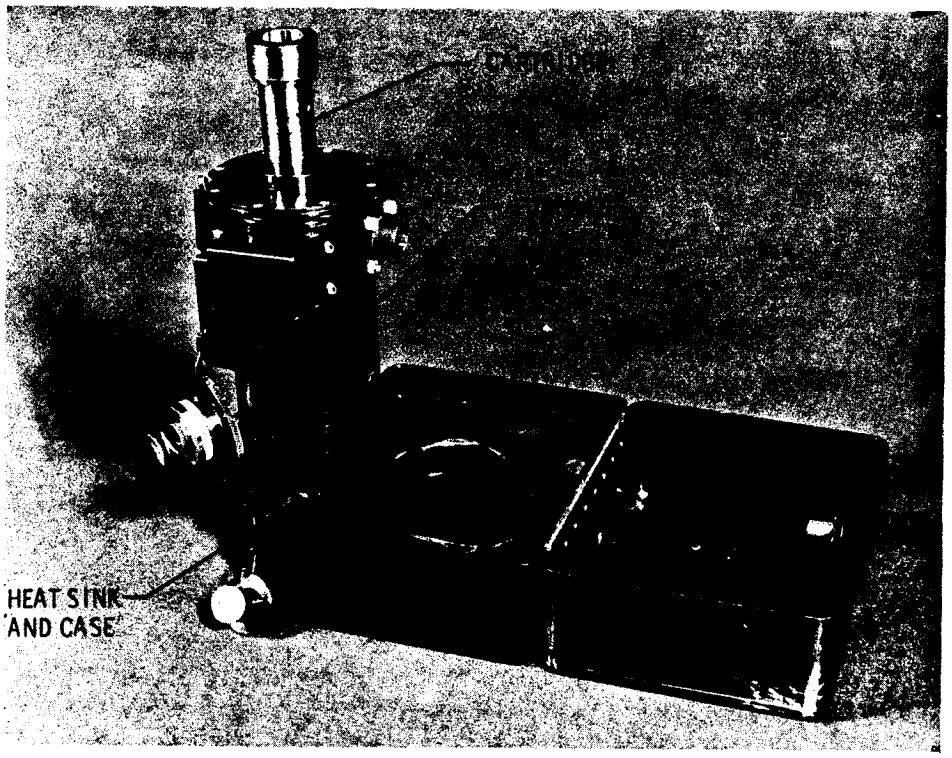

FIGURE 11. APOLLO 14 FURNACE FOR CASTING DEMONSTRATION

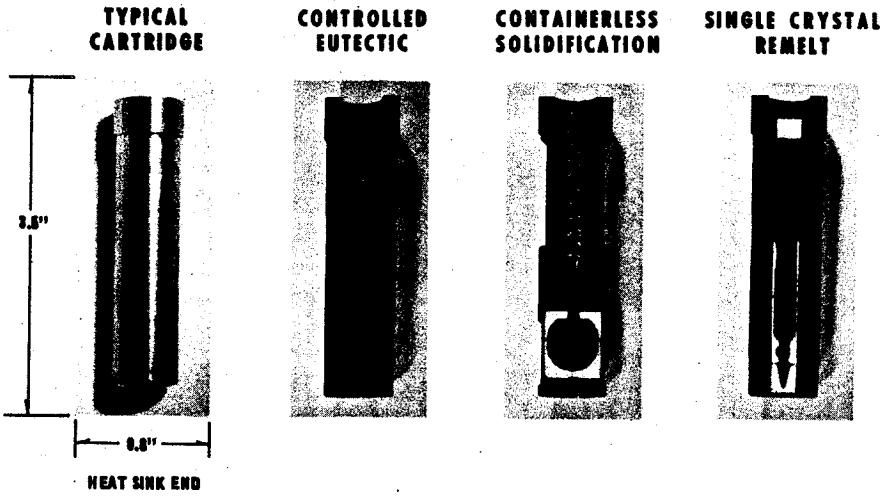

FIGURE 12. APOLLO 14 CARTRIDGES FOR CASTING DEMONSTRATION (INDIUM BISMUTH)

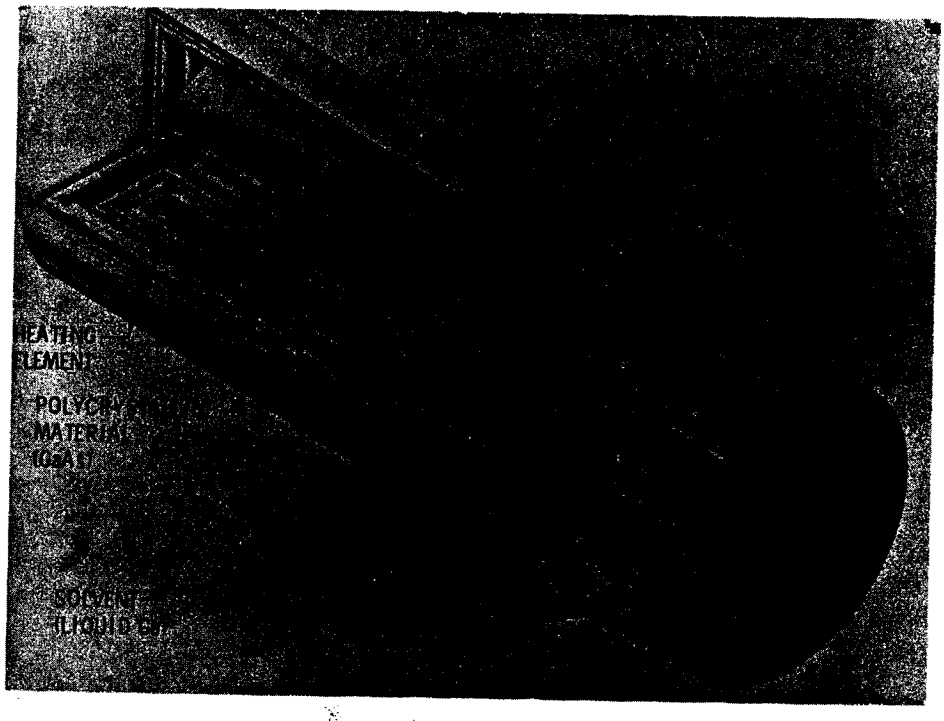

FIGURE 13. M555 - SINGLE CRYSTAL GROWTH EXPERIMENT

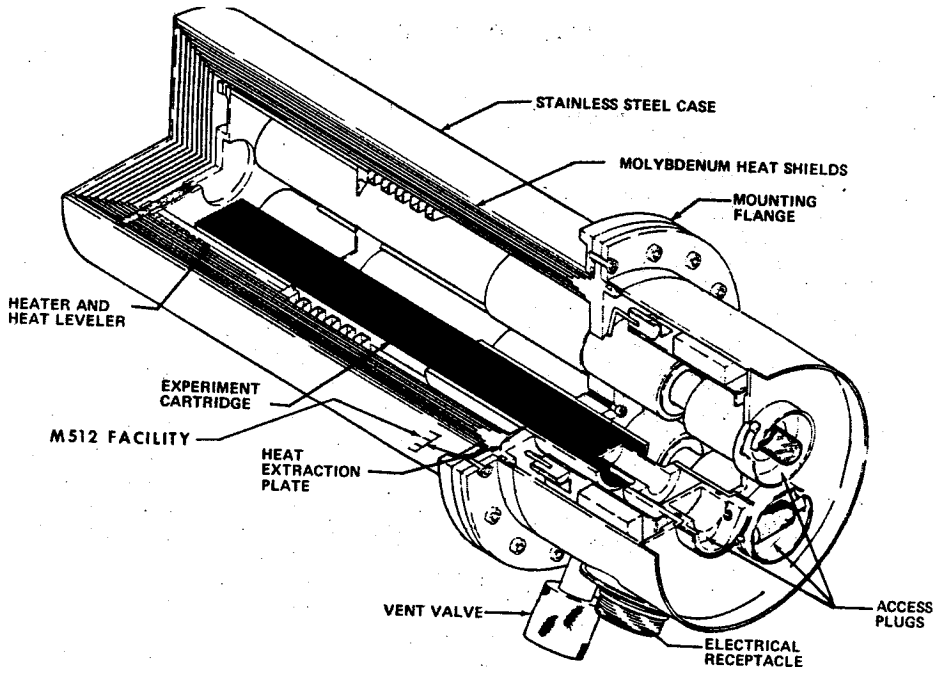

FIGURE 14. M518 - MULTIPURPOSE ELECTRIC FURNACE

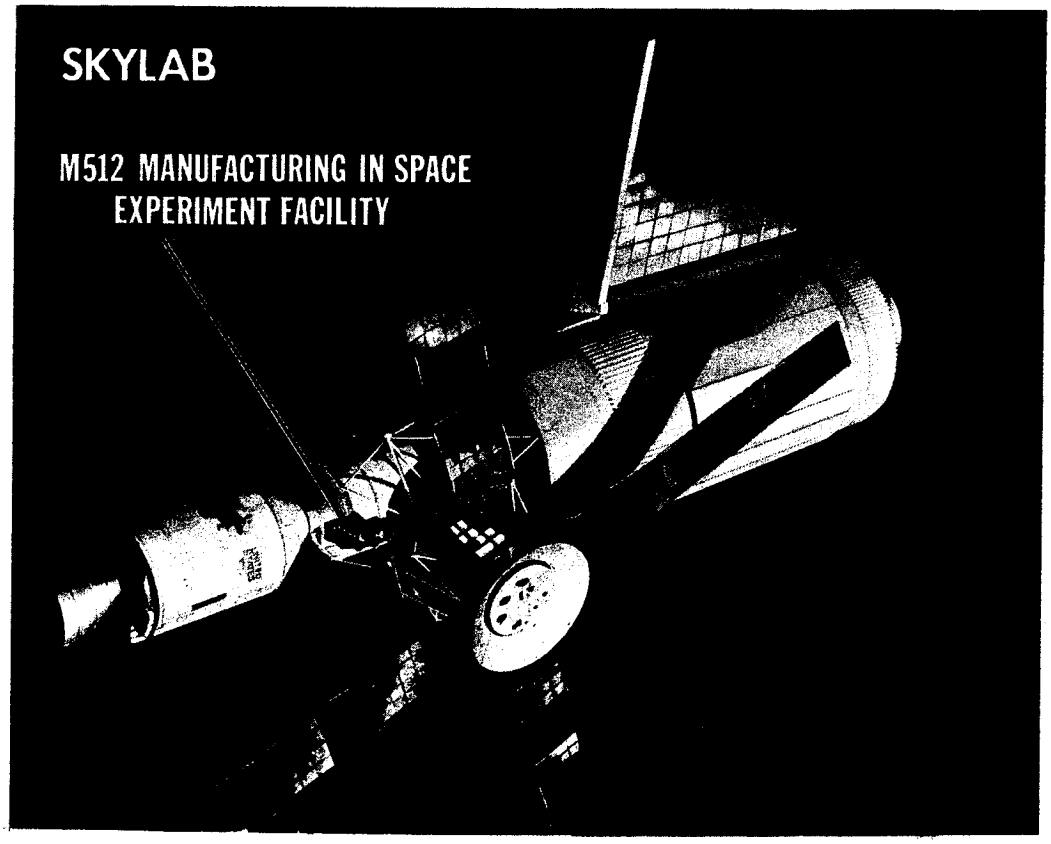

FIGURE 15. LOCATION OF M512 EXPERIMENT ON SKYLAB

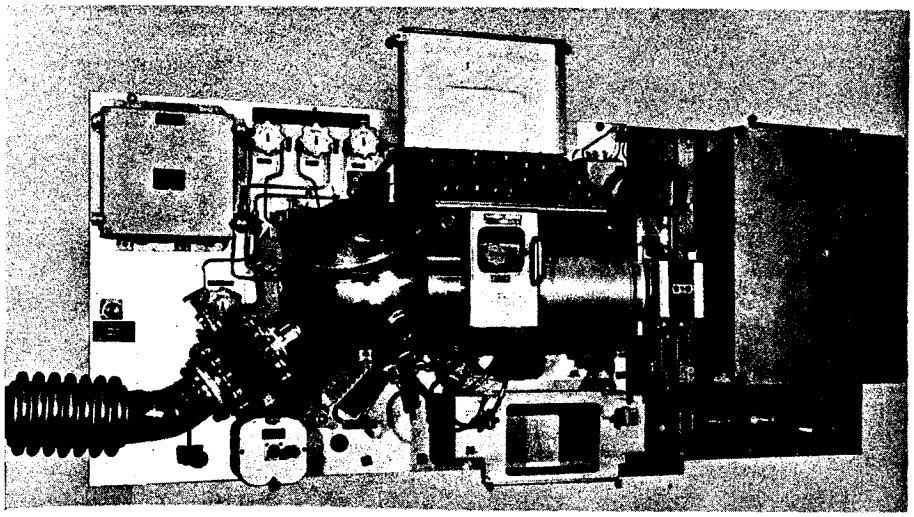

FIGURE 16. SKYLAB M512 MATERIALS PROCESSING IN SPACE EXPERIMENT FACILITY

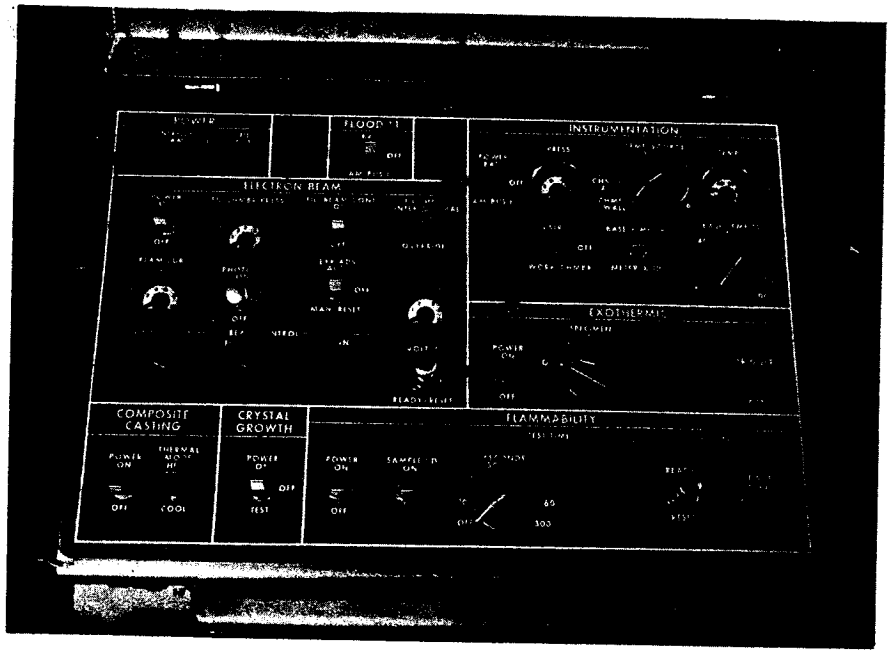

FIGURE 17. M512 EXPERIMENT CONTROL PANEL

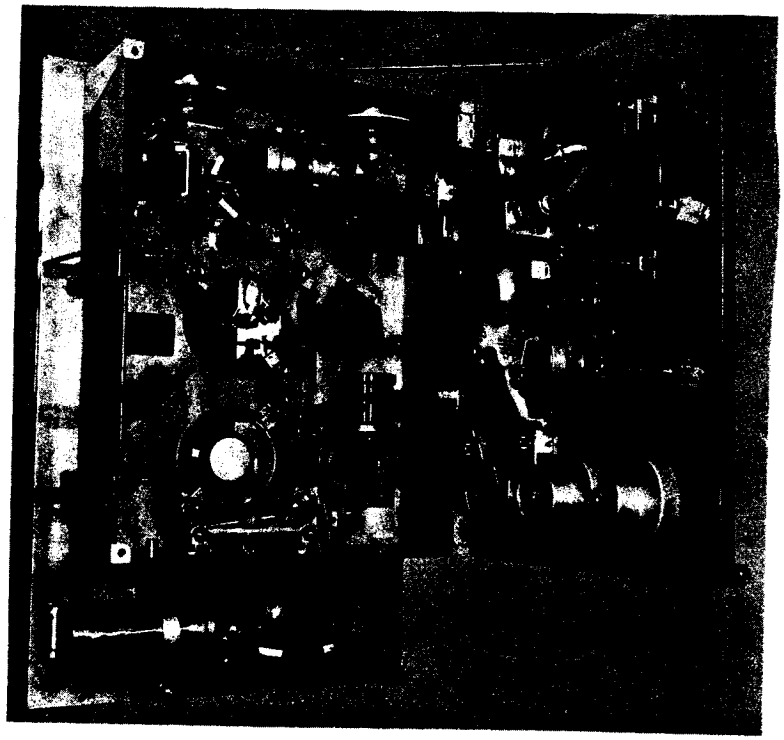

FIGURE 18. M512 EXPERIMENT ACCESSORIES STOWAGE CONTAINER

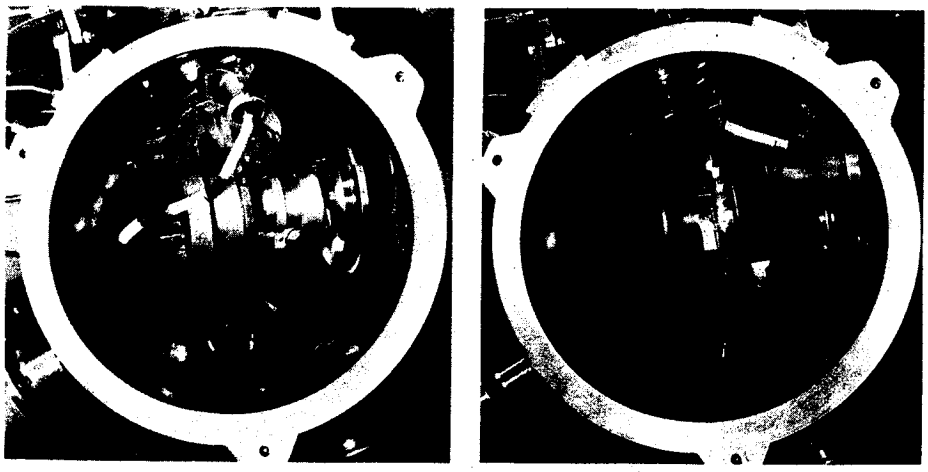

M551 METALS MELTING EXPERIMENT

M553 SPHERE FORMING EXPERIMENT

FIGURE 19. M551 METALS MELTING EXPERIMENT AND M553 SPHERE FORMING EXPERIMENT

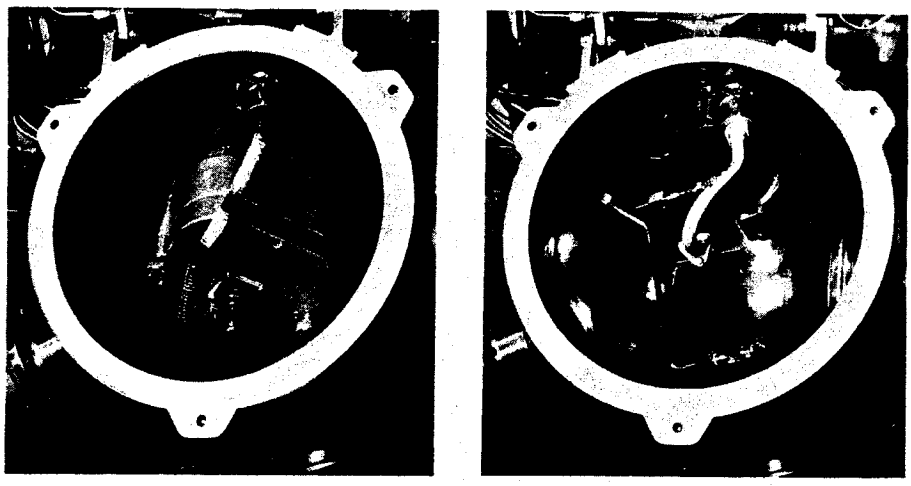

M552 EXOTHERMIC HEATING EXPERIMENT

M479 FLAMMABILITY EXPERIMENT

FIGURE 20. M552 EXOTHERMIC HEATING EXPERIMENT AND M479 FLAMMABILITY EXPERIMENT

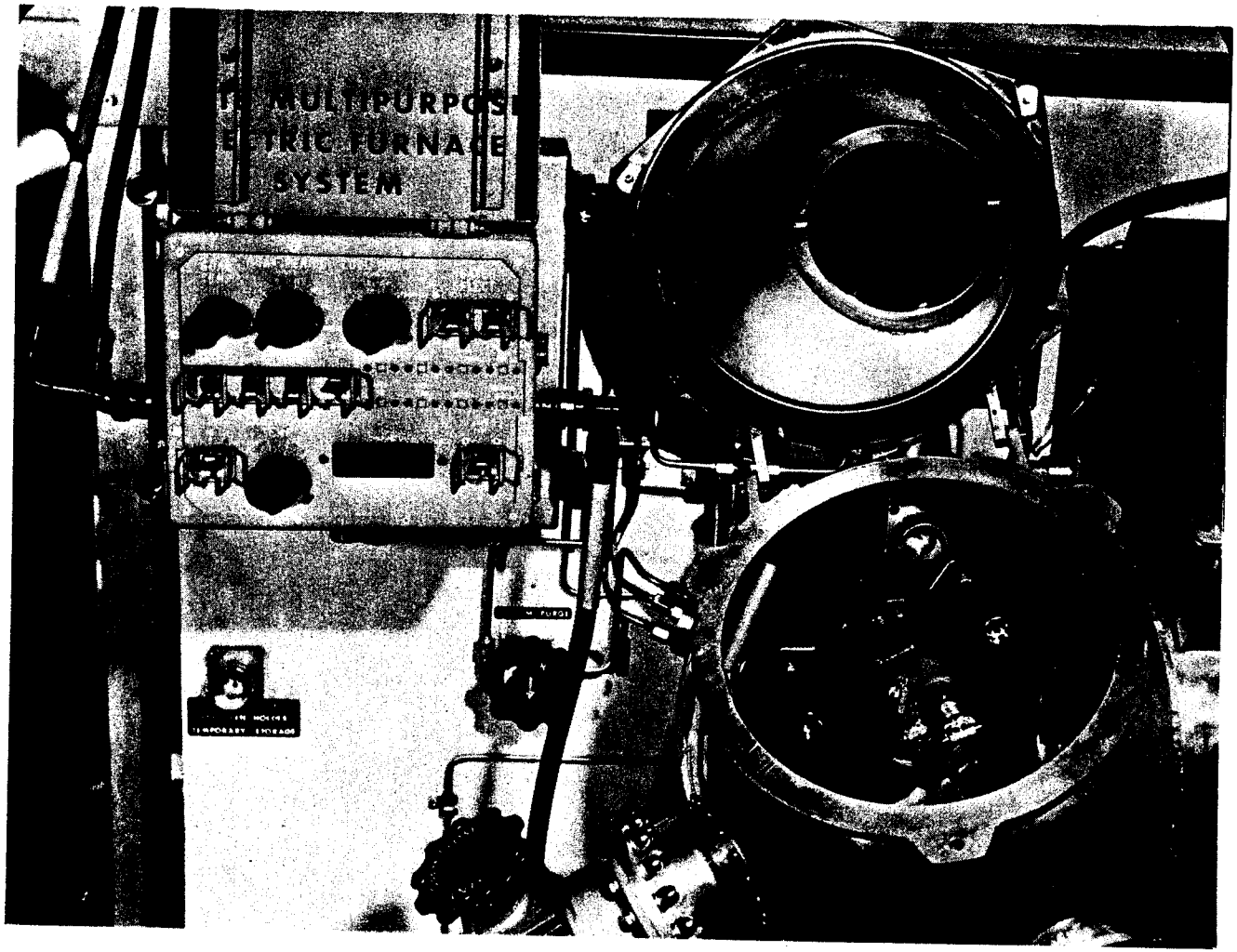

FIGURE 21. M518 MULTIPURPOSE ELECTRIC FURNACE SYSTEM

SKYLAB EXPERIMENT M552
EXOTHERMIC BRAZING

By

J. R. Williams
Process Engineering Laboratory
Marshall Space Flight Center
Alabama 35812

SUMMARY

The M552 Skylab experiment reveals that brazing in space is feasible. It successfully demonstrated the ability to retain molten metal within a braze tube joint system. Surface energy was the dominant operative force system controlling liquid metal for this experiment.

The zero gravity environment for brazing resulted in several differences; increased solubility, increased liquid spreading, more uniform menisci (liquid/vapor interface) and a reduction of braze alloy shrinkage defects. The residual radioactive intensity and location of the redistributed isotope was interpreted to provide a sequential history of braze alloy movement during the-melt-flow-solidification stages of the process.

Convection theory [4] applied to M552 was validated but some results were not explainable by it, i.e., increased nickel transport and the radial mixing of the silver isotope on samples SLN-2 and SLN-4. All characteristics of thermal analysis appeared to react as expected but heat conduction rates increased because of increased extent, rate and uniformity of braze alloy spreading [5].

INTRODUCTION

The objectives of this experiment were to evaluate brazing as a tube joining technique for the assembly and repair of hardware in space and to study the spreading, mixing and capillary action of molten braze material in near zero gravity.

Experiment Results presented by C. M. Adams - University of Wisconsin.

The Exothermic Brazing Experiment was proposed late in 1965 as the MSFC # 35 experiment for the Saturn IV-B Workshop, and in September 1966, it was approved as Experiment M492, Tube Joining in Space. The initiation of the proposal was motivated by Air Force programs with exothermic heating sources which could be operated at pressures as low as 10^{-6} Torr. In the ensuing years, under contracts with the Whittaker Corporation, exothermic material compositions and configurations were developed for the M492 experiment and verified by extensive testing at MSFC.

In 1968, the M492 experiment was re-evaluated and approved by NASA as the Exothermic Brazing task of the M512 series of experiments. Later the experiment number and name were changed to the M552 Exothermic Brazing Experiment. Qualification and hardware testing continued through 1972, preparing the experiment for the 1973 Skylab flight. On June 12 and 13, 1973, Astronaut Paul J. Weitz processed four (4) braze specimens on NASA's earth orbiting Skylab.

The following organizations assisted NASA in the design, testing and analyses of the experiment: Battelle Columbus Laboratories - Metallographic Analyses; Lockheed Missiles and Space Company - Solidification and Connection Theory; Massachusetts Institute of Technology - Thermal Analyses; Union Carbide Corporation (Oak Ridge National Laboratory) - Isotope Tracer Application; University of Wisconsin - Metallographic Analyses; Westinghouse Astronuclear Laboratory - Surface Tension and Adhesion Analyses; Whittaker Corporation - Exothermic Material Development; Hayes International - Test Operations and the Naval Research Laboratory - Experiment Consultation. To the personnel representing these organizations and many NASA personnel, the author wishes to express sincere thanks for their professional guidance and dedication to this historic and successful engineering endeavor.

HARDWARE DESCRIPTION

EXOTHERMIC BRAZING ASSEMBLY

Each of the four braze specimens consisted of a tube, sleeve, inserts (spacers), and silver-copper-lithium braze rings. Each specimen, possessing a different clearance gap between the tube and sleeve, was positioned in a separate canister containing the exothermic material, ignitors and insulation. This assembly is shown in Figure 1. Two of the four specimens contained pure nickel tubes and sleeves. An isotope, 110-Silver with a half life of 253 days, was added to a section of one braze ring in the nickel specimens to enhance analysis of capillary flow. The location of the isotope pellet prior to melting is shown in Figure 2. The other two tubes and sleeves were

type 304L stainless steel with the tube partially slit through the center cross section but with some solid portions for support and to simulate a butt joint. Sample identification, material and gap clearances between the sleeves and tubes are noted in Table I.

BRAZE ALLOY RINGS

Each braze alloy ring weighs 1.95 grams and was composed of 71.8 percent silver, 28.0 percent copper, and 0.2 - 0.4 percent lithium. The alloy's melting temperature was 760°C (1410°F).

EXOTHERM MATERIAL

Three exotherm rings with a combined weight of sixty grams were installed over the sleeve to provide the heat source required to produce a brazed tube and sleeve joint. Substantially all of the reaction products were solid, and no external oxygen supply was required for the reaction. The exotherm material ignites at 1104°C (2020°F) and produces 650 calories per gram. Approximately 90 seconds are required for the exotherm to complete its reaction. The exotherm used in the M552 experiment has the following composition:

Aluminum	24.8 percent
Boron	5.0 percent
Titanium Dioxide	55.2 percent
Vanadium Pentoxide	15.0 percent

IGNITORS

Two ignitors positioned against the exotherm ring, were used to initiate the exotherm reaction. Although one ignitor is normally sufficient, the second one was added to provide redundancy to the system. This ignitor exotherm material reacts at 510°C (950°F) and has the following composition:

Aluminum	14.8 percent
Boron	7.7 percent
Titanium	10.0 percent
Vanadium Pentoxide	67.5 percent

INSULATION

The exothermic material was surrounded with Fiberflax (fibrous aluminum oxide) insulating material which contained the heat generated for the brazing process and also protected the outside container from overheating.

HOUSING

The aluminum housing which held the four exothermic brazing packages was made in two halves, and after installation of four exothermic packages, was bolted together on the line shown along its median plane. See Figure 3. A thermocouple temperature sensor was bolted onto the top half portion of the housing, and electrical connections to this sensor and to the ignitor wires in the exothermic packages were soldered to an insulated terminal board attached to the top half of the housing. All electrical connections were led out of the case through the power connector on the cover. Figure 4 shows a photograph of the total exothermic assembly during final assembly of all major components including the brazing packages and the terminal board.

ELECTRICAL - TEMPERATURE CHARACTERISTICS

Power for initiation of the exothermic reactions was provided by the 28 vdc batteries contained in the M512 facility and controlled through selector and trigger switches on the facility's control panel within the Skylab's Multiple Docking Adaptor. Each initiating pulse is 120 amperes at 28 volts for 5 milliseconds (14.4 watt seconds per pulse). The temperature sensor output on the M512 chamber was read on the control panel's temperature gauge. The thermocouple sensor closes a circuit at approximately 110^{o}F and this action was displayed by a hot light indicator on the control panel. A schematic diagram of the experiment's electrical system is shown in Figure 5.

EXOTHERMIC PACKAGE WEIGHT AND SIZE

Equipment Item	Weight	Volume	Dimensions
Exothermic Brazing Assembly	3.7 Kg (8.2 lbs)	387 in^3	6.75" x 7.61" x 7.56"
Power Cable	.23 Kg (.5 lbs)	1.00 in^3	3/8" dia x 12"

A picture of the complete M552 Exothermic Brazing Package with its electrical power cable is shown in Figure 6.

PROCEDURES

PREFLIGHT DEVELOPMENT

During the development of the Exothermic Brazing Experiment, tests were performed at MSFC and at contractor facilities on over sixty prototype brazing packages similar to the four which were processed in the Skylab experiment. This testing included subjecting the units to relative humidity, vibration, exotherm aging, oxygen rich atmospheres and temperature profile tests under a simulated space experiment condition within the M512 experiment processing facility similar to that used in the Skylab flight experiment. A cataloging of the brazed specimens used in the qualification and evaluation phase of the experiment is shown on Table I.

These tests provided the base line data for the operational procedure of M552 Exothermic Braze Experiment in Skylab. Three M552 Exothermic Braze experiment assemblies (4 exothermic packages in each assembly - 12 packages total) similar to the flight configuration were used for astronaut training at JSC at Houston, Texas.

In addition, two nickel material specimens with a radioactive tracer, 110-Silver, were brazed for the Oak Ridge National Laboratory personnel who developed the isotope mapping techniques subsequently applied to the Skylab specimens. Testing was also performed to assure the safety of Skylab crew and photographic film relative to the radiation effect of the isotopes. Three specimens were brazed at MIT from which a thermal analysis for the experiment was derived. A temperature profile graph of the heat transferred to the tube's inside diameter is shown on Figure 7. Thermocouple locations for this test are shown on Figure 8.

Twelve other specimens of flight configuration were brazed at MSFC prior to the flight experiment. A typical laboratory test setup is shown in Figure 9. These brazed specimens served as radiographic and metallographic references for comparison with the specimens brazed during the Skylab flight which were jointly analyzed by the MSFC and experiment consultant personnel. One Exothermic Brazing Experiment assembly containing four tube and sleeve assemblies was reserved as a backup flight package or to be used for tests to duplicate any unexpected conditions encountered during the flight experiment.

As a result of the above engineering studies, confidence in the adequacy of the operational hardware and astronaut procedures was established.

FLIGHT PROCEDURE

Astronaut Weitz installed the M552 package in the M512 processing chamber in the Skylab MDA. The chamber door was sealed and the chamber atmosphere vented to space. After a 2 hour outgassing period, he initiated the ignition process. Approximately 2.75 hours was required for one exothermic package to be processed through its temperature profile. The other 3 units were processed similarly. All hardware and facility systems worked as designed; no anomalies were observed. The experiment package containing processed exothermic units was returned to earth on June 22 and to MSFC on June 26, 1973.

POST FLIGHT EVALUATION

The M552 package was received at MSFC and sequentially photographed during unpackaging. Visual observations were made and recorded. All four canister assemblies were x-rayed. The individual Skylab specimens, SLS-1, SLN-2, SLS-3 and SLN-4 were removed and cleaned via wire brush. Montage x-ray pictures were made of each specimen. Autoradiographs were made of the two nickel specimens. The negatives were printed and are shown on Figures 10 and 11. The 2 nickel specimens, SLN-2 and SLN-4, were transferred to Oak Ridge National Laboratory for sectioning and isotope mapping. The two 304L specimens were transferred to Battelle for sectioning. The identification plan for sectioned samples is shown on Figure 12.

Battelle subsequently provided the metallographic evaluation of both narrow gap samples SLS-1 and SLN-2. The University of Wisconsin provided the metallographic evaluation of the wide gap samples SLS-3 and SLN-4. A total matrix showing disposition, allocation, etc., of all preflight characterization and flight samples is shown on Table I.

FUTURE WORK

NASA Contract NAS8-28733, with the University of Wisconsin has been extended to study why certain liquid-solid reactions, such as the dissolution of nickel takes place more rapidly in the space environment. This effort will run through calendar year 1975.

RESULTS AND DISCUSSION

RADIOGRAPHY

I. SLS-1 (GAP .005" - 304L Material) specimen montage X-ray is shown in Figure 13 and is compared with a typical ground brazed sample MCS-1 of the same configuration. The Skylab sample exhibited a nearly perfect braze joint. One minor shrinkage defect was present adjacent to a ring groove at station F. Excess braze alloy had flowed inwardly through the slits in the tube and pooled over and adjacent to these slits on the tube I.D. The braze material was free from oxide. The braze alloy completely spread to the outermost ends of the sleeve. MCS-1 was typical of the ground brazed .005" GAP characterization samples, all of which exhibited voids adjacent to ring grooves and a much higher frequency of small defects throughout the solidified braze zone. It should also be noted that a .005" GAP exceed normal design specification for braze joint in one gravity application. A normal design clearance for optimum capillary braze flow in one-gravity would be approximately .002".

II. SLN-2 (GAP .010" - Nickel Material) specimen montage X-ray is shown on Figure 14 and is compared with a typical ground brazed sample MCN-1 of the same configuration. In this specimen the gap volume basically equals the volume of braze alloy. All specimens, Skylab and ground retained some braze metal in the ring groove. This would indicate equalizing forces between the ring groove to retain the molten metal and the gap zone to draw the metal into it. Both Skylab and Ground samples exhibited void areas in the braze gap zone.

III. SLS-3 (GAP .020" - 304L Material) specimen montage is shown in Figure 15 and is compared with a typical ground brazed sample of the same configuration. This specimeb was designed to represent a starved braze joint, possessing only about 50% enough alloy to fill the .020 gap zone. Note in the ground sample MCS-4, brazed horizontal, all the braze metal had pooled at the bottom section and gravity forces had completely drained the ring grooves. The Skylab sample is a classic example of what happens when surface energy is the dominate force. A small quantity of braze alloy was retained as fillets in both ring grooves and most braze alloy had bridged the .020 gap between the tube and sleeve. Some braze alloy was drawn through the 3 slits and pooled internal on the tube.

On the SLS-3 the braze material is free from porosity and voids. It is logical to assume that the .020" gap would have completely filled had there been adequate braze alloy.

IV. SLN-4 (GAP .000" - .030" - Nickel Material) specimen montage X-ray is shown in Figure 16 and is compared with a typical brazed sample MCN-4. The braze quality of the Skylab specimen was very good and much better than any ground brazed characterization sample. Note that nearly all of the braze alloy was drawn from the SLN-4 ring groove at the left side of the photograph and at the narrow end of the gap. Braze alloy fillets on both ground and flight specimens were retained in the ring groove adjacent to the wide gap end. Variation in the contour lines of the braze alloy were caused by slight variations in concentricity between the sleeve and tube. Radioactive tracings indicate alloy spreading the full length of the sleeve and some fillets of alloy were visible adjacent to the inserts at the wide end of the gap.

ISOTOPE - 110 SILVER TRACER APPLICATION [3]

I. AUTORADIOGRAPHS

Autoradiographs which were made from both samples SLN-2 and SLN-4 are shown in Figure 10. In these autoradiographs the darker areas correspond to higher levels of radioactivity. The 360° azimuth represents the circumference of the nickel sleeve, and the original position of the tracer-containing pellet is marked on the print. The autoradiograph for sample SLN-2 shows that the tracer alloy flowed mainly in a circumferential direction to areas at an azimuth of about 180° from the original tracer pellet location (0°). Most of the radioactivity is located in proximity to the pellet ring groove. An area of low radioactivity content can be seen just inside the tracer pellet location near the "upper" braze ring groove. After brazing in zero gravity, the tracer alloy in sample SLN-4 appeared to be concentrated in two areas; one above and the other below the tracer pellet location, although there was some mixing of the isotope throughout the total taper gap braze zone. This is shown in Figure 11.

II. ISOTOPE INTENSITY MAPS

The first use of a radioisotope tracer for mapping flow patterns during brazing of metal components in a space environment (near zero gravity) proved successful.

Radioisotope tracing consisted of measuring the intensity of radiation from the silver isotope at numerous points around the braze filled annulus at many transverse sections of the tube. Individual radiation intensity results for all sections were then combined to generate a two-dimensional radiation intensity map of the entire braze joint. These maps are shown in Figure 17 for SLN-2 and Figure 18 for SLN-4.

In both unit and near-zero gravity experiments, flow of braze material into "hot zones", generated by uneven ignition of the exotherm during the initial stages of the braze, was evident. This phenomenon would not have been observed without the use of the radioisotope tracer-containing alloy.

It is interesting to note that the areas void of solid braze alloy, yet wet by molten braze material, showed no residual tracer isotope activity. This observation would imply that the silver did not react nor adhere to the nickel surface.

The ^{110}Ag tracer maps for this experiment suggest that such tracing can provide a picture of the thermal history for any particular assembly as well as accurate braze alloy flow information. Since no other analytical technique would provide this unique composite view of surface, gravitational, and thermal forces, radioisotope tracing proved useful in interpreting other metallurgical aspects of this experiment.

SLN-2. The radiation intensity map for sample SLN-2 is shown in Figure 18. This sample had a nominal annulus clearance of 0.010 in. (0.025 cm). Some of the braze alloy flowed outside the nickel ferrule in the samples brazed in space. The effect of this extraneous flow is also shown by the movement of the tracer alloy which extended outside

the zero reference plane to areas with negative distance values. However, most of the tracer alloy was concentrated on either side of the ring groove from an azimuth of approximately 40^{o}, moving to the left to 200^{o}. An area of slight activity was found in the "upper" ring groove associated with a fillet of braze material. These results agree with those observed in the autoradiograph for sample SLN-2 showing high radioisotope content along the "lower" ring groove.

SLN-4. The radiation intensity map for sample SLN-4, having a 0.000-0.030 in. (0.000-0.076 cm) taper annulus, is shown in Figure 18. The braze extended beyond the nickel ferrule, and moderate concentrations of the radioisotope were detected outside the ferrule edge at negative distance values. However, most of the ^{110}Ag tracer isotope was concentrated in areas above and below the tracer ring groove at an azimuth of approximately 280 . Since SLN-4 was a taper-gap sample, it must again be remembered that the lower concentration area inside the ring groove actually gave higher radiation intensity values than the high concentration area outside the groove, but these latter values were normalized by dividing by a smaller volume increment. With this normalization in mind, comparison of the tracer map in Figure 18 to the autoradiograph in Figure 11 can be made. Both the map and autoradiograph show the presence of two regions of intense radioactivity, and they agree with respect to their azimuthal location.

CONVECTION ANALYSIS [1 & 4]

Specific evaluations performed for this experiment include:

Examination of the extent and uniformity of spreading using data supplied by other investigators.

Evaluation of the location of voids taking into account solidification shrinkage, buoyancy, Marangoni effect and the presence of the tube slot.

Analysis of the microstructure data obtained by others especially near the free surface where surface tension convection might occur even in low gravity.

Based on results reported to date, the following low-gravity variations have been observed.

I. Spreading of braze alloy: Visual and metallurgical examinations indicate the molten braze alloy spread further and more uniformly in the constant gap Skylab samples, SLS-1, SLN-2 and SLS-3, than in the corresponding ground samples [7 and 8]. A superior quality braze joint was noted in the SLS-1 sample [7]. Thus, the predictions of improved capillary flow [4] were confirmed. No firm conclusion can yet be reached on the absence or presence of turbulence during capillary spreading in microgravity. Turbulence was only expected to be possible in Skylab specimens SLS-3 and SLN-4.

II. Lack of hydrostatic pressure: A more symmetrical interface was noted in the meniscus of Skylab sample SLN-2. Spreading was more extensive in wide gap Skylab specimens SLS-3 and SLN-4 than in the corresponding ground samples [8]. These low-g variations agree with predictions dealing with the lack of hydrostatic pressure in microgravity brazing.

III. Void location: In Skylab sample SLS-1 there was an absence of voids and porosity compared to ground specimens. This low-g variation could be attributed to the more uniform capillary spreading in microgravity. In Skylab sample SLN-4 porosity existed near the narrowest position of the gap which was not seen on ground based tests MCN-4, -5 and -6. This porosity has been attributed to solidification shrinkage, thus Marangoni bubble migration cannot be a factor. From thermal conduction considerations the axial ends should solidify before the center and the igniter end should solidify before the opposite end. Thus, porosity should be centered between the middle section of the braze alloy and the end opposite the igniter. The wide gap ground samples, however, would be influenced by thermal convection, as well

thermal conduction, and the last portion to solidify in these vertically processed specimens would have been the wide gap (upper) end. Thus, ground specimens MCN-4, -5 and -6 would be expected to have less shrinkage induced voids near the narrow gap end than SLN-4, as actually occurred.

IV. Distribution of components: Two significant low-g variations have been reported thus far: (1) increased nickel transport in the SLN-4 wide gap, and (2) complete radial mixing of the silver isotope in SLN-2 and SLN-4. Nickel distribution was greater in the wide gap samples MLN-4, -5 and -6 [7]. This increased nickel transport cannot be attributed to surface tension convection because $\sigma_{Ni} > \sigma_{Ag-Cu}$. Furthermore, this mechanism, if possible, would have been operative on Earth also. Neither can gravity convection explain the increased Skylab nickel transport because $\rho_{Ni} \simeq \rho_{Cu} < \rho_{Ag}$. This would cause nickel to rise to the wide gap area in ground samples MLN-4, -5 and -6. The preceeding argument assumes that nickel is completely miscible in molten Ag-Cu. The phase diagram of Ag-Ni however, indicates a monotectic system with the possibility of two immiscible liquid phases if melt temperatures exceed 1435°C [9]. The silver-rich liquid is approximately 1.5 wt % Ni and the nickel-rich liquid is 3.65 wt % Ag. At the monotectic temperature the various molten components have the following densities:

Melt Component	Density at 1435°C (g/cc)
Copper	7.69
Ni-rich	7.81
Ag-rich	8.87

Thus, the narrow gap in samples MLN-4, -5 and -6 would be depleted in nickel, and again gravity convection would not explain the increased nickel in the wide gap of SLN-4. In conclusion the low-g variation of increased nickel transfer in SLN-4's wide gap cannot be explained by surface tension or gravity effects and must therefore be due to some as yet unexplained phenomenon such as nucleation or solidification effects. It should also be pointed out that no quantitative information has been reported on M552 alloy distributions, only qualitative results.

ρ - Density
σ - Surface Tension - Stefan - Boltzmann Constant

Silver isotope tended to settle (Ag is densest component) in ground samples MCN-1, -2, -3, -4, -5 and -6; whereas complete radial mixing of the isotope was reported in Skylab samples SLN-2 and SLN-4 [7]. As predicted in Section III-B, the ground based settling is due to gravity-induced sedimentation. The unexpected complete radial mixing which occurred on Skylab can be attributed to liquid-state diffusion and/or turbulence in the capillary flow.

V. Transport: The subject of transport and distribution of components was also addressed by R. W. Heine, C. M. Adams and T. A. Siewert [1]. These investigators offer the following comments:

Both Skylab nickel specimens (the one examined at Battelle and the other at the University of Wisconsin) exhibited appreciably higher concentrations of dissolved nickel in the braze alloy than did any of the ground characterization specimens. Several explanations, most of them unreasonable, may be hypothesized. It seems very unlikely that the absence of gravity would materially influence either the solubility or the diffusivity of nickel in a silver-rich liquid. In fact, the combinations of time, temperature, and liquid state diffusivity, and the dimensions of the capillary space in the nickel specimens, are such that diffusion cannot be the limiting factor. Even with the wide (0.020 inch) gap nickel specimen, the time, t, required for nearly complete diffusion throughout the capillary section can be estimated from

$$t = \frac{0.2L^2}{D}$$

where $L = 0.020" = 0.051$ cm., gap clearance

$D = 2.8 \times (10)^{-5} \text{cm}^2/\text{sec}$ (2, 3), diffusivity in liquid silver at 1000°C

$t = 18$ seconds

This specimen is obviously at elevated temperature much longer than 18 seconds. If diffusion is augmented by convection, the time becomes even less. However, the transport situation is evidently complicated

enough that it has not yet proven possible to establish a good analytical representation. It does seem that convection has an effect on transport at the interface between the solid nickel and the braze alloy. In both the ground characterization and Skylab specimens, there develops a layer of copper-nickel alloy at this interface. In the absence of convection, this layer develops sufficient thickness to act as an effective diffusion barrier. Weighing all the facts and observations, it seems likely convection was more vigorous in the Skylab than in the ground characterization specimens. The interface structure reflects this; there is a distinct tendency for the copper nickel interface layer to be thinner in the Skylab than in the ground characterization specimens. This is not uniformly true, in fact, the observation must be and has been made statistically by close scrutiny of many portions of the interface on each specimen.

In summary, the present conclusion is there was sustained convection after capillary flow in the Skylab specimens which was sufficiently vigorous to prevent development of an effective copper-nickel alloy diffusion barrier. It is postulated this sustained convection may have resulted from the interaction of the traveling Skylab specimens with the earth's magnetic field.

VI. Braze-base metal reaction: Nucleation of nickel phases in the nickel samples, both ground and Skylab, should vary with gap width [4]. This effect has been tentatively identified in SLN-2 [10] along with a possible gravity effect on this phenomenon. While the cause of this effect (surface energy considerations) should not vary with gravity, nickel transport variations due to gravity may have led to reported gravity variations in nickel-braze structure as well as reported gap size variations. The orientation of the nickel rich solid phase also seems to match the theories discussed in [4] as the nickel-rich needles are perpendicular to the walls [10].

VII. Microstructure: Different and/or unique microstructures were reported in Skylab samples SLN-2, SLS-4 and SLN-4. These low-g variations in microstructure are:

A. SLN-2: A unique structure appeared in which a globular copper-nickel second phase is in a matrix silver phase with the globular phase present at between 30 and 90 volume percent. Also, a unique structure appeared in which a needle-like second phase, high in copper, is present in a silver matrix phase. The needles are perpendicular to the joint interface.

B. SLS-3: The proeutectic silver-rich phase was more noticeable than in the ground samples and SLN-4 specimen.

C. SLN-4: Altered copper structure in the narrow gap end when compared to ground samples. Presence of proeutectic silver-rich phase not found in ground samples.

Based on the qualitative nature of these results, these variations have been attributed to some unknown nucleation effects and not to convection effects.

VIII. Variable-gap capillary pumping: As expected [4] the melt in both the Skylab and ground-based variable gap samples SLN-4, MCN-4, -5 and -6 moved to the narrow end of the tube. No low-g variation was expected because capillary forces predominate in this configuration.

III. METALLURGICAL STUDIES [1 & 6]

A. PHASE RELATIONSHIPS

The pertinent binary equilibrium systems, copper-nickel, silver-copper, and silver-nickel, are well established, but the ternary system, silver-copper-nickel, is not known with precision. Copper and nickel are mutually completely soluble in both the liquid and solid states; silver and copper exhibit complete liquid but limited solid solubility; silver and nickel exhibit very limited mutual solubility in both the liquid and solid states. The one published study of the ternary system suggests that silver-copper alloys rich in silver exhibit very limited capacity for dissolving nickel except at very high temperature [11]. Alloy element distributions observed in both the Skylab and ground characterization specimens exhibit appreciable concentrations of nickel in the solidified braze alloy. Moreover, much more nickel dissolved in the Skylab specimens than in the ground-based specimens.

The binary silver-copper alloy without nickel separates upon solidification into two solid phases, one rich in copper but containing some dissolved copper. When nickel is added to the silver-copper alloy, upon solidification the nickel preferentially associates with the copper-rich phase, being quite insoluble in the silver-rich phase. Moreover, silver and nickel appear to be mutually exclusive in the copper-rich phase. In fact, two kinds of copper-rich phase form, one which contains nickel but no silver, and the other which contains silver but almost no nickel. The solidification process is rendered quite complicated by the addition of nickel. The simple binary 72% silver 28% copper freezes substantially at one temperature, 780°C, and the product of solidification exhibits the classical eutectic structure, a finely dispersed mechanical mixture of silver-rich and copper-rich phases. The presence of nickel increases the temperature at which solidification begins, and the first solid crystals which form contain copper and nickel with practically no silver. These crystals become fairly large before the rest of the alloy freezes at about 780°C. These large copper-nickel crystals or dendrites are called primary because they form first upon cooling. Both the ground characterization and Skylab specimens of brazed nickel exhibited this characteristic strucfeature. Some primary copper-rich dendrites were also observed in the stainless steel specimens, but these contained much less nickel, because stainless only contains 8% nickel. As more and more nickel dissolves in

the silver-copper alloy, the fine eutectic structure progressively, and finally completely, disappears. Very abnormal structures, surprisingly high in nickel concentration, were observed only in the Skylab samples. The identification of these abnormal structures with high nickel concentration is still somewhat circumstantial; the important question is: Is the structure abnormal because of the absence of gravity, or is the structure abnormal because so much nickel has dissolved? And further, did more nickel dissolve because of the absence of gravity? At this stage of the study it appears that the increased nickel concentration in the Skylab specimens accounts for the abnormal structure.

The presence of dissolved nickel in the liquid silver-copper alloy has a subtle but logical effect on the formation of primary phases. In the absence of nickel, solidification of the 72% silver 28% copper substantially begins and ends at 780°C, and the structure produced is a finely dispersed classical eutectic mixture of silver-rich and copper-rich phases. The first effect of dissolved nickel is to increase the temperature at which solidification begins: A copper-rich primary phase, containing nickel, forms at a temperature well above 780°C. Upon cooling, when the temperature begins to approach 780°C; virtually all the nickel has been rejected from the liquid solution, because the nickel is virtually insoluble in the silver-rich liquid at temperatures below 850°C. Thus, it is the nickel which causes the primary copper phase to form at a relatively high temperature; however, this primary crystallization has the effect of removing copper from the liquid. The remaining liquid contains appreciably more than 72% silver, and primary silver-rich phase now must form at a temperature about 780°C. When the eutectic temperature, 780°C, is finally reached, whatever liquid still remains contains very nearly 72% silver-28% copper, and freezes to a fine eutectic structure. If the initial nickel concentration in the liquid is high enough, solidification will become nearly complete at a temperature above 780°C, and no normal eutectic structure will form. "The two-phase field resulting from the silver-copper eutectic decomposition terminates with the addition of 5 wt % Ni."[12] The quotation is an interpretation of early work done on the silver-copper-nickel ternary system[11], and is qualitatively correct. The limiting value of 5% nickel, in light of the present study, appears to be somewhat low; the actual value is probably closer to 10% nickel.

B. STRUCTURE AND COMPOSITION

(1) Wide Gap Specimens

The findings reported in the following paragraphs evolved primarily from brazed stainless steel samples SLS-3, and MCS-4,-5, and -6, and brazed Ni samples SLN-4 and MCN-4,-5, and-6. These have been referred to as "wide gap" samples, because, to develop effective capillary flow on earth using these materials, gap clearances are generally held below 0.005 inch. One objective which influenced specimen design was to observe wide-gap capillary flow in the absence of gravity.

(2) Nickel Specimens

In Figures 19, 20 and 21 are shown photomicrographs of structures found within the capillary brazed joint in specimen SLN 4. These structures are normal in most respects, being almost identical to corresponding sections taken from the ground characterization sample, Figure 22. The fine eutectic mechanical mixture occupies most of the field of view. The large dark regions are copper-rich and contain some nickel but almost no silver. The small dark regions are copper-rich and contain some silver but very little nickel. The white regions are silver-rich, containing some copper but essentially no nickel. In the Skylab specimens there occasionally appears a relatively large primary silver-rich dendrite; this has never been observed in any of the ground characterization specimens, and is an indirect result of high nickel concentration.

The alloy element distribution is typified in Figures 23, 24 and 25 which are, respectively, electron microprobe area scans showing nickel, copper, and silver distributions in the same field of view shown in Figure 22. In particular, it can be seen the large copper-rich dendrites contain copper and nickel but essentially no silver, and the small dark areas (sometimes referred to as secondary copper-rich phase) are rich in copper but contain no nickel. This pattern of alloy element distribution is repeated throughout in both the Skylab and ground characterization specimens, and supports the statement made above that silver and nickel are substantially mutually exclusive in the copper-rich phase, a feature which complicates the solidification sequence. Measurements were made of a structural feature called dendrite arm spacing. In the tree-like growth of dendrites, there occur regions in which the arms of the dendrites are

quite regularly spaced, and it has been found this spacing depends systematically on alloy composition and the cooling rate which prevailed during solidification. Dendrite arm spacings were found to be the same in the Skylab as in the ground characterization specimens, as had been expected. A typical view permitting measurement of dendrite arm spacing is shown in Figure 26, where the spacing is consistent with a dendrite containing 10% nickel 90% copper which solidified at a cooling rate of about 50°C per minute [13].

The structures observed in the nickel Skylab specimens have been characterized as normal, abnormal and mixed. These structures are shown in Figures 27 through 30. Figure 27 from Skylab sample SLN 4 shows the normal structure, which is to say it is substantially identical in all important features to the brazed nickel ground characterization specimens. There are occasional large nickel-containing copper-rich, silver-free dendrites to be found throughout the braze alloy. Then, near the interface, there are peninsular protuberances, epitaxial with the solid nickel, which are also rich in copper with appreciable concentrations of dissolved nickel. The rest of the structure is the fine eutectic mixture of silver-rich (white) solid solution containing relatively small particles of copper-rich, silver-bearing, low nickel solid solution. A detailed microprobe survey of this structure gave the following results?

a. Near the center of a large dendrite the composition is 20% nickel 80% copper.

b. Near one of the tips of the same large dendrite the composition is 10% nickel 90% copper.

This alloy distribution is consistent with the nature of dendrite growth. The first material to form upon cooling has the highest nickel content, and then, as the crystal grows, the exterior regions exhibit progressively lower nickel concentrations, and form at progressively lower temperatures. This is often referred to as a cored structure. The proturbances growing from the brazed nickel interface also present a logical variation in composition.

c. In the protuberance, very near the original interface, the composition is 35% nickel 65% copper.

d. Halfway out to the tip the composition is 20% nickel 80% copper.

e. At the tip the composition is 10% nickel 90% copper, the same as the tip of a large dendrite.

The small copper-rich particles within the finely dispersed eutectic structure contain something less than 10% nickel.

The abnormal structure is shown in Figure 28. There is a complete absence of the typically fine eutectic dispersion, and the relatively large dark particles contain nickel concentrations which range from about 40% nickel in their centers down to about 25% nickel near their exterior boundaries. These particles are therefore cored, but do not exhibit the usual morphology of dendrites. The total nickel concentration in the field of view shown in Figure 28 is quite high, estimated close to 10% nickel overall. Furthermore, the probe shows that the layer of nickel-copper alloy at the braze-nickel interface is quite thin compared to corresponding locations on ground characterization specimens. The thinner this layer the less effective it is as a diffusion barrier. Since it is unlikely any of these specimens reached temperatures much above 1000°C, the high nickel concentration is surprising in that it appears to exceed the maximum solubility which can be inferred from the published information on the ternary silver-copper-nickel system .

Figures 29 and 30 show mixed normal and abnormal structures. Figure 29 happens to be from a ring-groove location, where the cross-section of the braze alloy is relatively large, and Figure 30 shows a region within the capillary gap. All three structures, normal, abnormal and mixed, are found at various locations throughout the specimen; there is no systematic dependence on location.

(3) Stainless Specimens

Abnormal and mixed structures were not observed in any stainless

steel specimens, presumably because the stainless, containing only 8% nickel, does not introduce enough nickel into liquid solution to modify eutectic solidification appreciably. Within the capillary gap in the stainless Skylab specimens, there is a pronounced tendency for primary silver-rich dendrites to form, clearly shown in Figures 31 and 32. In fact, in these regions there has been some impoverishment in copper, apparently by dissolution into the stainless; the copper is soluble in the solid stainless, whereas silver is not. However, primary silver-rich phase has never been observed in the ground characterization specimens. This is yet further evidence for enhanced transport in the Skylab specimens, which must, for reasons already stated, relate to convection, i.e. convective disturbance overcomes any tendency for an effective diffusion barrier to form at the liquid-solid interface. In the ring-groove of the stainless Skylab specimen, the structure is identical to that in the ground characterization specimens, exhibiting primary copper-rich dendrites, containing generally about 2% nickel (sometimes less), surrounded by normal finely dispersed eutectic structure (see Figure 33).

For comparison, structures observed in stainless ground characterization specimens are shown in Figures 34 and 35; these exhibit primary copper-rich phase together with normal eutectic. In the stainless Skylab specimen, primary silver-rich but no primary copper-rich phase is observed in the capillary gap, and primary copper-rich but no silver-rich phase was observed in the ring-groove location. In the nickel Skylab specimen, primary silver-rich and copper-rich phases were frequantly observed together (Figures 19 and 20), both primary phases resulting from the presence of nickel dissolved in the liquid prior to solidification.

Another curious feature of the stainless Skylab specimen was the presence of finely dispersed stainless steel particles within the braze alloy. The first inclination is to attribute these particles to the presence of debris remaining from machining the specimens. However, the specimens were very thoroughly cleaned, and the particles are extremely small, ranging from 0.5 to 5.0 microns (micrometers) in diameter. Stainless does not readily fragment into such fine particles; it is more likely these inclusions, shown in Figures 36 and 37 are the consequence of erosive attack of the stainless by the liquid metal. This is taken as still further evidence of vigorous convection peculiar to the Skylab specimens, because these

particles were not detected in any of the ground characterization specimens.

Summarizing, the results of examining the stainless steel Skylab and ground characterization specimens have revealed significant differences and similarities. The formation of primary copper-rich dendrites and normal fine eutectic structure was observed in all stainless specimens in the groove location. The stainless Skylab specimens was distinguished by the presence of primary silver-rich phase and non-uniform dispersion of very fine stainless steel particles within the braze alloy.

(4) Narrow Gap Specimens [6]

The findings reported in the following paragraphs evolved primarily from brazed stainless steel samples SLS 1 and MCS 1, 2 and 3 and brazed Ni samples SLN 2 and MCN 1, 2 and 3. All of these samples incorporated narrower capillary gaps approaching those normally used in conventional brazing.

(5) Nickel Specimens

The micro structure of the braze alloy in Skylab specimen SLN 2 was frequently different from the structure exhibited by ground based specimens as shown in Figure 38. The resulting micro structures clearly indicate variations in the braze alloy composition and perhaps some variation in the cooling rate. However, these micro structures are considered normal and there is no obvious relation to an effect of the micro gravity environment.

(6) Stainless Specimens

Skylab specimen SLS 1 was an essentially void free braze. The micro structure and many other characteristics is this braze were similar to comparable ground-based specimens. Also, as noted in the preceeding discussion of wide gap specimens, no abnormal or mixed structures were observed.

Both the nickel and stainless narrow gap specimens exhibited smaller braze alloy gaps than intended or observed in the ground-based specimens. The smaller gap probably resulted from an end restraint condition that prevented unrestricted thermal expansion of the assembly. In the case of the stainless specimen, a diffusion bond was formed in a tight gap region as shown in Figure 39. This observation confirms that diffusion bonding can also be used as a joining method in the micro gravity environment.

C. MENISCUS FORMATION

The retention of braze alloy in the corners of the oversize ring grooves and fillets formation in the Skylab specimens are significantly different from the ground brazed specimens. This observation clearly supports the enhancement of surface tension forces in a zero gravity field. This difference is shown in Figure 40 of Skylab samples SLS-1 and a 304L stainless sample brazed on the ground. A classic retained fillet is shown on Figure 41 of Skylab sample SLN-2 where complete fillet symmetry was obtained.

CONCLUSIONS

I. The absence of gravity greatly extends the scope of brazing and, thereby, the applicability of brazing to fabrication in space. In zero gravity environment, the surface tension forces driving capillary flow predominate, while on earth these forces must complete with gravity. Study of braze alloy distribution in Skylab specimens clearly indicates that dimensional tolerances, especially braze gap clearances, will be far less critical to joining operations in space than on earth. The .020" radial gap specimen was brazed; greater gaps could also be brazed. This, of course, could not happen in 1 g. The practical significance of this fact, which had been predicted but never tested, can hardly be overemphasized. In space fabrication, many joints, which on earth would be produced by welding, should probably be brazed to allow wider fit up tolerances.

II. The absence of gravity definitely and surprisingly changes the ways in which liquid and solid metals interact. For example, for the same time and temperature conditions of exposure (a) liquid silver-copper alloy dissolves nickel more rapidly in space than on earth, and (b) solid stainless steel dissolves copper from liquid silver-copper alloy more rapidly in space than on earth. The detailed mechanisms by which these reactions are hastened have not been positively identified, and this effect of space environment had not been predicted. The space environment appears to offer unique advantages for implementation of some liquid-solid reactions, and also the measurement of solubilities. For example, the Skylab experience clearly indicates a higher solubility of nickel in liquid silver-copper alloy than had been found in the earth-bound studies (in this reaction the silver is rejected and appears as almost pure metal); this is not because nickel is more soluble in space, but rather because it dissolves more rapidly. This pattern of behavior suggests that saturated liquid metal solutions can be more easily produced, and true solubilities are more easily determined in space than on earth.

III. Liquid-vapor boundary surfaces (menisci), and the flow of liquid metal driven by surface tension are in close conformance with what had been predicted for zero gravity environment. There were no unexplained effects and in the Skylab specimens the surface tension of liquid silver-copper alloy appears to have been quite uniform.

IV. The addition of a radioisotope tracer to the M552 brazing experiment provided a unique picture of the thermal history of braze melting within the annulus as well as useful representation of the braze alloy flow pattern during the melting solidification process. Silver isotope tended to settle (Ag is densest component) in ground samples; whereas complete circumferential mixing of the isotope was reported in Skylab samples. As predicted the ground based settling is due to gravity-induced sedimentation. The unexpected complete circumferential mixing which occurred on Skylab can be attributed to liquid-state diffusion and/or turbulence in the capillary flow.

V. The presence or absence of gravity has no observable effect on the mechanism of alloy solidification. Such microstructural details as dendritic configuration, and eutectic structure were the same in space as on earth.

VI. The Skylab specimens exhibited fewer and smaller shrinkage defects that the comparative ground processed characterization samples indicating that gravity forces are significant during the capillary movement of the braze alloy.

VII. The oxide build-up on both the M552 Skylab braze alloy and the substrate materials was less than on ground based specimens indicating the adequacy of utilizing the space vacuum and its infinete pumping capacity for brazing operations of this type configuration.

REFERENCES

1. Heine, R. W.; Adams, C. M.; Siewert, T. A.; Report on Flight/Ground Sample Comparison Relating to Flight Experiment M552, Exothermic Brazing, University of Wisconsin - Contract NAS8-28733, December 4, 1973.

2. Tobin, J. M.; Kossowsky, R.; Final Report on M551, M552 & M553. Research Study on Material Processing in Space - Contract NAS8-78730, Westinghouse Astronuclear Laboratory, Pittsburgh, Pennsylvania, December 12, 1973.

3. Braski, D. N.; Adair, H. L.; Kobisk, E.H.; Radioisotope Tracer Studies in the NASA Skylab Exothermic Brazing Experiment M552 - Contract No. W-74-5-ENG-26. Oak Ridge National Laboratory, Oak Ridge, Tennessee - (Operated by Union Carbide Corporation for the Atomic Energy Commission, December 1973.

4. Bourgeois, S. V., Convection Effects on Skylab Experiments M551, M552, M553 - Contract NAS8-28015, Lockheed Missiles & Space Company, Inc., Huntsville, Alabama, December 1, 1973.

5. Muraki, T.; Masubuchi, K.; Thermal Analysis of M551, M552, and M553 Experiments - Contract NAS8-28732, Massachusetts Institute of Technology Cambridge, Massachusetts, December 1973.

6. Monroe, R. E. and Pattee, H. E.; Characterization of Exothermic Brazing Comments - Skylab Experiment M552 - Contract NAS8-28725 , Battelle Columbus Laboratories, Columbus, Ohio, December 4, 1973.

7. Williams, J. R.; 90-Day Report - Skylab Experiment M552, NASA - George C. Marshall Space Flight Center, Huntsville, Alabama, October 1973.

8. Visual Observation of M552 Skylab Specimens and Hardware During NDT at MSFC, NASA-George C. Marshall Space Flight Center, Huntsville, Alabama, July 17, 1973.

9. Hansen, M., The Constitution of Binary Alloys, McGraw-Hill, New York, 1958, pp. 36-37.

10. Monroe, R.E., Report on Skylab M552 Samples, Battelle Memorial Institute, Columbus, Ohio, September 21, 1973.

11. Guertler, W. and Bergmann, A., Study of the Ternary Ag-Cu-Ni, Zeitschrifte fur Metallkunde, 25, 53 (1933).

12. Metals Handbook, 8, 380 (1973).

13. Backerud, L. and Liljenvall, L. M., The Solidification Characteristics of 7 Constitutionally Different Types of Binary Copper Alloys, INCRA Project 165, Swedish Institute for Metal Research, Stockholm, 1971.

TABLE I. M552 GROUND CHARACTERIZATION/FLIGHT SAMPLE ALLOCATION

Exotherm Heaters		Application	Braze At	Tube Position	Type Material	Isotope Tracer	Thermal Profile	Gap Dimension	Identification #
1	EXOTHERM MATERIAL Jan & June - 71	Astronaut Training Stainless	MSC		347			.002	AT 5
2			MSC	Horz	347			.002	AT 6
3			MSC	(All)	347			.002	AT 7
4			MSC		347			.002	AT 8
5		Metallurgical Characterization Stainless	MSFC		304L		X	.005	MCS 1
6			MSFC		304L		X	.005	MCS 2
7			MSFC	Horz	304L			.005	MCS 3
8			MSFC	(All)	304L			.020	MCS 4
9			MSFC		304L			.020	MCS 5
10			MSFC		304L			.020	MCS 6
11		Metallurgical Characterization Stainless	MSFC	Horz	Ni	X @ 12:00	X	.010	MCN 1
12			MSFC	Horz	Ni	X @ 3:00	X	.010	MCN 2
13			MSFC	Horz	Ni	X @ 6:00		.010	MCN 3
14			MSFC	Vert	Ni	X @ Bot		.000 - .030	MCN 4
15			MSFC	Vert	Ni	X @ Bot		.000 - .030	MCN 5
16			MSFC	Vert	Ni	X @ Bot		.000 - .030	MCN 6
17		Isotope Mapping	MSFC	Horz	Ni	X @ 3:00		.010	IMN 1
18			MSFC	Vert	Ni	X @ Bot		.000 - .030	IMN 2
19		Thermal Flow Data	MIT	Horz	347		X	.002	TF 1
20			MIT	(All)	347		X	.002	TF 2
21			MIT		347		X	.002	TF 3
1	EXOTHERM MATERIAL Dec - 72	Skylab Flight Samples	SKYLAB		304L			.005	SLS 1
2			SKYLAB		Ni	X		.010	SLN 2
3			SKYLAB	N.A.	304L			.020	SLS 3
4			SKYLAB		Ni	X		.000 - .030	SLN 4
5		Skylab Backup Samples	TO BE DETER-MINED		304L			.005	SBS 1
6					Ni	X		.010	SBN 2
7				N.A.	304L			.020	SBS 3
8					Ni	X		.000 - .030	SBN 4

N.A. - Not Applicable

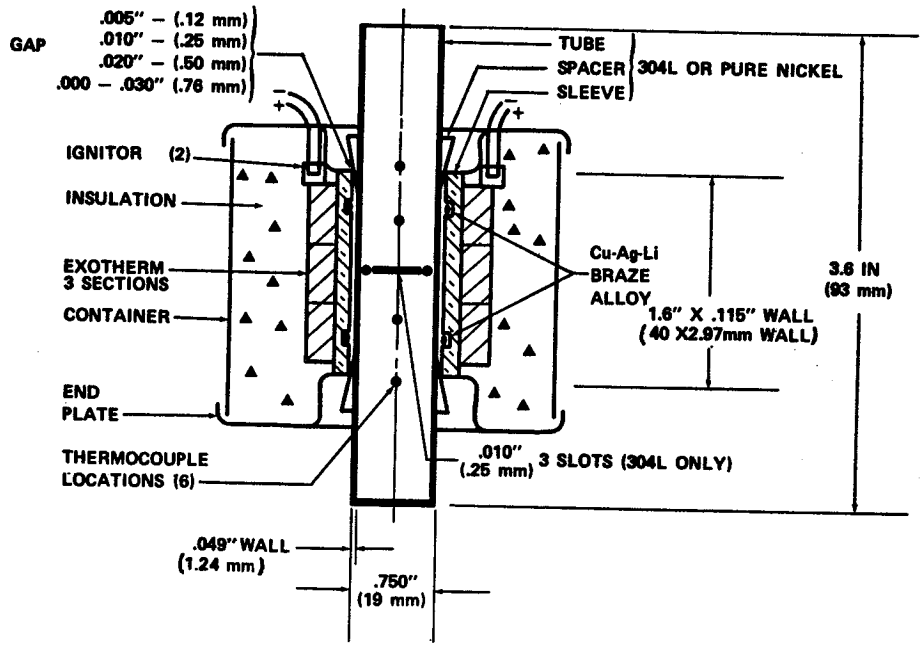

FIG. 1 CROSS SECTION - TUBE AND SLEEVE ASSEMBLY IN BRAZING CONTAINER

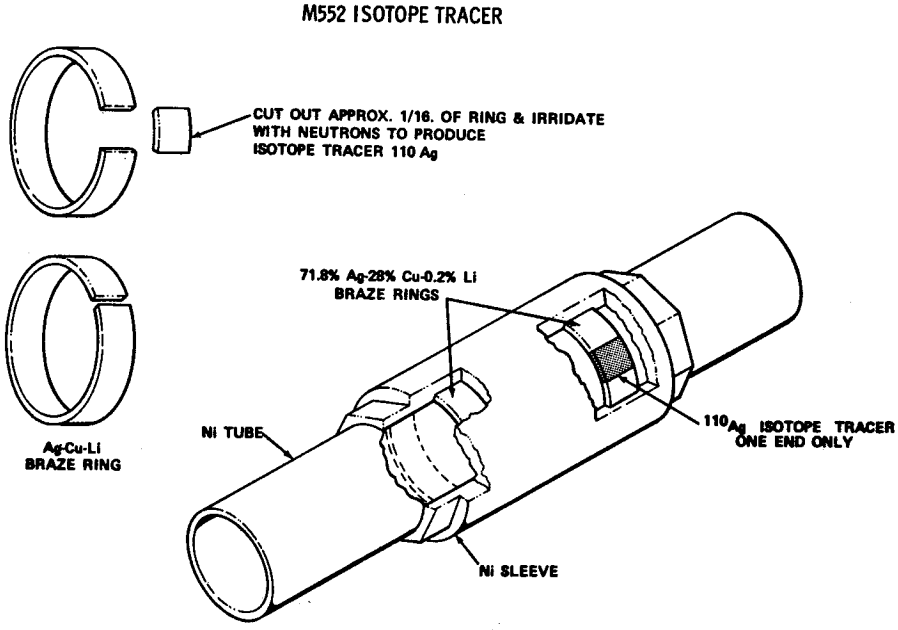

FIG. 2 ISOTOPE LOCATION - NICKEL SAMPLES

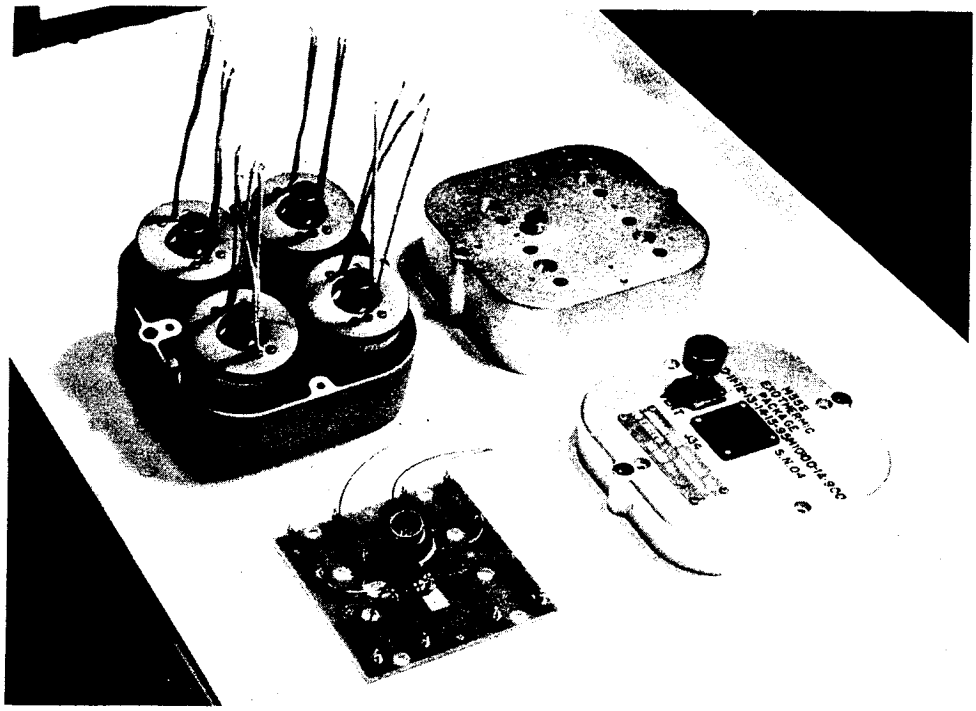

FIG. 3 HOUSING ASSEMBLY AND CONTENTS

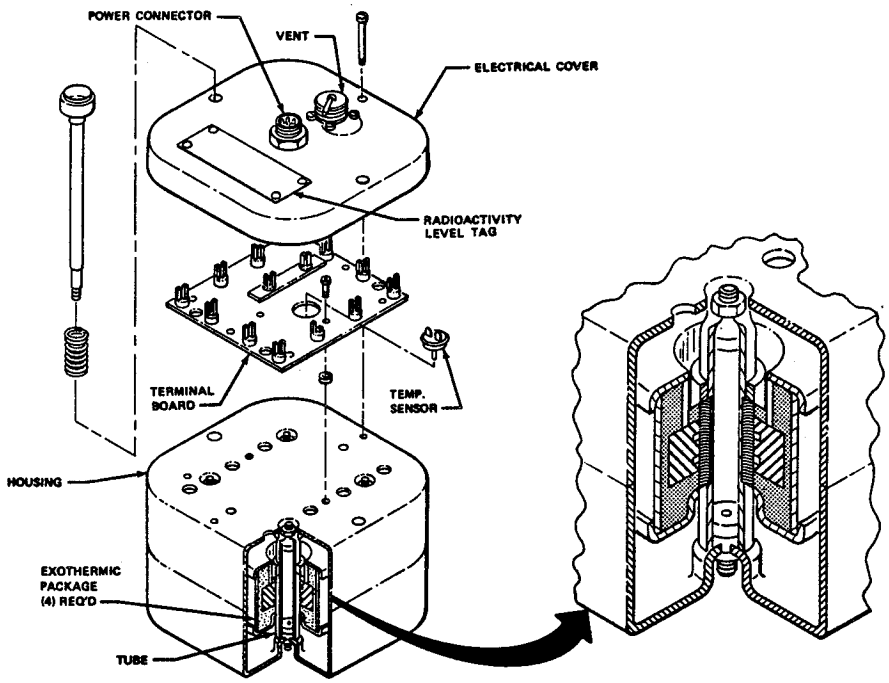

FIG. 4 M552 EXOTHERMIC PACKAGE AT ASSEMBLY

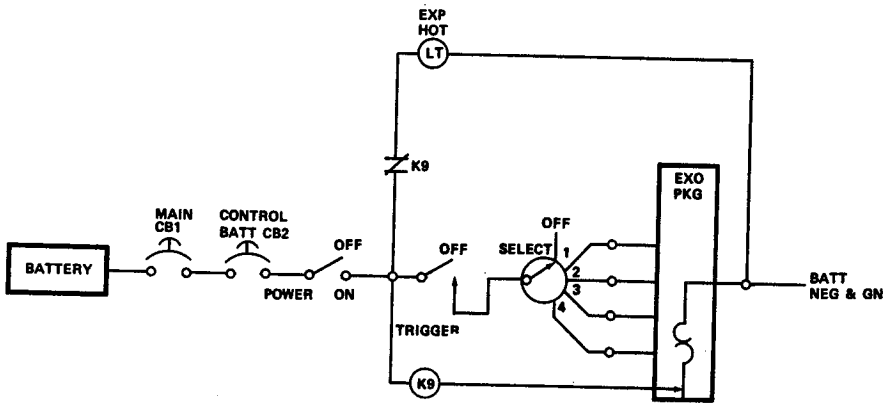

FIG. 5 SCHEMATIC OF M512 FACILITY ELECTRICAL CIRCUITS USED IN THE EXOTHERMIC BRAZING EXPERIMENT

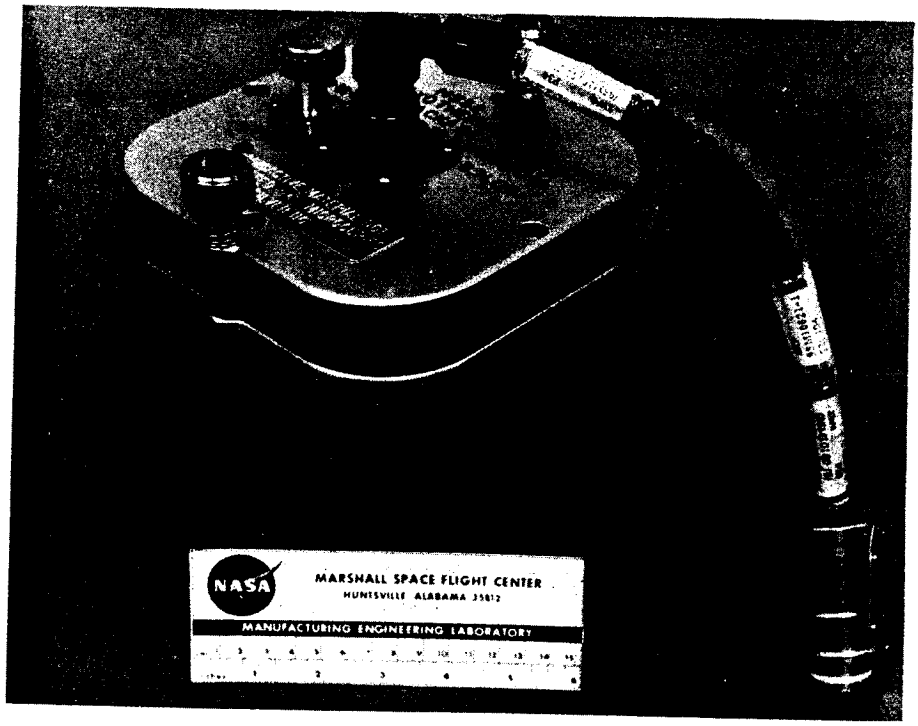

FIG. 6 M552 EXOTHERMIC PACKAGE AND ELECTRICAL POWER CABLE

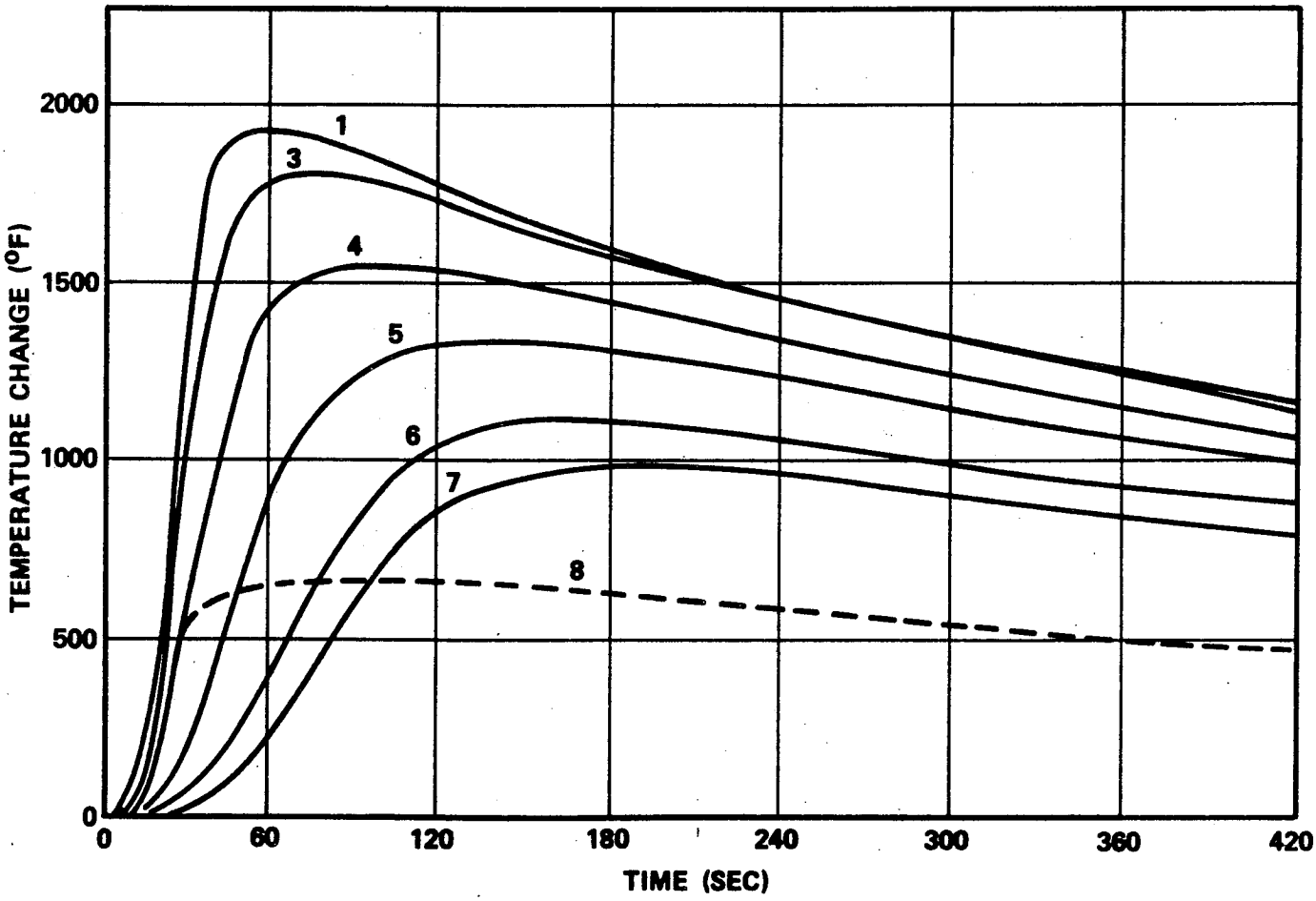

FIG. 7 TEMPERATURE PROFILE CURVES OF EXOTHERMIC HEATING OF TUBE

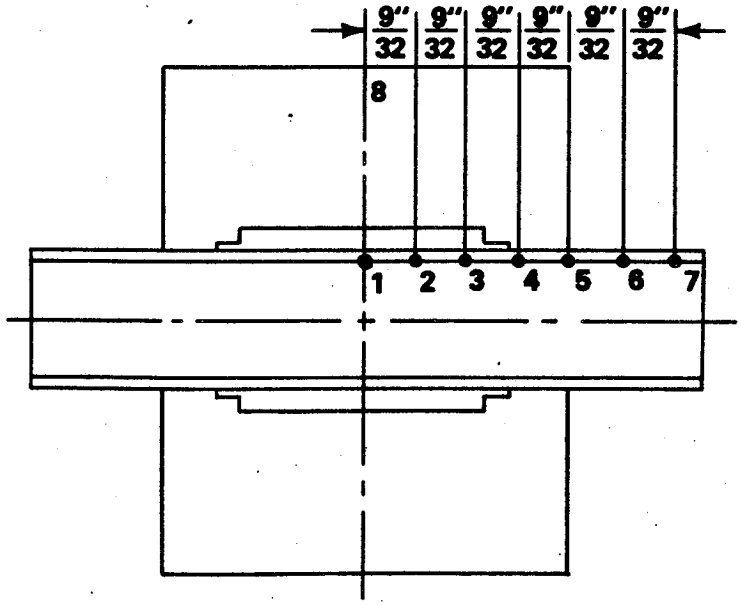

FIG. 8 THERMOCOUPLE LOCATIONS FOR TEST GENERATING CURVES IN FIGURE 7

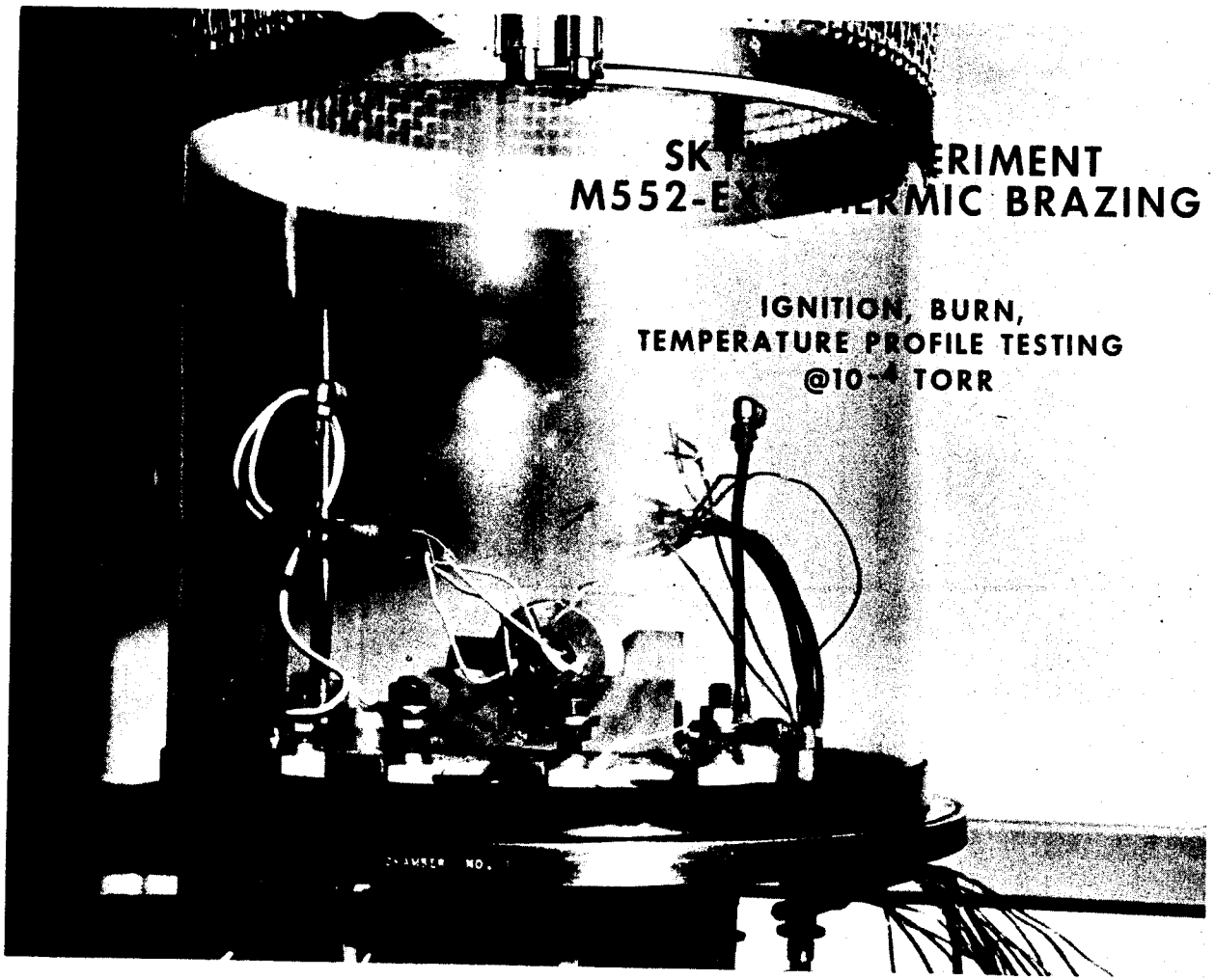

FIG. 9 IGNITION, BURN, TEMPERATURE PROFILE TESTING @ 10^{-4} TORR

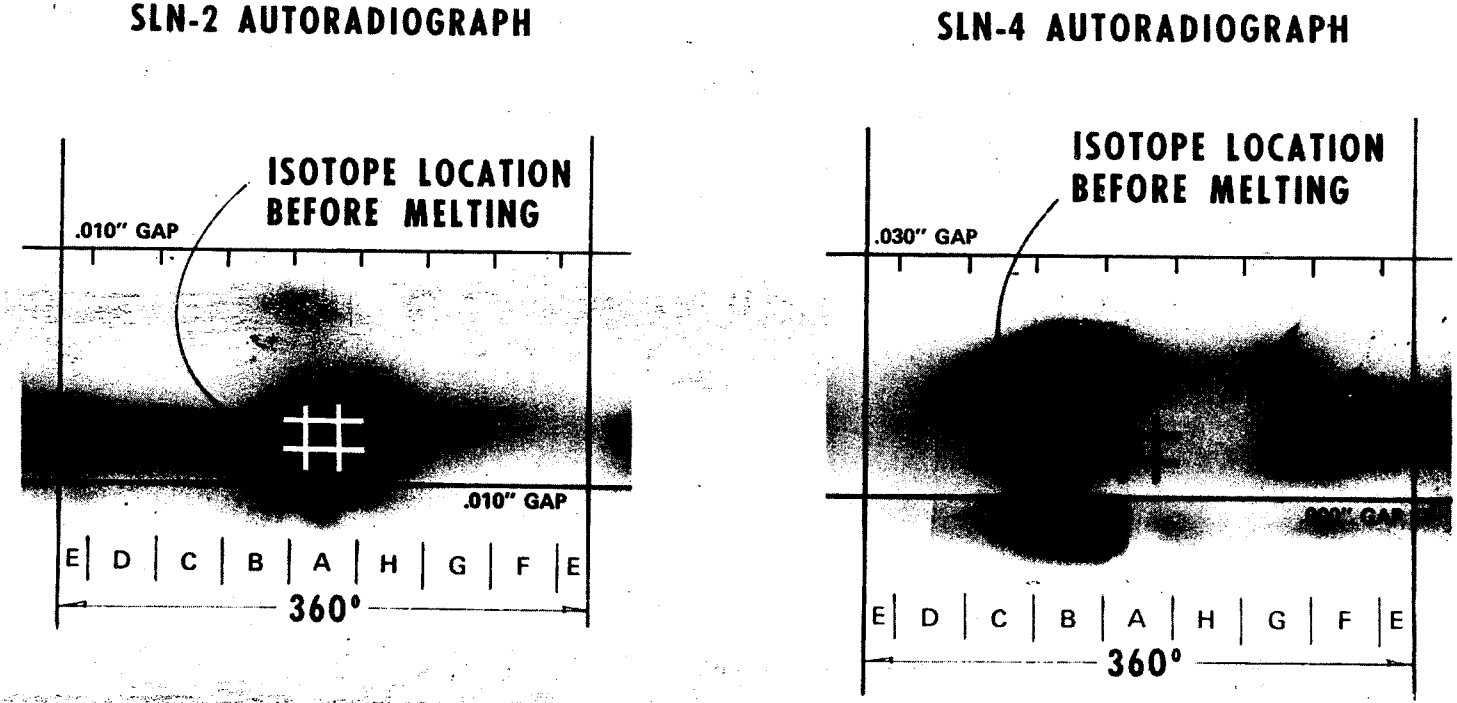

AUTO RADIOGRAPH OF 110 SILVER ISOTOPE AFTER MELTING, MOVEMENT VIA CAPILLARY FLOW & RESOLIDIFICATION IN PURE NICKEL SPECIMENS.

FIG. 10 AUTORADIOGRAPH OF SKYLAB SPECIMEN SLN-2

FIG. 11 AUTORADIOGRAPH OF SKYLAB SPECIMEN SLN-4

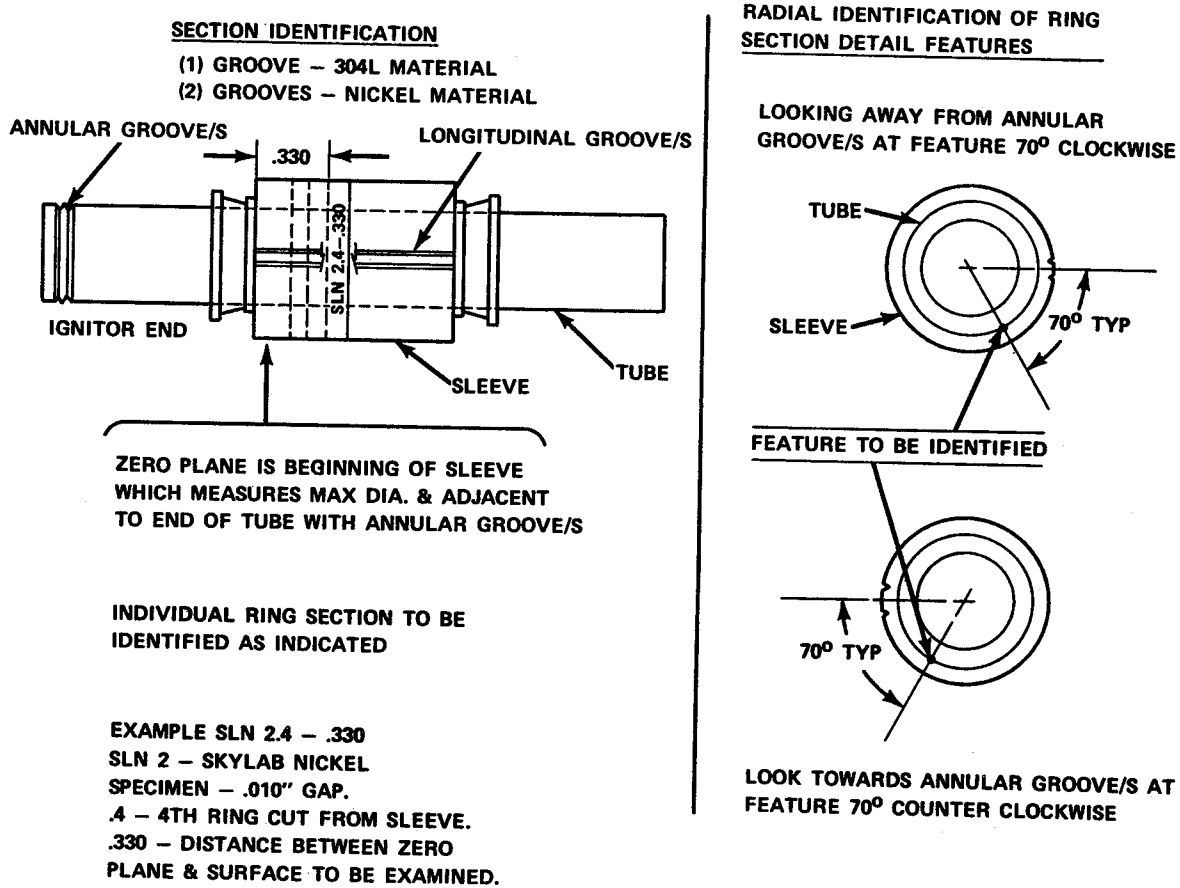

FIG. 12 M552 - IDENTIFICATION SECTIONING PLAN

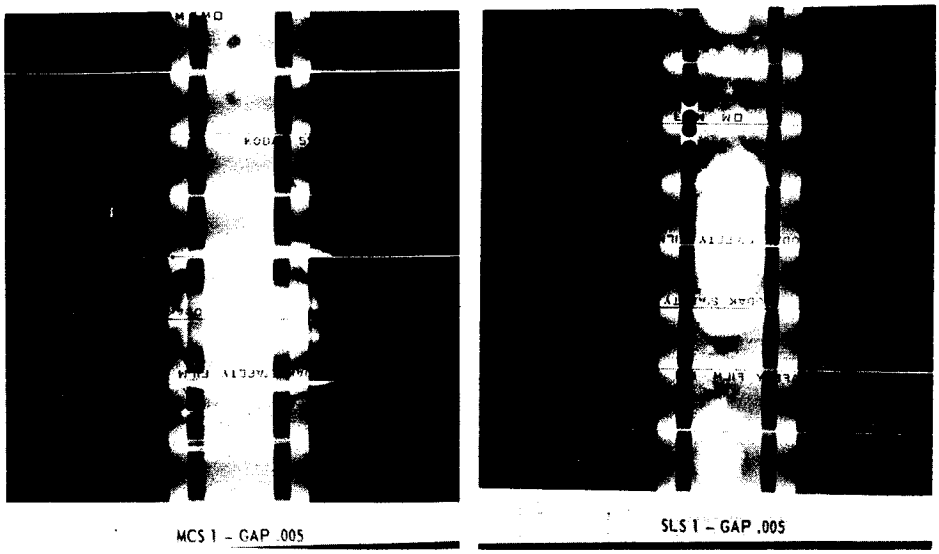

FIG. 13 MONTAGE RADIOGRAPH - SLS-1

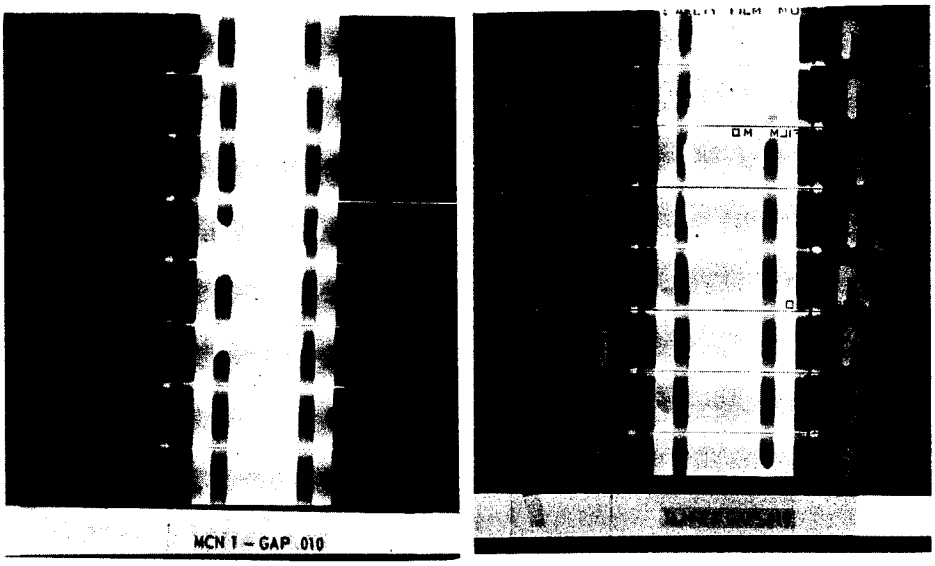

FIG. 14 MONTAGE RADIOGRAPH - SLN-2

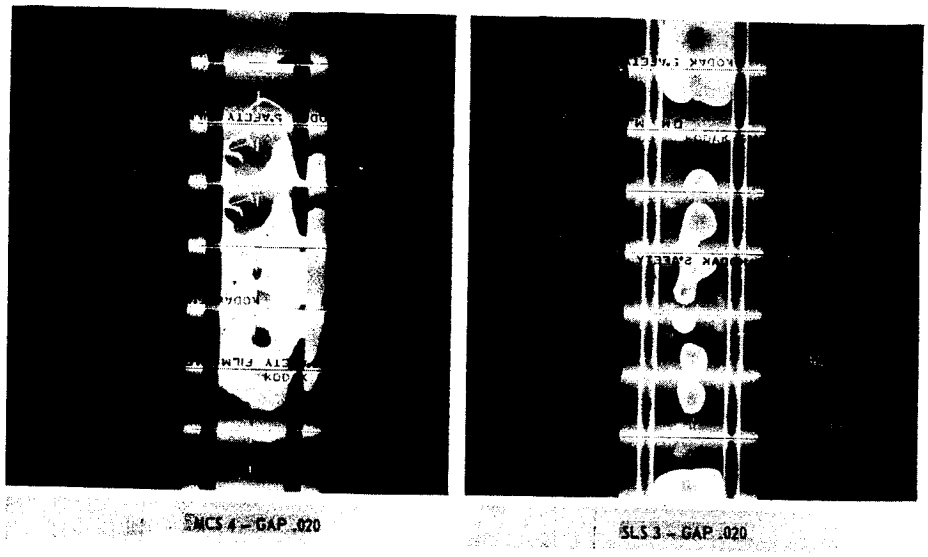

FIG. 15 MONTAGE RADIOGRAPH - SLS-3

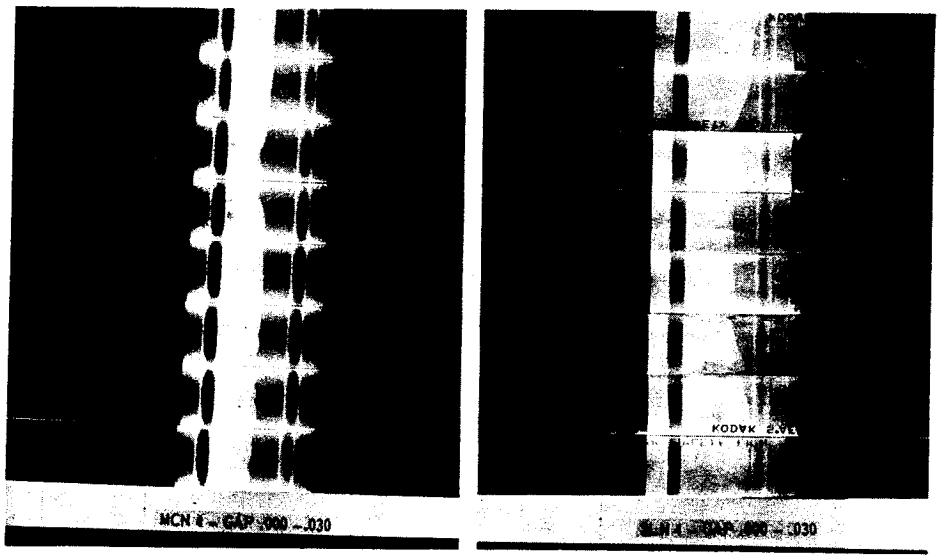

FIG. 16 MONTAGE RADIOGRAPH - SLN-4

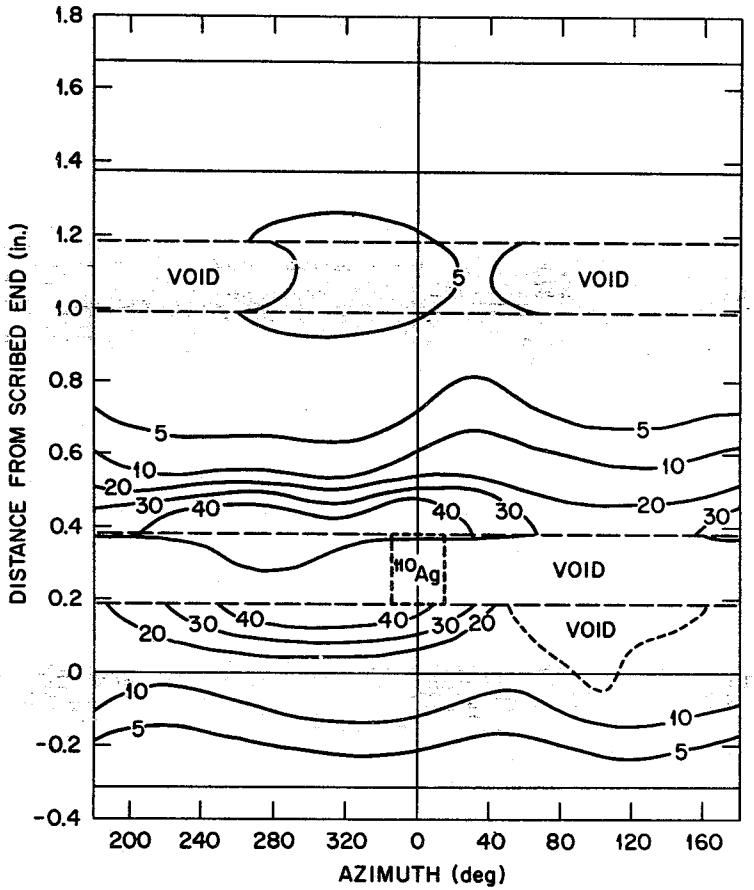

FIG. 17 ISOTOPE INTENSITY MAP - SLN-2

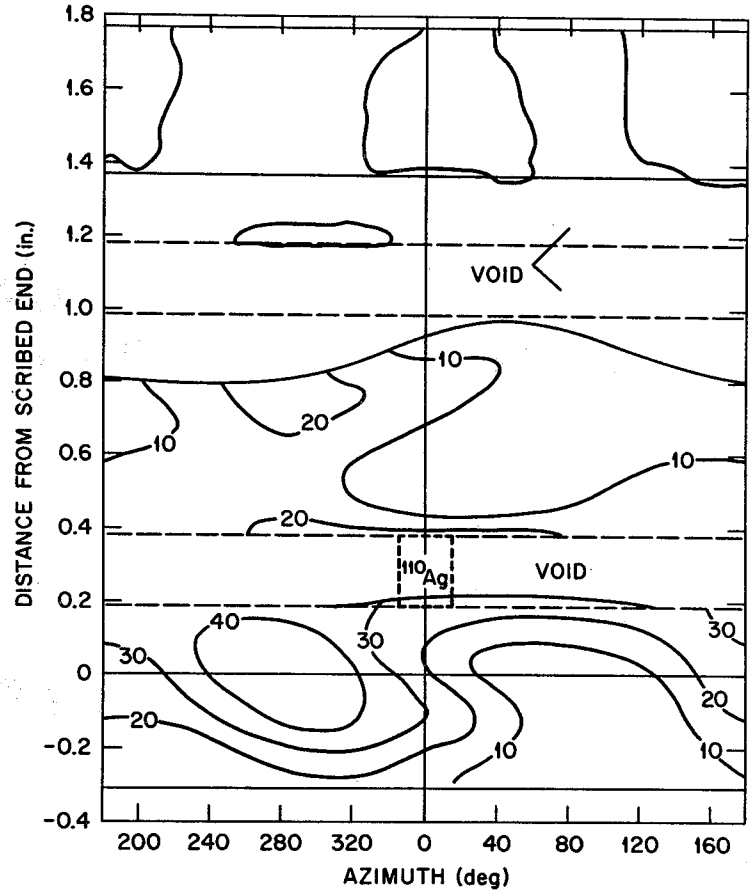

FIG. 18 ISOTOPE INTENSITY MAP - SLN-4

FIG. 19 SCANNING ELECTRON MICROGRAPH OF SLN-4-20mm - 120° SHOWING THE TWO KINDS OF PRIMARY PHASES. (250X)

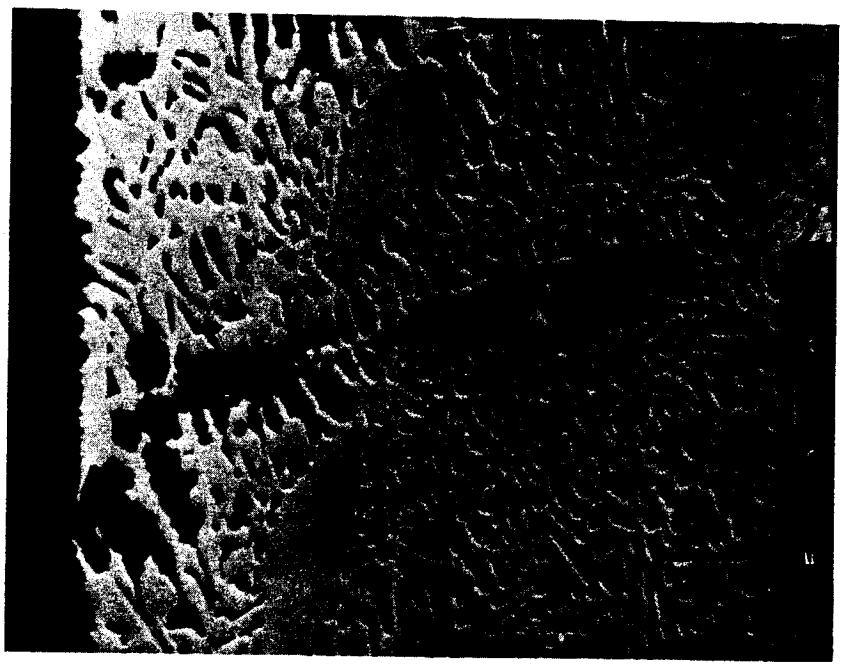

FIG. 20 CLOSE-UP OF THE SAME REGION SHOWN IN FIGURE 19. NOTICE THE DARK COPPER PHASE EXTENDING FROM THE NICKEL SURFACE WITH THREE LIGHT SILVER PHASE REGIONS AT ITS TIP. (500X)

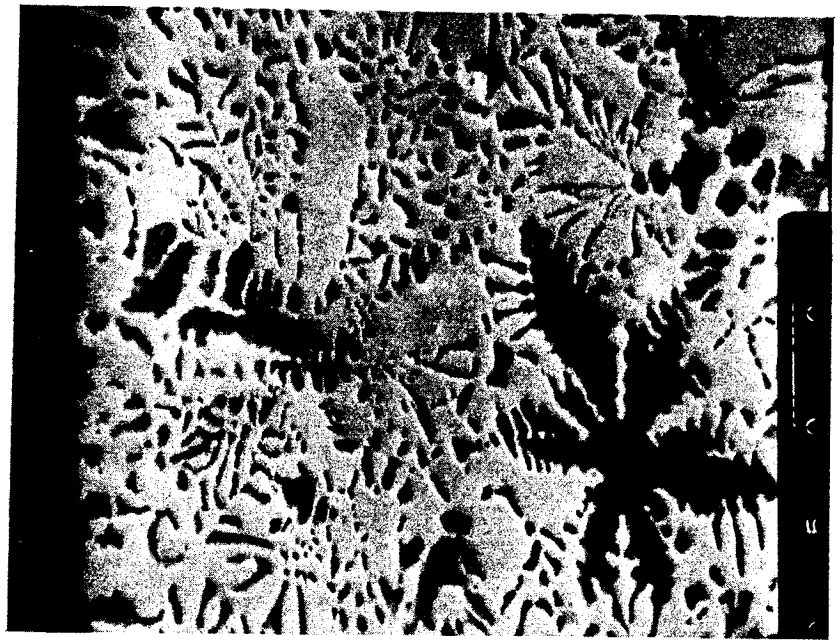

FIG. 21 SCANNING ELECTRON MICROGRAPH OF SLN 4-21mm -120° SHOWING SIMILAR STRUCTURE TO FIGURES 19 AND 20. (500X)

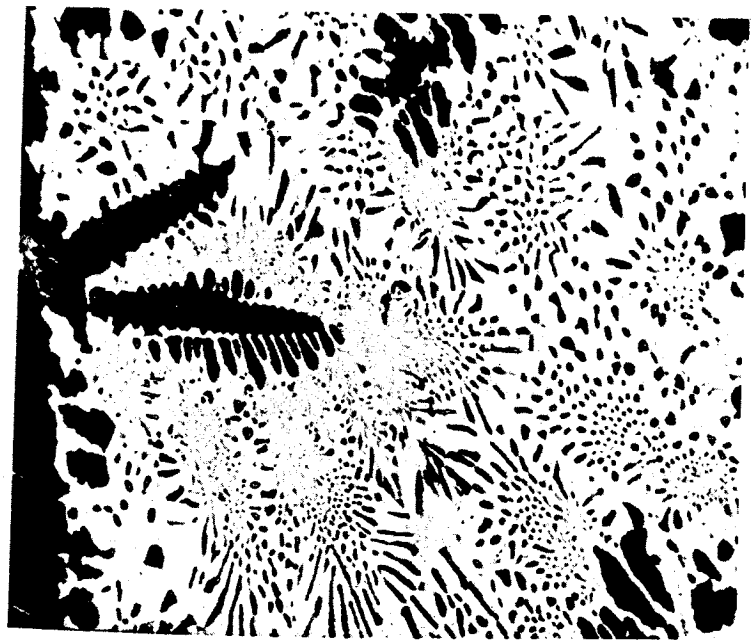

FIG. 22 SCANNING ELECTRON MICROGRAPH OF MCN 6-8mm - 90° SHOWING A TYPICAL COPPER-RICH DENDRITE AND COPPER-RICH REACTION LAYER ADJACENT TO THE PURE NICKEL AT THE FAR LEFT. (500X)

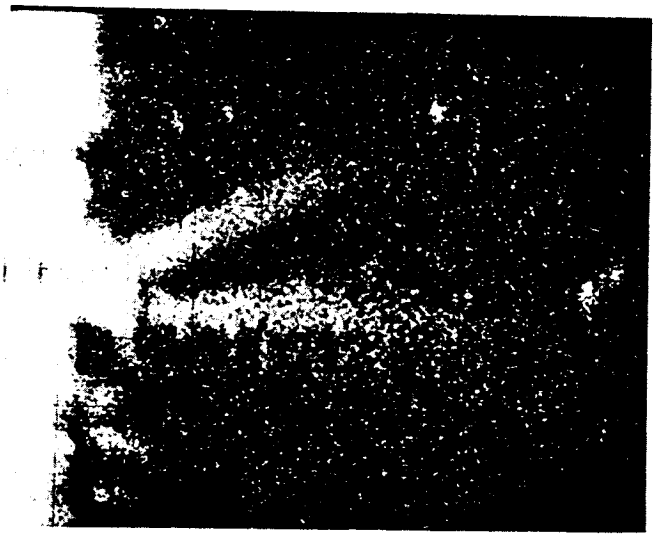

FIG. 23 NICKEL $K\alpha$ X-RAY SCAN OF THE SAME REGION AS FIGURE 22. THE LIGHT AREAS SHOW THE HIGHEST NICKEL CONCENTRATIONS. (500X)

FIG. 24 COPPER $K\alpha$ X-RAY SCAN OF THE SAME REGION AS FIGURE 22. (500X)

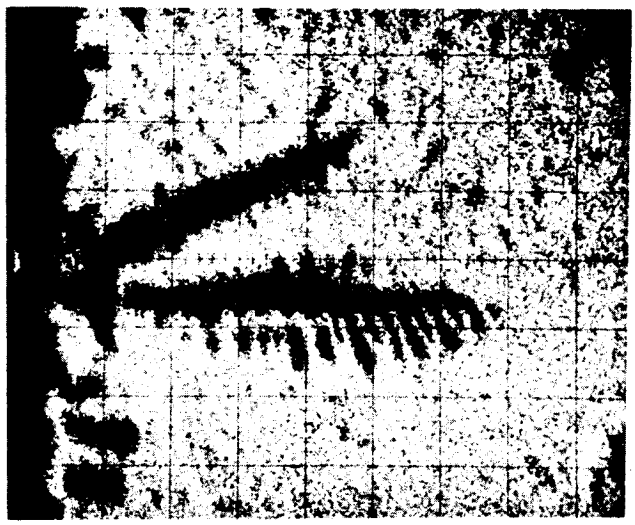

FIG. 25 SILVER Lα X-RAY SCAN OF THE SAME REGION AS FIGURE 22. (500X)

FIG. 26 SCANNING ELECTRON MICROGRAPH OF SLN 4-5mm - 290° WITH A LARGE DENDRITE. (250X)

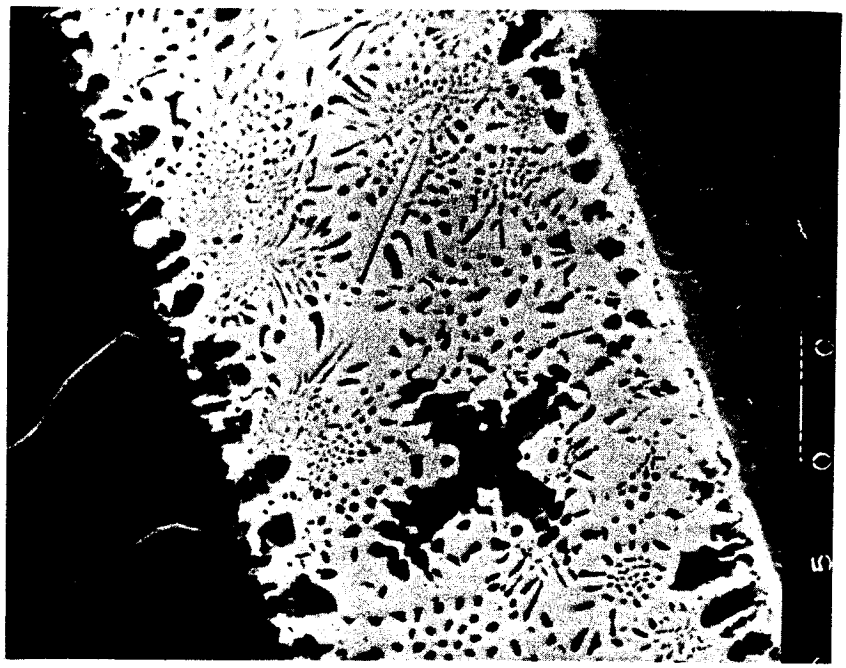

FIG. 27 SCANNING ELECTRON MICROGRAPH OF SLN 4-18mm - 90° ILLUSTRATING THE NORMAL STRUCTURE. (500X)

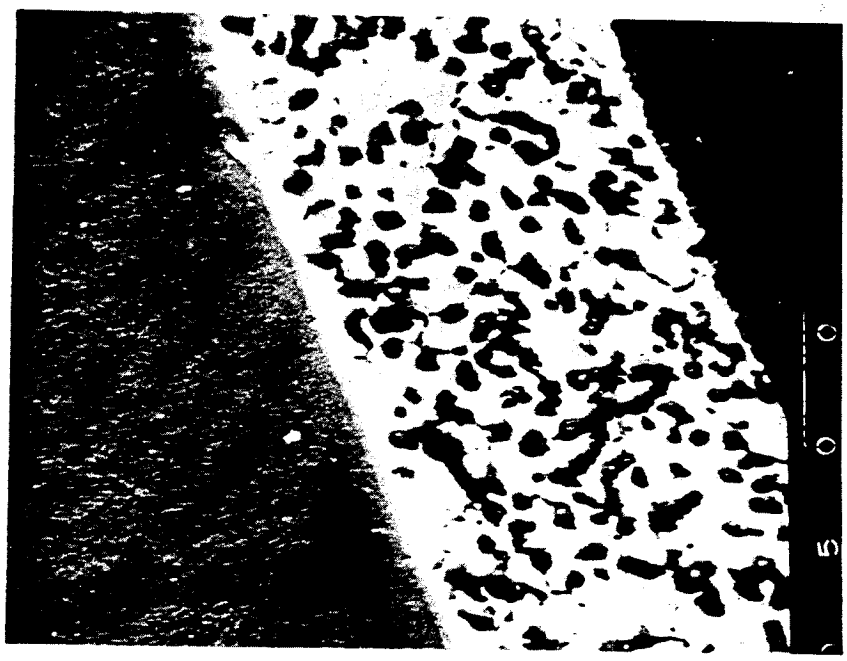

FIG. 28 SCANNING ELECTRON MICROGRAPH OF SLN 4-18mm - 65° ILLUSTRATING THE ABNORMAL STRUCTURE. (500X)

FIG. 29 SCANNING ELECTRON MICROGRAPH OF SLN 4-33mm - 220° ILLUSTRATING THE MIXTURE OF NORMAL AND ABNORMAL STRUCTURE IN THE RING-GROOVE FARTHEST FROM THE ZERO PLANE. (250X)

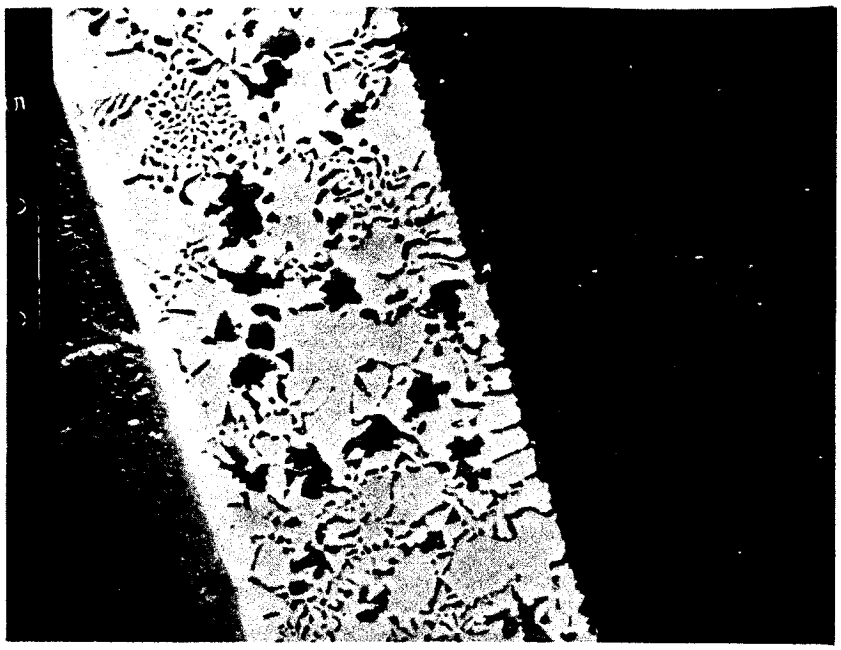

FIG. 30 SCANNING ELECTRON MICROGRAPH OF SLN 4-18mm - 75° ILLUSTRATING THE MIXED STRUCTURE. (500X)

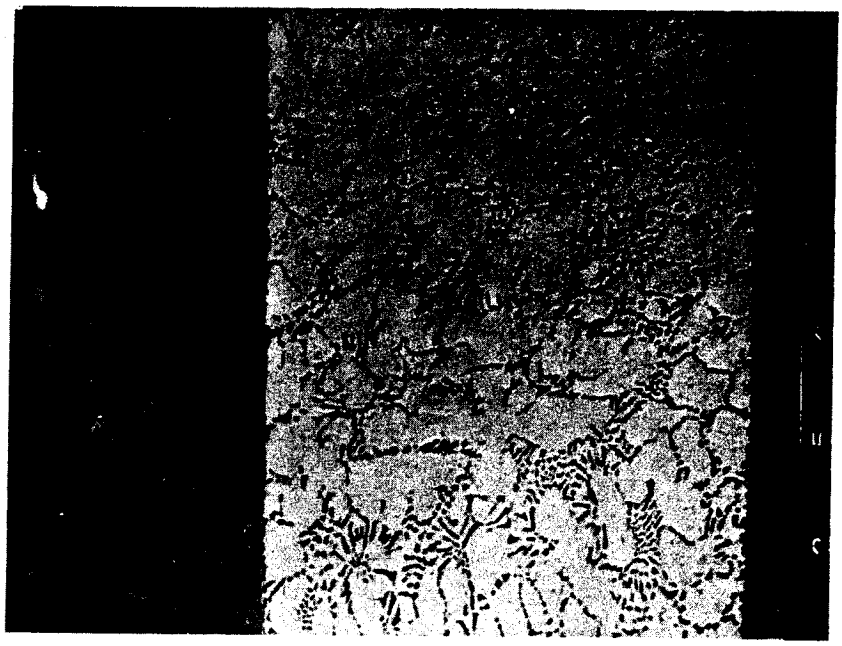

FIG. 31 SCANNING ELECTRON MICROGRAPH OF SLS 3-13mm - 150° SHOWING THE PRIMARY SILVER-RICH DENDRITES (LARGE WHITE AREAS) WHICH WERE NOT OBSERVED ON GROUND CHARACTERIZATIONS. (250X)

FIG. 32 SCANNING ELECTRON MICROGRAPH OF SLS 3-17mm - 5° SHOWING A MORE EXTREME CASE OF THE PRIMARY SILVER-RICH DENDRITES SEEN IN FIGURE 31. (500X).

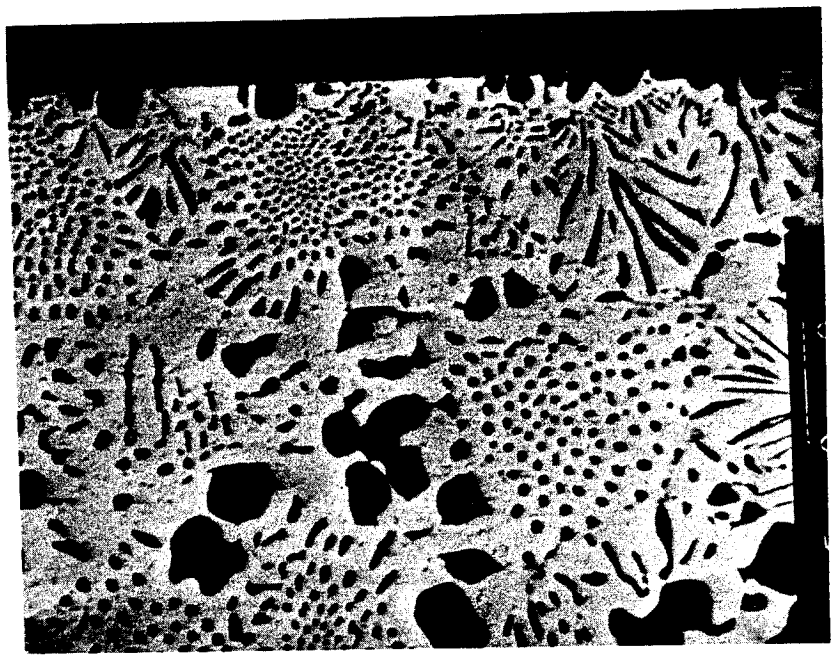

FIG. 33 SCANNING ELECTRON MICROGRAPH OF SLS 3-28mm - 5° SHOWING DENDRITES PRESENT IN THE RING-GROOVE ALONG WITH THE COMPLETE ABSENCE OF THE PRIMARY SILVER PHASE SHOWN IN FIGURES 31 AND 32. (250X)

FIG. 34 SCANNING ELECTRON MICROGRAPH OF MCS 6-11.7mm - 260° SHOWING THE NORMAL EUTECTIC ADJACENT TO STAINLESS SURFACE (AT TOP). (500X)

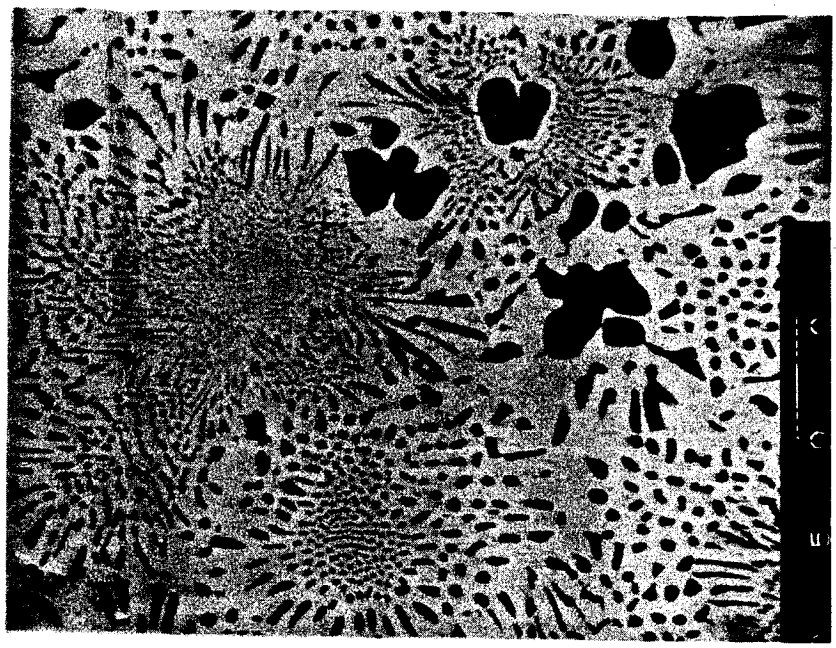

FIG. 35 SCANNING ELECTRON MICROGRAPH OF MCS 6-11.7mm - 280° SHOWING AGAIN THE GROUND CHARACTERIZATION MICROSTRUCTURE. (500X)

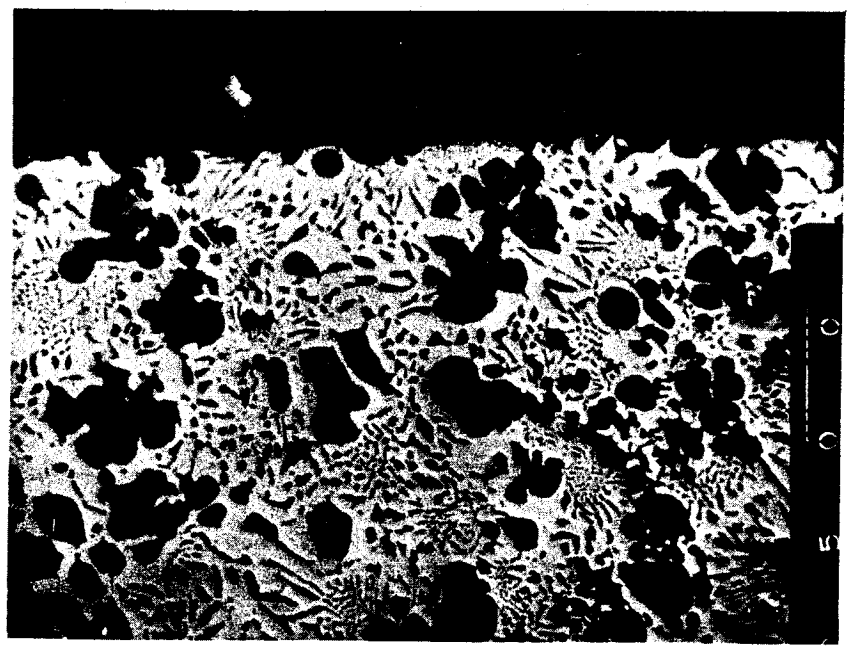

FIG. 36 SCANNING ELECTRON MICROGRAPH OF SLS 3-7mm - 315° SHOWING STAINLESS STEEL PARTICLES NEAR STAINLESS STEEL-BRAZE ALLOY INTERFACE. (500X)

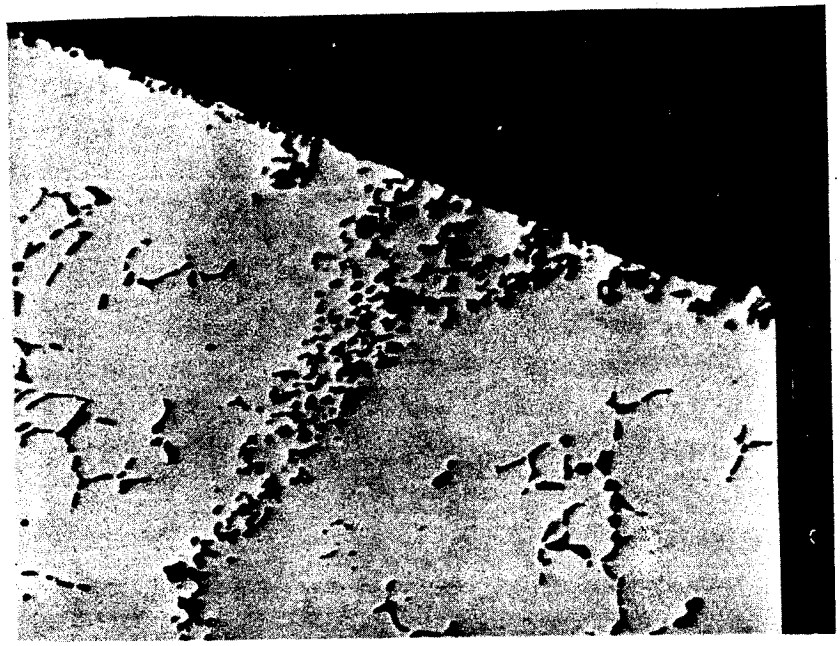

FIG. 37 SCANNING ELECTRON MICROGRAPH OF SLS 3-12mm -5° SHOWING STAINLESS PARTICLES IN BRAZE ALLOY. (500X)

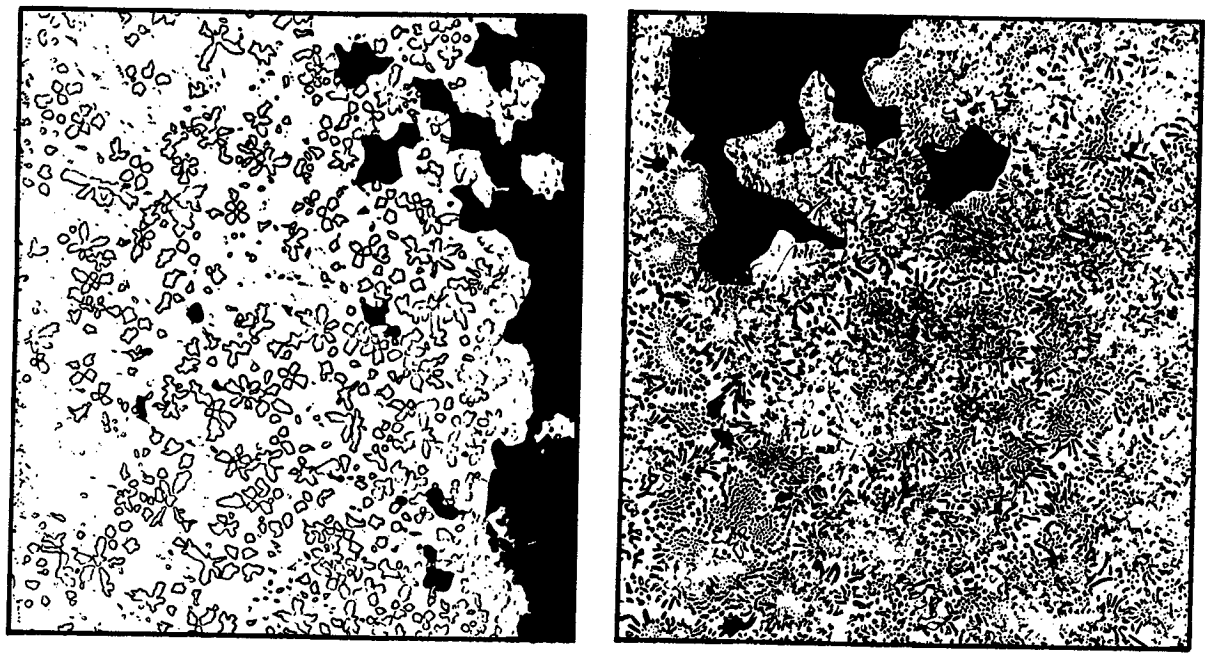

Skylab Ground

Microstructure Ring Groove 100X

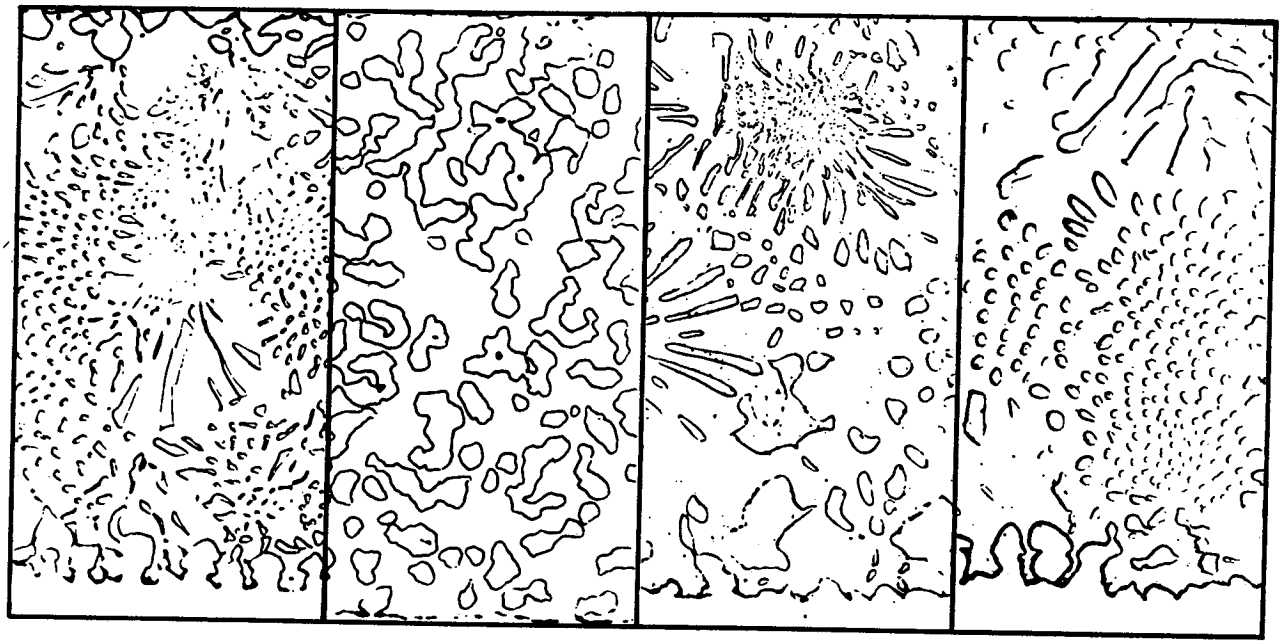

Skylab Ground

Microstructure in Braze Gap-500X

FIG. 38 COMPARISON OF MICROSTRUCTURES IN SKYLAB SPECIMEN SLN-2 AND GROUND BASED NICKEL BRAZE SPECIMENS.

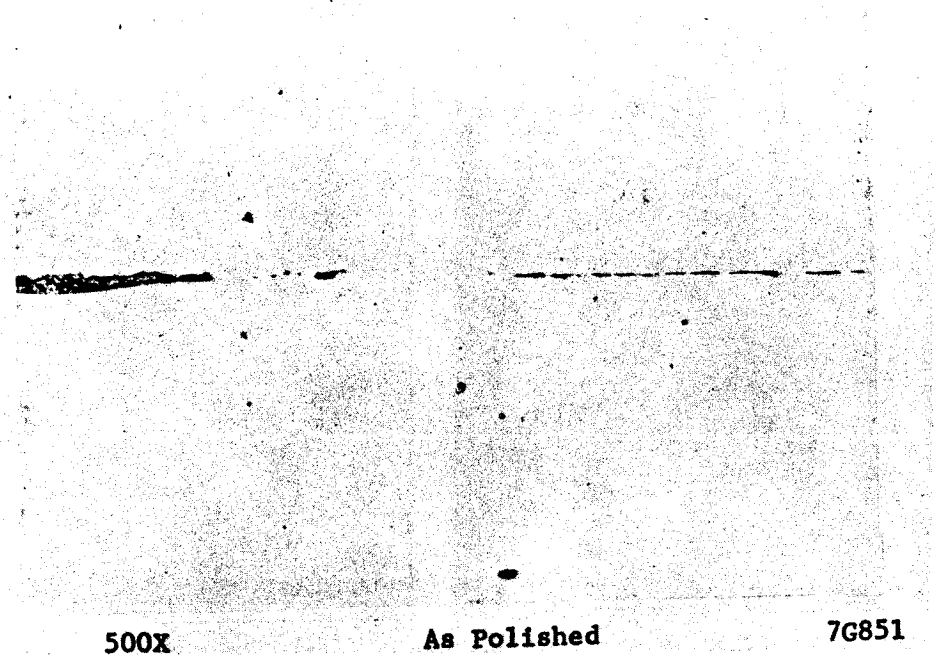

SOLID-STATE BOND AREA -
SECTION SLS-1.4 (14 mm and 0°)

FIG. 39 DIFFUSION BONDED AREA FORMED IN SKYLAB STAINLESS STEEL SPECIMEN SLS-1.

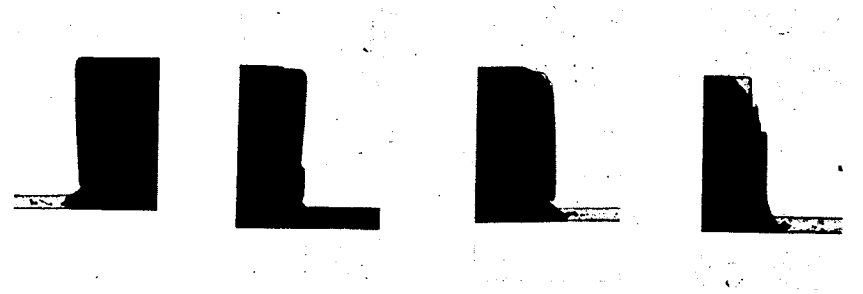

a. Ground Specimens

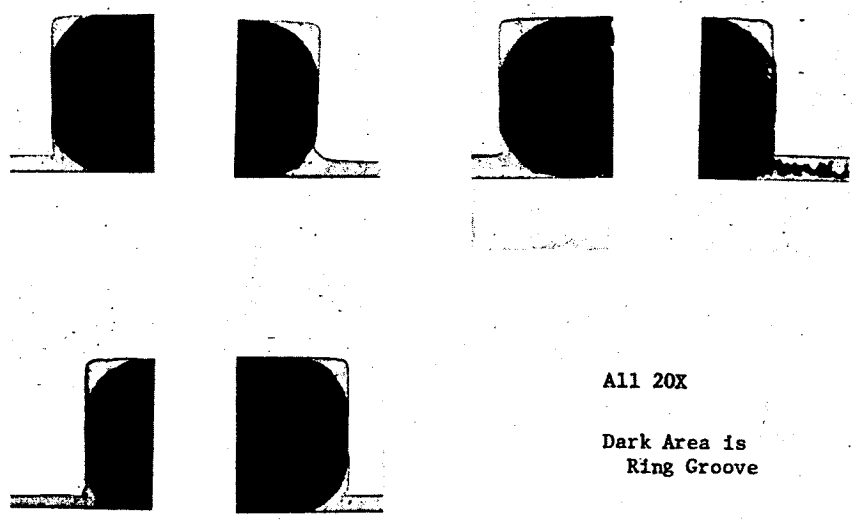

All 20X

Dark Area is
Ring Groove

b. Skylab Specimens

FIG. 40 COMPARISON BETWEEN RETAINED FILLET OF 304L GROUND BASED FILLET AND SKYLAB SLS-1 SPECIMEN

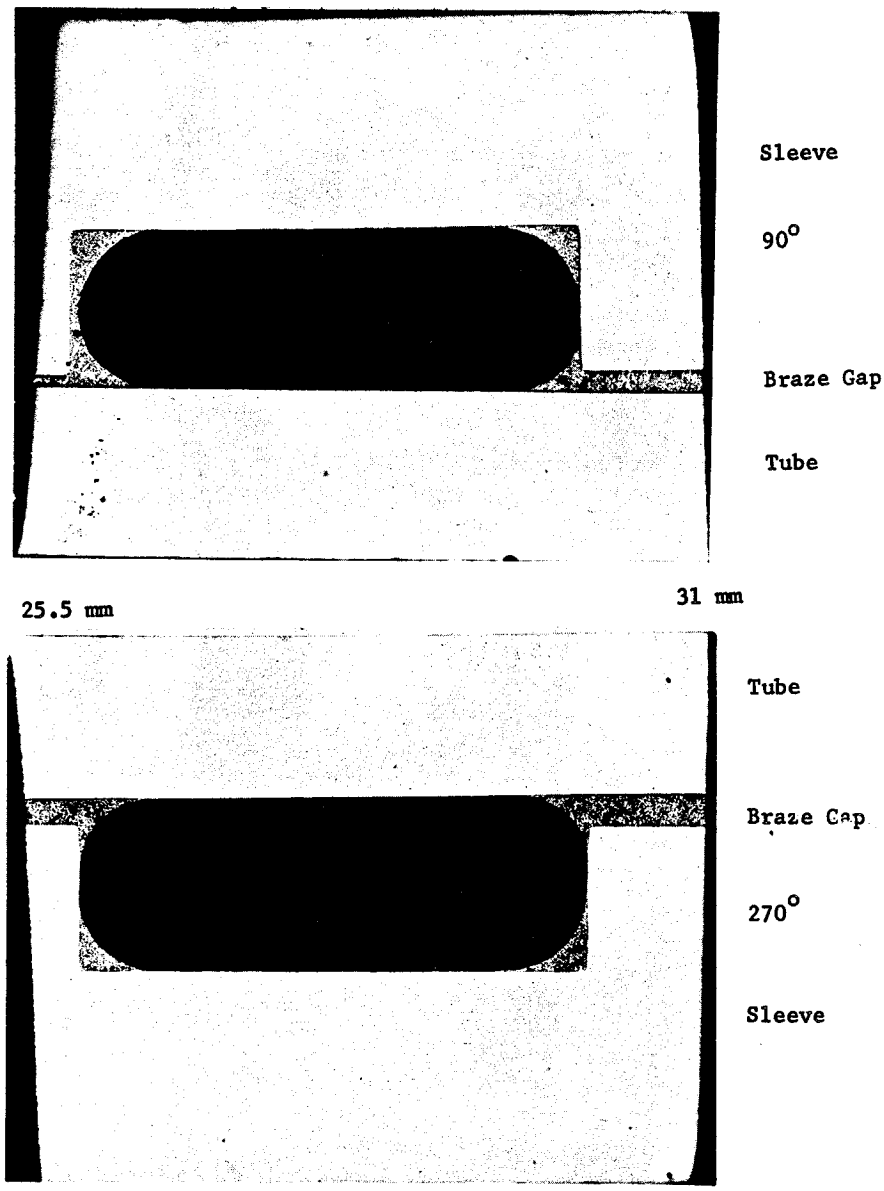

FIG. 41 CLASSIC EXAMPLE OF A BRAZE MATERIAL FILLET RETAINED IN RING GROOVE-SKYLAB SAMPLE SLN-2

SKYLAB M551 METALS MELTING EXPERIMENT

By

E. C. McKannan*, R. M. Poorman
George C. Marshall Space Flight Center, Alabama 35812

SUMMARY

The objectives of the M551 Metals Melting Experiment are to (a) study behavior of molten metal, (b) characterize metals melted and solidified in the low gravity space environment compared to one-gravity of earth, and (c) determine feasibility of joining metals in space. The experiment used the electron beam (EB) and chamber of the M512 apparatus to make a dwell puddle and a melt in a rotating disc of varying thickness. Hence, the EB performed cut-through, full and partial penetration melts, in addition to a re-solidified button. The three disc materials were aluminum 2219-T87, 304 stainless steel and pure tantalum to provide a wide range of density and melting conditions. Observations to date include (a) the proof that EB welding, cutting and melting can be done successfully in low gravity. Earlier, some welding authorities had postulated that without gravity the EB would force the molten puddle out of contact. However, the experiment proved that surface tension forces predominate. (b) From the view-point of cast-solidification, small, equiaxed grains in Skylab specimens compared to large, elongated grains in ground-based specimens were observed. The former are thought to be associated with constitutional supercooling and nucleation where the latter are associated with dendritic solidification. In further support of the more equiaxed grain growth in Skylab, symmetric subgrain patterns were frequently observed where there was much less symmetry in ground-based specimens. Further work is being done to explain the differences in solidification.

INTRODUCTION

The M551 Skylab Metals Melting Experiment evolved from an earlier plan for a welding experiment. It was changed and broadened to include melting and solidification of practical metals as speculation about the effect of low gravity on these phenomena increased. In this paper we will cover the status, background and history of that development, the final objectives, M512 electron beam apparatus and procedures used in ground studies, aircraft and Skylab. Emphasis will be placed on evaluation of results including a macro-view of the welding implications and a micro-structural view of the metallography of solidification in Skylab versus earth-bound experiments.

*Paper presented by E. C. McKannan.

OBJECTIVES

The objectives of the M551 Metals Melting Experiment are to (a) study behavior of molten metal in low gravity with particular attention to the stability of the molten puddle and its interface with the solidified metal. (b) Characterize metals solidified in low gravity with regard to grain size, orientation, sub-grain patterns as might be effected by the difference in convection during solidification. (c) Determine feasibility of joining and casting metals in space.

HISTORY

The M551 Metals Melting Experiment has evolved from several closely related lines of study and development work. Its original motivation came from studies performed in the early 1960's on methods of assembling structures in space. During that period it was expected that construction and maintenance of large orbital space stations would involve assembly of structural members in space, and the consensus of several studies was that electron beam welding would be the best process for performing the necessary joining operations.

Development work on compact electron beam welders was initiated by MSFC in 1963, and an electron beam welding experiment was proposed for the S-IVB Workshop in the fall of 1964. A portable welder was developed by the Westinghouse Electric Corporation for weld repair, limited weld fabrication and melting. The experiment was formally approved by the Manned Space Flight Experiments Board (MSFEB) in December 1966, as the M493 Electron Beam Welding experiment.

At about the same time, the MSFC began to explore the prospects for possible space materials manufacturing of products for use on Earth. Considerable interest was developed in the idea through contacts with industrial firms and studies performed in-house while development work on the experiment proceeded. As a result of this interest, it was suggested in 1968 that the capabilities of the apparatus should be exploited to perform some preliminary space materials experiments.

Concepts for additional manufacturing experiments were studied, and at the same time the M493 experiment was reassessed to determine its applicability to the new space materials manufacturing discipline. The outcome of these studies was a proposal of concepts for experiments to be performed in a modified version of the M493 apparatus. The concepts included a revision of the original welding experiment to pursue more general objectives under the title, Metals Melting.

SOVIET EXPERIMENT

While the Metals Melting Experiment was under development, a fairly extensive program of work on welding and cutting metals in space was carried on in the USSR by the E. O. Paton Welding Institute of the Ukraine SSR Academy of Sciences. This work was specifically directed toward space repair and

construction methods, and included electron beam, low-pressure plasma arc, and consumable electrode techniques. After an initial test program using ballistic trajectory aircraft flights, a space experiment was performed in October 1969, on the Soyuz-6 manned space mission.

Welding experiments were performed with stainless steel, aluminum alloy, and titanium alloy, and the space experiment seems to have been performed mainly to verify that satisfactory welding conditions for weightless materials had been established during the aircraft flights. The only available publication on this program does not mention that any intensive analysis was made of the grain structures produced by weightless solidification, but it points out that welding heat sources might also be used to process materials in space.

Planning for the Metals Melting experiment has taken account of what is known of the Soviet experiment and its results. Some of the Soviet work was duplicated. We believe that the data analysis of the Metals Melting experiment goes considerably beyond what has been done in the USSR to study fundamental solidification effects in weightless melts.

BALLISTIC TRAJECTORY AIRCRAFT

During June and July 1972, three flights were made in an Air Force KC-135 aircraft flying ballistic trajectories to achieve low gravity for a brief period. The M512 apparatus was mounted and specimens were installed to simulate operations in Skylab, albeit for 15-25 seconds only, at a time. While these flights were essential for developing and checking procedures and proving the operation of equipment, they did not provide enough time at low gravity to obtain a complete cycle of melting and solidifying before the aircraft pulled out of the low gravity trajectory and into a high gravity condition. Hence we were not able to make useful metallographic studies of low gravity solidification from this phase of the program.

EQUIPMENT DESCRIPTION

The M551 experiment was performed June 1973 in the M512 Materials Processing Facility on Skylab I. A detailed description of the facility and its interface with the Skylab system is given in Experiment Implementation Plan.

The basic equipment used for the Metals Melting experiment is shown in Figure 1; it consists of an electric motor drive mechanism which is attached to a three-legged mounting base and carries the disk-shaped experimental specimens as shown. The motor is a nominal 24 v. 1760 rpm D. C. motor, and the gear reduction in the drive mechanism is 300:1; in order to arrive at the output shaft speed of 2. 6 rpm required for the experiment, the motor armature speed is reduced by running at an actual input voltage of only 12 v. Power for the motor is supplied through the cable connector shown on the end of the assembly. The specimen track to be traversed by the electron beam is visible along the junction between the specimen's inner disk and outer ring.

Figure 2 is a sectional scale drawing of the M512 facility's work chamber with the Metals Melting fixture mounted in it. In this drawing the electron beam port is directly behind the specimen, and the beam direction is perpendicular to the plane of the figure. The sample is mounted at a distance of 1.5" from the beam port.

The mounting base of the fixture is attached by captive screws at three points around the opening of the heat sink well in the side of the work chamber. Electric power is led from the zero-g connector at the top of the chamber by a cable to the motor, and is controlled by a switch on the facility's control panel. The same switch initiates photographic recording by the sequencing camera during runs of the experiment.

The work chamber's camera port is in the lower hemisphere, and inside the chamber it is covered by an aluminum housing containing a diagonal mirror. A second mirror is just above the port, mounted in a recess in the flange surrounding the electron beam port, which is at the upper right inside the chamber. These two mirrors reflect the image of the beam impingement area on the specimen to the camera mounted outside the chamber. A third mirror mounted above the electron beam port permits the operator to view the face of the sample through the viewport in the cover of the working chamber. Light for this is provided by a small lamp in the recess to the left of the electron beam port.

The disk mounted on the drive mechanism is one of the specimens. The sample thickness required for the experiment is provided by milling channels to different depths in the back of the plate. A schematic drawing of the specimen used in the experiment is shown in Figure 4. Photographs of an actual specimen are shown in Figures 5 and 6. Materials are listed in Table I.

PROCEDURES

Three discs of varying thicknesses were processed in space by the electron beam welder: The first was 304 type stainless steel, the second a 2219-T87 aluminum, and the third pure tantalum. Singularly, each disc was placed in a work chamber, and the work chamber was vented overboard to space vacuum conditions. The electron beam was initiated in sharp focus on the target area of the disc, and the beam was adjusted and held at 80 Ma. and 20 Kv. Each disc was then rotated to provide 35 inches per minute travel speed on a 4.75 inch diameter. The specimens were designed with a thin section as the travel started. This provided a cutting action by the beam for 45 degrees of rotation. Here, the thickness gradually increased over 90 degrees of rotation to a value which provided a normal penetration of the electron beam weld. After 90 more degrees of rotation the thickness step increased to provide a partial penetration weld for 45 degrees. Here, at a 1/4 diameter hole, the beam was terminated. The disc was rotated another 22 degrees and was stopped at the dwell area. The electron beam was defocused and reinitiated for the dwell portion of the test. On the stainless steel and aluminum discs, dwell times were 15 seconds, while the dwell on the tantalum disc was 45 seconds. Thus, a large molten pool formed and solidified.

All discs were processed the same except that the tantalum weld used 70 Ma beam current. Thickness on the stainless steel and aluminum ranged from . 025 to . 250 inches. The tantalum values were . 017 to . 062 inches.

With each specimen the work chamber was vented overboard for two hours, and even so, the vacuum level during welding was only approximately 10^{-4} torr. Astronaut Pete Conrad performed the following steps in accomplishing the M551 Experiment:

a. Verify and check the M512 control panel.

b. Mount the first metals melting sample in the M512 vacuum chamber.

c. Establish vacuum.

d. Perform the weld cycle and make motion pictures at 24f/sec of the traversing beam.

e. Allow sample to cool (approx. 2 1/2 hrs.).

f. Pressure equalize the M512 vacuum chamber.

g. Remove and stow the metals melting sample.

h. Repeat steps b thru g for the remaining two metals melting samples.

During the metals melting experiment the vacuum conditions in the work chamber were reported as abnormal by the astronauts. Close examination of all flight data indicated vacuum sequencing was normal. The absolute pressure in the work chamber was somewhat higher than expected but within the normal operating limits of the experiment. The absolute pressure outside the Skylab was somewhate higher than expected. Hence, work chamber vent time to vacuum was greater than expected.

An extensive review of vacuum pressures and vent time by S&E-ASTN-ME shows all pressures and systems were normal. Values were within our operating range. No anomalies are believed to be related to the vacuum systems in the metals melting facility M512.

CHARACTERIZATION PLAN

After receiving specimens, both groundbased and Skylab flight, we at MSFC photographed for identification, measured distortions and weighed each one of them. R. E. Monroe at Battelle Memorial Institute radiographed, sectioned and sent designated pieces back to MSFC and others. Both groups did metallographic analyses and provided data to the following researchers for their analyses. At this time we are still involved in discussions of the implications of the microstructures presented here. The differences in interpretation, particularly with regard to the evidence of probable types and levels of convection, indicate that there is still much to be done to reap the full benefit of the experimental evidence from Skylab.

M551 METALS MELTING TEAM

Name	Affiliation	Specialty
Mr. Robert Monroe	Battelle Memorial Institute	Joining Research-Metals
Prof. C. M. Adams, Jr.	University of Wisconsin	Joining Research-Metals
Prof. Koichi Masubuchi	Massachusetts Institute of Technology	Stress Analysis & Thermal Treatment
Dr. Martin Tobin	Westinghouse	Surface Tension
Dr. Philamina Grodzka	Lockheed-Huntsville	Solidification & Convection Physics
Dr. M. R. Brashears	Lockheed-Huntsville	Solidification & Convection Physics
Dr. S. V. Bourgeois, Jr.	Lockheed-Huntsville	Solidification & Convection Physics
Dr. A. A. Smith	British Welding Institute England	Joining Research-Metals Physical Testing

The data packages included ground base data, flight and groundbase film of M551 experimental sequence, and flight data. Each member of the consultant team has been in constant touch with one another for experiment definition, plan, and data analysis.

WELDING ANALYSIS - A MACROVIEW

Gravity effects appear to be small in the weld nugget configuration and puddle control of all three materials when related to typical welding problems. In all cases there was greater puddle sagging in the groundbase specimen with one gravity compared to the Skylab specimen with low gravity. This was particularly true for the weld dwell periods of 15 and 45 seconds. In the over, full, and partial penetration phases, puddle sag was very slight. Frequency of surface ripple, beading and weld spatter appeared to be somewhat related to gravity. All three were slightly reduced in the Skylab specimens which were melted in low gravity. These parameters are of more interest to a scientific study of solidification than to the practical aspects of welding. Basically, this experiment indicates that molten metal surface tension is the predominant force controlling the weld puddle. In low gravity the weld nugget is more symetrical. All weld puddling and control techniques that are applicable on earth would be expected to be useful in welding in a space environment. Hence, this experiment has demonstrated the feasibility of welding in space. This subject is developed in detail in a report by R. E. Monroe of Battelle Memorial Institute. (1)

METALLOGRAPHIC ANALYSIS OF MICROSTRUCTURE

A typical cross-section, magnified 10 and 100 times, of the aluminum 2219-T87 partial penetration melt is shown in Figure 7. The groundbase melt shows the familiar large grains often seen in weldments and castings with columnar grain growth oriented perpendicular to the solidification front. It also shows heavy banding, the fine, equiax-grained chill zone and the grain growth of the unmelted, heat-affected zone. The large, elongated grains are explained on the basis of dendritic freezing and the finer-grained chill zone is described on the basis of greater super cooling (temperature differential), as described by Chalmers (2) and Reed-Hill. (3)

By contrast the Skylab specimen which was solidified in low gravity under otherwise identical conditions, shows a major reduction in large, elongated grains; an increased width of the finer-grained chill zone and almost no banding. This can be explained if there was, as predicted, a reduction in thermal convection which is accompained by a greater temperature differential at the solidifying interface. In addition, the reduced convection would provide less mixing and greater constitutional super cooling which would produce nucleation of many more but smaller grains of varying composition. Constitutional super cooling results when a solid freezes with a composition different than that of the liquid from which it forms. (3) Instability of the freezing interface results in sub-grain micro-segregation which breaks up the banding seen in the groundbase specimen. Hence, there are differences in the solidified microstructure between one and low (10^{-4}) gravity which may have important implications for obtaining finer-grained castings in space.

Figure 8 shows a cross-section (100X) of the solidified aluminum in the full penetration area of the specimen. It clearly shows the differences in the sub-grain microsegregation between the groundbase and Skylab specimens. A symmetrical, rosete pattern in the Skylab specimen indicates the lack of a directed gravity force when compared to the groundbase specimen in which there is an alignment from upper left to lower right. The more pronounced sub-grain structure in the Skylab specimen obtained by an identical etching procedure to that used on the groundbase specimen is another possible indication of increased microsegregation and constitutional super cooling in low gravity.

The partial penetration molten area of the 304 stainless steel is shown in Figure 9. The molten zone is thiner and the interface is sharper than the aluminum because of the lower thermal conductivity. The shape of the spike is a result of the electron beam power profile and beam focus; it is a single-pass weld. The root of the spike is an interesting place to study solidification phenomena. As in the aluminum, large elongated grains perpendicular to the solidification front can be seen in the groundbase specimen compared to the finer grains of the Skylab specimen which solidified at a low gravity. The bands of segregations which are interrupted by some grains appear to have occurred after solidification. These bands are being subjected to further study by microprobe analysis of composition and phase.

Figure 10 shows a cross-section and a top view (10X) of a pure tantalum full penetration melt. Being a commercially pure metal with almost no alloying except minor amounts of columbium, there were no complex precipitants during solidification and very large, clean grains were formed. The most interesting observation from the groundbase specimen is that the residual vortices left behind after the electron beam passed were frozen into the grain structure. These occurred because of the rapid cooling rate at the high melting temperature. Although the thermal characteristics and travel speeds were comparable for the Skylab specimens, the residual vortices were erased in the grain structure. This may have been due to the fact that final grain size of the solidified material was smaller in the Skylab specimen compared to the groundbase specimen. The finer grains in the Skylab specimen were observed in all three materials with a wide range of properties.

CONCLUSIONS

1. This experiment demonstrated the feasibility of doing electron beam welding, cutting and melting in the low-gravity environment of space.

2. Large elongated grains observed in groundbase specimens where there were smaller, equiaxed grains in Skylab specimens indicate that there was a major difference in convection during solidication of three metals with a variety of physical properties.

3. The more equiaxed grain growth in Skylab, with symmetric sub-grain patterns was observed where there was orientation associated with the solidification front in ground-based specimens.

REFERENCES

1. Monroe, R. E., Characterization of Metals Melting Discs: Skylab Experiment M551 NASA Contractor Report NAS8-28725, December 4, 1973.

2. Chalmers, B., Principles of Solidification, John Wiley and Sons, New York 1964

3. Reed-Hill, R. E., Physical Metallurgy Principles, Van Nostrand Company, New York 1964

ACKNOWLEDGEMENT

The authors wish to gratefully acknowledge the important participation of the following individuals in this work.

Wendell DeWeese
Herman Gilmore
Robert Hoppes
Richard Parr

TABLE I
MATERIALS USED IN EXPERIMENT M551
METALS MELTING

Identification	Aluminum 2219-T87		Stainless Steel 304		Tantalum	
Density, g/cc	2.83		8.03		16.6	
Melting Point, ^{o}C	638		1442		2996	
Thermal Conductivity cal/cm/sec/^{o}C	0.6		0.38		0.13	
Composition, %	Cu	6.2	C	0.05	Ta	99.5
	Mn	0.3	Mn	1.5	Cb	0.1
	Ti	0.15	Si	0.75		
	Mg	0.02	P	0.04		
	Fe	0.25	S	0.03		
	Si	0.15	Cr	19.0		
	Zn	0.10	Ni	8.5		
	Al	bal	Mo	0.5		
			Cu	0.5		
			Fe	bal		

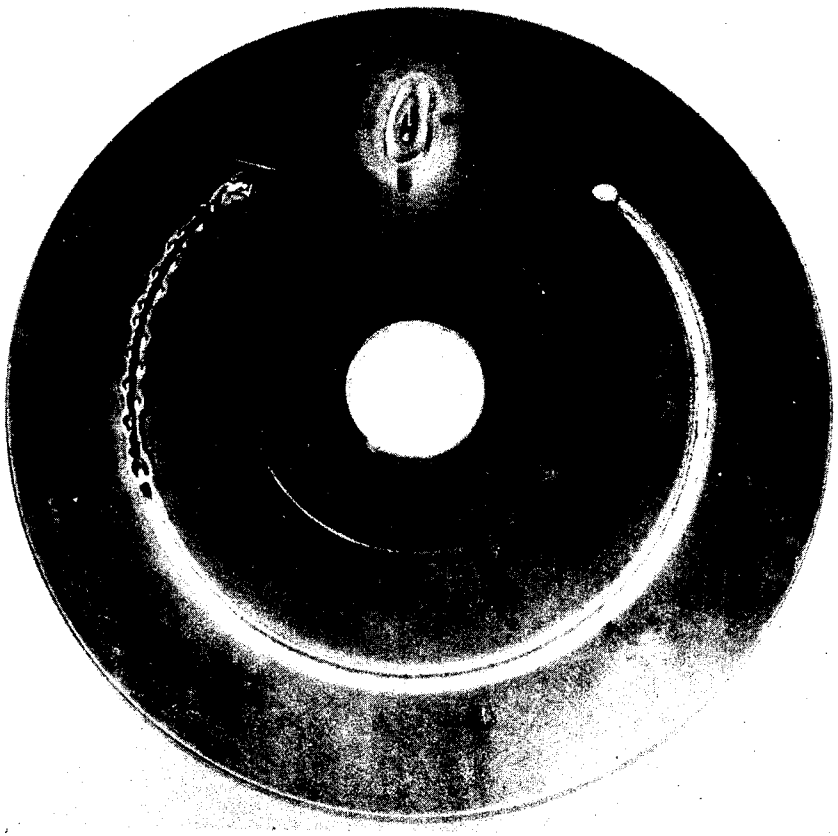

FIGURE 5. SKYLAB STAINLESS STEEL SAMPLES
S/N 106 (FRONT)

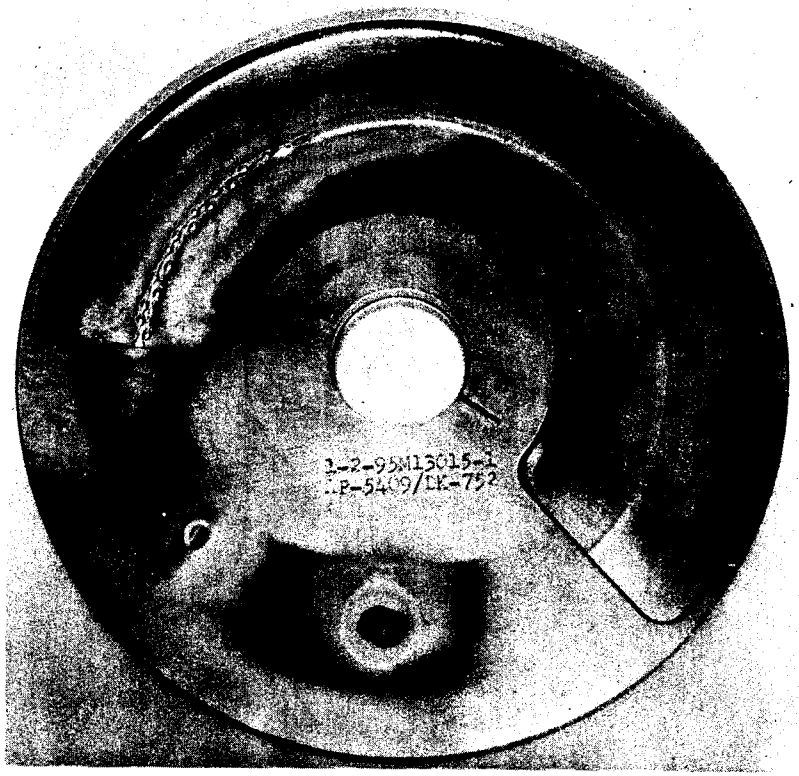

FIGURE 6. SKYLAB STAINLESS STEEL SAMPLES
S/N 106 (REAR)

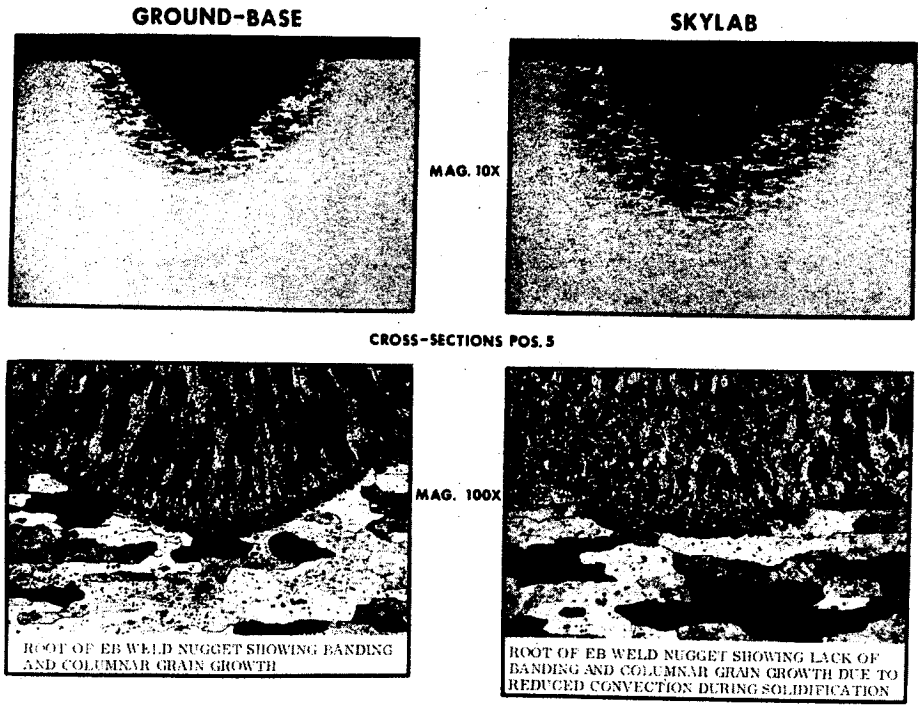

FIGURE 7. COMPARISON OF GROUND-BASE & SKYLAB EB WELDS IN 2219-T87 ALUMINUM

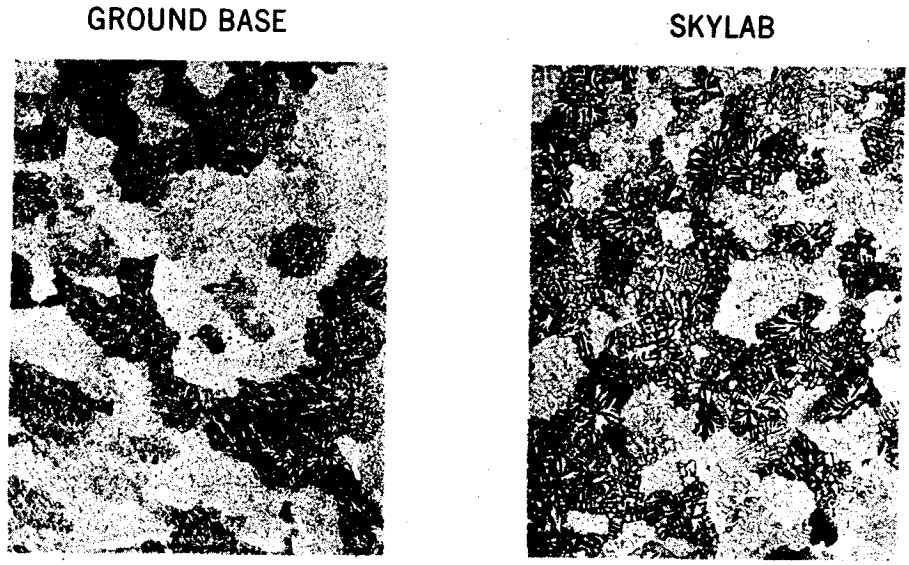

FIGURE 8. WELD STRUCTURES IN GROUND BASE & SKYLAB FUSION ZONES

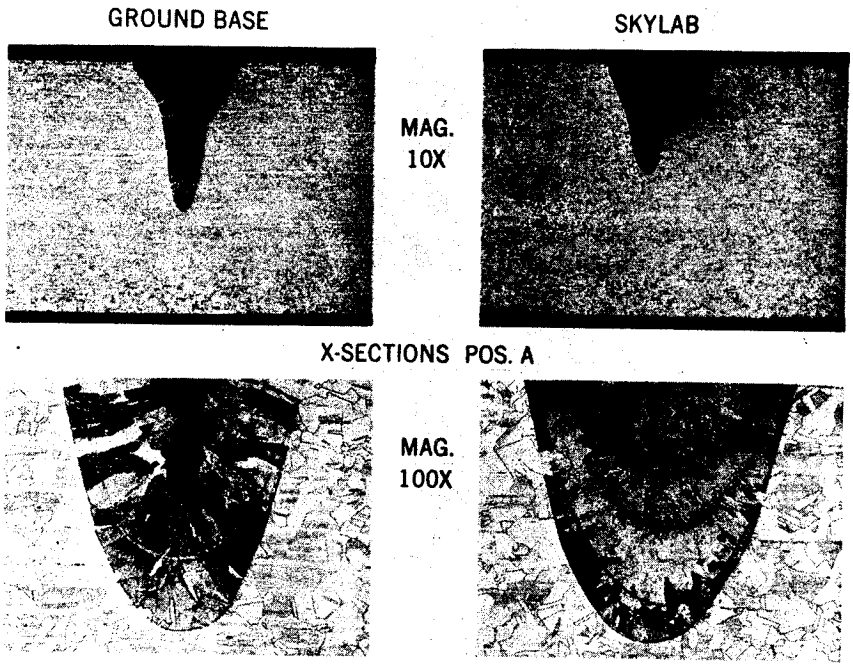

FIGURE 9. GROUND BASE & SKYLAB EB WELDS IN 304 STAINLESS STEEL

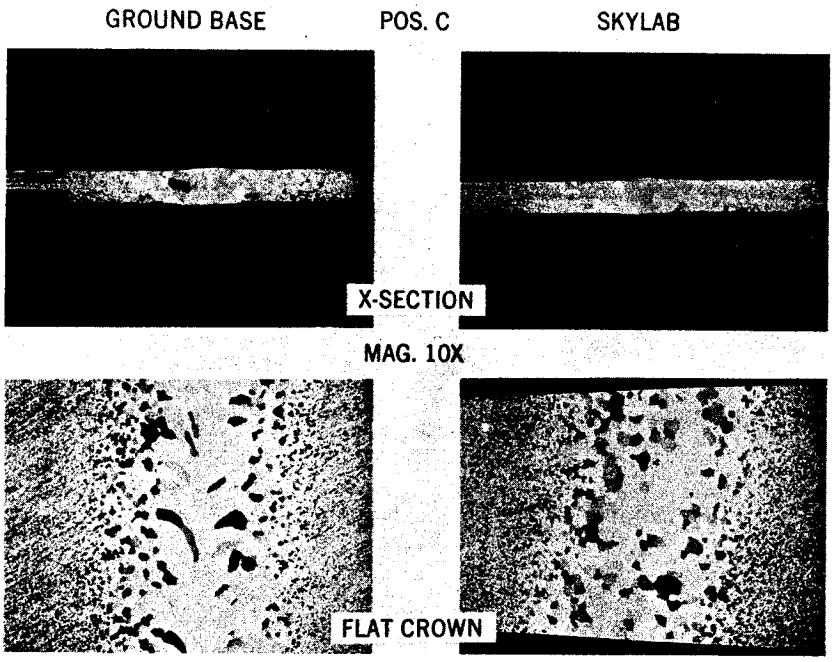

FIGURE 10. GROUND BASE & SKYLAB EB WELDS IN TANTALUM

SKYLAB M553 SPHERE FORMING EXPERIMENT

By

D. J. Larson
Research Department
Grumman Aerospace Corporation
Bethpage, New York 11714

SUMMARY

The M553 Sphere Forming Experiment was conducted in the M512 Furnace Facility during Skylab II. The experiment was designed to study the effects of weightlessness in solidification processes. Four face centered cubic materials of varying alloy contents and solidification reaction types were studied.

Careful analysis of the samples indicated that there was an outstanding record of both initial and terminal solute redistribution processes, and that this record may be substantially better than that obtained terrestrially for comparable experimental conditions. Further, the last regions to solidify evidence extensive solidification terracing; and for one alloy type, this terracing was found to be decorated with second phase precipitate particles. These particles were highly localized in systematic arrays which were frequently low index crystallographic systems.

Some of the samples underwent unanticipated solidification reactions rather than the anticipated solid/liquid processes. Subsequent consideration indicated that this phenomenon could have been anticipated and that it was a result of the reduced gravity environment — that is, the reduced gravity environment magnified a typically microscopic phenomenon terrestrially so that it became a macroscopic effect. Work is continuing on quantifying this effect.

It is felt that these and subsequent results will contribute to the detailed understanding of terrestrial solidification processes and have shown the importance of considering the gas phase during space processing. Whereas prior consideration of one-gravity

solidification dealt with liquid/solid reactions, this work indicates that consideration of solid/liquid/gas reactions is important and potentially beneficial in a reduced gravity environment.

INTRODUCTION

The M553 Sphere Forming Experiment conducted in the M512 Furnace Facility during Skylab II was designed to study the effects of a reduced gravity environment on the containerless solidification of face centered cubic metals. The metals studied were: pure Ni, Ni-1 wt % Ag, Ni-12 wt % Sn, and Ni-30 wt % Cu. The constant primary crystalline structure was selected because the solidification theory for face centered cubic materials is the most advanced (Reference 1) and offered an attractive basis for planning the experimentation and evaluating the results.

The materials were electron beam melted and were either retained on stings of the same composition as the specimen or were to be released while molten, and solidified while floating free within the chamber. The latter operation was not entirely successful and some specimens intended to be released remained on their ceramic pedestals.

The present paper presents an overview of results obtained in the metallographic characterization conducted by the four investigative groups: University of Connecticut, Georgia Institute of Technology, Grumman Aerospace Corporation, and Arthur D. Little, Incorporated. We first cover features of the alloys that were similar and then features that were unique to certain alloys. In the latter area we describe a reaction that is unique to the weightless environment.

DISCUSSION

Prior to considering the differences between the different alloys, we will first discuss those features which were similar among all the alloys. It was anticipated that the reduced gravity environment would enhance the sphericity of the processed samples and this enhancement is shown in Figs. 1a and 1b for 1 g and low g specimens, respectively. Typically, the 1 g specimens had a sphericity value (R_{max}/R_{min}) of 1.28, whereas the flight samples were typically 1.01 to 1.04, a substantial enhancement due to the reduction in gravity.

Figure 2a illustrates the variation in surface morphology of both the terrestrial and flight samples. The lower portion of this sample is composed of epitaxially nucleated columnar dendrites that have grown rapidly into the melt from regions of remnant unmelted solid, or from the pedestal region. As the ratio of thermal gradient (G) to growth rate (R) decreased to a critical level, the columnar growth decayed to an equiaxed free dendritic form (Reference 2). These dendrites are located in the mid region of Fig. 2a and were the last regions to solidify. The last region to be considered is uppermost in Fig. 2a and appears to cap the other regions. This is a region of nucleation and growth that occurred on the liquid surface. The cap has assumed the dimensions of the liquid sphere, and its dimensions are thus greater than that of the lower region, which is defined by the volume of the solid. This results in the obvious height increment at the interface between the liquid surface nucleated cap and the equiaxed dendrites (Reference 3). In the cap region adjacent to the last region to solidify, there are substantial interdendritic shrinkage cavities. These are shown in Fig. 2b. The growth in the surface nucleated region progressed laterally on the two dimensional liquid surface and radially inward. The radial growth is also shown in Fig. 2b.

The relative proportion of these three regions varied depending on the thermal history of the individual samples. The samples that solidified while freely floating after total melting and those that had only a point contact of remnant unmelted solid (sting samples) solidified via surface nucleation and growth over virtually the entire sample. The samples that remained in contact with the pedestal (all of the ground base samples), that had remnant unmelted solid, or that impacted on the chamber wall during solidification all evidenced extensive areas of epitaxial growth and reduced surface nucleated growth.

An interesting aspect of the flight alloys that solidified by a surface nucleation mechanism was that all three principal growth mechanisms (platelet, cellular, and dendritic) could be active on the same surface. Microcompositional mapping in ⟨100⟩ directions indicated that the selection of growth mechanism was determined more by local thermal conditions (G, R) than by compositional fluctuation. This underscores the importance of controlling thermal parameters in containerless solidification so that the growth mechanism can be preselected.

We have introduced the areas of constancy among the samples. The differences are of equal importance and they will now be discussed.

The materials differed in solute content and in solidification reaction type. It was anticipated that the differing alloy content would affect the degree of constitutional supercooling during the bivariant portion of the solidification and would, in concert with the thermal parameters, result in a diversity of solidification mechanisms. This anticipation was confirmed: the lowest solute content alloy is (Ni-1 Ag) solidified primarily by a cellular mechanism whereas the higher solute content alloys (Ni-12 Sn, Ni-30 Cu) solidified dendritically. The sequential appearance of solidification mechanisms occurred only as surface reactions when the G/R value was sufficiently high. These flight samples reverted to the above mechanisms within the bulk of the samples as the G/R value decreased.

An additional variation was that two of the alloys (Ni-1 Ag and Ni-12 Sn) demonstrated solidification in which the bivariant solidification is superceded by a univariant solidification reaction in the last regions to solidify. These reactions were, respectively, monotectic and eutectic in nature. These univariant reactions gave some interesting results.

Considering the eutectic solidification of the Ni-12 Sn alloy first, the proeutectic solidification in the last regions to solidify was dendritic. The interesting features were that the proeutectic dendrite tips were clearly terraced where they were exposed by interdendritic solidification shrinkage, and that some of those dendrites were decorated by arrays of the intermetallic (Ni_3Sn) eutectic constituent. Careful investigation of the platelet and cellular solidification regions of the flight samples indicated terracing during these mechanisms, as well, although they were not decorated with intermetallic particles. The platelet and dendritic terracing is shown in Figs. 3a and 3b, respectively. The highly localized decoration of the dendrite tips is shown in Fig. 4a and 4b. These latter results were not typical of the particle decoration found in the ground base samples and may be a manifestation of reduced convection level in the flight samples. Terracing, too, was substantially less marked and may have been enhanced by reduced convection.

The last feature to be discussed relates primarily to the Ni-1 Ag samples, but was noted to a lesser extent in some of the

Ni-12 Sn flight samples. These features were internal voids that formed during the processing. Their volume was such that they could not have resulted from solidification shrinkage. They actually caused distortions of the outer surfaces. This can be seen in Figs. 5a and 5b for Skylab Samples 1.2 and 1.13, respectively.

Transverse sections of the voids are shown in Figs. 6a and 6b for the Ni-1 Ag and Ni-12 Sn, respectively. Careful microchemical analysis of the inner surfaces of the voids indicated that they were not a result of interstitial contaminant gas, but were due to metallic gas evolution during the processing (Reference 3). This revealed some interesting internal artifacts of both melting and solidification, as shown respectively in Figs. 7a and 7b. In the former case (Fig. 7a) the microchemical banding of the starting material has resulted in preferential melting of solute rich regions in advance of the solute poor regions. The subsequent volatilization of the silver rich liquid has laid bare the melting interface of this partially melted sample. In the latter case, the advancing solidification interface has also been revealed because of volatilization of the solute enriched liquid. Whereas these results are intriguing and potentially useful as a technique for revealing melting or solidification interfaces, the question arises as to why these reactions occurred to a much greater extent in the Ni-1 Ag flight samples than in the ground base samples, and why they occurred in the Ni-12 Sn flight samples when they had not been noted in the ground base samples. Consideration of this anomaly led us to a rigorous review of the processing parameters and to how these parameters would affect the solidification reactions. In turn, this led us to consider pressure (P) - temperature (T) - composition (X) diagrams for the alloys in question, rather than the conventional temperature (T) - composition (X) diagrams, because the T-X phase diagrams were generated under 1 g and one atmosphere of pressure, whereas the experimental conditions during the flight were 10^{-3} g and 10^{-5} mm of Hg. Consideration of reduced pressure isobaric sections within both P-T-X diagrams indicated that metallic gas evolution could occur as a phase reaction within both systems, on cooling (Reference 3). The reason that the reduced pressure reaction was suppressed within the ground base samples was due to the hydrostatic pressure head within the liquid itself. The hydrostatic pressure head is given by Eq. (1) for a cylindrical column of liquid

$$\Delta P = \omega h = \rho g h \qquad (1)$$

where ΔP = pressure increment, ω = specific weight, h = distance from the surface into the liquid, ρ = density, and g = gravity. It is clear that the pressure head decreases with reduction in gravity, and the prescribed low pressure phase reactions may become bulk reactions rather than surface reactions. This substantially broadens the consideration of space processing from liquid/solid phenomena to liquid/solid/gas phenomena and emphasizes that the pressure of a reduced gravity environment might prove to be a significant consideration for future experimentation. This point is being actively pursued.

CONCLUSIONS

In conclusion, we might say that this space experiment confirmed many results that had been anticipated, but in several important respects the results were unanticipated. The record of terracing was excellent, although not unprecedented terrestrially. The highly localized precipitate arrays, however, are more unusual and these results should be considered in light of existing theory of solute redistribution. Further, an additional process has been demonstrated that can address the problem of revealing the solid/liquid interface. Lastly, the importance of a rigorous consideration of the process parameters during space processing has been demonstrated. Although thermal control has previously been considered important, pressure control may prove to be an important consideration as well.

We have demonstrated that the pressure head is directly (and in a manner that may be quantified) related to gravity, and that as a result of the reduction of this head low pressure phase reactions may occur in the bulk that could not occur otherwise. Applications of these phase reactions are only limited by the creativity of the experimentalist, and it should be pointed out that these reactions are sufficiently rare terrestrially as to be unnamed.

ACKNOWLEDGMENTS

This work was partially supported by NASA Contract NAS 8-28728. We would also like to acknowledge the support of Mr. Earl Hasemeyer (who was the COR on this program) and Mr. Charles Lovoy, both of NASA, Marshall Space Flight Center.

REFERENCES

1. Tiller, W. A., J. Metals, Vol. 9, p. 847, 1957.

2. Kattamis, T. Z., "Phase C. Report - Evaluation of Skylab Samples," Institute of Materials Science, the University of Connecticut, December 1973.

3. Larson Jr., D. J., "Final Report on Phase C - Specimen Analysis of Skylab, M553 Experiment, Flight Samples," Research Department, Grumman Aerospace Corporation, April 1974.

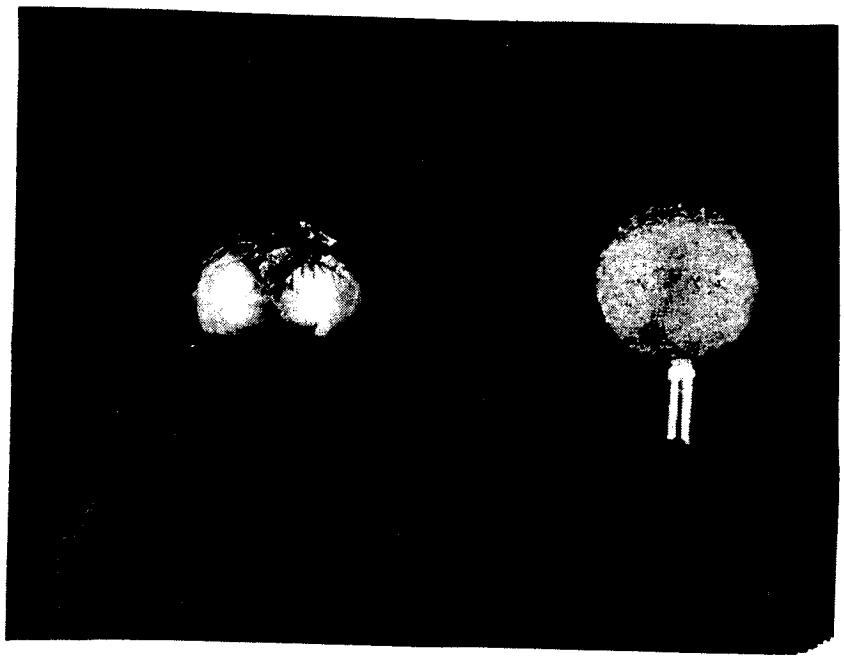

(a) (b)

FIGURE 1. MACROPHOTOGRAPHS OF 1 g PROCESSED AND LOW g PROCESSED SPHERES (2X)

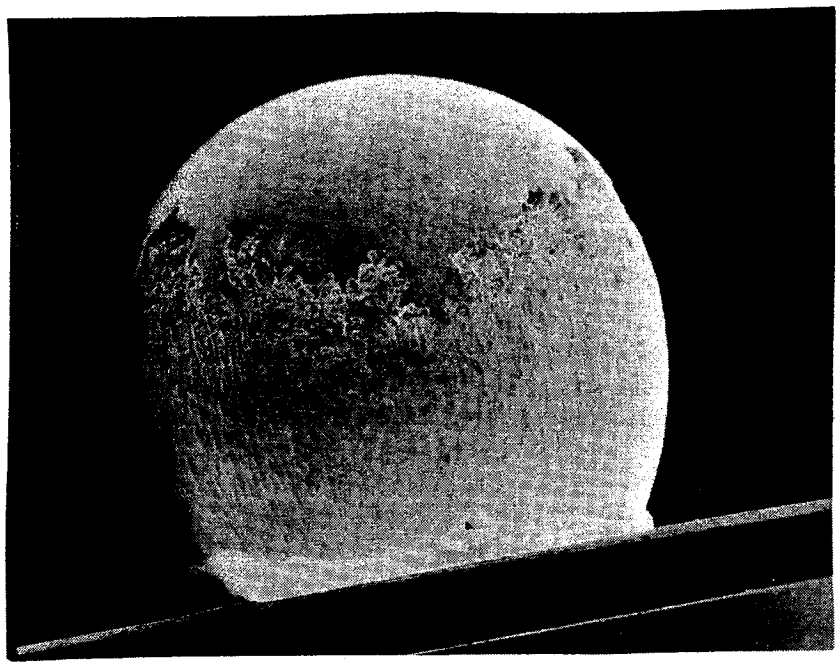

FIGURE 2A. MACROPHOTOGRAPH OF Ni-30 Cu SKYLAB SAMPLE 1.7 SHOWING REGIONS OF VARYING GROWTH MORPHOLOGY (15X)

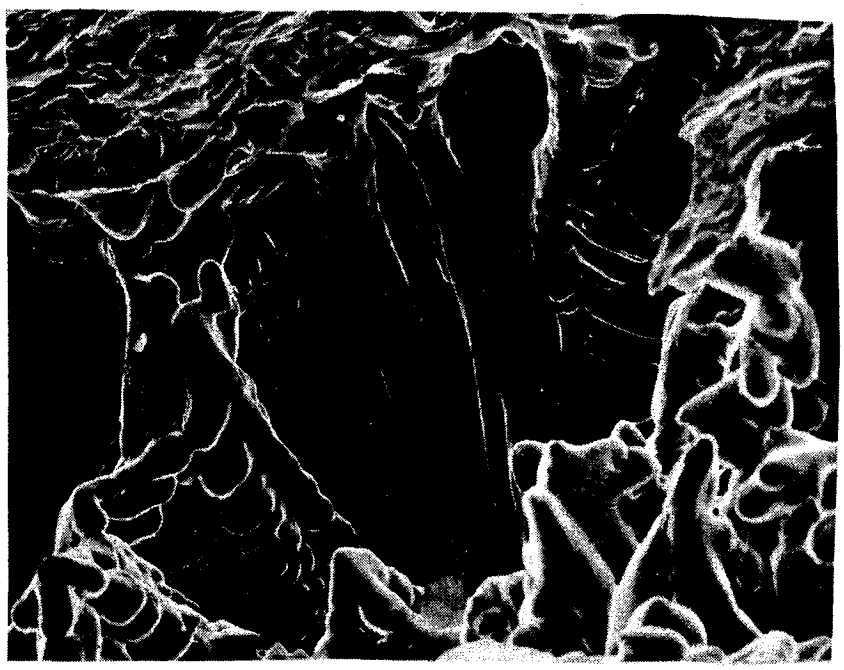

FIGURE 2B. ENLARGEMENT OF INTERFACE REGION OF THE Ni-30 Cu SKYLAB SAMPLE 1.7 SHOWING RADIAL GROWTH INWARD OF THE SURFACE NUCLEATED GRAINS (400X)

FIGURE 3A. TERRACING AT THE EXTREMITIES OF THE PLATELET GROWTH IN Ni-12 Sn SKYLAB SAMPLE 2.3 (3750X)

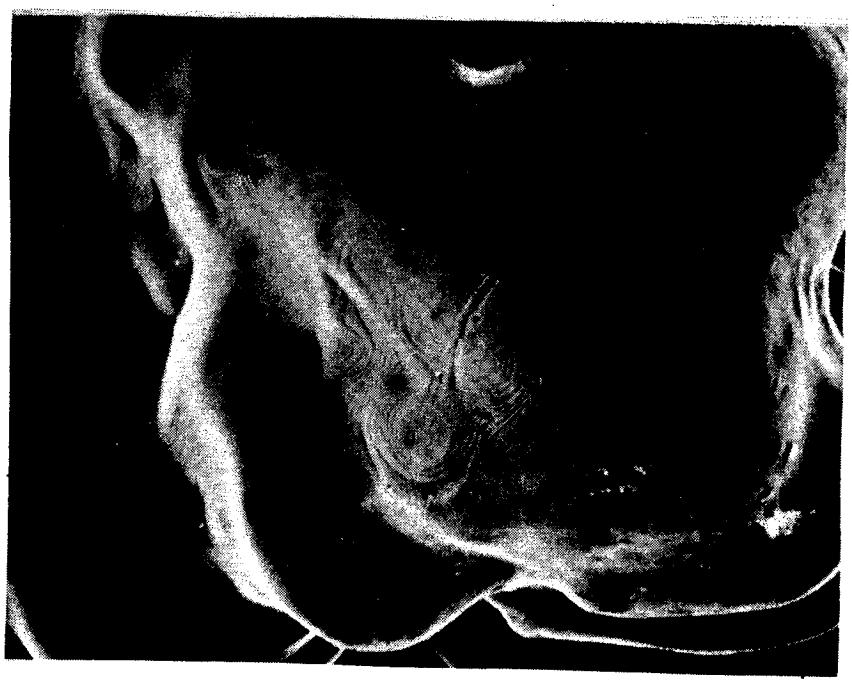

FIGURE 3B. TERRACING ON PRIMARY AND SECONDARY DENDRITE ARMS IN Ni-12 Sn SKYLAB SAMPLE 2.3 (3750X)

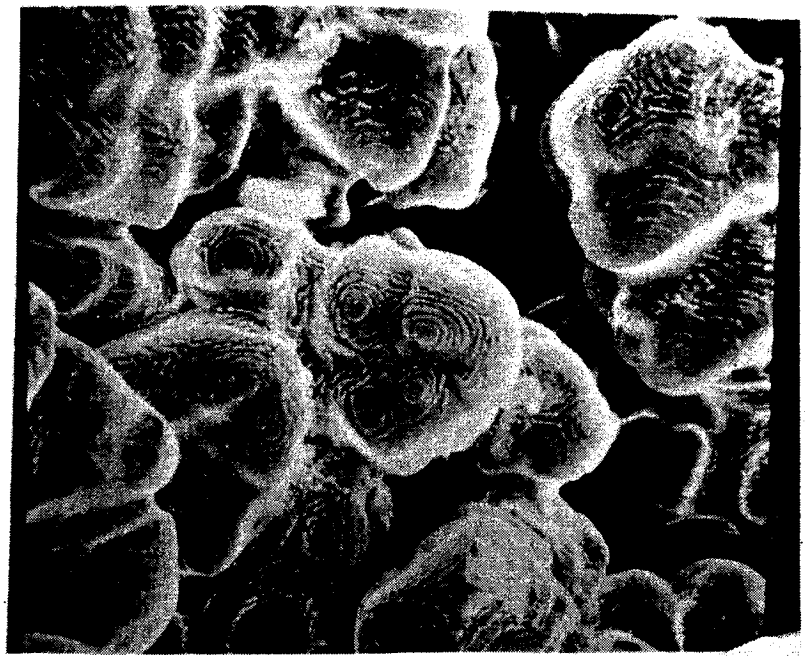

FIGURE 4a. DECORATION OF TERRACES BY Ni_3Sn EUTECTIC CONSTITUENT IN Ni-12 Sn SKYLAB SAMPLE 1.6 (1000X)

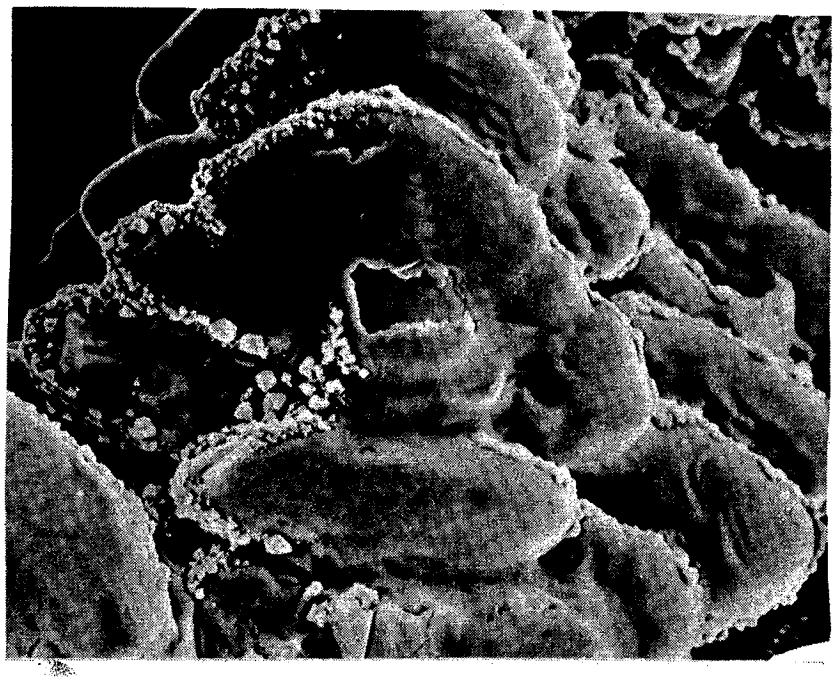

FIGURE 4b. DECORATION OF Ni_3Sn PARTICLES IN A CRYSTALLOGRAPHICALLY DEFINED ARRAY Ni-12Sn SKYLAB SAMPLE 2.3 (1500X)

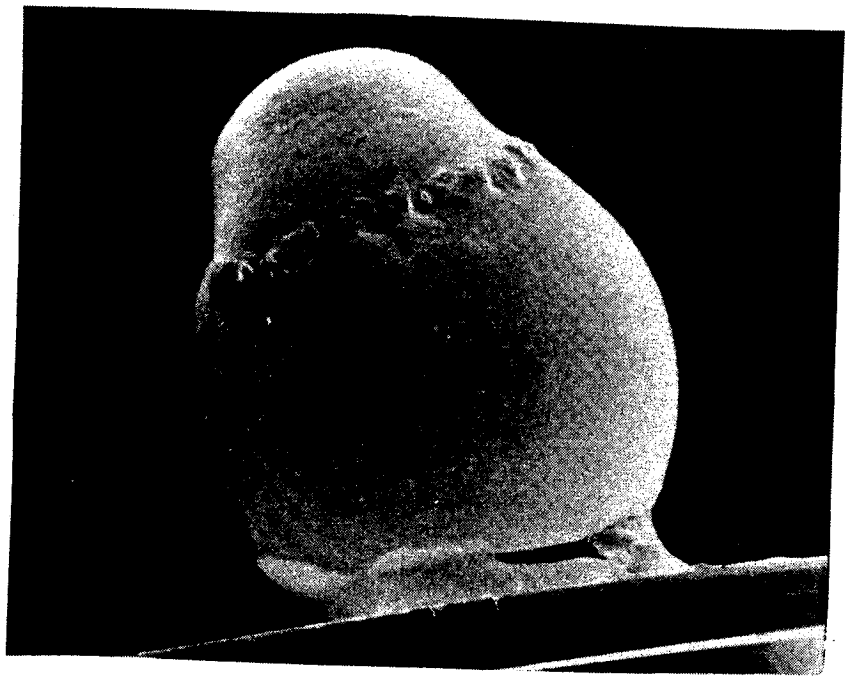

FIGURE 5a. MACROSCOPIC DISTORTION OF Ni-1 Ag
SKYLAB SAMPLE 1.2 (15X)

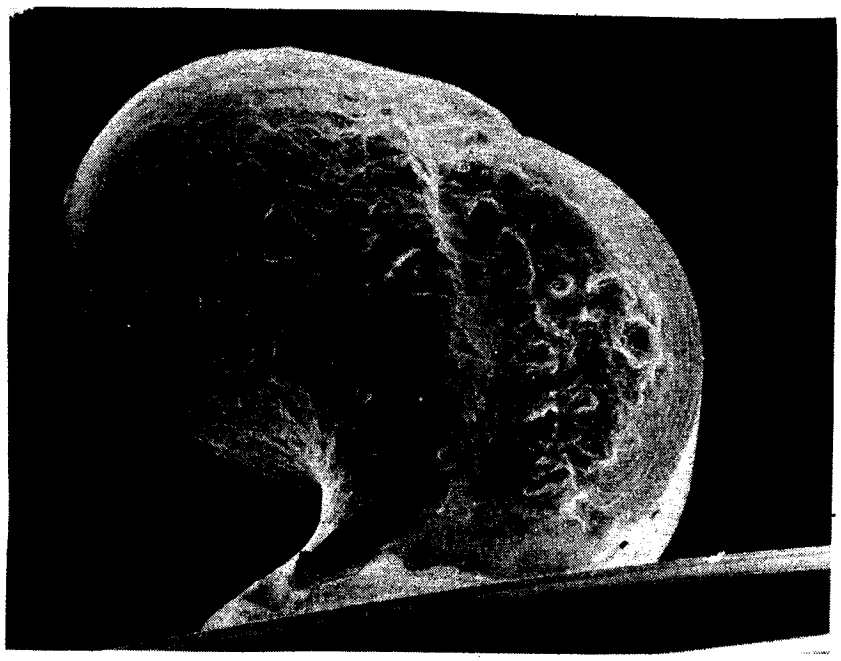

FIGURE 5b. MACROSCOPIC DISTORTION OF Ni-1 Ag
SKYLAB SAMPLE 1.13 (15X)

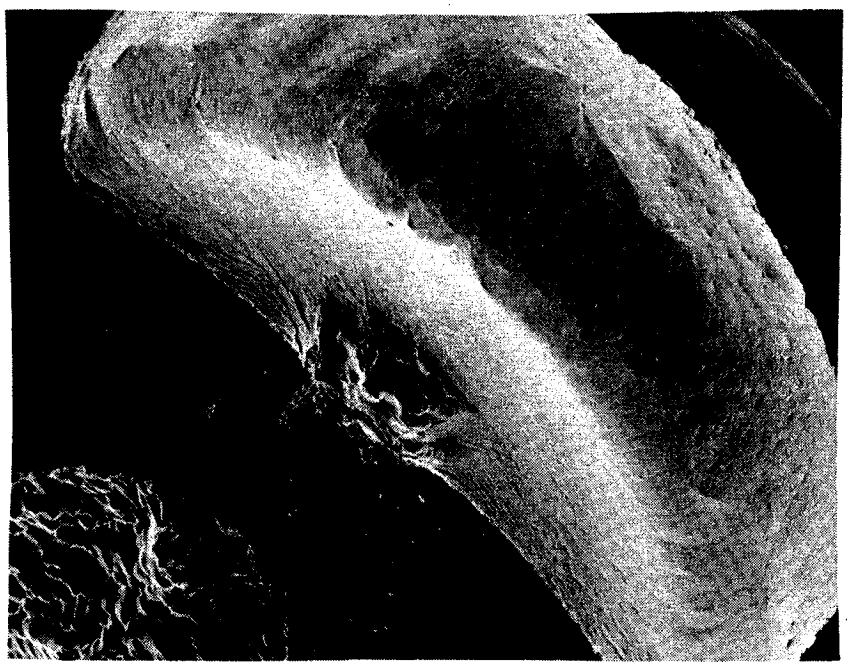

FIGURE 6a. MACROSCOPIC VIEW OF VOID AREAS IN Ni-1 Ag SKYLAB SAMPLE 1.2 (35X)

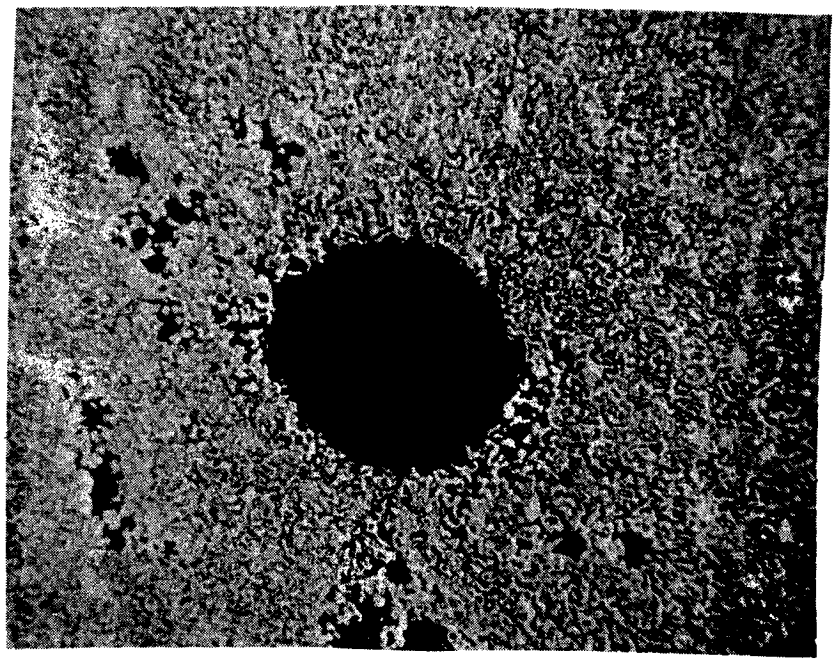

FIGURE 6b. MACROSCOPIC VIEW OF VOID AREA IN Ni-12 Sn SKYLAB SAMPLE 2.7 (60X)

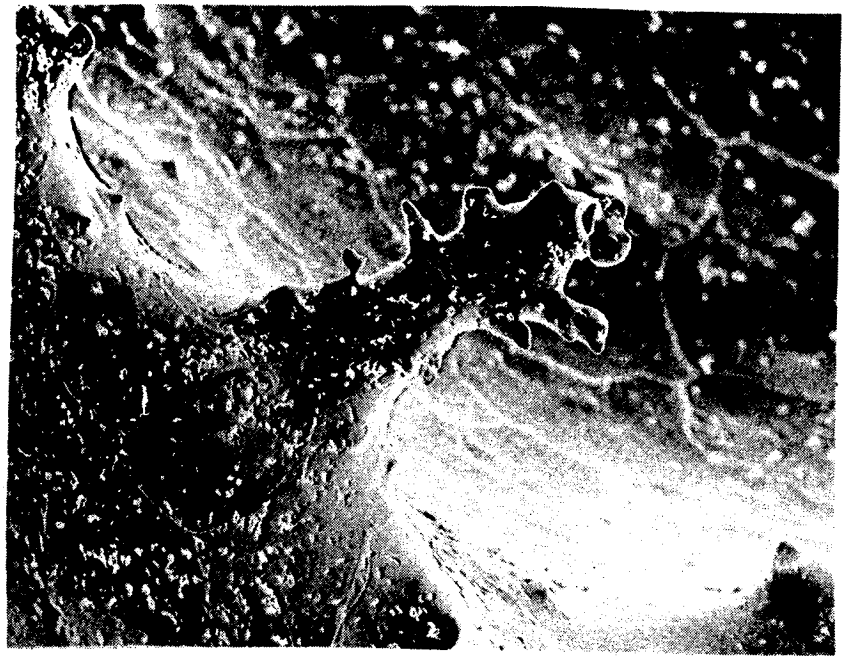

FIGURE 7a. MICROPHOTOGRAPH OF MELTING ARTIFACT REVEALED BY LIQUID/SOLID/GAS REACTION IN Ni-1 Ag SKYLAB SAMPLE 1.13 (400X)

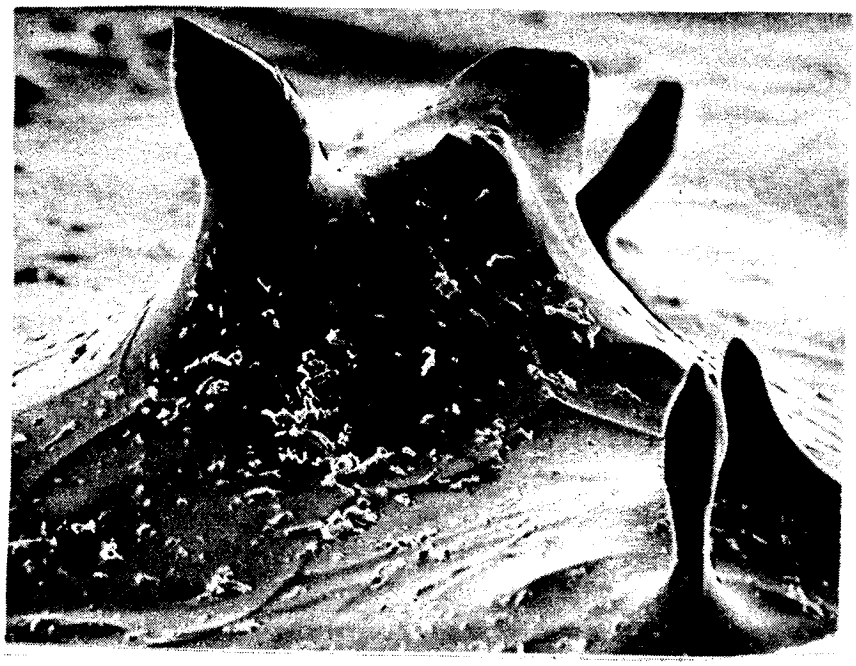

FIGURE 7b. SOLIDIFICATION ARTIFACT REVEALED BY LIQUID/SOLID/GAS REACTION IN Ni-1 Ag SKYLAB SAMPLE 1.13 (1500X)

SKYLAB EXPERIMENT M479
ZERO GRAVITY FLAMMABILITY

By

J. H. Kimzey
Lyndon B. Johnson Space Center
Houston, Texas 77058

SUMMARY

Flammability under conditions of weightlessness was investigated in Skylab 4. Thirty-seven tests using six materials were successfully carried out to learn more about how a flame acts in the absence of confection. Specific objectives were to note the extent of surface flame propagation and flash-over to adjacent materials, rates of surface and bulk flame propagation, self-extinguishment, and extinguishment by both vacuum and water spray. Data were returned in the form of crew comments on voice tapes and sixteen millimeter motion pictures taken at 24 frames per second. All tests were performed and all hardware functioned properly, although an operational oversight caused the water in the supply tank to be less than the minimum required pressure. Burning rates were significantly reduced as anticipated from earlier aircraft tests. Some reduction of total burning was also noted. The surface burn was not followed by continued inward burning as typically experienced on earth although some one-g tests at extremely low pressures have partially reproduced this condition. Ignition and extinguishment also appear to be similar to one-g. The typical soft blue flame was seen by the crew, but was not detected on the film emulsions used. Smoke patterns were also noted. This can be of value in studying Brownian movement of solids in gases under conditions of weightlessness.

INTRODUCTION

Skylab Experiment M479 was performed February 4, 1974, on Day 81 of the third and last manned mission. This was the latest in a study of flammability as applied to spacecraft.

BACKGROUND

An investigation of flammability under conditions of weightlessness began over 10 years ago. Without convection a flame as a somewhat spherical corona as seen on the right, figure 1. In such a case the fuel is surrounded by a corona which isolates the material from the surrounding atmosphere rather than extending above the fuel as noted on the left. Hardware for these aircraft tests was very basic consisting of a 10-inch diameter chamber in which the fuel was positioned. A motion picture camera recorded ignition and burning (figure 2). Fuels were selected to represent a variety of engineering materials with various melting points and flammability characteristics (figure 3).

AIRCRAFT TESTS

A typical float of the flammability chamber is seen in the motion picture film. Test times varied from 4 to 10 seconds. Burning rates from this series of tests were noted (figure 4) for some materials. Conclusions from these tests are given in figure 5. See also reference 1.

SKYLAB TESTS

Thirty seven tests were performed in Skylab mission 4, (figure 6). The hardware for Experiment M-479 consisted of many items used throughout the Skylab flight in eighteen different experiments. All of the M-479 hardware was designed, built, and tested by the George C. Marshall Space Flight Center. We are grateful for support by the many groups at Huntsville that provided this highly reliable and still functional equipment. The specimens (figure 7) were separately packaged in a designated container. Each one has a piece of test material, a Nichrome heater wire and an electric socket to support the material in the proper orientation.

A number tab served to identify the specimen both for the astronaut operator and for an aid in viewing the film. Once he installed the specimen in the work chamber (figure 8) and closed the cover he observed the test through the hatch window. Another port on the side provided for photographing the test with a motion picture camera. Controls for operating a water spray and a vent are also provided to evaluate these as a means of extinguishment. Tests were conducted in the Skylab atmosphere of 65 percent oxygen at 5.2 psia.

Skylab In-Flight Testing - Operation of the experiment was scheduled for day 81 of SL-4. Commander Gerald Carr performed these tests (figure 9).

Skylab Film Details - A 16 mm motion picture film shows:

1. Commander Carr in SL-4. Test number 2 was video recorded showing the specimen before test and following test as it was compared with speciment number 8 which had identical construction. Focus was poor but the fact that the 1-inch square specimen was not burned was readily apparent.

2. Commander Carr in SL-4. Tests numbered 16 and 17 were video recorded with the camera at the viewport recording the burning of the polyurethane foam specimen and the paper specimen. The test details are narrated as the materials were ignited and burned.

3. Test number 15. Neoprene coated nylon fabric was next ignited and burned using the film exposed in flight. This material exhibited the property of shrinkage on the nylon side and the tendency to curl and quickly roll up disturbing the burning.

4. Test number 16. Polyurethane foam covered in scene 2, above, is next. The flame is seen proceeding along the surface at 0.8 inches per second followed by a venting overboard of the atmosphere. The fire goes

out as the foam melts to a much smaller volume. No estimate of the unburned material is possible. No vent rates are given. Venting is through a 1-inch diameter screened orifice.

5. Test number 17. Paper, also described in the video recording of scene 2, is next. Ignition is noted but the film fails to show the soft blue glow of the flame described by Commander Carr, the same glow barely discernable in part of the video recording as the T.V. lens aperture opened fully. Evidence of the burning could be seen as the metal frame (near the top of the screen) began to glow as it was heated to a dark red heat (650 - 750 °C). The venting caused a significant flare up as burning rates and luminousity increased markedly due to the forced convection.

6. Test number 18. Teflon fabric is next. The igniter caused a flame of the material contacting the fabric. However, the flame did not persist. As the igniter cooled, after about three seconds, the flame went out.

7. Test number 1. The aluminized mylar is seen next. This material burned at 3.8 inches per second, with a bright light, indicating that the aluminum was burning and contributing significantly to the heat. This same material in one-g burns the same way irrespective of orientation as convection cannot overcome inertia as quickly as the flame moves.

8. Test number 2. Nylon of scene number 1 is next. Three ignition attempts are seen.

9. Test number 26. Nylon in this test has a different geometry but an identical igniter. The first attempt did not produce a flame. The second, however, did. The film shows two flame zones that start in a subtle, gentle glow that pulses as the material melts and liberates flammable gases. As time passes the agitation increases. The material burns for 10 minutes 43 seconds at which time the atmosphere was dumped to cause extinguishment. The effects of venting include intensified burning as seen earlier with polyurethane foam and paper in tests number 16 and 17.

In addition to video tape and motion pictures we have two still photographs. The first (figure 10) shows the burning of polyurethane foam in test number 10. Note the spherical shape of the flame. The diameter is estimated at more than 6 centimeters. This means that this material has a flame in zero-gravity (at this atmosphere) extending over 3 centimeters. Another picture immediately after the fire went out shows the smoke pattern (figure 11). It reportedly persisted for a long period of time.

SKYLAB SPECIMENS RETURNED

Two specimens were brought back, as requested (figures 12 and 13). These are the nylon from tests numbered 2 and 8. Neither ignited. This being the case, Col. Carr included the residue from test number 26 (figures 14, 15, and 16). After burning for nearly 11 minutes, this fire was deliberately extinguished by dumping the atmosphere. We still have over 10 percent of the material unburned in this specimen.

Another returned specimen was a piece of residue from test number 17 (figure 17). Paper burned with a very soft blue flame not visible to the camera. Carr reported that the residue "has remarkable strength." An estimation, based on area and weight, showed it was consumed between 74 and 79 percent. Similar paper ignited in one-g (in air) was consumed by 91 percent.

CONCLUSIONS

Several conclusions can be made regarding fire in zero-gravity (figure 18). These include ignition, burning rates, extinguishment by vacuum dump, water spray and self-extinguishment and the validity of one-g tests.

RECOMMENDATIONS

The M-479 experiment was an engineering study designed to assist in future manned space programs. The need for additional zero-gravity testing is obvious. Areas of concern are as follows (figure 19):

1. Fire detection - Document the light emission from various materials. Note specifically the wavelength and intensity for paper.

2. Ignition - Ignition energies should be quantitatively measured.

3. Propagation rates - Various fuel compositions, thicknesses and geometry.

4. Critical gap distances - Determine critical spacing for various materials.

5. Other fuels - Flammable liquids, flammable gases and metals could have unique mechanisms of burning in zero gravity. Metals do not have gaseous products of combustion therefore they probably burn in zero-gravity as vigorously as in one-g.

6. Extinguishment - The suitability of water as an extinguishment should be verified as well as the use of solids (bicarbonates) and gases (CO_2 and Halons such as 1301 bromotrifluoromethane).

REFERENCES

[1] Kimzey, J. H., "Zero Gravity Flammability," included in "Space Processing and Manufacturing" symposium held October 21, 1969, at the George C. Marshall Space Flight Center, Huntsville, Alabama. ME-69-1. N-70-14669, N71-11719, N70-20535.

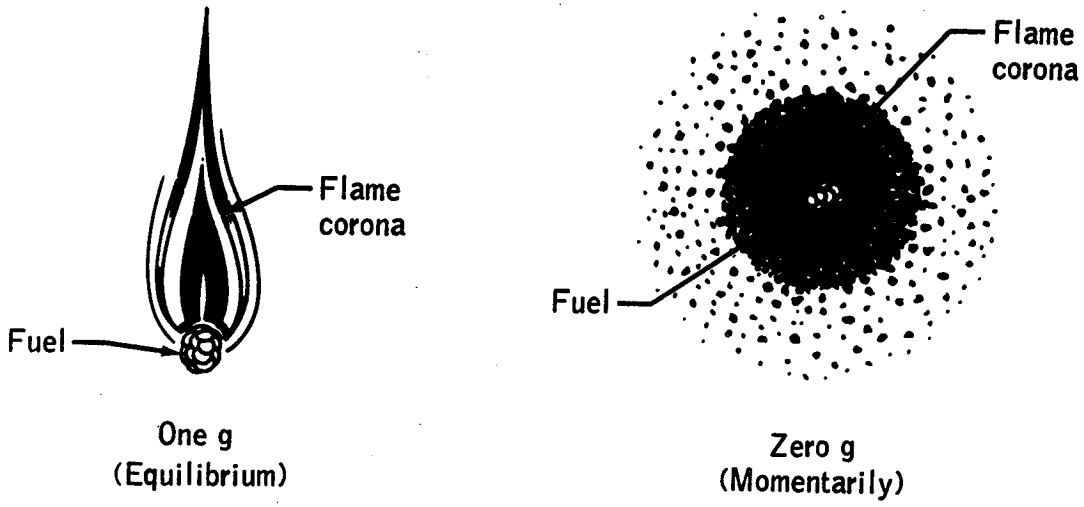

FIGURE 1. COMPARISON OF FUEL BURNING AT ONE-G AND ZERO-G IN OXYGEN ATMOSPHERE

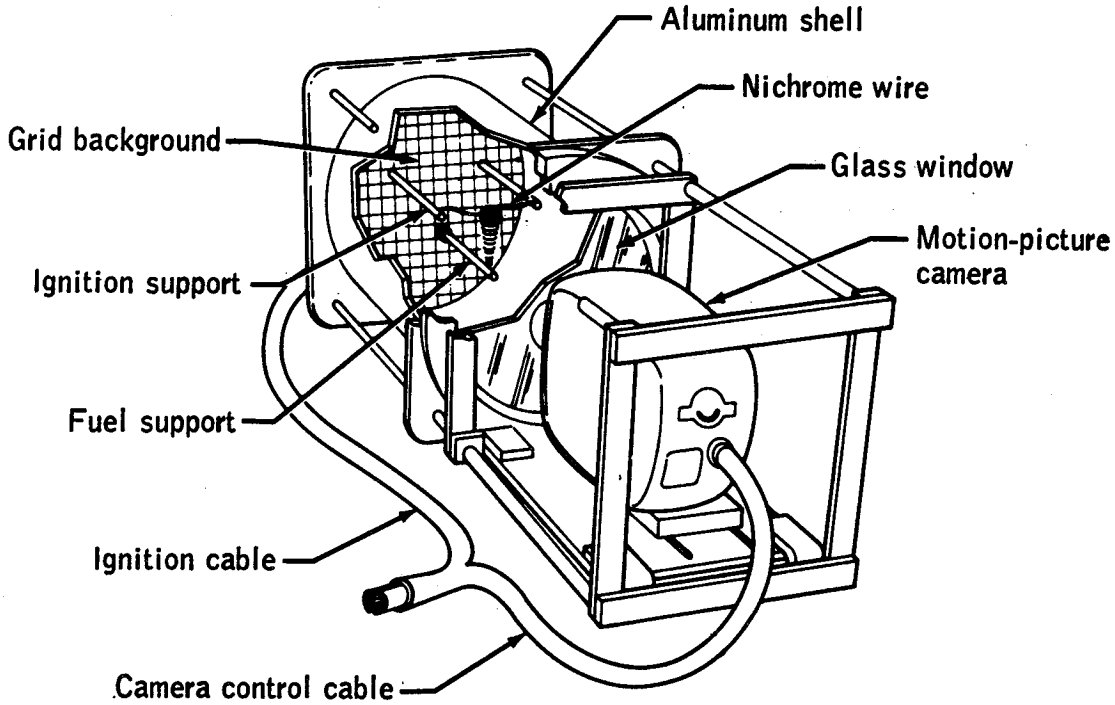

FIGURE 2. ZERO-G FLAMMABILITY CHAMBER

MATERIALS

DACRON THREAD

NEOPRENE RUBBER, FOAMED

NEOPRENE RUBBER TUBING

PARAFFIN

POLYURETHANE RUBBER

SILICONE RUBBER

STYRENE PLASTIC

TEFLON TUBING

FIGURE 3. AIRCRAFT FLAMMABILITY TEST

FUEL [1]	RATE OF BURNING, INCH PER SECOND					
	ONE-g			ZERO-g		
	15 PSIA AIR	5 PSIA O_2	15 PSIA O_2	15 PSIA AIR	5 PSIA O_2	15 PSIA O_2
NEOPRENE	0.0	0.2	0.4		0.10	
SILICONE	0.04	0.5	1.1	0.0	0.08	
TEFLON	0.0				0.00	
POLYURETHANE		0.6	0.7	0.0	0.08	0.15
DACRON [2]		0.6	0.7		0.08	0.15

NOTE:

1. FUEL IS TUBULAR (NO.10 AWG I D) AND THREADED OVER A STEEL OR CERAMIC MANDREL
2. DACRON THREAD IS WRAPPED AROUND POLYURETHANE
3. IGNITION IS PROVIDED BY ELECTRIC RESISTANCE COIL
4. TEMPERATURE OF ATMOSPHERE IS 65 ± 5°F

FIGURE 4. BURNING RATES IN ONE-G AND ZERO-G

CONCLUSIONS

IGNITION - NO DIFFERENT THAN ONE-G

BURNING RATES - SLOWER THAN ONE-G

- o FIRE WILL PROPAGATE ALONG A SURFACE

SELF EXTINGUISHMENT - HIGHLY PROBABLE

- o FIRE WILL NOT BURN INWARD AS GASEOUS PRODUCTS OF COMBUSTION WILL IMPEDE OXYGEN FLOW

CONVECTION - INTRODUCING CONVECTION PROMPTLY INCREASES FLAME SIZE AND INTENSITY.

- o FORCED AIR FLOW OR VENTING INCREASES BURNING

FIGURE 5. AIRCRAFT FLAMMABILITY TEST

(ZERO GRAVITY FLAMMABILITY)

DATE: FEBRUARY 4 & 5, 1974 - MISSION DAY 81

MISSION: SL-4

ASTRONAUT - OPERATOR: LT. COL. GERALD P. CARR

EQUIPMENT: M-512 FACILITY IN M.D.A.

FIGURE 6. SKYLAB M-479 EXPERIMENT

MATERIAL	DIMENSIONS	TEST NUMBERS
ALUMINIZED MYLAR	2 5/8" x 3 5/8" x .0003	1,7,13,19,25
NYLON SHEET	1" x 1" x .125	2,8,14,20,26
NEOPRENE COATED NYLON FABRIC	2 5/8" x 3 5/8"	3,9,15,21,27
POLYURETHANE FOAM	1/4" x 1/4" x 2"	4,10,16,22,28
BLEACHED CELLULOSE PAPER	2 5/8" x 3 5/8" x .009"	5,11,17,23,29
TEFLON FABRIC	2 5/8" x 3 5/8"	6,12,18,24,30
PAPER, 2 PIECES, MOUNTED IN PARALLEL FACE-TO FACE WITH A GAP OF 1/8, 1/4, 1/2"	2 5/8" x 3 5/8" x .009"	31 THROUGH 37

FIGURE 7. SKYLAB EXPERIMENT M-479

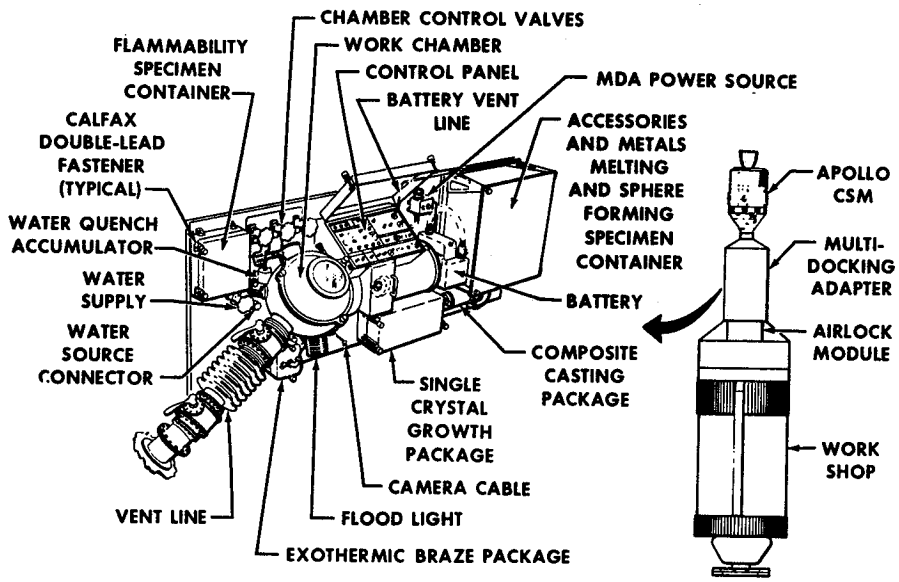

FIGURE 8. SKYLAB EXPERIMENT M-479 ZERO GRAVITY FLAMMABILITY

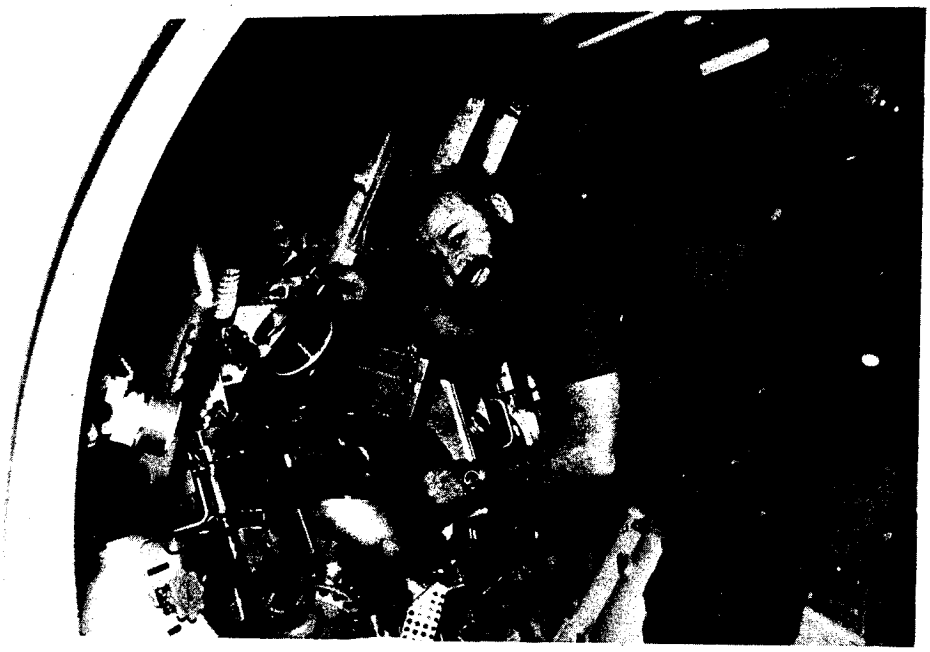

FIGURE 9. SKYLAB IN-FLIGHT TESTING

FIGURE 10. PHOTOGRAPH OF BURNING POLYURETHANE FOAM IN TEST NUMBER 10

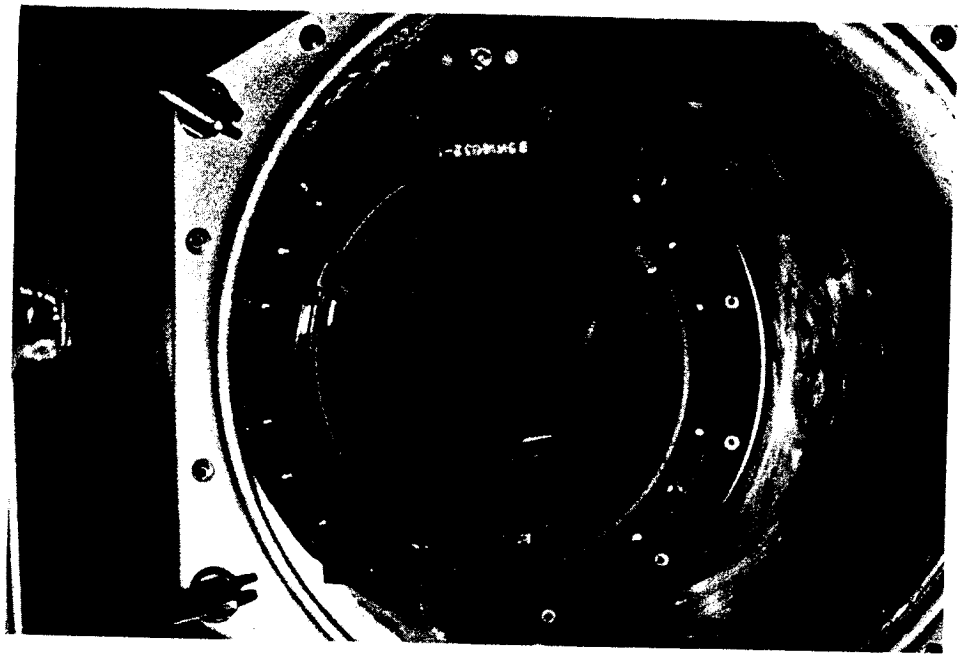

FIGURE 11. PHOTOGRAPH OF SMOKE PATTERN OF BURNING POLYURETHANE FOAM IMMEDIATELY AFTER FIRE WENT OUT

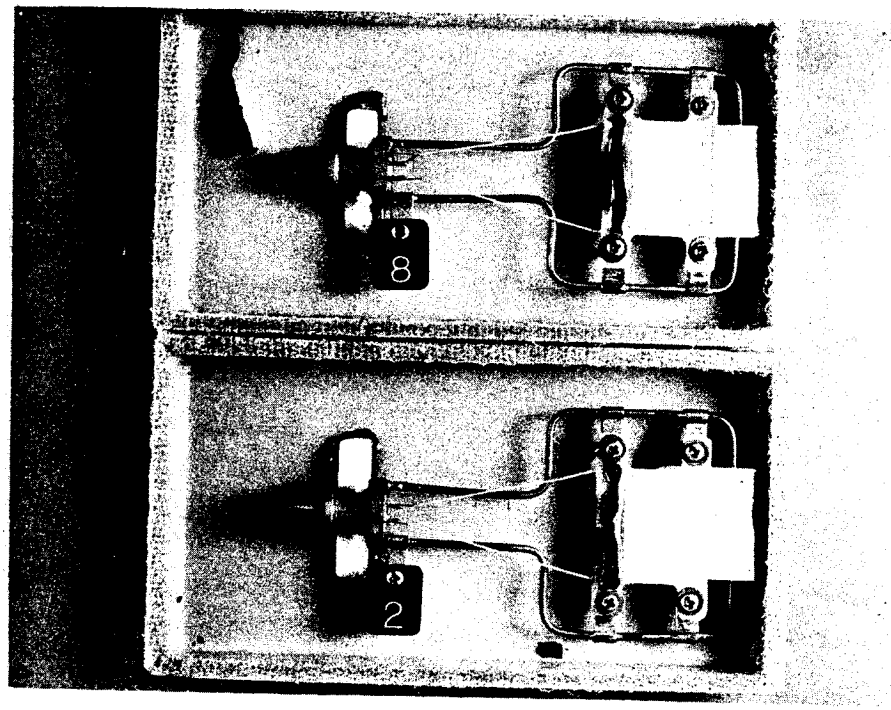

FIGURE 12. PHOTOGRAPH OF SPECIMEN RETURNED FROM TEST NUMBER 2 WHICH DID NOT IGNITE

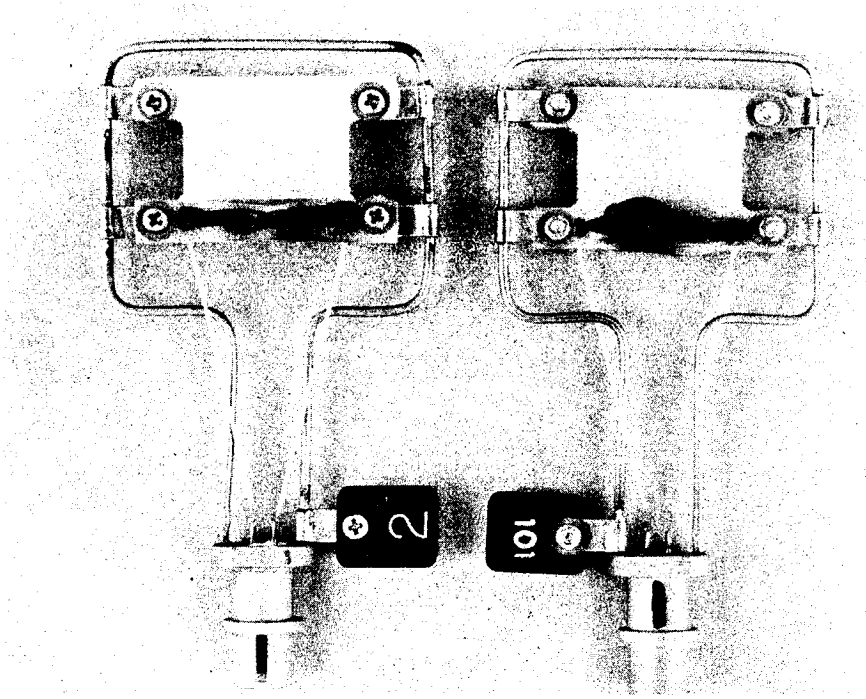

FIGURE 13. PHOTOGRAPH OF SPECIMEN RETURNED FROM TEST NUMBER 8 WHICH DID NOT IGNITE

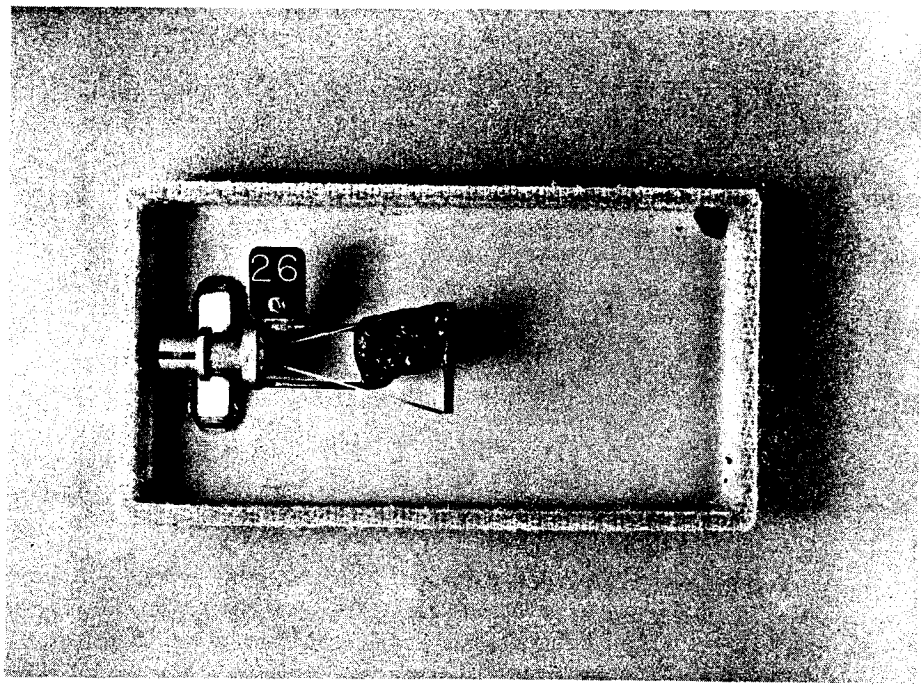

FIGURE 14. PHOTOGRAPH OF RETURNED RESIDUE FROM TEST NUMBER 26 WHICH AFTER BURNING FOR NEARLY 11 MINUTES WAS DELIBERATELY EXTINGUISHED BY DUMPING THE ATMOSPHERE.

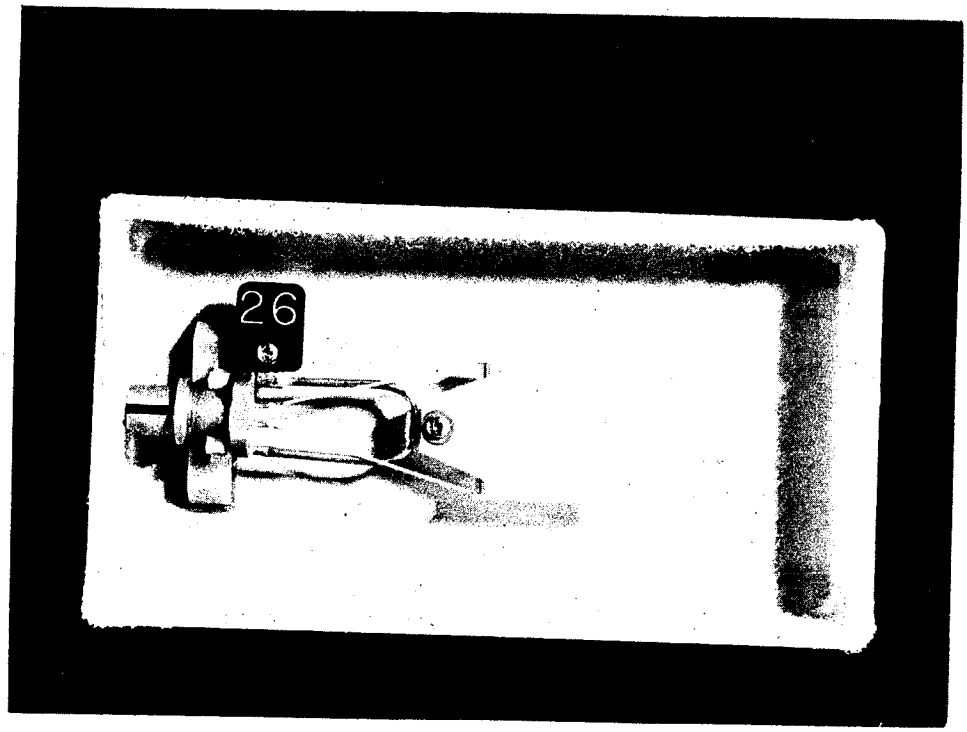

FIGURE 15. PHOTOGRAPH OF RETURNED RESIDUE FROM TEST NUMBER 26 WHICH AFTER BURNING FOR NEARLY 11 MINUTES WAS DELIBERATELY EXTINGUISHED BY DUMPING THE ATMOSPHERE.

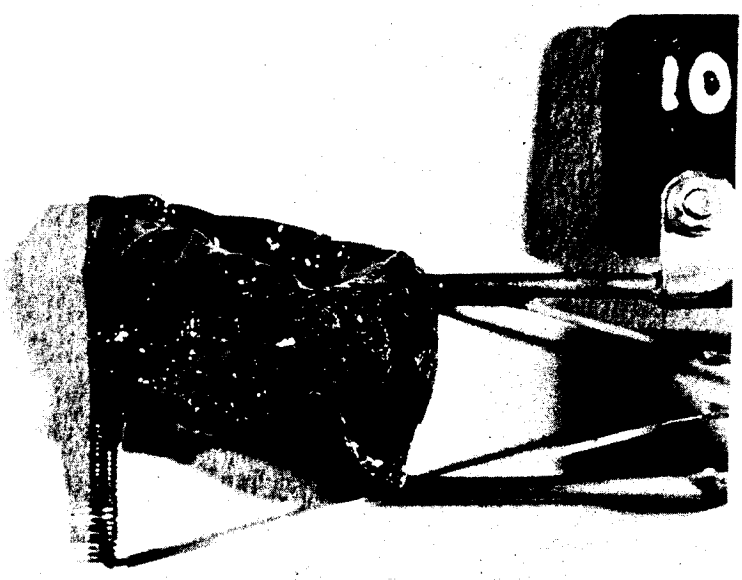

FIGURE 16. PHOTOGRAPH OF RETURNED RESIDUE FROM TEST NUMBER 26 WHICH AFTER BURNING FOR NEARLY 11 MINUTES WAS DELIBERATELY EXTINGUISHED BY DUMPING THE ATMOSPHERE.

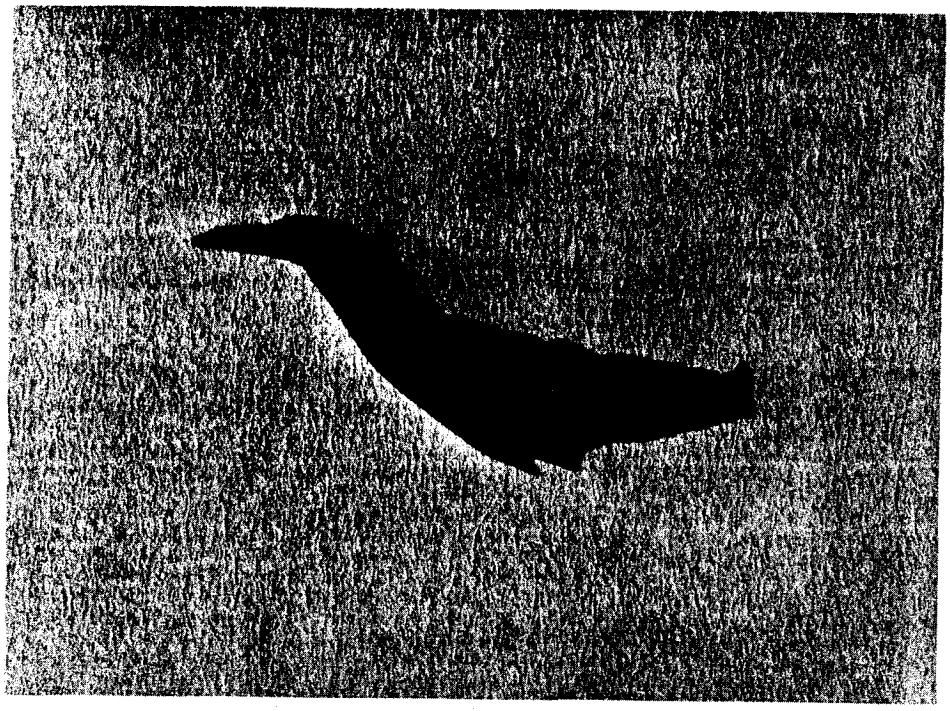

FIGURE 17. PHOTOGRAPH OF RETURNED RESIDUE FROM TEST NUMBER 17. PAPER BURNED WITH A VERY SOFT BLUE FLAME NOT VISIBLE TO THE CAMERA.

(CONCLUSIONS)

IGNITION - NO DIFFERENT THAN ONE-G

BURNING RATES - SLOWER THAN IN ONE-G. NO TENDENCY TO INCREASE WITH TIME AS ONE-G UPWARD BURNING

- o HIGHLY FLAMMABLE, THIN MATERIAL - FAST BURNING IN ONE-G REGARDLESS OF ORIENTATION. SIMILAR FAST BURNING IN ZERO-G.
- o THICKER MATERIAL, NONMELTING - A NEARLY INVISIBLE FLAME PASSES OVER THE SURFACE COMPLETELY SURROUNDING THE FUEL SLOWER THAN ONE-G.
- o PLASTIC MATERIAL, LOW MELTING POINT - SLOWER BURNING THAN ONE-G. NOT SELF EXTINGUISHING. WILL BURN FOR EXTENDED PERIOD OF TIME IN A VERY SMALL, NEARLY INVISIBLE FLAME WHICH IS ERRATIC DUE TO HIGH VISCOSITY DISTURBANCES.

FIGURE 18. SKYLAB EXPERIMENT M-479

- o FOAM MATERIAL, FLAMMABLE - SLOWER BURNING THAN ONE-G

EXTINGUISHMENT BY VACUUM - POSSIBLE BUT ADVERSE EFFECTS FROM EDDY CURRENTS CAUSE INCREASED BURNING

EXTINGUISHMENT BY WATER - POSSIBLE IF APPLICATION IS CONTROLLED

SELF EXTINGUISHMENT

- o YES - NONMELTING MATERIAL (PAPER, CARBON, ETC.) AND MATERIAL REQUIRING HIGH HEAT TO IGNITE (TEFLON)
- o NO - PLASTIC MATERIALS WITH A LARGE TEMPERATURE SPREAD BETWEEN MELTING POINT AND BOILING POINT (NYLON, ETC.) AND METALS - NO GASEOUS PRODUCTS OF COMBUSTION RAPIDLY BURNING MATERIAL (ALUMINIZED MYLAR, ETC.) MATERIALS CONTAINING OXIDIZERS AND MATERIALS TRAPPING OXYGEN (OPEN CELL FOAMED POLYURETHANE)

FLASHOVER TO ADJACENT MATERIAL - BURNING PAPER REQUIRES GAP DISTANCES OF OVER 1/2 INCH TO PREVENT FLASHOVER.

FLAME VISIBILITY - THE FUEL-RICH NATURE OF MANY KINDS OF ZERO-G FLAMES CAUSES A SOFT BLUE FLAME WHICH IS BOTH SMALL AND NEARLY INVISIBLE. FLAMES FROM RAPIDLY BURNING MATERIAL ARE GENERALLY VISIBLE.

MATERIAL TESTING - ONE-G TESTING FOR FLAMMABILITY PROVIDES AN ADEQUATE, SOMEWHAT CONSERVATIVE, TEST FOR FIRE SAFETY.

FIGURE 18. SKYLAB EXPERIMENT M-479 (CONT.)

FUTURE STUDIES OF ZERO-GRAVITY FLAMMABILITY

SHOULD INCLUDE:

- FIRE DETECTION - FLAME SPECTRA
- IGNITION ENERGIES
- PROPAGATION RATES
- OTHER FUELS
  - LIQUIDS
  - GASES
  - METALS
- EXTINGUISHMENT

FIGURE 19. RECOMMENDATIONS

INTRODUCTORY REMARKS TO M-518 MULTIPURPOSE FURNACE EXPERIMENTS PERFORMED ON SKYLAB

By

William R. Adams
George C. Marshall Space Flight Center
Marshall Space Flight Center, Alabama 35812

Ladies and gentlemen, it is indeed a pleasure to chair this portion of the symposium. Our next eleven presenters are Principal Investigators of Materials Processing Experiments in the M518, Multipurpose Furnace System, on the Skylab Program. Working with each of them over the past two years has been very pleasant and a personally rewarding experience. They have been invited here today to discuss the objectives, mechanics and scientific results of their individual experiments. Before introducing the first speaker, I'd like to take just a few minutes to familiarize you with the M518 Furnace Facility. This information will allow each speaker to go immediately into the details of his experiment without having to discuss general design and facility aspects.

Each investigator was asked to construct his desired sample materials to mutually agreed to dimensions. The material was then encapsulated in Quartz or a suitable metal sheath. This sample ampoule was then shipped to the Westinghouse Laboratories in Pittsburgh, our general contractor for the entire M518 experiment system, who chose suitable thermal inserts (conductors and resistors) required to establish a thermal gradient across the cartridge, in a manner suitable to the Principal Investigator. This entire system was then enclosed in stainless steel tubes, all having the same exterior dimensions. As you can readily see, the cartridge system presents a simple and clean interface between the facility and the highly varied experiments.

Each experiment was initiated by a Skylab astronaut inserting three cartridges, comprising a set for each experiment, into the M518 Furnace. Upon insertion, the cartridges became an integral part of the furnace design. Space vacuum was utilized to prevent convective heat transfer; therefore, radiative heating of the end of the cartridge located near the heater element was then conducted through the cartridges to the heat sink located at the other end of the furnace. Generally speaking, the total heat generated by the furnace flowed through the experiment cartridges at a rate which was dependent upon the thermal impedance of the individual cartridge designs. The desired parameters, maximum heat leveler temperature, time duration at max temperature, and rate of cartridge cool down, were "dialed in" by the astronaut on the facility control device. (These specific parameters were, of course, established through extensive ground testing.)

All mechanical aspects of the experiment system went well. All eleven experiment sets were processed during the second Skylab mission, and seven of the eleven were repeated during the third mission using the so-called "flight backup" cartridges. These repeat operations were for additional data. The previously unanticipated opportunity came as a result of time line openings which were generated by the crew members operating even more efficiently than planned. Some of the experiments were processed at identical parameters to the first operation, and some utilized modified operational parameters depending on individual Principal Investigator preference.

The facility functioned flawlessly and the thermal designs of the individual experiment cartridges apparently accomplished the desired thermal mechanics. The overall project results will be reflected in the interesting presentations to follow.

N74 29892

EXPERIMENT NO. M-557

IMMISCIBLE ALLOY COMPOSITIONS

By

J. L. Reger
TRW Systems Group
Redondo Beach, California 90278

SUMMARY

Ampoules containing materials exhibiting either liquid or solid state immiscibility were thermally processed in the M-518 Multipurpose Electric Furnace under low and one gravity conditions. Three cartridges, each containing three separate experiment ampoules were processed simultaneously during one furnace run.

Two of the experiment ampoules, gold-germanium (Ampoule A) and lead-zinc-antimony (Ampoule B), were processed in the isothermal portion of the furnace and one experimental ampoule, lead-tin-indium (Ampoule C), was processed in the gradient region of the furnace. Both the control (one gravity) and low gravity processed specimens were analyzed for their metallographic and electronic properties.

In all cases, the low gravity processed specimens exhibited better homogenization and microstructural appearances than the one gravity control specimens. The electronic behavior of the low gravity specimens were equal or superior in every respect and the Ampoule B specimens exhibited an anomalous superconducting transition temperature approximately 2 K higher than either the elements or the one gravity control specimens. In addition, the low gravity processed A and B ampoules exhibited X-ray diffraction lines not identifiable with any referenced diffraction patterns.

From these analyses, it is concluded that low gravity processing of materials processing liquid or solid immiscibility can produce compositions exhibiting unusual metallographic and electronic behavior.

INTRODUCTION

Immiscible systems, with few exceptions, are one of the unique classes of materials which are non-producible in bulk form on Earth. A number of these systems provides a potential class of new materials if they can be successfully produced in space. These potential applications include electronic, optical and other types of materials with unique physical characteristics.

Since segregation effects due to density differences and the relatively long time period necessary to solidify the materials from

the liquid state are the primary reasons for inability to secure bulk samples, processing in a low gravity environment should circumvent the majority of the problems associated with the immiscible systems.

This hypothesis has been verified to a large degree by investigations at TRW Systems Group utilizing NASA low gravity facilities to process materials having a miscibility gap in either the liquid or solid state [References 1, 2, 3].

In one of these investigations, however, it was found that the cooling rate during low gravity solidification had an influence on both the microstructure and electrical behavior of the immiscible system [References 2,4].

Thus, the opportunity of processing systems having either liquid or solid immiscibility on Skylab should provide extremely valuable information in corroborating both current information on the behavior of these systems, as well as a comparison of the effect of long cooling times with the results obtained in the short duration, low gravity facilities.

SKYLAB TESTS

Experiment M-557: "Immiscible Alloy Compositions", is comprised of three separate specimen ampoules per cartridge processed in the M-518 Multipurpose Electric Furnace; two in the isothermal portion and one in the gradient region of the furnace. The isothermal ampoules, designated A and B, contain 76.85 - 23.15 w/o gold-germanium and 45.05 - 45.06 - 9.89 w/o lead-zinc-antimony, respectively. Ampoule A, gold-germanium, exhibits almost complete solid state immiscibility and Ampoule B, lead-zinc-antimony, exhibits a liquid miscibility gap below a critical or consolute temperature. The gradient ampoule, designated C, contains 70.20 - 14.80 - 15.00 w/o lead-tin-indium, with tin as the precipitated second phase. Figure 1 shows the cartridge and ampoule configuration.

Two sets of three cartridges each were processed under one gravity conditions as controls; three horizontally and three vertically in the furnace. Three cartridges were then subsequently processed in the M-512/M-518 facility on board Skylab during the SL-3 mission. Basically, the processing consists of heating the isothermal section of the cartridges to 720°C, holding the temperature for a soak period of 4 hours, then allowing the cartridges to passively cool to ambient temperature. This temperature was set to allow Ampoule B to be heated above the critical or consolute temperature where the liquid immiscibility gap is exceeded and the liquid elements become single phase. The soak period is sufficiently long for complete mixing and diffusion of the elements. The temperature at the cold end is clamped such that Ampoule C is not completely melted, thus a comparison of the solidification behavior between one gravity and low gravity processed specimens can be made.

A AMPOULES

Figures 2 and 3 represent photomacrographs of one and low gravity processed gold-germanium specimens. As can be seen, precipitation/segregation

of the germanium mainly occurs at the top of the one gravity specimens, as opposed to the more random distribution in the low gravity processed specimens.

Microscopic documentation was primarily limited to the low gravity specimens, since the gross segregation of the one gravity processed specimens prevented any extensive interpretation. In essence, the density differences between the elements dominated to the extent that minimal interaction in terms of microstructural differences occurred.

Figures 4 through 6 are optical, electron microprobe and scanning electron photomicrographs of typical specimen areas. For the most part, the areas are identical for each type of instrument utilized and are representative of the specimen microstructure. Some differences in microstructural appearance are evident between the surface and the interior of the specimens; however, the presence of either a very fine dispersion or a compound is still evident. In addition, comparison of gold-germanium specimens from another program [Reference 3] cooled at much faster rates with those on this program (an example is Figure 7) show that cooling time does play an important role in the microstructural features of immiscible systems.

Table I presents the X-ray diffraction data of the specimens which do not correspond to the known diffraction data of the elements and the metastable gamma germanium gold. Both unknown lines of varying intensities were found. If the lines correspond to a metastable compound, the varying intensity may be due to the orientation within the specimen since it has been noted that both the d spacing and the intensity will vary as a function of orientation [Reference 5].

Superconductivity measurements were made on the bulk specimens by the inductance method as shown schematically in Figure 8 . None of the one gravity but all of the low gravity processed specimens superconducted at 1.5 K, although the signal was weak. This indicates that only a small portion of the specimen superconducts, possibly correlating to the fine dispersions. Superconducting transition temperatures are shown in Figure 9.

Resistivity measurements using a Leeds four point probe were made on the one and low gravity processed specimens and the results are shown in Figure 10 . As can be seen, the resistivity of the one gravity processed specimens decreases toward the gold rich end due to the gravity gradient. The values are higher than for pure gold since some germanium is present.

B AMPOULES

Figures 11 and 12 are photomacrographs of the one and low gravity processed lead-zinc-antimony specimens. As with the gold-germanium, extensive segregation occurred in the one gravity specimens and microscopic documentation was primarily limited to the low gravity processed specimens since the segregation again prevented meaningful interpretation. Figures 13 through 15 are optical, electron microprobe and scanning electron photomicrographs of typical specimen areas.

The low gravity processed specimens are not only more uniformly dispersed, but additionally zinc is the primary matrix, with lead as the dispersant and antimony is predominantly associated with the zinc, as opposed to the one gravity processed specimens.

As with the A Ampoules, the X-ray diffraction patterns of the low gravity processed specimens show additional lines which do not correspond with any of the known elements or compounds. Table II presents the d spacings and intensities.

Superconductivity measurements were made on the B specimens in the same manner as with the A specimens and the results are shown in Figure 16. Both the one and low gravity specimens exhibited the same superconducting behavior to 7.2K, but the low gravity specimens had an additional transition at 9.2K, which is 2K higher than any of the three compositional elements. The reason for this anomalously high transition temperature is not known, although it may be due to the fine dispersion of lead in the zinc-antimony matrix leading to a fine particle superconductivity effect [References 6 and 7].

As with the A specimens, resistivity measurement were made with the Leeds four point resistivity probe and are shown in Figure 17. Again, a more uniform resistivity was noted with the low gravity as compared to the one gravity processed specimens.

C AMPOULES

Due to the nature of the electronic testing performed on these materials, minimal metallagraphic documentation was done on these specimens. Figures 18 and 19 exemplify the transition zone where solidification started and the directional solidification that occurred during cooldown. In general, the directional microstructure of the low gravity processed specimens is finer and of better quality than the controls. Table III gives the X-ray data for the specimens; there was no appreciable difference between the one and low gravity specimens.

Magnetic measurements were carried out on the directionally solidified Pb-Sn-In C specimens processed in one and in low-gravity environment. Dispersion of the Sn-rich phase, which is non-superconducting at 4.2 K, may act as pinning sites to flux movement [Reference 8], resulting in hysteresis effects with large areas under the magnetization curves. If Pb-rich lamellar structures of small dimensions are formed by directional solidification, this may be apparent in an increase in H_{c2}.

Both the one and low gravity processed specimens were sectioned such that the maximum and minimum G/R ratio portions as shown in Figure 20 were measured to determine the effect of directional perfection, etc. on the magnetic properties. The samples were cut in 2 cm lengths and placed to fit tightly in the center of coils wound with 10,000 turns of #36 copper magnet wire to length of 3.4 cm. Permeability measurements were made as a function of the magnetic field by measuring the inductance with a bridge at 1 kHz with the coils placed in the center

of a superconducting solenoid with the axes approximately parallel to the field. Three coils could be arranged symmetrically about the axis of the solenoid with the center of the samples separated by 2.5 cm. This allowed the samples to be within a sphere of less than 1% inhomegeneity in the magnetic field. All measurements were made with the samples immersed in liquid helium at a temperature of 4.2K. A schematic diagram of the apparatus is shown in Figure 21.

A typical magnetization curve is shown in Figure 22 and the data is presented in Table IV, where "cold end" refers to the section of sample cut from the region processed with a high G/R ratio. Hysteresis effects are apparent indicating the presence of trapped flux. This is the region where the greatest amount of two phase directional solidification is expected [References 9,10].It is noted that with the one gravity processed samples there is little correlation in H_{c2} values between the high and low G/R specimens. The low gravity processed samples, however, show consistently higher H_{c2} values for the portion having a high G/R ratio. These samples also show somewhat more pronounced hysteresis with larger areas under the curves, indicating more extensive flux pinning by the Sn-rich phase. These results correspond to a greater extent of directional solidification with low gravity processing compared to the one gravity processed samples. In the region of high G/R ratio (cold end), the low gravity processed samples show an average increase in H_{c2} of 260 Oe, compared to the one gravity processed samples.

CONCLUSION

Three systems possessing either liquid or solid state immiscibility have been processed in the M-518 facility on board Skylab. From the metallurgical and electronic examinations, the low gravity processed specimens exhibited unique metallurgical features and enhanced electronic properties as contrasted to the one gravity processed controls.

The A specimens corroborated the effect of cooling rate on the metallurgical structure.

The unknown X-ray diffraction lines exhibited by the low gravity processed A and B specimens indicates that processing in this type of environment can lead to morphological structures not found in the one gravity processed specimens. It is not known at this time if the unusual superconducting transitions found in these systems are related to these diffraction patterns.

Inasmuch as a low gravity environment suppresses thermal convection, high G/R ratios can be utilized to obtain directionally solidified structures having superior metallurgical and electronic features, exemplified by the C specimens, as contrasted to the one gravity processed specimens.

It must be emphasized that these materials represent only a

fraction of the hundreds of systems possessing a miscibility gap which have been identified. However, the interesting electronic and metallurgical behavior of these processed materials has lead to cautious optimism regarding the potential use of this class of materials. Thus from this work, it is anticipated that future research into immiscible systems will benefit not only the basic understanding of materials behavior but ultimately enable materials to be produced which will have extremely useful applications.

REFERENCES

1. "Test and Evaluation of Apollo 14 Composite Casting Demonstration Specimens 6, 9 and 12," Contract NAS 8-27085, Phase I, TRW Systems Group, Redondo Beach, CA
2. "Test and Evaluation of Apollo 14 Composite Casting Demonstration Specimens 6, 9 and 12," Contract NAS 8-27085, Phase III, TRW Systems Group, Redondo Beach, CA
3. J. L. Reger, "Study on Processing Immiscible Materials in Zero Gravity," Contract NAS 8-28267, TRW Systems Group, Redondo Beach, CA
4. L. L. Lacy and G. H. Otto, "The Electrical Properties of Zero Gravity Processed Immiscibles" Paper No. 74-208, presented at the AIAA 12th Aerospace Sciences Meeting, Jan 30 - Feb 1, 1974, Washington, D. C.
5. T. R. Anantharaman, et al, Trans. A.I.M.E., 233, 2014 (1965).
6. J. Hurault, "Superconductivity in Small Crystallites," J. Phys. Chem. Solids 29, 1765 (1968).
7. J. H. P. Watson, "Possibility of Ultrahigh Critical Fields in Granular Hard Superconductors," Appl. Phys. Letters 15, 125 (1969).
8. J. D. Livingston, "Flux Pinning by Superconducting Precipitates," Appl. Phys. Lett. 8, 319 (1966).
9. F. R. Mollard and M. C. Flemings, "Growth of Composites from the Melt-Part I ," Trans. TMS - AIME 239, 1534 (1967).
10. F. R. Mollard and M. C. Flemings, "Growth of Composites from the Melt-Part II," Trans. TMS - AIME 239, 1534 (1967).

Table I. Unknown X-Ray Diffraction Lines for A Specimens

d Spacing, Å	I/I_o [1]	Specimens [2]
1.992	8	11
1.293	10	12
1.021	2,5,3	10,11,12
0.9108	7,26,29	10,11,12
0.8926	32	12
0.8334	7,33,30	10,11,12
0.8307	11	12

Table II. Unknown X-Ray Diffraction Lines for B Specimens

d Spacing, Å	I/I_o [1]	Specimens [2]
3.450	4,12	10,12
3.437	27	11
2.976	14	11
2.3.3	15,5	10,12
2.135	15,17	6,11
2.004	22	10
1.489	49	11
1.336	10	11
1.310	11,4	11,12
1.255	38	12
1.133	25,9	11,12
1.008	7,7,10	10,11,12
0.9503	11,8,10	10,11,12
0.8656	12	12
0.8346	7,7,5	10,11,12

Table III. Unknown X-Ray Diffraction Lines for C Specimens

d Spacing, Å	I/I_o [1]	Specimens [2]
3.048	42	All
2.840	60	All

1. Ratio of line intensity to strongest peak
2. Both one and low gravity processed specimens

Note: All other lines identified.

Table IV. H_{c2} Values for Pb-Sn-In Eutectic Alloys *

Sample (1-g)	H_{c2} (kOe)	Sample (low-g)	H_{c2}(kOe)
1 C cold end	3.62	10 C cold end	3.88
1 C hot end	3.69	10 C hot end	3.80
2 C cold end	3.76	11 C cold end	4.06
2 C hot end	3.66	11 C hot end	3.60
3 C cold end	3.67	12 C cold end	3.89
3 C hot end	3.90	12 C hot end	3.62

* Average H_{c2} values for Pb-Sn-In eutectic alloys

	One-g processed	Low-g processed
Cold end	3.68 kOe	3.94 kOe
Hot end	3.75 kOe	3.67 kOe

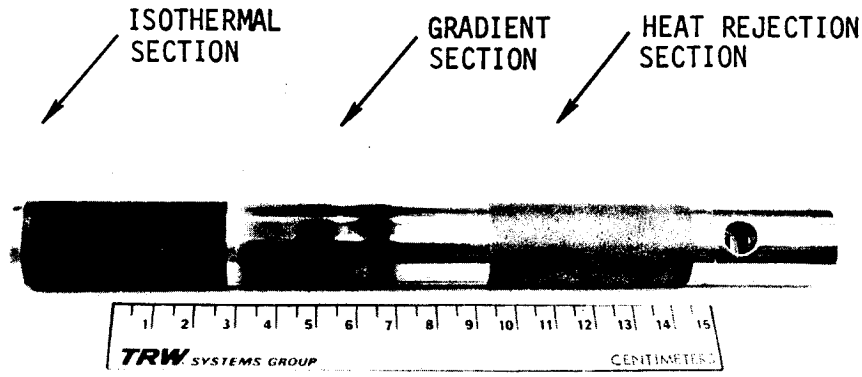

PROCESSED M-557 CARTRIDGE SHOWING EXTERNAL CONFIGURATION

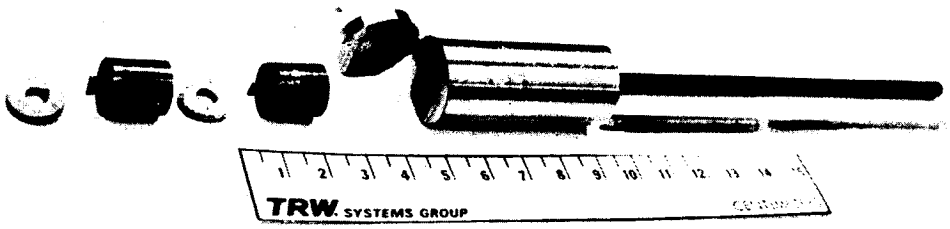

DISASSEMBLED AMPOULE SET

FIGURE 1. M-557 CARTRIDGE AND AMPOULE CONFIGURATION

Specimen 1A

Specimen 5A

Specimen 12A

FIGURE 2. ONE GRAVITY PROCESSED SPECIMENS 1A and 5A AND LOW GRAVITY PROCESSED SPECIMEN 12A (10X)

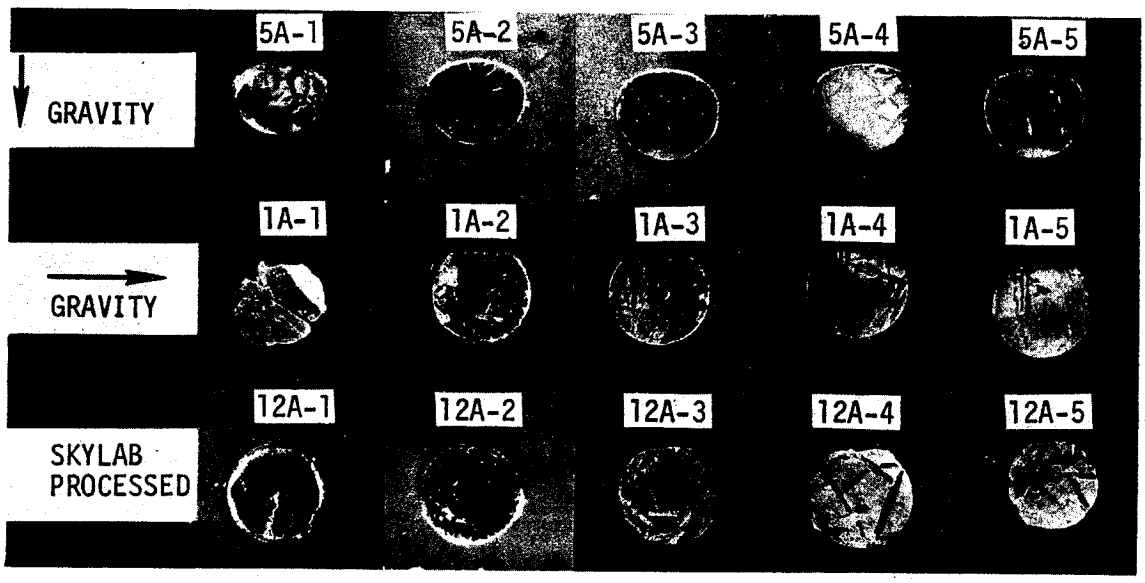

Figure 3. Axially Sectioned Specimens 1A, 5A and 12A (1.5X)

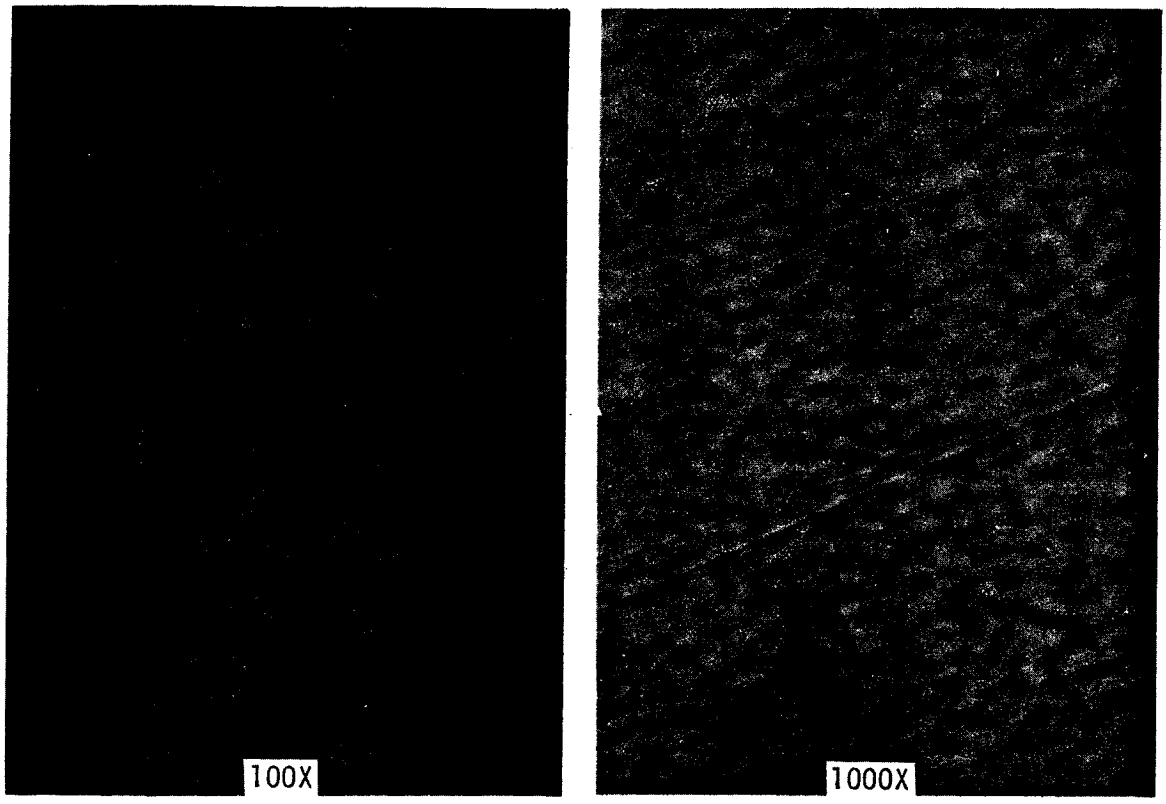

FIGURE 4. OPTICAL PHOTOMICROGRAPHS OF SECTION 12A - 2

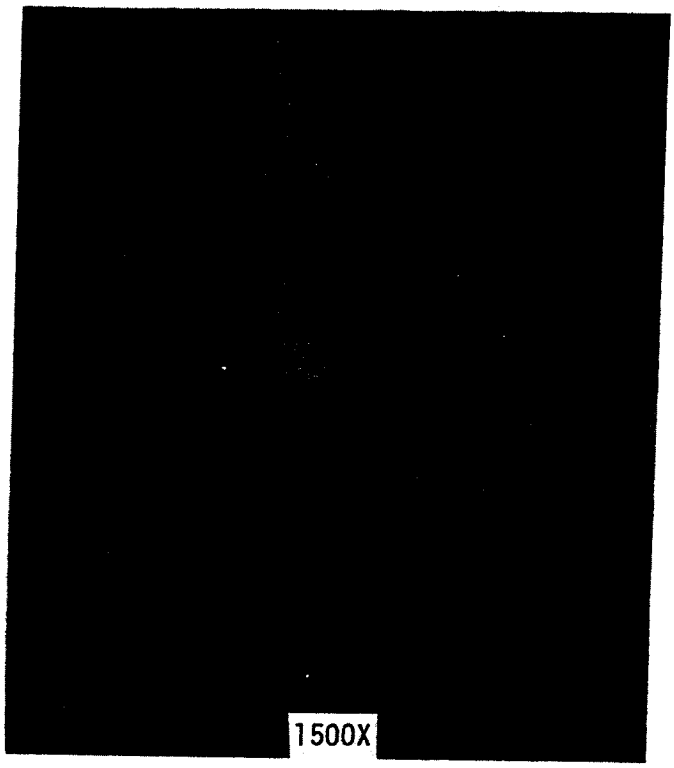

FIGURE 5. SEM PHOTOMICROGRAPHS OF SECTION 12A - 2

absorbed electron

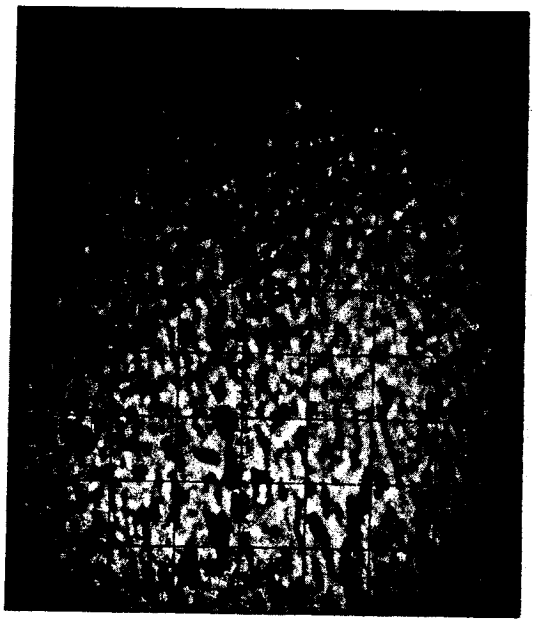

Au

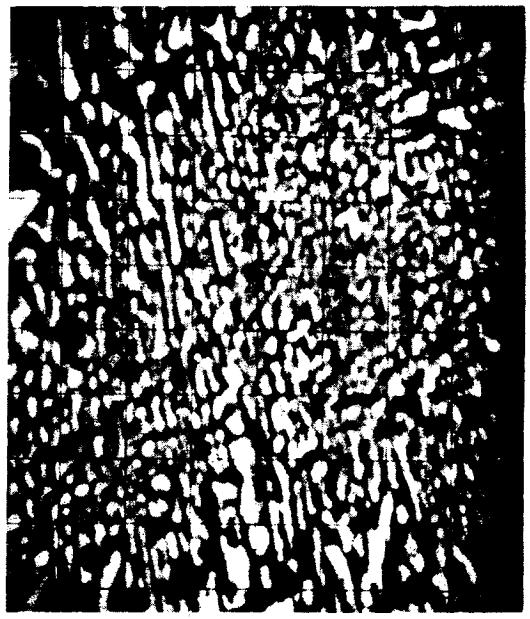

Ge

FIGURE 6. ELECTRON MICROPROBE PHOTOMICROGRAPHS
OF SECTION 12A - 2 (900X)

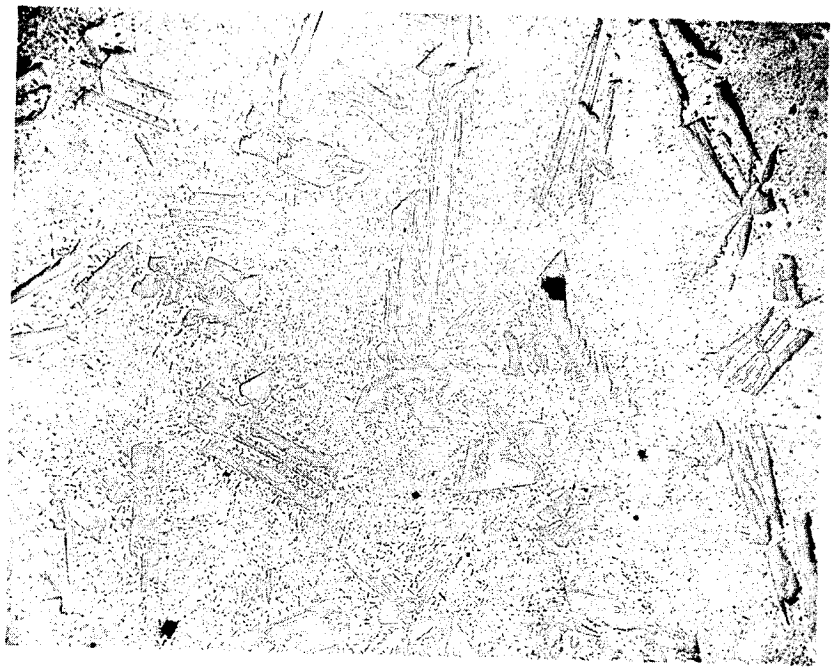

Specimen 1-C

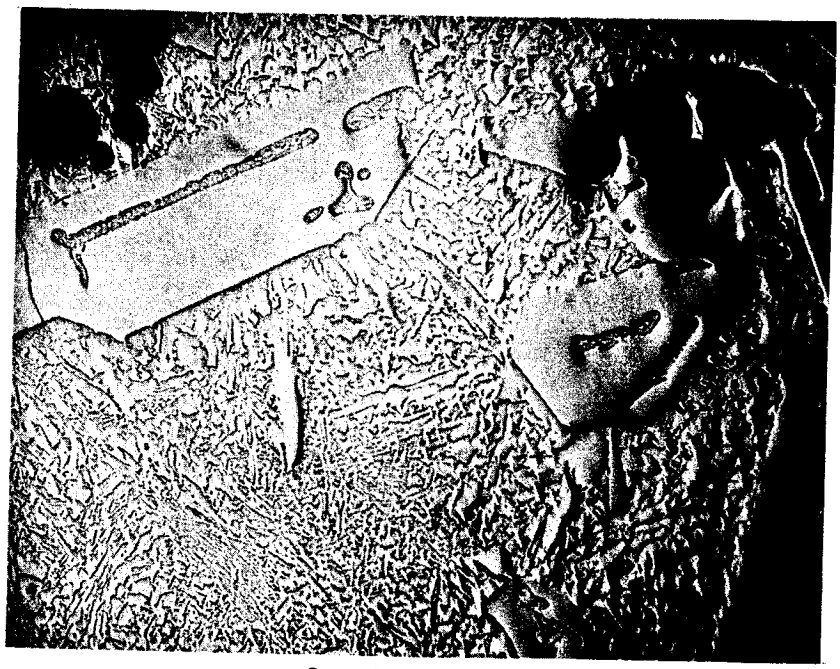

Specimen 12A

FIGURE 7. SPECIMEN 12A VERSUS KC-135 PROCESSED SPECIMEN 1-C (50X)

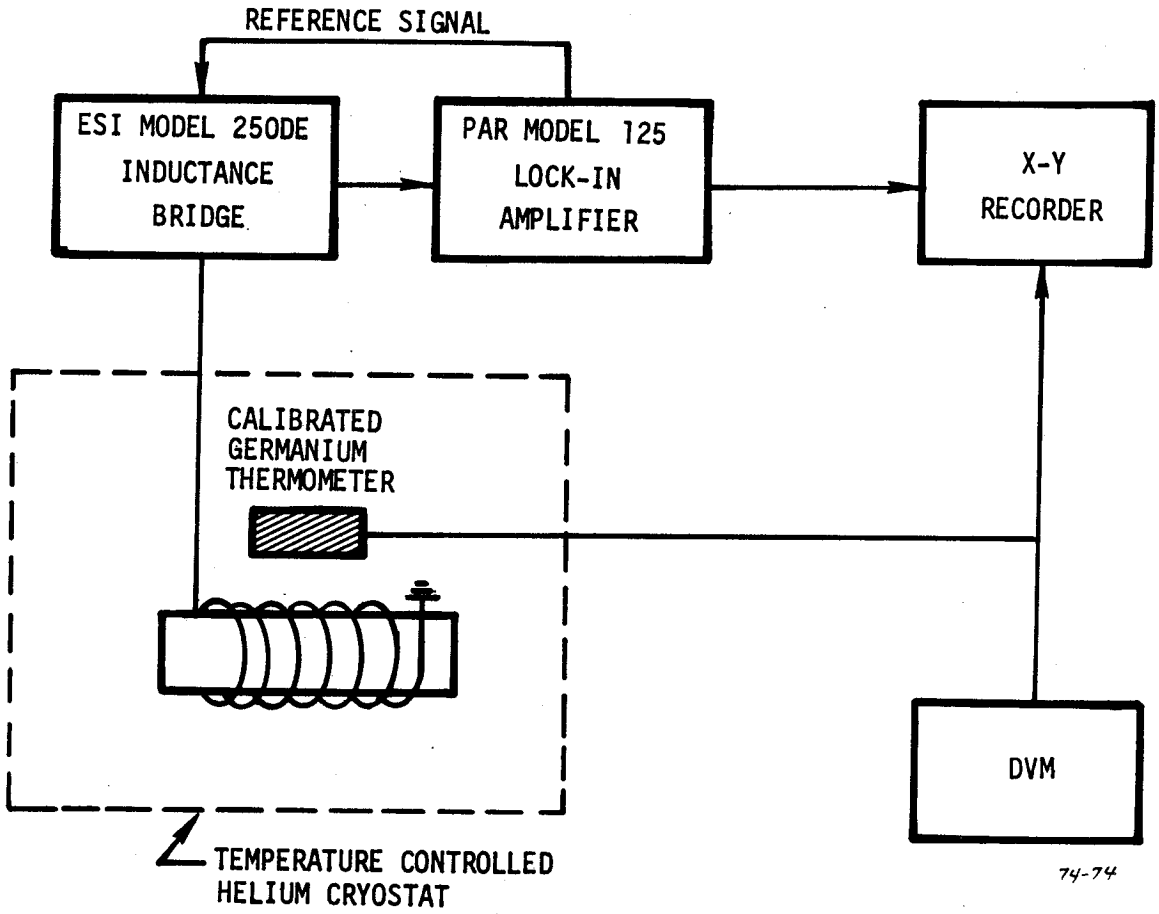

FIGURE 8. SCHEMATIC BLOCK DIAGRAM FOR INDUCTANCE MEASUREMENTS

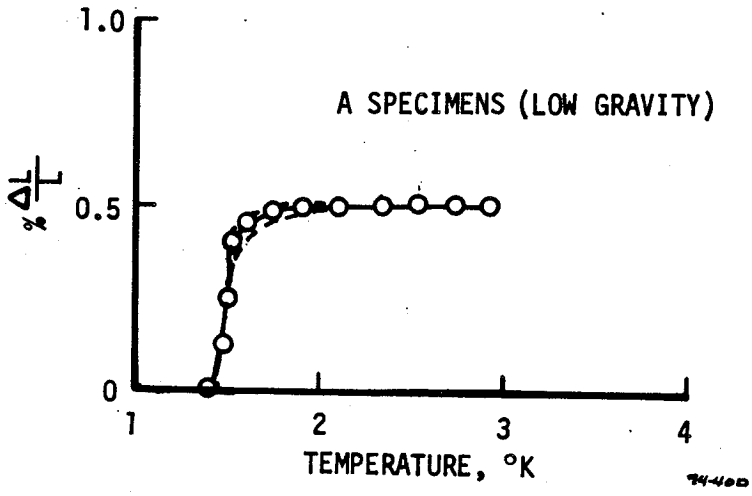

FIGURE 9. SUPERCONDUCTING TRANSITION TEMPERATURES OF A SPECIMENS

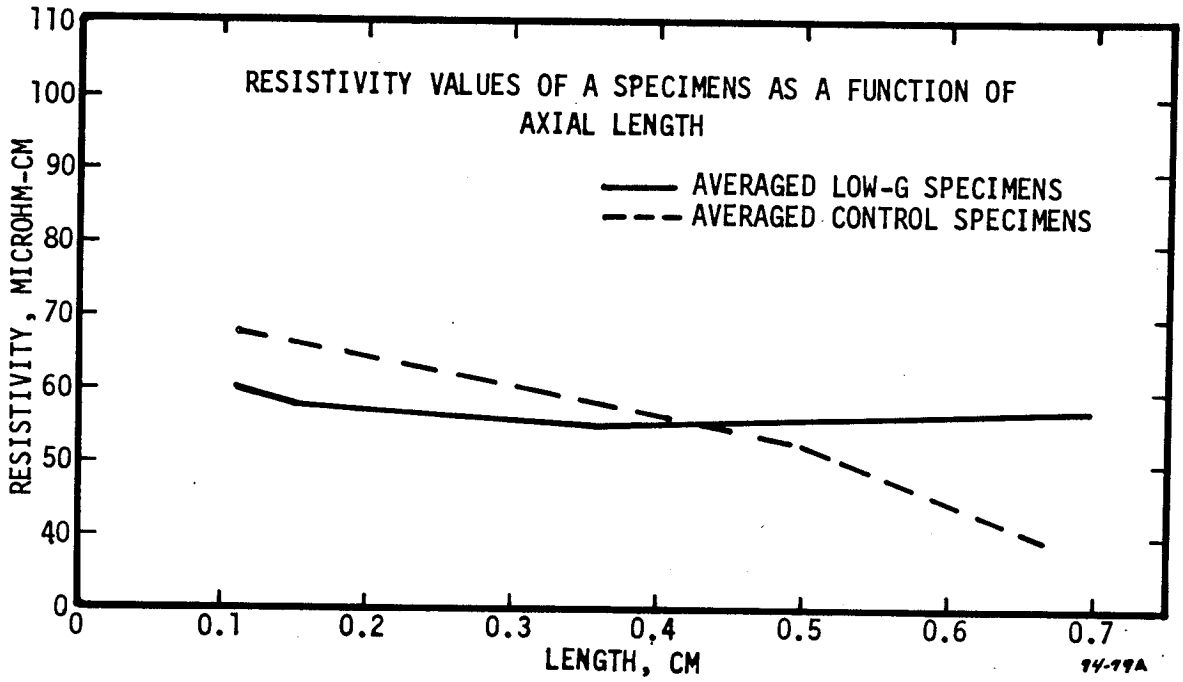

FIGURE 10. RESISTIVITY OF CONTROL AND LOW GRAVITY PROCESSED A SPECIMENS

Specimen 3B

Specimen 5B

Specimen 12B

FIGURE 11. ONE GRAVITY PROCESSED SPECIMENS 3B AND 5B AND LOW GRAVITY PROCESSED SPECIMEN 12B (10X)

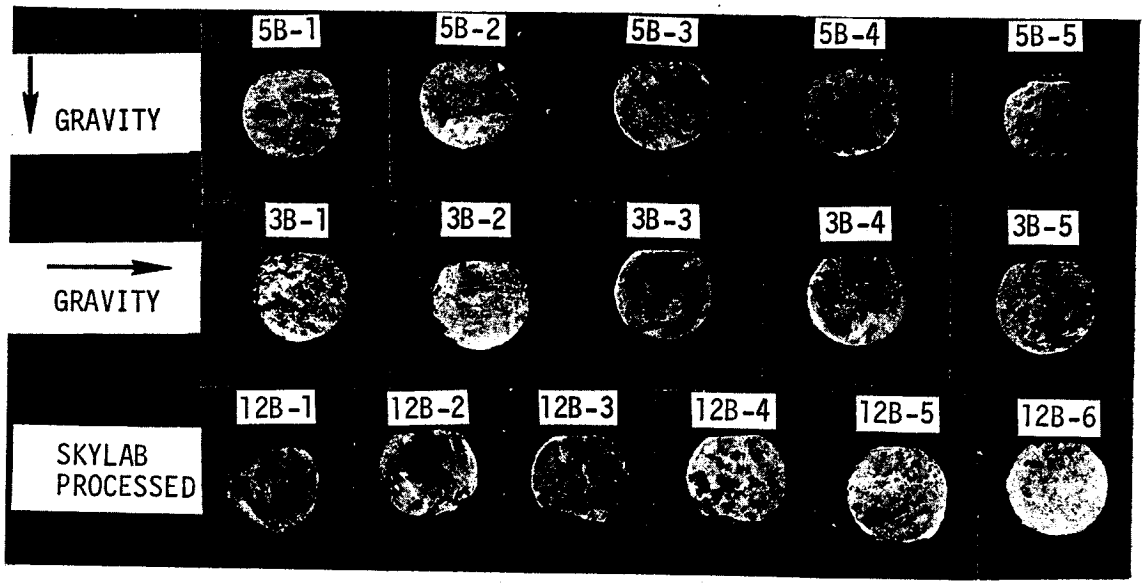

FIGURE 12. AXIALLY SECTIONED SPECIMENS 3B, 5B AND 12B (1.5X)

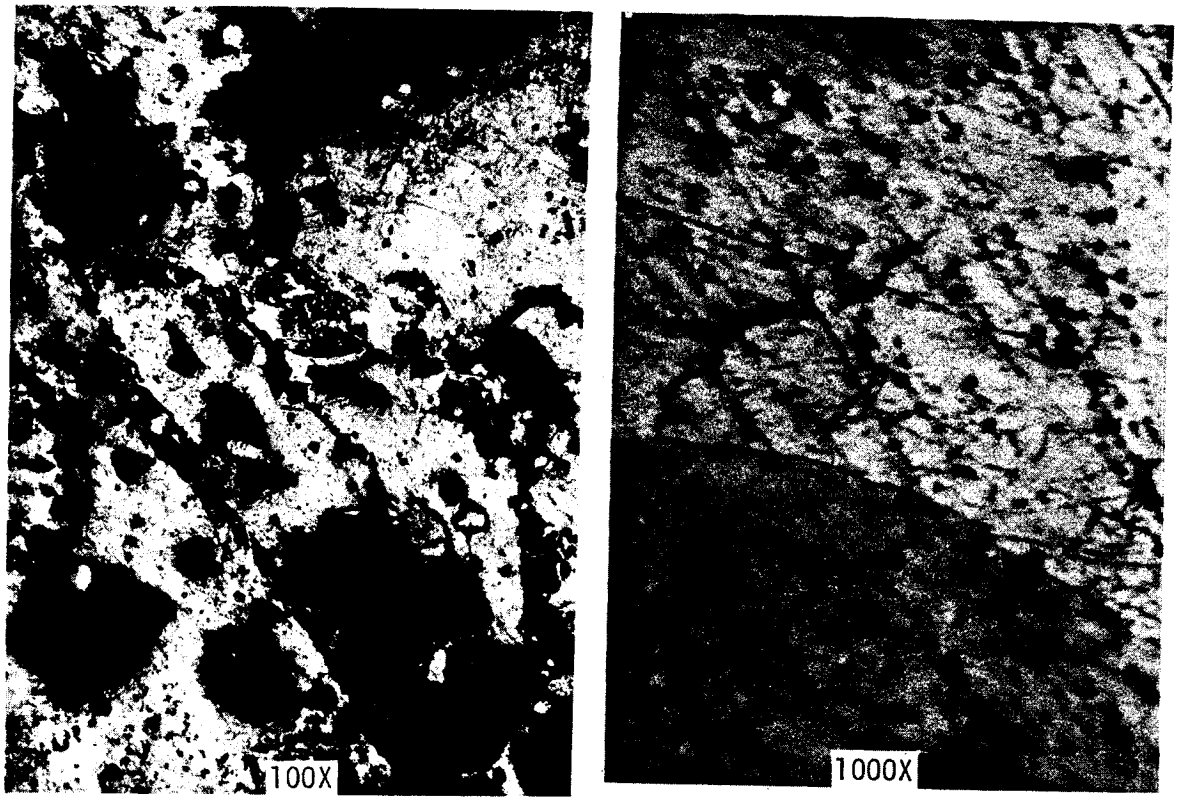

FIGURE 13. OPTICAL PHOTOMICROGRAPHS OF SECTION 12B - 2

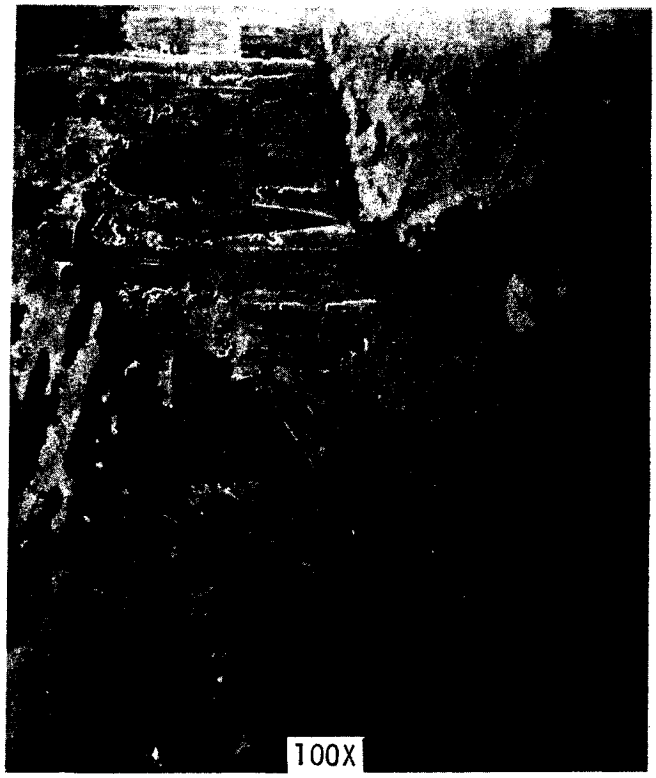

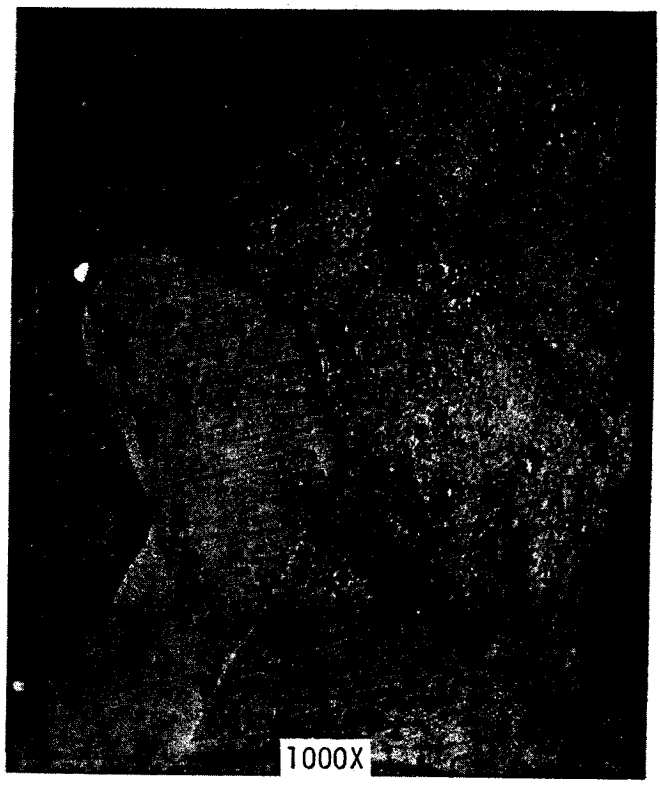

FIGURE 14. SEM PHOTOMICROGRAPHS OF SECTION 12B - 2

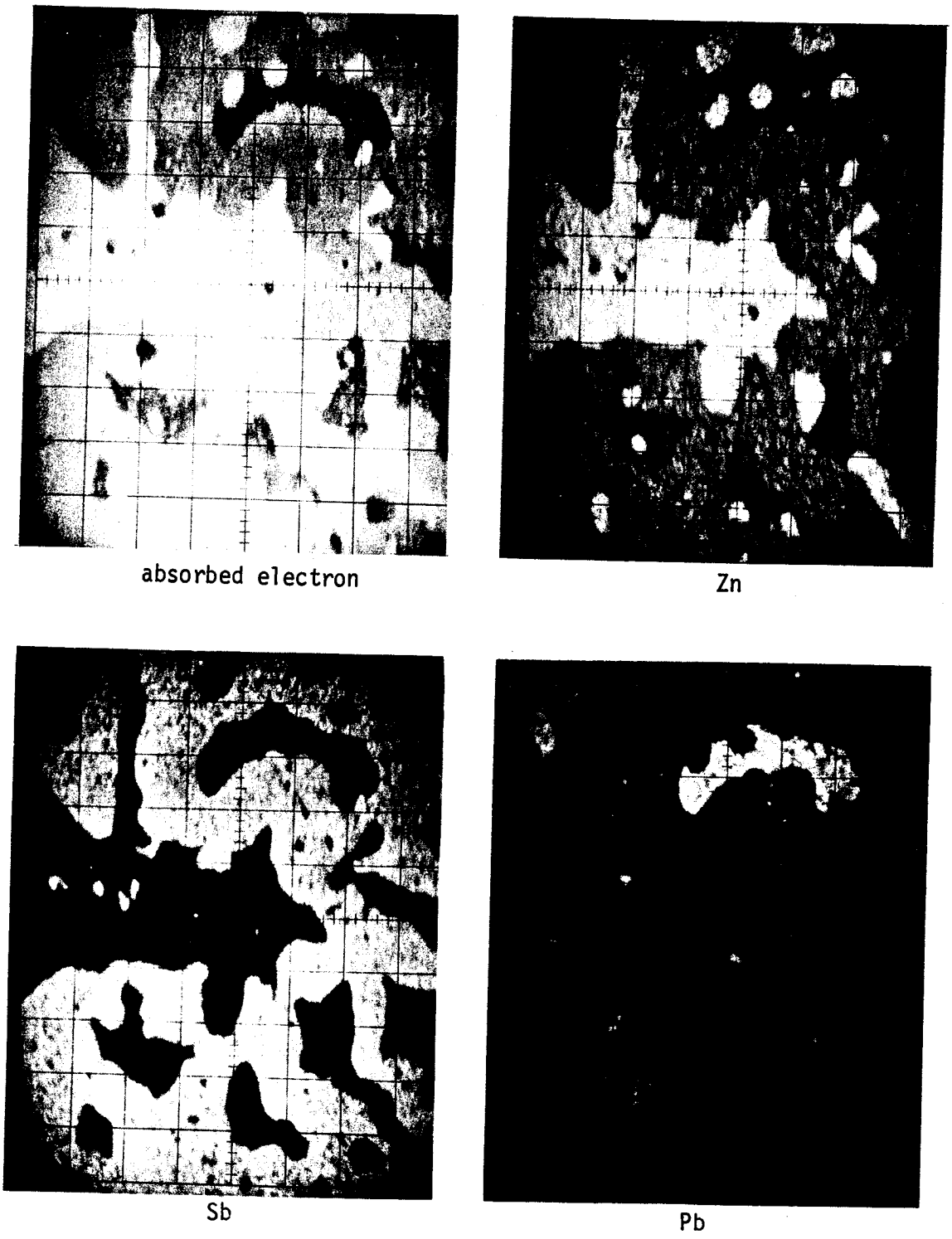

FIGURE 15. ELECTRON MICROPROBE PHOTOMICROGRAPHS OF SECTION 12B - 2 (900X)

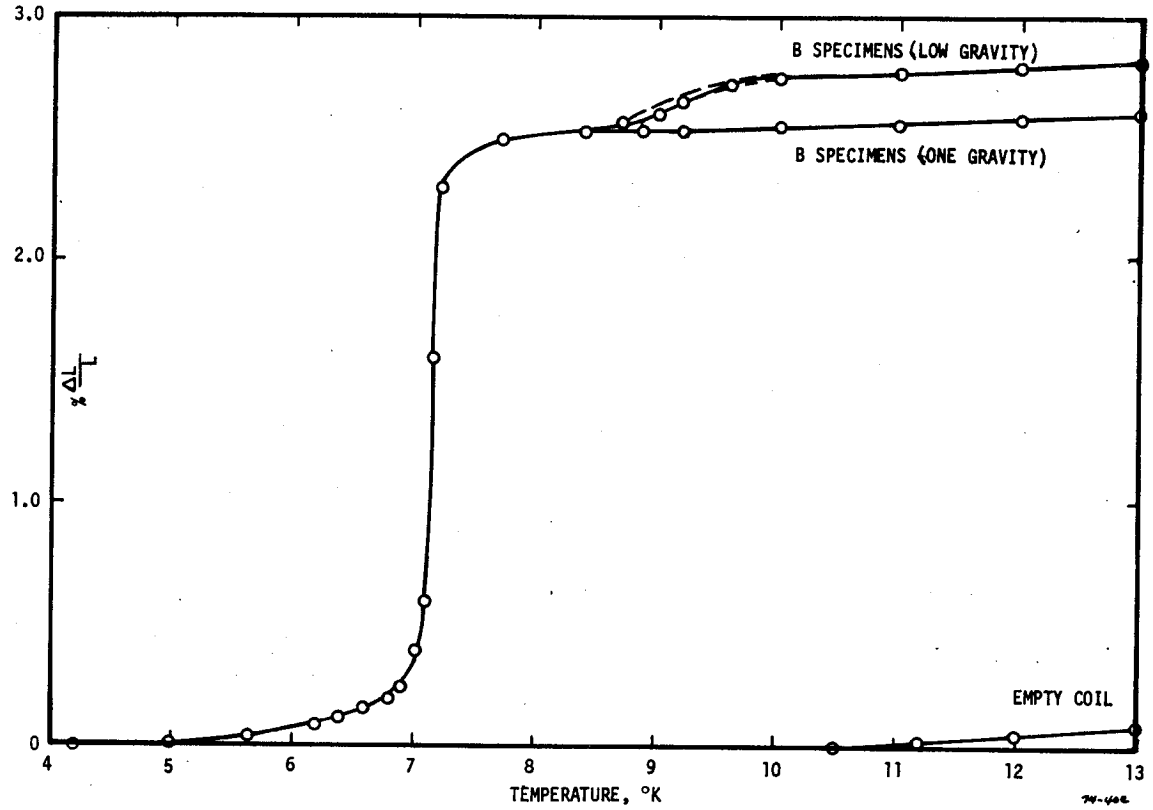

FIGURE 16. SUPERCONDUCTING TRANSITION TEMPERATURES OF B SPECIMENS

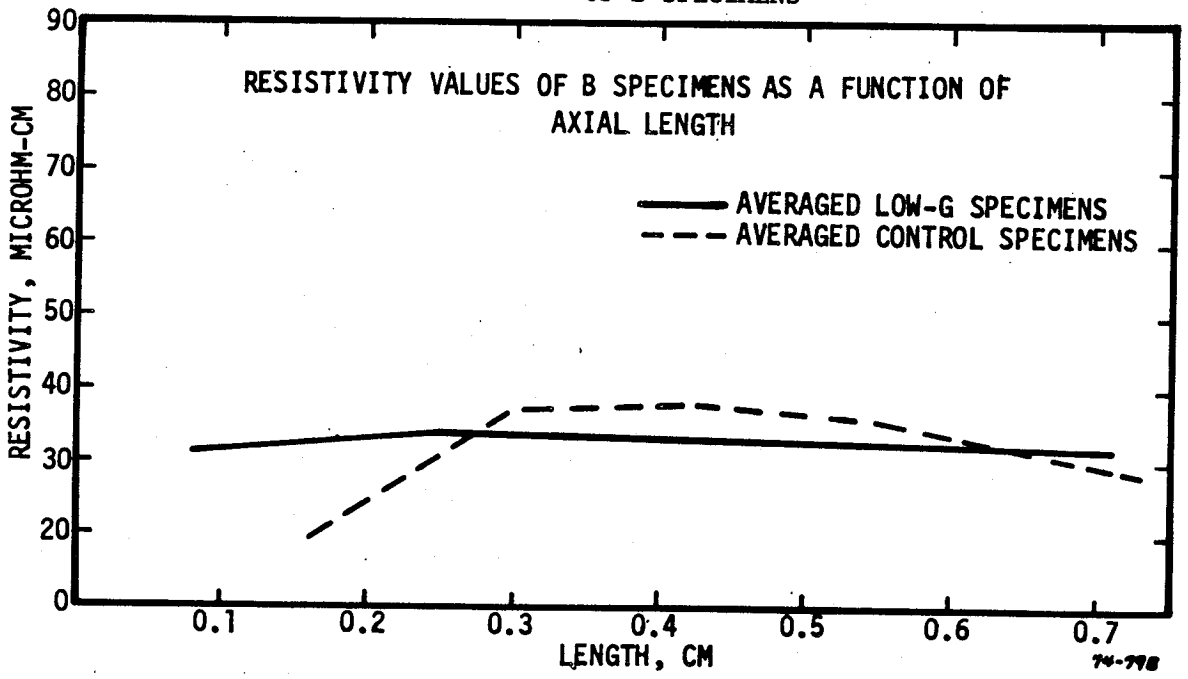

FIGURE 17. RESISTIVITY OF CONTROL AND LOW GRAVITY PROCESSED B SPECIMENS

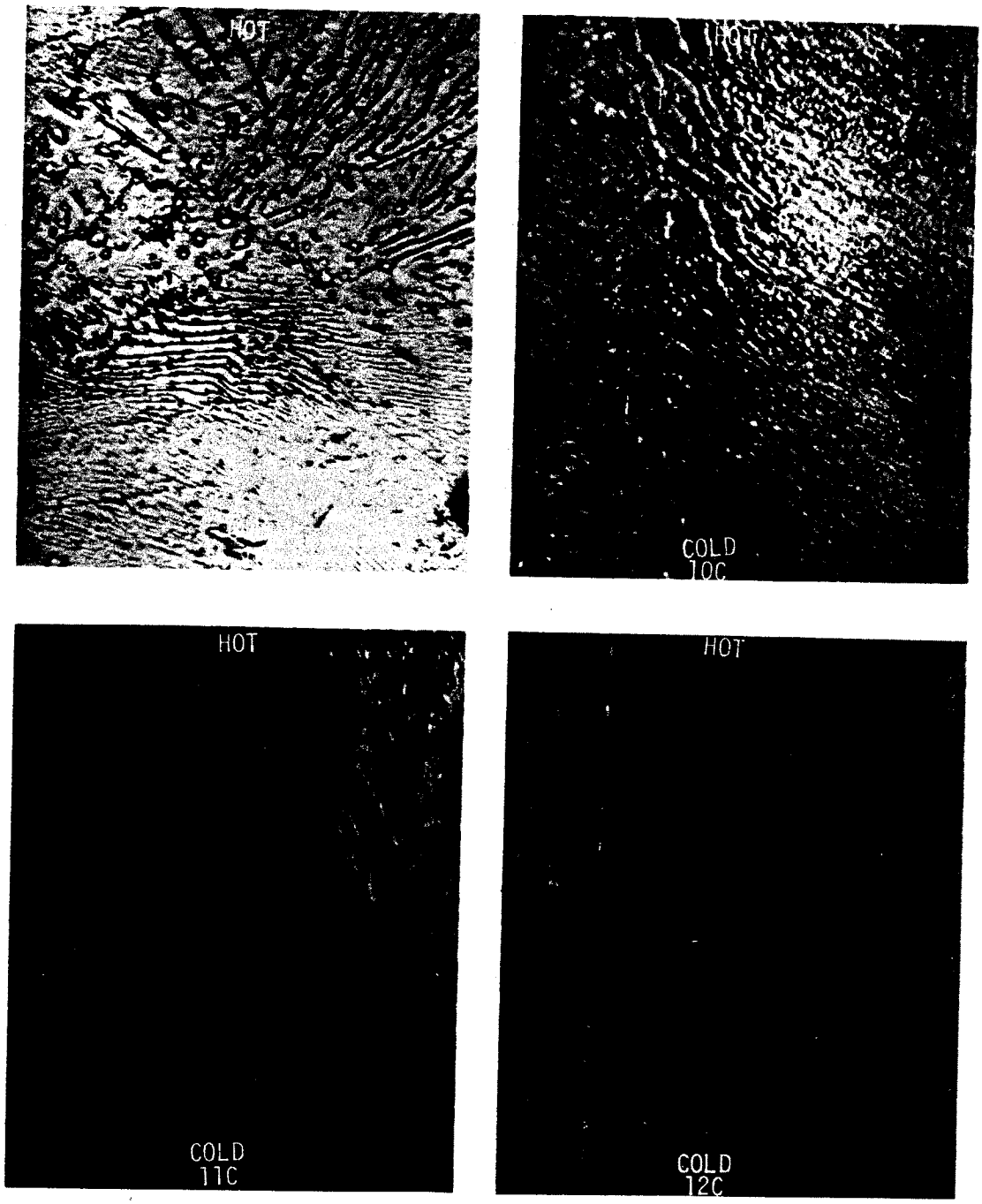

FIGURE 18. TRANSITION ZONE OF C SPECIMENS (500X)

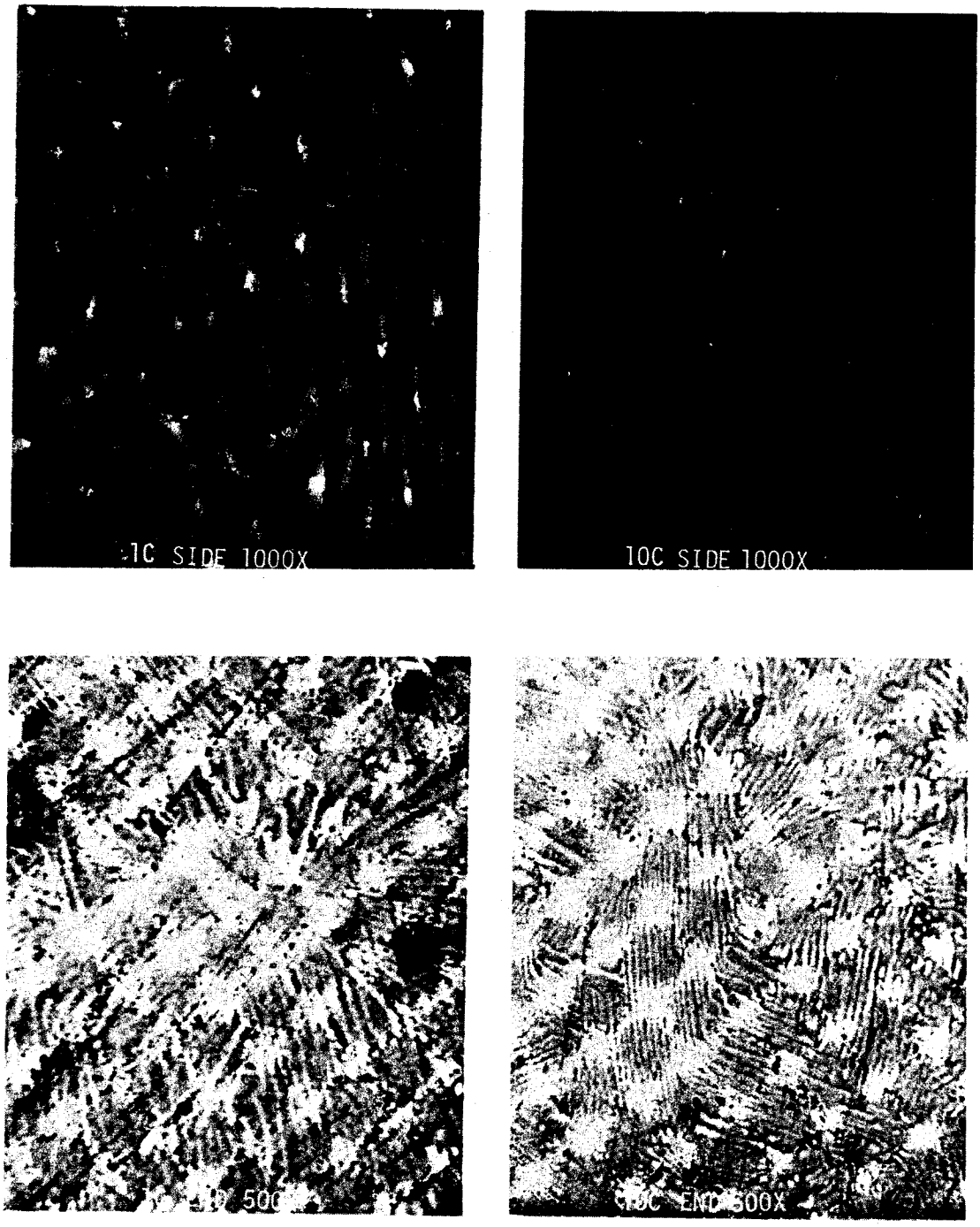

FIGURE 19. HOT ZONE PHOTOMICROGRAPHS OF C SPECIMENS

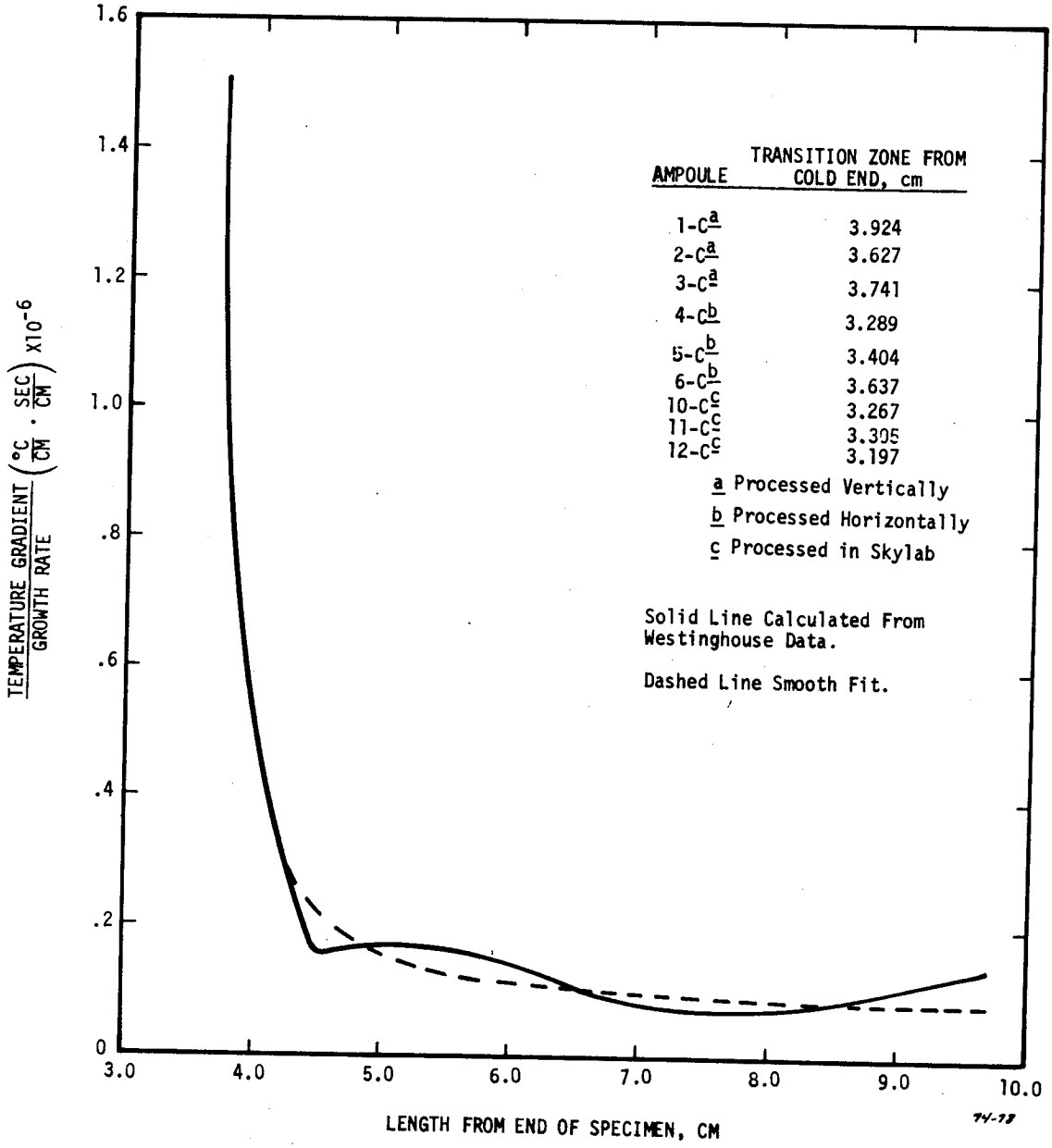

FIGURE 20. G/R RATIO AS A FUNCTION OF DISTANCE FROM COLD END

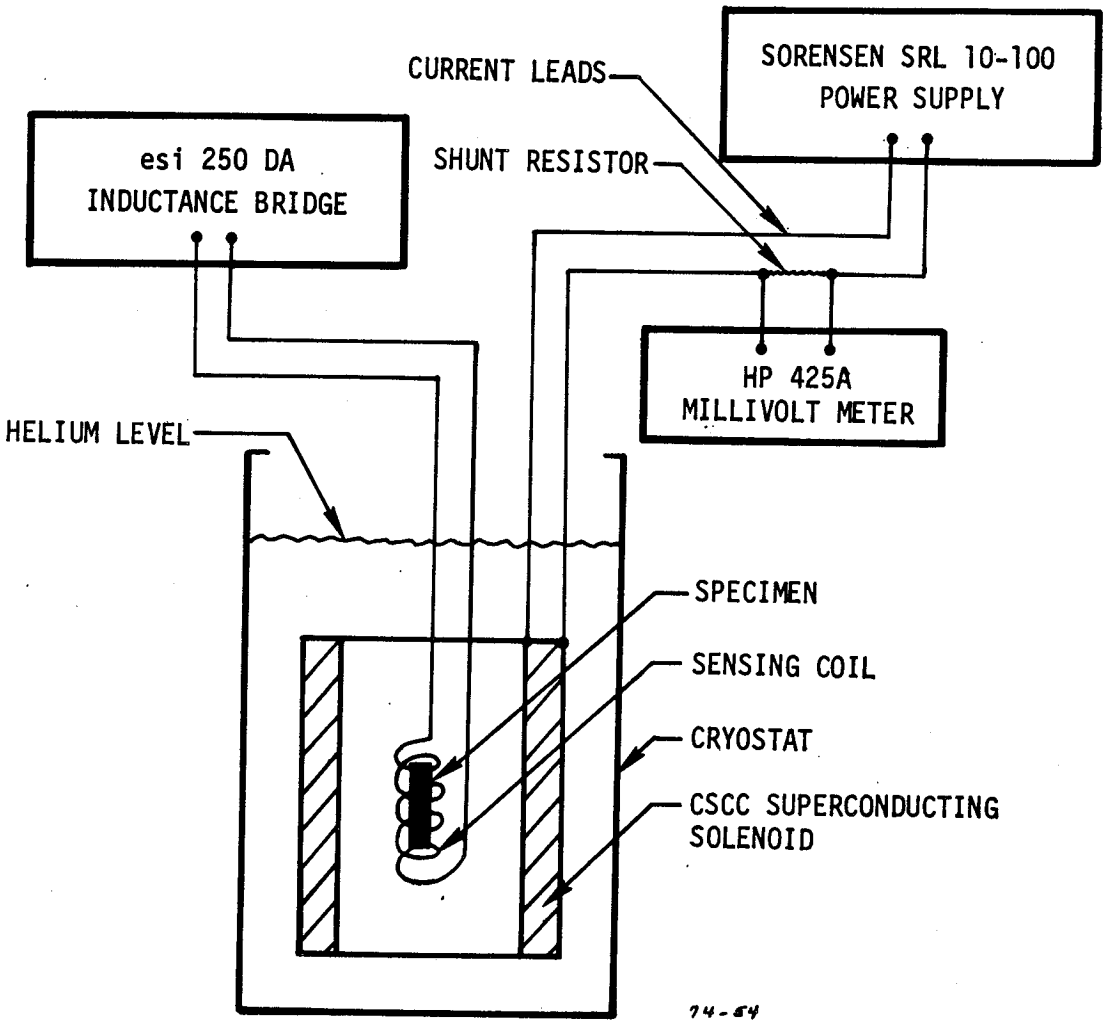

FIGURE 21. SCHEMATIC REPRESENTATION OF MAGNETIZATION MEASURING APPARATUS

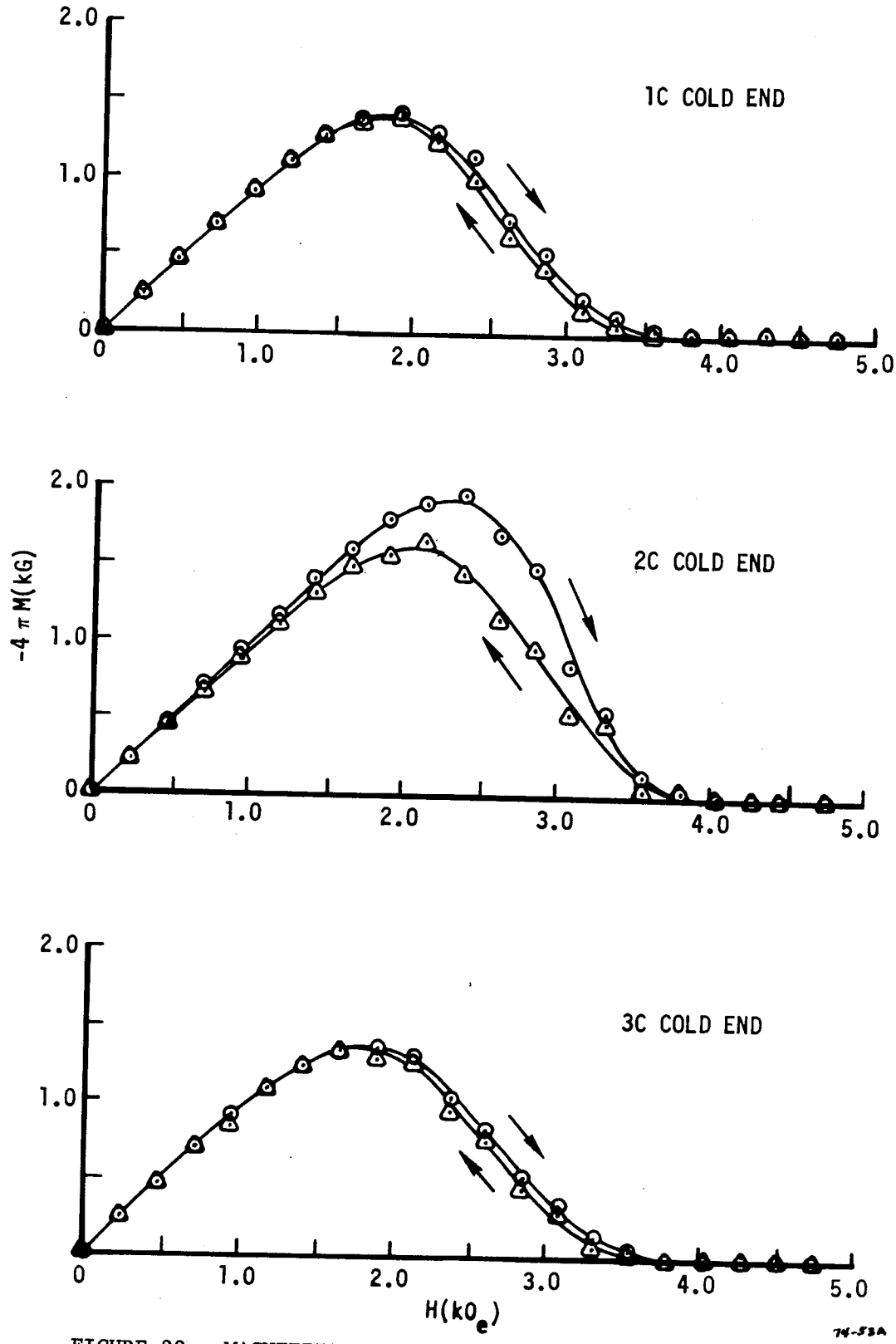

FIGURE 22. MAGNETIZATION CURVES FOR ONE GRAVITY PROCESSED C SPECIMENS

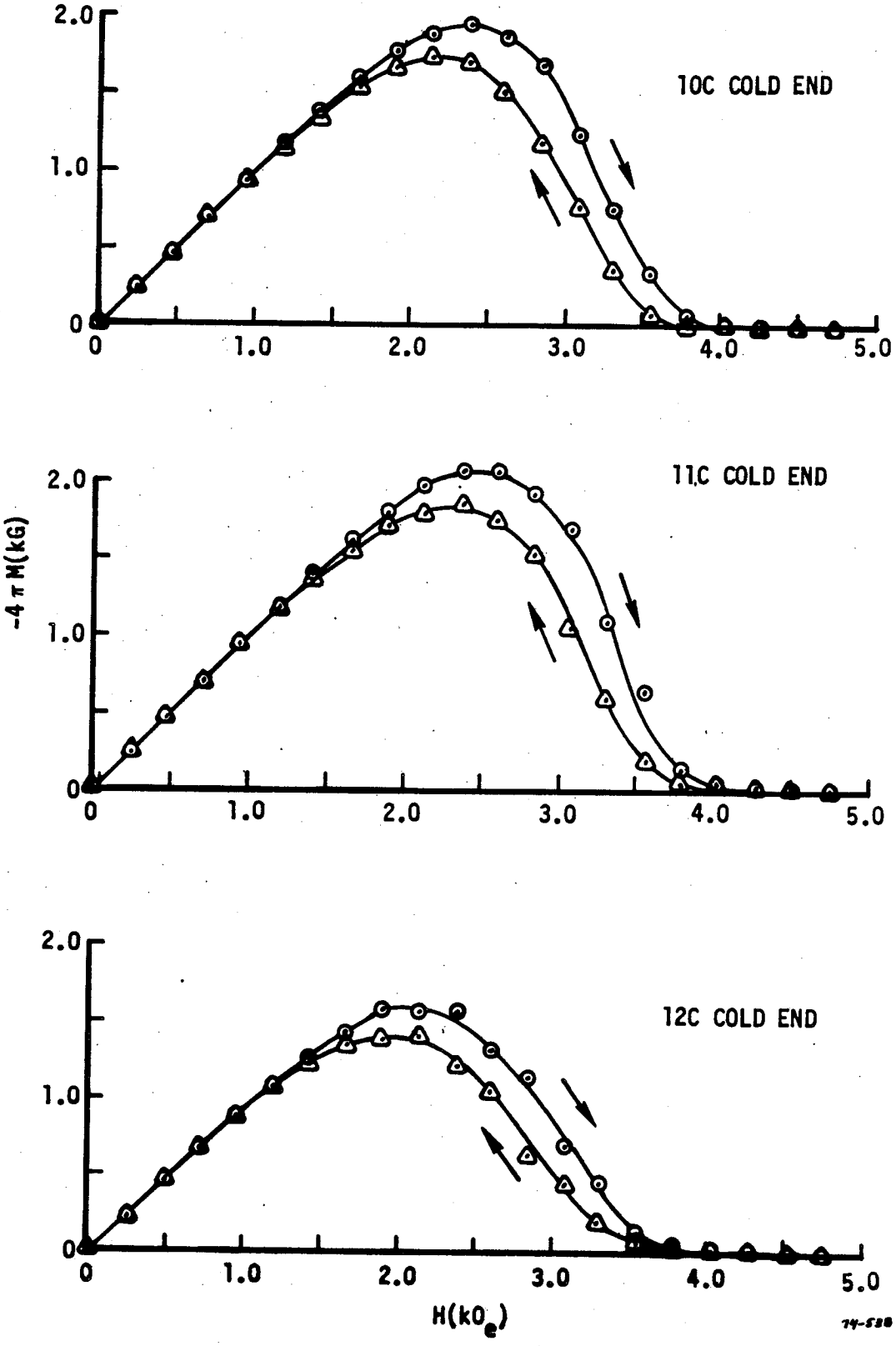

FIGURE 22. (CON'T) MAGNETIZATION CURVES FOR LOW GRAVITY PROCESSED C SPECIMENS

SILVER SAMPLES MELTED IN SPACE
SKYLAB EXPERIMENT M565

By

A. Deruyttere, E. Aernoudt*, H. Goeminne, J. Smeesters
O. Arkens, M. Verhaeghen
Department of Metaalkunde, Universiteit te Leuven
Leuven, Belgium

SUMMARY

The objective of the experiment was to make a preliminary study of the behaviour of porous material when melted and resolidified in weightless condition.

Two kinds of samples have been used: perforated discs and a fibre compact. The observations made on the various specimens are presented and compared with those made on similar specimens treated in the same manner on the ground.

Some provisional conclusions are:

(1) most of the original porosity in the samples has disappeared during the melting stage. This could possibly be avoided by different heating and pressure conditions or by using samples with closed pores. If necessary, the mobility of the pores could probably be reduced by the presence of a slowly diffusing gas

(2) even if samples were perfectly spherical in the liquid state, their shape is altered on solidification due to both shrinkage pipe formation and constitutional supercooling

*Paper presented by E. Aernoudt.

(3) the leveling out of impurity concentration gradients appears indeed to be slow in the molten metal when gravity induced convection is absent

(4) when only a part of a solid body is melted in zero gravity, the tendency of the molten part to become spherical may be much restricted.

OBJECTIVES OF THE EXPERIMENT

Some products made by powder and fibre metallurgy are intentionally porous, e.g., self-lubricating bearings, filters and damping devices. When a high porosity is desired, the necessary cohesion of the material can only be obtained through solid phase sintering, as any substantial melting would cause a rapid collapse of the porous structure. However, this may no longer happen when the melting is done in weightless condition. The melting of a porous material in space may produce a porous part in which size, shape and distribution of the pores are different from those obtainable on earth by classical powder metallurgy. Hence, some properties of the material, such as strength or filtering characteristics, may also be different from those that have been obtained so far. Knowledge gained through melting and resolidifying experiments on porous material in space, may therefore promote the development of new materials or the development of space techniques, e.g., repairing porous spacecraft parts by welding in space.

EXPERIMENTAL

The furnace

The Skylab multipurpose furnace M 518, designed and built by Westinghouse, can contain three stainless steel cartridges in which the specimen containing ampoules are sealed in (fig.1-3).
The main characteristics of the furnace are:

- ° outside diameter: about 10 cm
- ° overall length : about 30 cm
- ° powder of resistance heater: 150 watts
- ° maximum temperature: about 1000°C
- ° length of hot zone: 5 cm
- ° length of gradient zone: about 6 cm
- ° length of heat extraction zone: about 15 cm
- ° inner diameter of each of the three experiment chambres: about 2cm

The temperature is measured by two thermocouples located one in the graphite heat leveler, which separates the heater resistance from the experiment chamber, and the other in the heat extractor plate.

The cartridges

The cartridges (fig.4) were also designed and manufactured by Westinghouse. For the silver melting experiment they were made such as to provide a small temperature gradient in the hot zone. The purpose was that a part of the samples would not melt. This appeared to be the only way to be sure that the temperature had not exceeded too much the melting temperature, as the actual temperature of the samples could not be measured. Moreover, a varying temperature might yield additional information.

It had been anticipated to conduct the heating in such a way that the part of the samples which should melt, would stay only a short time at temperatures at or slightly above the melting point.

However, the ground based tests, made on similar samples and in a similar furnace as those used in flight, showed that the furnace had to be set on maximum power during heating up, and that there had to be a soak for one hour at the maximum allowed temperature in order to melt a little more than half of the samples. Because of these experimental limitations the most interesting experimental conditions such as very short holding times just above the melting point could not be obtained.

The ampoules

For the ampoules which had to contain the samples, the choice fell on silica tubes sealed in vacuo and designed in such a way (fig.5) that the various parts inside the ampoule were held together by a silica piston firmly enough as to avoid rattling. In fact rattling has not been avoided completely in every case, but this has not caused any serious trouble.

The samples

It appeared sensible to start with experiments on samples which are easy to characterise, at least in some ways. Originally it was intended to use two- and three-dimensional grids made of silver fibres arranged in regular arrays, as shown in fig.6. The possible variables were: wire diameter, mesh size, number of stacked layers, melting temperature, duration of melting and atmosphere (pressure). From melting and resolidifying such samples in space a wide variety of product shapes could be expected, ranging from many small spheres to a single massive sphere with in between various intermediate configurations.

When it became known that each experiment which NASA accepted for the Skylab furnace would have to be performed in a single run,

- i.e. that only one maximum furnace temperature and only one duration would be available, a drastic redesign of the experiment has to be made. A set of samples was finally selected as described below. The choice was also affected by the circumstance that a small temperature gradient would be provided in the high temperature zone of the furnace.

Silver was chosen as the experimental material because it is a typical metal, readily available with high purity, fairly unexpensive, easy to roll and draw, and melting at a temperature (961,9°C) below the maximum available temperature of 1000°C. The silver was of 99,999% grade (electrolytic silver melted under hydrogen in graphite crucible).

The ampoules were loaded as follows:
Ampoule A (fig.5) contained 8 silver discs of 14 mm diameter and 0.1mm thickness in which one or more holes had been spark cut or drilled as follows, when counting from the hot end of the ampoule:
P8: 1 central hexagonal hole of 3.5 mm side
P7: 1 central hexagonal hole of 3.5 mm side
P6: 1 central square hole of 1 mm side
P5: 4 square holes of 1 mm side and 6.4 mm apart
P4: 9 round holes of 1 mm diameter and 3.2 mm apart
P3: 21 round holes of 1 mm diameter and 1.6 mm apart
P2: 14 round holes of 2 mm diameter and 0.8 mm apart
P1: 21 round holes of 2 mm diameter and 0.4 mm apart

The silver discs were held apart by silica ring spacers and, in order to avoid mixing of the melting products from different discs, the silica ampoule was divided in compartments by stainless steel grids. The silica ampoules were sealed under a vacuum of about 10^{-5} mm Hg. Before sealing they were heated for one hour at 350°C in the same vacuum in order to decompose any Ag_2O present.

Ampoule B had exactly the same load as ampoule A, except that the discs had a thickness of 0.5 mm.

Ampoule C (fig.7) contained a single sample made of silver fibres of 0.4 mm diameter and 10-15 mm length. The fibres had been poured as randomly as possible into a cylindrical die, compressed into a disc of about 4 mm high and 50 mm diameter (maximum pressure about 10 kg/mm^2). The disc was sintered in hydrogen for two hours at 900°C. From this disc a prism was cut to dimensions 40 x 14 x 4 mm. The porosity was 30% for the Skylab sample and 33% for the ground based test sample.

The temperature

Fig.8 shows the uncorrected temperature-time curves for the actual Skylab experiment. The hot thermocouple rose from 35°C to its maximum 1035°C in 3 1/2 hours and remained for 1 hour at the maximum temperature, when the power was cut off. The initial passive cooling rate was 38°C for the first five minutes.

The exact thermal history (temperature of the samples themselves versus time) is not known. Especially for the fibre sample the time spent above the melting point may have been short because the molten part was sucked down the temperature gradient by the unmolten part as a result of surface tension.

RESULTS AND DISCUSSION

Plate specimens

Fig.9 shows radiographies taken from three different angles at 120° of the plate samples after the Skylab and ground experiments and before taking them out of the ampoules. In both Skylab ampoules (1A and 1B) five out of the eight plates melted, whereas in the ground

ampoules either four (3A) or five (3B) plates melted.

The Skylab samples which did melt are obviously more spherical than the ground samples, except one which remained in contact with a silica ring and wetted it. They are not complete because during solidification, due to small accelerations in Skylab, there was local contact, with limited wetting, with the stainless steel grid. In one instance (1B) two molten spheres must have come into contact with each other through the holes in the steel grid and one of them has sucked the other one right through the grid so that both spheres have united into one.

All the molten plates of 0.5 mm thickness have each turned into a single droplet of molten metal. On the contrary, of the plates of 0.1 mm thickness some have become one droplet and others have split into several small droplets. Model calculations are being made in order to attempt an interpretation of this result. It is unfortunate of course that the plates containing many holes (14 or 21) could not be melted.

An examination of the B samples with the scanning electron microscope shows that, even if they had had no contact during solidification with neither the stainless steel nor the silica, the spheres would have been far from perfect. This is shown by figs.10 (sample 1B P7-8) and 11 (sample 1B P6). Even if the spheres have been perfect in the liquid state, on solidification a network of grooves has appeared on their surface and a shrinkage pipe has been formed. The grooves are the traces of a cellular solidification substructure. Cellular solidification has been found in many systems, although observations are generally made on decanted solid-liquid interfaces (1,2). The cell formation is attributed to constitutional supercooling which itself is due to impurities which segregate to or from the cell boundaries (e.g. 20 ppm lead in tin).

In the present case, according to the manufacturer of the silver, any impurity in the ingots used has a concentration less than 1 ppm, except iron which is less than 1,5 ppm. The plate specimens had been made from these ingots by cold rolling and they were not heated until the degassing treatment just before sealing the ampoules. Nevertheless, it appears likely that at least the surface of the silver has been contaminated with oxygen, iron and other elements by contact with various products, such as tools, lubricants, cleaners, atmosphere (before and after sealing), stainless steel grids (after melting). Although the total contamination must be very low, the cellular substructure reveals the presence of impurities at least near the surface.

Similar traces of cellular substructure have been found on the ground tested specimens (fig.12). However, there the grooves are confined to a small region which was obviously the last to solidify (fig. 13). On the contrary, in the Skylab samples the grooves appear to occur all over the surface of the samples (fig.10 and 14), indicating that solidification has progressed in a different way.

It has been checked by X-ray diffraction that regions where a substructure is clearly visible, are monocrystalline with small disorientations.(fig.15).

The density of the samples has been measured to check if internal pores are present. The results are inconclusive. The samples are now being cross sectioned by gradually polishing away thin layers of material.

It is concluded that cellular solidification and shrinkage pipe formation may easily prevent the obtention of perfect spheres by melting and solidification in zero gravity. In principle, cellular solidification can be avoided by increasing the purity of the metal or by

increasing the temperature gradient in the solidifying melt. Pipe formation can also be controlled by the thermal conditions. Further study would be necessary to find out if both disturbing factors could be completely eliminated.

Fibre specimens

Figs. 16 and 17 show different views of the Skylab and the ground test melted fibre specimens. The amount melted in both cases is nearly the same, so the temperature distribution should have been very much the same in both experiments.

The ground test specimen stood upright during the test, hot end above, and the molten metal ran down the unmelted part and took the cylindrical shape imposed by the quartz half cylinders. On the contrary, the molten part of the Skylab specimen (henceforth called "the bead") did not touch any solid material except the unmelted part of the specimen: its shape is therefore determined by surface tension and by the constraints due to the shape of the unmolten metal. An attempt is being made to calculate the shape of the "bead". The shape of the "shoulders" (fig.17) between the solid and the molten silver appears to be similar in both specimens. In fact, the contact angle between solid and liquid silver is zero, but in the present case the spreading out of the liquid silver was halted by the temperature gradient.

In the Skylab specimen traces of the individual fibres can apparently still be distinguished on the entire surface of the "bead". Details of this surface can be seen on fig.18. It is suggested that the fibre traces are akin to the grooves observed on the plate specimens and that they also are due to impurities. Notwithstanding

the sintering in hydrogen and the heating in vacuo before sealing the ampoules, the fibres must have a surface layer enriched in impurity atoms. When the fibres melt and merge together, their impurity-rich surfaces can persist for some time in the pool of liquid, owing to the absence of gravity induced convection. Apparently such segregation of impurity atoms still existed when the metal solidified and gave rise to the traces or grooves visible all over the outer surface of the bead. Fig.19 shows small holes in such a groove, presumably due to the rejection of oxygen from the liquid. Such traces are not visible on the ground tested specimen even on the solidified surface which was not in contact with the silica, neither have they be seen on other specimens melted on earth without contact with crucible material. It is concluded that diffusion and surface tension induced convection (Marangoni effect) are much slower than gravity induced convection in equalizing concentration variations.

The central part of the bead (when seen in profile), corresponding to the original thickness of the sample, has a blackish appearance. There the surface is essentially made up of cross-sections through fibres. The black appearance seems to be due to small silver spheres (diameter 1-10 μ), which condensed from evaporated metal (fig.20). Condensed crystals have also been found on the silica tube walls but there they have a more faceted appearance (fig.21).

Fig.22 shows a longitudinal as-cut section parallel to the thickness direction of respectively the Skylab and the ground test sample. The section was made by very slow spark cutting, using a 0.5 mm diameter tungsten wire as electrode. The cutting speed was kept as low as about 0.1-0.2 mm/hour in order to minimize surface damage.

The ground sample shows some residual porosity mainly in the central part. There the metal did not melt as is shown by the irregular shape of the pores. In the outer regions the silver did melt and run down and only a few rounded pores are left. This has been confirmed by electrolytic etching (fig.23): the grains in the molten part are very large and without twins, those in the unmelted region are small and full of annealing twins. The etching has also revealed that the surface has been damaged only slightly by the cutting: some holes got covered by a thin film of material which is removed by the etching.

The Skylab sample (fig.24) shows a quite small residual porosity, and the pores are not necessarily spherical although the bead completely melted, as has been checked by etching (fig.25). Besides the few larger pores (diameter 0.1-1mm) seen in figs. 24-25, many small pores are also present (sizes 0.01-0.1mm) both on grain boundaries and inside grains (fig.26). Because of their rounded shape they can be identified as gas holes, not as shrinkage cavities. The observed (small) porosity can probably be explained as follows.

First of all it appears likely that only a few pores got trapped in the melting silver. Indeed, just below the "bead" the outside dimensions of the specimen (length and width of the cross-section) have not changed. Yet, the porosity has much decreased. This shows that liquid metal has infiltrated from the bead and has solidified on the still unmelted fibres, the twinned crystals of which have grown into the liquid. From this it can be inferred how the melting of the fibre specimen has actually occurred. Owing to the temperature gradient, the melting has of course started at the hot end (the top in the figures shown). As soon as some metal melted, it flowed into the open pores between unmelted neighbouring fibres which melted themselves a little later and provided liquid to fill the pores in the next layer. In this way only few pores got trapped in the liquid.

The few pores which were entrapped should have adjusted their size so as to fet equilibrium between the enclosed gas pressure and the surface tension restraint $p = \frac{2\gamma}{R}$, in which is the surface tension and R the pore radius. A pore of initial radius R_1 at a gas pressure p_1 should shrink or expand to a radius R_2 given by

$$R_2 = \left(\frac{p_1 R_1^3}{2\gamma}\right)^{1/2}$$

In the present case it can be taken that $p_1 = 4.10^{-5}$ mm Hg (taking into account the pressure increase by a factor four on heating from room temperature to the melting point of silver) and γ = 1000 dyne/cm.

Assuming that the entrapped pores had an original diameter of 1 mm or less the above formula shows that they should shrink to a diameter of 10^{-3} mm or less. This result is not so much influenced by a substantial decrease of the surface tension (such as due to impurities) or by using an initial pressure of, say one order of magnitude higher. It is concluded that pores entrapped on melting have become extremely small or have coalesced or left the metal while it was in the molten state. Indeed, even in the absence of gravity induced buoyancy and convection, pores in a liquid specimen may move because of surface tension induced convection, and they will tend to coalesce and to move to the free surface because of diffusion. Coalescence of pores in a weightless liquid is similar to the so-called Ostwald ripening or coarsening of a fine precipitate in a solid metal or to the coarsening of gas filled pores in solids (3). In these cases a small gas hole or second phase particle is gradually dissolved and reprecipitated on a larger pore or particle, simply because the solubility in the solid increases with the curvature of the interface. Such a process is either diffusion or interface controlled.

It has been concluded above that surface induced convection and diffusion appear to be relatively slow. Consequently, although it is not known how long the "bead" was actually molten (upper limit 1 hour), it seems improbable that all pores visible are residual porosity which persisted from melting till solidification. The size and distribution of the smaller pores suggest that they at least are rather due to dissolved oxygen being rejected from the liquid on solidification. The density of small gas holes is less near the free surface of the specimen where the gas could escape more easily. This kind of pores is much less frequent in the ground test sample, where buoyancy made them move faster than the solidification front at which they formed.

Besides the rounded gas holes there may be a few less rounded micro-shrinkage holes. Near the top of the bead there are two irregularly shaped cavities which apparently are shrinkage holes: they lie in the zone which was the hottest and the last to solidify.

The contour of the longitudinal section of the bead is fairly irregular which corresponds to the rather rough appearance of the outer surface of the bead as described above.

SUMMARY AND CONCLUSIONS

The examination and study of the experimental results is not yet finished. Some samples, such as the A series (thin plates), have still to be examined in detail. The presence and distribution of impurities in all specimens has to be checked. An attempt is being made to calculate theoretically the shape of the various specimens after melting and solidification. Moreover, other experiments should be performed. Therefore, the following conclusions are only provisional:

1. Most of the original porosity in the samples has disappeared during the melting stage. This has been favoured by the fact that the pores were of the open type, by the presence of a temperature gradient and by the low pressure. It should be possible to obtain a more porous product when starting from a material with gas filled closed pores, and if the stay above the melting point is not long enough to allow the pores to coalesce and to migrate to the free surface by diffusion and surface tension induced convection. Even with samples with open pores such as those used in the present investigation, the obtention of a porous product might be possible if the heat input was the same on all sides of the specimen so that a molten surface layer would enclose the still unmelted material. As regards the way in which the geometry of a porous specimen (e.g. a grid) changes with time on melting in weightless condition, one should perform experiments using levitation melting and high speed image recording.

2. The experiment has shown that the shape and surface condition of a sample melted and solidified in space is not only determined by surface tension: shrinkage may cause the formation of a pipe and constitutional supercooling, caused by impurities, may result in a cellular substructure leading to a network of grooves on the surface. These disturbing factors might be reduced by modifying the thermal conditions and by increasing the purity of the metal or avoiding any contamination.

3. The leveling out of concentration gradients, as may be caused by pick up of the impurities at the surface, appears to be slow in the molten metal when gravity induced convection is absent. Therefore the action of diffusion and of convection due to variations in surface tension, appears to be slow.

4. When only a part of a solid is melted in zero gravity, the tendency of the molten part to become spherical can be much restricted. This would be important for applications such as zone melting in space and welding of porous or massive material in space.

It is clear that the experiment performed in Skylab is only a crude and preliminary approach to the problem area outlined in the introduction of this report.

It is hoped that Spacelab will provide the opportunity to carry out more melting experiments on silver or other metal samples under conditions different from those available or applied in Skylab. It would e.g. be interesting to use levitation melting and high speed image recording so that the changes of shape during the whole process can be observed.

ACKNOWLEDGEMENTS

The authors thank NASA for providing the facilities and carrying out the experiment, METALLURGIE HOBOKEN-OVERPELT for providing the silver, N.V. BEKAERT (Zwevegem) for drawing the silver wire and the Belgian AIR FORCE and WESTINGHOUSE ELECTRIC CORPORATION for helping with transport problems.

REFERENCES

1. TILLER, W.A., JACKSON, K.A., RUTTER, J.W. and CHALMERS, B.
Acta Met., 1953, 1, 428

2. BILONI, H., BOLLING, G.F. and COLE, G.S.
Trans. Met. Soc. A.I.M.E., 1966, 236, 930

3. MARKWORTH, A.J.
Met. Trans., 1973, 4, 2651

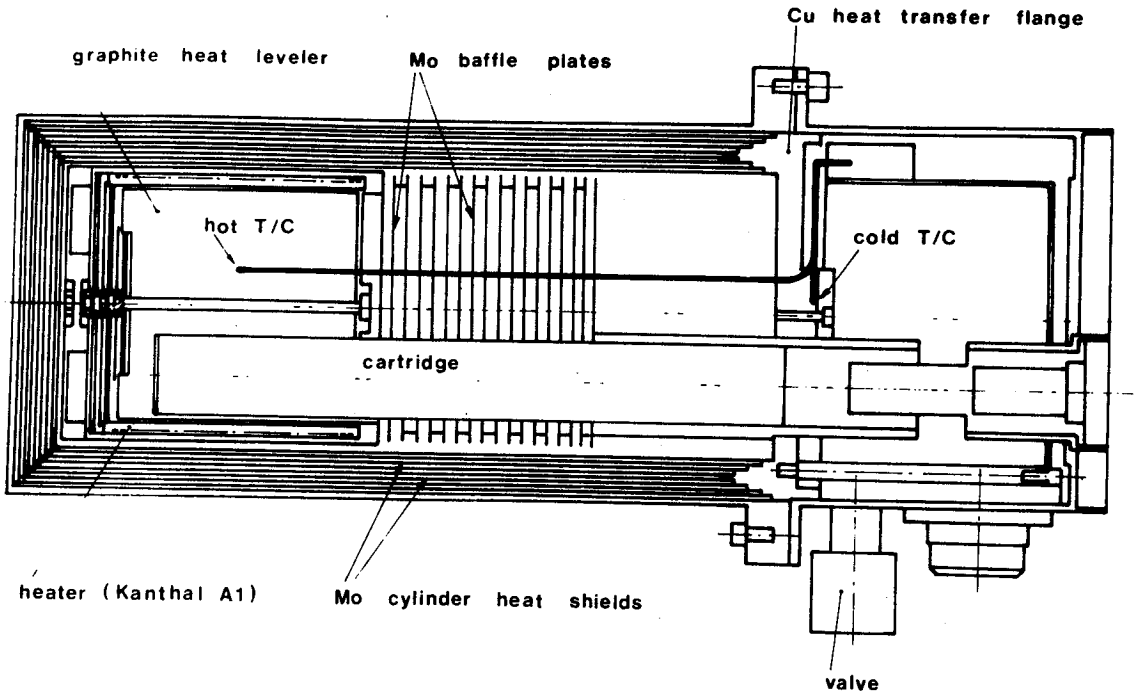

FIGURE 1. MULTIPURPOSE ELECTRIC FURNACE (SCHEMATIC)

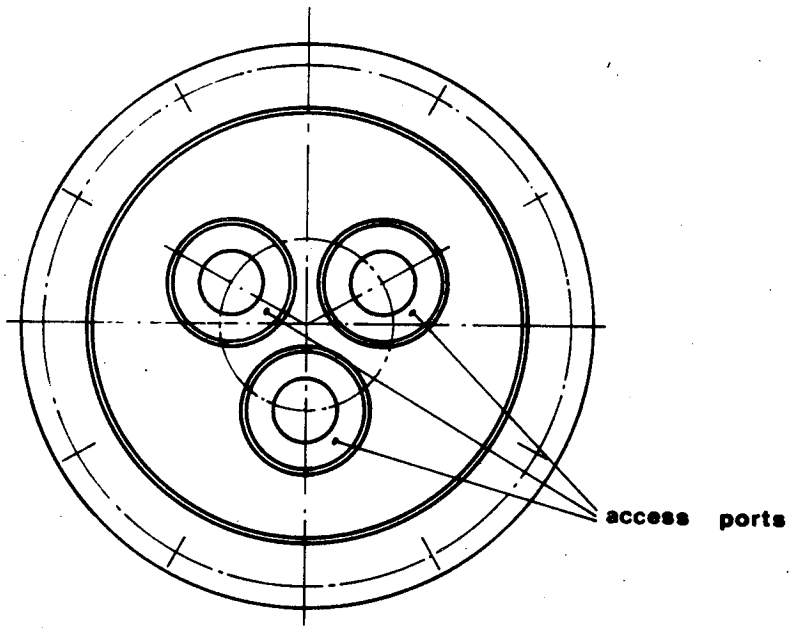

FIGURE 2. FRONT VIEW OF THE MULTIPURPOSE ELECTRIC FURNACE (SCHEMATIC)

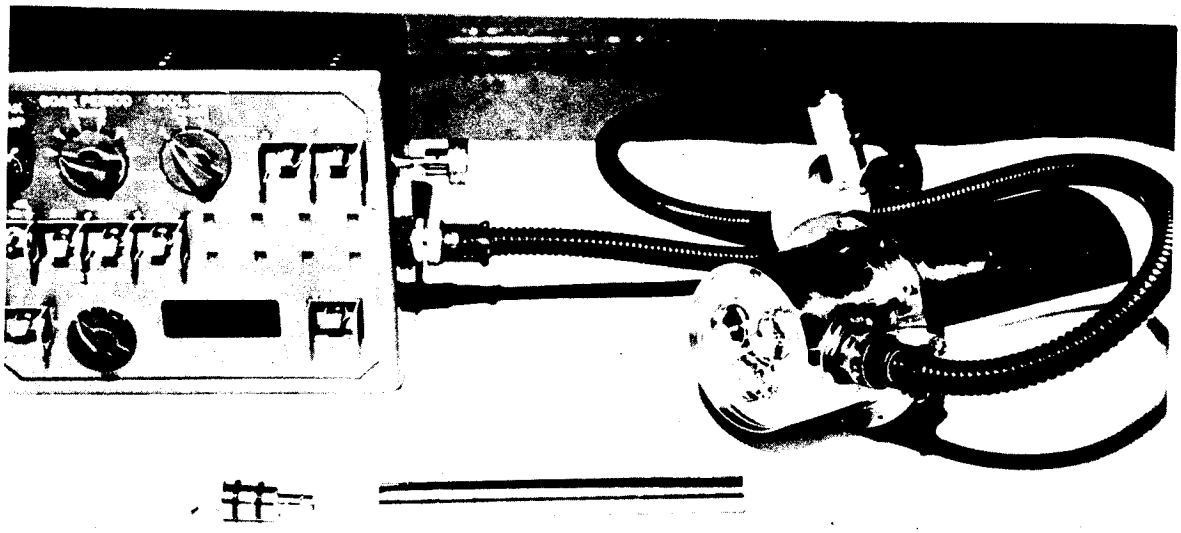

FIGURE 3. SKYLAB EXPERIMENT M518 MULTIPURPOSE ELECTRIC FURNACE

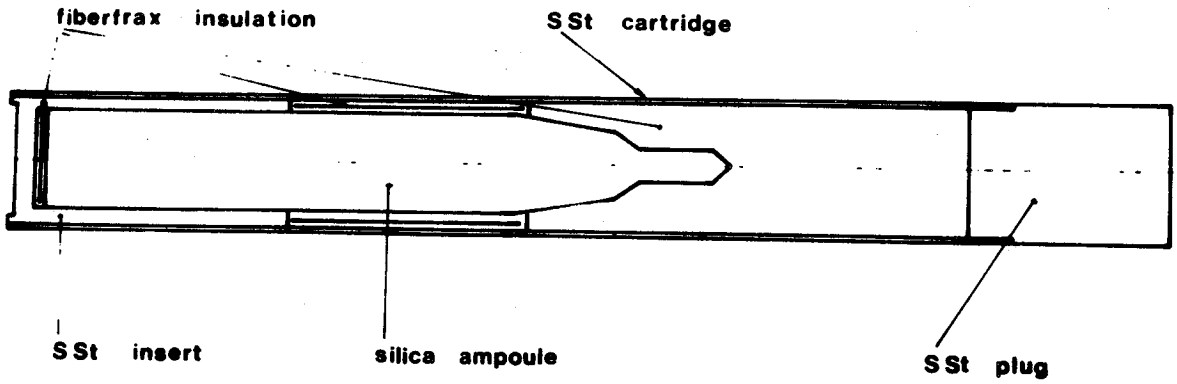

FIGURE 4. EXPERIMENT M565 CARTRIDGE ASSEMBLY
(SCHEMATIC)

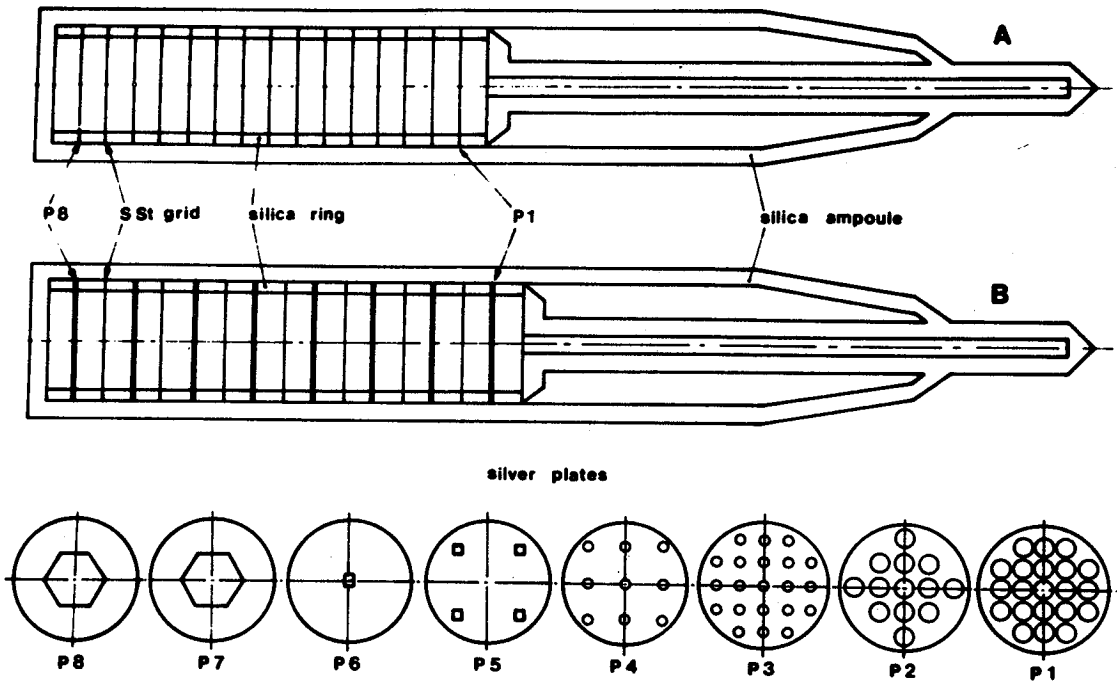

FIGURE 5. AMPOULES A AND B WITH PLATE SPECIMENS (SCHEMATIC).

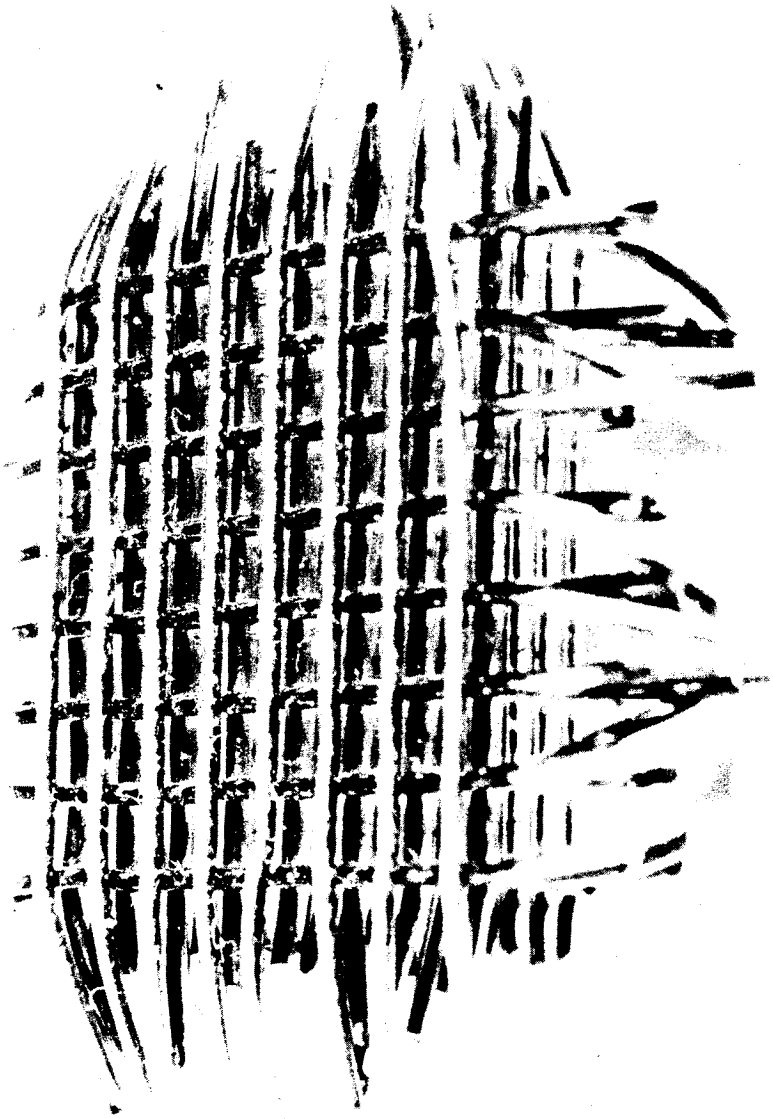

FIGURE 6. MULTI-LAYER SILVER GRID.

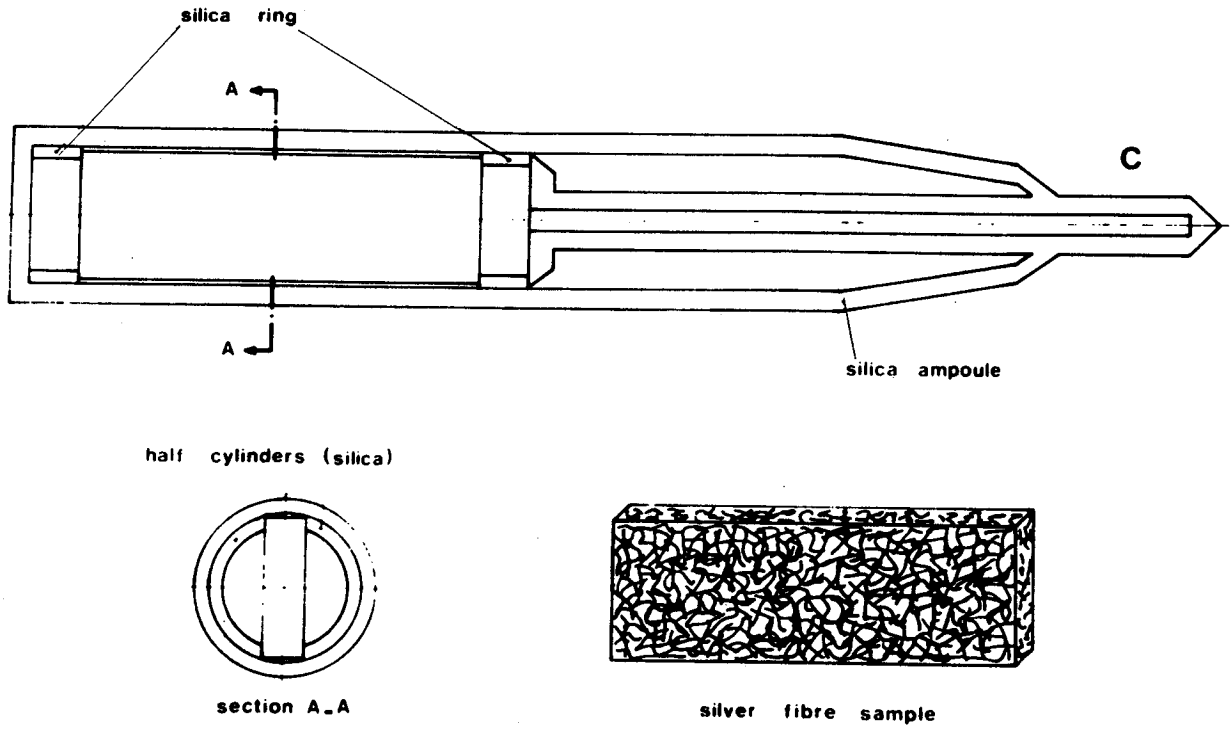

FIGURE 7. AMPOULE C WITH SPECIMEN (SCHEMATIC).

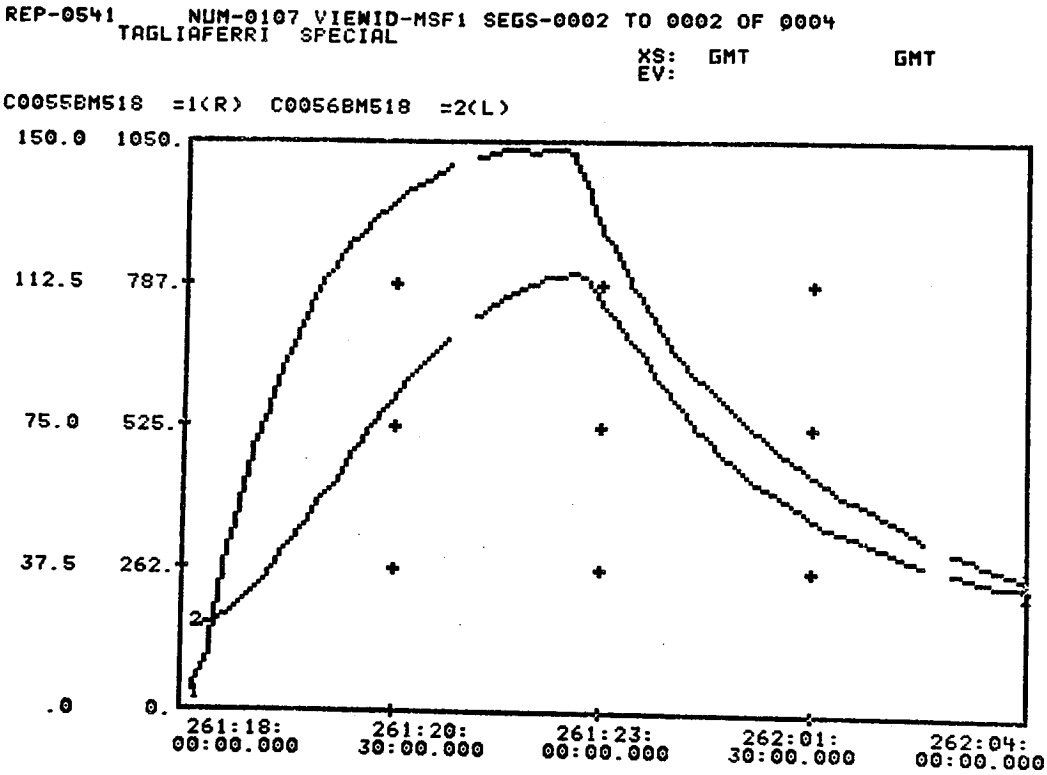

FIGURE 8. TEMPERATURE-TIME CURVES FOR THE ACTUAL SKYLAB EXPERIMENT. CURVES 1 AND 2 SHOW RESPECTIVELY THE HOT AND COLD THERMOCOUPLE READINGS.

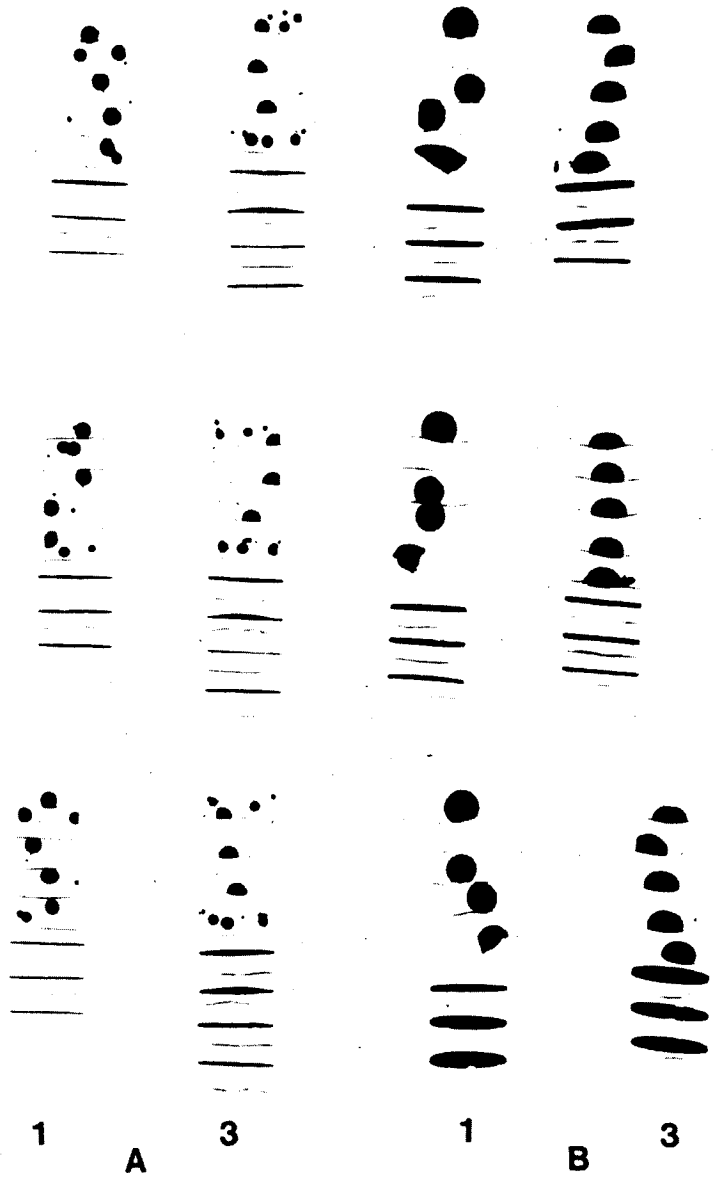

FIGURE 9. RADIOGRAPHIES OF THE SKYLAB (1A AND 1B) AND GROUND (3A AND 3B) TESTED SAMPLES IN THEIR UNOPENED AMPOULES. THREE RADIOGRAPHIES AT 120° OF EACH AMPOULE.

FIGURE 10. SKYLAB SAMPLE 1B P7-8 SHOWING CELLULAR SOLIDIFICATION SUBSTRUCTURE (X 20)

FIGURE 11. SKYLAB SAMPLE 1B P6 SHOWING PIPING AND SUBSTRUCTURE. (X 92)

FIGURE 12. GROUND SAMPLE 3B P4 SHOWING CELLULAR SOLIDIFICATION SUBSTRUCTURE (X 45)

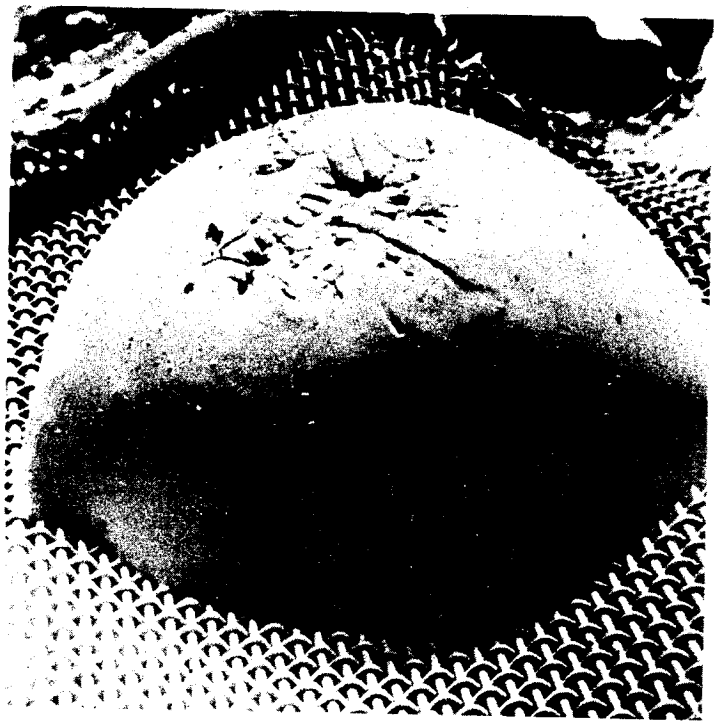

FIGURE 13. GROUND SAMPLE: SUBSTRUCTURE IS LOCALIZED (X 20)

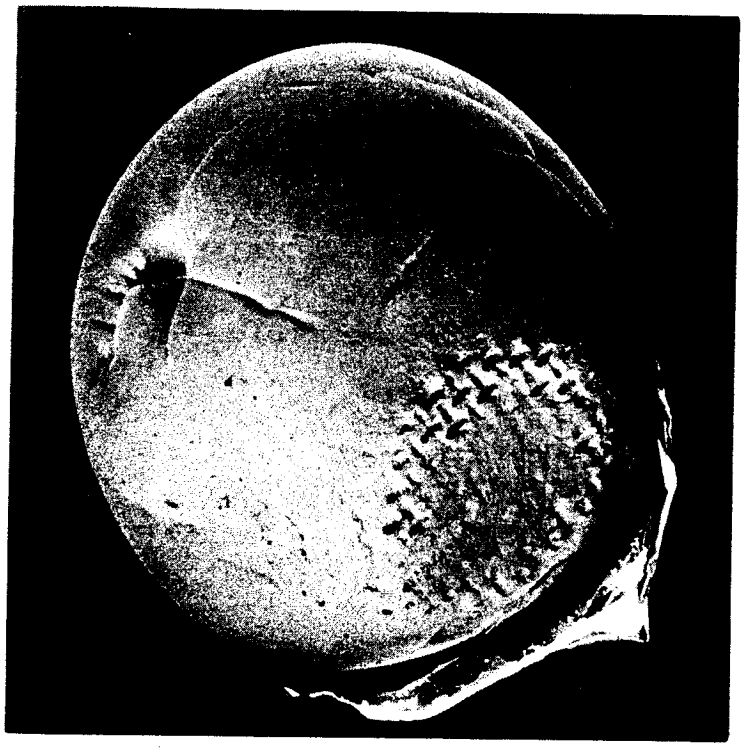

FIGURE 14. SKYLAB SAMPLE: SUBSTRUCTURE IS GENERALIZED (X16)

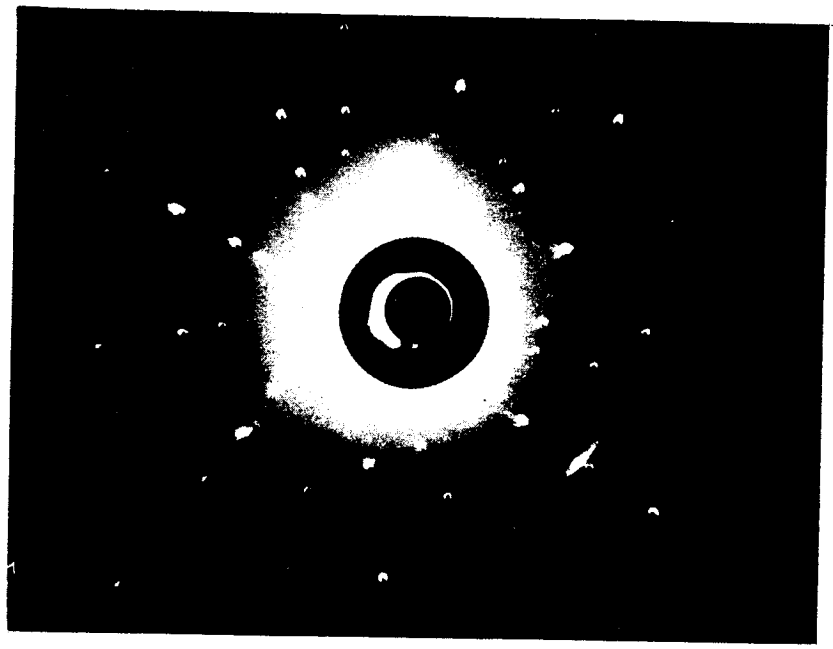

FIGURE 15. LAUE BACK REFLECTION PHOTOGRAPH OF SKYLAB SAMPLE 1B P6 (REGION SHOWN IN FIGURE 11)

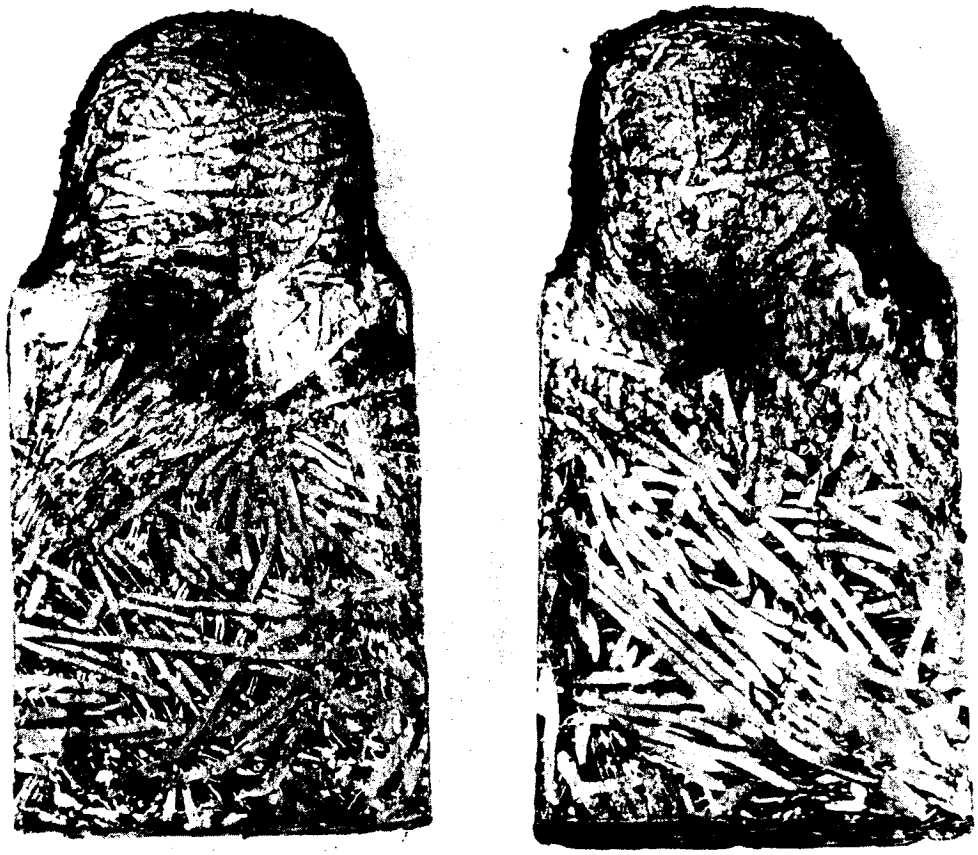

FIGURE 16a FRONT AND BACK VIEW OF SKYLAB TESTED FIBRE SPECIMENS. VERY APPARENT FIBRE TRACES ON "BEAD" OF SKYLAB SPECIMEN.

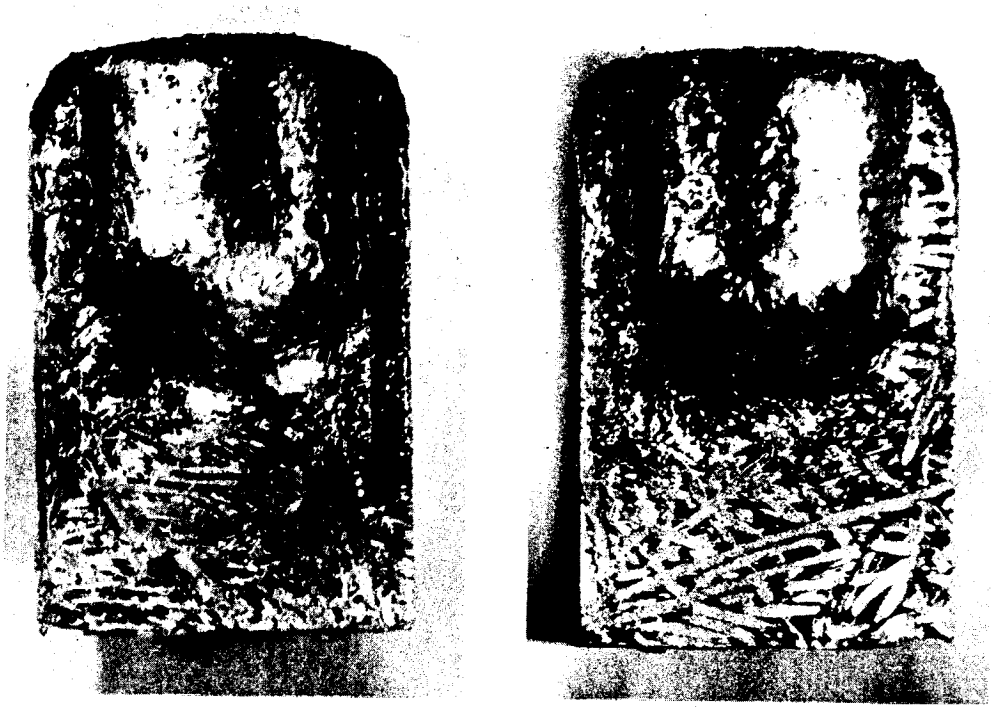

FIGURE 16b FRONT AND BACK VIEW OF GROUND TESTED FIBRE SPECIMENS.

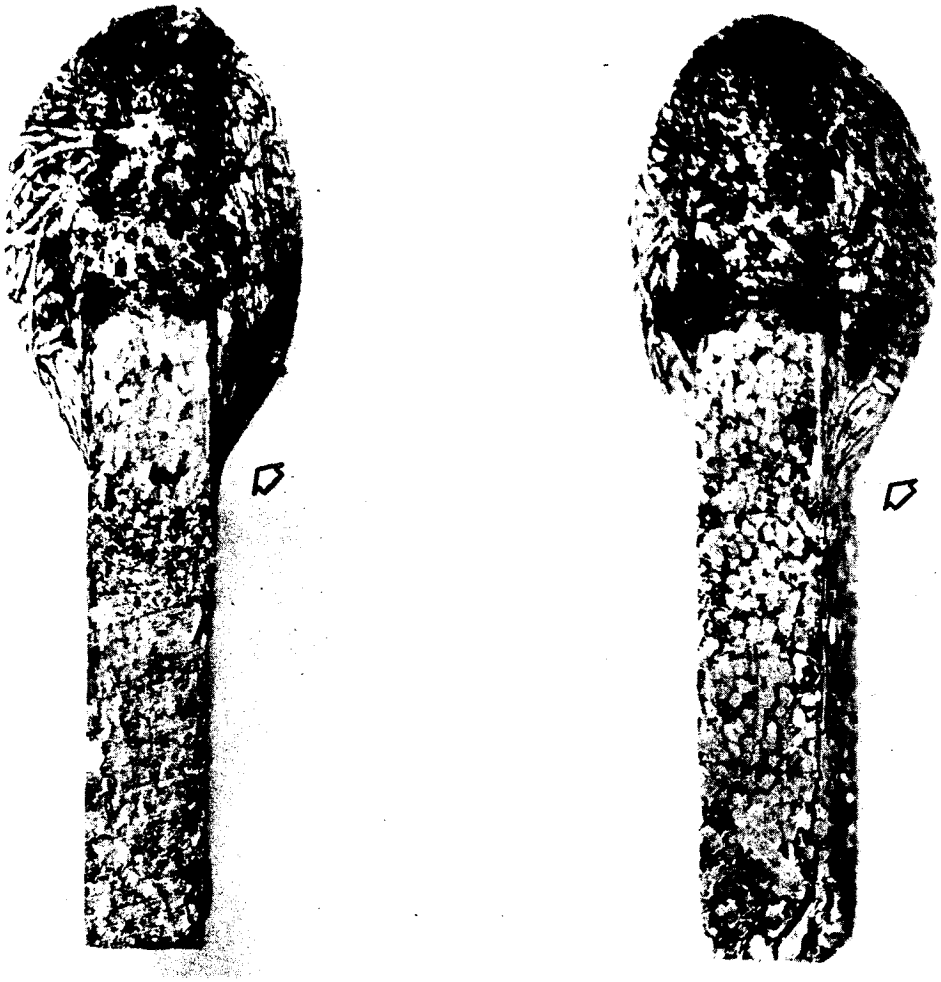

◁ = shoulders

FIGURE 17a. SIDE VIEWS OF SKYLAB TESTED FIBRE SPECIMENS.

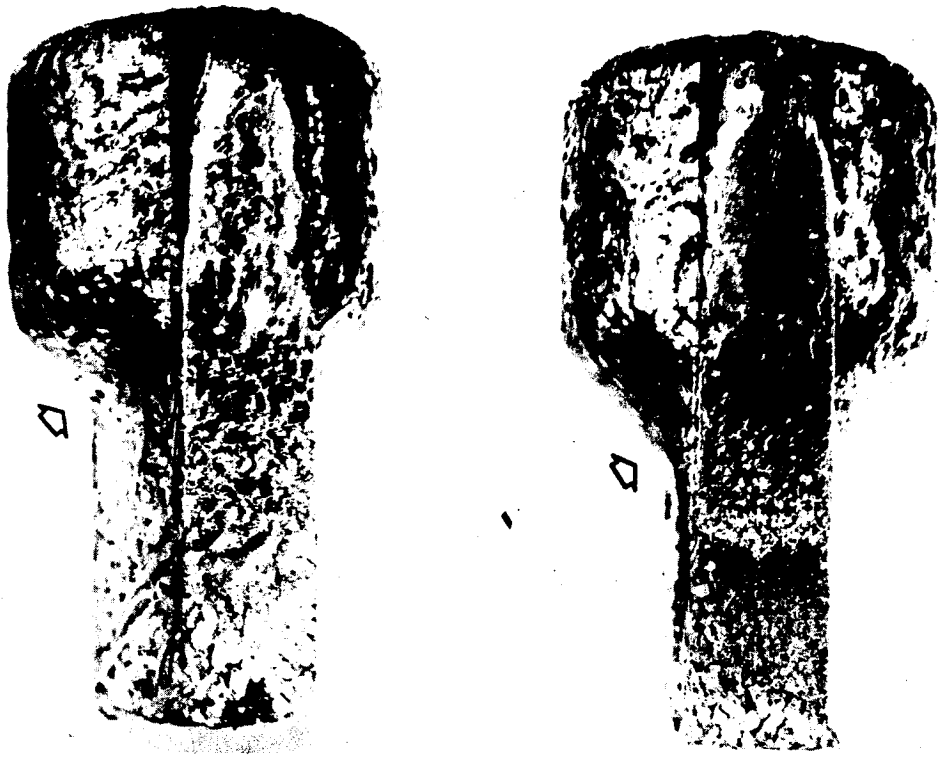

◇ = shoulders

FIGURE 17b. SIDE VIEWS OF GROUND TESTED FIBRE SPECIMENS.

FIGURE 18. SKYLAB MELTED FIBRE SPECIMEN (X 5).

FIGURE 19. GROOVE IN SKYLAB MELTED FIBRE SPECIMENS (X 1100).

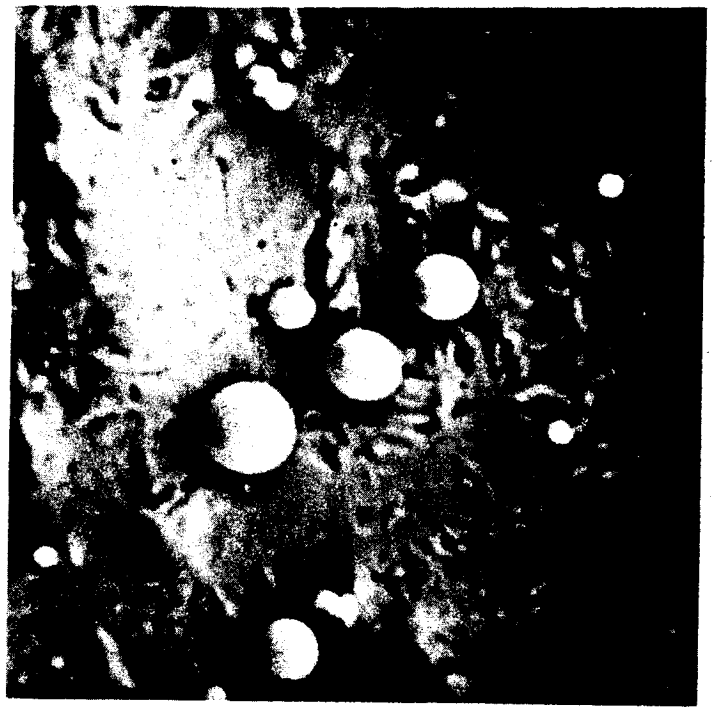

FIGURE 20. SILVER SPHERES CONDENSED ON SKYLAB MELTED FIBRE SPECIMEN (X 1300).

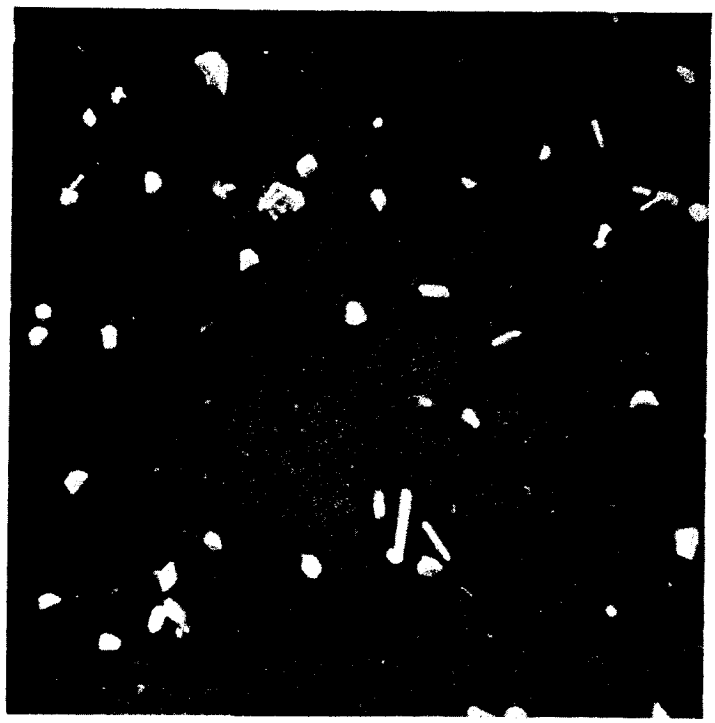

FIGURE 21. SILVER CRYSTALS CONDENSED ON SILICA TUBE WALLS (X 400)

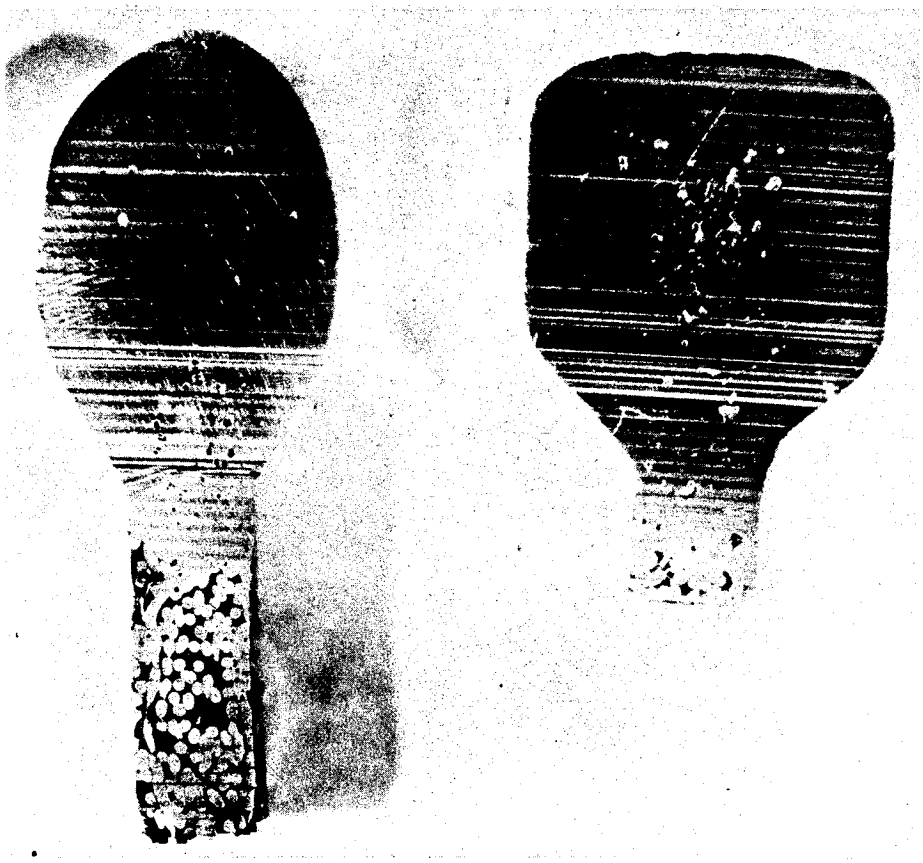

FIGURE 22. AS CUT SECTION THROUGH SKYLAB (LEFT) AND GROUND (RIGHT) SAMPLES (X 4).

FIGURE 23. POLISHED AND ETCHED SECTION THROUGH GROUND SAMPLES (X 9).

FIGURE 24. POLISHED SECTION THROUGH SKYLAB SAMPLE (X 6).

FIGURE 25. POLISHED AND ETCHED SECTION THROUGH SKYLAB SAMPLE (X 6).

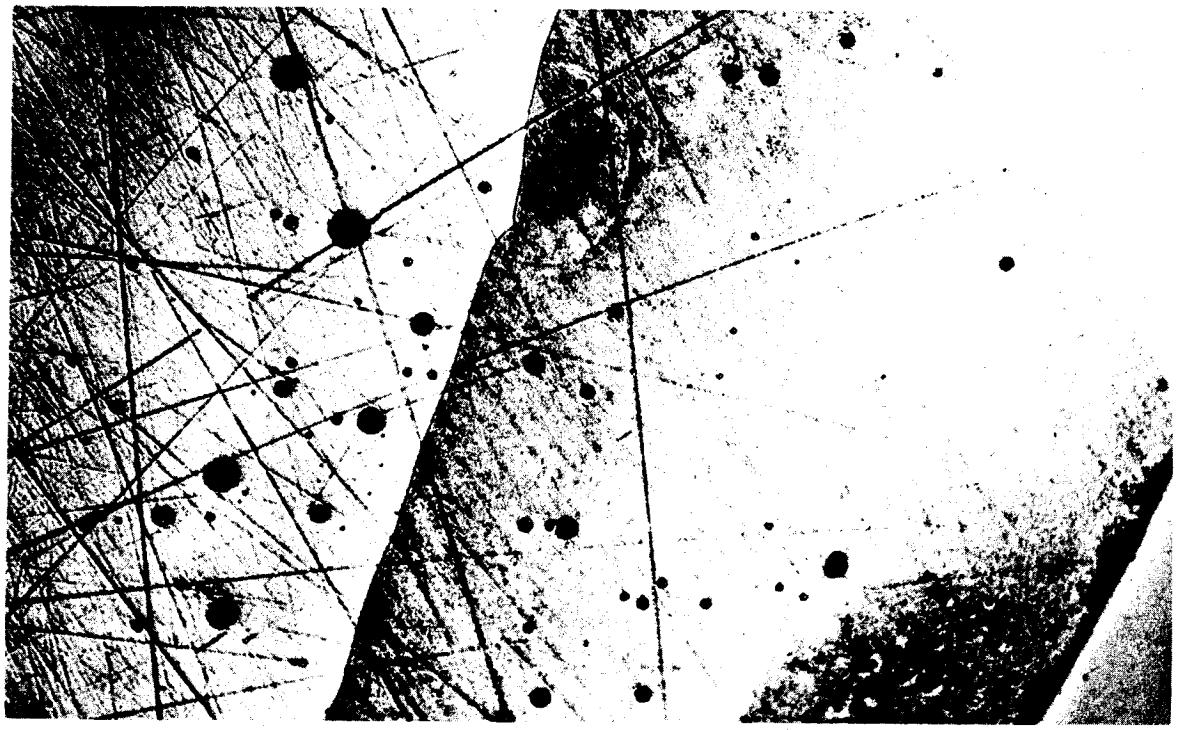

FIGURE 26. SMALL PORES IN SECTION OF SKYLAB SAMPLE (X 60).

PREPARATION OF SILICON CARBIDE WHISKER REINFORCED SILVER COMPOSITE MATERIAL IN A WEIGHTLESS ENVIRONMENT SKYLAB EXPERIMENT M561

By

Tomoyoski Kawada
(Principal Investigator)
Sennosuke Takahaski*, Susumu Yoshida,
Eiichi Ozaqa and Renpei Yoda
National Research Institute for Metals
2-3-12, Nakameguro, Meguro-ku, TOKYO

SUMMARY

The object of the experiment was to get Ag and SiC whisker composites with high density and uniform distribution of whiskers by heating and pressurizing sintered products above the melting point of Ag in a weightless environment.

This report describes the results of the examination carried out on the samples processed on Skylab and comparison with those prepared on the ground. The SiC nominal volume fraction is 2, 5, and 10%. The size of each sample is 8mm in diameter and about 30mm in length. The microhardness is measured on a longitudinal section of the sample. Also the distribution density of whiskers is estimated by observing the section under an optical mocroscope. The difference between the Skylab samples from the ground based test samples is clearly revealed in the uniform distribution of hardness values and the nonexistence of any floating whiskers.

INTRODUCTION

Composite materials of metallic matrix reinforced by high-strength whiskers such as SiC and Al_2O_3 have been attracting much attention as promising candidates for high-strength materials. At present, however, their practical application has not been realized. The greatest trouble in processing such whisker composite materials is that it is difficult to obtain sufficiently high-density material by applying the usual powder metallurgical techniques of mixing, compacting and sintering.

As for a method to cope with this difficulty, it may be expected that a process of melting and pressurizing the metal matrix is effective for raising the density of the product in processing such materials. Unfortunately, there is a possibility that the mixture might separate into

*Paper presented by Sennosuke Takahaski

two components, i.e., metal and whiskers, as soon as the metal matrix is melted down, and lose its unity as a composite material, because the specific gravity of the whisker is generally lower than that of the matrix.

If in a weightless environment such as on Skylab a metal-whisker composite which is prepared by the conventional powder metallurgical technique is kept in a molten state, it would be possible to obtain a homogeneous composite material, because there is no influence of buoyancy and thermal convection in a weightless environment. But by the melting process only, it will be impossible to raise the density of the composite by removing voids further than that of the sintered state. Therefore, one of the points of our proposal was laid in a procedure to positively remove voids by pressurizing the sample during melting.

The present report describes the result of comparative evaluation on the samples of SiC whisker reinforced Ag composite material processed on Skylab and those processed on the ground under otherwise similar conditions. The experiment was carried out following the line of the above-stated idea.

The samples and the ampoules containing them were designed and prepared by NRIM and the cartridges containing the ampoules by Westinghouse Astronuclear Laboratory. The coordination of the experiment was performed by MSFC.

The melting experiments on Skylab were carried out twice, the first in the SL-3 mission in September 1973 and the second in the SL-4 mission in December 1973. In this report the results are described for the samples processed during the SL-3 mission.

PREPARATION OF SAMPLES

The selection of materials for the experiment was done bearing in mind the following:

1) the temperature range of the multipurpose electric furnace to be used in this experiment,
2) the significant difference in the specific gravity between the whisker material and the matrix metal,
3) there was to be little chemical reaction between the whisker material and the metal matrix,
4) the need for easy availability of the materials which are well controlled in their particle size and shape.

After the screening of some materials, silver of m.p. 961°C and specific gravity 9.4 at molten state was selected as the matrix and silicon carbide (SiC) whiskers of specific gravity 3.1 as the reinforcing material. The particle size of fine powder of silver used was under

0.5 μm in diameter. The SiC whiskers used were about 0.1 μm in diameter on average and 10μm in length on average.

In a preliminary measurement the contact angle between Ag and bulk SiC crystal turned out to be about 120°. Any significant reaction as observed in the interface between SiC and molten Cu was not shown in the case of SiC and molten Ag.

SiC whiskers of 2, 5, and 10 volume % were mixed in Ag powder. Before mixing they were coated with Ag. Cylindrical green samples of 8mmϕ in diameter and about 35mm in length were prepared by well mixing the shiskers and Ag powder, compacting the mixture in a press, sintering it at about 900°C in a hydrogen gas atmosphere and finally hot-pressing it lightly.

Figure 1 shows the ampoule that contained the sample. The ampoule assembly consisted of a silica tube, a graphite sheath, a piston rod of graphite and silica and a coiled spring for pressurizing the sample from one end. The spring was made of special heat-resistant alloy. The applied force by the spring was adjusted to about 30kg in the initial condition before melting. The pressurizing mechanism was designed so as to crush voids in the material in molten state by hydrostatic pressure applied to the sample. Now let us assume that the whiskers are uniformly and unidirectionally arranged in a state of the closest packing and that the molten metal with a surface tension γ forms a contact angle Θ with the whiskers. The pressure P which is necessary to crush voids between the whiskers is given by the following equation,

$$P = \frac{-2\gamma v \cos\Theta}{r}$$

where r is the radius of the whisker and v is its volume fraction. For example, if it is assumed that r=0.05μm, Θ=120°, γ=890dyne/cm and v=0.1 in the above equation, P turns out to be 18kg/cm.

EXPERIMENTAL PROCEDURE

The sample ampoule was loaded and sealed into the cartridge made of stainless steel. Three sample ampoules were set together in the multipurpose electric furnace and heat treatment was performed under a prescribed condition.

1) Skylab experiment

Figure 2 shows the temperature profile during processing of the Skylab samples. As shown in the figure, the samples were heated at the maximum heat leveler temperature of 1010°C for about 4 hrs and then cooled in the switched-off furnace. It was estimated from the results of the ground-based tests that the measured temperature was about 20°C higher than that at the center of the sample. Accordingly, the temperature of the samples is thought to have been kept above the melting point of Ag for about 5 hrs.

2) Ground-based experiment

In the ground-based experiment the samples were heated and cooled in a furnace that was quite similar to the multipurpose electric furnace on Skylab. The sample axes were held in the vertical position and their spring ends were kept downward. Table I shows the maximum heating temperature and the soaking time at that temperature. Experiments under different conditions with the maximum temperatures of 980°C and 985°C were also carried out. But the samples for these experiments are not evaluated in this report because the metal matrix did not seem to have attained a sufficiently molten state in these cases.

EVALUATION OF SAMPLES

The evaluation tests were carried out for six samples shown in Table I, three for the Skylab test and the other three for the ground-based test (GBT).

1) X-ray radiography

X-ray radiographs were taken on the samples at NASA-MSFC with the cartridges unopened. Examples are shown for the Skylab sample 1A′ and the GBT sample 5A in Figure 3(a), (b), respectively. It was recognized that the piston mechanism in the ampoule had worked without trouble. But it was presumed that relaxation in the applied pressure had occurred to some extent during heating as some permanent deformation was observed in the coiled spring at its higher temperature end.

2) Macroscopic appearance

Figure 4 (a), (b) show macroscopic appearances of the samples. The samples 1A′ and 1B′ were contaminated with graphite from the graphite sheath at their bottom sides. This contamination is thought to be due to the fact that the temperature of the furnace was a little too high (1010°C). There was observed some flowed out material due to a crack in the graphite sheath in 1C′ sample as shown in Figure 4. At the bottom side of the GBT samples was recognized a tarnished zone. This shows that floating and coagulating of whiskers occurred during melting at the bottom side of the GBT samples.

3) Measurement of bulk density

The bulk density of the samples was measured for each sample both before and after the experiment. The density ratio was determined from the bulk density. Here the density ratio means the ratio of the bulk density to the ideal theoretical density.

Table II shows the weight, size, and density ratio of the samples. The density ratio of the Skylab samples 1A′ and 1B′ was 3 and 5% larger than that of the green samples, respectively.

A decrease of 2% in the density ratio was measured for the Skylab sample 1C′. As already described, some material flowed out in this sample

through a crack in the graphite sheath. The sheaths of 1A' and 1B' samples were not broken, but their weights decreased by about 1.3 g. It was perhaps due to loss of material by penetration of molten material through the graphite sheaths. For the GBT samples 5A and 5B a decrease of a small amount of weight was measured.

4) Macrostructural observation

Each sample was cut longitudinally at about one half of the radius off the center axis as shown in Figure 5. The cut section was polished and used for measurements.

Figure 6(a), (b) show the macrostructure revealed on the section. A considerable number of voids were observed on every section. In every Skylab sample, a transversal zone where voids diminished was observed. It corresponded to a region which bounded the graphite contaminated part (cf. Figure 4). It seems that the occurrence of this zone depended on the temperature distribution in the sample during melting.

5) Microstructure and measurement of distribution density of whiskers

Figure 7(a), (b) show the microstructures at both ends, the spring side and bottom side, of the sections. There is observed a difference in the void distribution between the Skylab Samples and the GBT ones. For the GBT samples 5A and 5B there were more voids at the bottom end, i.e., the upside of the sample, than at the spring end. For the Skylab samples no such difference in void density between both ends was observed and the voids themselves were generally less than for the GBT samples.

The same situation was observed for sample 5C but at its bottom end was seen a layer of 0.1mm in thickness, which was thought to be the result of exudation of metal. Those voids found at the bottom end of GBT samples are considered to be the traces of whiskers which fell off the metal matrix after floating up and coagulating during melting.

Figure 8 (a), (b) show photomicrographs of a large magnification of the section. Using these photographs the distribution density of whickers was measured by counting the spots which appeared to be whisker sections. In this case the counted numbers of whiskers depended on the resolving power in the microscope and photographic conditions, because the diameters of whiskers varied over a wide range around the mean diameter of 0.1um. Accordingly, these measured distribution densities are to be regarded only to indicate relative values.

Figure 9 (a), (b) show the distribution density of whiskers for the Skylab sample 1A and the GBT sample 5A. In the measurement of the distribution density, mocrophotographs were taken at several positions as shown in Figure 5. The dimension of a region taken on one photograph was $85 \times 60 \mu m^2$. In each region three squares of $20 \times 20 \mu m^2$ were picked up at random. The number of whiskers contained in the square was counted and the distribution density was calculated. The average value and the standard deviation were calculated for each three values corresponding to each position on the sample section in Figure 9. The left side origin of the abscissa in Figure 9 corresponds to the spring end of the sample.

These values have only a relative meaning as mentioned above. However, the following could be said from the comparison of the result for 1A′ with that for 5A:
no significant difference in the scatter in the distribution density is noticed between 1A′ and 5A; the density for 1A′ is generally a little larger than that for 5A; the density for 5A decreases towards the bottom end along the axial direction, but no such tendency is observed for 1A′. For B and C samples, reliable measurement of the distribution density could not be made because of large volume fractions of whiskers.

6) Measurement of microhardness

Figures 10 (a), (b), 11 (a), (b), and 12 (a), (b) show the microhardness of the samples. The measurement of hardness was carried out by a microvickers hardness tester with a load of 100g. Measured positions are shown in Figure 5. At each position the hardness was measured on five points at intervals of about 500μm. The mean values and the standard deviations were calculated for each five hardness numbers and plotted in figures 10, 11, and 12 corresponding to the positions on the section. The origin of the abscissa of the figures corresponds to the spring end of the sample.

The hardness for the Skylab samples showed a tendency of smaller change with position than for the GBT samples. To examine in more detail the change of hardness with position, the microhardness for the Skylab sample 1A′ and the GBT sample 5A was measured at 2mm intervals in the longitudinal direction and at 200μm intervals in the transversal direction. The results are shown in Figure 13 (a), (b). These histograms show the following trends:
the median value of the hardness number is apparently higher for 1A′ than for 5A; its fluctuation along the longitudinal direction is larger and oscillatory for 5A as compared with 1A′; the scatter of the hardness number on the same longitudinal positions is on the whole larger for 5A than for 1A′.

CONCLUSIONS

A melting experiment was carried out on Skylab for a sintered composite material consisting of a Ag matrix reinforced by SiC whiskers of 2 to 10 volume percent. The ampoule containing the sample was equipped with a device to pressurize the sample during melting.

Melting experiments were also performed on the ground under otherwise similar conditions. The products processed on Skylab and on the ground were subjected to comparative evaluation and the following conclusions were obtained:
1) An increase in the density ration was obtained by melting and pressurizing. The degree of increase was approximately the same for the Skylab and the GBT samples.

2) Floating and coagulation of whiskers were observed at the upside end of the GBT samples. The GBT samples showed a decreasing tendency in the distribution density of whiskers towards the upside end. No such phenomena were observed for Skylab samples.
3) The microhardness was generally smaller for the GBT samples than for the Skylab samples and showed large fluctuations along the axial direction as compared with the Skylab samples.
4) The above results are considered to indicate clearly the influence of buoyancy and thermal convection in the melted GBT samples, while the Skylab samples were devoid of such influence since they were processed in a weightless environment.

TABLE I. COMPOSITION OF SAMPLES AND SOAKING CONDITION

Sample		Volume Fraction of Whisker (%)	Maximum Heating Temperature (C)	Soaking Time (hrs)
Skylab Sample	1A′	2	1010	4
	1B′	5		
	1C′	10		
GBT Sample	5A	2	990	2.5
	5B	5		
	5C	10		

TABLE II. DENSITY RATIO OF SAMPLES BEFORE AND AFTER EXPERIMENT

Sample		Weight (g)		Length (mm)		Dia-meter (mm)	Density Ratio (%)	
		green material	after test	green material	after test		green material	after test
Skylab Samples	1A′	15.99	14.70	33.4	31.4	8	92	95
	1B′	14.61	13.29	33.7	31.0	8	87	92
	1C′	14.17	12.47	32.4	28.0	8	89	87
GBT Samples	5A	14.32	13.98	35.0	31.0	8	81	89
	5B	13.82	13.57	35.0	34.4	8	79	85
	5C	11.76	11.76	32.4	31.2	8	74	84

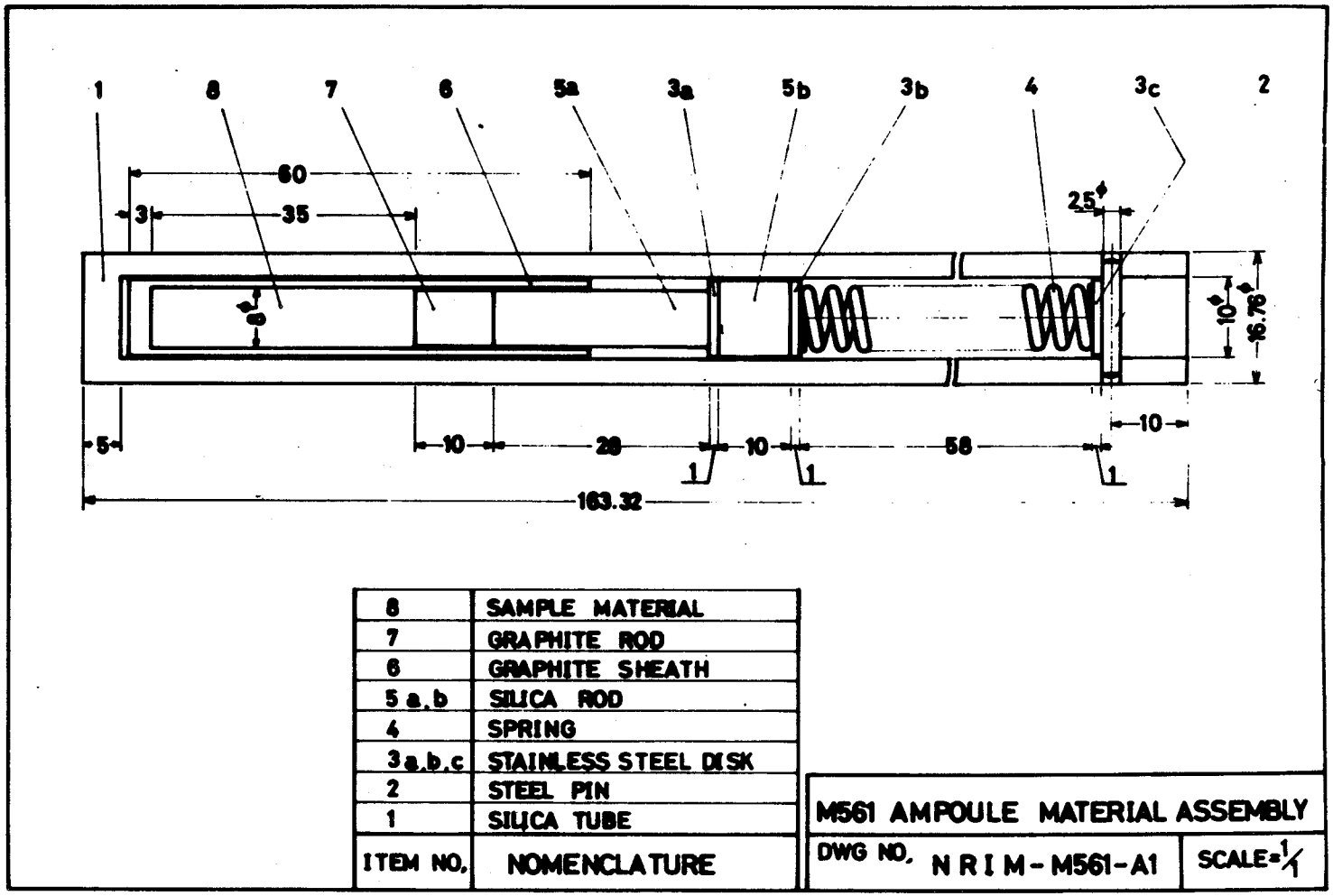

ITEM NO.	NOMENCLATURE
8	SAMPLE MATERIAL
7	GRAPHITE ROD
6	GRAPHITE SHEATH
5 a,b	SILICA ROD
4	SPRING
3 a,b,c	STAINLESS STEEL DISK
2	STEEL PIN
1	SILICA TUBE

M561 AMPOULE MATERIAL ASSEMBLY

DWG NO. N R I M - M561 - A1 SCALE=1/1

FIGURE 1. CROSS SECTION OF SAMPLE AMPOULE

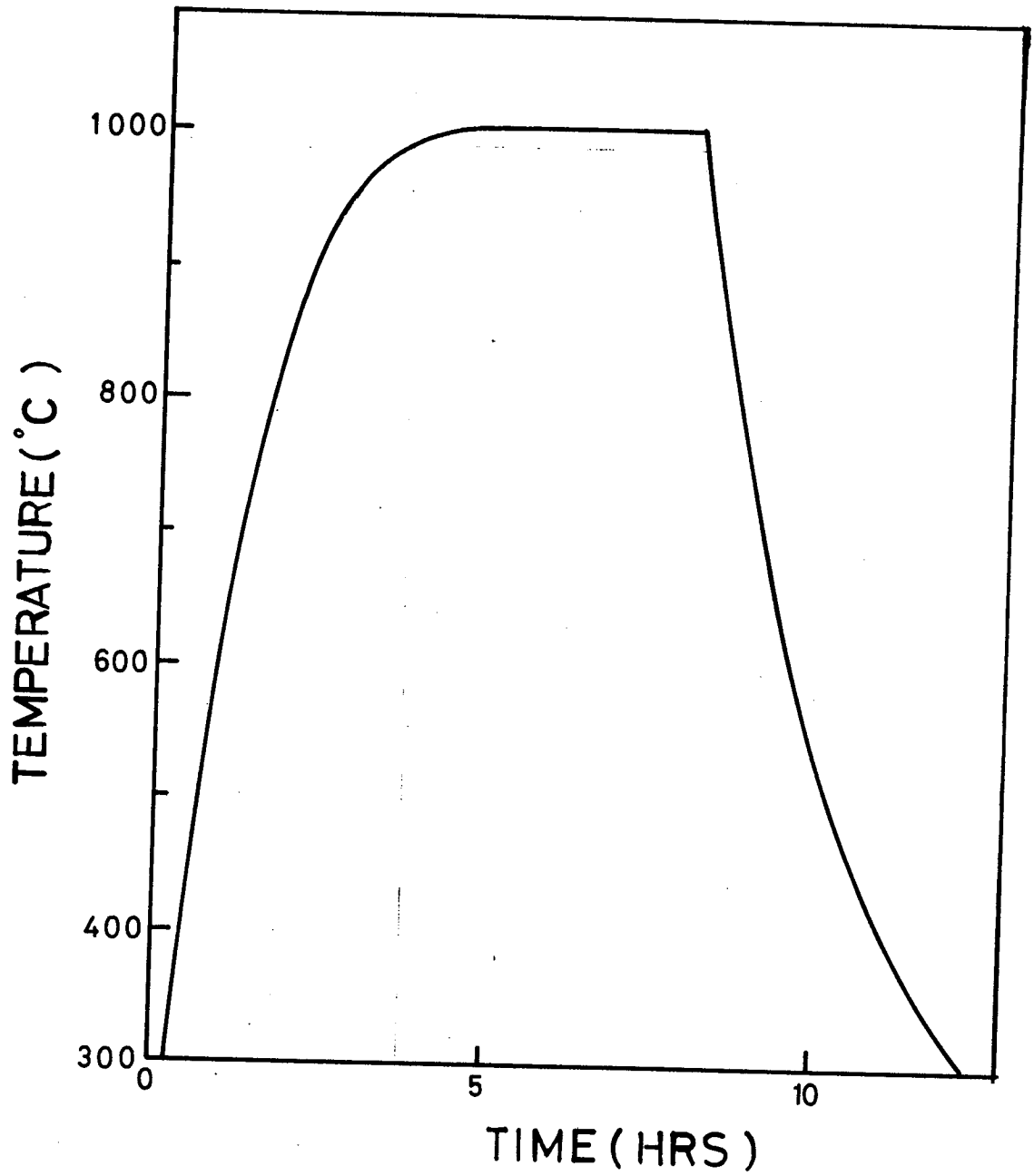

FIGURE 2. TEMPERATURE PROFILE DURING PROCESSING OF SKYLAB SAMPLES

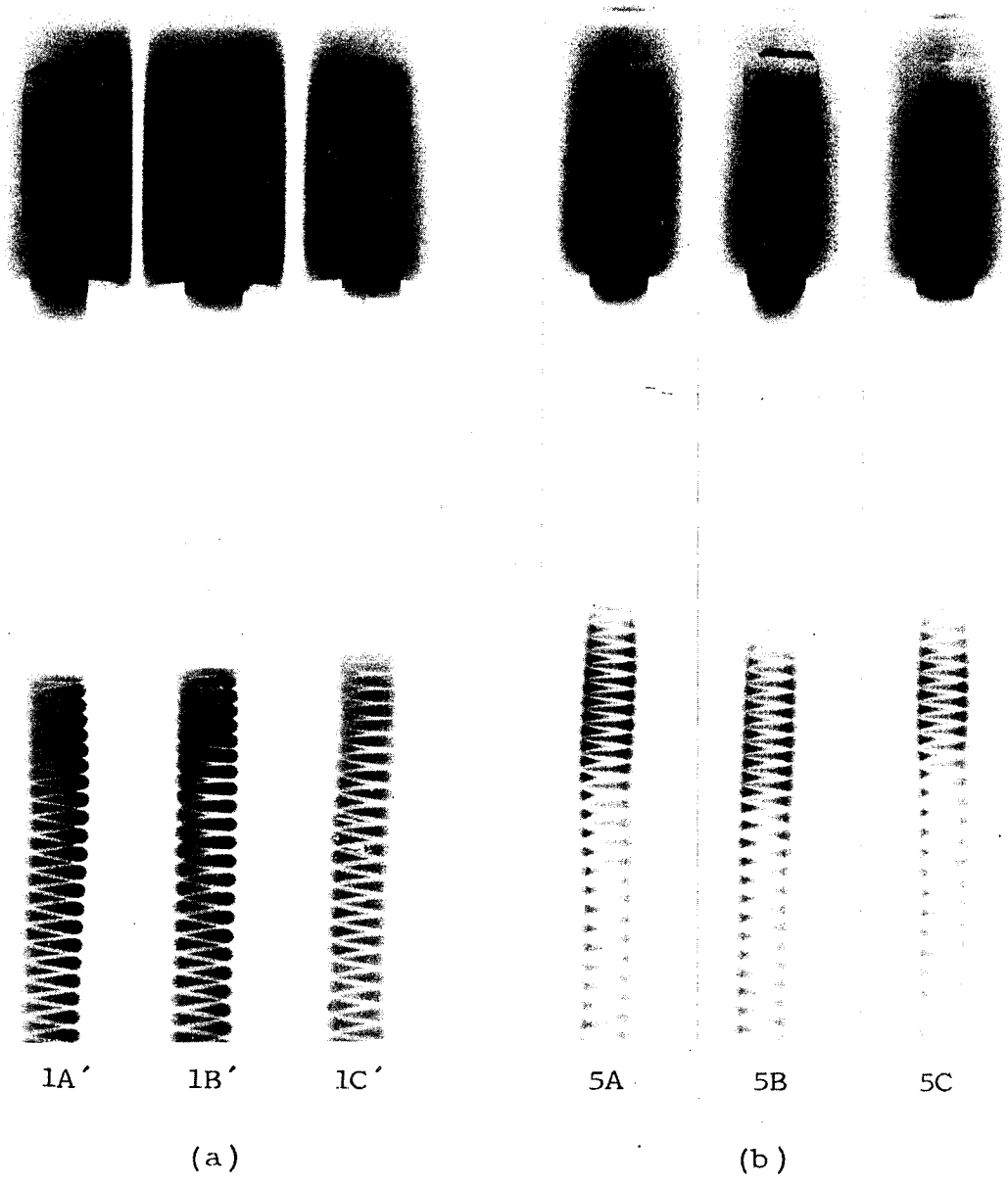

FIGURE 3. X-RAY RADIOGRAPHS, SKYLAB SAMPLES 1A´, 1B´, 1C´, (a) AND GBT SAMPLES 5A, 5B, 5C (b)

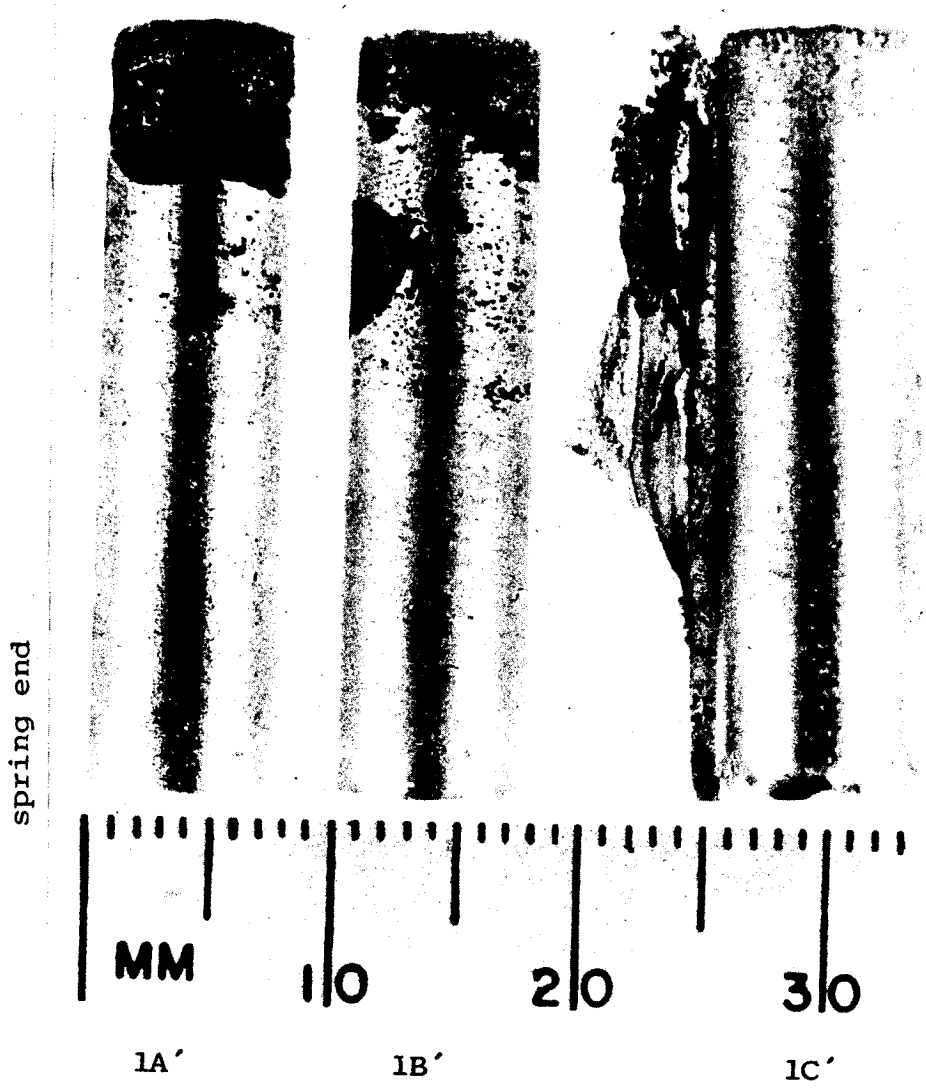

FIGURE 4A. MACROSCOPIC APPEARANCE OF SKYLAB SAMPLES 1A', 1B', AND 1C'

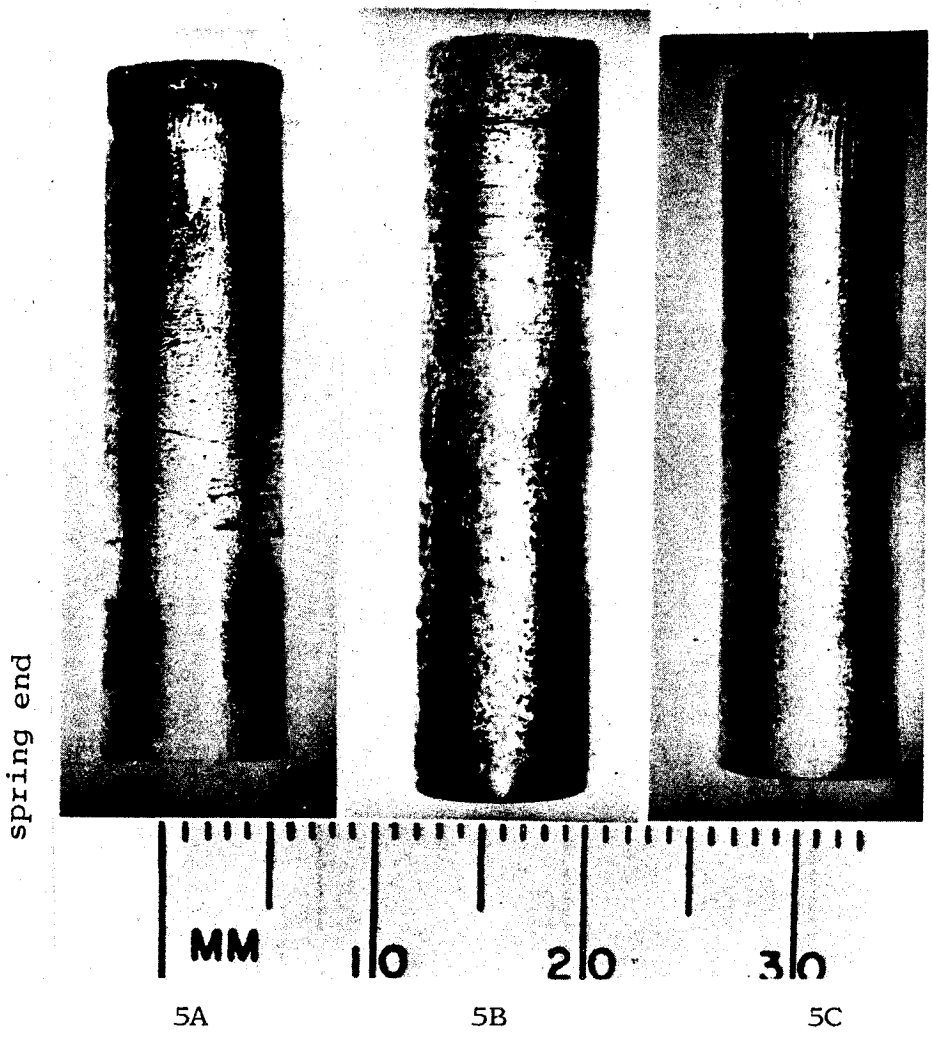

FIGURE 4B. MACROSCOPIC APPEARANCE OF GBT SAMPLES 5A, 5B, AND 5C

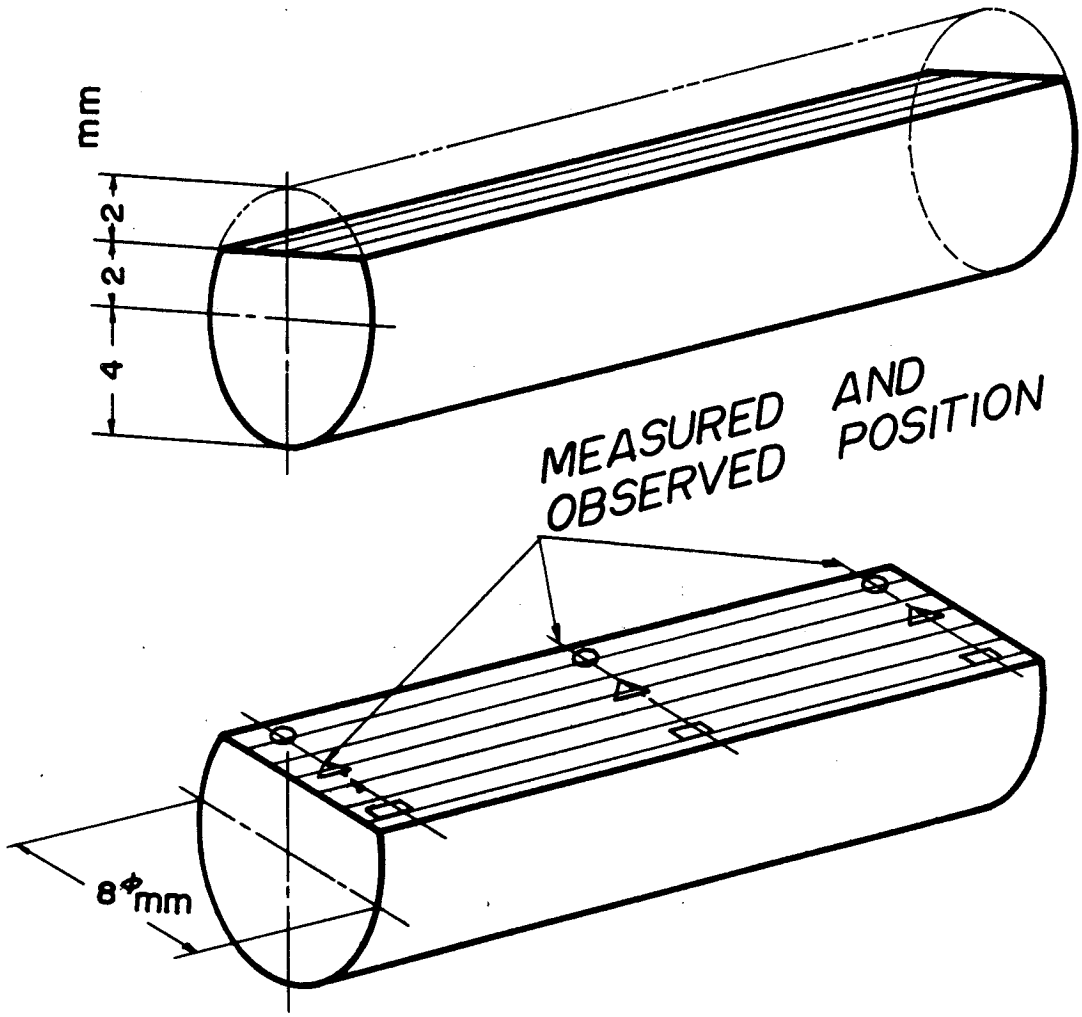

FIGURE 5. SCHEMATIC DIAGRAM OF CUT SECTION

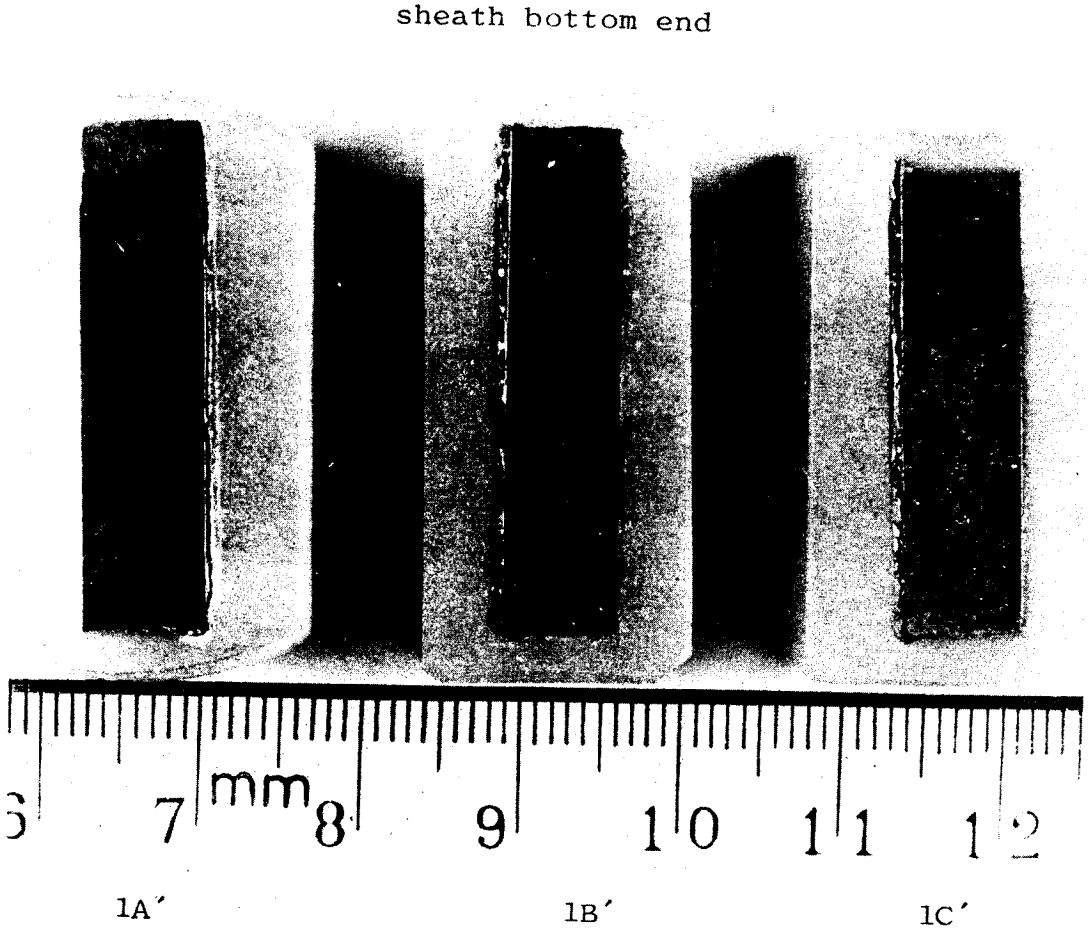

FIGURE 6A. PHOTOGRAPHS SHOWING MACROSTRUCTURE ON THE SKYLAB SAMPLES 1A′, 1B′, AND 1C′

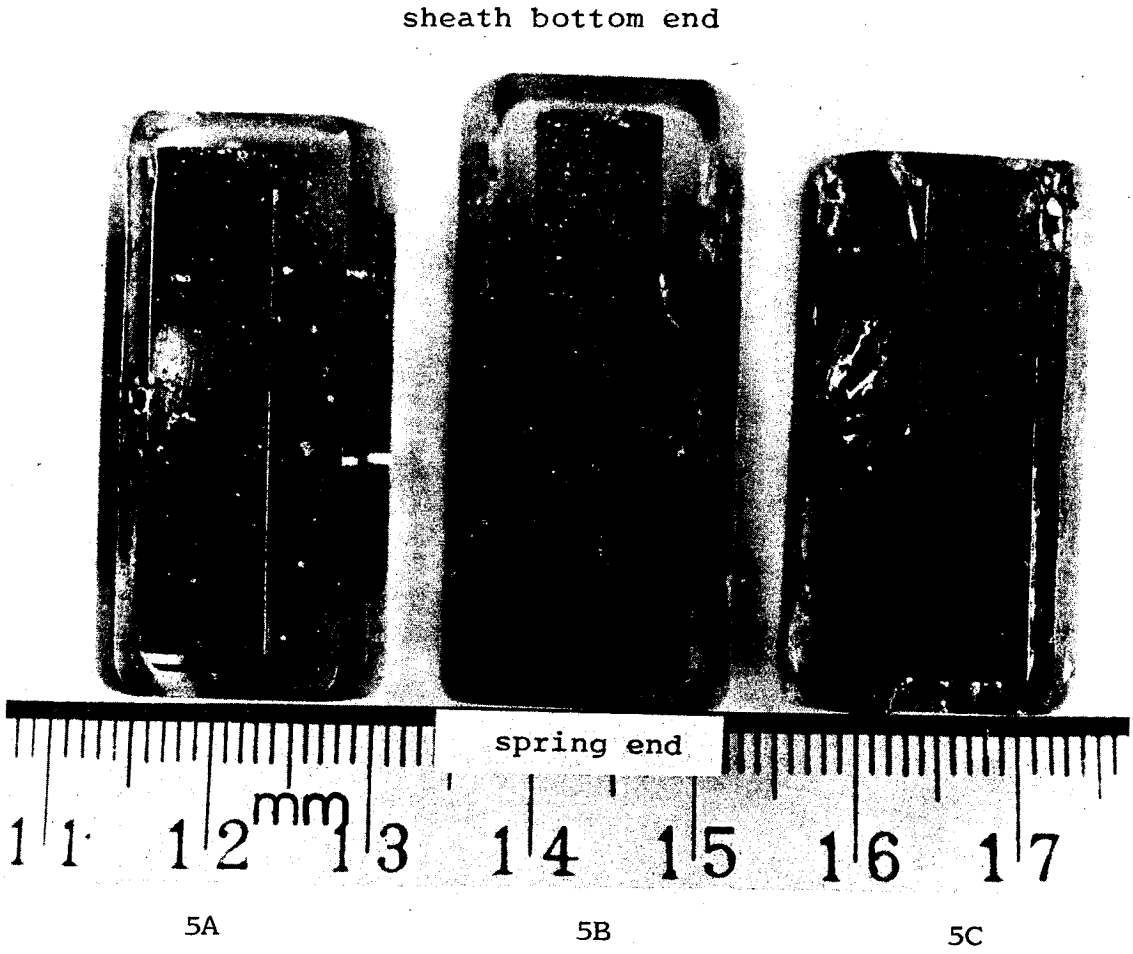

FIGURE 6B. PHOTOGRAPHS SHOWING MACROSTRUCTURE ON THE GBT SAMPLES 5A, 5B, AND 5C

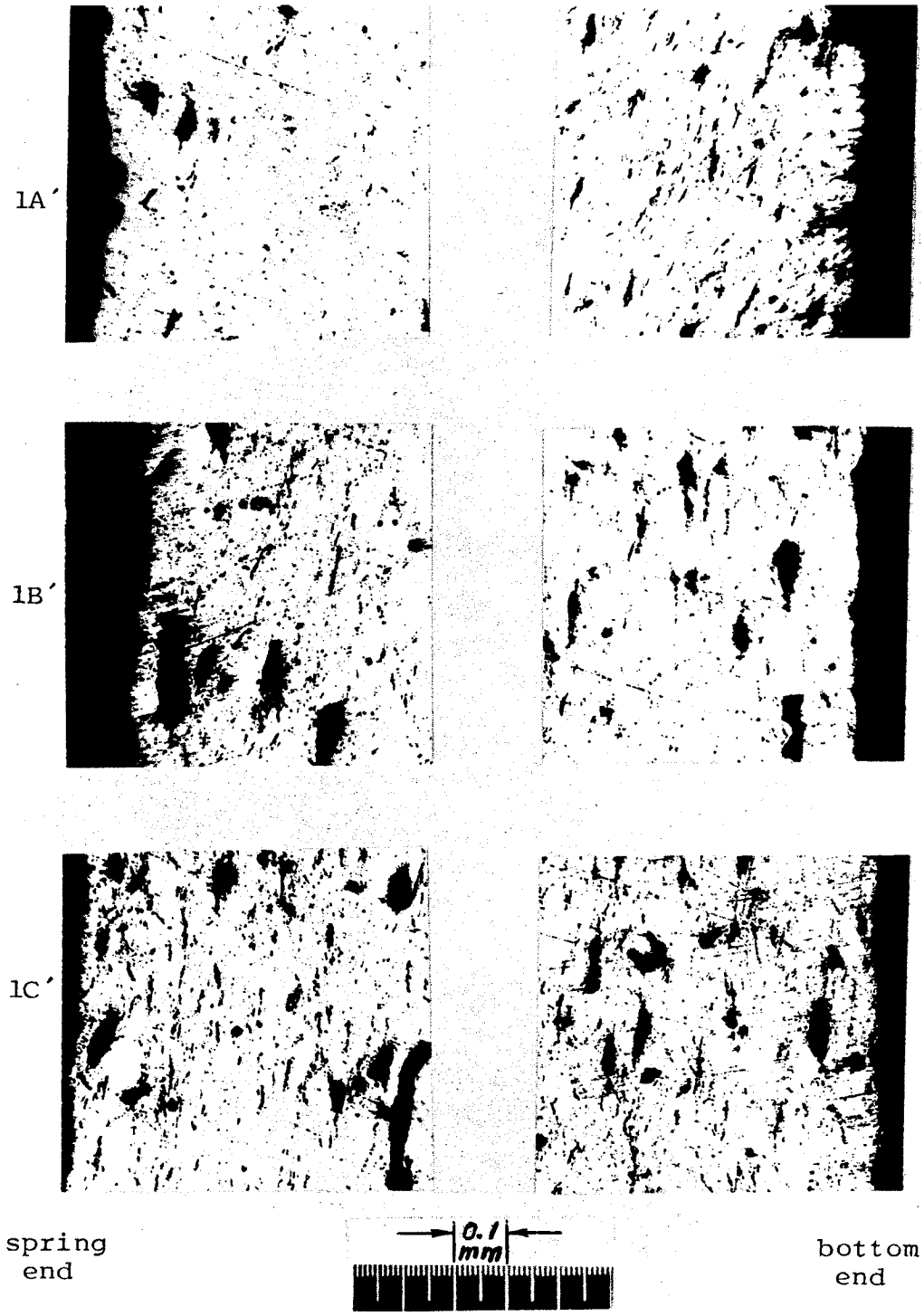

FIGURE 7A. PHOTOMICROGRAPHS SHOWING MICROSTRUCTURE AT THE SPRING END AND THE BOTTOM END, SKYLAB SAMPLES 1A′, 1B′, AND 1C′

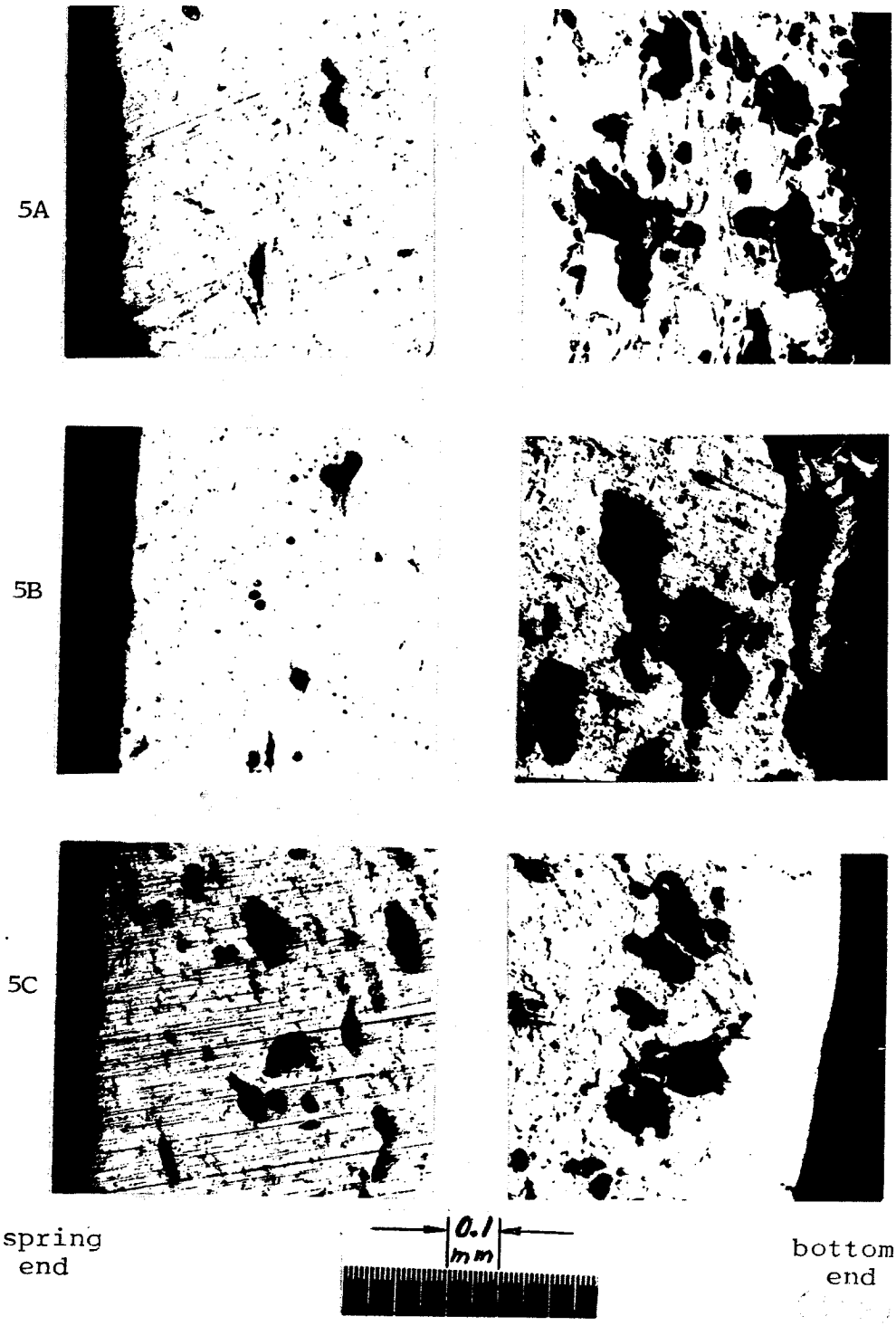

FIGURE 7B. PHOTOMICROGRAPHS SHOWING MICROSTRUCTURE AT THE SPRING END AND THE BOTTOM END, GBT SAMPLES 5A, 5B, AND 5C

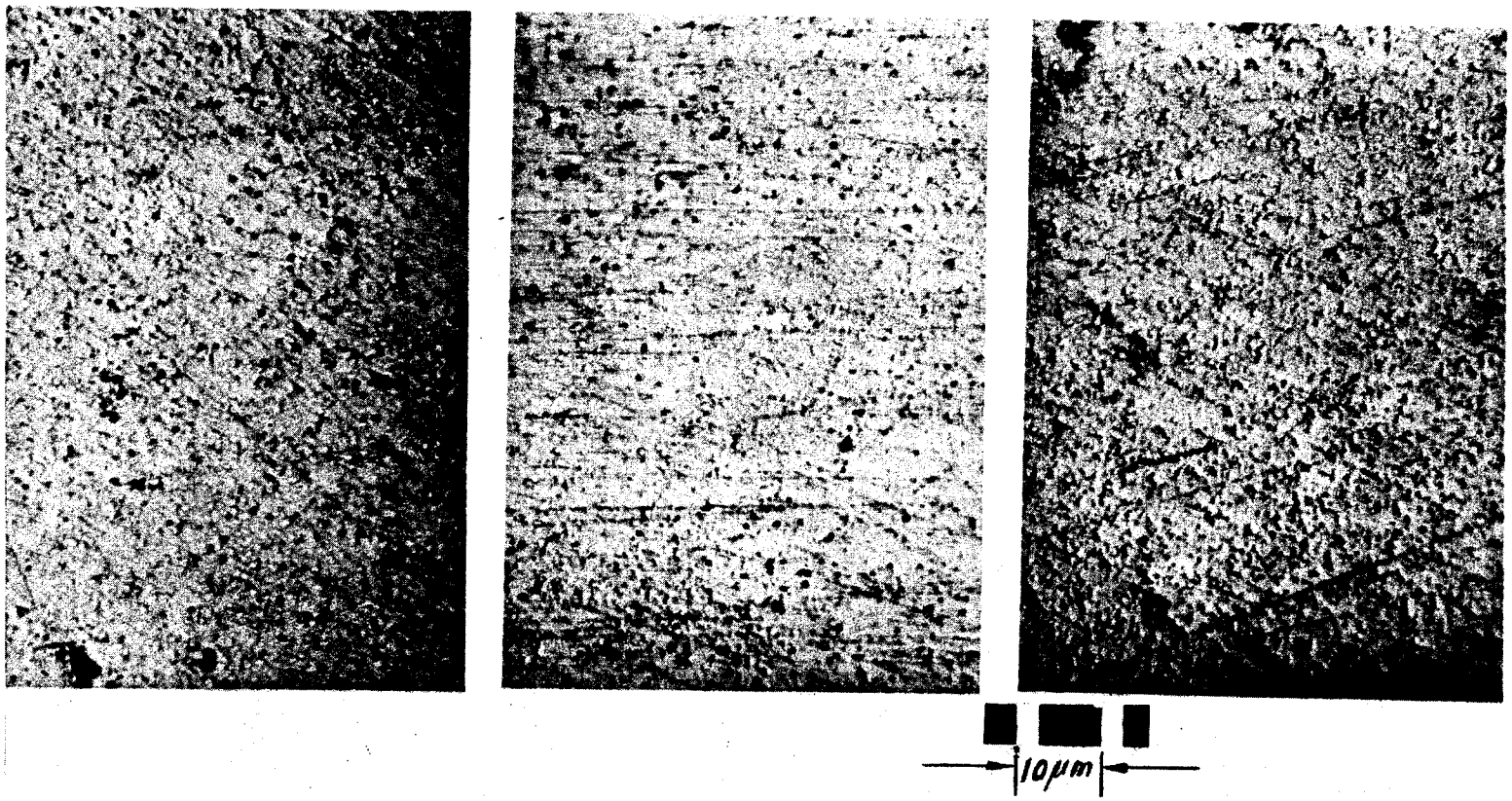

FIGURE 8A. PHOTOMICROGRAPHS SHOWING THE WHISKER DISTRIBUTION, SKYLAB SAMPLE 1A′

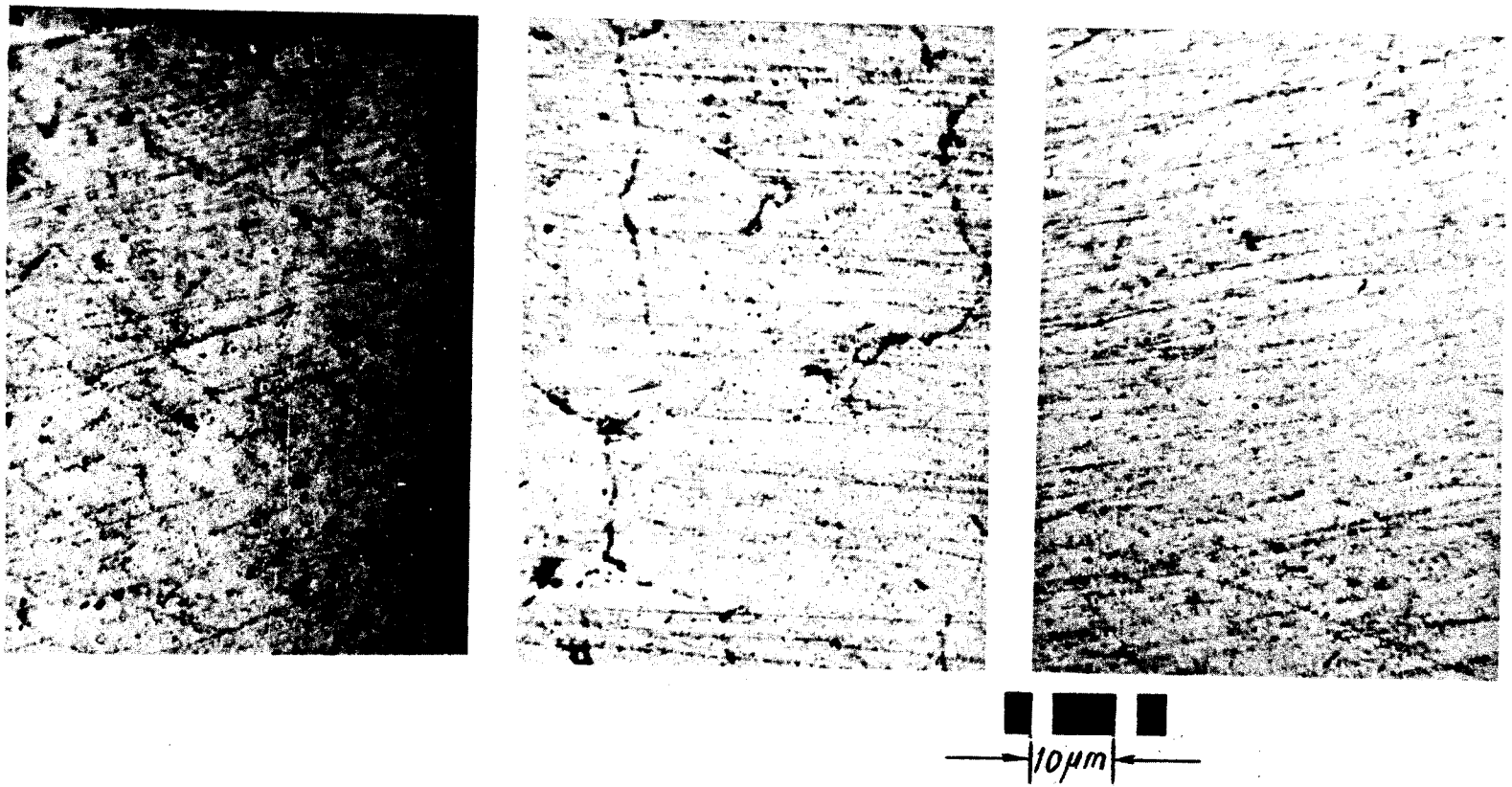

spring end

center

bottom end

FIGURE 8B. PHOTOMICROGRAPHS SHOWING THE WHISKER DISTRIBUTION, GBT SAMPLE 5A

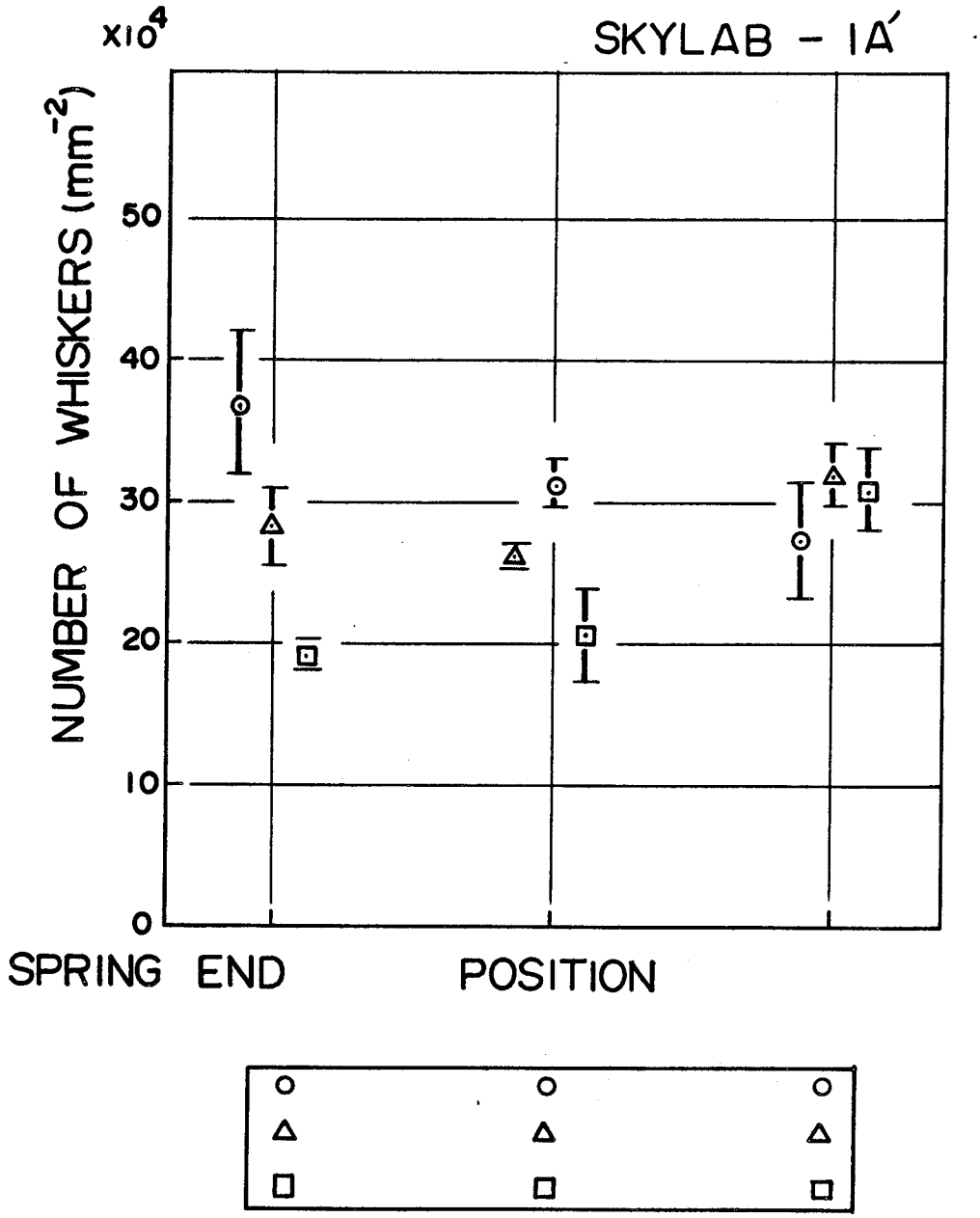

FIGURE 9A. DISTRIBUTION DENSITY OF WHISKERS, SKYLAB SAMPLE 1A´

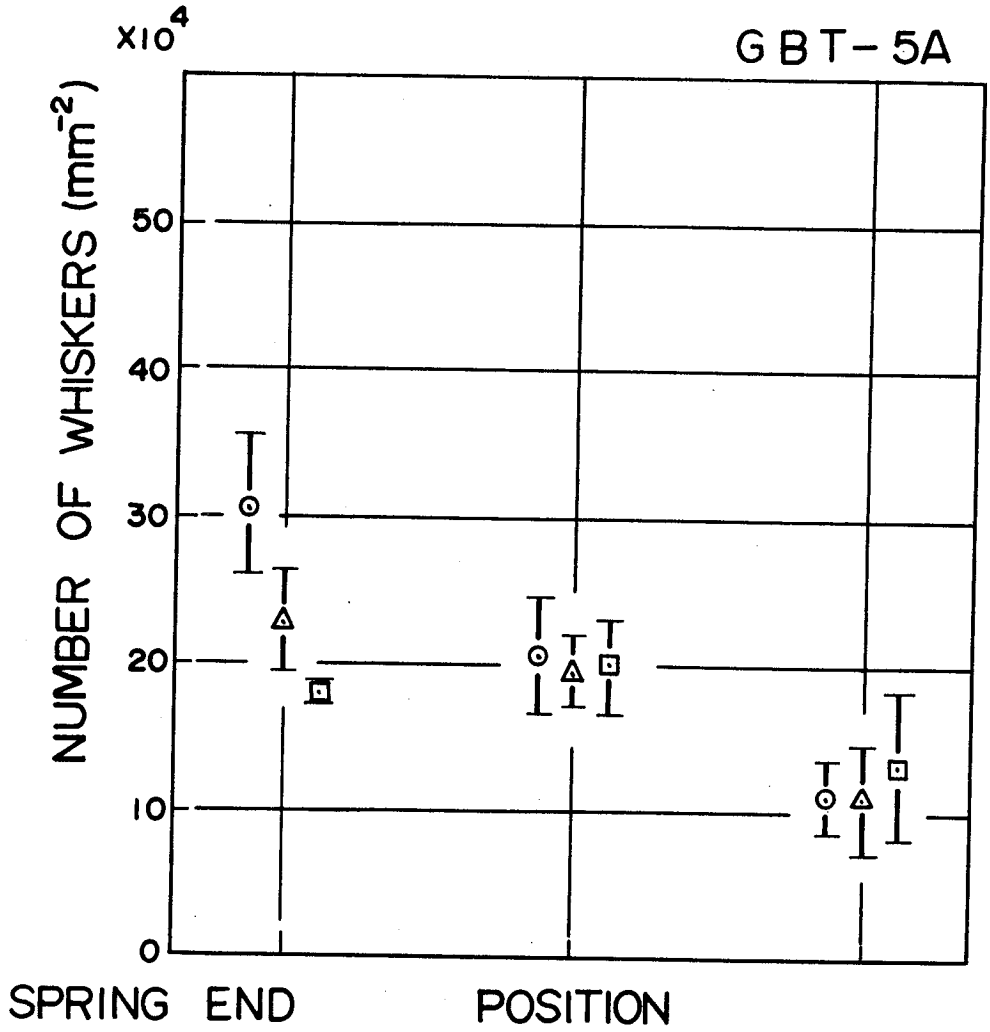

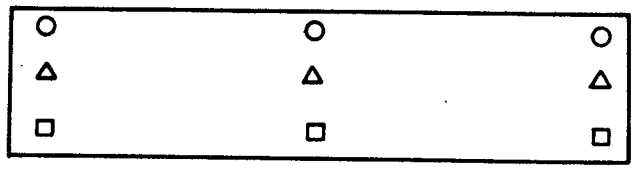

FIGURE 9B. DISTRIBUTION DENSITY OF WHISKERS
GBT SAMPLE 5A

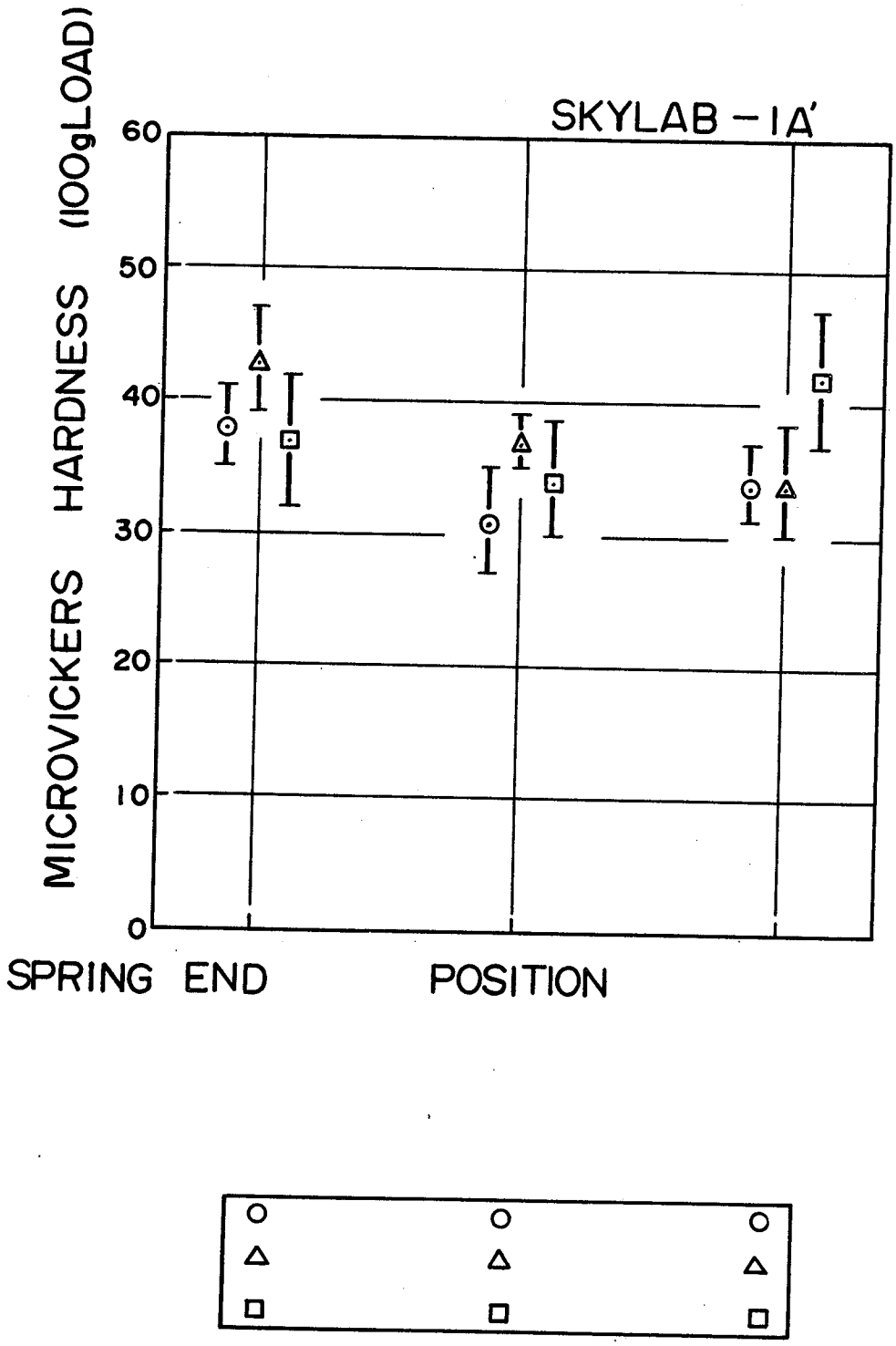

FIGURE 10A. MICROHARDNESS ON THE SECTION, SKYLAB SAMPLE 1A'

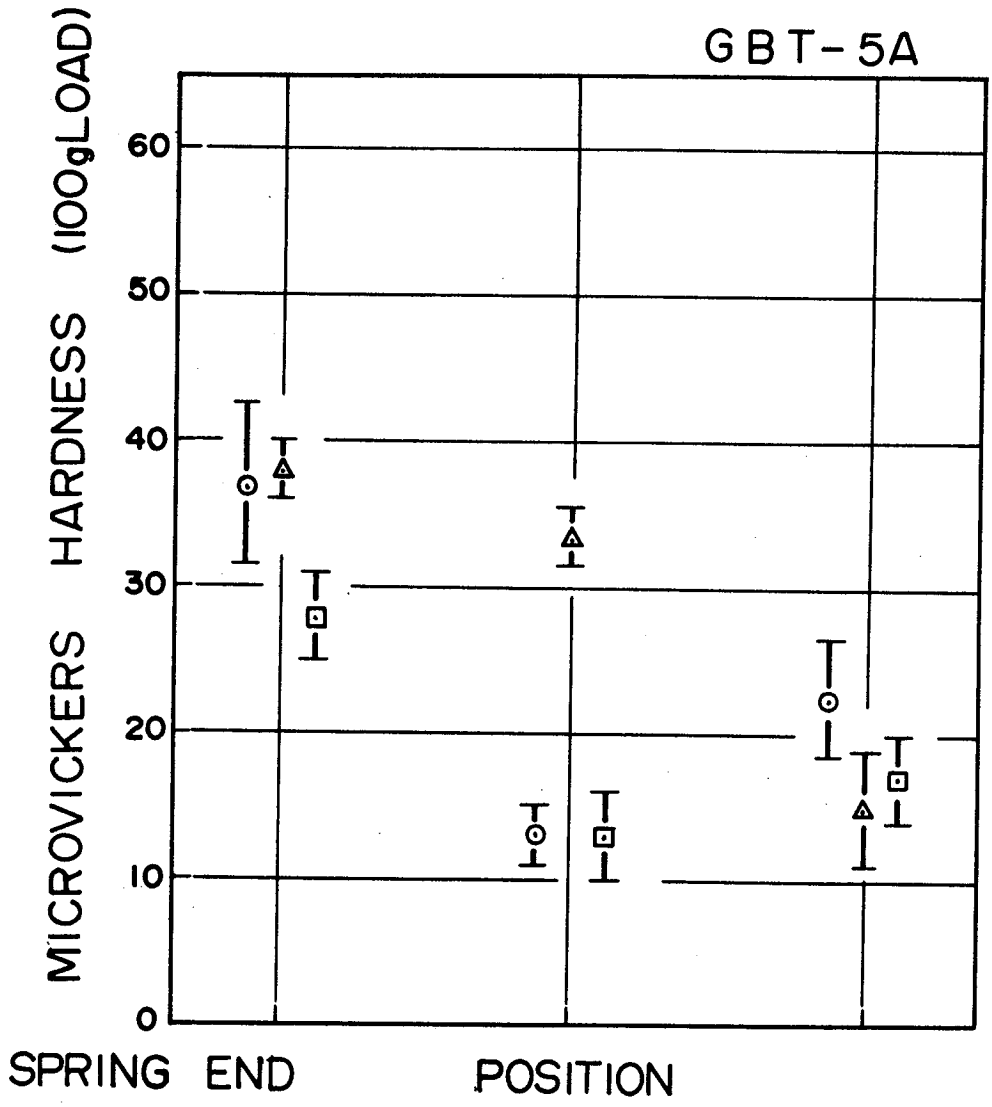

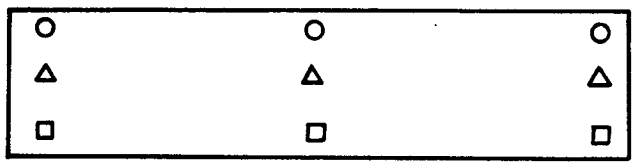

FIGURE 10B. MICROHARDNESS ON THE SECTION, GBT SAMPLE 5A

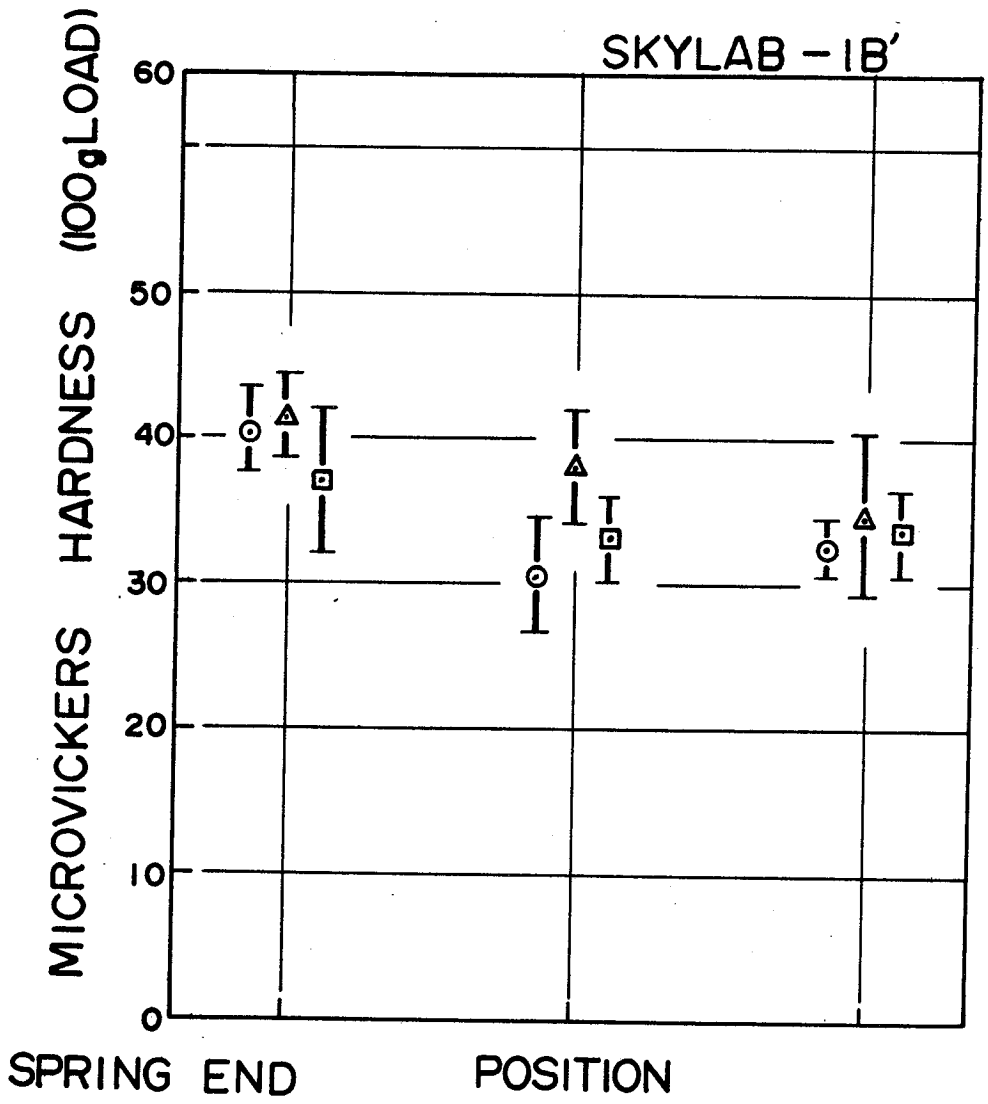

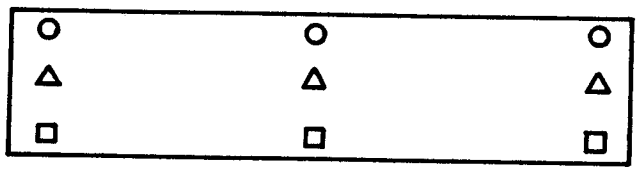

FIGURE 11A. MICROHARDNESS ON THE SECTION, SKYLAB SAMPLE 1B'

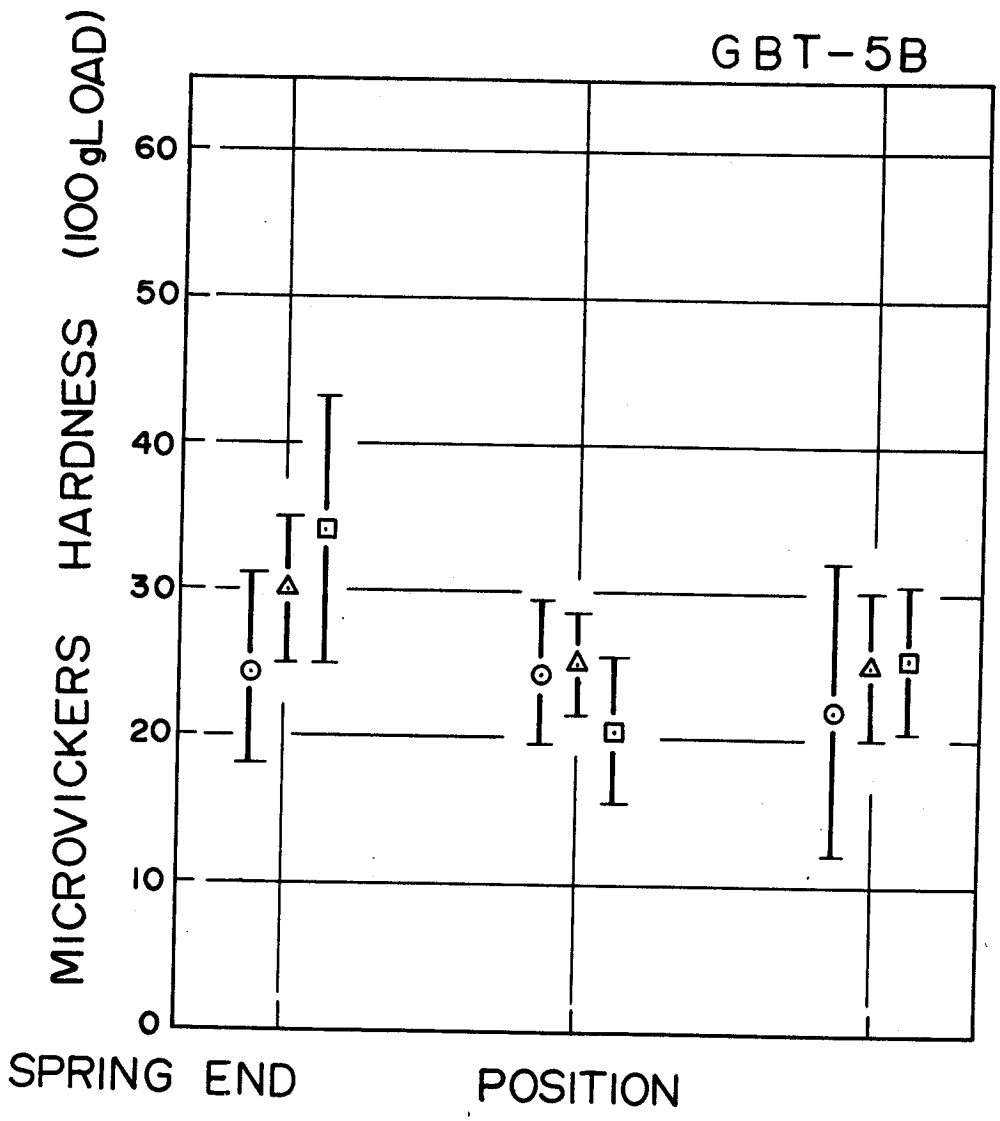

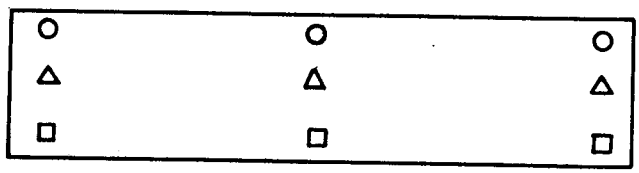

FIGURE 11B. MICROHARDNESS ON THE SECTION, GBT SAMPLE 5B

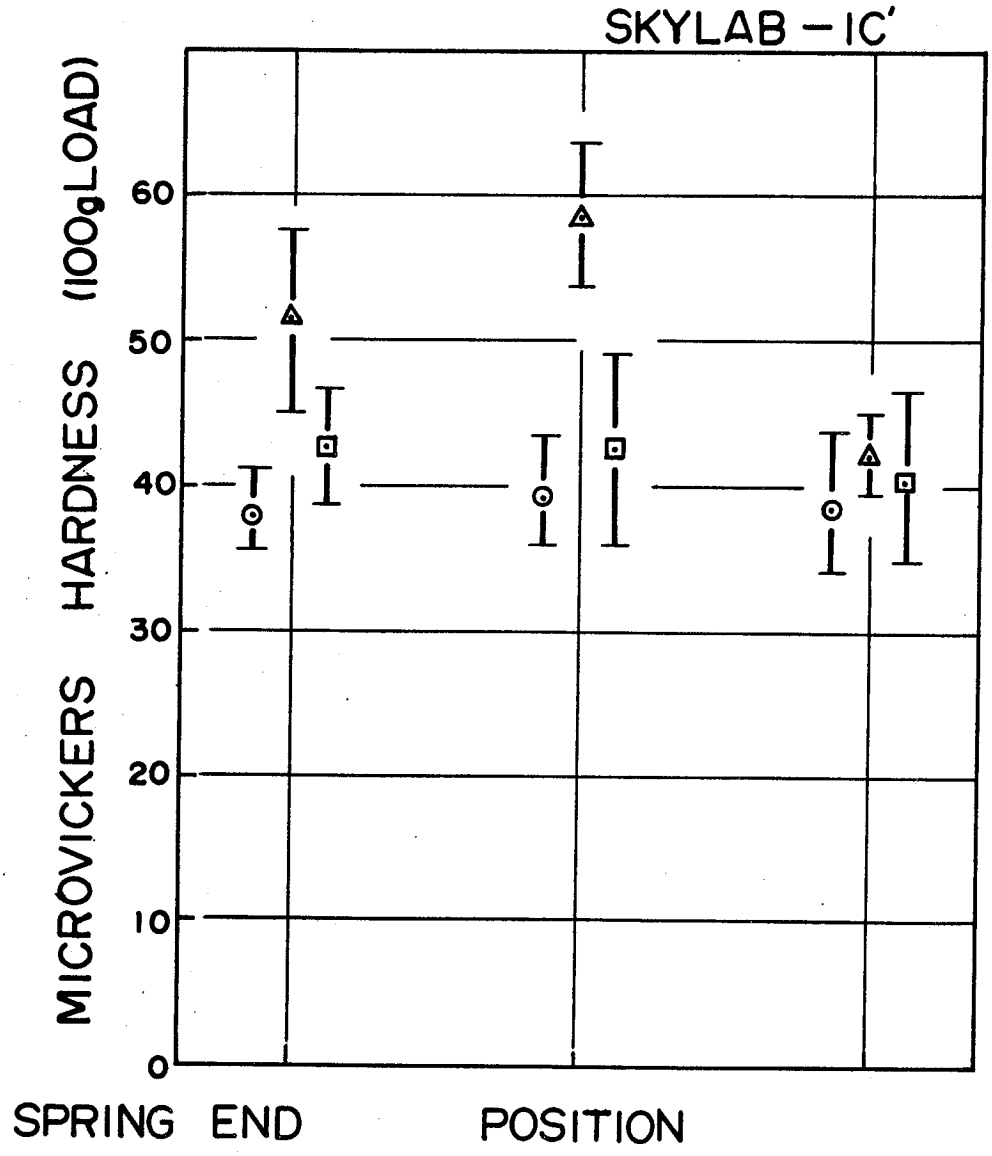

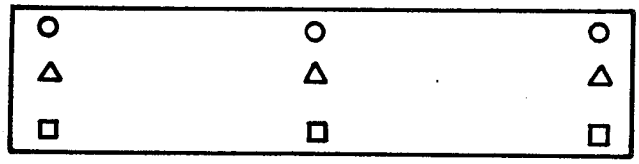

FIGURE 12A. MICROHARDNESS ON THE SECTION, SKYLAB SAMPLE 1C'

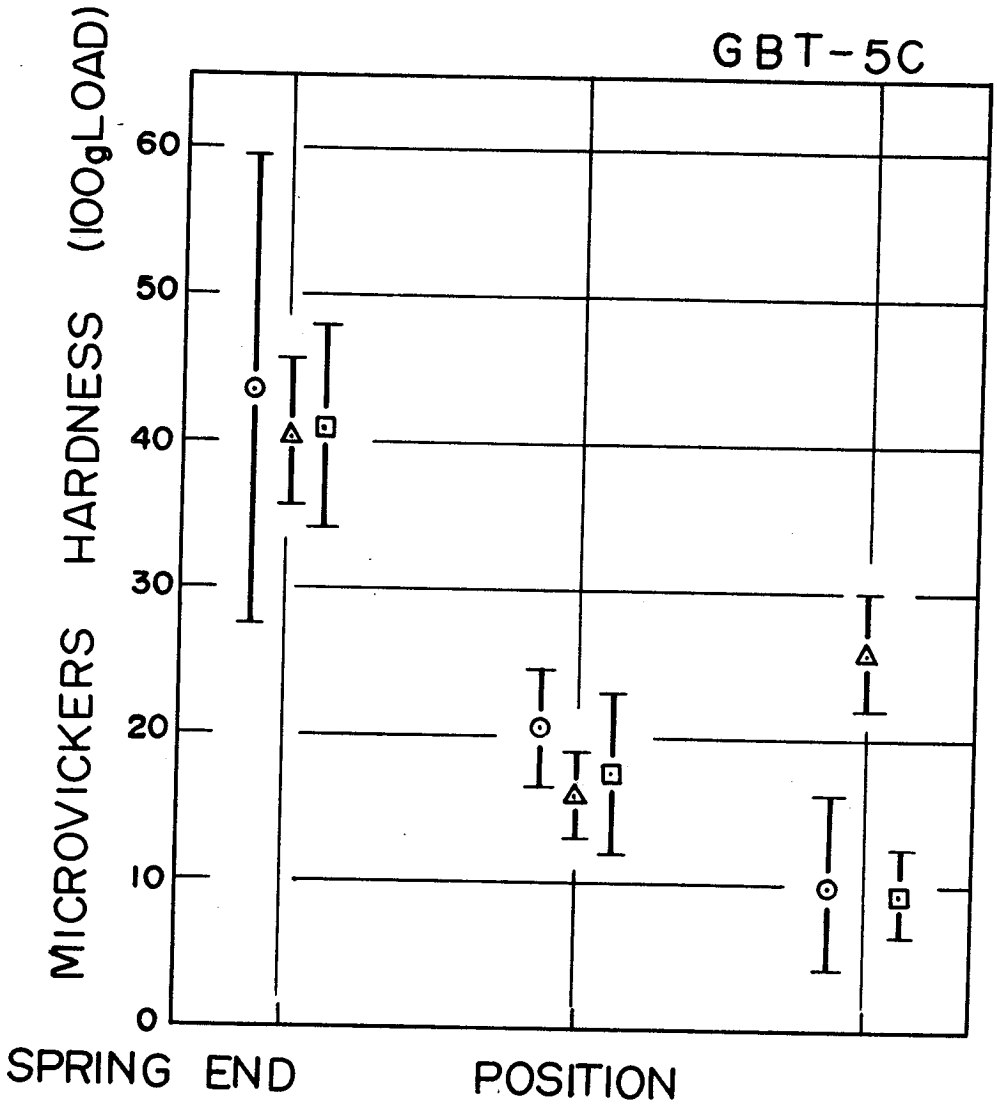

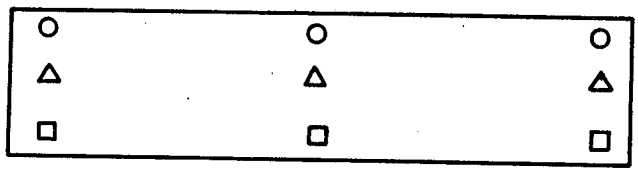

FIGURE 12B. MICROHARDNESS ON THE SECTION, GBT SAMPLE 5C

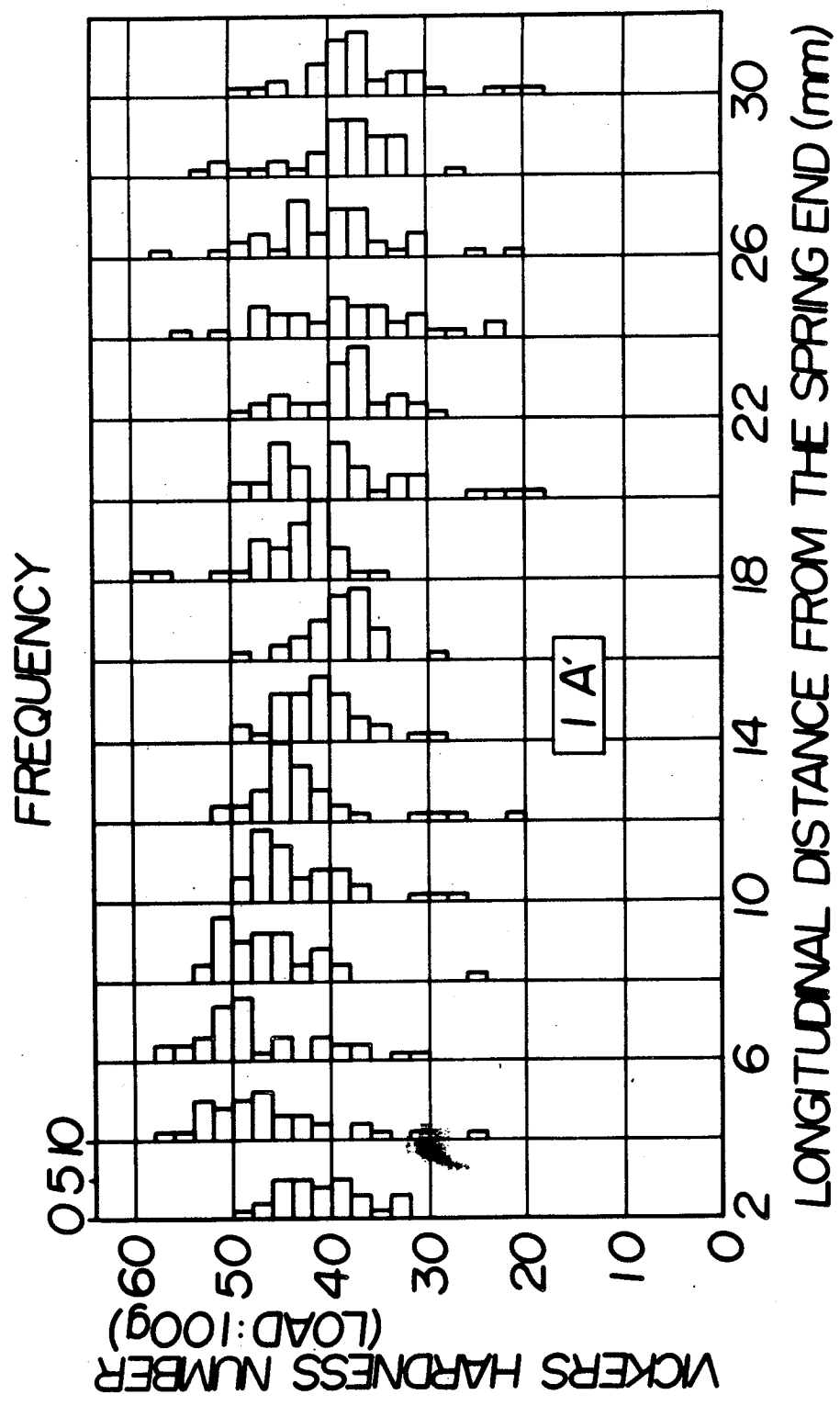

FIGURE 13A. HISTOGRAM SHOWING THE DISTRIBUTION OF HARDNESS ON THE SECTION, SKYLAB SAMPLE 1A'

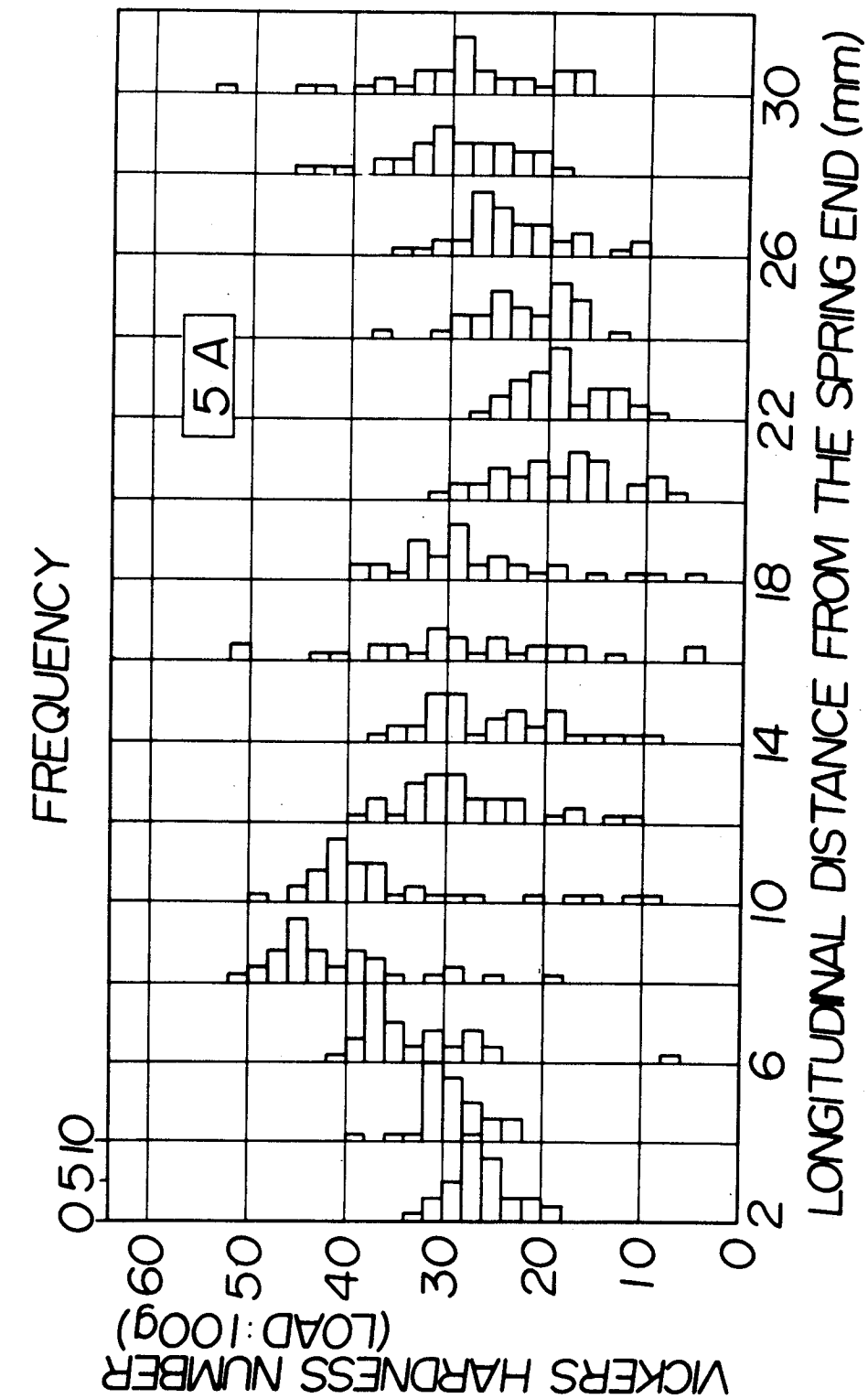

FIGURE 13B. HISTOGRAM SHOWING THE DISTRIBUTION OF HARDNESS ON THE SECTION, GBT SAMPLE 5A

VAPOR GROWTH OF GeSe AND GeTe SINGLE CRYSTALS IN MICRO-GRAVITY

By

H. Wiedemeier*, F. C. Klaessig , S. J. Wey and E. A. Irene
Department of Chemistry, Rensselaer Polytechnic Institute
Troy, New York 12181

SUMMARY

The positive effects of micro-gravity on crystal growth and fundamental properties of the vapor transport reaction were established by analyzing the results of GeSe and GeTe vapor transport experiments performed on board Skylab.

The analysis is based on a direct comparison of GeSe and GeTe crystals and of mass transport rate data obtained on earth and in space. For this purpose, a total of six transport experiments employing different concentrations of transport agent (GeI_4) and two temperature gradients were performed during the Skylab 3 and 4 missions. Extensive ground-based studies demonstrated that the crystal morphology and the mass transport rates of the above systems are affected by the transport conditions, in particular by gravity-driven convection. With increasing contribution of the convective component to the transport process the crystal quality decreases. This shows that on earth the negative effects of convection can only be minimized but not eliminated. The analysis of space and ground crystals is based on a comparison of deposition patterns, growth habits, optical and scanning electron microscopy of as-grown and cleaved crystal faces and thermal etching. The results demonstrate unambiguously a considerable improvement of the space crystals in terms of surface perfection, crystalline homogeneity and defect density. The observation of greater mass transport rates than expected in micro-gravity environment is of basic scientific and technological significance. This indicates that conventional transport models are incomplete and demonstrates that crystals of improved quality can be grown at reasonable rates by this technique in space. These results are of practical importance for the modification of crystal growth techniques on earth.

The combined results confirm the unique conditions of weightlessness for materials processing and for the observation of basic transport phenomena.

INTRODUCTION

Crystal growth by vapor transport is of technological importance in the production of bulk and layer type single crystalline materials used in various

*Paper presented by H. Wiedemeier.

electronic devices. It is well established that the properties and performance characteristics of materials are critically dependent on the degree of homogeneity and crystalline perfection which, in turn, are affected by the transport conditions and condensation mechanism of a particular system. Control of these growth parameters under ground-based conditions is limited due to the presence of gravity-driven convective motion in the gas phase.

Crystal growth studies without convective interference in a micro-gravity environment should yield fundamental data for the vapor transport technique and reveal the inherent transport properties of a chemical system. This basic information obtained from the space experiments will enhance our understanding of crystal growth phenomena and will be useful for the improvement of crystal growth techniques on earth. Due to its inherent simplicity in terms of a defined solid-gas phase system, the vapor transport technique is well suited to observe micro-gravity effects and other unexpected phenomena.

This report contains the results of the present evaluation of six crystal growth experiments performed during the Skylab 3 and 4 missions. Four of these experiments were concerned with the growth of GeSe and two of GeTe crystals. Although these systems are presently of limited interest as electronic device materials, their structural properties are favorable for the detection of morphological changes. The conclusions drawn from these exploratory space experiments are readily adaptable to the growth of crystals of other electronic materials.

EXPERIMENT OXJECTIVES

The primary objective of our crystal growth experiments in space was to observe and to measure changes in the mass transport rate of a chemical system and in the morphology of crystals of IV-VI compounds. In the absence of gravity-driven convection and for given experimental conditions, the transport should be controlled by the thermochemical parameters of the solid-gas phase reaction. The crystal habit and morphology should be primarily determined by the crystallographic properties of the respective crystal structures. In addition, information concerning the number and distribution of crystal defects is expected from these experiments.

In view of the structural and thermochemical properties of these materials, any micro-gravity effects on the above parameters should be more pronounced for the GeSe system than for GeTe. The platelet type growth habit of GeSe is very suitable for microscopic and electrical measurements. In addition, thermal etching techniques have been developed for this material in our laboratory. The multi-purpose furnace available for crystal growth on Skylab required the use of a common temperature gradient and heating cycle for a set of three ampules. For this reason, the conditions for the space experiment were selected to yield optimal results for GeSe and supporting data from the GeTe system. The definition of these conditions and the suitability of the above materials for crystal growth in space are based on extensive ground-based studies in our laboratory.

GROUND-BASED STUDIES

Scientific Basis

In a chemical transport reaction [1], a gaseous transport agent reacts at a given temperature with the solid source material to form exclusively gaseous products. The vapor species migrate from the source to the condensation zone of the reaction vessel where, at a different temperature, the reverse reaction occurs with formation of the solid. The necessary concentration gradient is established by means of a temperature gradient. Under optimal experimental conditions well defined single crystals are formed by the condensation reaction. The transport reaction is carried out in evacuated sealed ampules of fused silica which are subjected to the desired temperature gradient in a horizontal two-zone tubular resistance furnace.

The transport of species via the gas phase can be described by diffusion and by gravity-driven convection. In a gravitational field and temperature gradient both transport modes occur simultaneously. It is a unique feature of the vapor transport technique to select experimental conditions such that one or the other mode can be predominant. Under ground-based conditions, the convective contribution to the overall transport process can be minimized, but not eliminated. Based on present models for diffusive and convective gas flow [1], the material flux from the source to the condensation region is affected by the pressure in the transport ampule. At very low pressures of transport agent, the mass transport rate is controlled by the rate of the heterogeneous solid-gas phase reaction, and the material flux is proportional to the concentration of transport agent. At medium pressures, the transport rate is inversely proportional to the total pressure. The overall transport is diffusion controlled in this range. At higher pressures, the material flux increases with increasing total pressure indicating the predominance of the convective transport mode. For the diffusion and convection controlled pressure regions, the heterogeneous solid-gas phase reactions in the source and condensation zone are in the state of near-equilibrium.

Transport Properties of GeSe and GeTe

Mass transport rate studies in our laboratory on GeTe [2] and GeSe [3] using elemental iodine or GeI_4 as the transport agent have confirmed the above models. Details of the experimental procedures and results have been discussed previously [2,3]. These studies demonstrated that the habit and morphology of single crystals grown by this technique are significantly affected by the transport conditions. With increasing contribution of the convective component to the transport process the crystal quality decreases. For GeTe, the crystal habit changes from octahedral bulk type crystals via distorted and hollow octahedra to platelets with nearly macroscopic surface imperfections. The corresponding morphological changes for GeSe from platelet to dendritic type crystal growth are even more pronounced. These observations are explained by gravity-driven convection which causes inhomogeneities and turbulence in the gas phase and negative effects on the condensation process and crystal morphology. The convective component is always operative on earth in the vapor transport system. The observed trend in the change of crystal quality suggests the possibility to grow nearly perfect crystals in zero-gravity environment. The experimental conditions of the above ground-based studies are the same as those employed in space, except for gravity.

EXPERIMENTAL SKYLAB PROCEDURES

The transport experiments were performed in the multi-purpose electric furnace built by the Westinghouse Electric Corporation. The furnace consisted essentially of a cylindrical furnace chamber and an instrumentation compartment. The furnace chamber contained three tubular reaction cavities for the individual metal cartridges and quartz ampules discussed below. Since the Westinghouse facility was a one-zone resistance furnace, the desired temperature gradient and stability were achieved by various heat shields surrounding the quartz ampules in the metal cartridges and by appropriate heat shields in the furnace. The temperature gradient used for the experiments performed during the SL 3 mission was 520 → 420°C with a nearly linear gradient between the hot and cold zone of the reaction chamber.

In order to increase the range of experimental conditions a temperature gradient of 412 → 346°C was employed for the second series of transport studies carried out on the SL 4 mission. The primary goal of the SL 4 experiments was to confirm the unexpected mass transport rates observed during the SL 3 mission discussed below. In addition, supporting evidence for the morphological changes in crystal habit was expected.

The transport ampules were made of fused silica tubing of 13.7 mm inner diameter and 150 mm in length. Close to one end the ampule contained three shallow indentations to hold the source material in place. The other ampule end was sealed after loading at a pressure of 10^{-6} torr or less. Prior to loading the cleaned ampules [2,3] were outgassed at a temperature of about 1000°C for 10 hours and a vacuum of 10^{-6} torr. The polycrystalline starting materials GeSe and GeTe were synthesized by annealing stoichiometric mixtures of high purity elements (99.999%) and subsequent sublimation of the product [2, 3]. The crystallographic identity of the materials was established by X-ray diffraction techniques. High purity GeI_4 (99.999%) was used as a transport agent. The ampule designated 3A in this experiment contained 2.0 gm of GeSe and 14.28 mg of GeI_4 per cm^3 tube volume. Ampule 3B was loaded with 1.0 gm GeSe and 1.28 mg/cm^3 GeI_4, and ampule 3C contained 1.0 gm GeTe and 7.14 mg/cm^3 GeI_4. After sealing the ampule, the starting material was quantitatively sublimed to the source end. For the temperature gradient 520 → 420°C, these conditions corresponded to a high (GeSe, 3A), low (GeSe, 3B) and medium (GeTe, 3C) contribution of the convective component to the overall transport under ground-based conditions. This set of ampules was used for the SL 3 mission experiments.

For the SL 4 mission experiments the back-up ampules 5A, 5B and 5C were employed. The quantities of GeSe and GeTe and the initial amounts of transport agent GeI_4 used in these ampules was the same as in the corresponding SL 3 transport tubes. Due to the lower temperature gradient used for the SL 4 experiments (412 → 346°C), a partial precipitation of transport agent occurred in ampules 5A and 5C during transport. No precipitation of GeI_4 occurred in ampule 5B. The resulting pressure conditions corresponded to a medium (GeSe, 5A and GeTe, 5C) and to a low (GeSe, 5B) convective contribution to the overall transport under ground-based conditions.

The transport tubes were enclosed with the proper heat shields in evacuated metal cartridges by Westinghouse. These cartridges were inserted into the multi-purpose furnace by the astronauts. The chemical transport reactions for

the GeSe and GeTe systems and the experimental conditions employed for the studies in micro-gravity environment are summarized in Table I. The GeI_4 pressures are calculated for the mean temperature of the gradient and ideal gas conditions.

Table I

TRANSPORT REACTIONS AND
EXPERIMENTAL CONDITIONS

$$GeSe(s) + GeI_4(g) = 2\ GeI_2(g) + 1/2\ Se_2(g)$$

$$GeTe(s) + GeI_4(g) = 2\ GeI_2(g) + 1/2\ Te_2(g)$$

ΔT:	520 → 420°C (SL 3 Mission)
GeSe (3A)	$P(GeI_4(g)) = 1.50$ atm
GeSe (3B)	$P(GeI_4(g)) = 0.13$ atm
GeTe (3C)	$P(GeI_4(g)) = 0.75$ atm
ΔT:	412 → 346°C (SL 4 Mission)
GeSe (5A)	$P(GeI_4(g)) = 0.42$ atm
GeSe (5B)	$P(GeI_4(g)) = 0.12$ atm
GeTe (5C)	$P(GeI_4(g)) = 0.60$ atm

After initiating the heating cycle aboard Skylab 3, a temperature of 520°C at the source end and of 420°C at the condensation region of the ampule were achieved after 2.75 hours. These conditions were maintained (± 3°C) for 33 hours, during which transport and crystal growth occurred. After termination of the experiment, cooling of the ampules to ambient temperature took place in the multi-purpose furnace over a period of about 12.5 hours. The heating cycle for the SL 4 experiments consisted of a heat-up period of 1.5 hours, a soak-time of 34 hours during which the temperature remained constant within ± 3°C, and a cool-down period of 7 hours.

The cartridges were returned to the George C. Marshall Space Flight Center. Radiographic examination of the ampules in the cartridges showed that none of the ampules had any mechanical damage. After opening the metal cartridges, the ampules were brought to our laboratory for further evaluation of the experiment. An opened cartridge and a ground-based GeSe transport ampule are shown in Fig. 1. A similar ampule used for the space experiment was inserted into the section of the cartridge shown next to the ampule in Fig. 1. This part fit into the upper half of the cartridge which was sealed at the right edge of the first section. The ground-based ampule reveals the dendritic type deposition of GeSe typical for convection controlled transport conditions.

RESULTS AND DISCUSSION

After recording the deposition profile of transported material in the closed ampules, the tubes were opened and the crystals and residual source materials were carefully removed for further examination.

Crystallographic Identification of Transport Product

The crystallographic identification of space grown crystals was established by means of Debye-Scherrer and Laue X-ray diffraction techniques. The results in terms of lattice parameters and crystallographic orientation of as-grown faces are summarized in Table II together with corresponding data of ground-based crystals.

Table II

CRYSTALLOGRAPHIC PARAMETERS OF
SKYLAB AND GROUND-BASED CRYSTALS

System	Lattice Parameters (Å)			Orientation (hkℓ)
	a_0	b_0	c_0	
		SL 3 MISSION		
GeSe (Ground-Based)	4.383 ± 0.01	3.827 ± 0.01	10.770 ± 0.02	(001)
GeSe (M556-3A)	4.387 ± 0.01	3.840 ± 0.01	10.768 ± 0.02	(001)
GeSe (M556-3B)	4.387 ± 0.01	3.836 ± 0.01	10.787 ± 0.02	(001)
GeTe (Ground-Based)	5.982 ± 0.003	α = 88.25 ± 0.05°		(111)
GeTe (M556-3C)	5.981 ± 0.003	α = 88.30 ± 0.05°		(111)
		SL 4 MISSION		
GeSe (M556-5A)	4.386 ± 0.01	3.835 ± 0.01	10.783 ± 0.02	(001)
GeSe (M556-5B)	4.375 ± 0.01	3.826 ± 0.01	10.757 ± 0.02	(001)
GeTe (M556-5C)	6.072 ± 0.01	α = 87.20 ± 0.2°		(111)

A comparison of the data in Table II shows that the lattice constants of the respective systems are identical within limits of error. There is no change in the orientation of native faces of crystal platelets. Within the detection limits of X-ray diffraction techniques there is no measurable effect of micro-gravity on the crystallographic parameters of space grown crystals. The increase in the unit cell dimensions of GeTe (5C) can be explained by the formation of a limited solid solution between GeTe and transport agent which was anticipated under the experimental conditions of the SL 4 mission. The above results are expected in view of the relative magnitude of chemical bonding and gravitational forces.

Mass Transport Rates

A summary of the mass transport rate or flux data observed in micro-gravity and under ground-based conditions is given in Tables III and IV.

Table III

MASS TRANSPORT RATE UNDER
MICRO-GRAVITY AND GROUND-BASED CONDITIONS

SL 3 MISSION (520 → 420°C)

System	Mass Flux ((moles/cm^2·sec) × 10^{-9})			Ground-Based Transport Mode
	Micro-G	1-G	Extrapolated Diff. Mode	
GeSe (A)	∿5	39	∿4 × 10^{-1}	High Convective
GeSe (B)	∿10	5.3	∿3	Low Convective
GeTe (C)	∿3	2.5	∿2 × 10^{-1}	Medium Convective

A comparison of these data reveals a rather significant result. The flux in micro-gravity is greater than expected if gas phase diffusion would be the only parameter contributing to the material transport from the source to the condensation region. For systems (A) and (C) the difference between observed and predicted mass fluxes is about one order of magnitude. These observations indicate the existence of other than gravity-driven convective transport components contributing to mass flux in a reactive solid-gas phase system. Thermodynamic and kinetic considerations suggest that the additional transport modes are related to the thermochemistry of the gas phase reaction and to secondary effects of the temperature gradient. These factors have been largely ignored in the conventional treatment of transport phenomena.

The above trend in the mass transport rates is confirmed by the flux data of the SL 4 transport experiments listed in Table IV.

Table IV

MASS TRANSPORT RATE UNDER
MICRO-GRAVITY AND GROUND-BASED CONDITIONS

SL 4 MISSION (412 → 346°C)

System	Mass Flux ((moles/cm^2·sec) × 10^{-9})			Ground-Based Transport Mode
	Micro-G	1-G*)	Extrapolated Diff. Mode	
GeSe (A)	∿0.8	0.9	∿0.1	Convective
GeSe (B)	∿1.8	0.8	∿0.5	Diff. + Conv.
GeTe (C)	∿1.0	1.7	∿0.1	Convective

*) Based on 420 → 350°C temperature gradient

Despite the lower temperature gradient and the associated partial precipitation of transport agent for the SL 4 experiments, the flux data of Table IV are in good agreement with the overall pattern observed during the SL 3 mission.

The technological significance of these results is the possibility of growing crystals in space at reasonable rates and improved quality by this technique. The scientific importance is the demonstration that the conventional transport models are incomplete.

Morphological Characteristics

A comparison of ground-based and space grown crystals reveals distinct morphological differences of the as-grown faces and crystal habits.

Representative GeTe crystals (Table I, system 3C) are shown in Fig. 2. Crystals obtained under ground-based conditions (Fig. 2a) show distorted surfaces of the platelets and needles. Aggregation and twinning are frequently observed. Nearly all octahedral type crystals grown under these conditions reveal partially hollow growth habits. The corresponding space crystals (Fig. 2b) have considerably more compact habits. The as-grown faces of these crystals show a higher degree of smoothness and crystalline perfection. The edges of these crystals are better defined. The apparent slight difference in the metallic luster of the ground-based and space crystals is due to a partial condensation of the residual gas phase during the cool-down period of the multi-purpose furnace. In our laboratory, this is avoided by removing the ampule from the furnace and quenching the residual vapor phase at the source region.

The typical appearance of the condensation region of a GeTe ground-based and space transport ampule is shown in Fig. 3. The curvature of the dendritic-type crystals is characteristic of the GeTe deposition pattern under

convection controlled transport conditions (Fig. 3a). This pattern strongly indicates turbulent flow of the gas phase in the ground-based ampule. Under micro-gravity conditions no such pattern is observed (Fig. 3b).

A rather interesting phenomenon is observed on some of the as-grown faces of GeTe crystals obtained in ampule 3C under micro-gravity conditions (Fig. 4). The triangular pattern reveals three-fold symmetry which is characteristic of the (111) orientation of the GeTe crystal face. This pattern is probably due to a very slow condensation of vapor species which can lead to a decoration of the defects in the (111) plane. Since such a decoration effect requires a rather homogeneous and undisturbed condensation, this phenomenon is difficult to observe under ground-based conditions due to localized convective interference.

A representative selection of ground-based and space grown GeSe crystals (Table I, system 3B) is shown in Fig. 5. The concentration of transport agent used in this case corresponds to the onset of the convection controlled range in a gravitational environment. For this reason, the external morpological differences are expected to be less pronounced than for systems 3C and 3A (Table I). However, the difference in surface quality between ground-based (Fig. 5a) and space crystals (Fig. 5b) is obvious. The as-grown faces of the ground crystals have steps and ledges while the space crystals reveal a more uniform surface. A comparison of internal faces of GeSe (system B) crystals will be discussed below.

The most pronounced difference in growth morphology was predicted and observed for GeSe (Table I, system 3A). The GeI_4 pressure employed yields a convention controlled transport mode under ground-based conditions. A typical view of the condensation region of a GeSe ground-based (high convective) transport ampule is compared to the corresponding space ampule (3A) in Fig. 6. The ground-based ampule (Fig. 6a) shows clearly the dendritic type growth and distinct curvature of the individual dendrites. This morphology reveals the effects of convective turbulence on crystal habit. In the absence of convective interference individual well-developed single crystal platelets (Fig. 6b) are obtained. The space ampule 3A (Fig. 6b) contains the largest GeSe single crystal grown under present experimental conditions. (The photographs of Fig. 6 were taken through the quartz wall of the closed ampules.)

Close-ups of the two sides of the largest GeSe single crystal platelet (system 3A) grown in space are shown in Fig. 7. The actual dimensions of this platelet are about 4 mm in width and 16-18 mm in length. The thickness is about 50 μ. The spotty appearance of the native surfaces is due to the above mentioned partial condensation of residual gas phase during the cool-down period.

The lower temperature gradient employed for the SL 4 experiments (412 → 346°C) yielded smaller transport rates as compared to the SL 3 mission experiments. In addition, the lower temperature of the condensation region leads to a reduction in mobility of species on the surface of the crystal. This results in a decrease of crystal size and quality. However, despite these restricting parameters a comparison of ground-based and space crystals grown in the above temperature gradient confirms the trend observed for the morphological changes of the SL 3 crystals.

This is illustrated in Fig. 8 for GeSe ground-based and space (5B) crystals. The major difference here is that the ground crystals (Fig. 8a) reveal a higher growth rate in the c-direction (perpendicular to the (001) plane) relative to the space crystals (Fig. 8b) which show a preferential growth parallel to the (001) plane. This yields single crystal platelets with (001) orientation. This observation is interesting with respect to the orthorhombic structure of GeSe which is characterized by primary bonding within the (001) double-layers and secondary bonding between adjacent planes of two sets of (001) double-layers. Based on these bonding properties, the predominant growth of (001) platelets is expected under near-ideal conditions. This is also in agreement with the corresponding results (GeSe, 3B) of the SL 3 experiments. In addition, the as-grown faces of the space crystals (Fig. 8b) show a higher degree of crystalline perfection. The spotty appearance of the surface of the space grown material is due to the above discussed condensation of residual vapor species during the cool-down period.

Analogous to the SL 3 results, the morphological differences between ground and space crystals are more pronounced for the GeSe system (5A) corresponding to high-convective transport under ground-based conditions. This is illustrated in Fig. 9. Ground-based GeSe transport leads to massive aggregation of smaller GeSe platelets and to polycrystalline condensation (Fig. 9a). (This corresponds to dendritic aggregation for the higher temperature gradient of the SL 3 experiments.) Under micro-gravity conditions individual single crystal platelets of (001) orientation (Fig. 9b) are obtained. The apparent roughness of the surface of the space crystals is caused by the above mentioned precipitation of transport agent due to supersaturation during growth and the condensation of residual vapor species in the cool-down period. However, despite these secondary reactions imposed by the experimental conditions of the SL 4 mission, the characteristic morphological differences between ground and space condensation are clearly exhibited.

The combined experimental evidence from the changes in deposition pattern and crystal habits demonstrates unambiguously the positive effects of micro-gravity on the external morphology and quality of crystals. The results of scanning electron microscopy and thermal etch studies discussed below are consistent with the above conclusions.

Scanning Electron Microscopy Studies

Scanning electron photomicrographs (400X) of cleaved faces of GeSe ground-based and space grown (3B) crystals compared in Fig. 10 show interesting morphological differences.

The irregular cleavage pattern of the ground-based crystal (Fig. 10a) is partially due to crystalline inhomogeneities causing a nonuniform separation of (001) layers upon cleavage. The origin of the holes in cleaved faces of ground-based crystals is not yet unambiguously identified. Other cleaved faces of ground crystals revealed shallow indentations. Present data indicate that some of these cavities could be native defects. The rather homogeneous cleavage pattern of the space crystal (Fig. 10b) reflects the higher degree of crystalline perfection. The diagonal edge is due to cleavage and represents the border between (001) planes of different depths with respect to the native surface. Both crystals were cleaved in the same manner which emphasizes the differences in crystallinity of the space and ground-based material.

Scanning electron photomicrographs (1000X) of the native edges of GeSe ground-based and space (3B) crystals in Fig. 11 reveal a pronounced difference in crystalline perfection. In both cases the crystal area at the left-hand side of the photograph is the (001) face of the crystal platelet. The edge is perpendicular to the (001) face. The edge of the ground-based crystal (Fig. 11a) shows regions of crystalline imperfections containing holes which penetrate into the bulk of the material. The morphology of a cleaved (001) face (perpendicular to the edge) will be affected by the location of the cleavage plane with respect to edge inhomogeneities. This could explain morphological differences of cleaved GeSe faces of ground-based crystals. The nearly perfect edge of the space crystal (Fig. 11b) is consistent with the high quality of cleaved (001) faces.

The morphological differences between GeSe dendrites obtained under ground-based high-convective conditions and GeSe single crystal platelets obtained in space (3A) are illustrated in Fig. 12 by scanning electron microscopy (200X). The native surface of the dendrite (Fig. 12a) reveals a series of steps which mark the onset of growth of different segments of the dendrite. In the presence of convection currents the onset of new layers is not always perpendicular to the growth direction of the preceeding crystal leading to the observed curvature of dendrites. The irregular growth also explains the formation of macroscopic cavities which penetrate into the bulk of the dendrite. The overall morphology of the cleaved (001) face of the space crystal (Fig. 12b) reflects the degree of homogeneity of the gas phase and condensation process under micro-gravity conditions.

Thermal Etching Studies

In order to investigate the effects of micro-gravity on crystalline perfection for the bulk of the material, internal faces of GeSe (system 3B) crystals are examined by thermal etching and optical microscopy. Due to the bonding properties of GeSe the single crystal platelets can be cleaved parallel to the (001) plane. For the etch studies, freshly cleaved GeSe crystal platelets are mounted in the hot stage of a metallographic microscope. Under vacuum ($\sim 10^{-4}$ torr) the temperature of the crystal is gradually raised until a change in surface morphology is first observed. Based on studies in our laboratory, at this temperature any mass-loss from the crystal surface is very small and changes in surface morphology are mainly due to a mobility of species on the surface [4,5]. In addition, the surface mobility is initiated at surface defects.

The cleaved faces of GeSe ground-based specimens selected for thermal treatment were of the highest quality and were indistinguishable at magnification 500X from the space crystals. The results of a short-term thermal etching (5 min at about 190°C) of inner planes of ground and space crystals (3B) of GeSe are shown in Fig. 13. The ground crystal (Fig. 13a) is completely covered with thermal etch pits. The average density of pits based on the upper left and lower right areas of Fig. 13a is about 8×10^5 cm^{-2} and the diagonal length of the largest pits is approximately 8×10^{-3} cm. The number and distribution of etch pits is related to the corresponding quantities of defects in this plane. The morphology of the space crystal (Fig. 13b) is considerably less affected by short-term thermal etching. The density of pits based on the entire area of Fig. 13b is in the order of 10^3 cm^{-2}, and the diagonal length of the largest pits is in the low 10^{-3} cm range. Allowing for

large error limits in the etch pit count of the space crystal, there remains a significant difference compared to the density of pits of the ground crystal. This indicates a higher degree of crystalline perfection and homogeneity of the space grown material. (The edge in the upper right area and the line in the right section of Fig. 13b are due to cleavage of the crystal.)

The above observations are supported by the results of long-term etching of GeSe single crystal platelets at the same temperature for 2.5 hours. After extended time periods, mass-loss from the crystal causes a complete roughening of the surface. Representative areas of thermally treated internal (001) faces of ground and space (3B) crystals are shown in Fig. 14. The differences in surface morphology are obvious. The density of etch pits in the upper left quadrant of the ground-based crystal in Fig. 14a is about 8×10^5 cm^{-2}. The diagonal length of the largest well defined etch pit in the lower right corner of Fig. 14a is about 10^{-2} cm and the depth is approximately 33×10^3 Å. These etch pits reveal the two-fold symmetry of the (001) plane. In addition, the surface of the ground-based crystal has developed several nearly macroscopic etch pits in the lower left area of Fig. 14a. The high reflecting broad region in the upper right section of Fig. 14a is a large step to a lower (001) plane. The morphology of the ground crystal is contrasted by the much more uniform appearance of the (001) face of the space crystal in Fig. 14b. The density of etch pits based on the entire area of Fig. 14b is 4×10^4 cm^{-2}, the average diagonal length is about 4×10^{-3} cm and the depth of the larger pits is approximately 17×10^3 Å. The etch pits reveal the two-fold symmetry of the crystal plane. There are no macroscopic changes of the space crystal even after extensive thermal etching.

A comparison of the results of thermal etching shows that the number of etch pits of the space crystal after long-term etching is at least one order of magnitude lower than the density of pits for the ground-based crystal after short-term etching. The overall morphology of the (001) plane of the space crystal after short and long thermal treatment reveals a higher degree of perfection than the plane of the ground-based crystal. Based on the relation between the effects of thermal etching and crystalline imperfections, the combined experimental information from the etch studies demonstrates the improved quality of the space grown crystals.

A cleaved section of a ground-based GeSe dendrite and the cleaved (001) face of the corresponding space platelet (3A) are compared in Fig. 15. The internal face of the dendrite (Fig. 15a) reveals a distinct line pattern and the curvature typical for the macroscopic habit of dendritic growth. The face of the GeSe space crystal (Fig. 15b) appears to be mirror smooth under these conditions. (The magnification applied for the dendrite is 250X and for the crystal platelet 500X.) The edge in the plane of the space crystal is due to cleavage and represents the boundary between layers of different depths with respect to the native surface.

The results of thermal etching (30 min, ~190°C) of cleaved faces of a ground-based GeSe dendrite and the corresponding single crystal platelet (3A) grown in micro-gravity (Fig. 16) are consistent with the external morphological differences between these growth habits. Thermal treatment of the dendrite face (Fig. 16a) caused the formation of large aggregated etch pits and nearly macroscopic ledges. This observation demonstrates that removal of

mass due to vaporization is highly irregular with respect to the surface area as a result of the intrinsic inhomogeneities of the dendritic crystal. The morphology of the thermally etched (001) face of the space crystal (Fig. 16b) is considerably more homogeneous. The well defined etch pits reveal the two-fold symmetry of the (001) plane. The average diagonal length of the larger etch pits is about 5×10^{-3} cm, their depth is approximately 3×10^{4} Å and the etch pit density is in the low 10^{5} cm^{-2} range. The absence of steps even after extensive thermal treatment of the (001) face of the GeSe space crystal reveals a very uniform removal of mass from the surface. This in turn requires a rather homogeneous crystalline structure of the surface and subsurface layers. The combined differences between the growth habits and the thermal etch patterns of GeSe dendrites and platelets demonstrate unambiguously the positive effects of micro-gravity on external morphology and bulk crystalline perfection.

CONCLUSIONS

The combined experimental evidence from the analysis of space grown crystals confirms the predicted positive effects of micro-gravity on crystal quality. This is based on a comparison of macroscopic crystal habits, deposition patterns, optical and scanning electron microscopy, and the results of thermal etching of cleaved crystals obtained under ground-based and micro-gravity conditions.

In addition to improved crystal quality, a second major result of the Skylab experiment M556 is the observation of greater mass transport rates than expected in micro-gravity environment. This observation is of scientific and technological significance with respect to the theoretical extension of conventional transport models and the possibility of growing higher quality crystals at reasonable rates by the vapor transport technique in space. Continuing ground-based studies indicate that the interaction between gravity-driven and other convective components causes turbulence and the negative effects on crystal quality as observed on earth. The ultimate goal of these studies is to approximate the effects of micro-gravity on crystal quality under earth-bound conditions.

The internal consistency of results obtained for two materials (GeSe and GeTe), two different temperature gradients and various pressures of transport agent strongly support the validity of the above conclusions.

ACKNOWLEDGEMENTS

The authors would like to express their sincere appreciation to the National Aeronautics and Space Administration for giving us the opportunity to participate in this unique endeavor of space experimentation. We are particularly grateful to the scientific and technical staff of the George C. Marshall Space Flight Center for their encouraging, understanding and enthusiastic support and cooperation which actually put our experiment into space. Special thanks are due to Dr. M. C. Davidson, our scientific monitor, W. R. Adams and A. Boese of MSFC for their continuous and most valuable guidance throughout the various phases of this program. We are grateful to the astronauts of the SL 3 and SL 4 missions for their excellent performance of experiment M556. The authors would like to thank Dr. R. G. Seidensticker

(Westinghouse Electric Corporation) for his contributions in designing the multi-purpose furnace facility and achieving the desired temperature conditions. Thanks are due to all members of our group whose continued interest in this project provided many stimulating discussions.

REFERENCES AND BIBLIOGRAPHY

1. H. Schäfer, "Chemical Transport Reactions," Academic Press, New York, 1964.

2. H. Wiedemeier, E. A. Irene and A. K. Chaudhuri, J. Crystal Growth, 13/14, 393 (1972).

3. H. Wiedemeier and E. A. Irene, Z. Anorg. Allg. Chem., 400, 59 (1973).

4. E. A. Irene, Ph.D. Thesis, Rensselaer Polytechnic Institute, Troy, New York, 1972.

5. F. C. Klaessig, work in progress.

J. J. Gilman, Editor, "The Art and Science of Growing Crystals," J. Wiley & Sons, Inc., New York, 1963.

J. P. Hirth and G. M. Pound, "Condensation and Evaporation," (in Progress in Materials Science, Volume 11, Ed. B. Chalmers) Pergamon Press, MacMillan Company, New York, 1963.

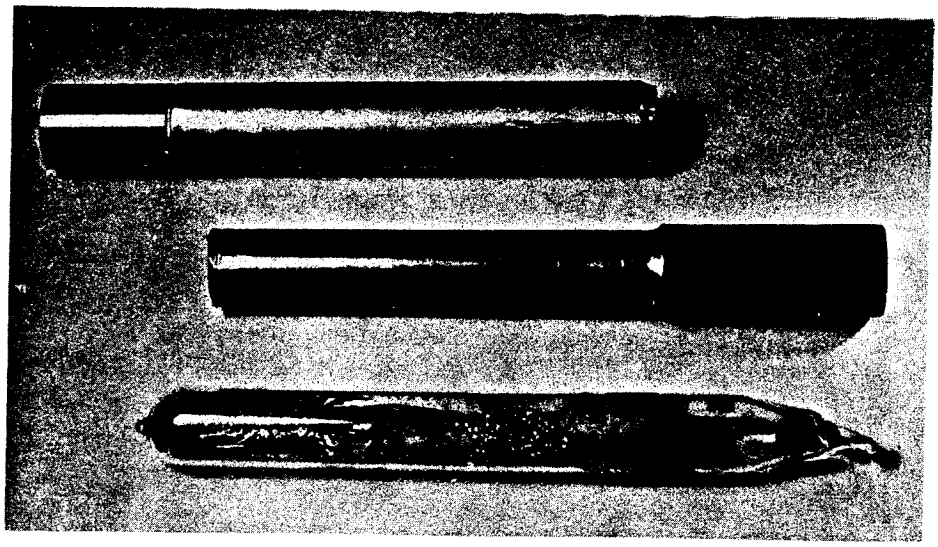

FIGURE 1. METAL CARTRIDGE FOR TRANSPORT AMPULE USED IN SKYLAB EXPERIMENT. THE QUARTZ AMPULE SHOWN WAS USED FOR GROUND-BASED STUDIES. THE AMPULE IS 150 mm LONG, 13.7 mm INNER DIAMETER AND REVEALS THE DENDRITIC DEPOSITION OF GeSe TYPICAL FOR CONVECTIVE CONDITIONS.

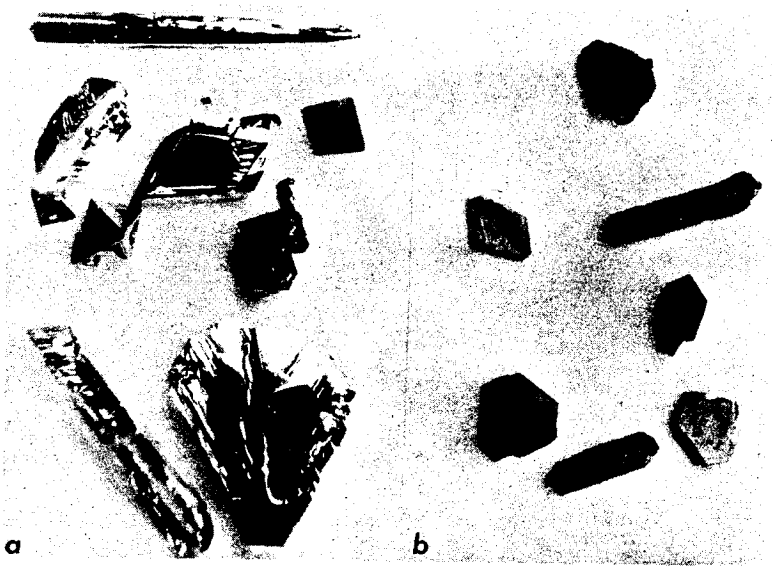

FIGURE 2. REPRESENTATIVE GeTe CRYSTALS OBTAINED UNDER BROUND-BASED CONVECTIVE (a) AND SPACE (b) CONDITIONS. THE LENGTH OF THE GROUND-BASED (a) NEEDLE IS ABOUT 4mm AND THE EDGE LENGTH OF THE HOLLOW OCTAHEDRA ABOUT 0.7 mm. THE LENGTH OF THE SPACE (b) NEEDLE IS ABOUT 2mm AND THE AVERAGE EDGE LENGTH OF THE PLATELETS IS 1mm.

FIGURE 3. DEPOSITION PATTERN OF GeTe CRYSTALS UNDER GROUND-BASED CONVECTIVE (a) AND MICRO-GRAVITY (b) CONDITIONS. LENGTH OF INDIVIDUAL DENDRITES (a) IS 1.5-4mm.

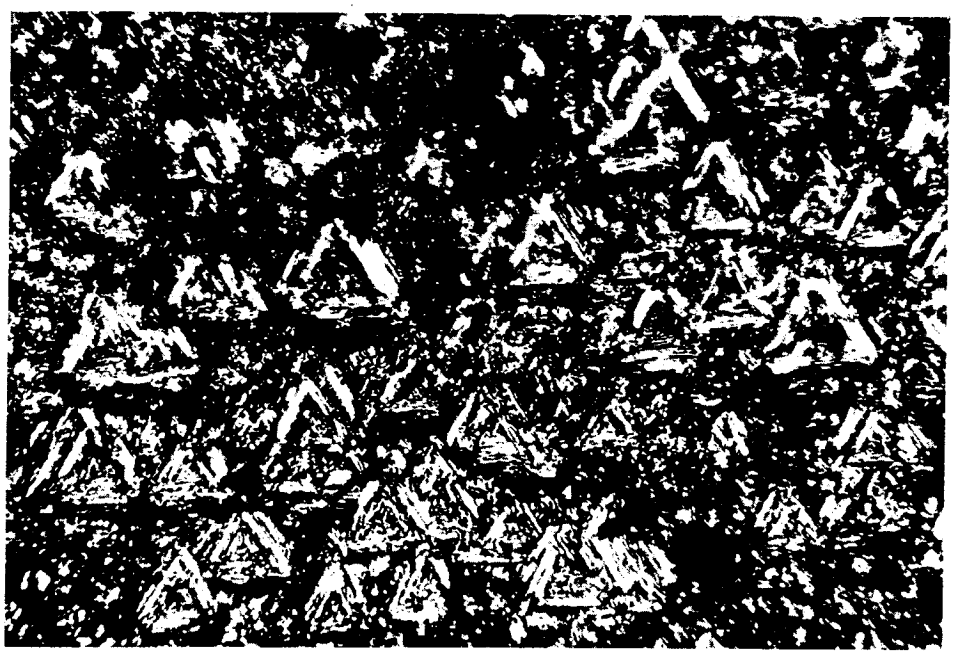

FIGURE 4. PHOTOMICROGRAPH (300X) OF (111) NATIVE FACE OF GeTe SPACE-GROWN CRYSTAL (3C). TRIANGULAR PATTERN INDICATES POSSIBLE DECORATION OF DEFECTS.

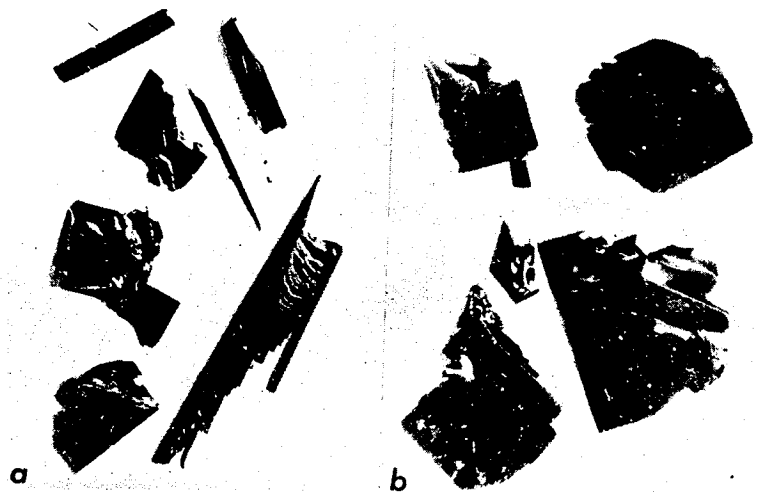

FIGURE 5. REPRESENTATIVE GeSe CRYSTALS (3B CONDITIONS) GROWN ON EARTH (a) AND IN SPACE (b). THE EDGE LENGTH OF THE GROUND-BASED CRYSTALS (a) IS 1-5mm AND OF THE SPACE CRYSTALS (b) 2-5mm.

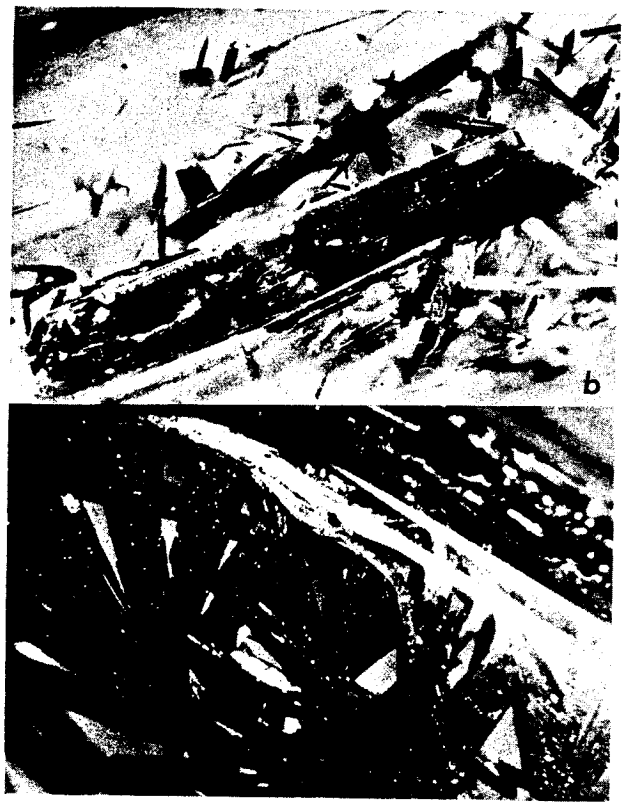

FIGURE 6. VIEW OF THE DEPOSITION REGION OF A GeSe (3A CONDITIONS) GROUND-BASED (a) AND SPACE (b) TRANSPORT AMPULE. EDGE LENGTHS OF SPACE CRYSTALS (b) RANGE FROM 0.2-18mm.

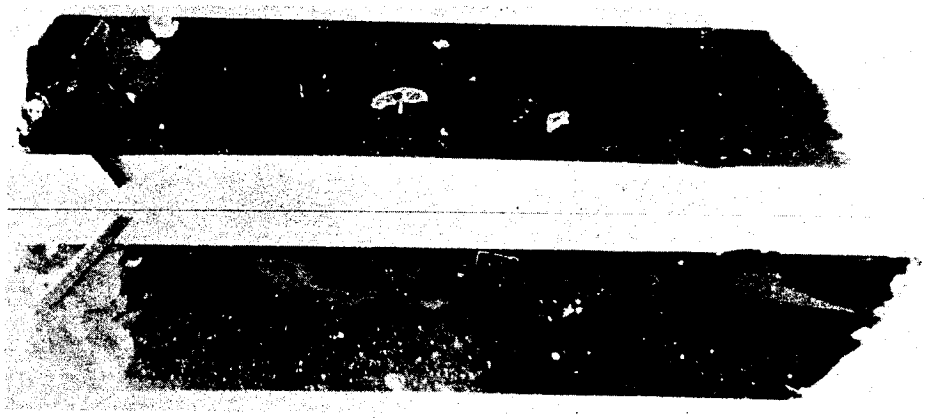

FIGURE 7. FRONT AND BACK SIDE OF THE LARGEST GeSe SINGLE CRYSTAL PLATELET GROWN UNDER MICRO-GRAVITY CONDITIONS (3A). DIMENSIONS ARE 4 X 8 18mm, THICKNESS IS ABOUT 50 μ.

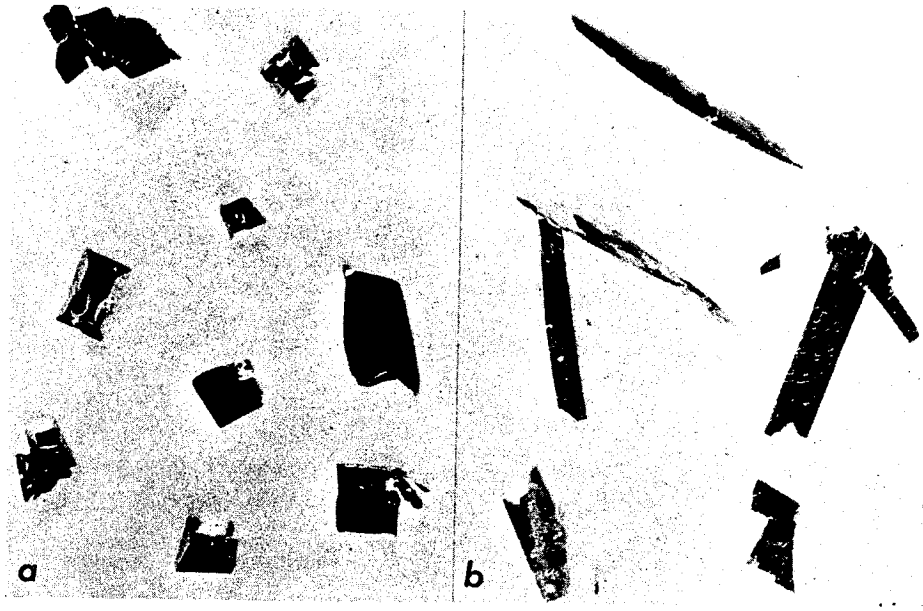

FIGURE 8. REPRESENTATIVE GeSe CRYSTALS (5B CONDITION) GROWN ON EARTH (a) AND IN SPACE (b). AVERAGE DIMENSIONS OF GROUND-BASED (a) CRYSTALS ARE 1-2mm AND OF SPACE CRYSTALS (b) 1mm WIDTH AND 5mm LENGTH.

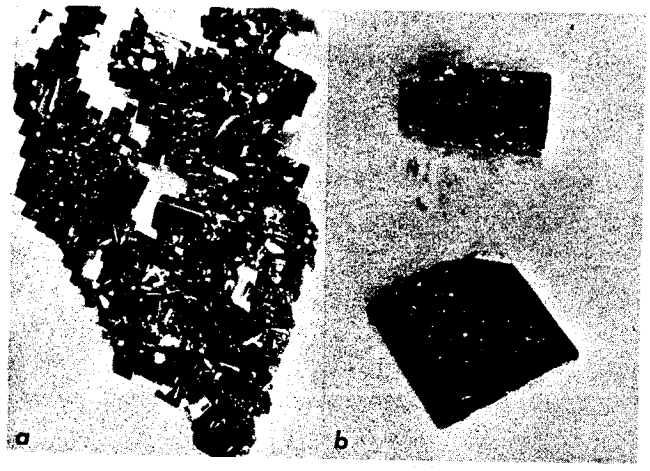

FIGURE 9. REPRESENTATIVE GeSe CRYSTALS (5A CONDITIONS) OBTAINED UNDER GROUND-BASED (a) AND MICRO-GRAVITY (b) CONDITIONS. TOTAL LENGTH OF CRYSTAL AGGREGATE (a) IS 5mm. EDGE LENGTHS OF SPACE CRYSTALS (b) IS 0.8-1.5mm.

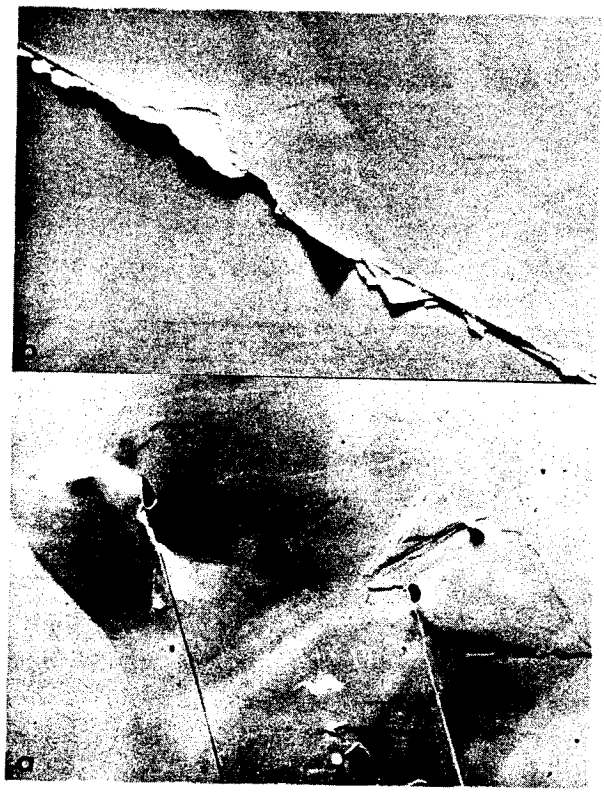

FIGURE 10. SCANNING ELECTRON PHOTOMICROGRAPHS (400X) OF CLEAVED (001) FACES OF GeSe (3B CONDITIONS) CRYSTALS GROWN ON EARTH (a) AND IN SPACE (b).

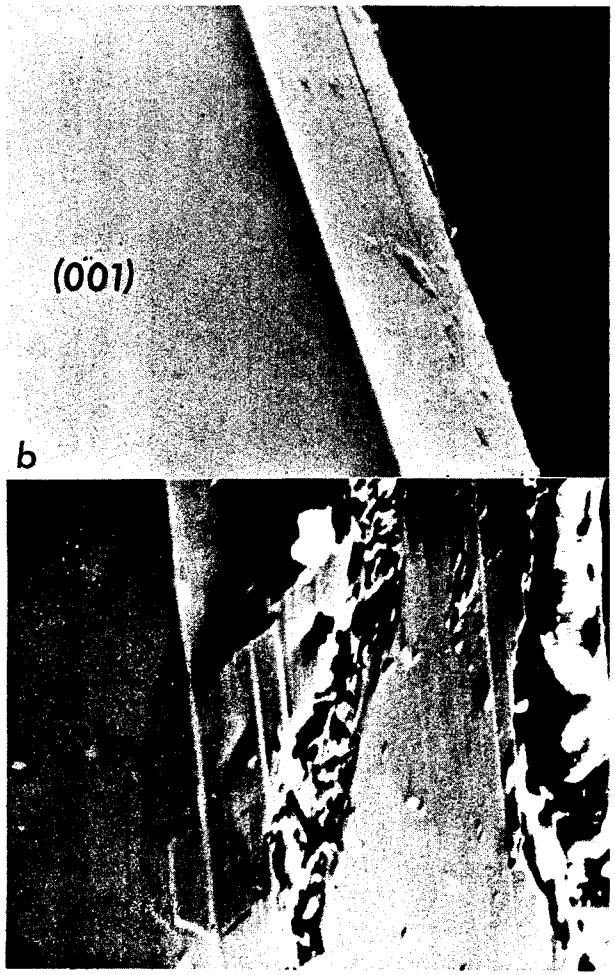

FIGURE 11.

SCANNING ELECTRON PHOTOMICROGRAPHS (1000X) OF NATIVE EDGES OF GeSe (3B CONDITIONS) CRYSTALS OBTAINED UNDER GROUND-BASED (a) AND MICRO-GRAVITY (b) CONDITIONS.

FIGURE 12.

SCANNING ELECTRON PHOTOMICROGRAPHS (200X) OF THE NATIVE SURFACE OF A GeSe GROUND-BASED DENDRITE (a) AND OF THE CLEAVED (001) FACE OF A SPACE-GROWN GeSe (3A) CRYSTAL (b).

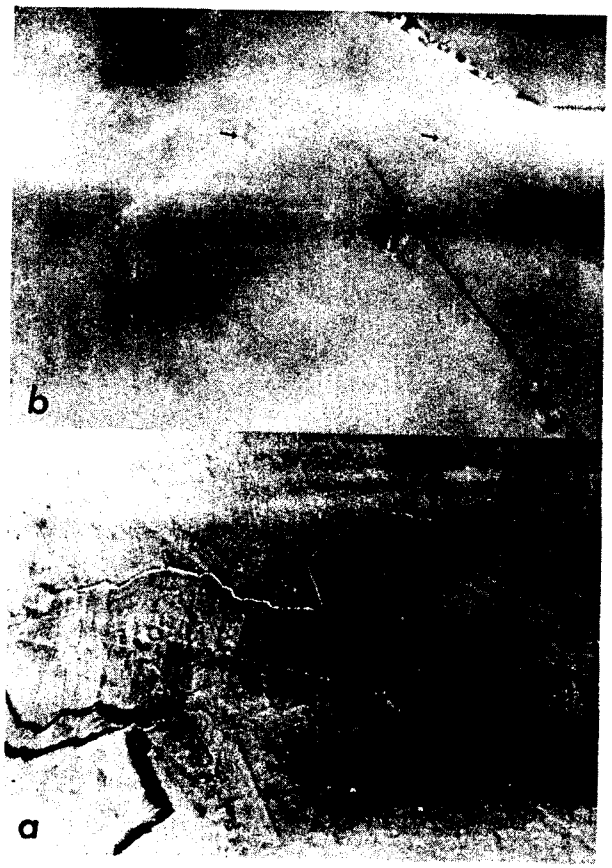

FIGURE 13.

OPTICAL PHOTOMICROGRAPHS (125X) OF CLEAVED (001) FACES OF GeSe (3B CONDITIONS) SINGLE CRYSTAL PLATELETS OBTAINED ON EARTH (a) AND IN SPACE (b) AFTER THERMAL ETCHING (5 MIN, ~190°C). THE LOCATIONS OF TWO OF THE THERMAL ETCH PITS OF THE SPACE CRYSTAL (b) ARE INDICATED BY ARROWS.

FIGURE 14.

OPTICAL PHOTOMICROGRAPHS (125X) OF CLEAVED (001) FACES OF GeSe (3B CONDITIONS) SINGLE CRYSTAL PLATELETS GROWN ON EARTH (a) AND IN MOCRO-GRAVITY (b) AFTER THERMAL ETCHING (2.5 HR, ~190°C).

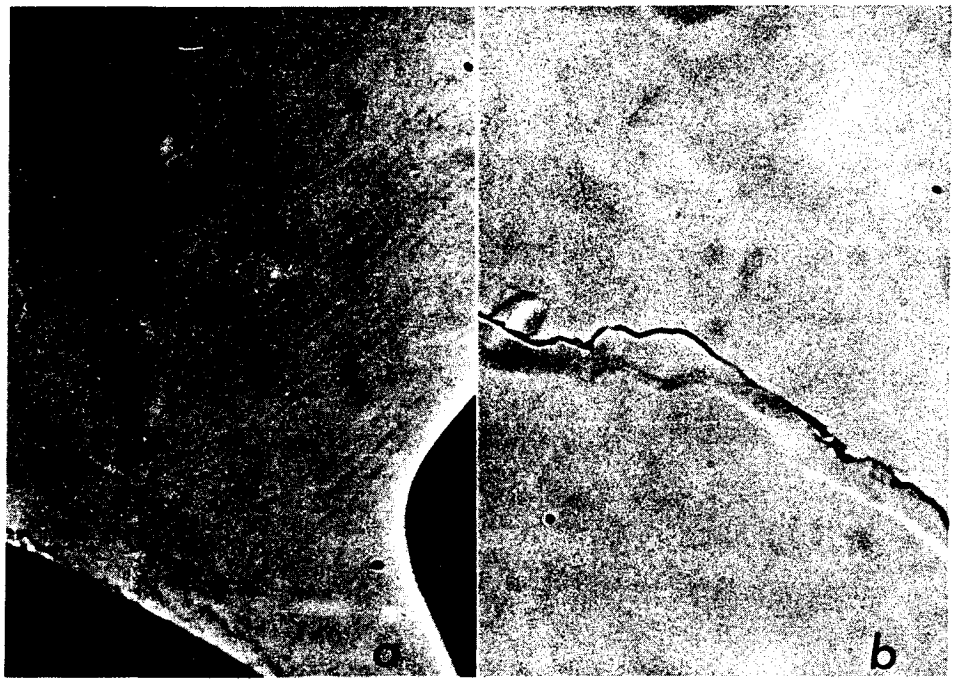

FIGURE 15. OPTICAL PHOTOMICROGRAPHS OF A CLEAVED SECTION OF A GeSe GROUND-BASED DENDRITE (a) (250X) AND OF A CLEAVED (001) FACE OF A SPACE-GROWN GeSe (3A) SINGLE CRYSTAL PLATELET (b) (500X).

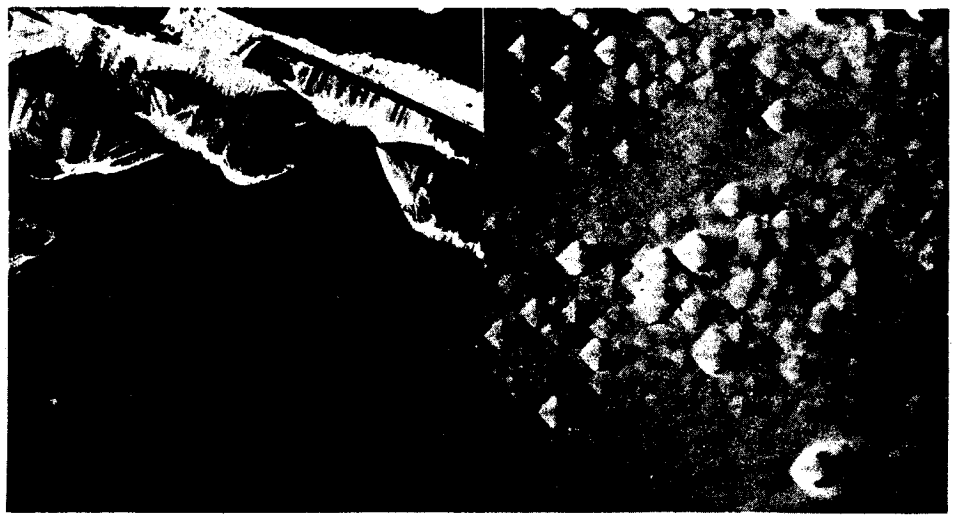

FIGURE 16. OPTICAL PHOTOMICROGRAPHS (125X) OF A CLEAVED GeSe GROUND-BASED DENRITE (a) AND A CLEAVED (001) FACE OF A SPACE-GROWN GeSe (3A) CRYSTAL PLATELET AFTER THERMAL ETCHING (30 MIN, ~190°C).

SEEDED, CONTAINERLESS SOLIDIFICATION OF INDIUM ANTIMONIDE

(Skylab Experiment M-560)*

By

H. U. Walter
The University of Alabama in Huntsville, Department of Physics
Huntsville, Alabama 35807

SUMMARY

Directional solidification of a containerless melt that was suspended at the end of a seed crystal was employed to produce crystals of InSb during Skylab missions(SL3 and SL4).

Single crystals with well developed growth facets ({110}, {111}, {$\bar{1}\bar{1}\bar{1}$}) were obtained. Analysis by X-ray topography and chemical etching shows that the crystals are of high structural perfection. Virtually no dislocation clusters were observed; average dislocation density is of the order of $10^2/cm^2$. The density of dislocations decreases linearly in the center section of space-grown crystals.

A sample that was heavily doped with selenium ($N \approx 10^{19}/cc$) appears to be homogeneously doped in the center section only. Striated solute distribution is observed in the first and the last portion of the space-grown crystal.

*This work was supported by NASA under Contract NAS8-28304.

INTRODUCTION

One of the major attractions of space for processing of materials from the melt is the possibility of handling large quantities of molten materials without the use of containers. This possibility is particularly attractive for highly reactive and high melting temperature materials.

Since gravity-driven convection, which is the major factor that limits the control of directional solidification processes, is lacking as well, space should provide an ideal environment for materials processing from the melt. Provided that second-order effects such as surface tension gradient driven convection are negligible or can be controlled, steep temperature gradients could be established without generating fluid flow. Consequently, unidirectional, steady-state solidification could be achieved. Incorporation of dopant could be controlled perfectly and problems stemming from constitutional supercooling could be overcome.

It can be assumed, however, that for a given material, a practical upper limit for thermal gradients exists. Above this limit, convection driven by surface tension gradients would create similarly uncontrolled conditions as gravity-driven convection does on earth. After initial studies on the feasibility of containerless processing, these limits will have to be investigated and established.

The present study on "Seeded, Containerless Solidification of InSb"* (Skylab Experiment M-560) deals with some of the basic aspects of containerless crystal growth. The objectives of the investigation were defined as follows:

(1) Investigate the feasibility of containerless processing of single crystals in space environment.

(2) Obtain information on the structural perfection of space-grown crystals as compared to samples grown on earth.

(3) Demonstrate the potential of space for producing homogeneously-doped semiconductor material.

---

* This study was initially proposed for germanium; proper melting and temperature gradients could not be established with the existing furnace and it was consequently changed to the lower melting InSb.

EXPERIMENTAL APPROACH AND ARRANGEMENT

A multipurpose electric furnace (M-518) was provided by NASA.* Maximum furnace temperature was 1000°C. Three experiment chambers that could be loaded with different sets of sample cartridges allowed for simultaneous processing of three samples at identical thermal conditions. Each experiment chamber, which is 2.14 cm I.D. and 25 cm deep, has three temperature zones: a 5 cm hot zone in a graphite heat leveler, a 6.3 cm gradient zone, and a heat extraction region of approximately 14 cm. Active control of the heated section of this gradient furnace was provided; the temperature profiles in the samples were determined by the heat-flow characteristics of the sample and sample container.

The basic experimental approach can be described as follows: An oriented, cylindrical single crystal of InSb is mounted into a graphite base that is located at the cold end of the gradient furnace. From this support, the sample extends through the gradient section of the furnace into a hemispherical heating cavity that is located in the hot zone of the furnace. As the graphite cavity is heated, a temperature gradient is established along the crystal, and the sample slowly melts back starting at the bottom of the graphite cavity. The melt adheres to the end of the seed crystal and detaches from the graphite. A spherical melt that is suspended at the end of the seed crystal is formed in the gradient region. During soak, the melt will homogenize; inclusions will partly be accumulated at the surface of the melt and static conditions will be established. During cool down, the seed crystal will grow according to temperature gradients into the containerless melt, and a single crystal will eventually be formed.

The design of the ampoule is shown in Fig. 1. Only high purity materials were used; a major design consideration was to avoid possible contamination of the samples and degradation of materials during the period of approximately 1 year from delivery of ampoules to return of processed samples.

The outer quartz envelope was manufactured from precision-drawn (i.d. = 18 mm $\pm$ 0.025 mm) and precision-ground (0.789 $\pm$ 0.001") clear fused quartz tubing. Single crystals of InSb were grown by the Czochralski technique. Prior to seal off, the ampoules were evacuated to 10^{-9} torr. Ultrahigh purity hydrogen was then admitted to 350 torr and the ampoules were sealed off.

Thermal testing had the objective to establish furnace settings to obtain reproducible meltback of 13 $\pm$ 3 mm as measured from the bottom of the heating cavity.

---

* Design, construction and testing by Westinghouse Electric Corp. under NASA contract.

Furnace settings were established for flight as follows:

Heat leveler temperature	$653^{\circ}C \pm 8^{\circ}C$
Soak time	60 min.
Cool-down rate	$0.6^{\circ}C$/min.

Interface position of 13 mm ± 3 mm and growth rates of 1 - 3 cm/h were expected with these settings.

RESULTS AND DISCUSSION

I. Morphology of Space-Grown Samples

Two sets of cartridges were processed during Skylab missions SL3 and SL4. All cartridges were returned undamaged. With both sets of experiments, recommended soak temperature ($653^{\circ}C \pm 8^{\circ}C$), soak time (1 hr.), and cool-down rate ($0.6^{\circ}C$/min) were met. A temperature versus time plot for two thermocouples, one located in the hot zone, the other in the heat extraction region of the furnace is given in Fig. 2. The upper curve, which represents temperatures measured in the graphite heat leveler at the hot zone of the furnace, indicates constant temperature at $657^{\circ}C$ (printout) for 1 hour. This period is followed by a linear cool-down of $0.6^{\circ}C$/min.

X-ray shadowgraphs of SL3 samples taken prior to opening are shown in Fig. 3. For comparison, a shadowgraph of a sample that was processed on the ground is shown in Fig. 4. Samples processed during SL4 mission show similar silhouettes. Meltbacks of 17.5 mm (E1), 16 mm (D2), 16.5 (D1), 16 mm (D3), 16.5 mm (E3), 16 mm (E2) were obtained as compared to a desired 13 mm ± 3 mm.

Overall views of two representative samples processed during SL3 and SL4 missions are given in Fig. 5 and Fig. 6. Prior to more sophisticated analysis of structural perfection of the samples, single crystallinity could be assessed due to the following reasons: (1) As determined by optical reflection goniometry, well-developed growth facets agree with the crystallographic symmetry of the samples, (2) Single crystal Laue diffraction patterns were obtained, (3) With the exception of two samples (E1 and E3), no grain boundary grooving could be observed. Grooving in the two samples could later be related to a twin-boundary parallel to $\{\bar{1}\bar{1}\bar{1}\}$ which could be traced into the seed; the second twin boundary, apparently (211), was initiated at the periphery of the sample. The generation of this boundary appears to be related to oxide specks that were accumulated at the surface in this area.

An EREP maneuver that was conducted during solidification of SL3 samples (see Fig. 2) apparently caused a disturbance of growth that left a distinct ring-shaped mark on all of the SL3 samples

(see Fig. 5). This time mark in conjunction with the time where cool-down was initiated allows determination of an average growth rate as follows: D1: 10.4 mm/hour, D2: 12.8 mm/hour, E1: 13mm/hour, Since identical furnace settings were used on SL4, an average growth rate of 12 mm/hour can realistically be assumed for SL4 samples.

The general shape of the crystals implies that the melt did adhere to the graphite of the heating cavity instead of being freely suspended at the end of the seed crystal. A teardrop-shaped melt was, therefore, formed that was supported at one end of the seed and that was attached to the bottom of the heating cavity at the other end. The small protrusion at the end of the crystal can be explained by the fact that InSb expands by approximately 11% upon solidification; directional solidification would consequently result in a small amount of melt having to escape when the solidifying crystal meets the bottom of the heating cavity.

Contact angles of InSb at 530°C to 550°C on graphite substrates prepared from the same material and having comparable surface finish as the graphite cavity were determined by sessile-drop methods as $130^{\circ} \pm 3^{\circ}$. No hysteresis could be observed. Since the shape of liquids is determined by minima of free surface energy, a situation where the melt is attached to the seed as well as to the bottom of the graphite heating cavity is energetically instable.

Alternatively, directional solidification of a spherical melt that is suspended at the end of a cylindrical seed crystal can be described as follows: In the most simple case, no volume changes are involved with the transition from liquid to solid, and the surface of the solid follows the surface of the liquid which meets the solid surface tangentially at all times during solidification. The resulting solid will be a true replica of the melt. If volume changes are considered, different shapes of the solid will result. In the case of expansion, elongated, bulb-shaped samples will be formed; in case of contraction, a geoid shape with flattened end will result.

Since as a rule little change of volume is observed in the melting process of metals (only about 3% or less), replicas of melt shapes are obtained. Our early experimentation had been confined to solidification of metals[1,2] and the initial title of the experiment "spherical crystals" stems from this.

With germanium, where an increase in volume of about 5% is associated with solidification, nonspherical shapes are observed. Samples prepared by directional solidification of sessile drops of germanium with solidification starting from the base, have characteristic onion shapes; a behaviour that has been observed previously.[3]

The next complication that can be added to this model is that the surface of the growing solid does not follow the shape of the liquid. Instead, a situation exists as shown in Fig. 7a and 7b, where the meniscus of the liquid meets the solid at an angle. As shown in Fig. 7c and 7d, upper and lower limits for this angle can be introduced. Angles higher or lower than this limit would represent an instable wetting situation where surface breakdown and rearrangement would result. Evidence from space-grown crystals supports this model of free solidification.

Extremely well-developed {110} facets, generally more disturbed {111} facets and small {211} facets are observed. Six {110}* facets ($1\bar{1}0$, $10\bar{1}$, $01\bar{1}$, $\bar{1}10$, $\bar{1}01$, $0\bar{1}1$) are parallel to the [111] growth direction. Similar to the example given in Fig. 7a, these facets are primarily responsible for the rather prismatic shape of the samples. Three {$\bar{1}\bar{1}\bar{1}$} facets ($11\bar{1}$, $\bar{1}11$, $1\bar{1}1$) and three {111} facets ($1\bar{1}\bar{1}$, $\bar{1}1\bar{1}$, $\bar{1}\bar{1}1$) are inclined $19^{\circ}28'$ to the direction of growth. {111} facets which are terminated with Sb atoms would grow away from the seed axis, the {$\bar{1}\bar{1}\bar{1}$} would grow toward the seed. With the facet growing into the melt as with {$\bar{1}\bar{1}\bar{1}$}, a situation should be created similar to the one shown in Fig. 7c, where the facet becomes instable and growth is periodically interrupted. Terracing caused by periodic surface breakdown can indeed be observed on {$\bar{1}\bar{1}\bar{1}$} facets.

Facets are observed with crystals grown on the ground as well. Facets on the space-grown samples are, however, generally less disturbed. Aside from hillocks and scattered pits, facets of undoped crystals are exceptionally flat.

Hillocks cannot be avoided with InSb; they are formed above 350 - 400°C[5,6] because Sb evaporates preferentially from heated InSb surfaces. At the melting point, partial pressures of In and Sb are 10^{-6} and 10^{-3} mm/g respectively.[7] As a result, indium-rich droplets are formed; these droplets solidify at lower temperatures and appear as hillocks.

Aside from hillocks which would not be found with monocomponent systems such as germanium or silicon, the facets are of remarkable optical quality and flatness. Tolanski multiple-beam interference microscopy (Fig. 8) shows straight and equally-spaced interference fringes. Using the Tolanski microscope with the Fizeau-flat parallel to the surface of the facet (interference contrast), a single dark fringe can be made to cover a complete facet. This latter phonemenon is proof for overall flatness of some facets to a few hundred Å.

---

*Dewalt[4] denomination.

II. Assessment of Structural Perfection and Chemical Homogeneity

The two ruling parameters, composition (stoichiometry, dopant distribution, inclusions, precipitates, etc.) and structure of a crystalline material can be considered separately to a limited extent only. As an example, variation in dopant concentration is associated with variation in lattice parameters, inclusions and precipitates disturb the periodicity of the lattice. Similarly, low defect density and in particular absence of grain boundaries is a prerequisite for electronically useful material as well as chemical homogeneity.

As mentioned above, overall single crystallinity could be verified by optical reflection goniometry and Laue diffraction. As can be expected, all facets are low Miller index planes ({111}, $\{\bar{1}\bar{1}\bar{1}\}$,{110}, {211}).

Reflection X-ray topography[8] (Berg-Barrett geometry) was used to study the structural quality of the crystals prior to cutting or any surface preparation. The experimental arrangement is shown in Fig. 9. The actual apparatus used was a Lang camera that was modified for taking scanning reflection topographs. A standard X-ray tube with copper target was used. The technique can briefly be described as follows: A divergent beam of X-rays is emitted from an X-ray focal spot and passes through a set of slits of defined separation (L_1) onto the crystal. The crystal is set at the appropriate angle to diffract the incoming X-rays into an X-ray counter set at $2\theta_B$, twice the Bragg angle. The counter is used to align the crystal for maximum diffracted intensity. An X-ray sensitive film is inserted between the crystal and X-ray counter and the diffracted beam image is recorded on the film. In order to prevent the direct beam from exposing the film, a second slit system (L_2) is placed between crystal and film. This slit is adjusted to allow passage of only the diffracted beam. L_1 is kept so that the divergence of the primary beam is small enough to allow separation of $K\alpha_1$ and $K\alpha_2$ images. During exposure, film and sample are simultaneously translated so that the X-ray beam slowly scans the surface of the sample, and an image of a larger area of the surface of the crystal is recorded.

Examples of reflection topographs obtained in this manner are shown in Figs. 10, and 11. Symmetrical reflections about [111] and [110] were used to obtain the topographs shown in the figures. One single Bragg reflection is obtained that reflects all of the crystal surface exposed to the X-ray beam. No grain or lattice misorientation can be observed. Geometrical irregularities of the surface show up on the topograph as well; shadows are cast by small oxide specks which can be seen on some of the pictures. Aside from this, the space-grown portion exhibits flawless single crystals. Only at the very end of the space-grown samples, irregularities show up; this is, however, to be expected since this portion was grown under increasing radial thermal gradients and the material was then in contact with the mold.

Etching of dislocations is a well-established procedure with InSb. In particular In-dislocations can reliably be revealed by etching of {111} planes in CP4 etchants. Crystals were cut into thin wafers perpendicular to the axis of growth. In-dislocations in one sample as revealed by etching are shown in Fig. 12. This sample was prepared during SL3 mission; a sample grown during SL4 mission has not yet been investigated.

Dislocation density in the earth-grown seed has a rather wide spread. This scatter seems to be less in the space-grown portion of the crystal. Since the wafers that were etched are presently used for electrical measurements, no additional data points could be taken so far. After the electrical measurements are completed, further step-etching will be done to obtain more data points. Additional dislocations are generated during the initial period of growth; a linear decrease follows and in the last portion of the space-grown crystal, the density increases due to increasing radial temperature gradients. A small maximum seems to appear at the beginning of the last third of the space-grown crystal. This maximum coincides with the perturbation caused by the EREP maneuver; this event is also marked on the surface of the sample as has been mentioned earlier. The dislocation density profile for a second sample (also SL3) shows similar features. Consistent with the sample just described, the density of dislocations decreases rather linearly in the middle section of the space-grown crystal. The density is reduced by a factor of about 6 over a growth distance of 1 cm.

To answer questions concerning redistribution of dopant and convective flow in the melt, one of the samples of the flight set was heavily doped with selenium ($N \approx 10^{19}$/cc). With this sample, three regions where dopant was incorporated in different manners could be discerned. As determined by etching and X-ray topography, no inhomogeneities could be detected so far in the center section of the crystal. The part of the sample that solidified last, shows distinct banding; a wave-like variation of dopant concentration is indicated in X-ray photographs and etched surfaces. An unusual sequence of striations that is also reflected on the surface of the crystal can be observed in the first third of the crystal. Distinct decoration of the interface can be observed; starting from the seed, the spacing increases exponentially; the period then becomes constant and the markings disappear. For conclusive interpretation of this behavior, dopant profiles will have to be determined. It seems, however, that the sequence described could develop only if no appreciable fluid flow would have disturbed the solidification process. This would indicate that not only gravity-driven convection but surface tension gradient-driven convection as well were insignificant.

CONCLUSION

Based on this investigation, the following conclusions concerning containerless processing of single crystals from the melt in low gravity environment can be reached:

(1) Highly perfect single crystals can be prepared by seeded, containerless solidification. For processing of highly reactive materials and high melting temperature materials, the technique described should be especially valuable; large crystals could be prepared by this technique as well.

(2) Even though dopant inhomogeneities are observed, all indication points to essentially no-fluid-flow conditions. Consequently, production of homogeneously doped single crystals by containerless techniques appears to be feasible.

ACKNOWLEDGMENT

This study was only possible with the direct and indirect support given by a large number of persons. The author is indebted to all of them. Special thanks are due to Messrs. W. R. Adams, T. C. Bannister, A. Boese, Dr. J. H. Bredt, M. C. Davidson, R. Fatheree, L. Gibbs, J. Levie, D. P. Nicolas, Dr. R. S. Snyder, Prof. A. F. Witt and J. Zwiener for technical and administrative support as well as for helpful suggestions and interesting and stimulating discussions.

REFERENCES

1. H. U. Walter, R. S. Snyder, J. Less Common Metals, 24 (1971) 467-469.

2. H. U. Walter, J. Crystal Growth, 10 (1971) 309-312.

3. G. A.Kurov, A. I. Petrin, V. V. Ignatev, Sov. Phys. - Crystallography, 14 (1969) 122.

4. K. F. Hulme, J. B. Mullin, Solid State Electronics, Pergamon Press 1962, Vol. 5, 211-247.

5. D. Haneman, J. Appl. Phys., 31 (1960) 217.

6. M. F. Millea, C. T. Tomizuka, J. Appl. Phys., 27 (1956) 96.

7. V. K. Ilin, S. I. Aksenov, Inorganic Materials, 7 (1970) 1114.

8. J. Auleytner, "X-ray Methods in the Study of Defects in Single Crystals," Pergamon Press (1967).

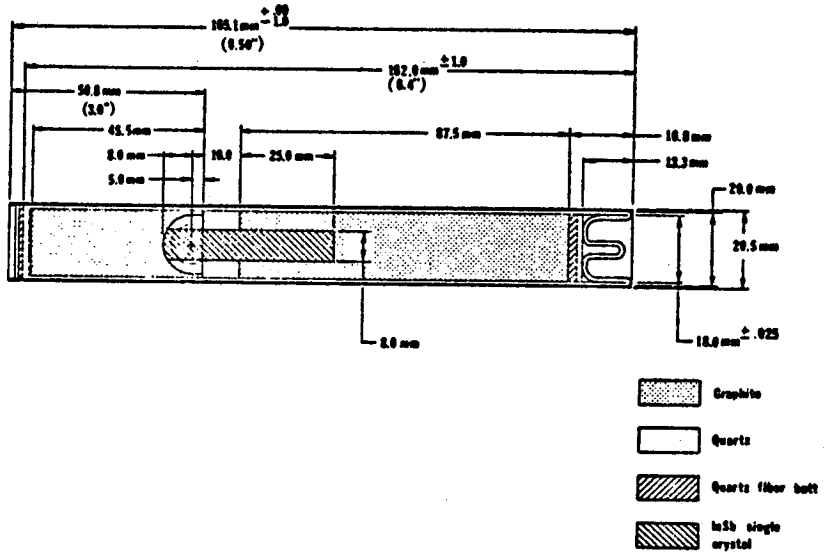

FIGURE 1. AMPOULE DESIGN

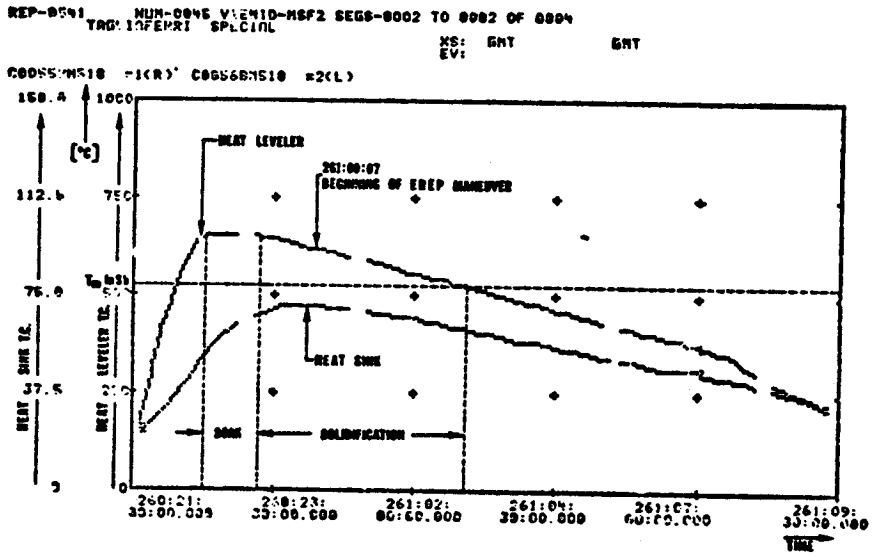

FIGURE 2. HEAT LEVELER AND HEAT SINK TEMPERATURE DURING PROCESSING OF M-560 SAMPLES (SL-3 MISSION)

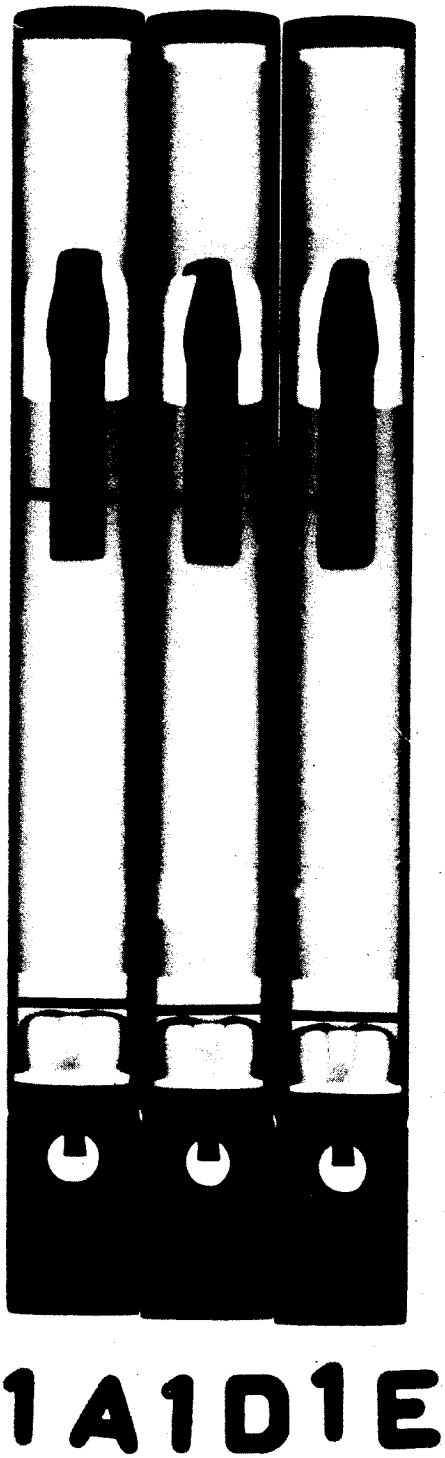

FIGURE 3. X-RAY SHADOWGRAPHS OF CARTRIDGES PRIOR TO OPENING

FIGURE 4. X-RAY SHADOWGRAPH OF TEST SAMPLE AFTER THERMAL TESTING

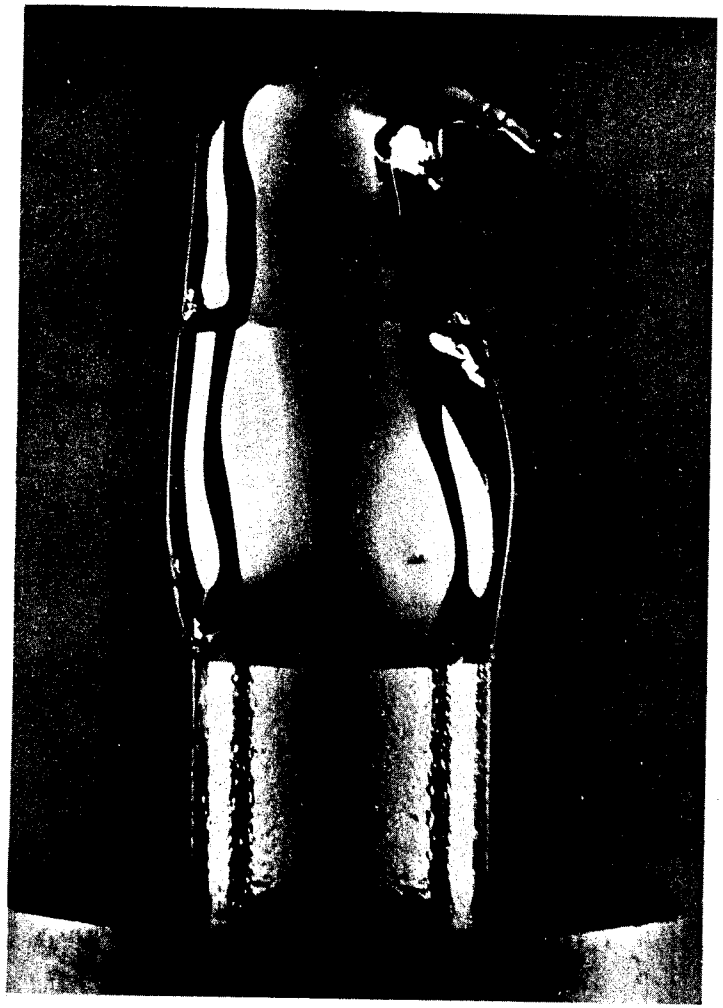

FIGURE 5. SAMPLE PROCESSED DURING SL-3 MISSION

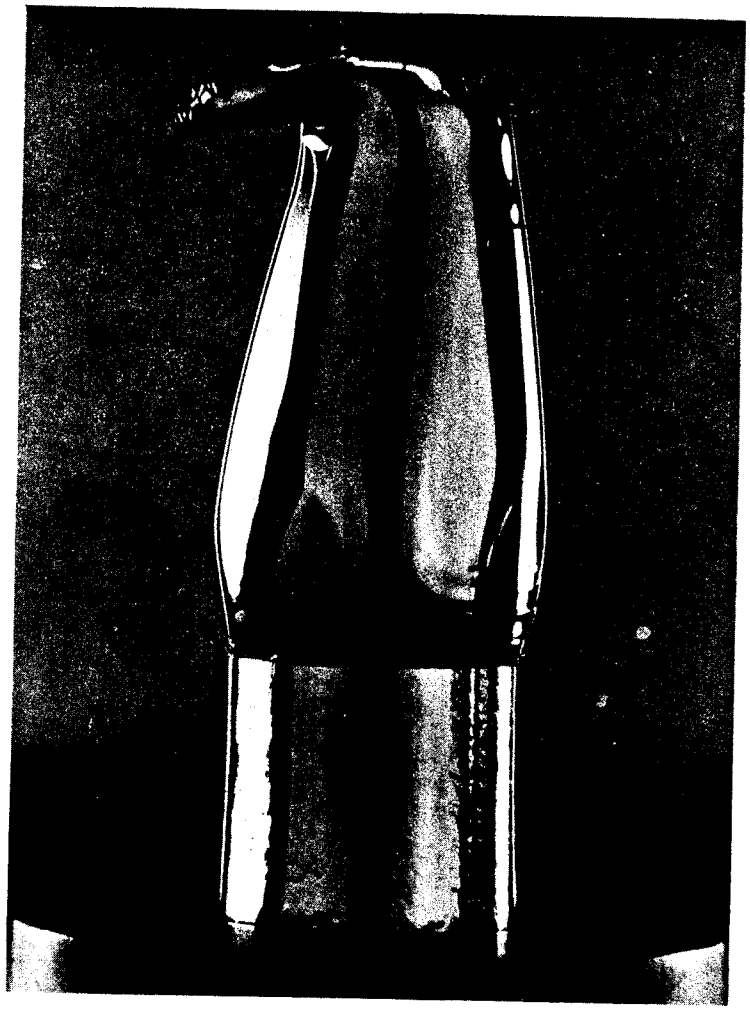

FIGURE 6. SAMPLE PROCESSED DURING SL-4 MISSION

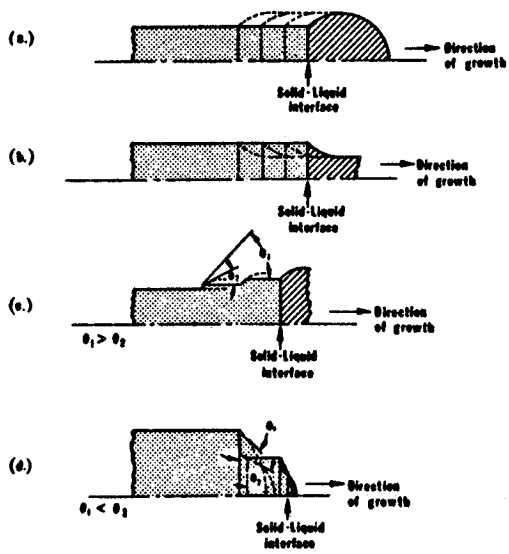

FIGURE 7. DIRECTIONAL SOLIDIFICATION OF DROPS.

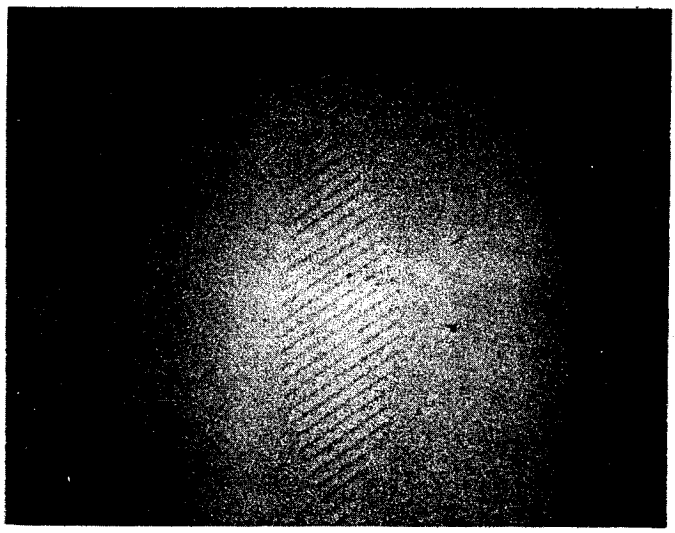

FIGURE 8. TOLANSKI PHOTOGRAPH OF (111) FACET

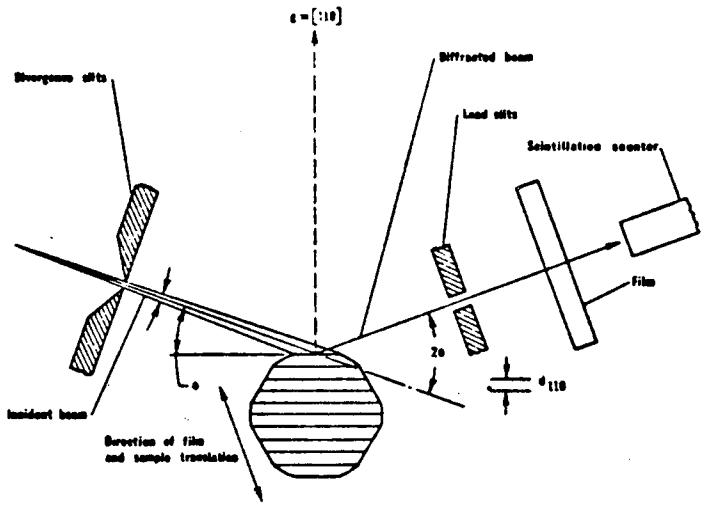

FIGURE 9. SCHEMATIC OF SCANNING REFLECTION TOPOGRAPHY

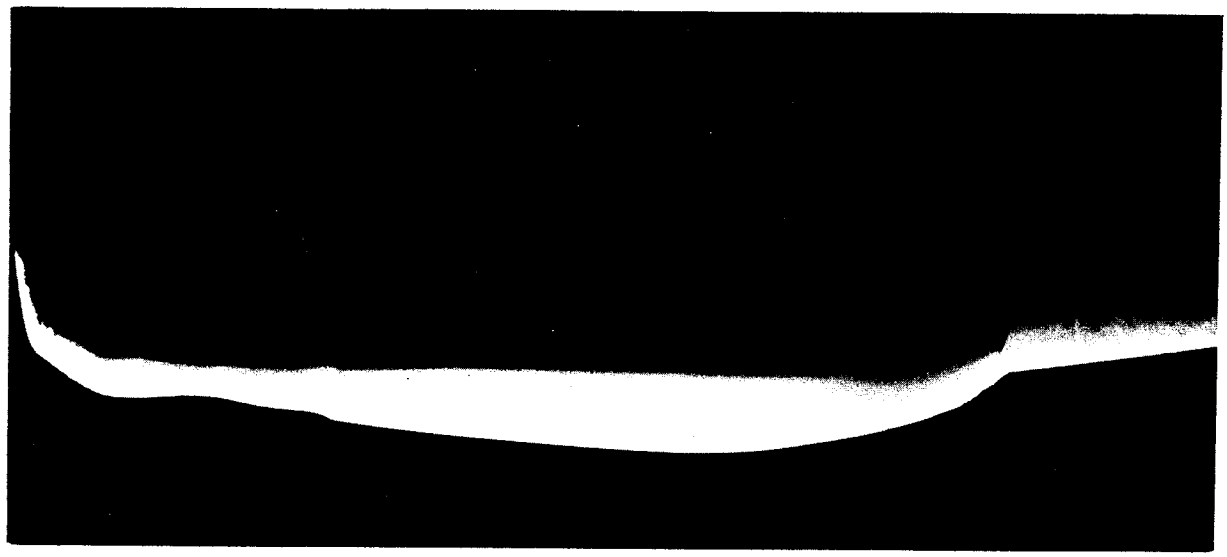

FIGURE 10. SURFACE TOPOGRAPH, (220) REFLECTION.

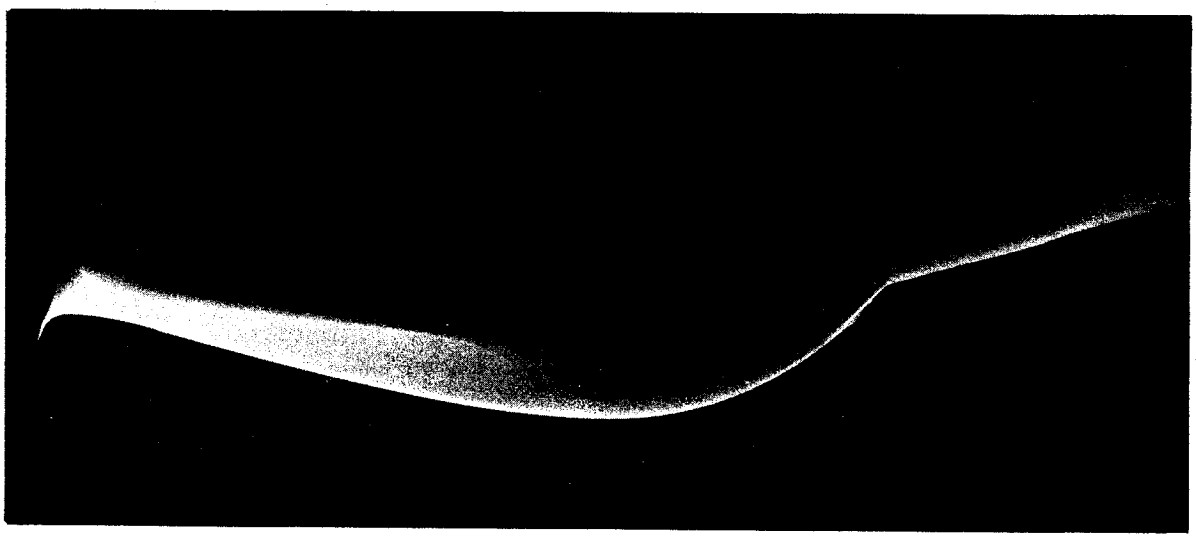

FIGURE 11. SURFACE TOPOGRAPH, (111) REFLECTION

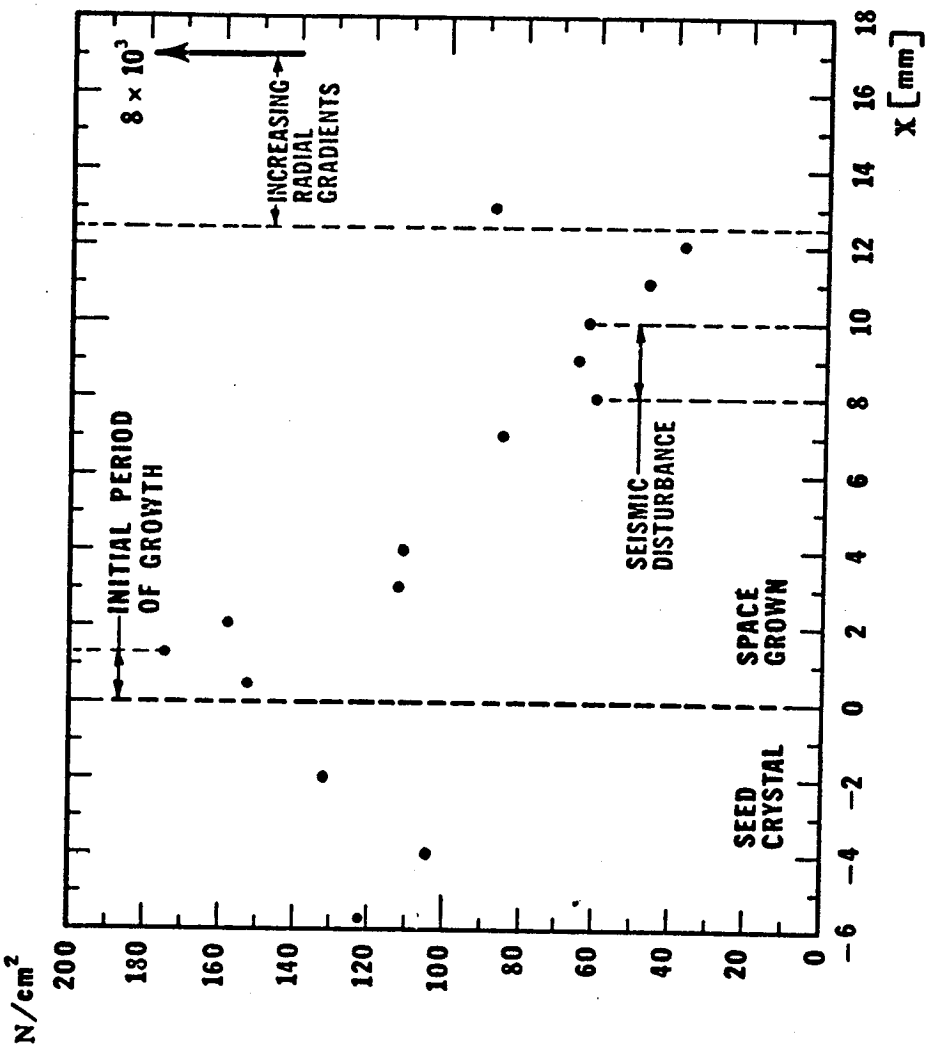

FIGURE 12. INDIUM DISLOCATIONS IN SAMPLE PROCESSED DURING SL-3 MISSION

N74 29897

STEADY STATE GROWTH AND SEGREGATION UNDER ZERO GRAVITY: InSb

By

A. F. Witt*, H. C. Gatos, M. Lichtensteiger,
M. C. Lavine, C. J. Herman
Massachusetts Institute of Technology
Cambridge, Massachusetts 02139

SUMMARY

It was established that ideal diffusion controlled steady state conditions, never accomplished on earth, were achieved during the growth of Te-doped InSb crystals in Skylab. Surface tension effects were found to establish non-wetting conditions under which free surface solidification took place in confined geometry. It was further found that, under forced contact conditions, surface tension effects led to the formation of surface ridges (not previously observed on earth) which isolated the growth system from its container. In addition, it was possible for the first time to identify unambiguously: the origin of segregation discontinuities associated with facet growth, the mode of nucleation and propagation of rotational twin boundaries, and the specific effect of mechanical-shock perturbations on segregation.

The results obtained prove the advantageous conditions provided by outer space. Thus, fundamental data on solidification thought to be unattainable because of gravity induced interference on earth are now within reach.

*Paper presented by A. F. Witt.

INTRODUCTION

Structural and compositional control during solidification of materials is impeded by gravity-induced effects in the melt. Thermal gradients necessary for crystal growth lead, in the presence of gravitational forces, to thermal convection which in general causes uncontrolled variations in the solidification rate and in diffusion boundary layer thickness; such variations lead directly to periodic and/or random microscopic and macroscopic segregation inhomogeneities. Furthermore, in the presence of gravity, establishing steep thermal gradients, often required to prevent constitutional supercooling, is impossible and consequently interface breakdown is unavoidable.

Gravity effects are, thus, primarily responsible for the present lack of reliable solidification data and the existing gap between theory and experiment. Consequently, crystal growth and associated segregation phenomena are still based on empiricism, and the properties and performance of solids are not at their theoretical limits.

Gravity-free conditions made accessible through the space program of NASA provide a unique opportunity to obtain reliable crystal growth data and, therefore, to advance our quantitative understanding of solidification processes; in addition this program makes possible the exploration and assessment of the potential of outer space for materials processing.

Indium antimonide was chosen for the presently reported Skylab experiment because its relatively low melting point (525°C) made the experiment compatible with the available electrical power. In addition, chemical etching, the only high-resolution technique available, at the time, for the study of segregation inhomogeneities on a microscale, had been developed on InSb to its most advanced level.

The experiments performed during the Skylab-III and -IV missions included the growth of undoped, tellurium-doped, and tin-doped indium antimonide. The present report is concerned primarily with results obtained on tellurium-doped InSb.

OBJECTIVES

The objectives of growing Te-doped InSb in Skylab were to confirm the advantages of zero-gravity environment, to obtain basic data on solidification, and to explore the feasibility of electronic materials processing in outer space. Thus, the experiment was designed to achieve diffusion-controlled, steady-state solidification and to investigate the associated growth segregation behavior on a micro- and macro-scale. Direct comparison of growth and segregation on earth and in space was to be achieved by melting and resolidifying in space a portion of each crystal grown on earth.

EXPERIMENTAL APPROACH

Crystal Growth Apparatus

The InSb growth experiment was carried out in the "multipurpose furnace" (Fig. 1) designed and constructed by Westinghouse Electric Corporation. The furnace provides for three tubular cavities into which three stainless steel

cartridges containing the crystal growth assemblies are inserted. Heat levelers, lateral heat-shields, and the heat extractor plate insure controlled heat flow from the heating element to the heat extractor plate through the crystal. Melting is initiated at the end of the crystal (to be referred to as hot end), located inside the heating element and the crystal-melt interface is advanced to the desired position (back-melting) by appropriate power input. Regrowth, in turn, is achieved by controlled power reduction.

From heat transfer calculations and ground-based growth experiments, it was concluded that, in Skylab, a power input of 99 watts to the furnace containing three encapsulated InSb crystals should result in a melt zone approximately 6 cm long, with an initial thermal gradient of about 46°C/cm.

In ground-based tests it was found that the morphology of the crystal-melt growth interface was slightly convex (viewed from the melt). No prediction could be made, however, about the growth interface morphology under zero gravity conditions since the wetting characteristics of InSb melts and the associated radial heat transfer behavior was not known.

Crystal Preparation and Assembly

Indium antimonide used for ground-based tests and the Skylab experiment was synthesized in the Electronic Materials Laboratory at M.I.T. The single crystals for the experiment were pulled from the melt in the <111> direction by the Czochralski technique. The as-grown crystals (approximately 1.8 cm in diameter and 17 cm long) were centerless ground to a diameter of 1.4 cm, and cut to a length of 11 cm. The cylindrical crystals were etched in modified CP-4 (2 parts HF + 1 HNO_3 + 1 CH_3COOH) to remove surface damage and reduce their diameter to the desired value. Each crystal was subsequently inserted between graphite spacers into a quartz ampoule of 3 mm wall thickness. The diameter of every crystal was 0.25 mm smaller than the inside diameter of its ampoule.

The spacer at the hot end had a peripheral cylindrical cavity to provide additional space for the melt in case unforeseen surface tension effects under zero gravity conditions resulted in increased clearance between the regrown crystal and the quartz wall; the cylindrical graphite spacer at the other end of the crystal (to be referred to as cold end) was designed to enhance heat transfer from the crystal to the heat extractor plate. The crystals were positioned in the ampoules so that their B <111> direction coincided with the regrowth direction.

All ampoules were repeatedly flushed with purified helium and evacuated to 10^{-7} torr prior to sealing. The crystals were anchored near their cold end to the ampoules by means of a small depression in the quartz wall formed by local heating of the evacuated ampoules.

Each sealed ampoule was encapsulated by the Westinghouse Electric Corporation in an evacuated stainless steel cartridge and subjected to simulated launch and re-entry conditions; they were subsequently examined by radiography. One set of three cartridges containing an undoped crystal, a Te-doped crystal ($\sim 10^{18}/cm^3$) and a heavily Sn-doped crystal ($\sim 10^{20}/cm^3$) was selected for the

zero gravity growth experiment (Skylab-III mission). A second set was selected for back-up purposes and was eventually used in an unscheduled second experiment in space (Skylab-IV mission). A sealed ampoule and its metal cartridge used in the Skylab experiment are shown in Fig. 2.

Crystal Growth Procedure in Space

Skylab-III Mission Experiment: The samples were inserted into the multi-purpose furnace and back-melting was initiated by turning on the power. The desired back-melting was achieved in 120 minutes. Then the system was kept at temperature for a period of 60 minutes (soaking period), to achieve thermal equilibrium in the system and homogenization of the melts.* Subsequently, a cooling rate of 1.17°C/min was established by controlled power reduction at intervals of 14.4 sec. Four hours after initiation of regrowth the power was turned off and passive cooling to the ambient temperature took place. The thermal history of the growth system (hot end temperature) obtained from a chromel/alumel thermocouple in the furnace is shown in Fig. 3.

Skylab-IV Mission Experiment: The remelting and thermal soaking procedure was identical with that of the Skylab-III experiment. However, in this (originally scheduled) experiment the growth system was subjected to a mechanical shock by striking the furnace assembly at a predetermined time; furthermore, the constant cooling rate of 1.17°C/min was interrupted 140 minutes after initiation of regrowth and a second thermal soaking period of 60 minutes was introduced by maintaining the furnace power at a constant level. The power was subsequently turned off and the system was allowed to reach ambient temperature (see Fig. 3). These changes in the growth procedure were intended to provide time reference markings in the crystal and to obtain data on the dependence of transient segregation on growth rate.

RESULTS AND DISCUSSION

The extent of regrowth achieved during the Skylab experiment was virtually the same for all crystals (about 6 cm) and in excellent agreement with theoretical calculations and ground-based testing; in each crystal the regrowth interface was clearly delineated (see for example Fig. 2).

Before proceeding with the analysis of the Te-doped crystals, it is of interest to discuss briefly the morphological characteristics of the Sn-doped and undoped crystals. The space-grown segments of the two Sn-doped crystals are shown in Fig. 4; the regrowth interface is clearly seen on the left-hand side of the figure. In both instances (as in the case of undoped InSb) the crystal surfaces, viewed through the quartz ampoule, are smooth and highly reflective, indicating that they formed in intimate contact with the confining walls. The presence of randomly distributed cavities of varying size, attributed to entrapped gas, indicates that the melt was also in intimate contact with

*A soaking period of 180 minutes was originally specified for this purpose; however, an inadvertent power shortage necessitated the reduction of the soaking period to 60 minutes.

(wetted) the quartz walls. The morphological characteristics of the two crystals are identical; differences in phase (Sn) segregation are associated with differences in growth conditions.

MORPHOLOGICAL CHARACTERISTICS

All crystals were separated from their containers, without affecting their morphological characteristics, by dissolving the quartz ampoules in 48% HF.

The two Te-doped InSb crystals will be discussed individually since they exhibit seemingly significant differences in morphological characteristics.

Tellurium-Doped InSb Grown in Skylab-III

This crystal was of the same diameter as the earth-grown segment (seed), two portions of which are shown in Figures 5 and 6; they correspond to the early and late stages of growth, respectively. The surface of the crystal, in contrast to that of the Sn-doped and undoped crystals, has a dull appearance which indicates that during growth it did not establish contact with the confining quartz wall. This conclusion is reinforced by the absence of peripheral cavities which generally characterize growth under confined geometry.

The surface of the regrown crystal in the vicinity of the seed (Fig. 5) exhibits several bands of differing width oriented normal to the growth direction. These bands were identified as the external boundaries of rotational twins (see below) which are frequently encountered in InSb grown in the <111> direction.

Conspicuous in Fig. 6 is the presence of irregularly spaced "surface ridges" oriented preferentially in the direction of growth (left to right). The ridges are shiny at the top indicating contact with the quartz wall; they are, on average, 25 μm high and increase in width towards the hot end of the crystal. Over the last 10 mm of the crystal the ridges become irregular and branch out. The regions between the ridges exhibit, in general, the characteristics of growth from free (unconfined) melts. In some isolated areas inclined lines, which have the appearance of stress-induced defects, originate at the surface ridges. These defects were shown to be confined to the surface region and to have no detectable effects on the growth and segregation behavior of the system. To the authors' knowledge, the phenomenon of surface ridge formation has not been previously observed in solidification under confined geometry; it will be further discussed below.

Tellurium-Doped InSb Grown in Skylab-IV

As seen in Fig. 7, regrowth, following the thermal soaking period, proceeds (left to right) first with decreasing and then essentially constant crystal diameter. With continuing growth the crystal diameter decreases, again, then increases and assumes a constant value of 12.8 mm (right-hand side of Fig. 7) which is the same as that of the I.D. of the confining quartz ampoule. (The reasons for the differences in diameter between the two Te-doped crystals in the early stages of regrowth will be discussed below.)

From volume considerations, it is concluded that the increase of the crystal diameter, with continuing growth coincides in time with the initial contact of the melt with the graphite spacer at the end of the quartz ampoule. Since crystal growth over the first 30 mm proceeded with a decreased diameter, and solidification of InSb is accompanied by a volume expansion of 12.9%, the volume available to the residual melt is less than during the Skylab-III experiment at the same time in growth. Thus, towards the final stages of solidification some melt was ultimately forced into the peripheral cavity available in the hot-end graphite spacer. Indium antimonide solidified in the spacer cavity weighed 2.52g. Accordingly, the total available volume for the melt in the ampoule itself (excluding the volume of the cavity in the graphite spacer) was occupied after the crystal had reached a length of 34 mm, i.e., 5 mm after the crystal diameter reached its maximum value. Since the clearance between the spacer and the quartz wall was less than 0.1 mm, the melt was under substantially increased pressure during the last 25 mm of growth. This increased pressure, however, did not lead to forced wetting between the melt and the quartz wall since contact between the crystal and the wall remained confined to the surface of the irregularly spaced ridges as in the Skylab-III crystal.

The surface characteristics of the crystal grown with a diameter smaller than the I.D. of the ampoule are typical of free-surface solidification. They are identical with those encountered between the surface ridges in the Skylab-III crystal and are similar to those observed on crystals grown by the Czochralski technique on earth.

Figure 8 shows the surface characteristics of the crystal portion grown with constant reduced diameter at a distance of about 10 mm from the initial regrowth interface; the surface irregularities are the same as those commonly observed in non-faceted crystal growth from the melt. In addition, randomly spaced lines oriented normal to the <111> growth direction are visible. These lines are not continuous over the whole periphery and are confined to the three relatively flat portions of the crystal surface. They are not present on the centrally located "white" band which was identified as a rotational twin (see also below).

It is of interest to note that the crystal portion with a reduced diameter does not exhibit surface ridges observed on the previously discussed crystal. Surface ridges do, however, appear as the crystal diameter increases and approaches the value of the I.D. of the ampoule. Details of surface ridge patterns are shown in Fig. 9. The ridges in this crystal are of the same height as those on the crystal grown in Skylab-III ($\sim$25 μm); here again they have no measurable effect on growth and segregation in the bulk of the crystal. They appear, however, less oriented along the growth direction and more branched. From the propagation patterns of these ridges, it is concluded that they are not the result of anomalous solidification, but, rather, that they are formed on the melt prior to solidification.

So far all attempts to account for ridge formation on the basis of known phenomena, such as wetting and convection induced by surface tension gradients, have met with fundamental inconsistencies.

Bulk Characterization

The bulk characterization of the space-grown crystals was aimed primarily at the growth and segregation behavior employing various analytical techniques. For this purpose the crystals were sectioned as shown in Fig. 10.

Dopant Segregation

The analysis of dopant segregation by high resolution differential etching was carried out on longitudinal sections of (211) surface orientation (see Fig. 10). All crystal sections were polished with Syton and etched for 40 seconds in a solution of 1 HF(48%) + 1 CH_3COOH (glacial) + 1 $KMnO_4$ (saturated aqueous solution); they were subsequently rinsed, dried in purified nitrogen and studied by means of interference contrast microscopy.

The striking difference in dopant segregation during growth under the influence of gravity and under zero gravity conditions is evident in Fig. 11 where a portion of earth-grown (upper part) and space-grown crystal (lower part) is shown. Compositional inhomogeneities which characterize the earth-grown segment (including pronounced coring effect) are absent in the segment grown in space. It is further seen that the regrowth interface morphology, established during thermal soaking, is convex (viewed from the melt).

The sharp demarcation line separating the earth- and space-grown segments is the result of an abrupt decrease in Te concentration which is dictated, for initial regrowth, by the thermodynamic characteristics of the system; i.e., the distribution coefficient, k_o of Te in InSb is less than one ($k_o = C_S/C_L < 1$, where C_S and C_L are the concentration of Te in the solid and the melt, respectively).

The microscopic segregation behavior for the peripheral part of the crystal in the vicinity of the regrowth interface (right-hand side of Fig. 11) is shown in Fig. 12. Pronounced segregation fluctuations (compositional inhomgeneities) in the earth-grown segment reflect irregular variations in growth conditions which are due to rotation effects and to uncontrolled gravity-induced thermal convection in the melt. No microscopic compositional fluctuations are present in the crystal segment grown in space. In the central part of the crystal also (Fig. 13) irregular microsegregation variations are present in the earth-grown segment but not in the corresponding space-grown segment. The segregation behavior in the equivalent region of the crystal grown during the Skylab-III mission was identical to the behavior presented above.

According to theory, the area of the space-grown region shown in Fig. 13 must be part of a transition region over which the dopant concentration increases continuously until it reaches the same value as that of the dopant concentration present in the bulk of the melt; at this point steady state segregation conditions are established and the dopant concentration in the solid remains constant except at the very terminal stage of solidification.

Quantitative Dopant Segregation Analysis

Since one of the major objectives of the Skylab experiment was to achieve steady state segregation, quantitative dopant concentration analysis of the transition region was undertaken by means of Hall-effect measurements and ion-microprobe scanning.

Hall-effect measurements were carried out by the Van der Pauw technique in a 6" field-regulated electro-magnet employing a constant current source and a calibrated, high impedance micro-volt detector. The Hall-effect samples were squares, 2 mm x 2 mm and 0.5 mm thick. Quadrant-shaped silver contacts were evaporated at the four corners of each sample and were annealed at 350°C for two hours to ensure ohmic behavior. Subsequently, gold wire leads were soldered with indium onto the contacts (Fig. 14). More than thirty individual Hall-effect measurements (at different field strengths) were carried out on each sample to optimize the validity of the data. The reproducibility of the results was better than one per cent.

Hall-effect measurements were carried out on the Te-doped crystal grown in the Skylab-III mission. Twelve successive crystal slices, 0.5 mm thick, were cut, as shown in Fig. 10. Two adjacent Hall-effect samples (2 mm x 2 mm) were chosen from each slide, in most instances near the central part of its straight edge (corresponding to a central location in the crystal). For some slices the Hall-effect samples could not be taken from the central location since twin or grain boundaries were present.

The compositional (carrier) profile together with the corresponding resistivity and carrier mobility obtained at 77°K are shown in Fig. 15. Hall-effect measurements on all samples were also performed at room temperature. The room temperature data are not significantly different than those shown in Fig. 14 in view of the relatively high level of carrier concentration.

The carrier concentration curve (N_{space}) in Fig. 15 shows clearly the decreased dopant concentration in the initial part of the space growth region, as predicted from theory; it delineates further the transient region in which the dopant concentration increases steadily and reaches its maximum value at a distance of about 0.5 cm from the regrowth interface. Beyond this distance the dopant concentration remains constant for the entire crystal length analyzed (5 cm); it is, thus, shown that ideal steady state segregation and homogeneous dopant distribution was achieved under zero gravity conditions. Ideal steady state segregation has never been achieved on earth. In the ground-based tests performed in an identical experimental configuration and under "stabilizing thermal gradients" as seen in Fig. 15, the dopant profile for the ground-based experiment (N_{earth}) indicates clearly a steadily increasing dopant concentration which reflects the presence of convective interference apparently due to convection caused by unavoidable lateral thermal gradients.

The ratio of the dopant concentration in the initially grown region and in the steady state-grown region is a direct measure of the equilibrium distribution coefficient, k_o, which cannot be reliably determined on earth. Unfortunately, the low spatial resolution of Hall-effect measurements does not permit, at this time, the accurate determination of k_o. From the width of the region of transient segregation and the associated compositional change, the diffusion coefficient of the dopant in the melt can be determined, provided the microscopic growth rate is known and constant; this condition was not met in the present experiment, since only the nominal growth rate is known.

It should be pointed out that the observed variation in carrier concentration between adjacent Hall samples is not surprising since extensive

twinning took place in this InSb crystal in view of the fact that its diameter was the same as that of the confining wall and solidification is accompanied by 12.9 per cent volume expansion. In addition to twinning, growth under these conditions leads to high dislocation densities which account for the measured relatively low, carrier mobilities. In contrast, in the crystal grown during the Skylab-IV mission, with a smaller diameter than that of the quartz ampoule (unconfined solidification) the dislocation density was found to be 40 per cent smaller than that in the earth-grown segment.

The compositional profile in the same crystal was in parallel investigated by means of an ion microprobe analysis since this technique was expected to provide a similar sensitivity as the Hall-effect measurements but a resolution in the micron range. Measurements carried out with a CAMECA, IMS 300 Ion Analyzer and with an Applied Research Laboratory, Ion Microprobe Mass Analyzer are essentially consistent with the results of the Hall-effect measurements; however, due to the relatively low yield of sputtered Te-ions, the linear resolution and accuracy were found to be limited. Thus, as seen in Fig. 16, the precision of the ion-microprobe results with a scanning beam of 25 μm was only of the order of ±16%.

Intentionally Introduced Segregation Discontinuities

As pointed out earlier, the growth process during the Skylab-IV mission was perturbed 90 minutes and 140 minutes after initiation of the cooling cycle by a mechanical shock and by an arrest of cooling, respectively; the cooling arrest was sustained for a period of 60 minutes. These perturbations were intended to introduce time reference markers in the crystal and to study their specific effect on segregation behavior under steady state conditions.

Etching analysis of the crystal revealed the presence of only two distinct segregation discontinuities manifested as curved lines, extending over the entire cross-section of the crystal, 15 mm and 28.8 mm from the initial regrowth interface. As seen from the sketch in Fig. 17, the first discontinuity coincides with an abrupt decrease in crystal diameter and is of relatively low intensity as viewed in interference contrast. The second discontinuity was formed after the crystal had reached its maximum constant diameter and is very pronounced as seen in Fig. 18.

The nature of these segregation discontinuities was investigated by double beam interferometry. As seen in Fig. 19a the first perturbation (15 mm from the initial regrowth interface) resulted in a small and localized increase in tellurium concentration; on the other hand, the second perturbation (Fig. 19b) resulted in a pronounced segregation discontinuity (decrease) which persisted for an extended period of time. Thus, this second discontinuity is unambiguously identified as a transient segregation region associated with regrowth following thermal soaking. Accordingly, the first, short-lived, segregation discontinuity is associated with the mechanical shock.

Identification of the two segregation discontinuities permits their use as time markers for the determination of average microscopic growth rates in two different portions of the crystal. Thus, the average growth rate from

the initial regrowth interface to the first discontinuity, 90 minutes into growth, is found to be 2.8 μm/sec and the growth rate from the first to the second discontinuity is 4.6 μm/sec. The average growth rate over the first 2.88 cm of growth (see Fig. 17) is 3.4 μm/sec.

The above growth behavior is consistent with theory: for the thermal configuration in the multipurpose furnace the thermal gradient in the melt is expected to decrease with continuing solidification and consequently the growth rate must correspondingly increase.

It is of interest to note that the fringe deflection at the second compositional discontinuity (Fig. 19b) is constant over the entire crystal diameter. Since the fringe deflection is proportional to the concentration change across the discontinuity and since the dopant concentration in the initial regrowth portion at the discontinuity (following thermal soaking) must be constant across the crystal diameter, it must be concluded that the tellurium concentration in the crystal above the discontinuity, which is constant along the growth axis, (fringes parallel to the growth axis) must also be constant in the radial direction.

Crystal Morphology

As discussed earlier, the surface morphological characteristics of both space-grown crystals indicate that the Te-doped InSb melt does not wet the confining quartz wall. Accordingly, the contact angle between the seed and the melt at the peripheral contact line is controlled by the interfacial tensions of the three phases involved and the meniscus of the melt (which determines the shape of the growing crystal) becomes a function of the radius of curvature of the crystal-melt interface. The decrease in crystal diameter observed during the early stages of growth in the Skylab-IV experiment (Fig. 7) is, thus, a direct consequence of the pronounced convex configuration of the crystal-melt interface (as viewed from the melt) brought about by the thermal characteristics of the system.

The ensuing gradual change to constant crystal diameter reflects the decrease in lateral heat-transfer (due to the increasing distance of the growing crystal from the quartz wall) which results in an increase of the radius of curvature of the regrowth interface. The second decrease in crystal diameter, which coincides with the intentional, mechanical-shock perturbation, is attributed to a deformation of the melt (stretching towards the hot end) which established a melt menicus leading to decreasing crystal diameter. The subsequent increase in the diameter of the crystal is due to the fact that the volume available to the growth system becomes limited.

In the Skylab-III experiment the radius of curvature of the initial growth interface was significantly larger than in the Skylab-IV experiment; accordingly, the crystal diameter in the Skylab-III experiment conformed to the size of the confining quartz wall.

Peripheral Facet Effect

Basic thermodynamic parameters are responsible for the fact that during growth of InSb in the <111> direction a facet is generally formed at the growth interface. Since facet formation is associated with kinetic supercooling, the facet is centrally located at concave interfaces and peripherally at convex interfaces (as viewed from the melt). It is generally believed that dopant segregation within facets is controlled by lateral layer growth rate which is sensitive to thermal perturbations and gravity induced convection.

Consistent with the above considerations, peripheral facet formation is observed in both space-grown crystals (Fig. 20) since in both experiments the growth interface assumed convex morphology (Fig. 17). The well-defined segregation discontinuities on the facet grown region cannot, however, be explained on the basis of thermal and/or convective perturbations in the melt since segregation in the bulk of the crystals was found to be homogeneous.

The observed segregation effects in the peripheral facet can be explained by considering that kinetic supercooling for peripheral facet formation assumes its highest value at the outermost part of the growth interface, which thus becomes the location with the highest probability for nucleation of lateral layer growth. Under these conditions, any perturbation, such as a vibration or the arrival of a foreign particle at the peripheral three-phase contact line may trigger spurious nucleation of lateral layer growth and, thus, result in the formation of the observed segregation discontinuities. Their magnitude (intensity) is seen to decrease with decreasing supercooling from the periphery to the interior. Furthermore, depending on their magnitude, the facet segregation discontinuities extend more or less into the adjacent off-facet region; accordingly, it must be concluded that a finite amount of kinetic supercooling is associated with growth adjacent to facet regions. There is some evidence that the randomly spaced lines visible on the surface of the grown crystal (Fig. 8) correspond to the external boundaries of the presently discussed facet segregation discontinuities.

It should be pointed out that the same type of facet segregation discontinuity has been observed superimposed on compositional inhomogeneities in facet regions of earth-grown InSb; their origin could not, however, be explained.

Rotational Twinning

The bands of varying width appearing on the left-hand side of the crystal grown during the Skylab-III experiment (Fig. 5) were identified as the external boundaries of $(\bar{2}11)$ rotational twins. Each band is the result of two consecutive rotations by 60° of the (111) plane normal to the growth direction.

Analysis of the rotational twins on etched crystal segments of (211) surface orientation (Fig. 21) shows that some propagate across the entire crystal, some terminate within the crystal, and others deteriorate to grain boundaries, eventually leading to breakdown of the single crystal matrix.

In view of the convex interface morphology, nucleation during growth is essentially restricted to the outermost peripheral part of the growth interface which, as discussed previously, is susceptible to spurious nucleation. Rotational twin formation initiated by a nucleus having a 60° misorientation within the growth plane can thus be explained as the result of spurious nucleation of the crystal periphery.

Because of inherent thermal asymmetry in the multi-purpose furnace, the convex growth interface morphology is to some extent inclined to the growth direction. Therefore, any misoriented nucleus formed at the lowest part of the three-phase contact line (periphery of the growth interface) encounters no constraints in propagating and results in the formation of a twin boundary which crosses the entire crystal. Spurious nucleation at any higher part of the periphery, however, can propagate only through part of the crystal, since a varying fraction of the plane of propagation has solidified already in the original orientation. Considering that a twin boundary cannot terminate within the crystal, its direction of propagation must change to form a curved grain boundary which may either terminate at a subsequently nucleated twin boundary or lead to a polycrystalline matrix (see Fig. 21). It is of interest to note that the tendency of twin formation is strikingly reduced (only one rotational twin was observed) in the crystal grown with reduced diameter during the Skylab-IV experiment.

SUMMARY

The present InSb experiment proves unambiguously the uniqueness of zero-gravity conditions for obtaining directly fundamental data on crystal growth and segregation associated with solidification. Furthermore they demonstrate the striking advantages of processing materials in space.

Specifically the following results and conclusions were obtained for the first time:

Ideal steady state growth and segregation (exclusively diffusion controlled) were achieved leading to three-dimensional chemical homogeneity on a microscale over macro-scale dimensions (several centimeters in the present case); the transient segregation profile preceeding steady state solidification was determined; limitations in the experimental arrangement and in the presently available microanalytical techniques do not permit, at this time, the extraction of fundamental data pertinent to solidification.

Surface tension effects led to phenomena previously never observed and theoretically not predicted: the Te-doped melt, not wetting the quartz wall, solidified with a free surface (unconfined) configuration. Under forced contact conditions, intimate contact between the melt and the confining walls was prevented and the growth system was essentially isolated from its container by the formation of narrow surface ridges. It was also shown that surface tension effects in space remained localized on the surface and did not effect growth and segregation in the bulk.

In the absence of convective interference it was possible to identify segregation discontinuities associated with facet growth and to explain their origin on the basis of spurious nucleation. The absence of convective interference permitted, further, the determination of the mode of nucleation (formation of misorientated nuclei at the three phase boundary line) and propagation of rotational twinning.

A mechanical-shock perturbation intentionally introduced during growth was identified in the crystal and found to cause a localized increase in dopant segregation; this dopant discontinuity was used as a time reference for the determination of the average macroscopic growth rate.

On the basis of the present results it is no longer a matter of speculation that fundamental data necessary for bridging the gap between theory and experiment can be reliably obtained in the absence of gravity and that outer space presents one of the greatest opportunities ever afforded science and technology.

ACKNOWLEDGEMENTS

The authors wish to express their appreciation to the National Aeronautics and Space Administration, and particularly to the Staff at the Marshall Space Flight Center for their uncompromising efforts, cooperation and enthusiastic support during all stages of the experiment. They are indebted to Dr. K. M. Kim for carrying out much of the ground-based testing, to Drs. J. R. Carruthers and J. Colbey for stimulating discussions and to Mr. W. J. Fitzgerald and J. Baker for their skillful assistance with the characterization program. Finally, the authors are grateful to Dr. R. K. Lewis and the CAMECA Instruments, Inc., for their generosity in carrying out Ion-Microprobe Analyses of the crystal.

BIBLIOGRAPHY

The following bibliography is intended to provide pertinent background information.

J. C. Brice, "The Growth of Crystals from Liquids", North-Holland Publishing Co., 1973.

B. Chalmers, "Principles of Solidification", J. Wiley, 1964.

J. J. Gilman, editor, "The Art and Science of Growing Crystals", J. Wiley, 1963.

P. F. Kane and G. B. Larrabee, "Characterization of Semiconductor Materials", McGraw-Hill Book Company, 1970.

R. A. Laudise, "The Growth of Single Crystals", Prentice-Hall, 1970.

W. G. Pfann, "Zone Melting", 2nd ed., J. Wiley, 1966.

D. P. Woodruff, "The Solid-Liquid Interface", Cambridge University Press, 1973.

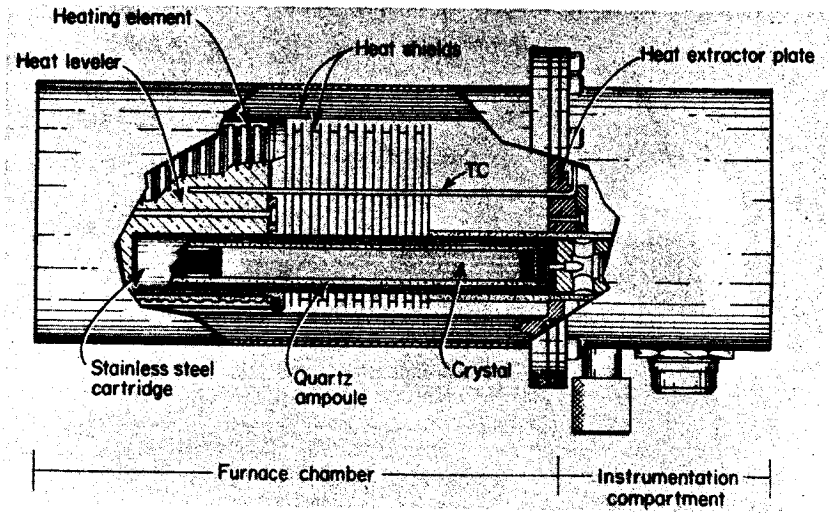

FIGURE 1. SKETCH OF THE MULTIPURPOSE FURNACE EMPLOYED FOR THE InSb GROWTH EXPERIMENT IN SKYLAB

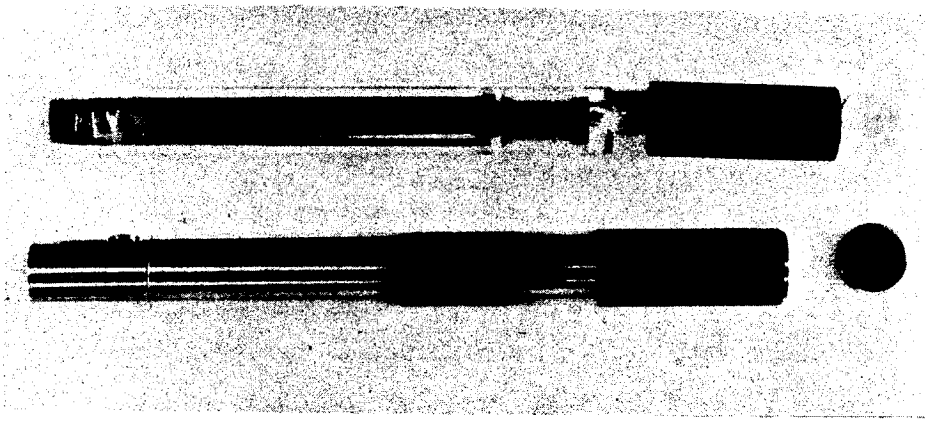

FIGURE 2. TOP: QUARTZ AMPOULE CONTAINING InSb CRYSTAL USED IN THE SKYLAB EXPERIMENT; THE COLD-END GRAPHITE SPACER, THE EARTH-GROWN CRYSTAL SEGMENT, THE SPACE GROWN SEGMENT AND THE HOT END GRAPHITE SPACER WITH A PERIPHERAL CAVITY ARE SEEN FROM LEFT TO RIGHT: AT EXTREME RIGHT IS GRAPHITE SLEEVE POSITIONED BETWEEN AMPOULE AND THE METAL CARTRIDGE. BOTTOM: STAINLESS STEEL CARTRIDGE IN WHICH CAMPOULE WAS ENCAPSULATED.

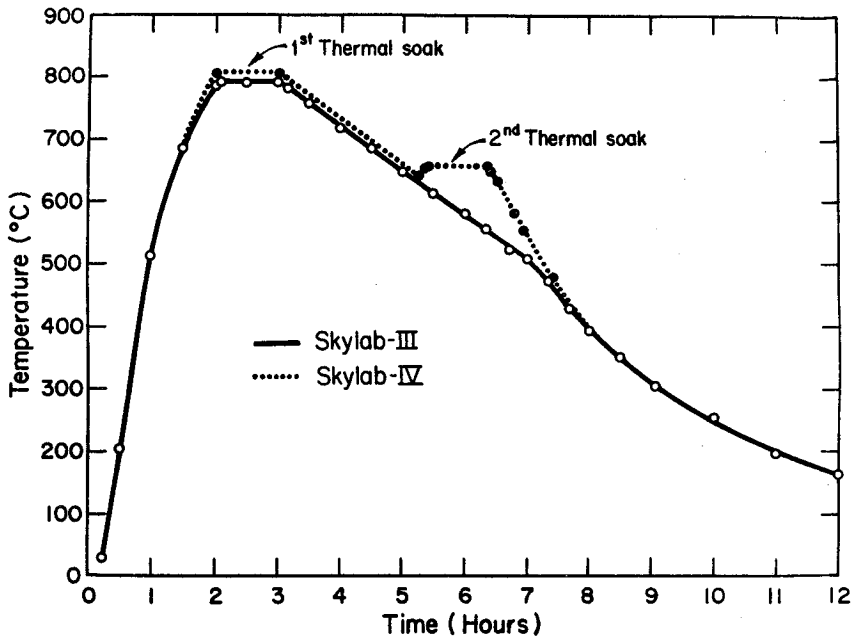

FIGURE 3. "HOT END" TEMPERATURE CYCLES FOR SKYLAB-III AND SKYLAB-IV EXPERIMENTS AS OBTAINED FROM A CHROMEL/ALUMEL THERMOCOUPLE.

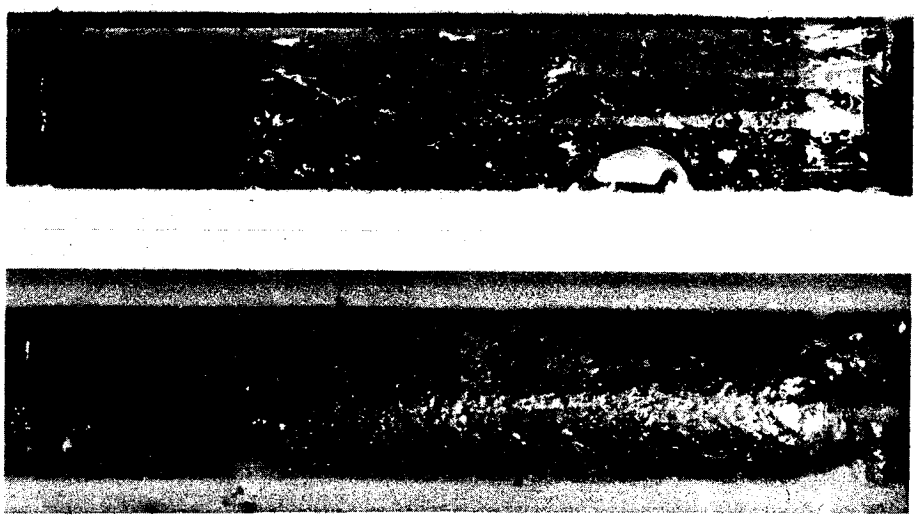

FIGURE 4. HEAVILY Sn-DOPED InSb CRYSTAL GROWN IN SPACE DURING SKYLAB-III (TOP) AND SKYLAB-IV MISSIONS CONTAINED IN THEIR QUARTZ AMPOULES. THE INITIAL REGROWTH INTERFACES ARE VISIBLE ON THE LEFT-HAND SIDE OF THE FIGURE; 2.6X.

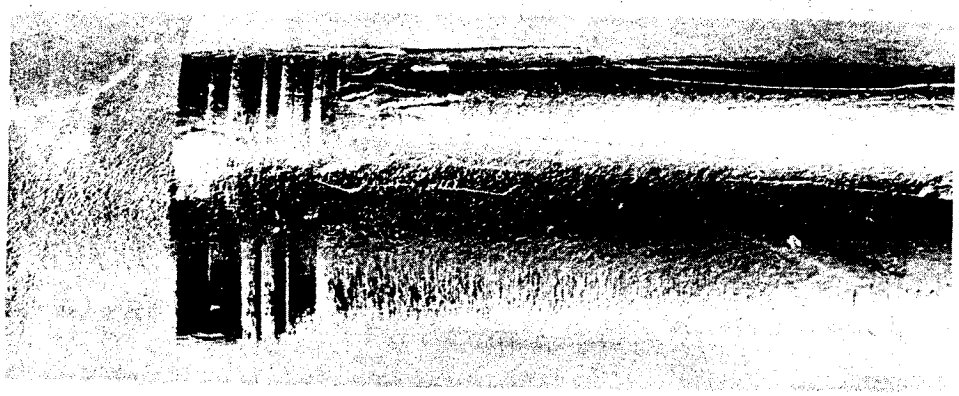

FIGURE 5. Te-DOPED CRYSTAL GROWN DURING SKYLAB-III MISSION. NOTE INITIAL GROWTH INTERFACE (LEFT-HAND SIDE), ROTATIONAL TWIN BANDS AND SURFACE RIDGES PROPAGATING ALONG THE GROWTH DIRECTION: THE DIAMETER OF THE SPACE GROWN SEGMENT IS THE SAME AS THAT OF THE EARTH GROWN SEGMENT; 4.9X.

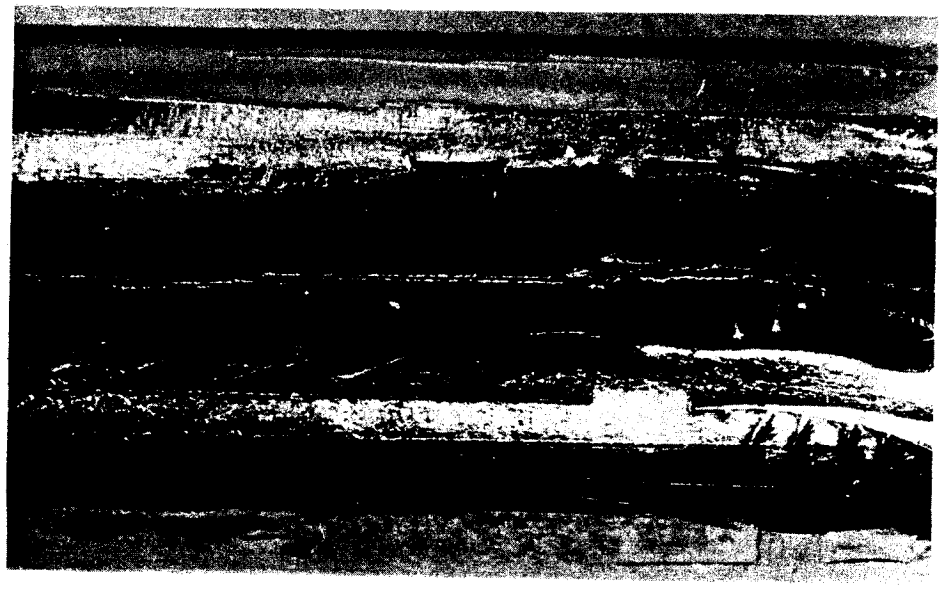

FIGURE 6. PART OF THE Te-DOPED CRYSTAL, GROWN DURING SKYLAB-III MISSION, 3.7 TO 5.9 cm FROM THE INITIAL REGROWTH INTERFACE. SURFACE RIDGES BROADEN AND BRANCH-OUT AT THE LATE STAGES OF GROWTH (RIGHT-HAND SIDE); 6.8X.

C-4

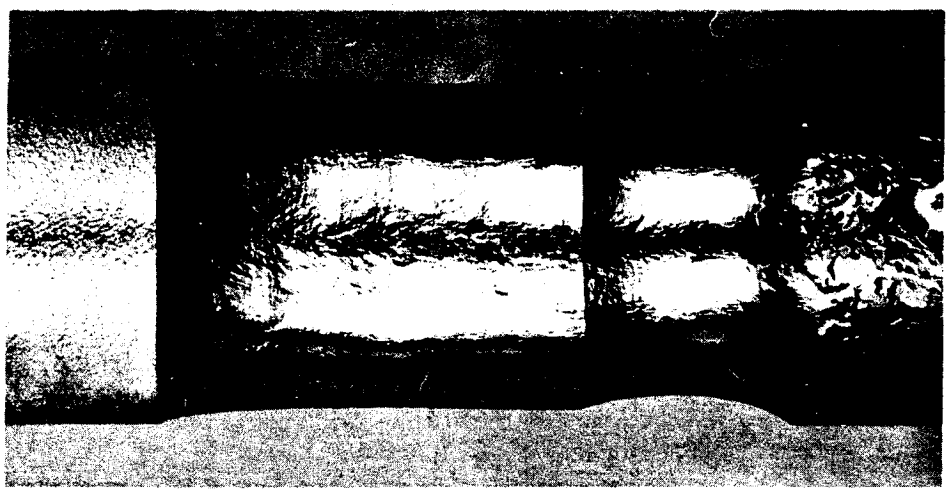

FIGURE 7. Te-DOPED CRYSTAL GROWN DURING THE SKYLAB-IV MISSION; NOTE DECREASE IN CRYSTAL DIAMETER UPON INITIATION OF GROWTH; SURFACE RIDGES APPEAR ON RIGHT-HAND SIDE AFTER CRYSTAL DIAMETER REACHES ITS MAXIMUM CONSTANT VALUE; 4.8X.

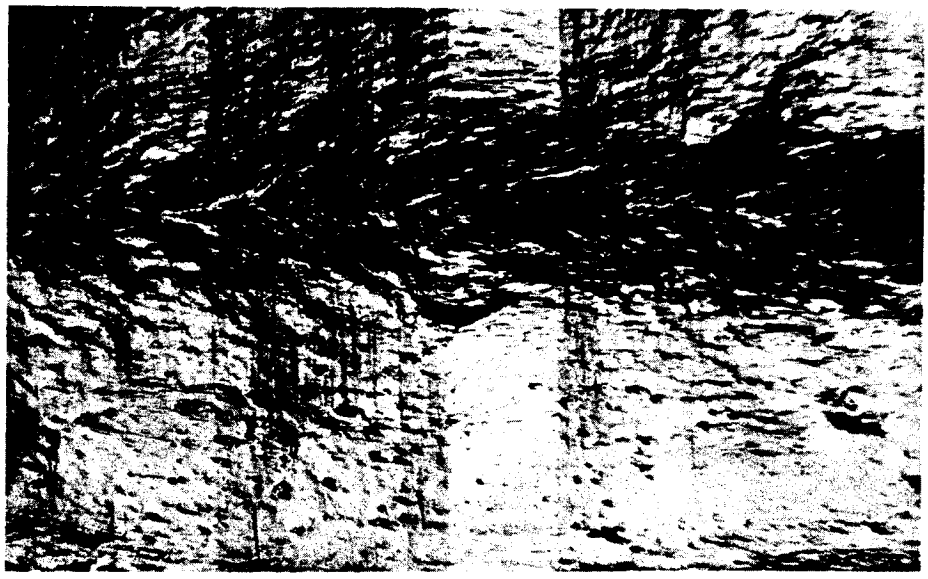

FIGURE 8. PART OF Te-DOPED CRYSTAL SHOWN IN FIGURE 7; SURFACE CHARACTERISTICS ARE TYPICAL FOR UNCONFINED SOLIDIFICATION: NOTE RANDOM DISTRIBUTION LINES NORMAL TO THE GROWTH DIRECTION; ROTATIONAL TWIN IS VISIBLE (WHITE BAND); 19X.

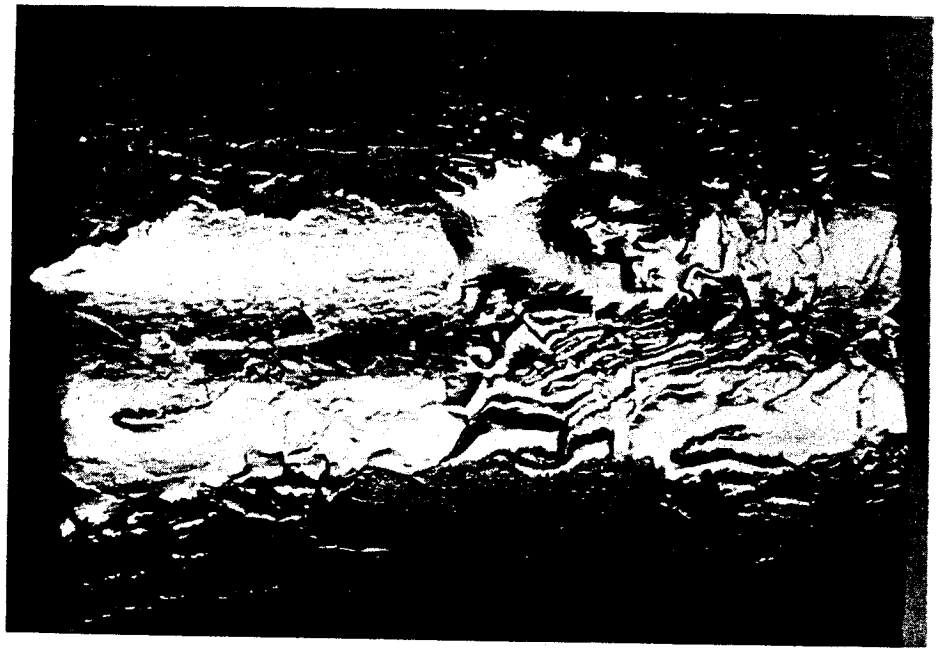

FIGURE 9. SURFACE RIDGE PATTERNS FORMED AFTER CRYSTAL REACHED MAXIMUM CONSTANT DIAMETER DURING SKYLAB-IV EXPERIMENT; NOTE DISCONTINUITY IN SURFACE MORPHOLOGY ASSOCIATED WITH SECOND THERMAL SOAKING (SEE TEXT); 21X.

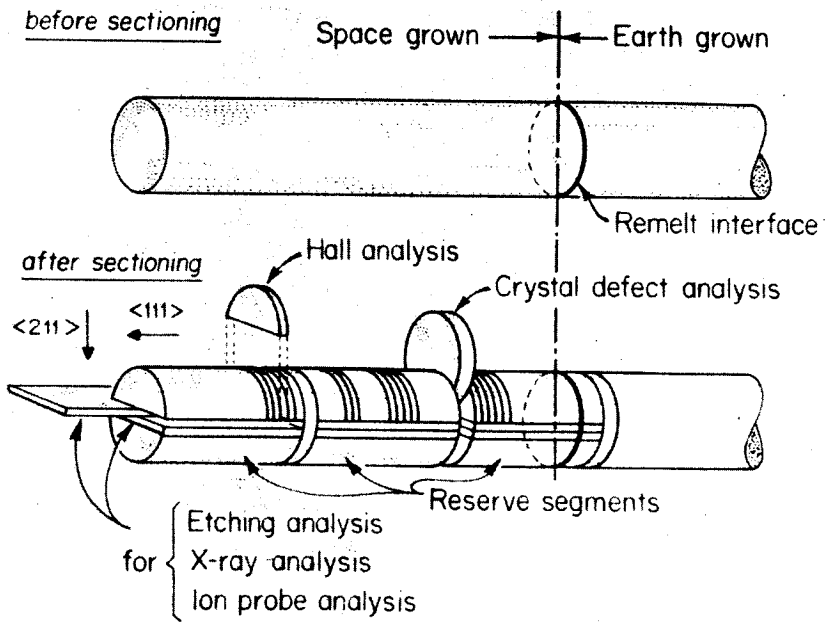

FIGURE 10. SECTIONING SCHEME FOR ANALYSIS OF SPACE GROWN CRYSTAL.

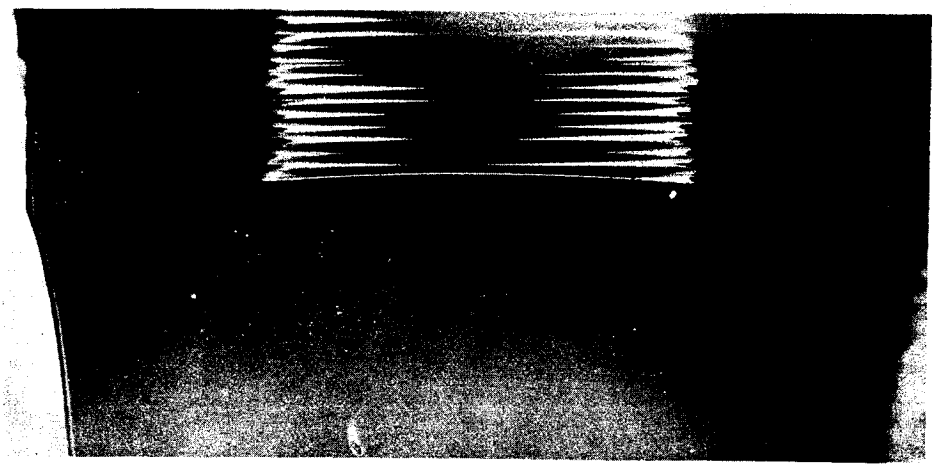

FIGURE 11. ETCHED CROSS-SECTION (UNDER DARK-FIELD ILLUMINATION) OF CRYSTAL GROWN DURING SKYLAB-IV MISSION; SPACE GROWN REGION (BOTTOM), IN CONTRAST TO EARTH GROWN REGION (TOP), EXHIBITS NO COMPOSITIONAL INHOMOGENEITIES: 12X.

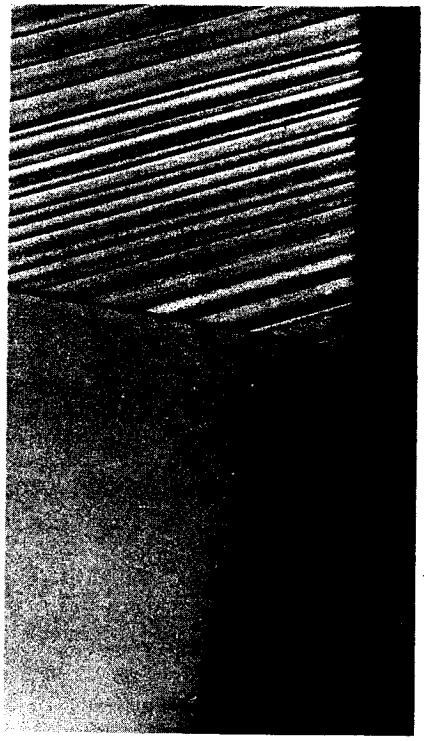

FIGURE 12. DOPANT SEGREGATION CHARACTERISTICS NEAR THE PERIPHERY OF INITIAL REGROWTH INTERFACE (RIGHT-HAND SIDE OF FIGURE 11); 300X.

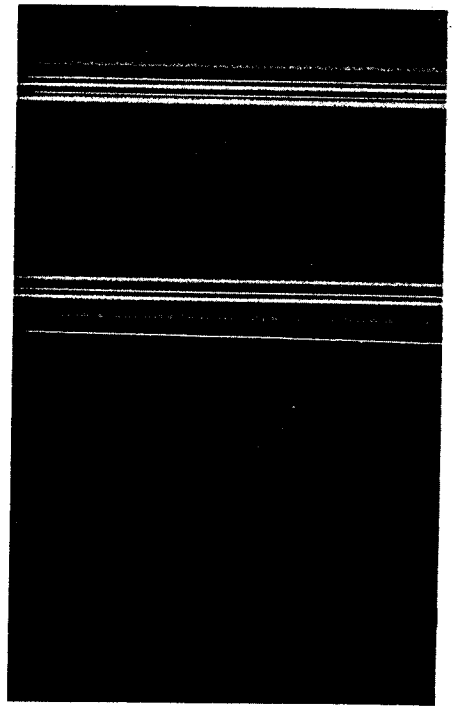

FIGURE 13. DOPANT SEGREGATION CHARACTERISTICS NEAR THE CENTRAL REGION OF INITIAL REGROWTH INTERFACE OF CRYSTAL GROWN DURING SKYLAB-IV MISSION; 580X.

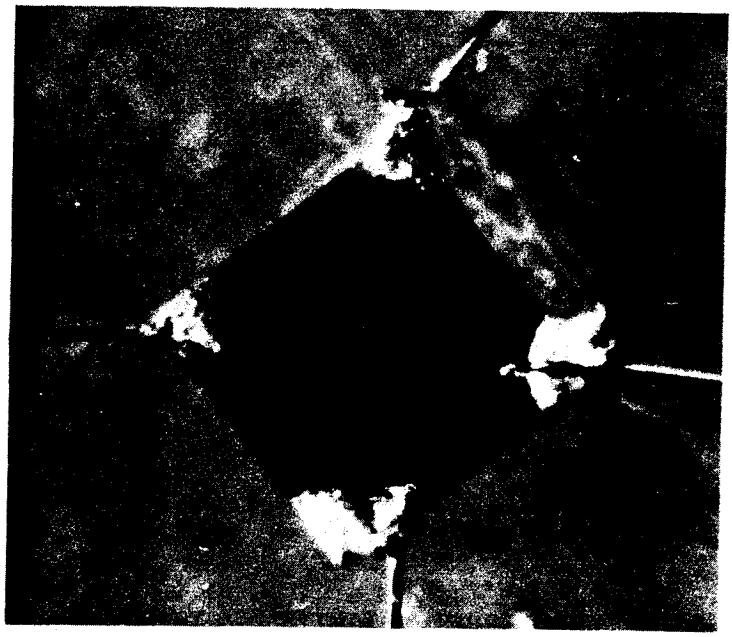

FIGURE 14. SAMPLE OF HALL-EFFECT MEASUREMENTS (VAN DER PAUW CONFIGURATION).

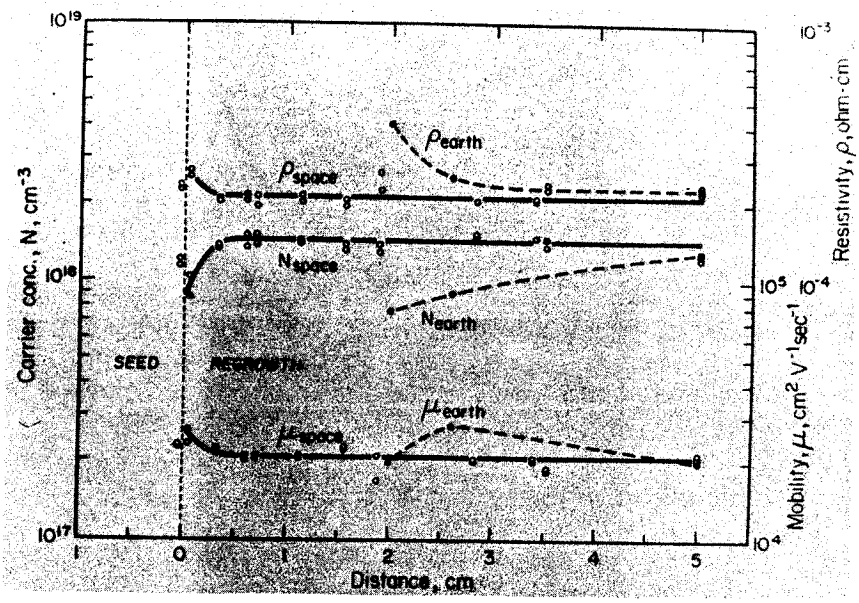

FIGURE 15. CARRIER (DOPANT) CONCENTRATION PROFILE OBTAINED FROM HALL-EFFECT MEASUREMENTS FOR Te-DOPED CRYSTAL GROWN DURING SKYLAB-III MISSION (N_{space}) AND FOR Te-DOPED CRYSTAL GROWN DURING GROUND-BASED TESTING.

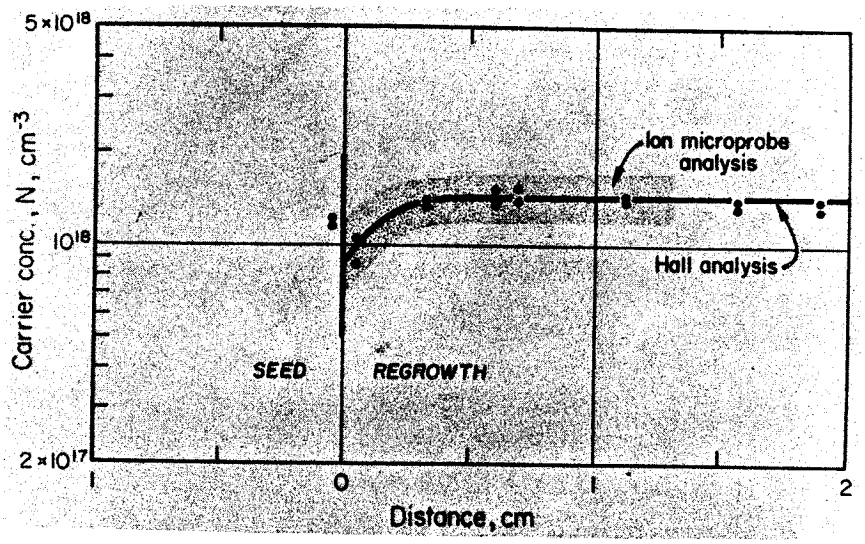

FIGURE 16. ION-MICROPROBE PRECISION LIMITS FOR Te IN InSb FOR A BEAM SIZE OF 25 μm SUPERIMPOSED ON PROFILE OBTAINED BY HALL-EFFECT MEASUREMENTS.

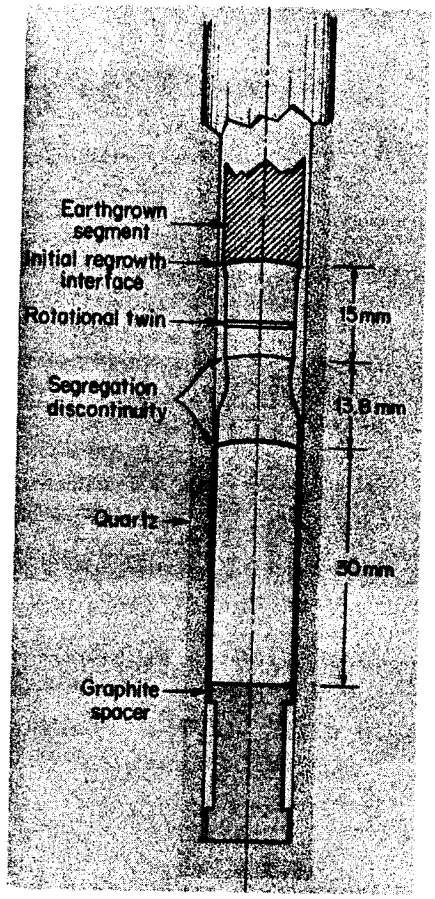

FIGURE 17. CROSS-SECTION OF CRYSTAL GROWN DURING SKYLAB-IV MISSION.

FIGURE 18. DOPANT SEGREGATION DISCONTINUITY CAUSED BY COOLING ARREST AND THERMAL SOAKING DURING GROWTH IN SKYLAB-IV MISSION; 400X.

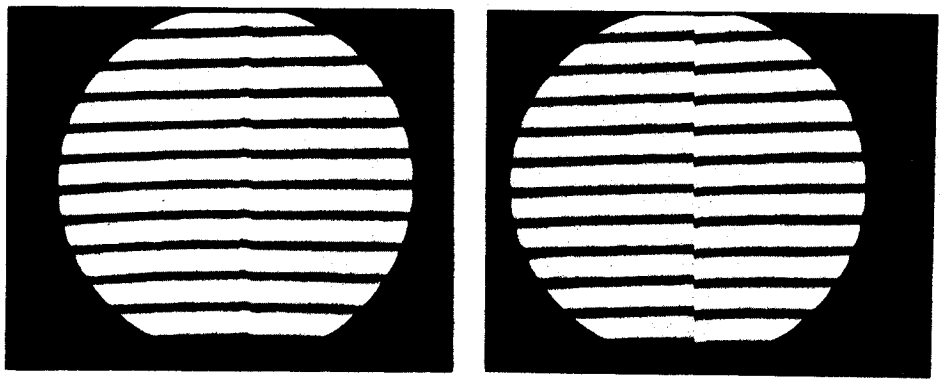

FIGURE 19. DOUBLE BEAM INTERFEROGRAMS OF SEGREGRATION DISCONTINUITIES AS REVEALED BY ETCHING (a) CAUSED BY MECHANICAL SHOCK AND (b) CAUSED BY REGROWTH AFTER THERMAL SOAKING (SEE TEXT).

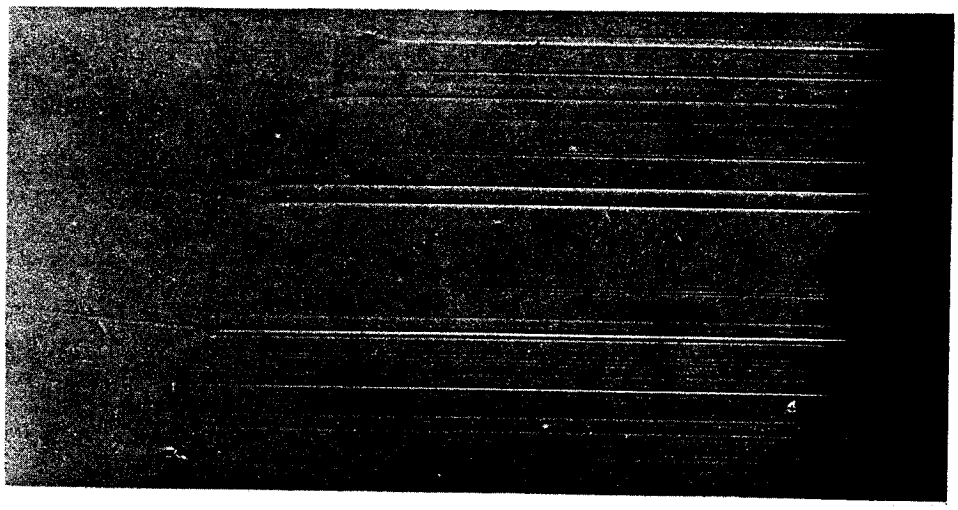

FIGURE 20. PERIPHERAL FACET GROWTH WITH SEGREGATION DISCONTINUITIES IN CRYSTAL GROWN DURING SKYLAB-IV MISSION; 300X.

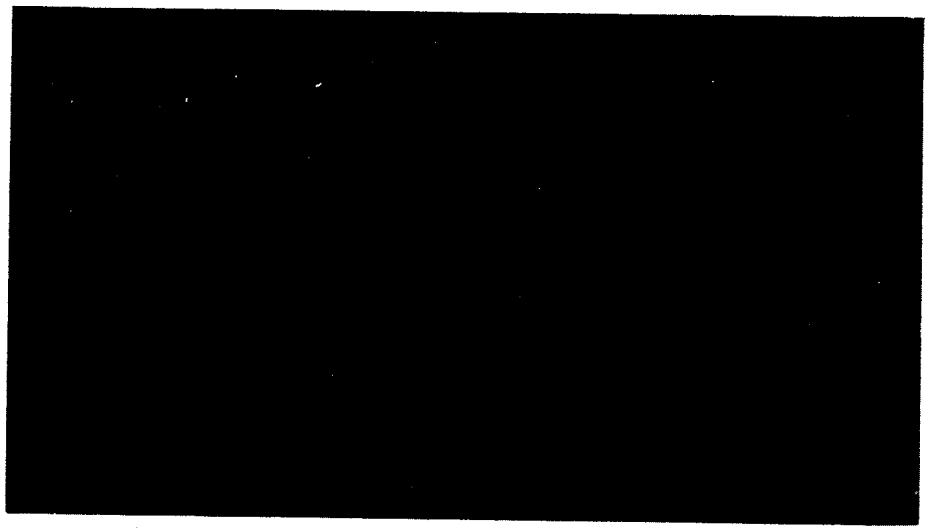

FIGURE 21. CROSS-SECTION OF CRYSTAL GROWN DURING SKYLAB-III MISSION EXHIBITING ROTATIONAL TWINNING (SEE ALSO FIGURE 5); 12X.

DIRECTIONAL SOLIDIFICATION OF InSb-GaSb ALLOYS

N74 29898

By

James F. Yee, Sanghamitra Sen, Kalluri Samra,
Mu-Ching Lin and William R. Wilcox*
University of Southern California
Los Angeles, California 90007

SUMMARY

$In_xGa_{1-x}Sb$ with x = 0.5, 0.3 and 0.1 was directionally solidified under a variety of conditions. Identical gradient-freeze experiments were performed vertically with the heater on top, horizontally and in Skylab (SL-3). Experiments were also performed in SL-4 with the heater temperature increased. Bridgman-Stockbarger and vertical gradient freeze experiments were performed at USC. A transverse magnetic field was used to inhibit convection in some of the USC Bridgman experiments. A wide range of grain sizes was observed, but with no influence of growth conditions yet observed. The number of twins in the space-processed samples was much less than in the earth-processed samples. Equilibrium between the growing crystal and the bulk melt was more nearly achieved in the horizontally processed ingot, because of the enhanced free convection. Gas bubbles were trapped in the ingots when the ampoules were back-filled with helium. The bubbles were more evenly distributed in the Skylab ingots. Micro-cracks were more numerous in inhomogeneous regions of the ingots. The ingots formed in SL-3 had a smaller diameter than the tube, but those in SL-4 did not. The grains were very difficult to distinguish from one another in five out of six Skylab ingots.

*Paper presented by William R. Wilcox.

I. INTRODUCTION

Although a wide variety of semiconductor compounds are available, the selection of electronic and other physical property combinations is limited. The range of available property combinations becomes much larger if one considers solid solution alloys. For example, the electronic properties of InSb-GaSb alloys are such that Gunn microwave oscillation can be observed with some compositions, but not in pure InSb or GaSb (1). Unfortunately, large homogeneous single crystals of concentrated alloys are not produced. Films of many alloys can be produced by chemical vapor deposition or by liquid phase epitaxy, but many applications require bulk single crystals.

Directional solidification of concentrated alloy semiconductors produces a polycrystalline material. Homogeneous polycrystalline ingots may be produced by very slow zone leveling either with or without a solvent added, under conditions such that interface breakdown due to constitutional supercooling is avoided. One may speculate that grains are generated by the compositional variations arising from hydrodynamic fluctuations in the melt. In order to test this suggestion, directional solidification experiments were performed on InSb-GaSb alloys. These were carried out on the earth in vertical and horizontal positions, with and without a magnetic field, and in Skylab. While dramatic differences in grain size were not observed, several interesting phenomena were discovered.

II. SOLIDIFICATION EXPERIMENTS

The phase diagram for InSb and GaSb is shown in Figure 1. The conditions required to avoid constitutional supercooling were estimated from the phase diagram by use of the equation (3)

$$\left(\frac{G}{V}\right) > \frac{m}{D}\frac{C_c}{C_m}(X_c - X_m) , \qquad (1)$$

where G is the temperature gradient at the interface, V is the freezing

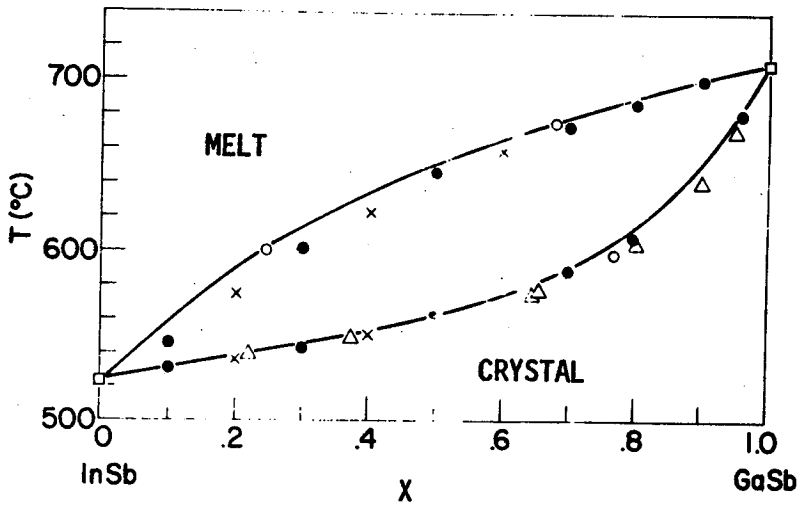

Figure 1. The InSb-GaSb pseudobinary phase diagram (2). X is mole fraction GaSb.

rate, m is the slope of the liquidus at the interfacial melt composition X_m, X_c is the mole fraction composition of the crystal, C_c is the total molar concentration in the crystal, C_m is the total molar concentration in the melt, and D is the binary diffusion coefficient (assumed to be 2×10^{-5} cm^2/sec). The results are shown in Figure 2. Conditions were chosen such that G/V was in the stable region at the beginning of solidification in each experiment. Mixtures initially containing 10%, 30% and 50% InSb were employed.

A. NASA Experiments

For the NASA earth and SL-3 experiments the value of G/V at the beginning of resolidification was estimated by use of heat transfer calculations (performed by Westinghouse (6)) to have been 816°C hour/cm^2. For SL-4 processed ingots the initial G/V was similarly estimated to have been 866°C hour/cm^2.

Fused silica tubing of 8 mm nominal inside diameter and 1 mm wall thickness was cut into nine-inch lengths and sealed at one end to prepare them for casting. Each such tube was cleaned in soap and water, followed by aqua regia and a rinse in semiconductor grade

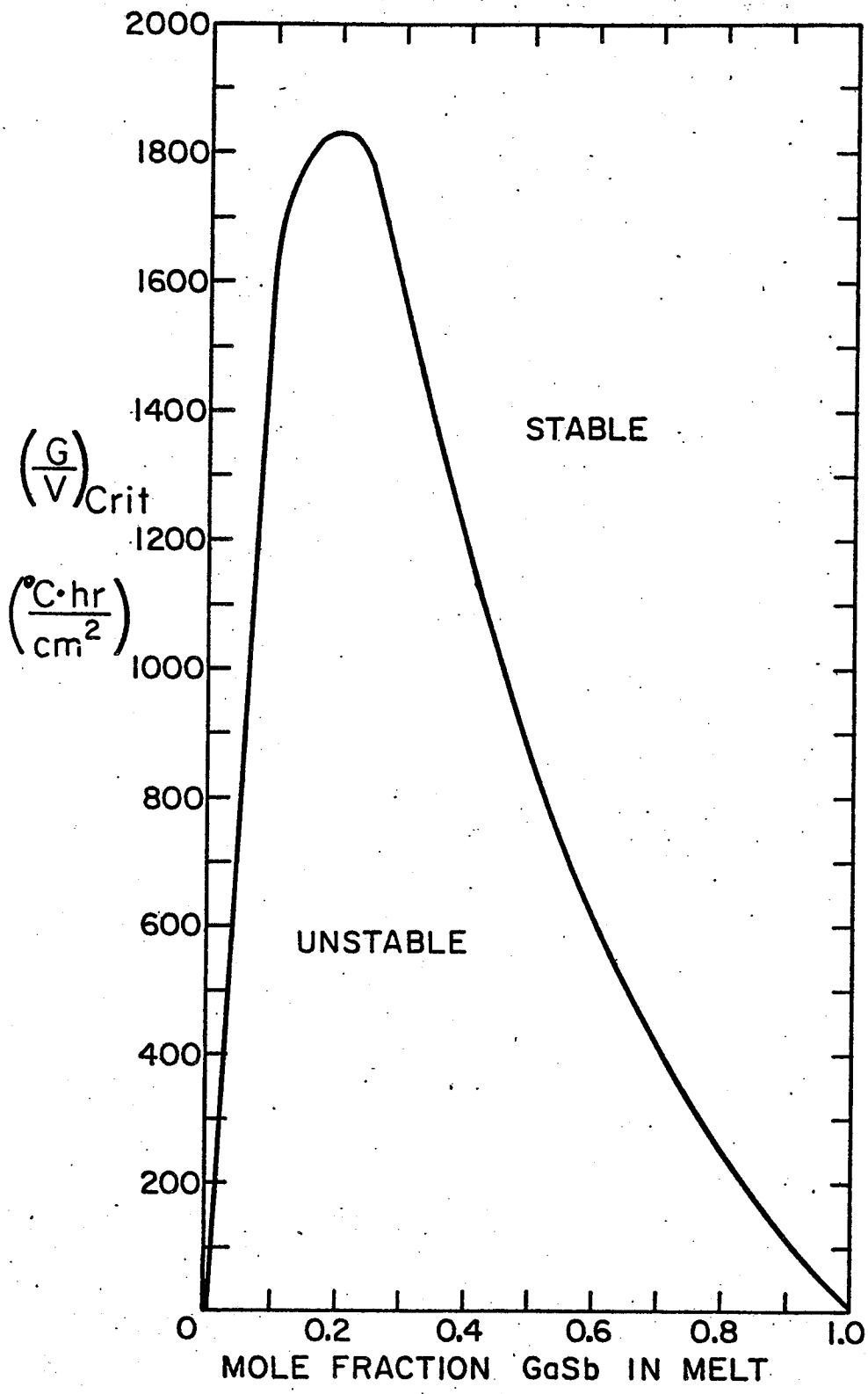

Figure 2. Critical G/V for constitutional supercooling in $In_xGa_{1-x}Sb$ calculated from Eq. (1).

deionized water. They were then heated in a horizontal furnace to over 920°C. Helium or argon was passed over acetone and into each capsule for a minimum of ten minutes, causing a layer of carbon to coat the interior walls of the capsule. The purpose of this coating was to prevent the sticking of the solid $In_xGa_{1-x}Sb$ to the walls of the silica capsule.

The elements were weighed in appropriate amounts and placed into the tubes. Each tube was sealed under a vacuum of less than 10^{-2} Torr. The ampoules were then heated in a vertical furnace at over 900°C for at least one hour. Frequent vigorous shaking was employed to enhance mixing of the melt. The ampoule usually cracked during cooling. Sometimes all of the silica could be mechanically removed quite easily from the ingot; sometimes it could not. In the latter case, HF was used to dissolve the quartz in one to two days. HF did not visibly attack the alloys in this period.

A typical cast ingot is shown in Figure 3. Longitudinal and cross-sectional slices of two $In_{0.3}Ga_{0.7}Sb$ ingots are shown in Figure 4. As can be seen, dendrites grew along the entire length of the ingot, as expected for such rapid solidification.

Each such ingot was cut to 9 cm length and chemically etched in 1 HNO_3:1 HCl in order to remove enough material at the surface so that it would fit loosely into carbon-coated 8 mm I.D. silica tubes. Graphite plugs, quartz wool and a small piece of silica tubing were used to encapsulate the sameles, as shown in Figure 5. The graphite plugs, made of high-purity Poco graphite DFP-2 rods (impurities < 5 ppm), were used as spacers to position the ingot and to confine the melt during crystal growth. The quartz wool was used as a spring to allow for the expansion of the ingot longitudinally during heating and crystal growth. The piece of quartz tubing was used to compress the assembly. The ampoules were evacuated and backfilled with 10 Torr of helium prior to sealing.

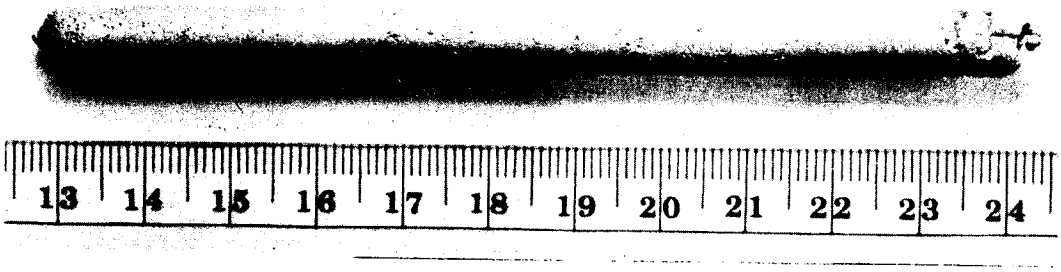

Figure 3. Photograph of casting.

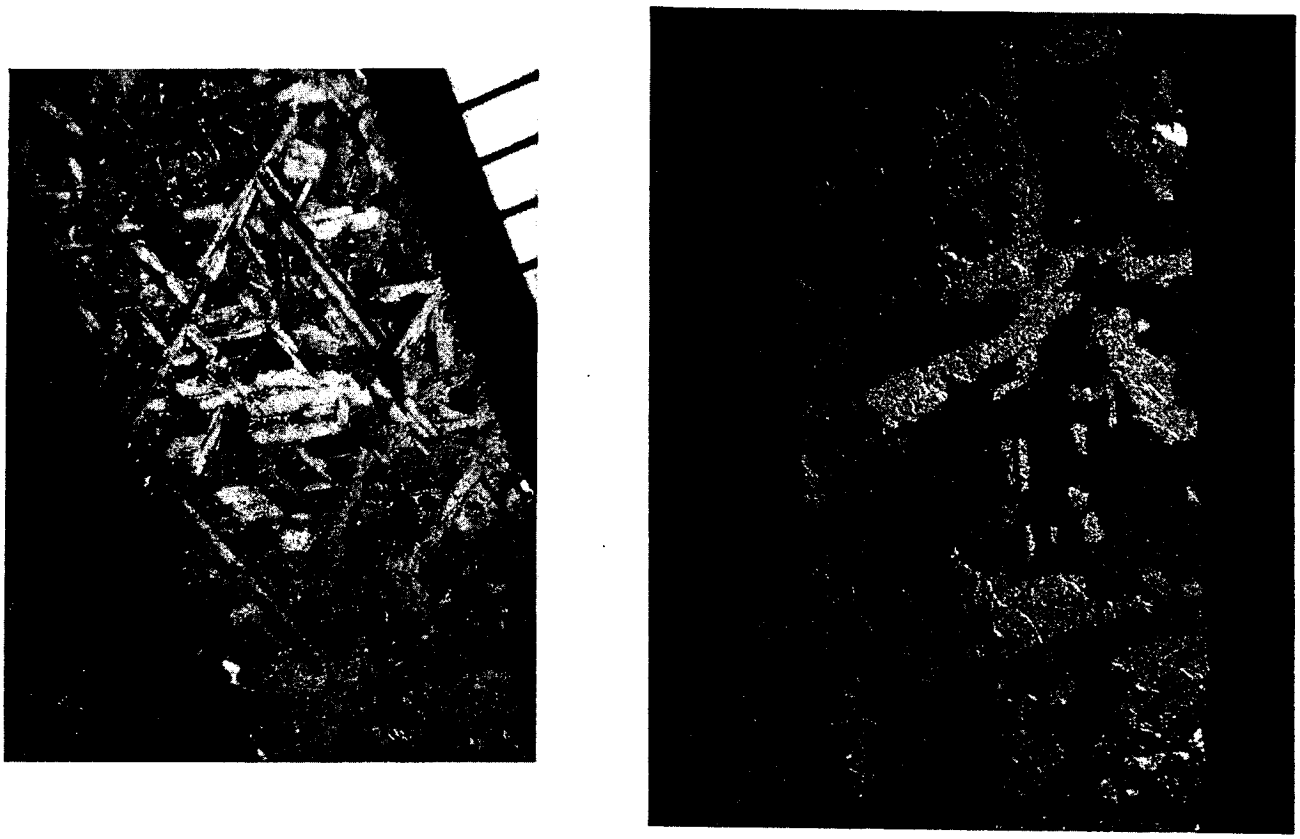

$In_{0.3}Ga_{0.7}Sb$ $In_{0.1}Ga_{0.9}Sb$

Figure 4. Photographs of cast ingots.

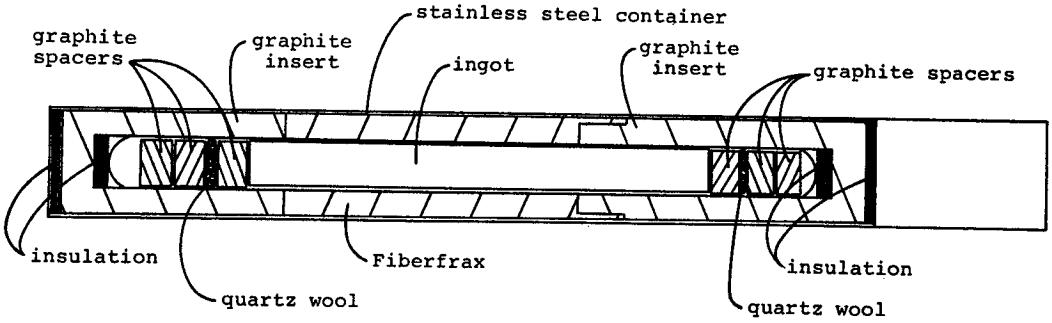

Figure 5. Diagram of completed ampoule in experimental cartridge.

These ampoules were then sealed by Westinghouse in stainless steel cartridges under a vacuum of $\leq 10^{-4}$ Torr. The cartridges were then processed by NASA in the Westinghouse Multipurpose Electric Furnace (6). This furnace consisted of a resistance heater at one end, a graphite heat extractor at the other, and an insulated region in between. Three cartridges were processed simultaneously in each run. As shown in Table I, three samples were processed vertically with the heater on top, three horizontally, three on the second Skylab mission, and three on the last Skylab mission. Power was applied so that the heater was at 960°C or 1020°C. This resulted in melting of somewhat over half of each ingot. After soaking for 16 hours to allow homogenization to occur, directional solidification was accomplished by programming down the heater temperature at 0.6°C per minute. This resulted in a steadily increasing freezing rate since the temperature gradient decreased as solidification proceeded. When the solid-liquid interface moved within the heater, the freezing rate increased rapidly because of the low temperature gradient there.

B. USC Experiments

Silica tubes of 9 mm I.D. were cleaned as before, but were not carbon coated because sticking and cracking were not a problem at the low solidification rates employed. Cleaner ingots with less oxides on their surfaces were obtained by etching the Sb and In shot in

TABLE I. SUMMARY OF NASA EXPERIMENTS

No.	Starting Composition	m.p. (°C)	Heater (°C)	Deviation from <111>	Length in Heater/Cooler[1]	Meltback x (cm)[2]
			Vertically Processed			
1A[3]	$In_{0.1}Ga_{0.9}Sb$	700	960		8.5/27.5 = 0.31	3.5
3B	$In_{0.3}Ga_{0.7}Sb$	678	960	18°	10.0/26/0 = 0.38	4.2
2C	$In_{0.1}Ga_{0.9}Db$	700	960	16°	12.0/24.0 = 0.50	3.7
			Horizontally Processed			
3A	$In_{0.5}Ga_{0.5}Sb$	646	960		9.5/26 5 = 0.36	4.6
4B	$In_{0.3}Ga_{0.7}Sb$	678	960	17°	14.0/22.0 = 0.64	4.6
4C	$In_{0.1}Ga_{0.9}Sb$	700	960	6°	8.5/27.5 = 0.31	4.0
			Skylab (SL-3) Processed			
2A	$In_{0.5}Ga_{0.5}Sb$	646	960		16.7/19.3 = 0.87	4.4
1B	$In_{0.3}Ga_{0.7}Sb$	678	960	9°	19.1/16.9 = 1.13	4.0
1C	$In_{0.1}Ga_{0.9}Sb$	700	960	9°	17.4/18.6 = 0.94	3.7
			Skylab (SL-4) Processed			
5A	$In_{0.5}Ga_{0.5}Sb$	646	1020		10.1/25.9 = 0.39	4.7
2B	$In_{0.3}Ga_{0.7}Sb$	678	1020		15.0/21.0 = 0.71	4.5
3C	$In_{0.1}Ga_{0.9}Sb$	700	1020		11.3/24.7 = 0.46	4.2

[1] In min.

[2] See Figure 13.

[3] Incorrectly labelled. Should have been 50% GaSb.

$1HC\ell:2H_2O$ for 10 to 15 minutes and then rinsing in methanol. The tubes were sealed under a vacuum of 5 to 10 x 10^{-3} Torr. An ampoule was then lowered into ~12 mm I.D. heater tube. The temperature was raised above the melting point of the desired alloy for 24 hours, with occasional shaking in order to produce a homogeneous melt.

Two different techniques were employed--the vertical Bridgman-Stockbarger technique and the vertical gradient freeze technique. Both furnaces were constructed by winding 22 gauge Kanthal wire on a grooved alundum furnace core. A diagram of the gradient-freeze apparatus is shown in Figure 6. The temperature gradient was produced by a cooled copper rod which projected 3 to 4 inches into the bottom of the furnace and contacted the ampoule. The heater tmperature was then slowly reduced by means of a temperature programmer. The initial value of G/V is estimated to have ranged from 300 to 500°C hour/cm^2.

A diagram of the Bridgman apparatus is shown in Figure 7. The voltage to the heater was held constant by a Sola constant voltage transformer in series with a variable autotransformer. The heater temperature was about 900°C, while the circulating coolant was at 4 to 5°C. The ampoule was lowered at 4 to 8 mm/day.

Temperature profiles in the Bridgman ampoule were measured by sealing a 5 mil chromel-alumel thermocouple in the tube. The thermocouple leads were in a two-holed alumina tube inside a silica tube. The alumina tube extended from the end of the silica tube. The thermocouple bead, formed at the end of the alumina tube, was coated with a ceramic cement to protect it from the melt. With the thermocouple fixed thereby, lowering the tube through the furnace produced the temperature profiles shown in Figure 8. The initial value of G/V in the growth experiments is estimated thereby to have been 930 to 1500°C hour/cm^2. The furnace profile in Figure 8 was measured by means of a thermocouple between an identical ampoule and the furnace tube wall.

Previous work on solidification of InSb in a horizontal boat showed that free convection could be greatly reduced by means of a

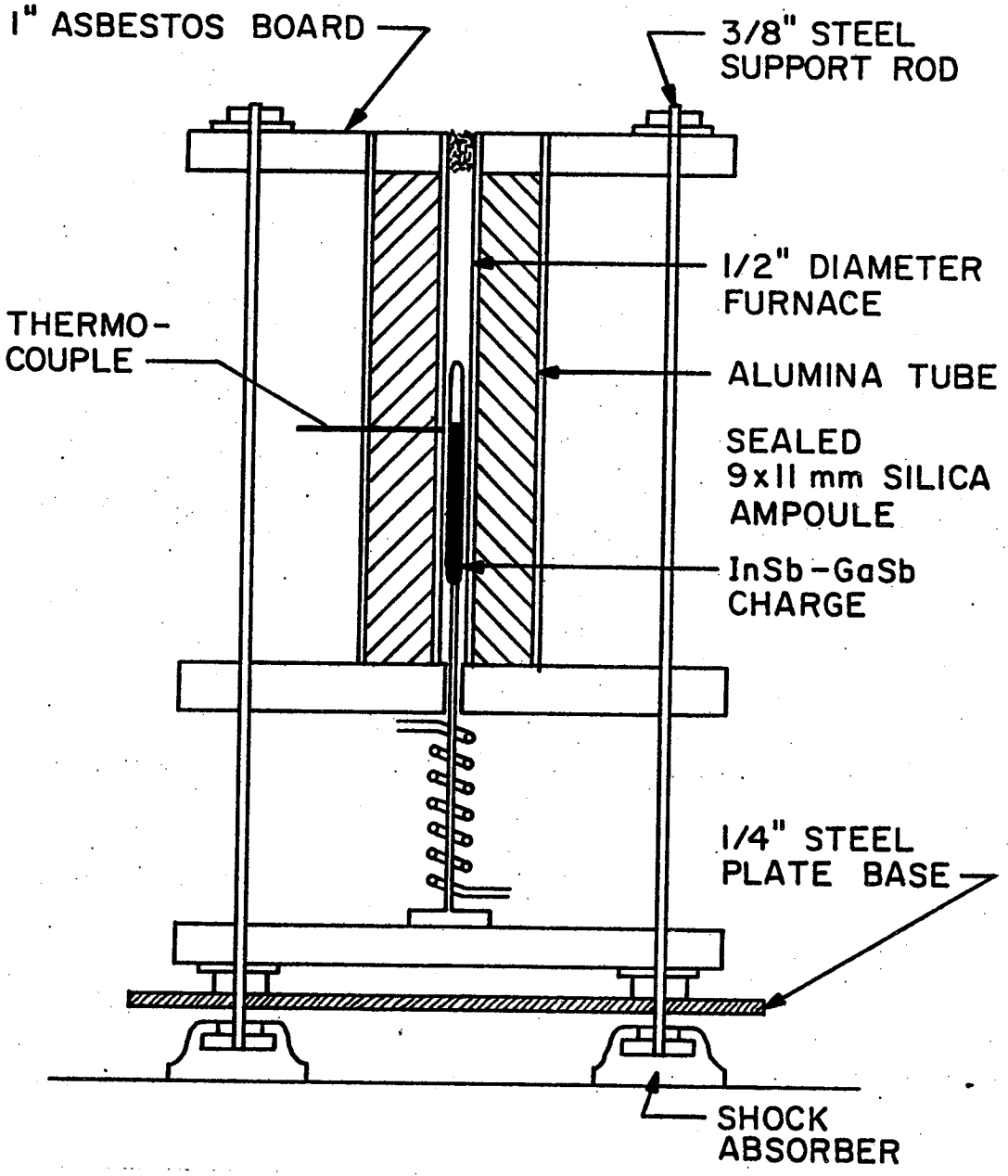

FIGURE 6. DIAGRAM OF GRADIENT-FREEZE APPARATUS FOR GROWTH OF $In_xGa_{1-x}Sb$.

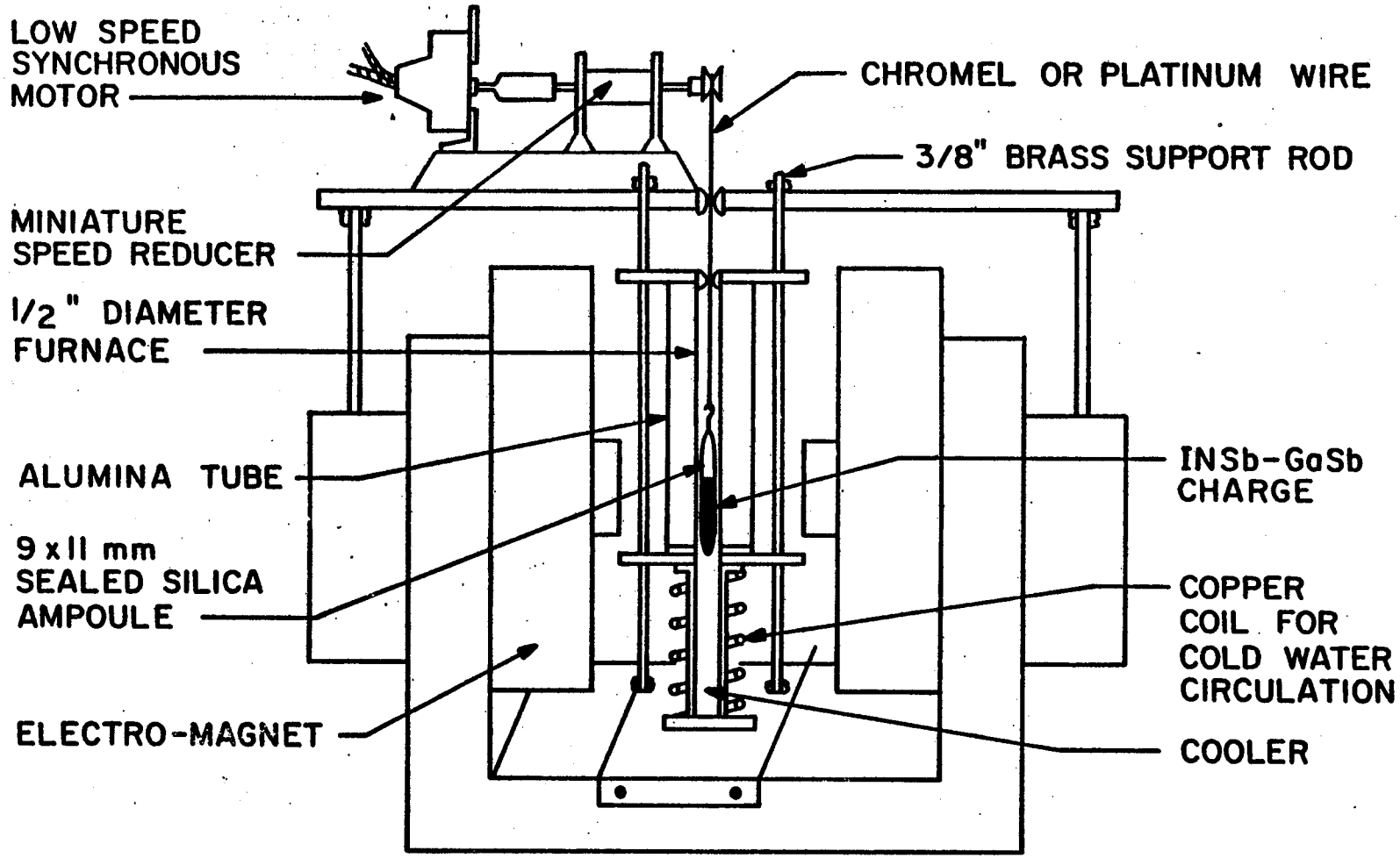

Figure 7. Diagram for vertical-Bridgman growth under magnetic field.

transverse magnetic field (4). We found that a transverse field in our Bridgman experiments altered the temperature profile as shown in Figure 9. This is indicative of reduced convection. No change in temperature distribution was noted as field strength was increased from 2 kilogauss to 4 kG, so 4 kG was used for the growth experiments. In several runs the field was turned on or off part way through the run.

III. RESULTS

A. Morphology

NASA provided X-radiographs of the unopened sampled cartridges after thermal processing, as shown in Figures 10-13. Note that the cross sections of the ingots processed horizontally were not circular. Those processed in SL-3 had irregular wavy surfaces with diameters somewhat less than the tube diameter. Ingot 1C had a diameter of only ~6.4 mm at one point. On the other hand, those ingots processed in SL-4 did have the tube diameter.

The radiographs, Figures 10-13, also allowed us to measure the melt-back position, as defined in Figure 14 and summarized in Table I. There was considerable variation in the amount of material initially melted in the thermal processing. There were two factors influencing the amount of melt-back: the thermal parameters of the semiconductor and the exact geometry of all components in the cartridge. The most important thermal parameter of the solid is its melting point, which increases as the gallium content increases. The lower the melting point, the more melt-back expected. The most important geometric factors are the length of solid in the heater and the length of solid in the cooler. The higher the ratio of the portion in the heater to that in the cooler, the more melt-back expected. If we examine Table I we see in comparing ingot 2C to 1A that the geometric effect was responsible for the larger melt-back. Comparing ingot 3B to 2C, the melting point effect predominated. The horizontally-processed ingots had appreciably more melt-back than the vertically-processed ingots.

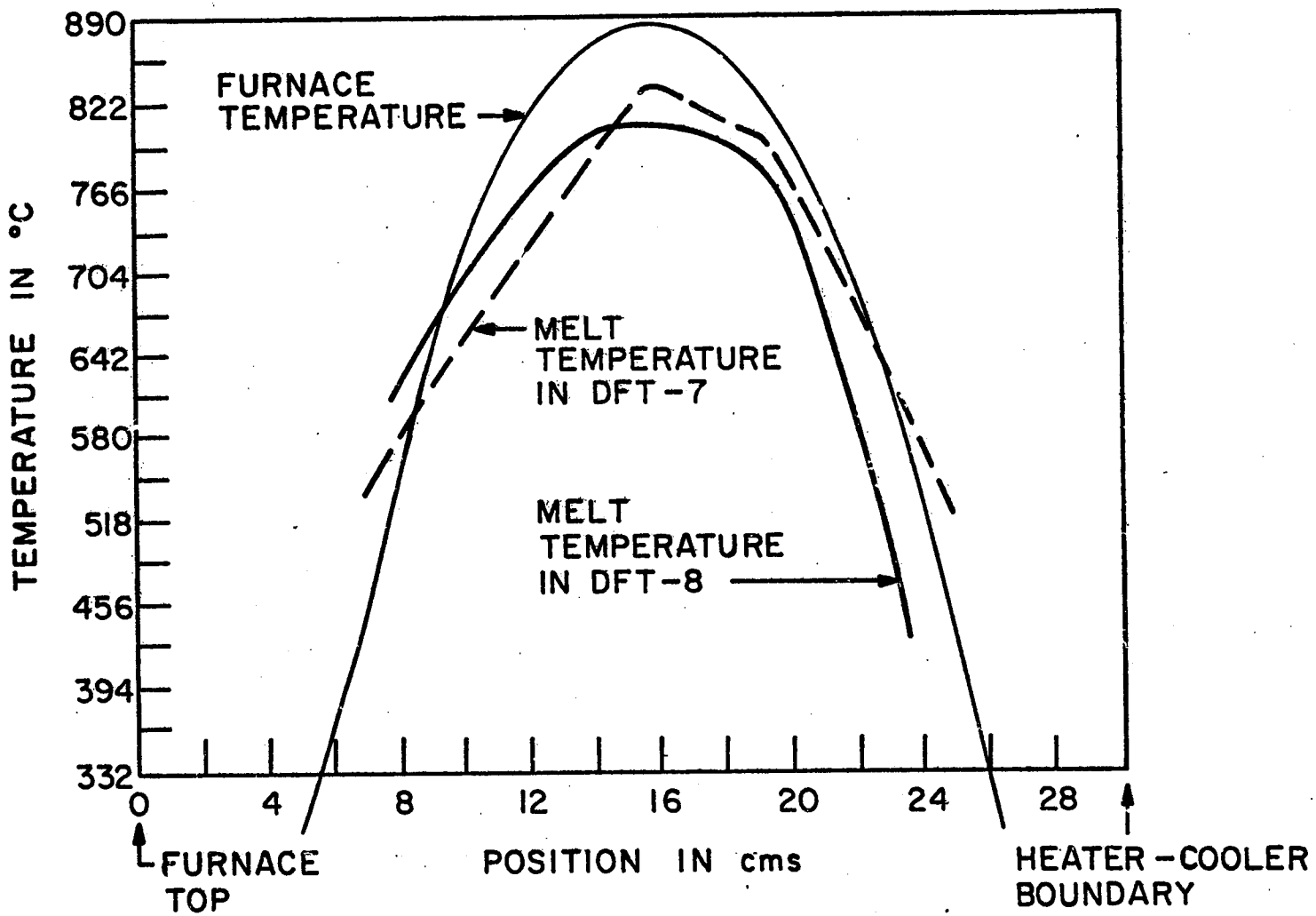

Figure 8. Measured temperature profile inside and outside vertical Bridgman growth ampoule (DFT-7 was $In_{0.1}Ga_{0.9}Sb$; DFT-8 was $In_{0.5}Ga_{0.5}Sb$).

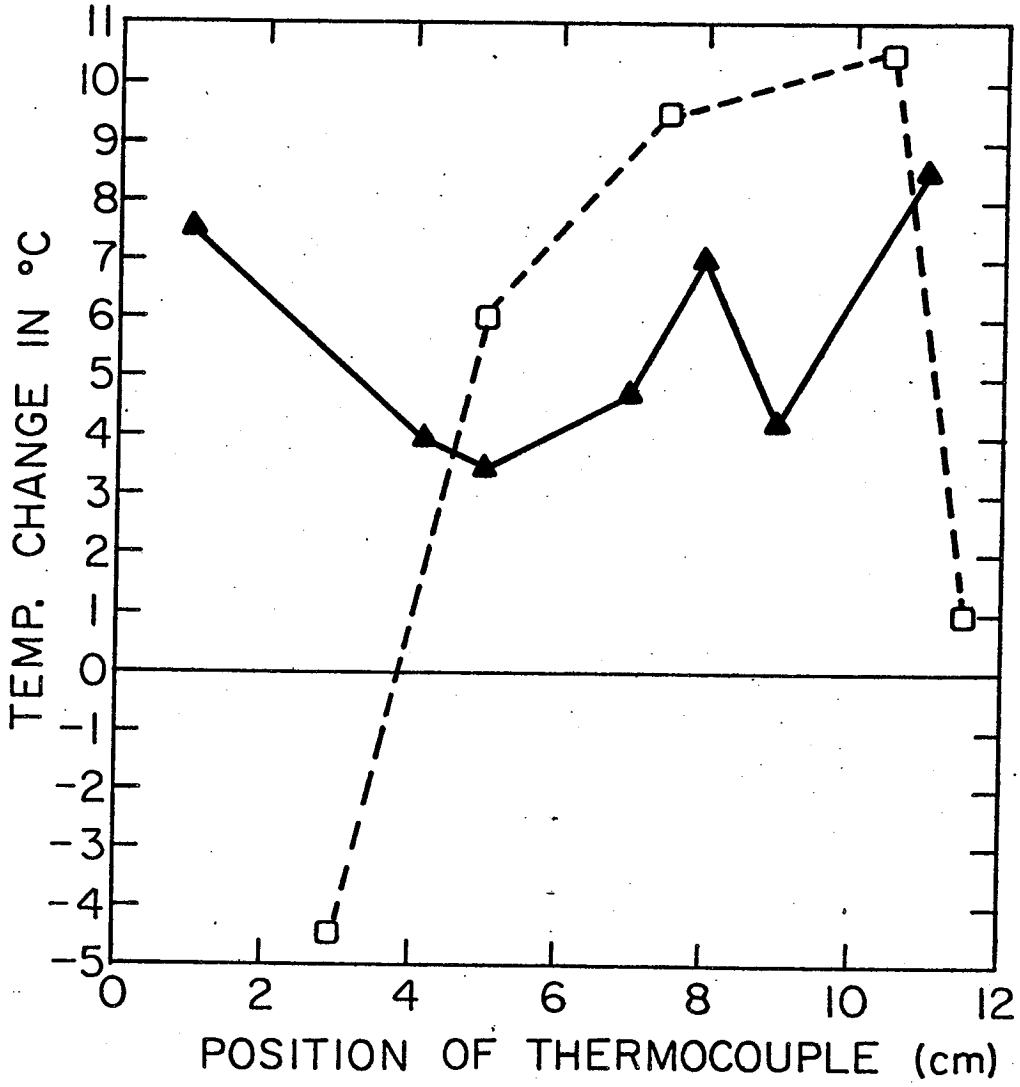

Figure 9. Change in temperature in Bridgman ampoule due to application of transverse magnetic field.

△ = DFT-8 ($In_{0.5}Ga_{0.5}Sb$)

□ - DFT-7 ($In_{0.1}Ga_{0.9}Sb$)

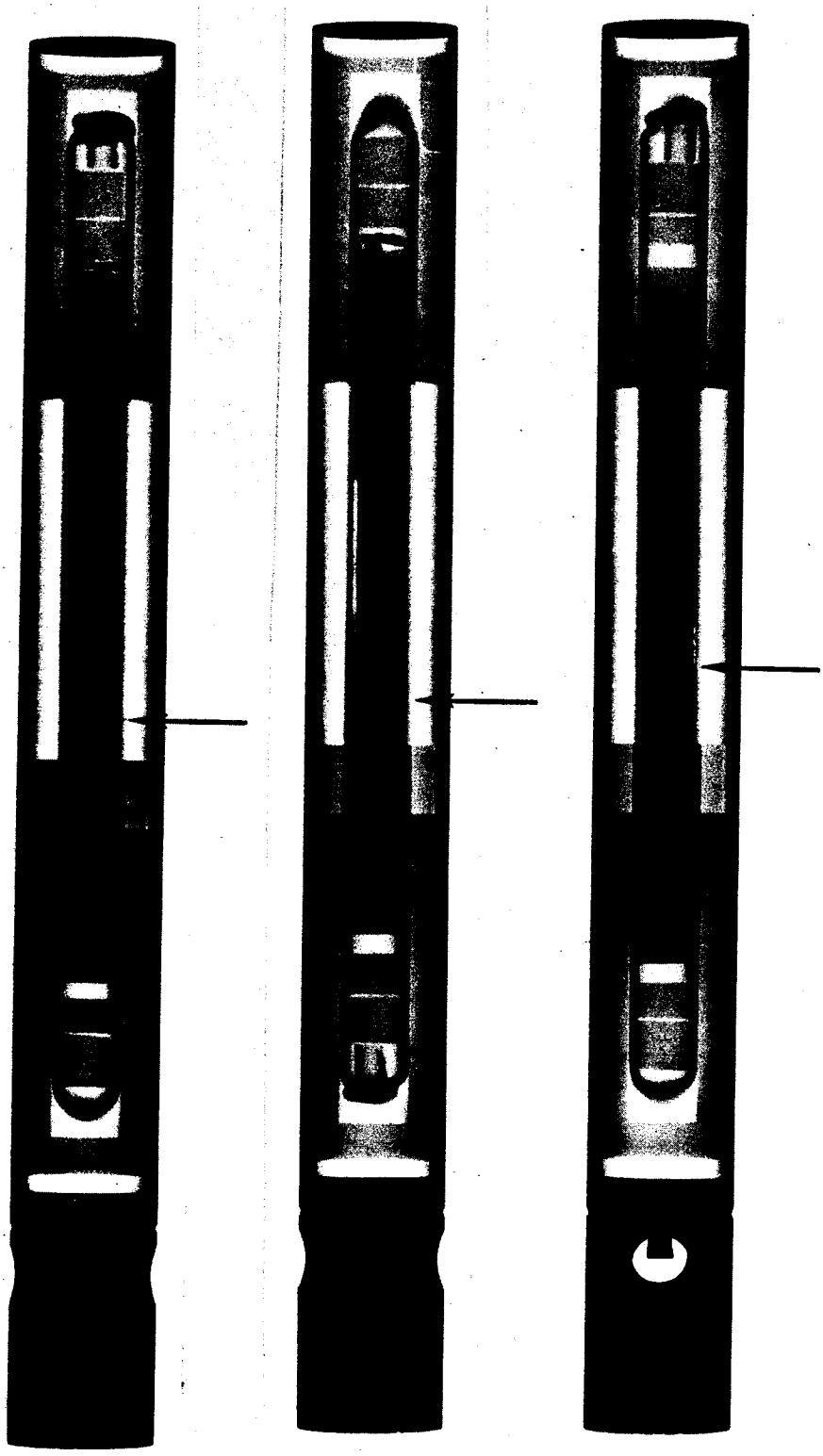

3A 4B 4C

Figure 10. X-ray images of cartridges processed on the ground in a horizontal position. Arrows indicate melt-back position.

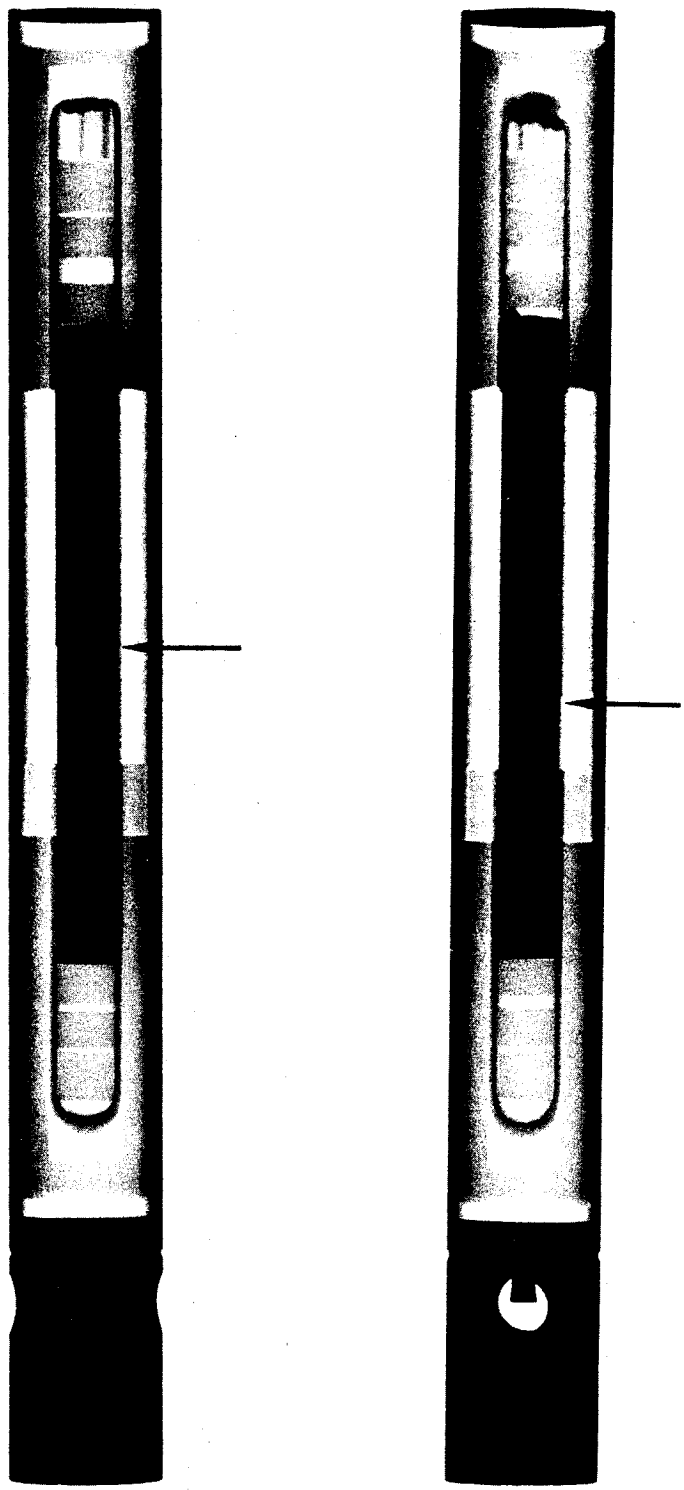

1A 3B

Figure 11. X-ray images of cartridges processed on the ground in a vertical position with the heater on top. Arrows indicate melt-back positions.

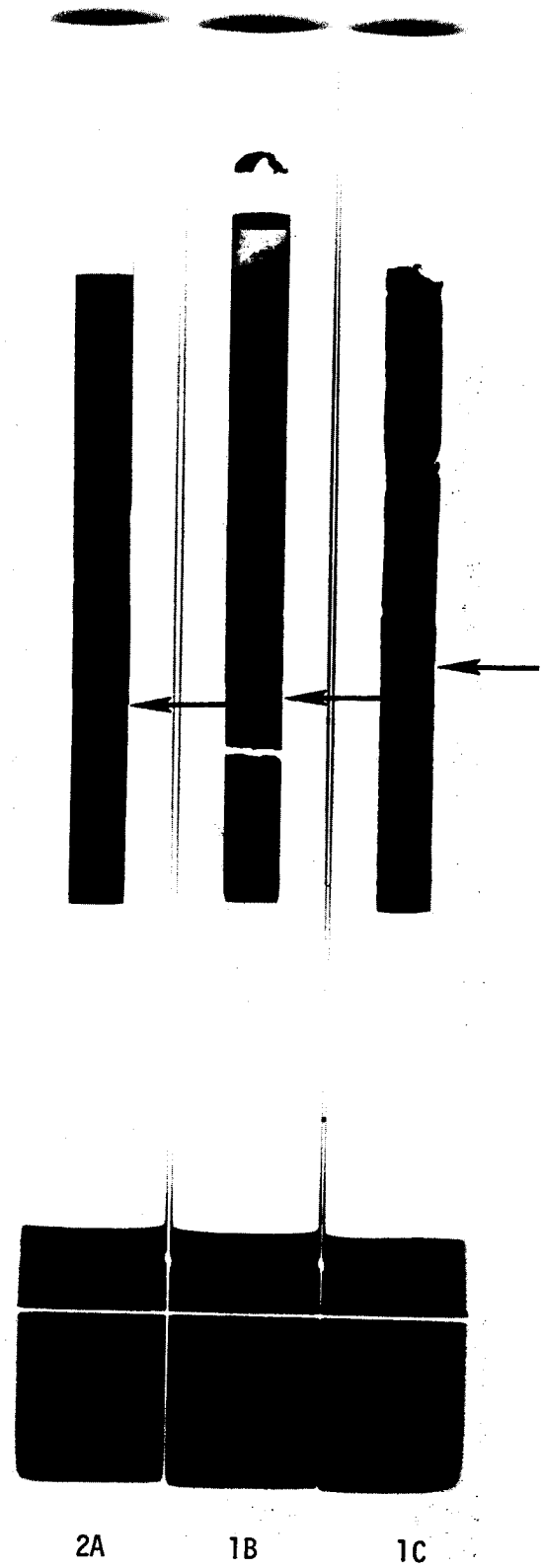

Figure 12. X-ray images of cartridges processed in SL-3. Arrows indicate melt-back positions.

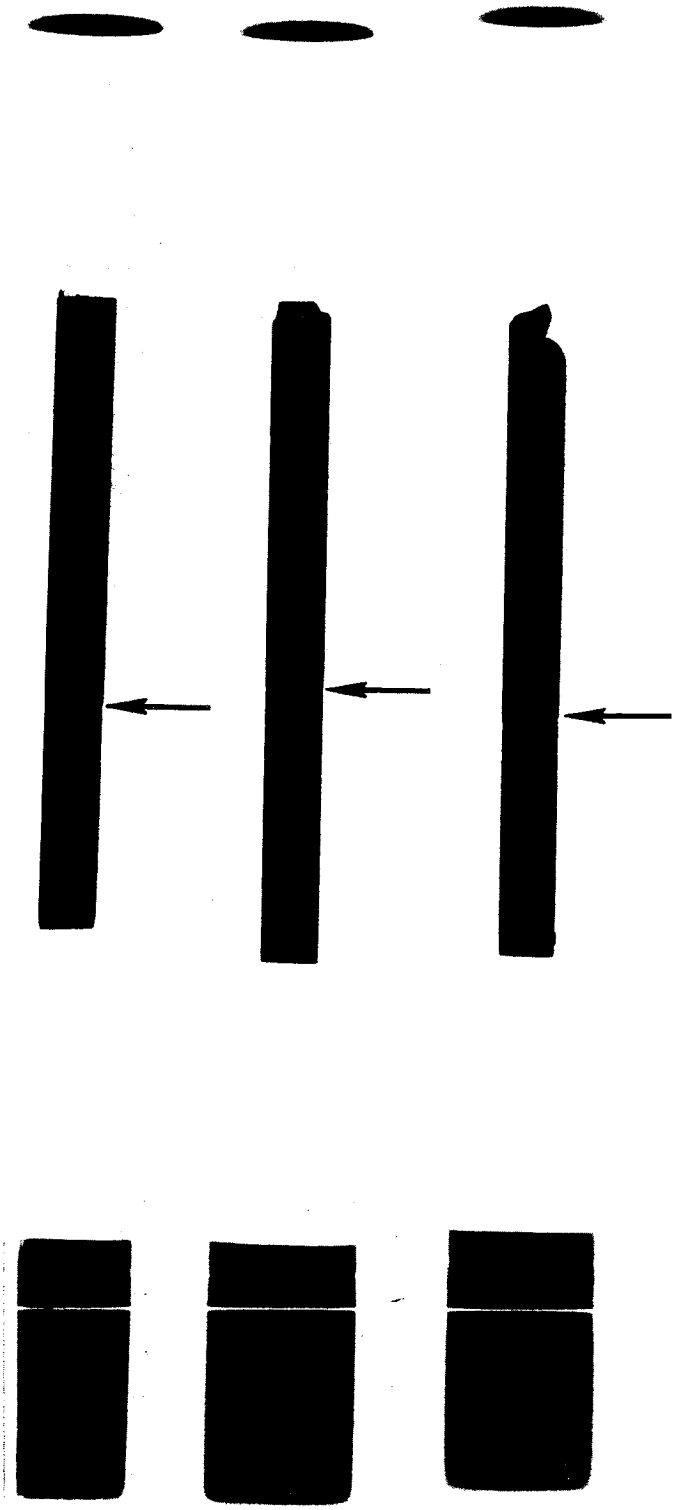

Figure 13. X-ray images of cartridges processed in SL-4. Arrows indicate melt-back positions.

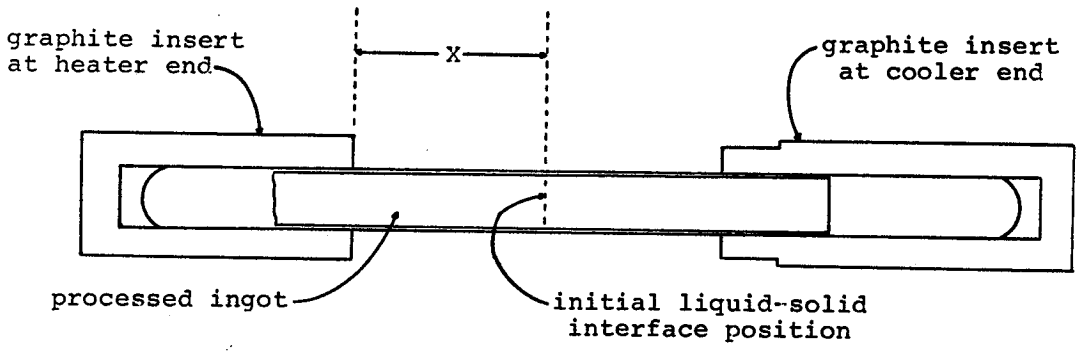

Figure 14. Definition of melt-back position

Free convection was clearly responsible--increasing the thermal transport in the melt without influencing that in the solid. Comparing ingot 3A to 4B, we see that the melting point and geometric effects cancelled. Comparing 4C to 3A, the melting point increase caused the melt-back to decrease, as expected. The first set of Skylab samples showed less meltback than the earth grown samples; from the geometric factors we would expect more meltback. This was probably due to the melt not contacting the ampoule wall. The second set of Skylab samples showed more melt-back due to the higher initial temperature of the heater.

The silica ampoules were removed from both the NASA and the USC processed ingots by soaking in HF for up to 2 days. The NASA samples were then sandblasted to reveal the external grain structure, as shown in Figure 15. In all ingots, the slowly refrozen region contained elongated grains. The original casting and the portion in the heater which refroze rapidly were both dendritic.

Both the NASA and the USC ingots were cut longitudinally with an abrasive wire saw. The horizontally-processed ingots were cut parallel to the gravitational field during solidification. One-half

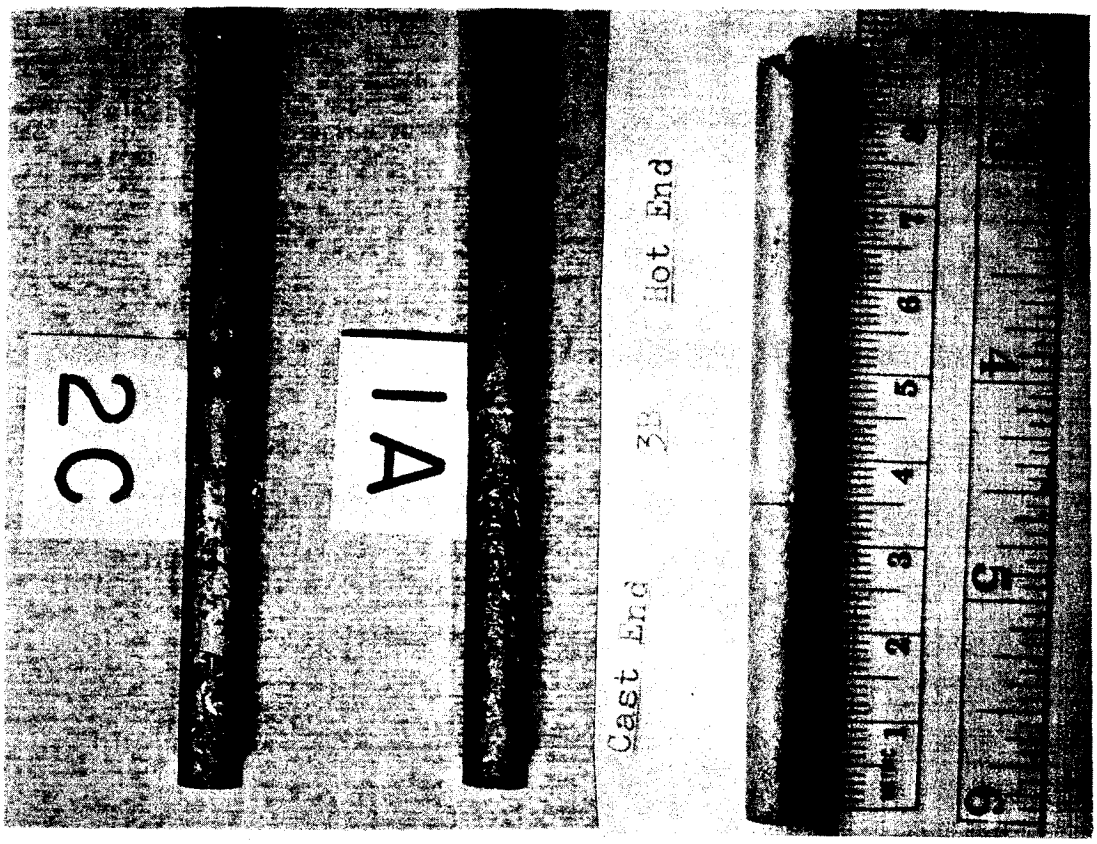

Figure 15(a). Sandblasted NASA ingots processed vertically. Furnace end on top.

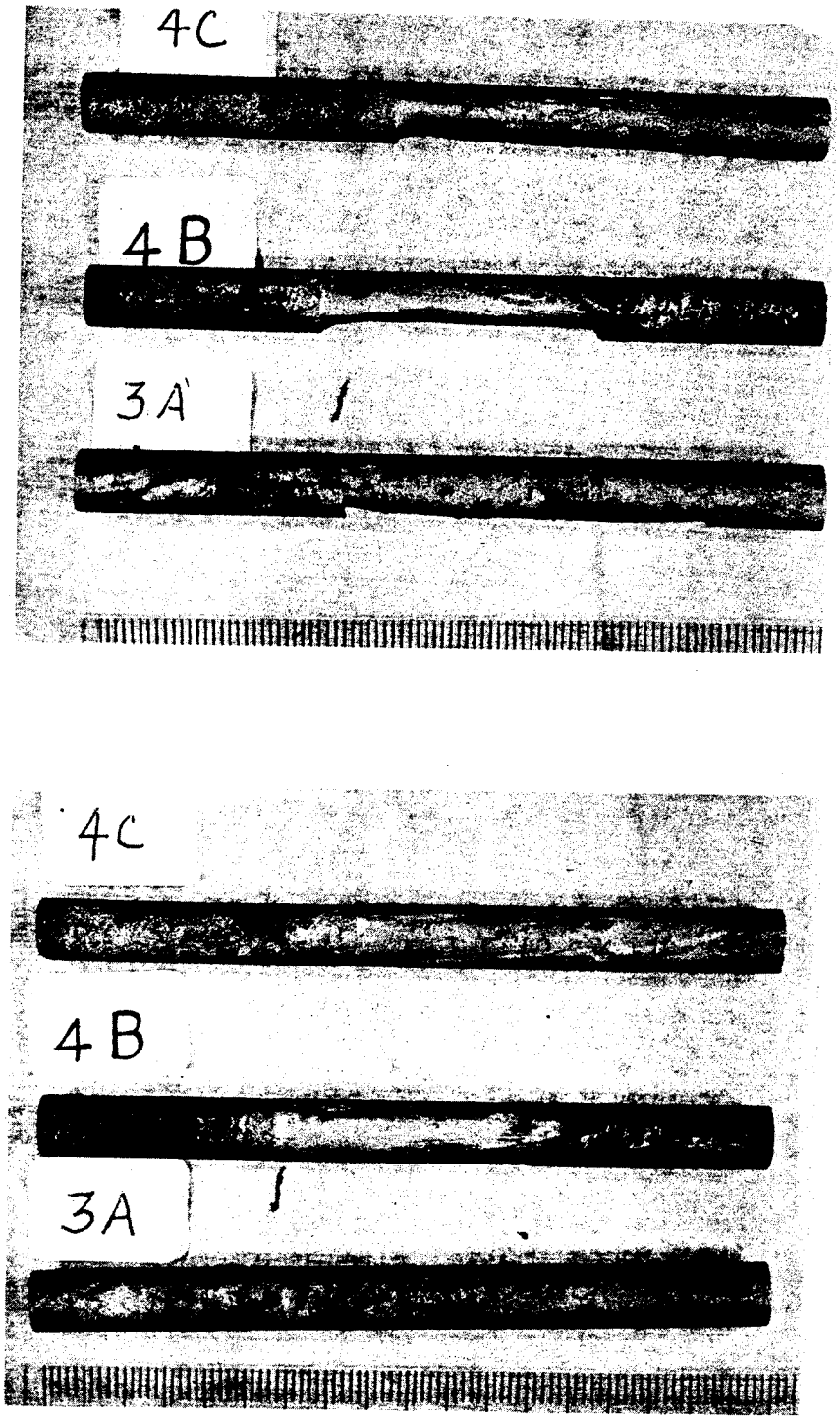

Figure 15(b). Sandblasted NASA ingots processed horizontally. Furnace end on right.

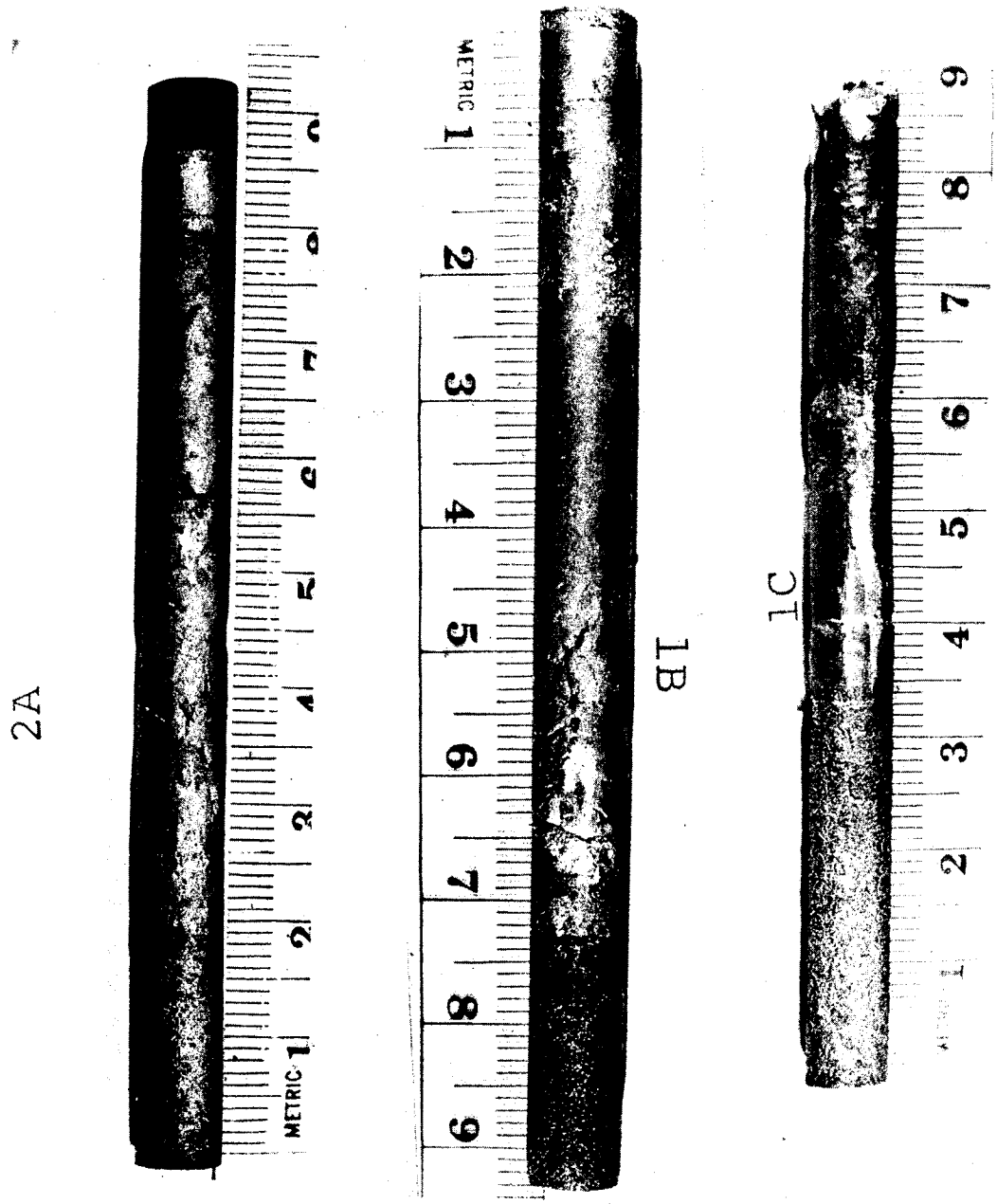

Figure 15(c). Sandblasted NASA ingots processed in SL-3. Furnace end on top.

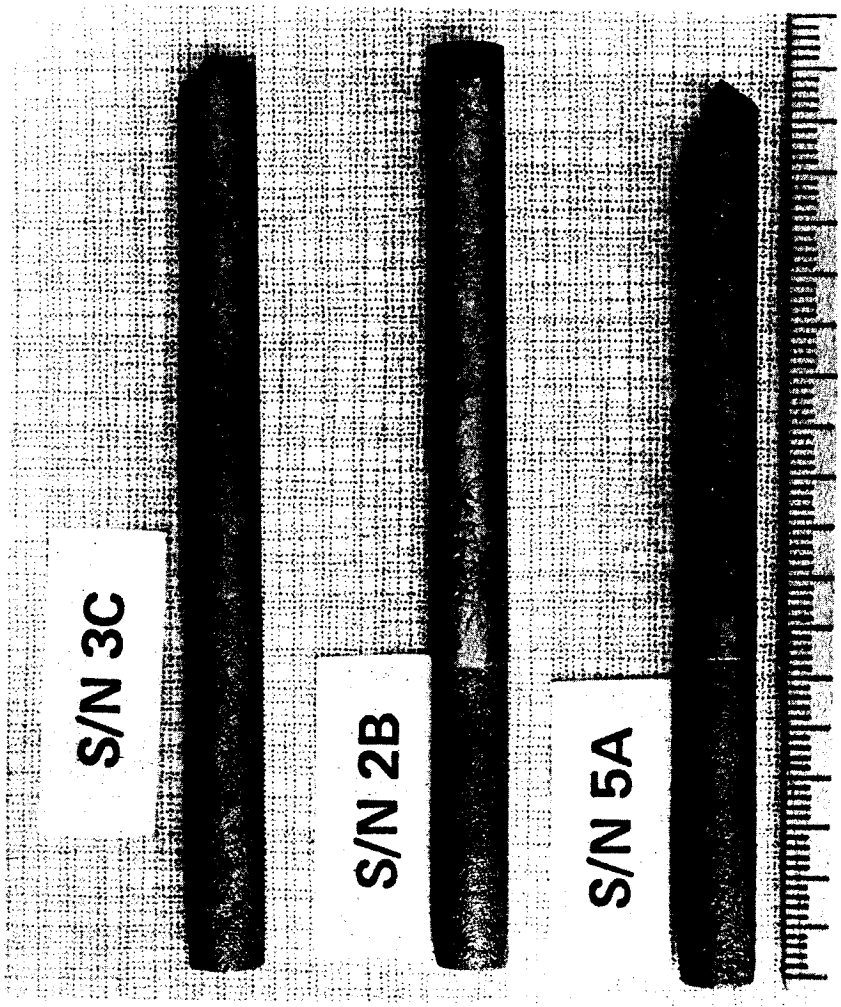

Figure 15(d). Sandblasted NASA ingots processed in SL-4. Furnace end on top.

1A

2C

Figure 15(e). Close up photographs of sandblasted NASA ingots processed vertically, with heater portion on top.

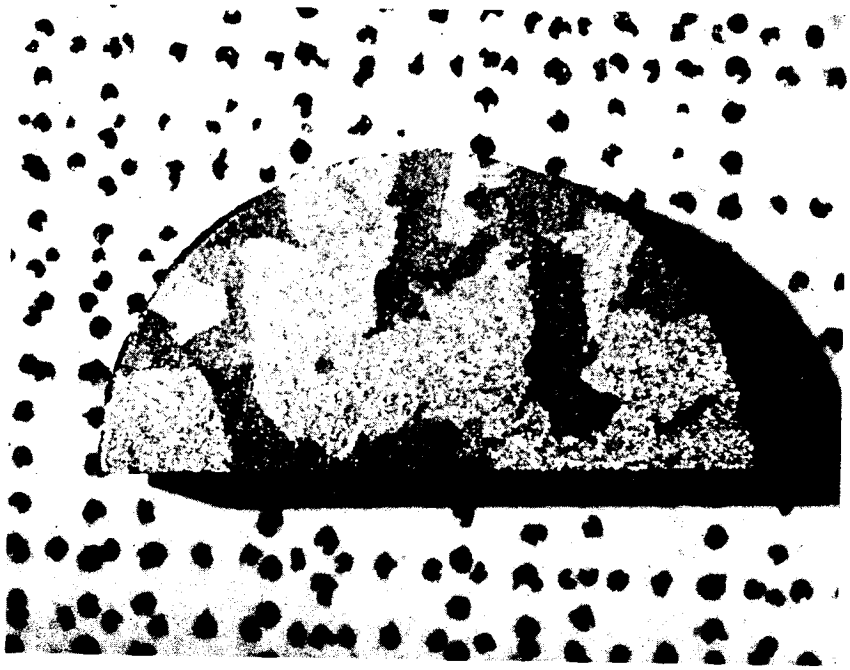

Figure 17(a). Sandblasted cross-sectional slice from ingot 1C (SL-3) about 4 mm from initial interface position.

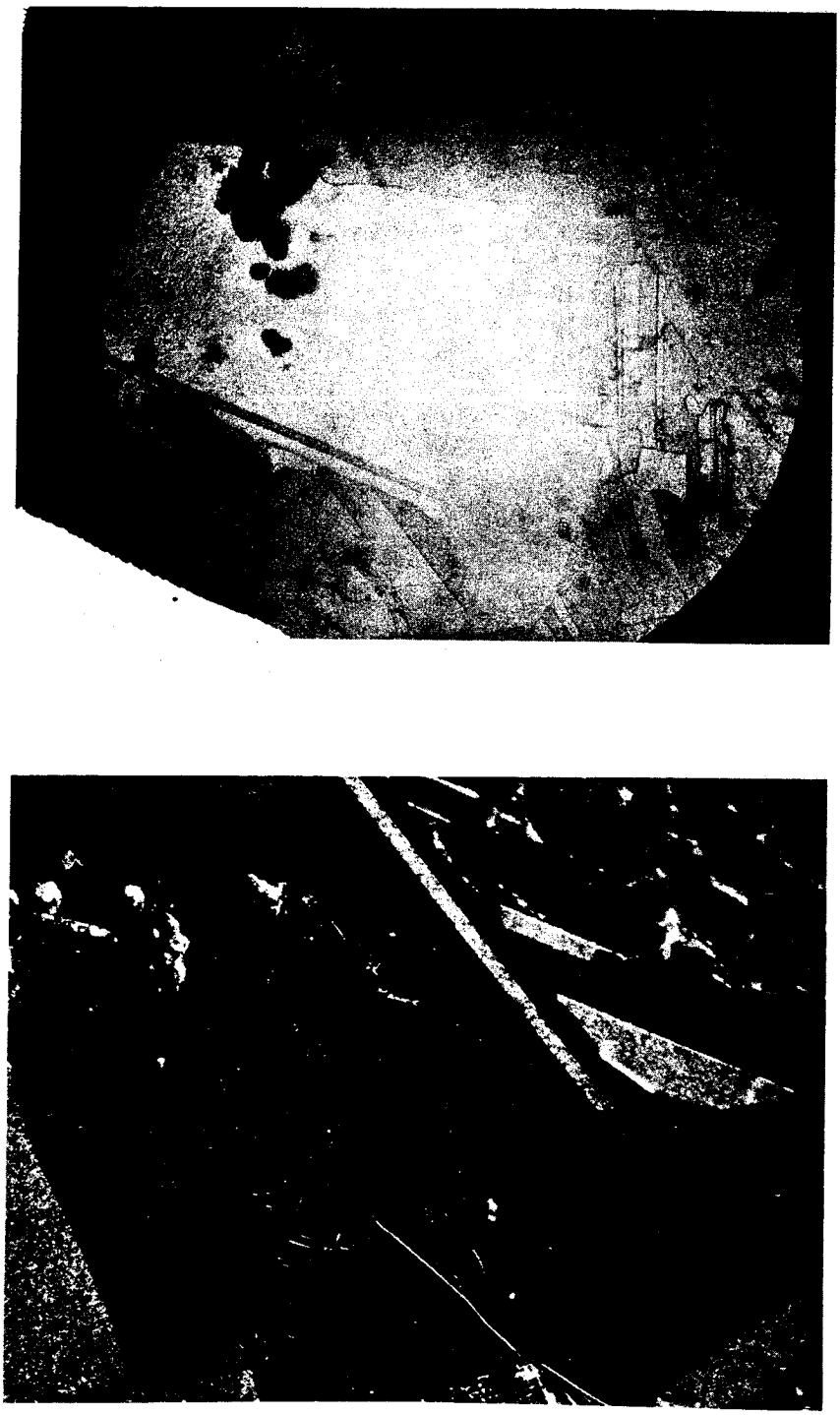

Figure 17(b). Cross-sectional slices of ingot 2C, processed vertically by NASA.

Etched in $2HF:2HA_c:3HNO_3$.

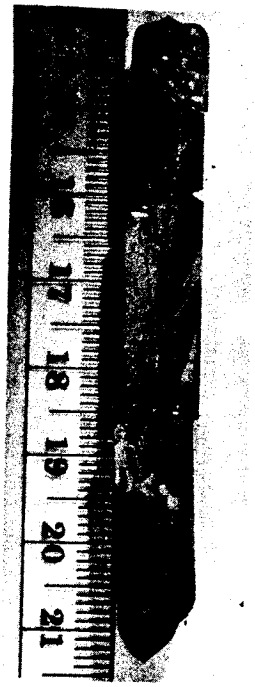

DF-9
$In_{0.5}Ga_{0.5}Sb$

DF-11
$In_{0.5}Ga_{0.5}Sb$

Figure 18(a). USC Bridgman-grown ingots.

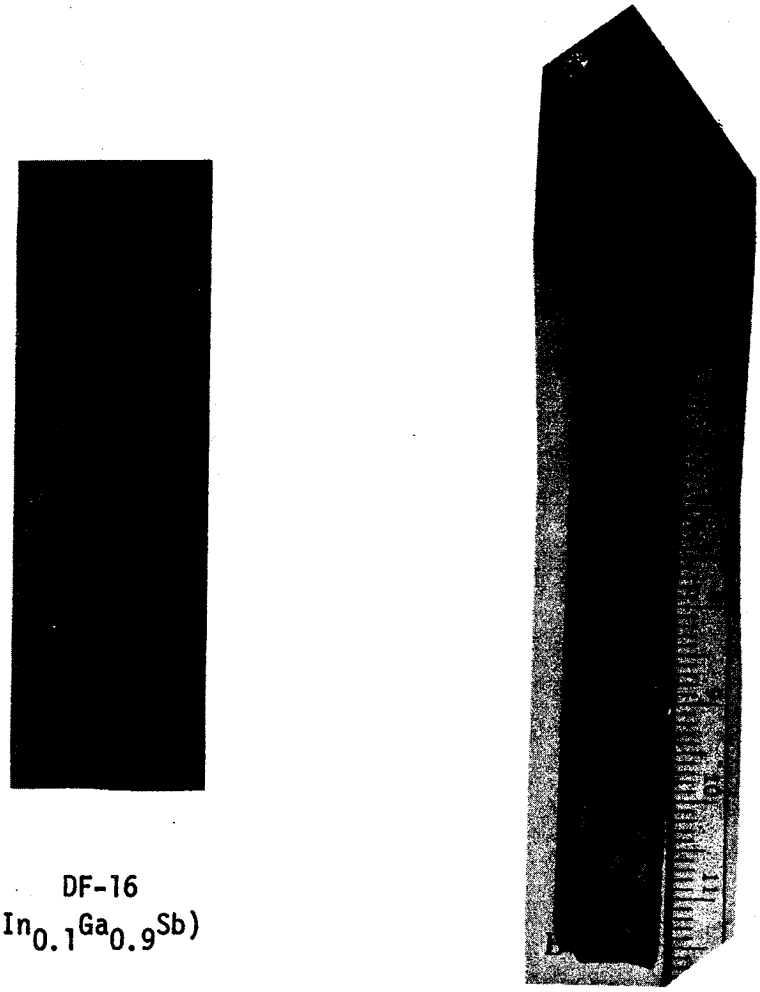

DF-16
($In_{0.1}Ga_{0.9}Sb$)

DF-17 ($In_{0.1}Ga_{0.9}Sb$)

Figure 18(b). USC Bridgman-Grown ingots.

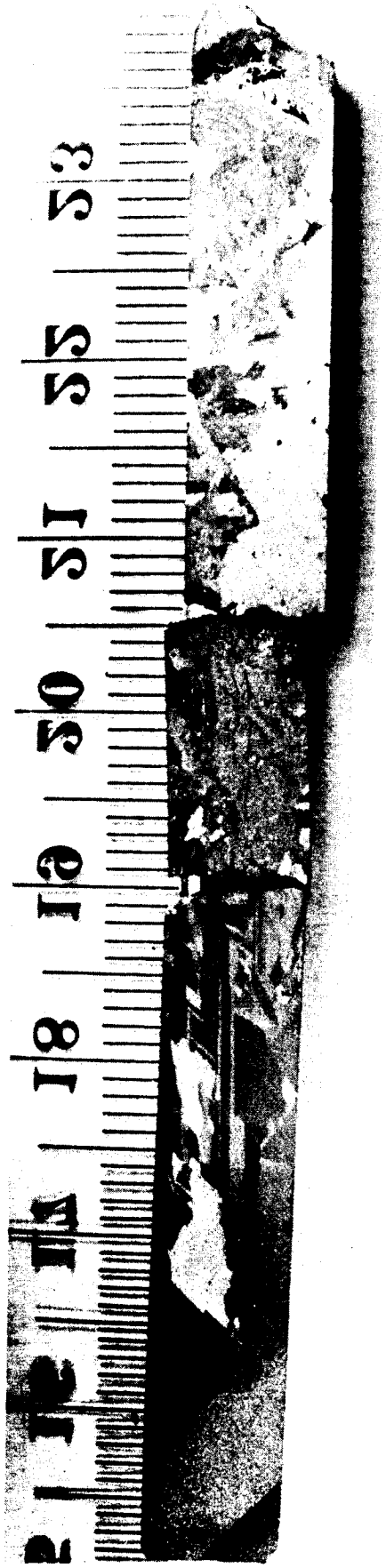

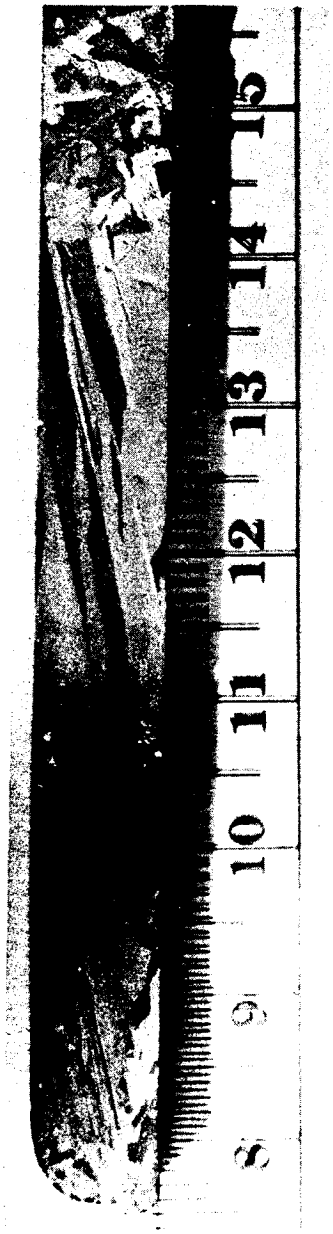

GF-6

GF-10

Figure 19. USC Gradient-frozen ingots of $In_{0.1}Ga_{0.9}Sb$.

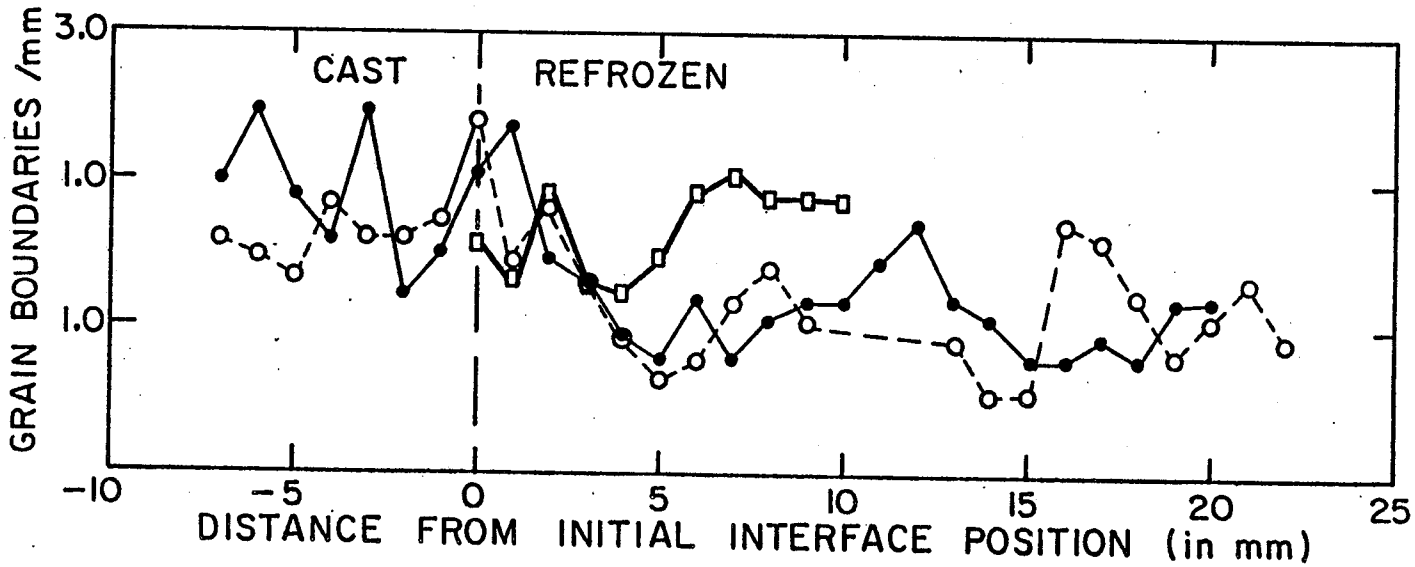

Figure 20. Distribution of grain boundaries in NASA $In_{0.5}Ga_{0.5}Sb$ ingots.

□ - Horizontally processed

○ - SL-3 processed

● - SL-4 processed

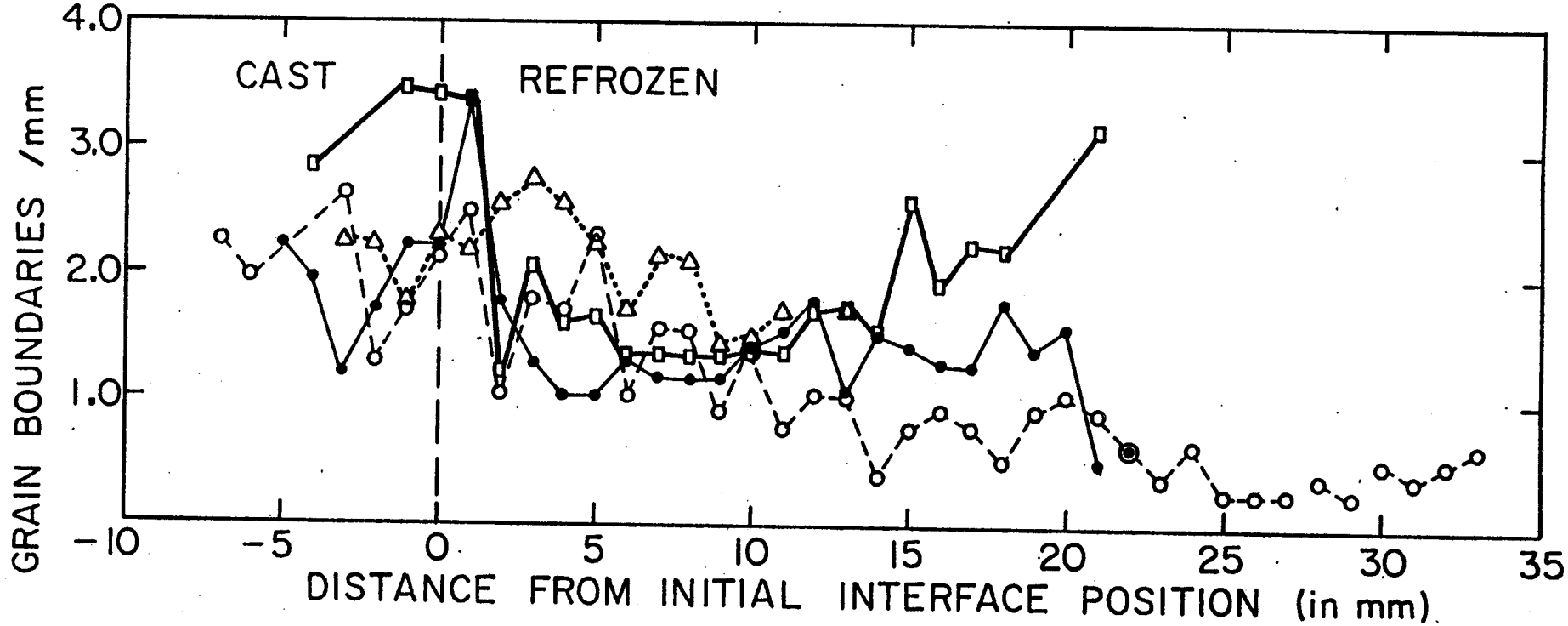

Figure 21. Distribution of grain boundaries in NASA $In_{0.3}Ga_{0.7}Sb$ ingots.

△ - Vertically processed

□ - Horizontally processed

○ - SL-3 processed

● - SL-4 processed

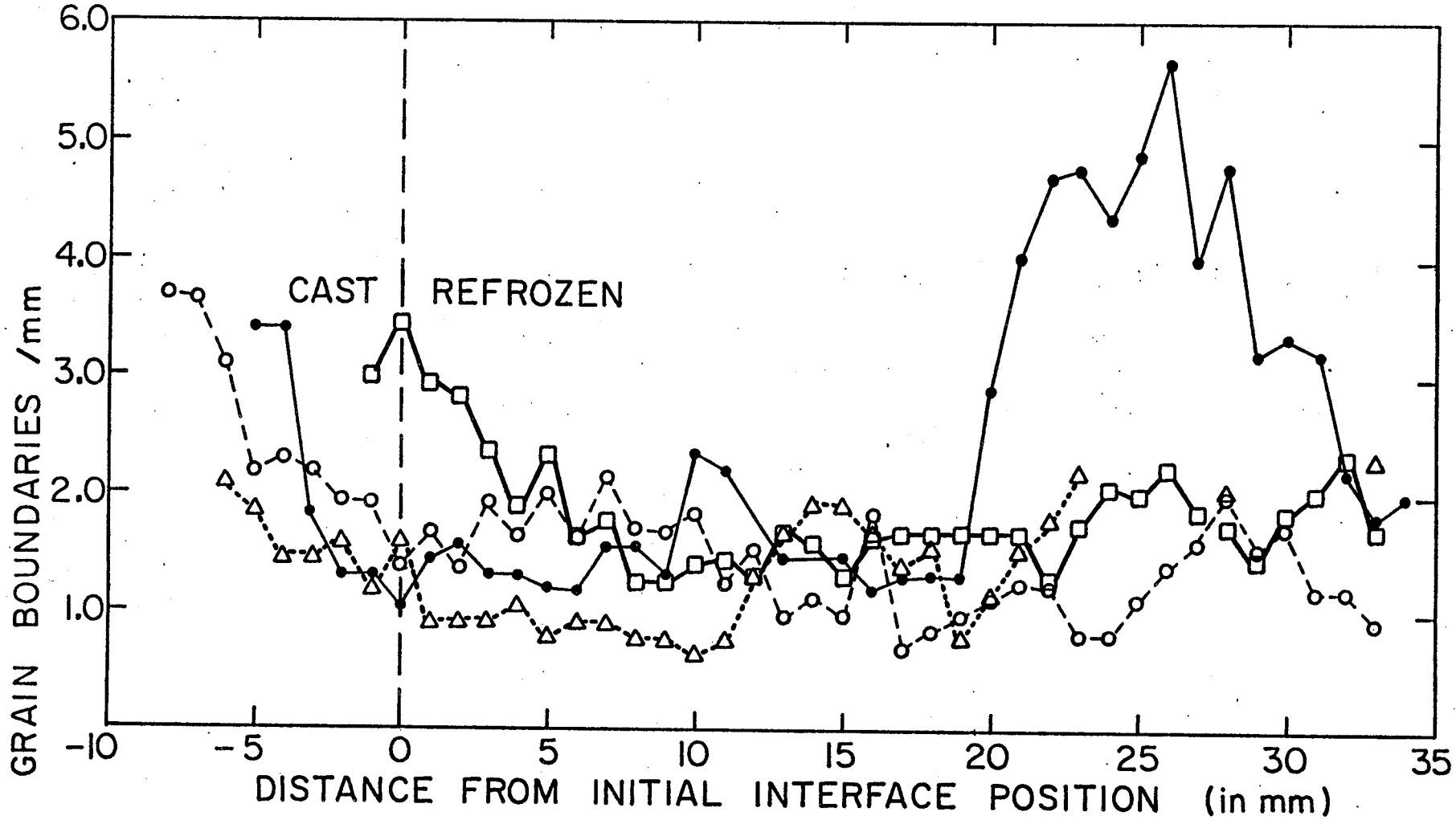

Figure 22. Distribution of grain boundaries in NASA $In_{0.1}Ga_{0.9}Sb$ ingots.

△ - Vertically processed

□ - Horizontally processed

O - SL-3 processed

● - SL-4 processed

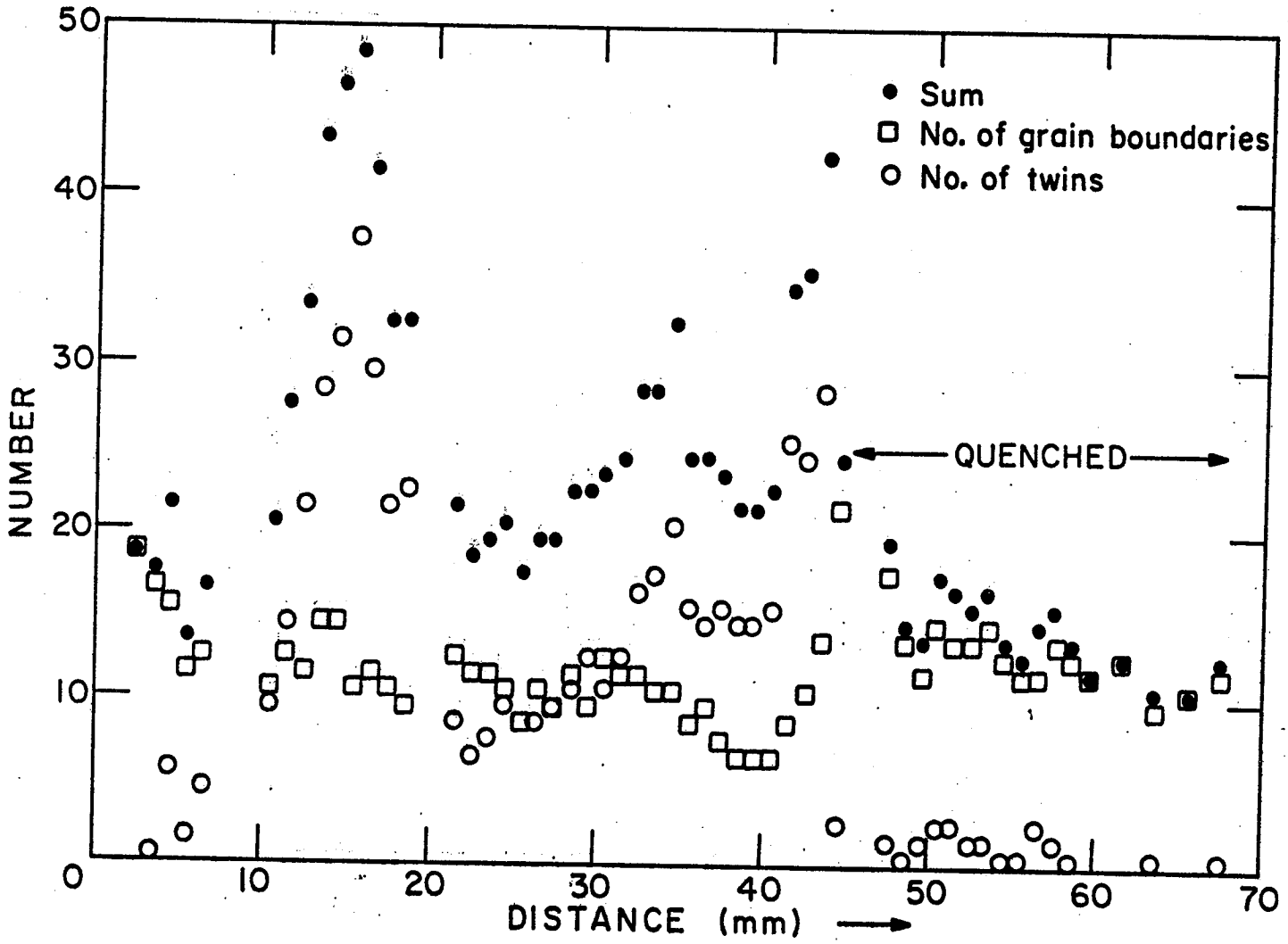

Figure 23(a). Distribution of grain and twin boundaries for USC Bridgman ingot DF-9 with original composition $In_{0.}$ $Ga_{0.}$ Sb.

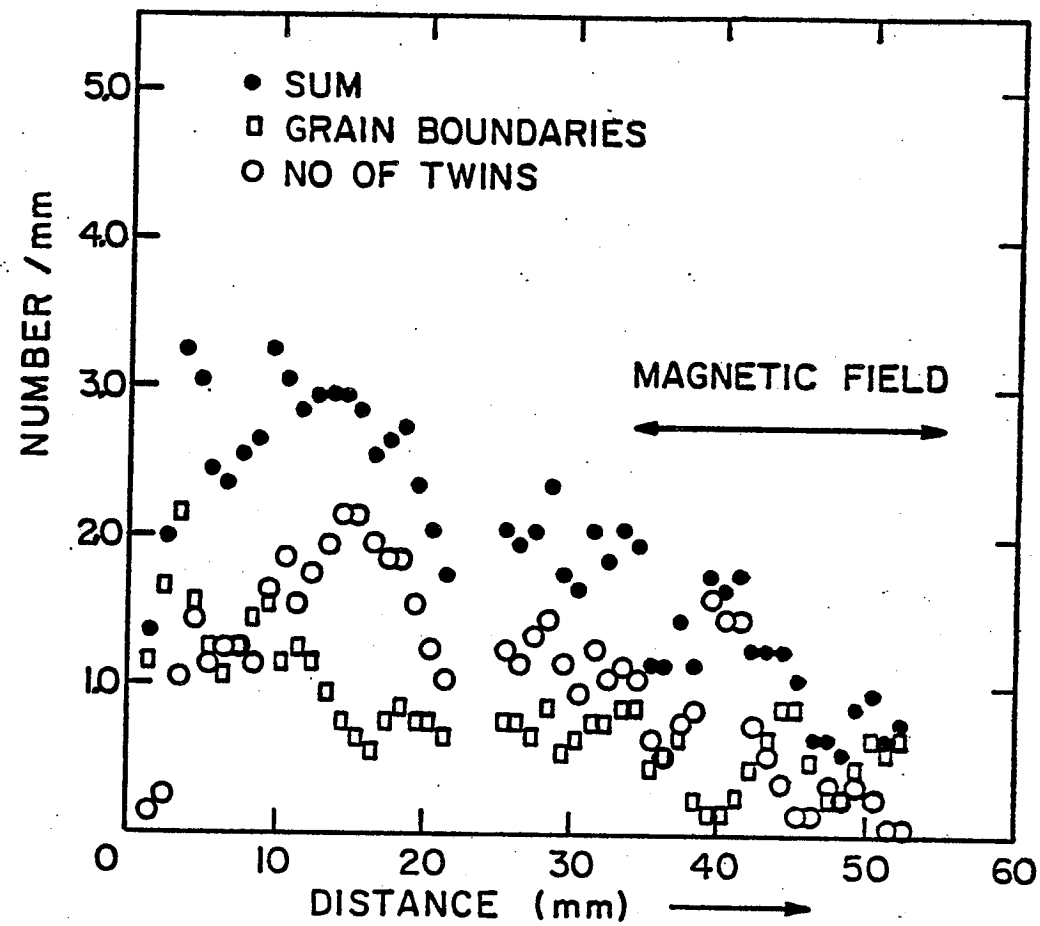

Figure 23(b). Distribution of grain and twin boundaries for USC Bridgman ingot DF-11 with original composition $In_{0.}$ $Ga_{0.}$ Sb.

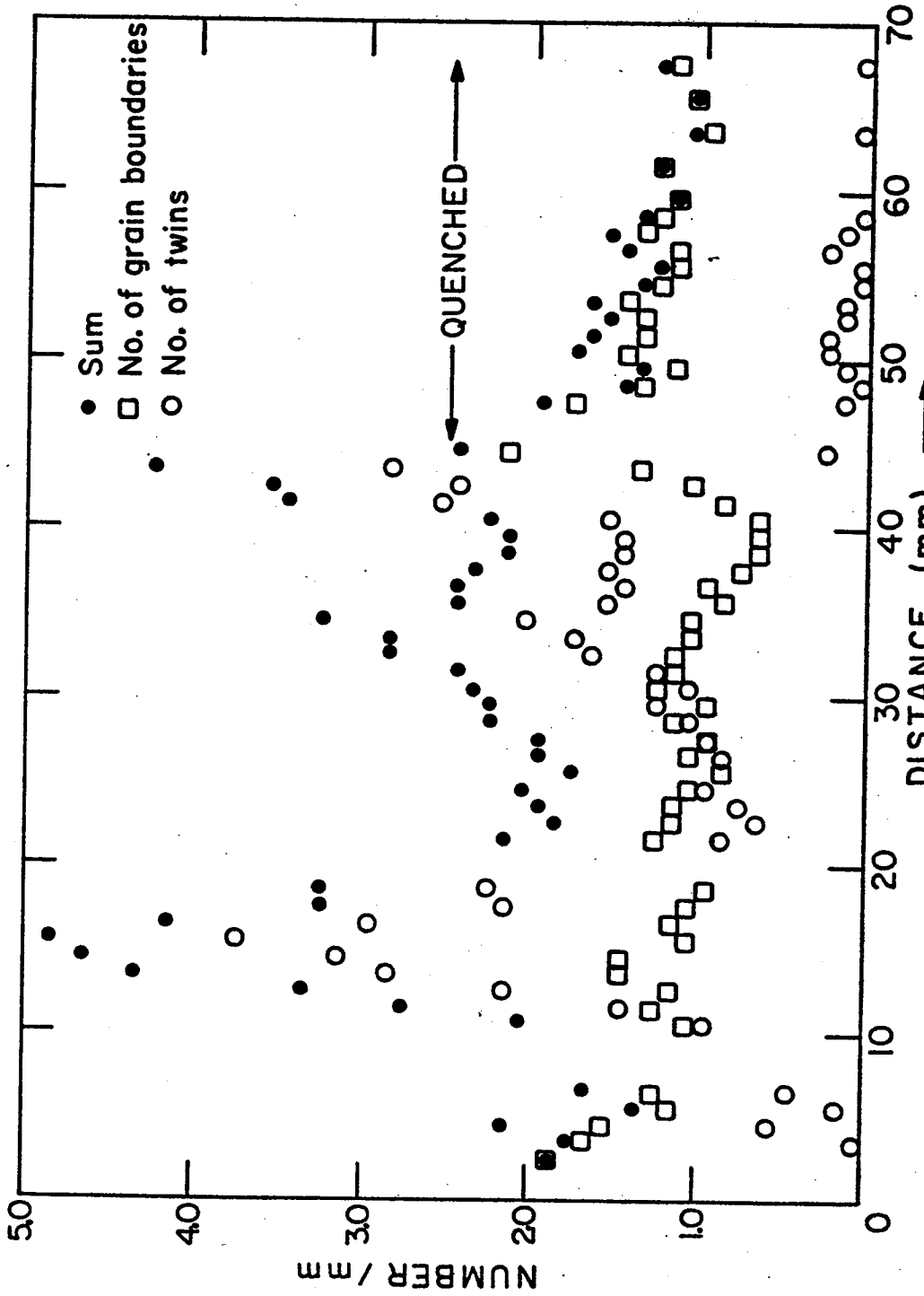

FIGURE 24. Distribution of grain boundaries and twin boundaries for sample DF-9 $In_{0.5}Ga_{0.5}Sb$

D. Twins

The number of twin boundaries was similarly counted, as shown in Figures 23-27. The number of twins increased at first, particularly in the earth-processed ingots. After the initial increase, the number of twins decreased, except in the horizontally-processed ingots. Twinning decreased as the In content of the initial melt increased. Twinning was much less in the space-processed ingots, particularly as the In concentration increased. The USC Bridgman experiments seem to indicate that imposition of the magnetic field caused twinning to decrease, but more experiments are needed to verify this.

E. Bubbles

Gas bubbles, or voids, were found in all of the NASA samples. Examples are shown in Figure 28. Since the NASA ampoules were back-filled with some helium, these were presumably filled with helium. The USC ampoules were sealed with a much lower gas pressure, and so no bubbles formed, as expected (5).

As shown in Figures 29-31, the void distribution was different in the earth-grown and space-grown samples. For the samples grown on earth, particularly those processed horizontally, the voids were concentrated at the initial liquid-solid interface. This congregation also served to show that the initial interface was planar, indicating that the heat flow was longitudinal as desired. For the samples grown horizontally, in addition to the voids at the initial interface, there were also voids along the side which was on top (at the free melt surface) during solidification. The space-processed ingots had voids dispersed throughout the slowly grown region. Those processed in SL-4 seemed to have somewhat fewer bubbles than the SL-3 ingots.

F. Cracks

Figures 15 and 16 show that microcracks developed in the ingots. Examination of the grain structure near the cracks indicated that some cracks inhibited grain growth, others initiated new grains,

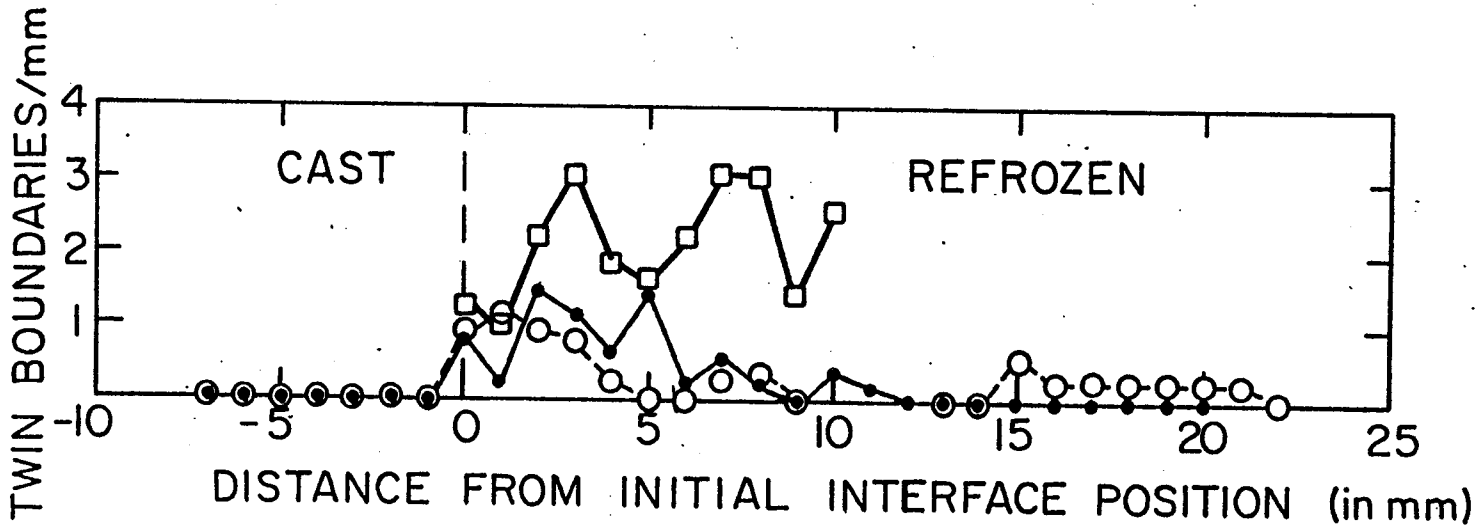

Figure 25. Distribution of twin boundaries in NASA $In_{0.5}Ga_{0.5}Sb$ ingots.

□ - Horizontally processed

○ - SL-3 processed

● - SL-4 processed

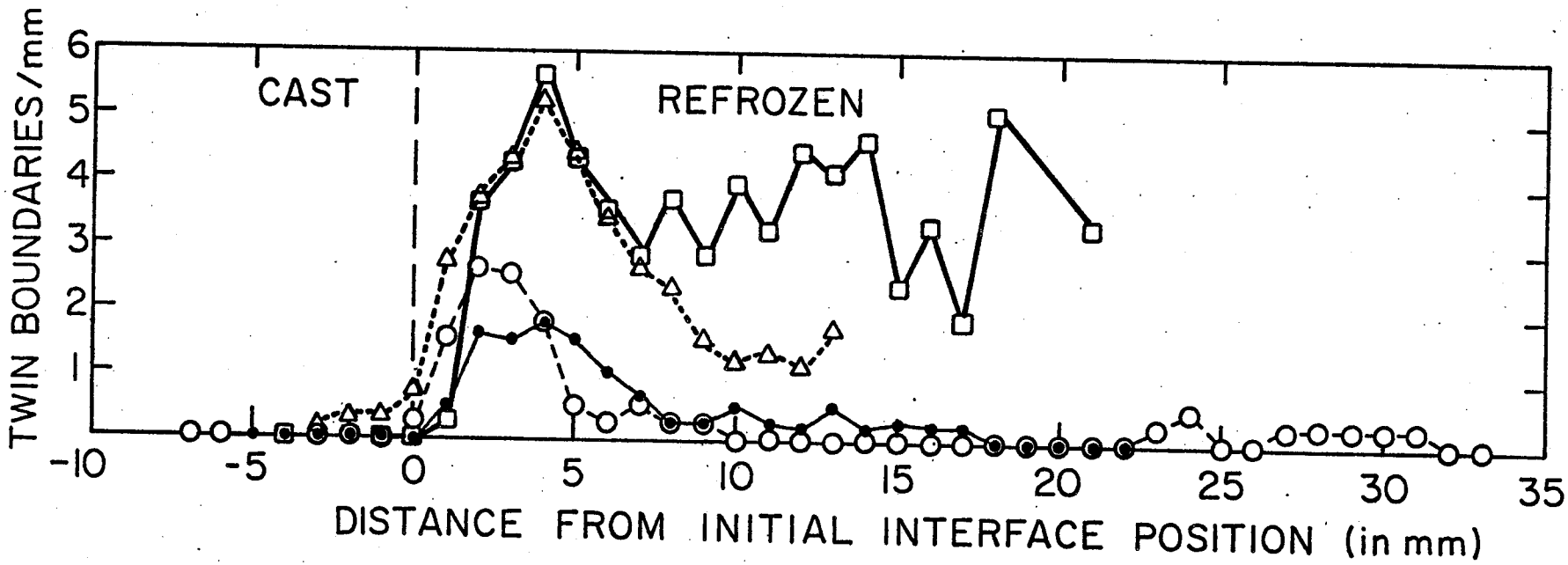

Figure 26. Distribution of twin boundaries in NASA $In_{0.3}Ga_{0.7}Sb$ ingots.

□ - Vertically processed
△ - Horizontally processed
○ - SL-3 processed
● - SL-4 processed

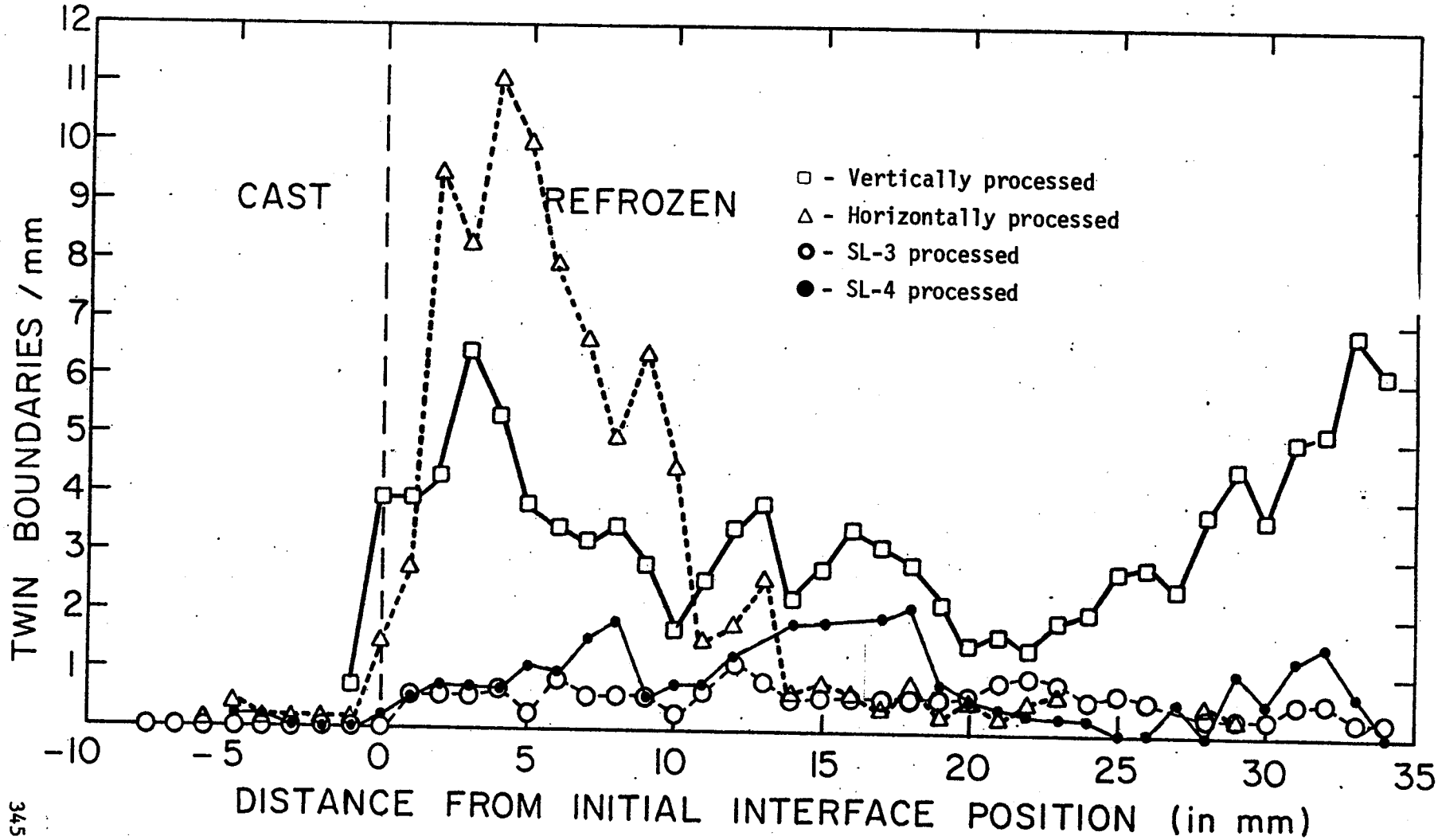

FIGURE 27. DISTRIBUTION OF TWIN BOUNDARIES IN NASA $In_{0.1}Ga_{0.9}Sb$.

3A

4A

Figure 28(a). Gas bubbles as seen on cross-sectional slices of NASA horizontally processed ingots, near initial interface.

Figure 28(b). Gas bubbles as seen in SL-3 ingot 1B.

Figure 28(c). Gas bubbles as seen in SL-3 ingot 2A.

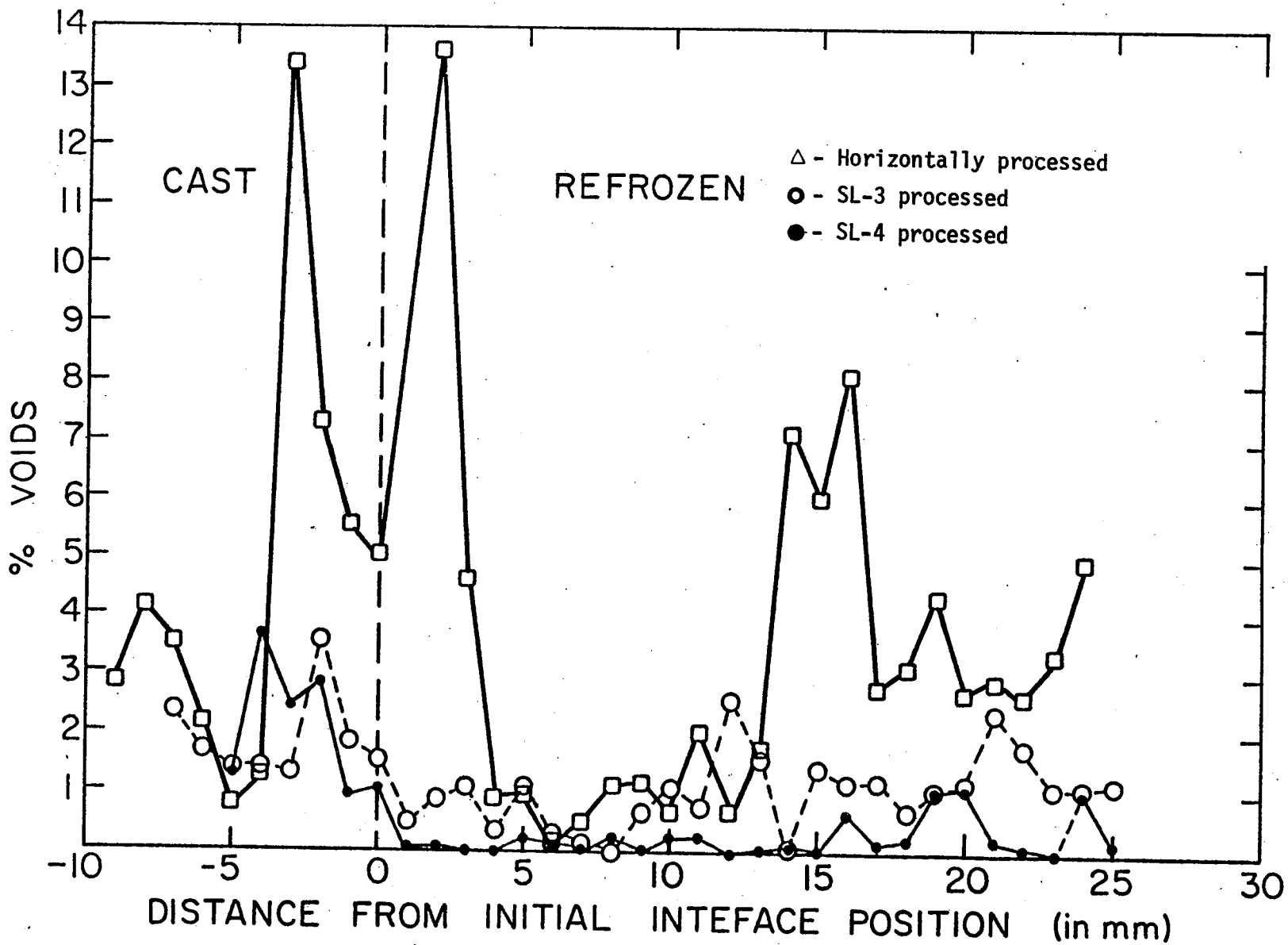

FIGURE 29. VOID DISTRIBUTION IN NASA $In_{0.5}Ga_{0.5}Sb$ INGOTS

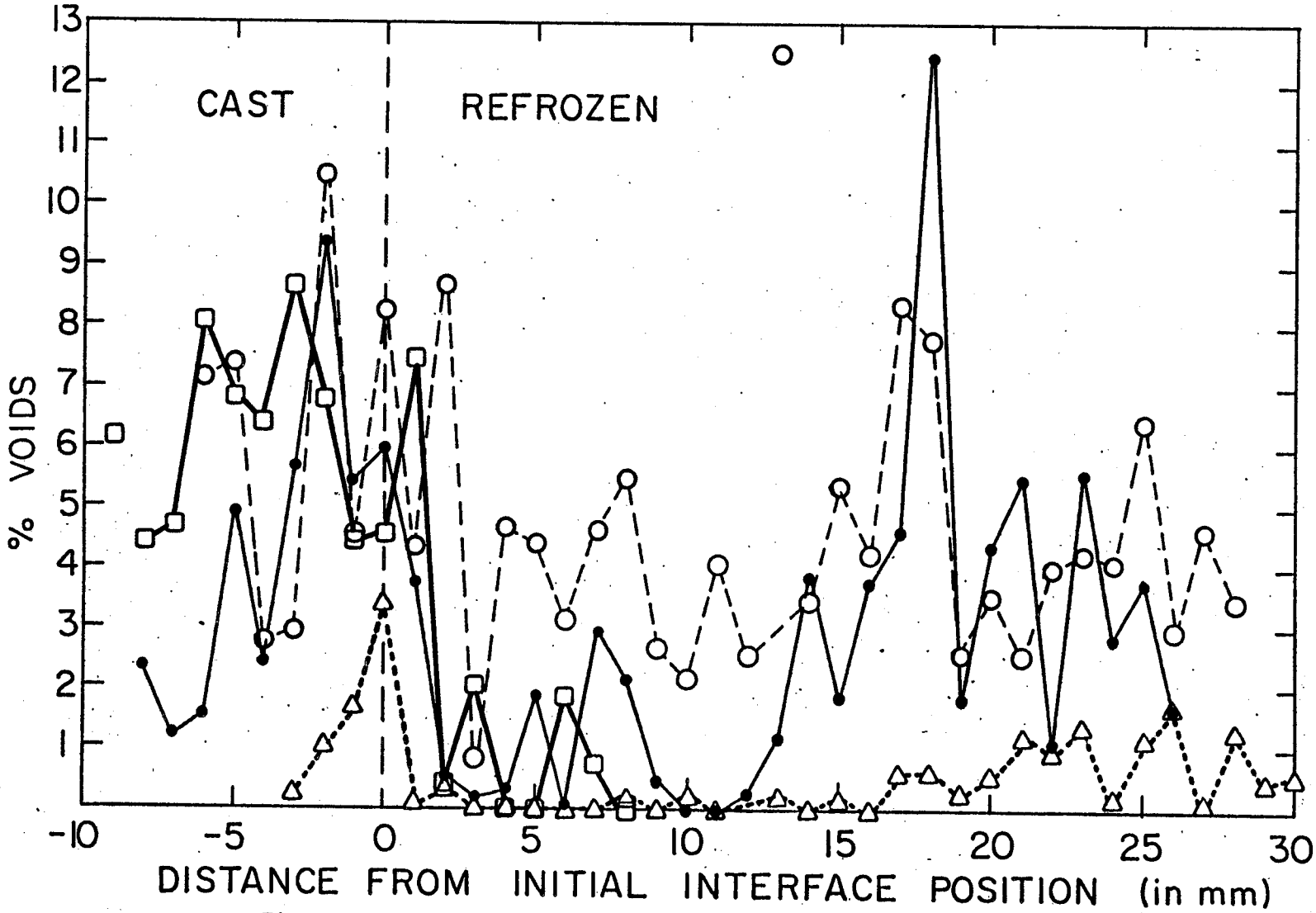

Figure 30. Void distribution in NASA $In_{0.3}Ga_{0.7}Sb$ ingots.

□ - Vertically processed

△ - Horizontally processed

○ - SL-3 processed

● - SL-4 processed

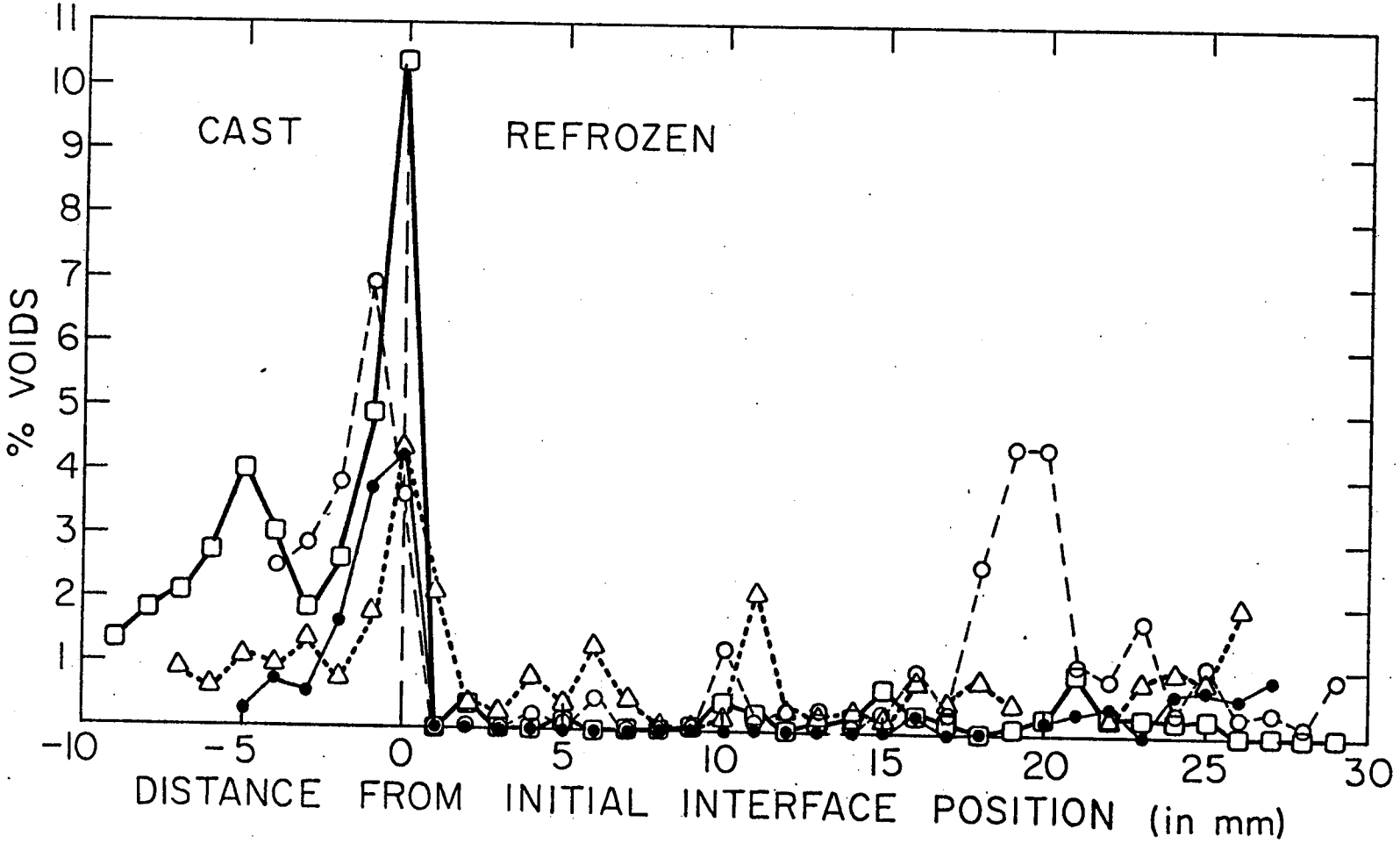

Figure 31. Void distribution in NASA $In_{0.1}Ga_{0.9}Sb$ ingots.

□ - Vertically processed

△ - Horizontally processed

O - SL-3 processed

● - SL-4 processed

and still others did not appear to influence the grain structure. The latter probably developed after solidification during the cool-down. At some cracks, the growth direction of the grains changed.

The distribution of cracks was counted by the same method used for grain boundaries and twins. As shown in Figures 32-34 there were more cracks in the cast portions and the last regrown regions. This is probably due to compositional stresses brought about by constitutional-supercooling generated inhomogeneities.

G. Atomic Absorption Analyses

A Perkin Elmer 306 Atomic Absorption Spectrophotometer was used to analyze for average Ga and In concentration of every third or fourth cross-sectional slice of all NASA ingots. Each slice was ultrasonically cleaned in acetone, chemically polished with 2 HF:3 HNO_3:2 HAc, rinsed in methanol, dried, weighed, dissolved in 5% HCℓ, diluted with deionized water, and analyzed. Figures 35-37 show that the vertically-processed and the Skylab-processed ingots had nearly identical concentration profiles. The concentration profiles in the horizontally-processed ingots are quite different because of the free convective stirring present in those runs. Note also the changes in concentration in the cast portions. These must have occurred during the soak period prior to programming down the heater. Since the castings were not homogeneous, the solid-liquid interface would actually have been a two-phase "mushy zone" in which recrystallization and compositional redistribution would be fairly rapid.

H. Electron Microprobe Analyses

The longitudinal slices were cut into one-inch lengths and final polished. These were analyzed at one millimeter intervals with an electron microprobe in the In characteristic X-ray mode. At least three passes were made over the length of the sample. The results are shown in Figure 38. The scatter which began to occur after several mm of resolidification is indicative of a non-planar interface caused by

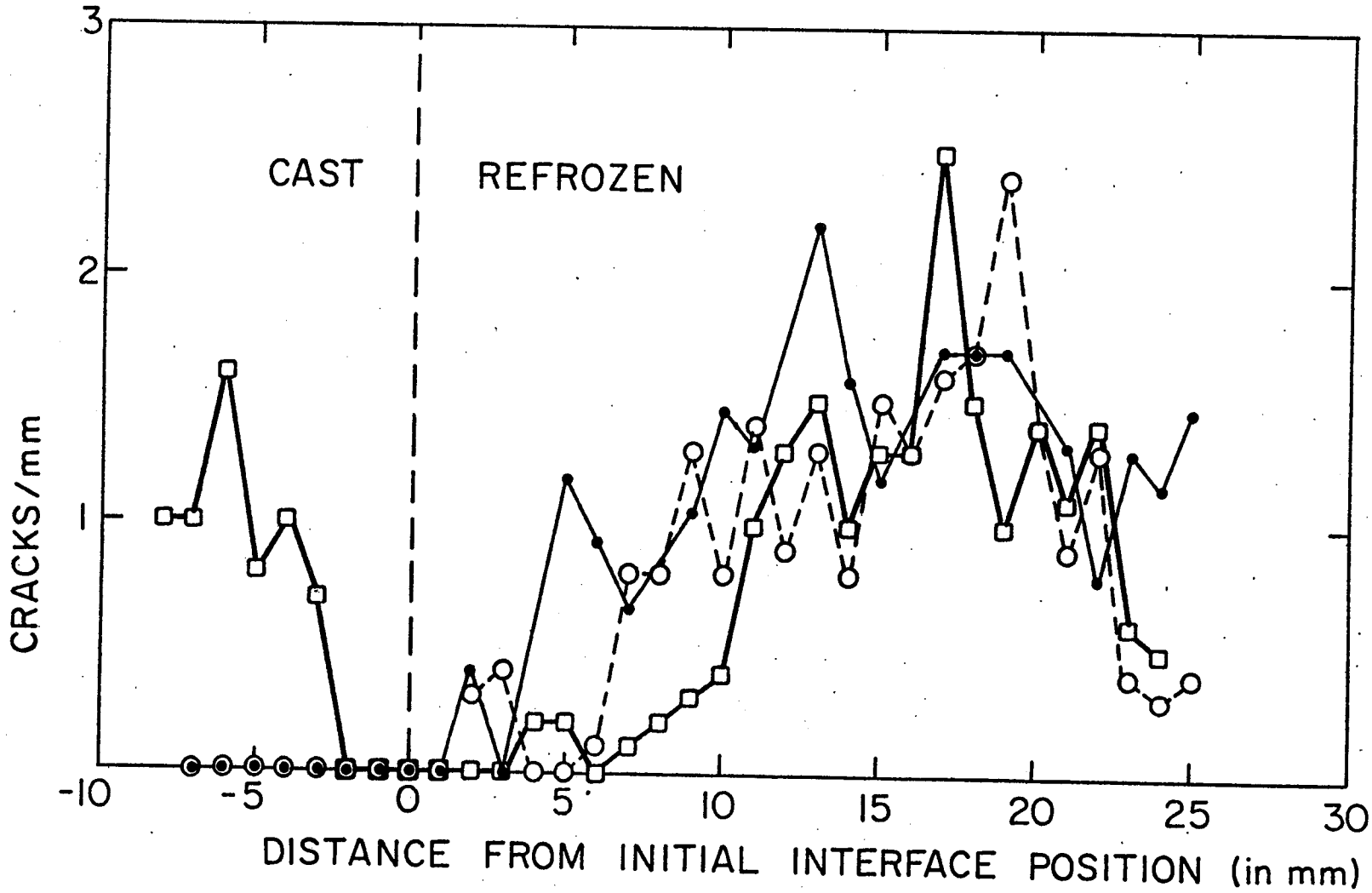

Figure 32. Crack distribution in NASA $In_{0.5}Ga_{0.5}Sb$ ingots.

□- Horizontally processed

O- SL-3 processed

●- SL-4 processed

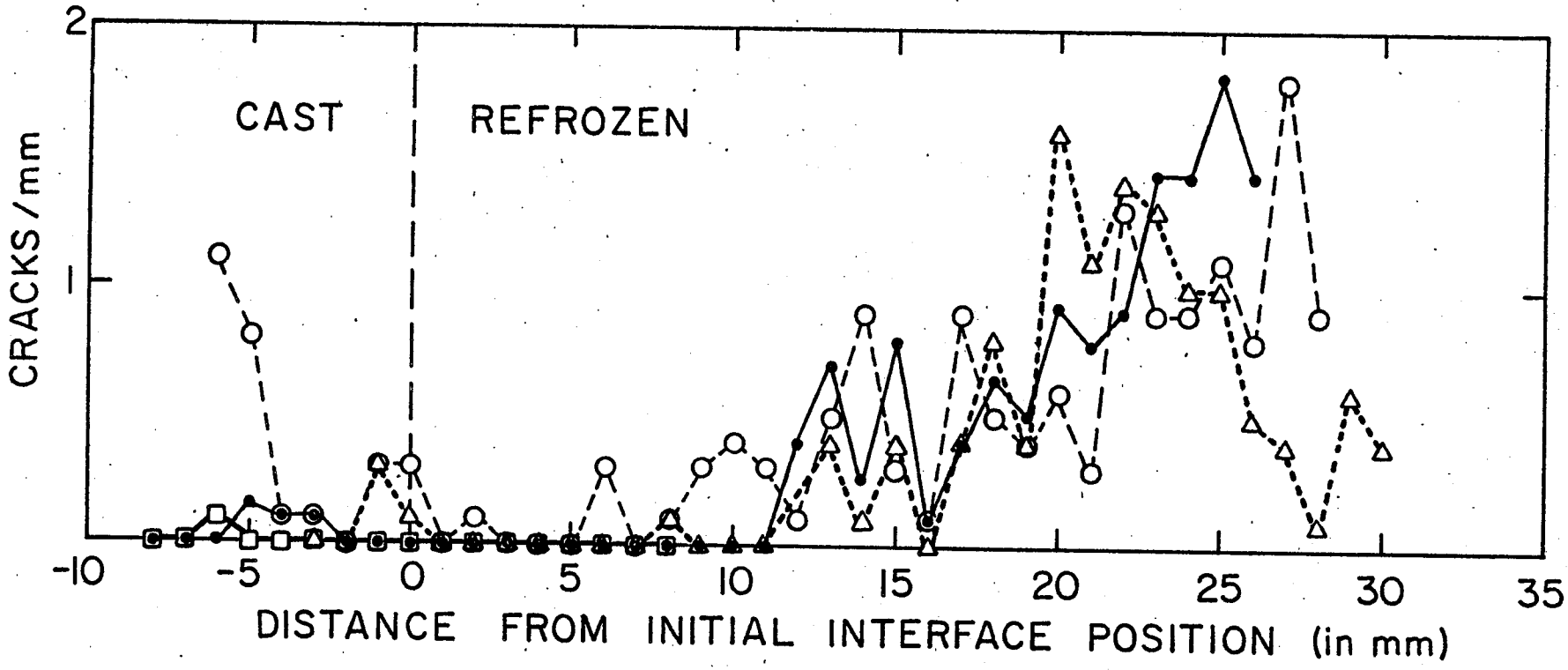

Figure 33. Crack distribution in NASA $In_{0.3}Ga_{0.7}Sb$ ingots.

△ - Vertically processed

□ - Horizontally processed

○ - SL-3 processed

● - SL-4 processed

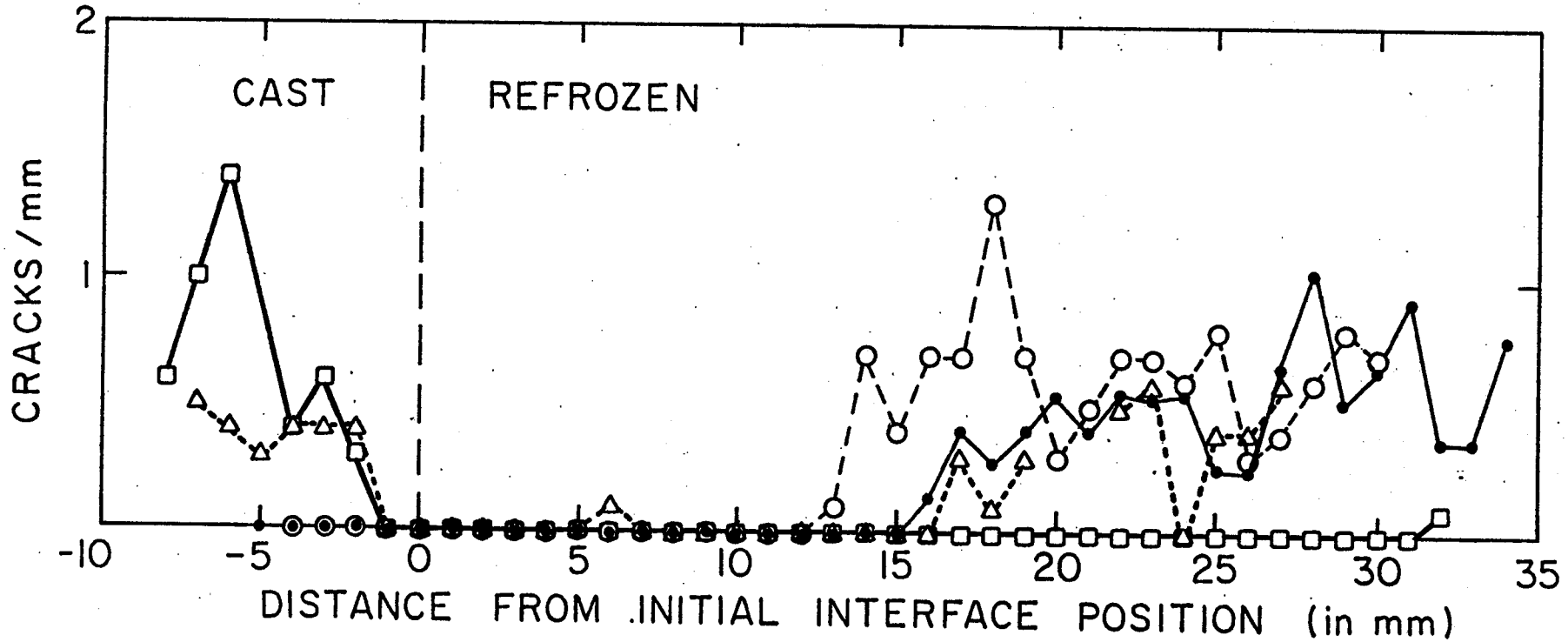

Figure 34. Crack distribution in NASA $In_{0.1}Ga_{0.9}Sb$ ingots.

△- Vertically processed

□- Horizontally processed

O- SL-3 processed

●- SL-4 processed

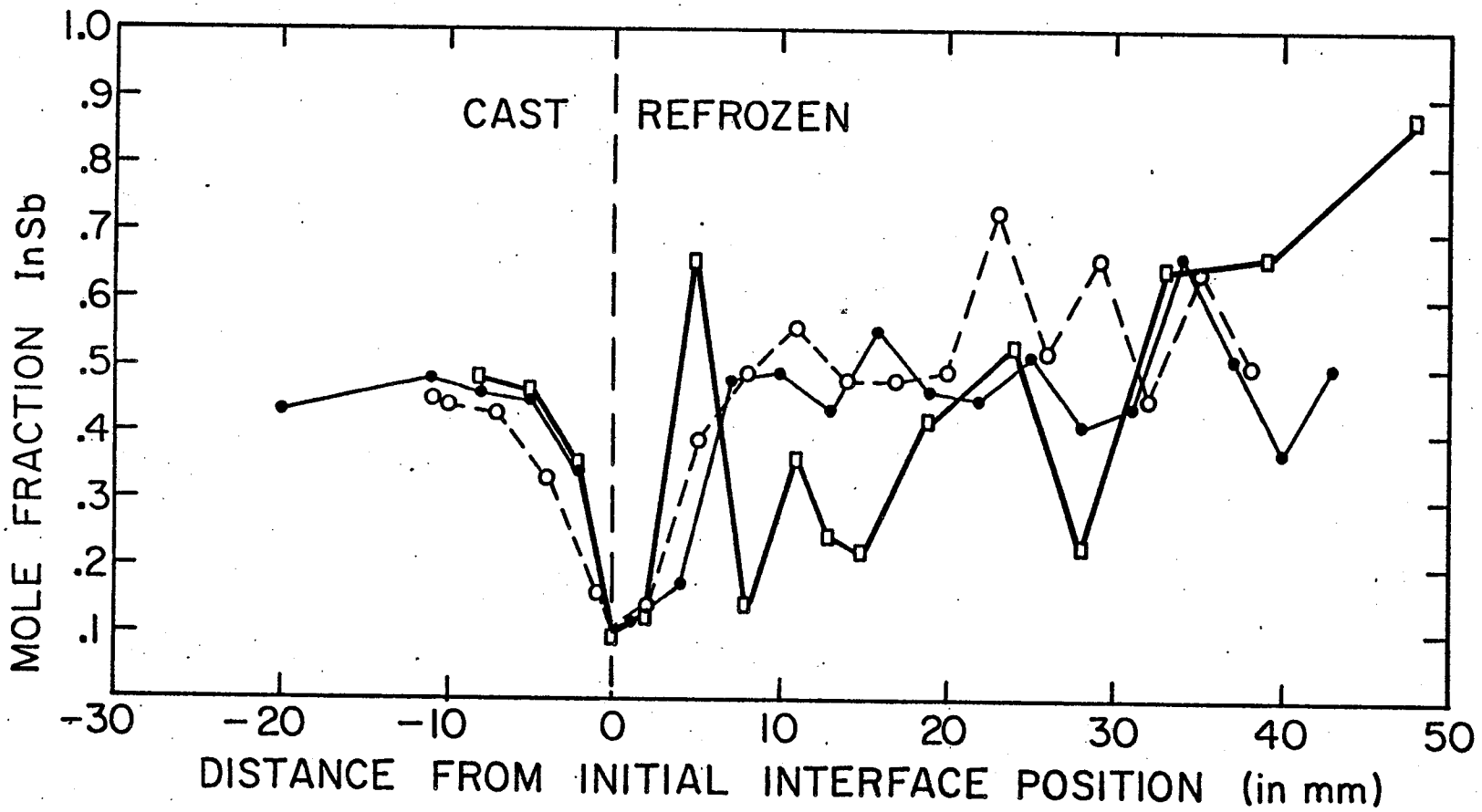

Figure 35. Indium concentration profiles in NASA $In_{0.5}Ga_{0.5}Sb$ ingots, as determined by atomic absorption spectrometry.

□ - Horizontally processed

○ - SL-3 processed

● - SL-4 processed

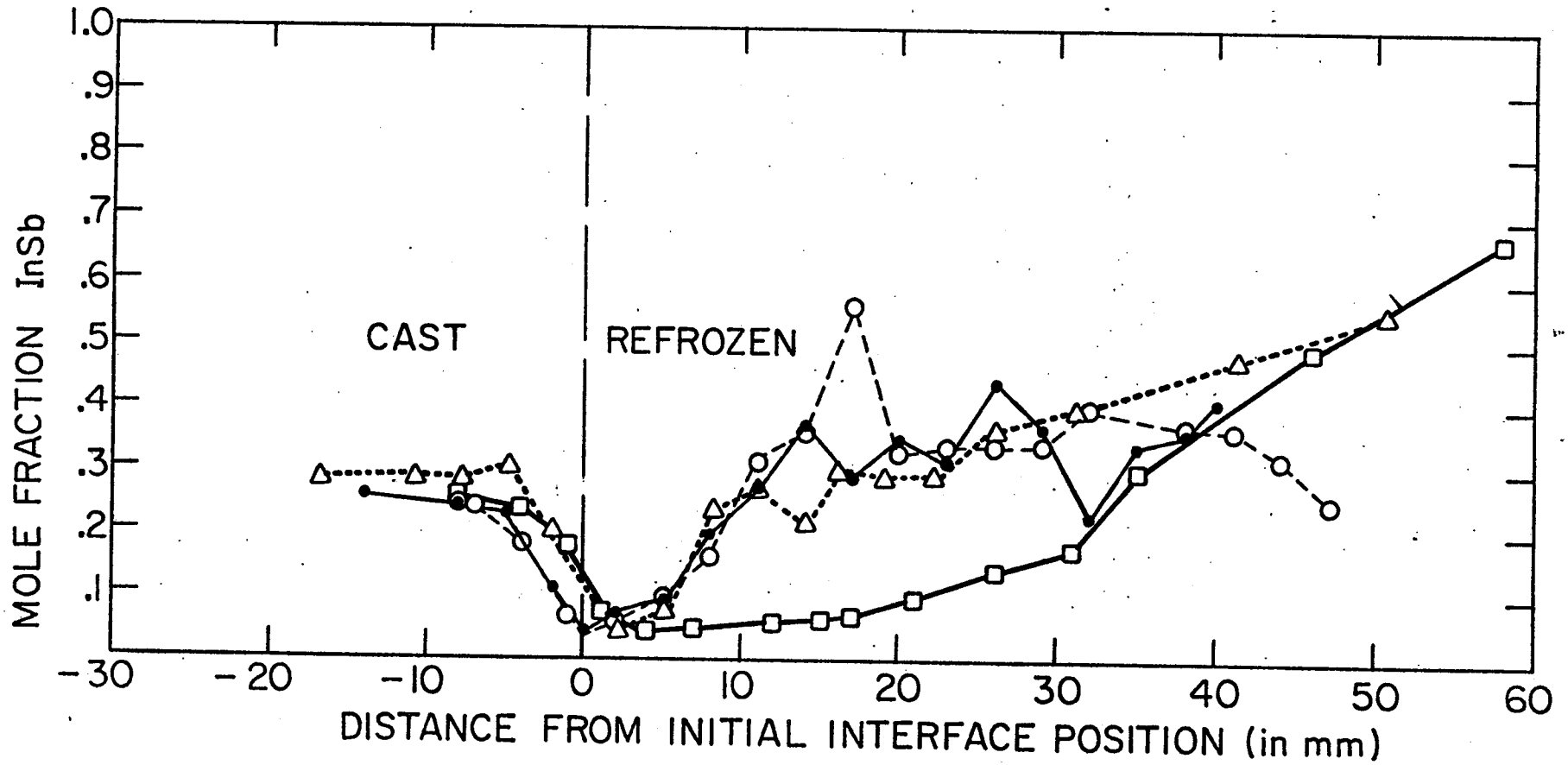

Figure 36. Indium concentration profiles in NASA $In_{0.3}Ga_{0.7}Sb$ ingots, as determined by atomic absorption spectrometry.

△ - Vertically processed

□ - Horizontally processed

○ - SL-3 processed

● - SL-4 processed

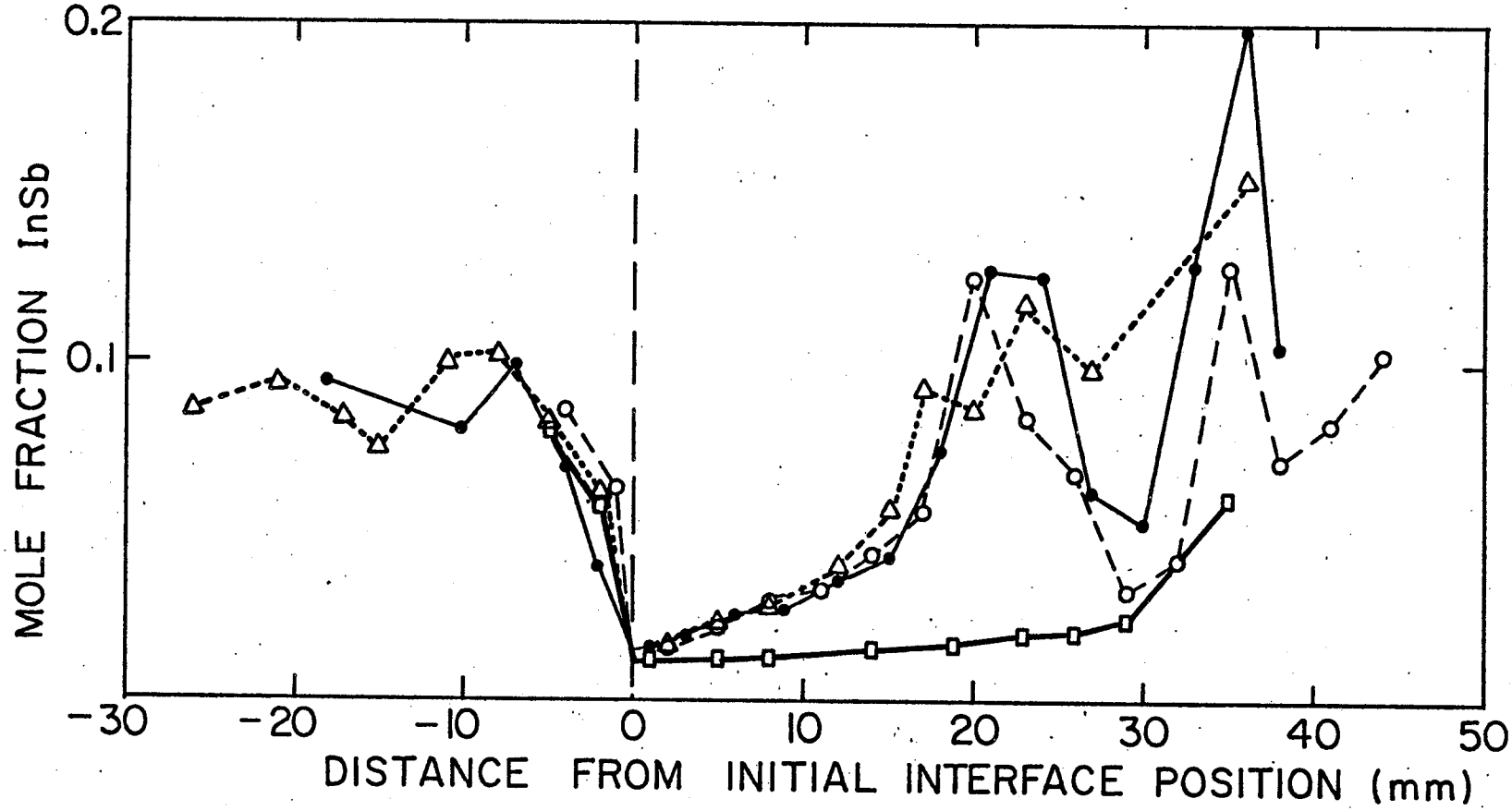

Figure 37. Indium concentration profiles in NASA $In_{0.1}Ga_{0.9}Sb$ ingots, as determined by atomic absorption spectrometry.

△ - Vertically processed

□ - Horizontally processed

○ - SL-3 processed

● - SL-4 processed

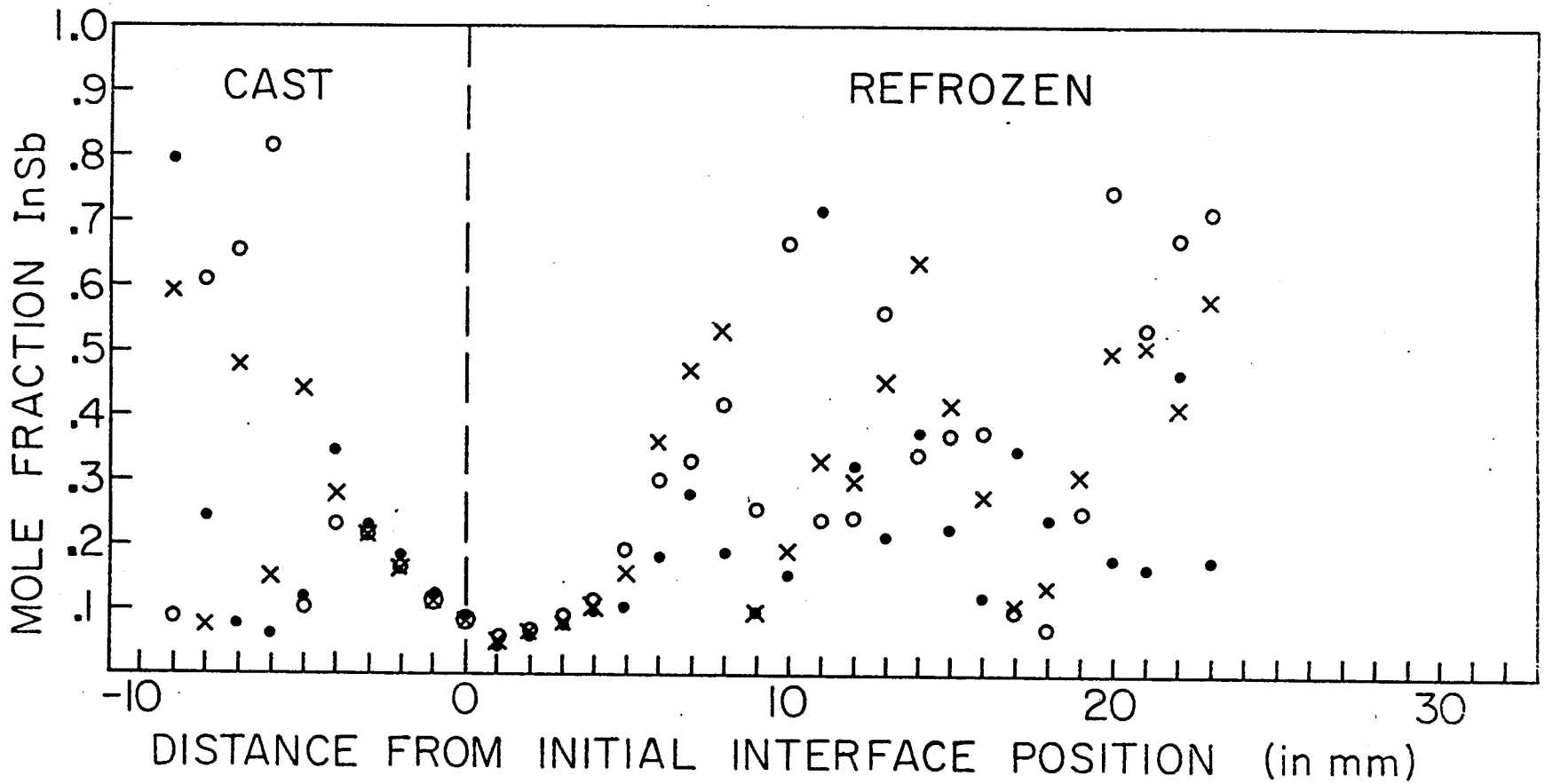

Figure 38. Electron microprobe results on NASA ingot 3B ($In_{0.3}Ga_{0.7}Sb$ processed vertically).

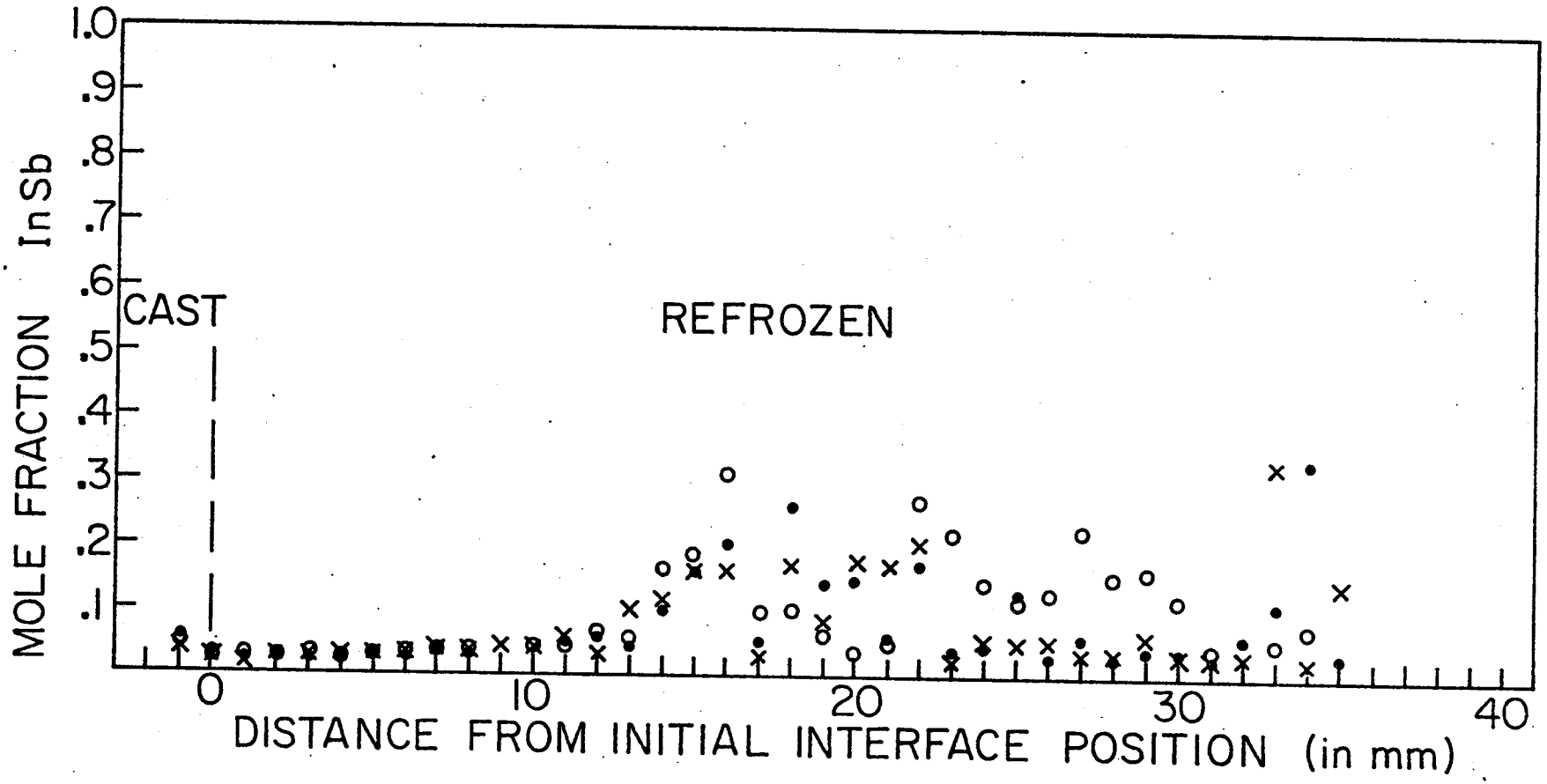

Figure 39. Electron microprobe results on NASA ingot 2C ($In_{0.1}Ga_{0.9}Sb$ processed vertically).

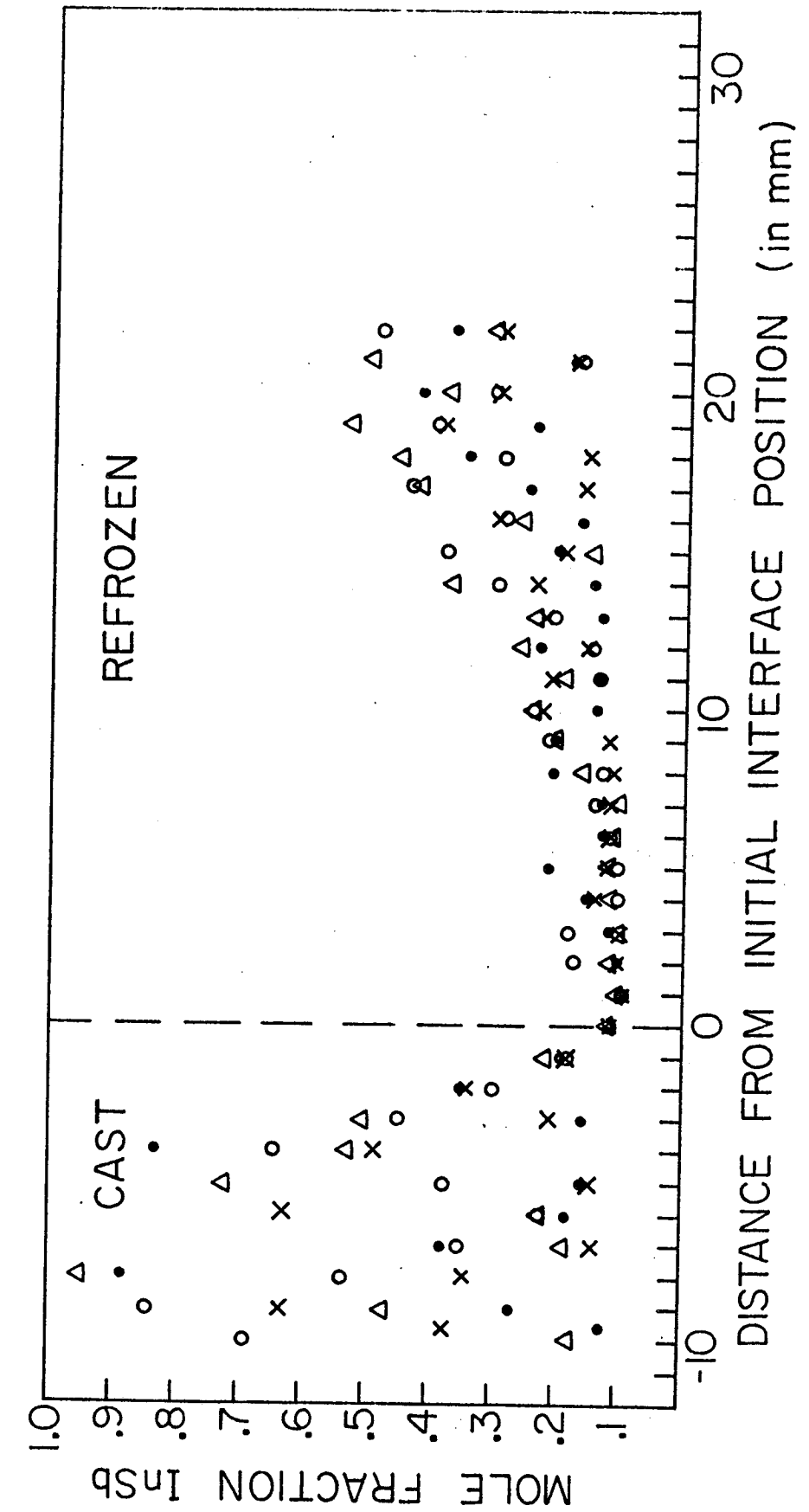

Figure 40. Electron microprobe results on NASA ingot 3A ($In_{0.5}Ga_{0.5}Sb$ processed horizontally).

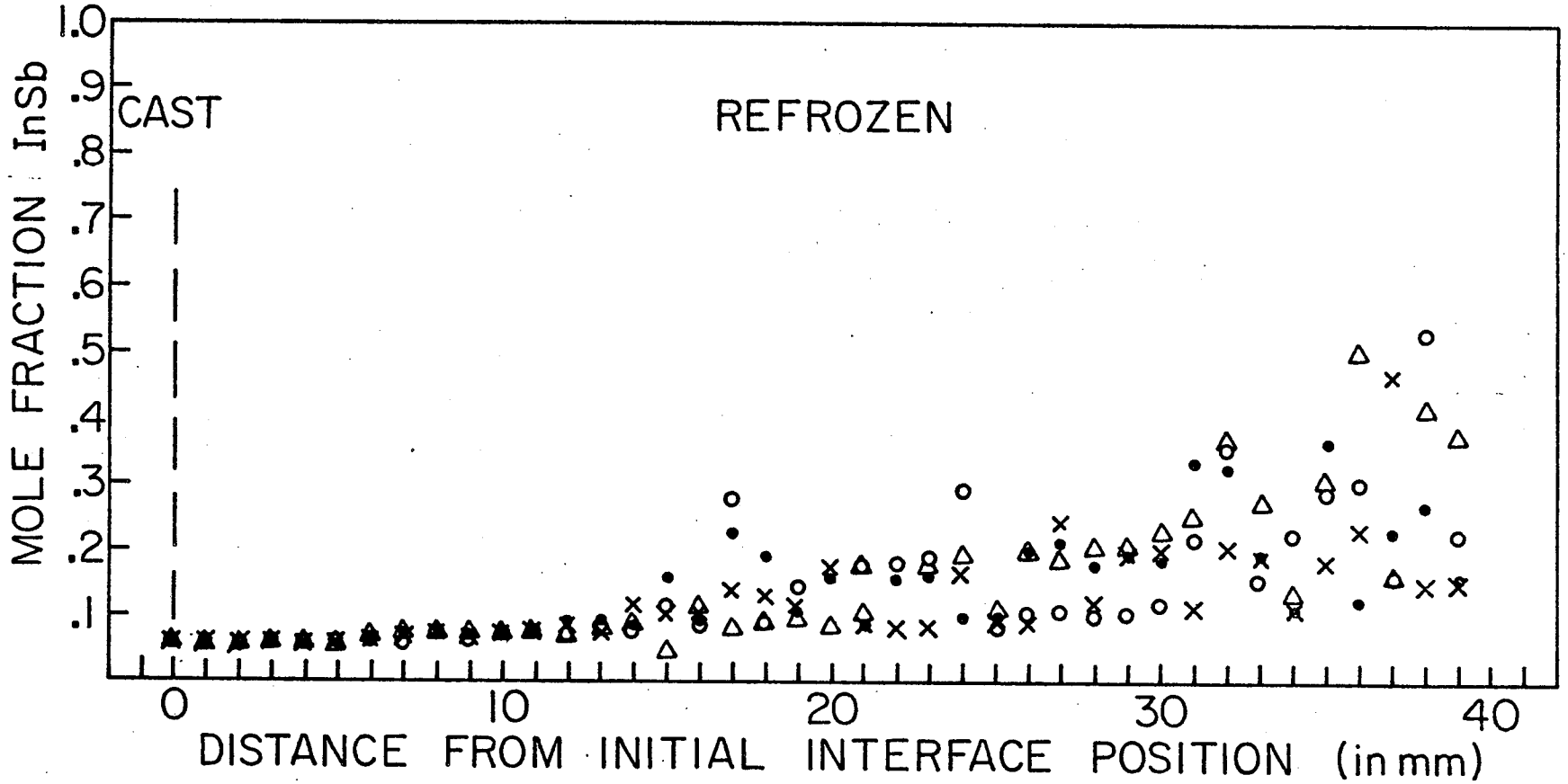

Figure 41. Electron microprobe results on NASA ingot 4B ($In_{0.3}Ga_{0.7}Sb$ processed horizontally).

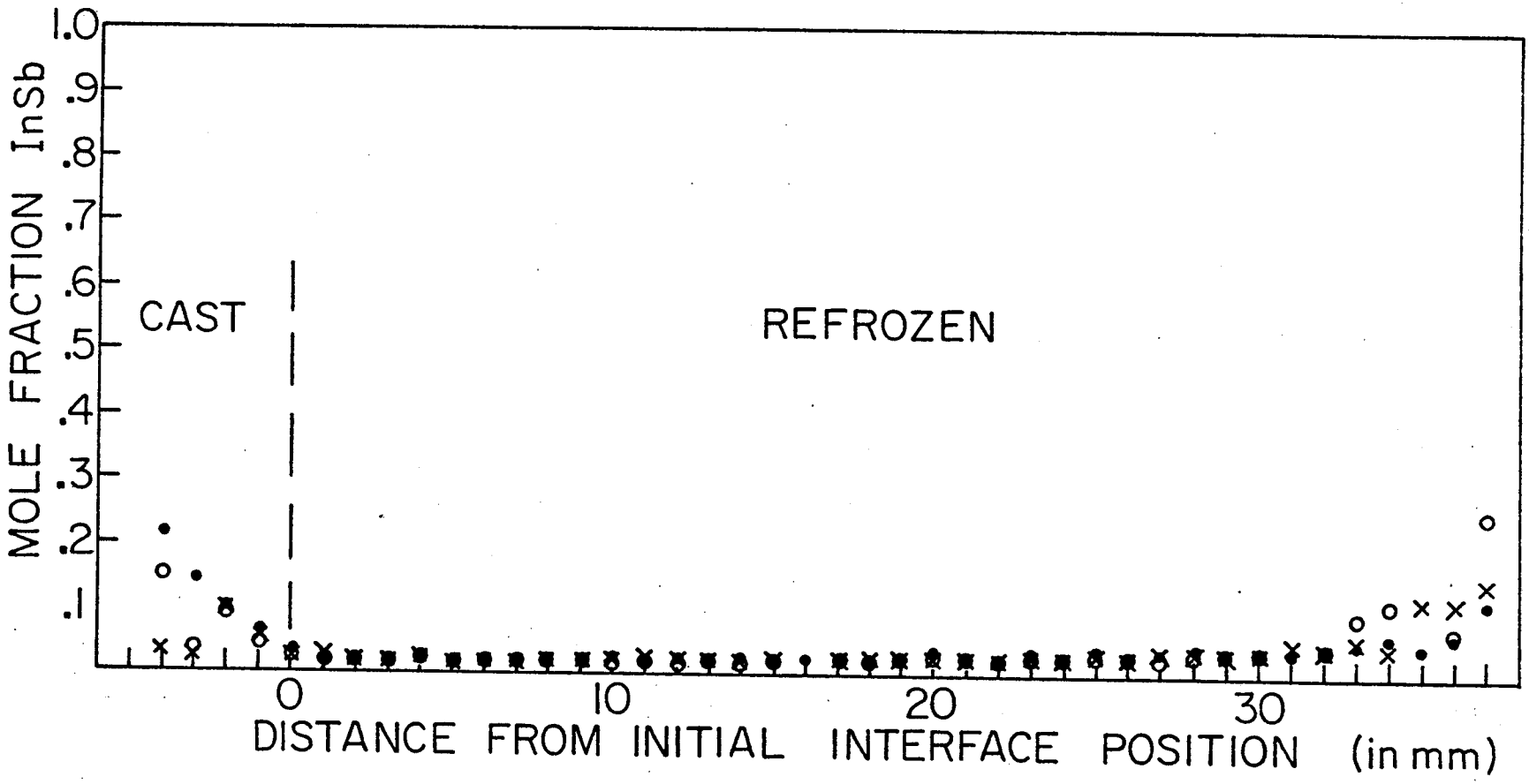

Figure 42. Electron microprobe results on NASA ingot 4C ($In_{0.1}Ga_{0.9}Sb$ processed horizontally).

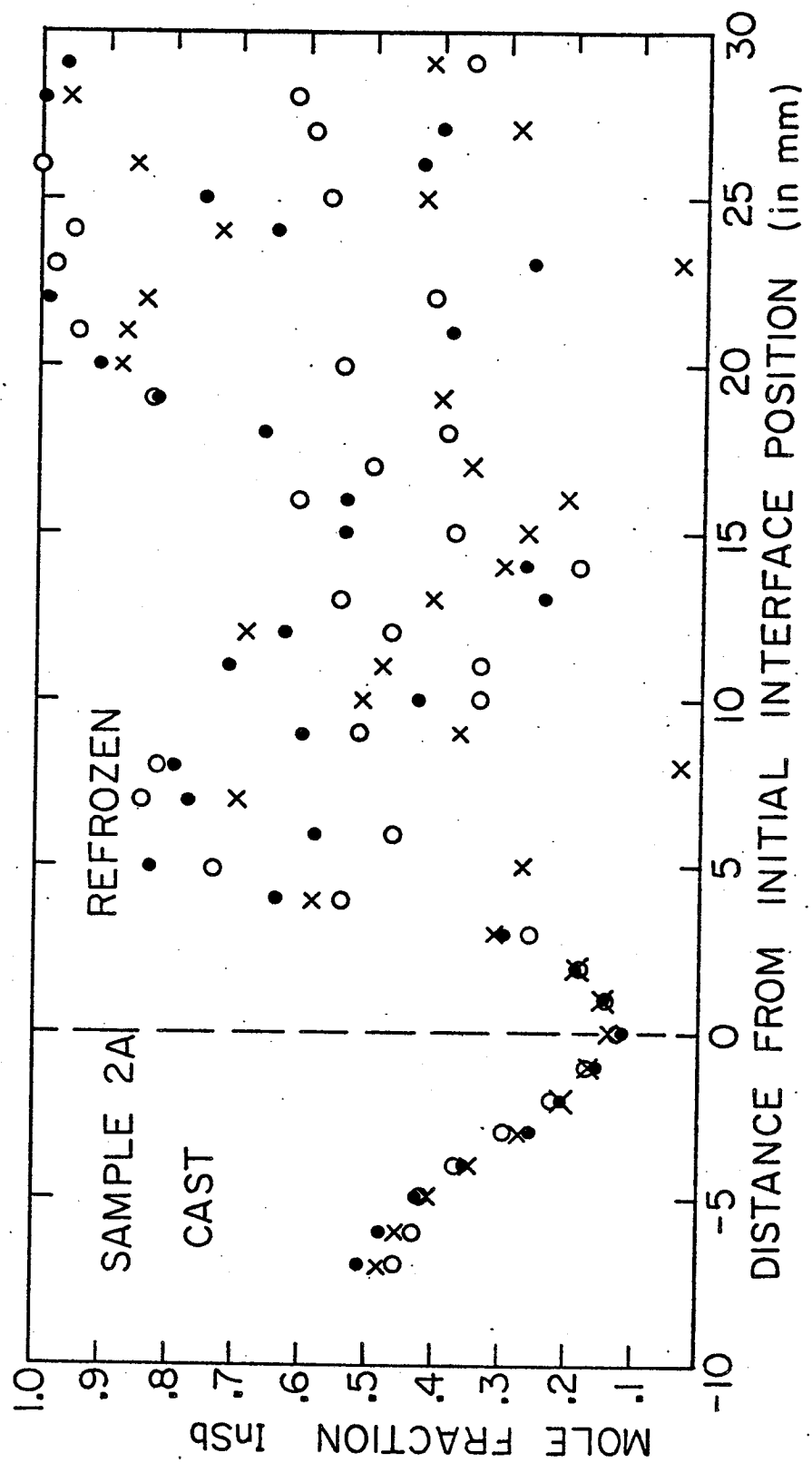

Figure 43. Electron microprobe results on NASA ingot 2A ($In_{0.5}Ga_{0.5}Sb$ processed in SL-3).

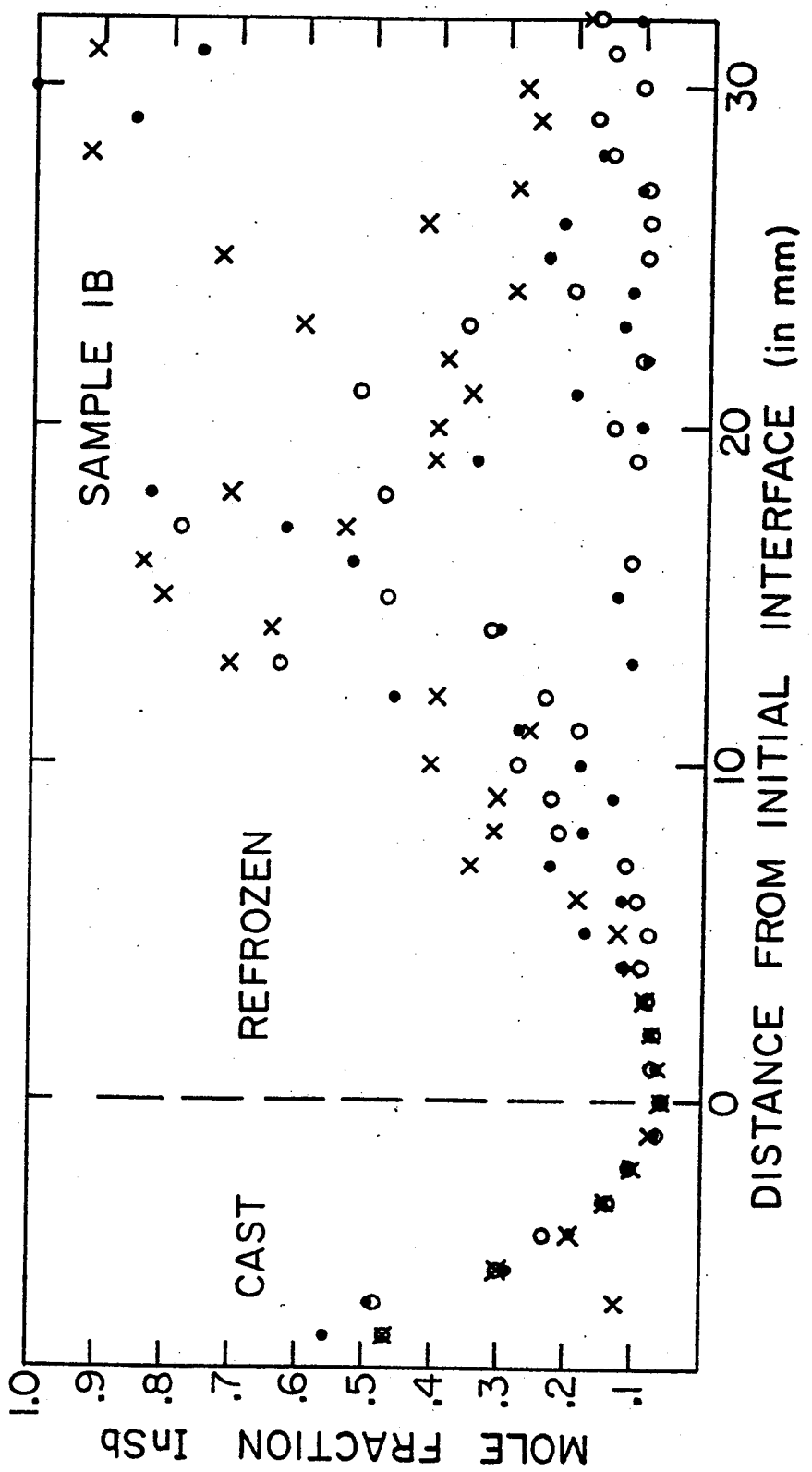

Figure 44. Electron microprobe results on NASA ingot 1B ($In_{0.3}Ga_{0.7}Sb$ processed in SL-3).

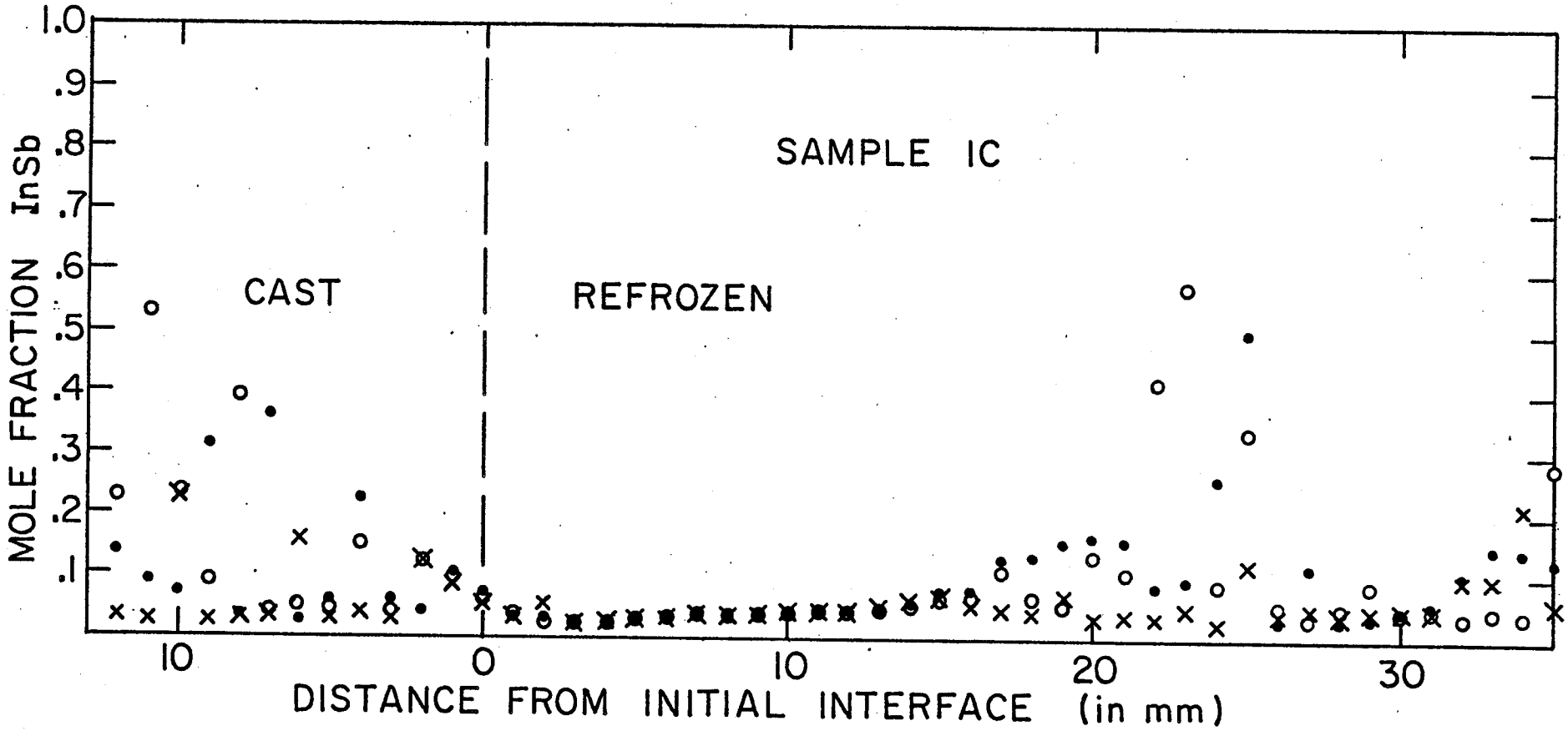

Figure 45. Electron microprobe results on NASA ingot 1C ($In_{0.1}Ga_{0.9}Sb$ processed in SL-3).

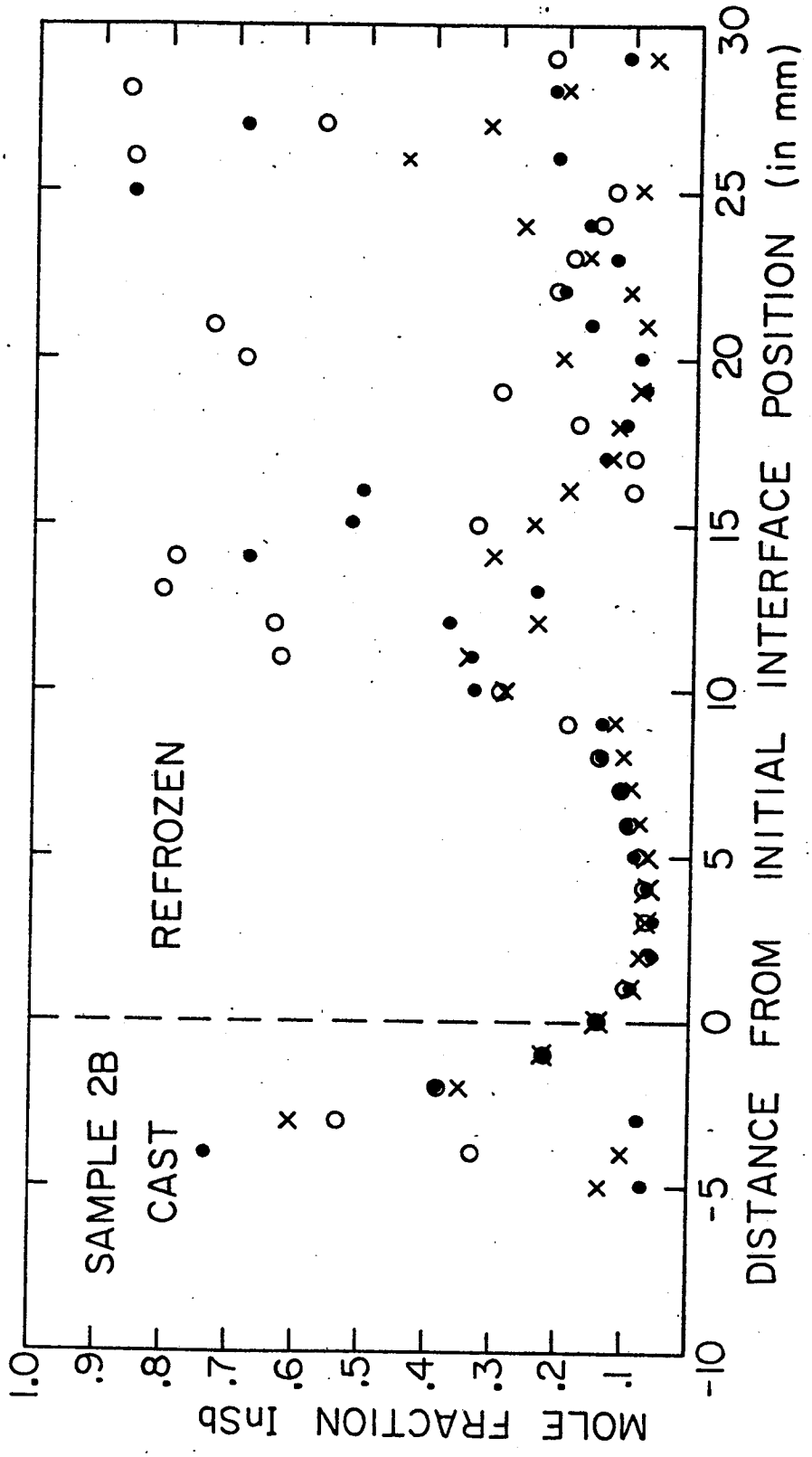

Figure 46. Electron microprobe results on NASA ingot 2B ($In_{0.3}Ga_{0.7}Sb$ processed in SL-4).

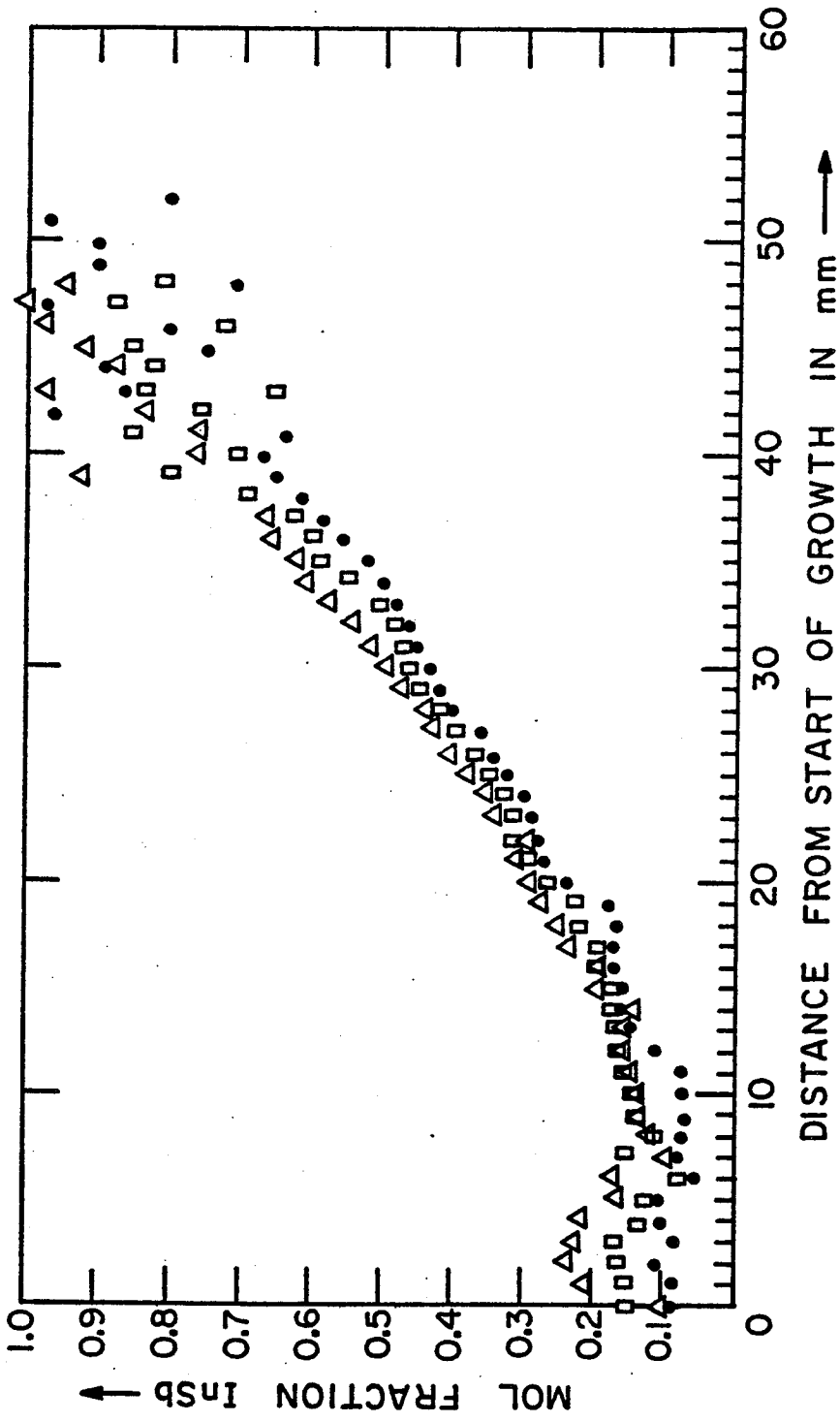

Figure 47. Electron microprobe results on USC ingot DF-9 (Bridgman-grown).

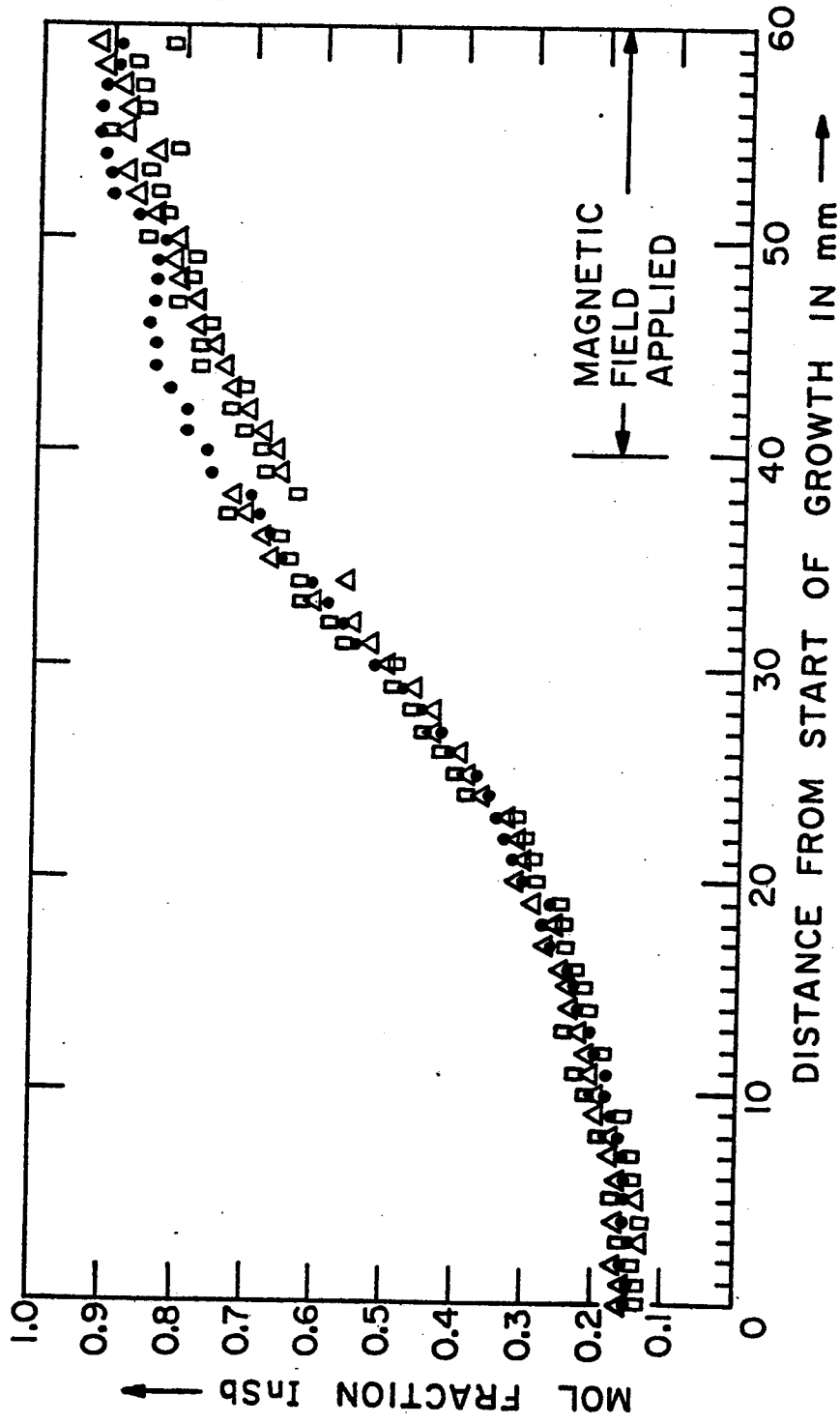

Figure 48. Electron microprobe results on USC ingot DF-11 (Bridgman-grown).

constitutional supercooling. From Figure 2, the tendency toward instability should increase as the In content of the melt at the interface increases, as the temperature gradient decreases, and as the freezing rate increases. All three of these trends occurred as solidification proceeded. Note, however, that a much longer length of stable growth was obtained with horizontal processing. There were two reasons for this, both related to free-convective stirring. The melt-back was greater with horizontal processing, as noted in Table I. This caused the interfacial temperature gradient to be larger since the distance from the interface to the heat sink was decreased. Secondly, the free convective stirring of the melt decreased the In concentration in the melt at the interface, which was also reflected in the difference in macroscopic concentration profiles, as noted earlier. Table III compares values of G/V from the Westinghouse heat transfer results (6) with those from Figure 2 for constitutional supercooling under the conditions at which the inhomogeneities began. The agreement is only fair.

The scanner on the electron microprobe was not operational so that possible micro-inhomogeneities could not be scanned in detail. An attempt was made to detect fluctuations in In concentration along the growth direction in the slow regrowth region of vertically-processed sample 2C near the initial interface by taking point counts two microns apart over a distance of twenty microns. No variation was detected. This means either that there was no variation or that this method was not sufficiently sensitive to detect it.

An attempt was also made to determine if gravity segregation occurred in the horizontally-grown sample 4C by taking point counts 0.4 mm apart across the width of the sample. If gravity segregation had occurred, there would have been a vertical compositional variation due to the combination of free convection and segregation at the growing interface. No variation was detected, probably because of the very slow growth rates.

TABLE III. VALUES OF G/V ESTIMATED AT POINTS AT WHICH INHOMOGENEITIES BECOME NOTICEABLE IN ELECTRON MICROPROBE RESULTS ON NASA INGOTS

Run	From Westinghouse Calculations[6]	From Figure 2 for Constitutional Supercooling with $D = 2 \times 10^{-5}$ cm^2/sec
	Vertical	
1A(c)	570	500
3B	670	1000
2C	570	500
	Horizontal	
3A	670	1200
4B	550	870
4C	330	400
	SL-3	
2A	800	1800
1B	670	1000
1C	550	500
	SL-4	
2B	710	1000

IV. CONCLUSIONS AND DISCUSSION

Several interesting effects of gravity were revealed by these experiments. The concentration profiles and the compositional homogeneity were both strongly influenced by the magnitude and direction of g, as expected from free convection effects. The lack of convective stirring in space-processing leads to a significant initial compositional transient which cannot be entirely avoided, although it can be greatly reduced by lowering the freezing rate. A lower freezing rate would also avoid compositional inhomogeneities due to constitutional supercooling. Production of a homogeneous ingot would probably eliminate cracking.

The most exciting development was the great reduction in twinning brought about by space processing. Since the cause of growth twinning is not really known, we can only speculate that foreign particles are responsible and that these interact more frequently with the growing interface when convection is present.

The ingots processed in SL-3 had a smaller diameter than the tube. Apparently the melt did not wet the carbon coating. Surface tension decreases with increasing temperature, and the temperature increased with distance from the interface down the melt. This would have forced the melt to contract near the interface and to expand at the hot end. Those processed in SL-4 had the same diameter as the tube. The only difference between these two runs was that the heater temperature was higher in SL-4. Since the compositions were the same, the interface temperatures were the same, although the portion of the melt in the heater would have been hotter in SL-4. We can only speculate that this higher temperature caused the melt to first wet the tube wall and then to spread down to the interface.

A wide variety of grain sizes was observed, but with no trend yet observed. Sadly, there appears to be no large advantage to space processing of alloys from this standpoint.

The preferred grain orientation was <111> in all cases.

We have no explanation for the great difficulty in distinguishing grains in the space-processed ingots.

Gas bubbles were more uniformly distributed in the space-processed ingots, but this is not significant since they can be avoided entirely by solidification in a reasonable vacuum (5).

Acknowledgments

The fabrication and characterization of the NASA samples was supported by NAS8-28305. The X-ray Laue patterns and the USC solidification experiments and characterization was supported by the Joint Services Electronics Program monitored by the Air Force Office of Scientific Research under Contract No. F44620-71-C-0067.

We are grateful to Vincent Yip for assisting with the fabrication of the NASA ampoules and to Jack Worrall for the electron microprobe work.

References

1. J. C. McGroddy, M. R. Lorenz and T. S. Plaskett, Solid State Commun., 7, 901 (1969).

2. G. M. Blom and T. S. Plaskett, J. Electrochem. Soc. 118, 1831 (1971).

3. W. R. Wilcox, J. Crystal Growth 12, 93 (1972).

4. H. P. Utech and M. C. Fleming, J. Appl. Phys. 37, 5 (1966).

5. W. R. Wilcox, J. Crystal Growth 19, 221 (1973).

6. R. G. Seidensticker and J. W. Chi, "Ground Base Test Report of the Multipurpose Electric Furnace System M-518", Westinghouse Report WANL TME 2838 (Pittsburgh, 1973), under Contract NAS8-28271.

INFLUENCE OF GRAVITY-FREE SOLIDIFICATION ON MICROSEGREGATION

N74 29899

By

John T. Yue* and Fred W. Voltmer
Texas Instruments Inc.
Dallas, Texas 75222

SUMMARY

Single crystalline germanium has been grown for the first time in space aboard SKYLAB Mission No. 2. The crystal growth experiment, designed to characterize the influence of gravity-free solidification on microsegregation of a semiconductor material, contained three crystals. One was doped with Ga with an initial doping concentration of 8×10^{16} atoms/cc; the second with Sb, with 4×10^{14} atoms/cc; and the third with B, with 2×10^{15} atoms/cc. Portions of the germanium crystals were remelted and subsequently resolidified at 5 μm per second under controlled conditions by the gradient freeze technique. The space grown crystals were compared with identical germanium crystals resolidified in a terrestrial environment in horizontal and vertical positions. Detailed spreading resistance measurements made on the Ga doped Ge crystals indicate that microsegregation in space is reduced by two to five-fold in the bulk and eight-fold near the surface, while macrosegregation in space is reduced by six-fold in the bulk. The effective segregation coefficient for Ga in Ge is analyzed extensively and is found to be larger for space solidification. This has the implication that the solute boundary layer at the growth interface in space is correspondingly thinner. The solidification interface is significantly smoother and is found to be initially convex toward the melt in space. A convective mixing model based on a BPS interpretation has been advanced to explain the absence of gravity on convective mixing and solute segregation during solidification.

*Paper presented by John T. Yue

I. INTRODUCTION

This report presents the results of an experiment in joint collaboration between Texas Instruments Inc. and the National Aeronautics and Space Administration on the Influence of Gravity-Free Solidification on Solute Microsegregation. The experiment provides a unique environment for crystal growth, namely space, and allows, for the first time, a quantitative characterization of the influence of gravity on convective mixing during crystal growth of a semiconductor material. The objective of the experiment is to investigate whether or not an improvement can be obtained in solute microsegregation for crystal growth of a semiconductor material in a gravity-free environment, and if improvement can be obtained whether or not it can be quantified.

Solute microsegregation is defined as micro-inhomogeneities of the solute species which occurs during solidification in crystal growth.[1] Solute microsegregation, which leads to resistivity variations in the semiconductor material both in parallel and perpendicular directions of crystal growth, can have adverse effects on semiconductor device performance.[2] The present interest in the semiconductor industry is to grow semiconductor materials with homogeneous dopant distributions.

A major contribution to segregation behavior is the always-present convection current[3] in the melt during crystal growth. Presently, the magnitude of gravity-induced convective mixing on segregation and particularly microsegregation is not known. For terrestrial crystal growth, contributions to convective mixing associated with gravity are intrinsically coupled with contributions arising from temperature gradient differences and fluctuations and it is therefore, nearly impossible to isolate the influence of gravity. By comparing crystals grown in a space environment, with identical crystals grown in a terrestrial environment, the effects of gravity can be isolated for the first time.

Germanium was chosen for the experiment for its lower melting point in comparison with silicon*. In order to define the influence of gravity on terrestrial crystal growth, both horizontal and vertical directions of solidification were used. The vertical crystals were grown in temperature stabilizing positions.[4] The process chosen for crystal growth was the gradient freeze method[5] because of the simplicity involved: 1) no movement was required of the melt during crystal growth and 2) a constant rate of solidification could be controlled by lowering the furnace temperature by a uniform power reduction.

Three identical sets of germanium crystals were prepared. Each set contained three differently doped crystals: gallium, antimony, and boron.

*The Westinghouse furnace was constrained to temperatures below 1000°C.

Two sets were used as ground control samples with one set grown in the temperature stabilizing position and the other in the horizontal position. The third set of germanium crystals was grown in space. The experiment consisted of remelting a portion of the germanium crystal and then resolidifying the remelted portion under controlled conditions. The ground-based experiments were performed at Marshall Space Flight Center (MSFC) in January, 1973 and the space experiments were performed aboard SKYLAB Mission Number 2 on September 13, 1973.

Information on solute microsegregation in the resolidified regions was obtained from detailed spreading resistance measurements on all crystals at the Semiconductor Research and Development Laboratory at Texas Instruments Inc.

II. EXPERIMENTAL PROCEDURE

IIA. Crystal Preparation

Three identical sets of germanium crystals were prepared. Each set contained three differently doped crystals of gallium, antimony, and boron with respective initial concentrations of approximately 7.8×10^{16} atoms/cc, 0.42×10^{15} atoms/cc, and 2×10^{15} atoms/cc. The samples were prepared by grinding Ge boules to a fine powder along with desired quantity of dopant. The powder was then mixed and fused grown in the $\langle 1\text{-}1\text{-}1 \rangle$ direction. One set was sent to NASA for crystal growth experiment in a zero gravity environment aboard SKYLAB Mission No. 2. The other two sets were sent to NASA for the same crystal growth experiment in a normal gravity environment at Marshall Space Flight Center. One of the two sets of terrestrial crystals grew in a horizontal position; the other set, in a vertical temperature stabilizing position. The orientation of these two sets of crystals, with respect to the gravitational field, is shown in Figure 1.

Each germanium crystal was enclosed in a graphite tube and then encapsuled in an evacuated stainless steel ampoule. The ampoule was inserted in a metal cartridge, specially designed by Westinghouse Electric Corporation. The cartridge was subsequently inserted in an evacuated furnace with a pressure less than 10^{-4} torr. The ampoule assembly is schematically illustrated in Figure 2. All crystals in the SKYLAB experiment were labeled such that the gallium doped ones were denoted by C, the antimony doped ones by A, and the boron doped ones by B.

IIB. Cartridge and Furnace Design

The metal cartridge shown in Figure 3a was designed to provide a temperature profile shown in Figure 3b when inserted into the Westinghouse Multipurpose Electric Furnace. The unique feature of the cartridge is the presence of a heat leveler which maintains a constant temperature for about 6 cm. from the hot end of the cartridge toward the cold end. Since the heat leveler is adjacent to the ampoule, the temperature of the Ge crystal is effectively maintained at a constant value within that region. A constant temperature gradient of about 20°C/cm is maintained from the cold end of the heat leveler to the cold end of the cartridge. In order to facilitate heat extraction at the cold end of the ampoule, a copper heat trap was used. A temperature characterization of the ampoule and cartridge was performed by J. W. H. Chi at Westinghouse[7] and is roughly indicated in Figure 3b.[8]

IIC. Furnace Temperature Cycle

Both the terrestrially grown and space grown germanium crystals underwent similar remelt temperature cycles. For any one set, all three crystals were exposed to the same furnace conditions as each multipurpose electric furnace was able to contain three cartridges simultaneously. At the start of the remelt cycle, the furnace temperature was increased to the soaking temperature of 1000°C within 3 hours. It can be seen from Figure 3b that at this temperature, an appreciable portion of the original germanium crystal would be remelted (the melting point of germanium is 938°C). The soak temperature was held for about 2 hours at a steady level in order to allow the system to reach steady state conditions. The cool-down cycle was then initiated by reducing the temperature at the hot end of the cartridge at a rate of 0.6°C per minute, which enabled the crystal to re-solidify. As the cool-down cycle proceeded, rapid freezing would suddenly occur in the crystal when the heat leveler temperature fell below 938°C. Microsegregation characterization only in the region of slow solidification was examined.

Two temperatures were monitored during the entire "oven-on" cycle, that at the hot end and that at the cold end (see Figure 3a). Results of telemetry monitoring of the entire temperature cycle for space growth aboard SKYLAB are compared with those for terrestrial growth at MSFC in Figure 4. A cool-down rate of 0.62°C was recorded for both terrestrial and space growth, but the temperature gradient dT/dX beyond the heat leveler appears to be slightly greater for crystal growth in space.

IID. Spreading Resistance Measurement Procedure

In characterizing segregation and microsegregation behavior, spreading resistance (SR) probes were used to obtain resistivity fluctuations. Both two-probe and one-probe spreading resistance measurements were made. A schematic illustration of the manner in which the measurements were made is shown in Figure 5. Both longitudinal and radial resistivity measurements were made as shown by the dotted lines in Figure 5a. For most crystals, the resistivity measurements were made at step intervals of 25 microns. Resistivity calibration of the spreading resistance instrument was obtained from known germanium standards.

In order to study the interface structure during solidification, several longitudinal measurements were made at different radial locations along the length of the resolidified crystal.

All crystal surfaces were ground down to one-half the diameter in depth by using No. 600 silicon carbide. The flats were then mechanically polished with Buehler Polishing Compound No. 2 and Lustrox. For the gallium doped germanium crystals, spreading resistance measurements were made at shallow flat depths first, before they were ground down to flat depths of one-half the crystal diameter.

IIE. Surface Morphology

X-ray radiographs were taken for all crystals before opening the capsules and ampoules. The radiographs showed no mechanical fractures for

the resolidified germanium crystals. The radiographs for the space grown crystals are shown in Figures 6 and 7.

The crystals were removed from the stainless steel ampoules by cutting open their ends. No physical damage was inflicted upon the surfaces of the crystals in this way. The disassembled parts are shown in detail for the space grown germanium crystals in Figures 8, 9, and 10.

Detailed examination of the resolidified regions showed distinction in surface features between the slowly frozen portions and rapidly frozen portions during resolidification. Characteristic to all the germanium crystals in the SKYLAB experiment, a relatively smooth surface feature, denoting single crystalline growth, was observed up to 1.6 to 2.5 cms. away from the original solid-liquid interface. The smooth surface regions corresponded to the slow solidification process. Immediately following the smooth surface regions, rough and nearly polycrystalline surface morphologies ensued until the ends of the crystals. These rough surface features observed for all crystals, are a result of the rapid solidification process.

Results of the Berg-Barrett X-ray topograph, however, indicated that despite the poly-crystalline surface morphologies, all the crystals grew single crystalline in the bulk (except for possibly near the surfaces and near the very ends of the crystals). X-ray topographs for the space grown crystals 2C, 3A and 4B are shown in Figure 11.

Twin-like structures associated with the three facet growths in the $\langle 1\text{-}1\text{-}1 \rangle$ direction were also observed. Such features began from the original solid-liquid interface and disappeared as the polycrystalline surface regions began. Pictorially, the twin-like structures are indicated in Figure 12. Since the results of the Berg-Barrett topography indicate single-crystalline growth in the bulk, it is concluded that the twin-like surface structures may have been assisted by surface contacts of the crystals with the graphite tubes.

III. RESULTS AND DISCUSSIONS

The results are tabulated in Tables I, II, and III for Ga, Sb, and B doped Ge crystals respectively. Extensive spreading resistance measurements have been made for the gallium doped crystals. Results from these measurements will be presented first. The influence of gravity on macrosegregation, microsegregation, and the effective segregation coefficients will be discussed. Interface shapes during resolidification and a model interpretation of the observed results will also be given. The section will finally conclude with the spreading resistance measurements of the Sb and B doped germanium crystals. The interpretation of these results are more difficult as contamination had entered the germanium melt during the oven-on cycle in sufficient quantities to interfere with electrical readings of Sb and B in Ge. However, the Ga crystals were sufficiently highly doped so that electrical interference from the contaminants was negligible.

IIIA. Gallium Doped Germanium Crystals

Figure 13 shows the results of spreading resistance measurements for terrestrially grown Ga doped Ge crystal (4-C) resolidfied in the horizontal

position. The measurement was made in the longitudinal direction near the axial center of the crystal at 25 μm step intervals and with two-probes. The flat depth used in the measurement (see Figure 5) was approximately 0.15 inches or about one-half the diameter of the crystal. The profile gives a history of Ga solute redistribution during re-solidification near the center of the Ge crystal.

Several prominent features should be pointed out in Figure 13. The sharp drop in resistivity marks the original solid-liquid interface. Distinct resistivity undulations attributed to irregular segregation behaviors are observed in this region (solidification rate was about 5 per sec.). The segregation coefficient at the interface is about 0.12 in approximate agreement with the reported values for Ga in Ge.[9] However, there appears to be no definite values for the effective segregation coefficient in this range. Assuming the theory of complete mixing by Pfann[10], k_e (obtained from the slope of concentration curve as a function of the fraction of solidification g) ranges from a value of 0.32, at g = 0.26 to 0.4, to nearly a value of 1.0 for g = 0. Additional comments on this behavior will be made in Section IIID. The unique stepped peaking feature at the on-set of resolidification is an indication that the cool-down cycle may have been unsteady during its initial stage.

Figures 14-17 show the radial resistivity profiles perpendicular to the growth direction for crystal 4-C at the same flat depth but taken with 10 μm steps and with the two-probe method. Significant fluctuations are observed both on macro and micro scales. A measure of these fluctuations can be defined by

$$\Delta\rho / \rho_{avg} \qquad (1)$$

where $\Delta\rho$ is the difference in resistivity between the highest and lowest values in any given region of interest and ρ_{avg} is the average resistivity in that region. For example, in Figure 15, at 0.5 cm away from the original solid liquid interface, the value for $\Delta\rho/\rho$ in the radial direction is 15% on the macro scale. This large variation occurs despite the slow solidification rate.

The terrestrially grown Ga doped Ge crystal will now be compared with the space grown Ga doped Ge crystal, sample 2-C. Figure 18 shows the longitudinal resistivity profile near the center of the crystal, measured with the two-point probe and 25 μm steps. The flatness of this resistivity profile for crystal grown in space, is to be contrasted with the longitudinal resistivity undulations observed for identical terrestrial growth shown in Figure 13. The large spike at 4000 microns is due to a crack. The unusually flat resistivity profile (up to 1.6 cm away from the interface) is, however, not observed when resistivity measurements are made near the edge of the flat depth as shown in Figure 19. This difference in the resistivity profile between the center and the edge of the resolidified region is attributed to temperature gradient induced convection currents. The segregation coefficient at the interface near the center of the crystal has a value of 0.23, while it is somewhat less at 0.17 near the edge. The disagreement in the segregation behavior can be attributed to an uneveness in temperature gradient induced convective current,

and to uneven interface shapes at the start of re-solidification. A detailed interface study will be mentioned in Section IIIE.

Figures 20 and 21 show the resistivity behavior perpendicular to the growth direction. The smooth behavior in resistivity and thus in Ga distributions across the slice is attributed to the absence of gravity induced convective mixing and should be compared with the resistivity profile at identical positions away from the interface for terrestrial crystal growth as shown in Figures 14-17.

For the gallium doped crystal which resolidified in the vertical temperature position (5-C), significant resistivity undulations are also measured. Figure 22 shows the longitudinal spreading resistance measurements made at the center and edge of the flat superimposed on each other. The pronounced dip present for both measurements is attributed to a sudden increase in solidification. Figures 23 and 24 indicate that large macrosegregation in resistivity also exist in radial directions. All measurements for 5-C have been performed at 25 μm steps with the two-probe method.

IIIB. Macrosegregation : Influence of Gravity

We define macrosegregation as solute concentration fluctuations with a periodicity of 100 to 1000 microns. It is to be distinguished from microsegregation which are defined as solute concentration fluctuations with smaller periodicity. At present, the effect of gravity on either microsegregation or macrosegregation has not been clearly understood.(11) One idea, however, is that gravity does play a major role on convection currents in the melt during crystal growth.

The results of the radial resistivity profiles for the Ga doped Ge crystals indicate that macrosegregation is strongly effected by the presence of gravity. Comparison of Figures 14-17, Figures 20-21, and Figures 23-24 show that for the SKYLAB experiments, solidification in space gives rise to a six-fold reduction in macrosegregation. The large macro-resistivity fluctuations of the order of 15% to 22% are not observed for the space grown Ga doped Ge crystal. The values have been obtained from the radial slices at 0.5 cm away from the original solid-liquid interface by using Equation 1 and by neglecting the high rise in resistivity near the surface. These macrosegregations seem to occur at intervals of 600μm. The results are summarized in Table I.

Since macrosegregation is a result of the degree of randomness in convective mixing, it can be deduced from the above information, that perhaps for crystal growth in space, the degree of convective mixing is reduced by as much as five to six times.

IIIC. Microsegregation : Influence of Gravity

Microsegregations, defined as resistivity fluctuations in the range of 10-100 microns, are clearly evident from spreading resistance measurements in Figures 13-24. All these measurements were obtained from the two-probe method at either 10 or 25 steps at flat depths corresponding one-half the diameter of the crystal. Special attention has been given to the radial resistivity measurements at 0.5 cm beyond the original solid-liquid interface. At this distance the re-solidification rate is known to be slow (approximately 5 μm per sec.). At this slow rate, any large resistivity fluctuations are less likely to

be attributed to gross changes in the solidification rate but are more likely to be attributed to changes in thermal and convective changes and randomness in the melt.

From Figures 15, 20, and 23, the degree of microsegregation, defined by Equation 1, averaged over regions less than 100 microns are of 2% and 1.4% for horizontal and vertical terrestrial crystal growth and at about 0.5% for space crystal growth. It should be pointed out that these are estimates obtained from measurements made at 25 μm steps.

Microsegregation measurements of the gallium doped germanium crystals have been made at 5 μm steps with the one-probe spreading resistance probe and are shown in detail in Figures 25 and 26 for the space and terrestrial crystals. Again, these are measurements across the radial slices at 0.5 cm away from the original solid-liquid interface at the same locations as shown in Figures 15 and 20. It is seen that microsegregation in the space crystal ranged from 0.4% to 1.5% (Figure 25) while it is more consistently 1.5% in the terrestrial crystal (Figure 26). However, the macrosegregation feature mentioned in Section IIIB is confirmed to be present in the ground crystal (Figure 26) while it could not be found in the radial slice measurements for the space crystal (Figure 25).

In order to examine microsegregation behavior near crystal surfaces, surface measurements were made on the gallium crystals 4-C and 2-C before they were ground to flat depth of one-half the crystal diameter. Spreading resistance (SR) measurements were taken at flat depths of 0.011 inch for the ground sample and 0.017 inch for the space crystal. The results of the SR measurements for these shallow flat depth are shown in Figures 27-30. Figures 27-28 are resistivity profiles for the terrestrially grown Ga doped Ge crystal 4-C taken perpendicular to the growth direction and at 25 μm steps. Figures 29-30 show the similar measurements for the space grown gallium crystal 2-C. No macrosegregation features are observed in radial measurements. The surface microsegregation, however, is extremely pronounced in the terrestrial sample and is nearly eight times greater than that in the space sample. Interestingly enough, the large microsegregation effects disappeared at the deep flat depth of 0.15 inch as indicated in Figures 14-17. The large surface microsegregation for the terrestrial crystal is measured 275 microns beneath the crystal surface. Presently, it is not clear how deep into the crystal such microsegregation behavior exists. Apparently, surface related convective mixing is strongly influenced by gravitational forces.

In the bulk, there is less influence of gravity on microsegregation than on macrosegregation. The additional randomness introduced to convective mixing by gravity tends to show up more in macrosegregation although there also appears to be some effect on microsegregation. The measured decrease of an order of two-fold in microsegregation for crystal growth in space indicates that perhaps other mechanisms are more dominant in determining microsegregation than convective mixings.

IIID. Segregation Coefficient : Influence of Gravity

Enough information has been obtained on the segregation coefficient from the Ga doped Ge crystals that a definite trend is indicated due to the influence

of gravity. As a common starting point, the BPS definition[12] for the effective segregation will be used,

$$k_{eff} = k_o / \left[k_o + (1-k_o)\, e^{-\Delta} \right] \qquad (2)$$

where

k_o = equilibrium segregation coefficient
$\Delta = \delta v / D$

and

δ = solute boundary layer thickness
D = diffusivity of solute in solution
v = solidification speed

For most purposes, it is safe to assume that k_o does not change in space since it is determined by activation energies between the solid and liquid phases.[13] Gravity has little influence in that category. The exponential function Δ contains all the information attributed to convective mixing, to diffusion of solute away from the growth interface, and to the rate of solidification. Equation 2 is simple, yet general enough to account for the influence of these three mechanisms on solute segregation.

The results of SR measurements give a set of values for the effective segregation coefficient (k_{eff}) for both space and terrestrially grown Ga crystals during different stages of solidification and at different depths within the crystal. The results are tabulated in Table 1. Two conclusions can be made: 1) k_{eff} measured at the original solid liquid interface is higher for solidification in space than it is on earth at both the center and edge of the initial interface. It could therefore be deduced that k_{eff} is probably higher for all corresponding points along the original interface in the space case; 2) the effective segregation coefficient as obtained from the slope of the concentration distribution defined by Pfann,[14]

$$k_{eff}^{-1} = d\left[\log C_L\right] / d\left[\log (1-g)\right], \qquad (3)$$

indicates that it decreases as the fraction solidified (g) increases. Observation 1) implies that Δ is greater at the initial interface for crystal growth in space. Assuming D and v to be the same in both space and on earth, the solute boundary layer must be larger at the initial interface during solidification in space. Observation 2) implies that as solidification proceeds, the solute boundary layer δ decreases for both space and terrestrial crystal growth.

III E. Interface Shape

Information obtained thus far indicates that the initial interface shape during the first 2.8 minutes of solidification is convex toward the melt for the Ga doped Ge crystal grown in space. The shape is indicated in Figure 3 as obtained from SR measurement at equally spaced intervals across the

flat surface near the interface. The bars indicate error brackets associated with alignment of the SR measurements. The non-smoothness in the interface shapes indicate changes in convection mixing during the onset of resolidification.

The interface profile for the terrestrially grown Ga doped Ge crystal 4-C Figure 32 is more irregular during the first 2.1 minutes of resolidification and is consistent with the increased nature of convective mixing associated with the large macrosegregation at 0.1 and 0.5 cm from the original solid-liquid interface (Figures 14-15) and the smaller solute boundary layer δ for that crystal. It is conceivable that the irregularity in the interface shape continues during resolidification for crystal 4-C and thus would be consistent with the large macrosegregation features observed in the longitudinal direction in Figure 13. Additional SR measurements are in progress in an effort to define the interface shapes in greater detail.

IIIF. Model Interpretation

A convective mixing model is proposed to explain the results of the SKYLAB experiment. It is suggested that the model is consistent with the three major observed facts deduced from the spreading resistance measurements. They are (see Table I):

1. k_{eff} appears to be greater in space than on earth
2. both macrosegregation and microsegregation are reduced for solidification, and
3. the solidification interface appears to be convex toward the melt in space.

Figure 33a illustrates the proposed convective mixing model. The convective currents indicated are consistent with the temperature profile of the ampoule during re-solidification and can lead to an initial convex interface as measured and shown in Figure 31. This convective mixing model, which has axial symmetry with respect to the growth direction, has a greater degree of mixing towards the edge of the interface. The increased mixing can lead to a smaller value for k_{eff} near the edge of the advancing interface based on a BPS interpretation of the solute boundary layer defined by Equation 2.

Figure 33b illustrates the situation which could exist at the initial solid-liquid interface in order to explain the large differences in k_{eff} between space and terrestrial growth. An increased convective mixing gives rise to a thinner solute boundary layer which, in turn, leads to a smaller k_{eff}. Furthermore, if during resolidification, the degree of convective mixing increases at the advancing interface, as it is conceivable, based on a dynamic model shown in Figure 33a, the effect of solute redistribution due to the decrease in δ as a fraction of solidification can be compensated by the normal increase of solute concentration in the melt. If this compensation occurs, the net result can lead to a relatively flat segregation profile for a considerable length as observed in Figure 18.

IIIG. Results of the Sb and B doped Ge

Unfortunately, the amount of contaminants which entered the Ge melt

during the "oven-on" cycle was large enough to interfere with the electrical properties of both Sb and B doped Ge samples. The initial doping levels were low, about 0.4 2 X 10^{15} atoms/cc for Sb and 2 X 10^{15} atoms/cc for B. The major constituents of the contaminants in samples taken from the melt ends of the crystals were shown by emission spectroscopy to be Mn, Cu, and Fe. As the graphite tubes did not contain such large quantities of these transition metals, (see Tables 2 and 3) it is deduced that they entered the melt from the stainless tube during the oven-on cycle.

Mn, Fe, and Cu are known to have deep energy levels and they enter as bands near the middle of the Ge energy gap. They enter as "p" donors in Ge. This explains the type change for the Sb doped Ge crystals after resolidification. Similarly, the segregation coefficients for B and Sb have completely been reversed. It is estimated that the quantity of electrically active contaminants were of the order of 6 X 10^{15} atoms/cc, "p" type.

Spreading resistance measurements for the Sb and B doped Ge crystals will not be included in this manuscript, but the results of those measurements are reported in Tables II and III. The Sb doped samples were extremely difficult to interpret, as they had erratic segregation and macrosegregation behaviors. The B doped samples, however, tend to follow the segregation theory of solute resistivity based only on the diffusion mechanism.(15) There appears to be a real improvement in both macro- and microsegregation behaviors for the boron sample.

It is unfortunate that the B and Sb samples were contaminated as they would have allowed a characterization of microsegregation as a function of activation energies. The equilibrium segregation values are 20 and 0.003 for B and Sb respectively.

IV. CONCLUSIONS AND RECOMMENDATIONS

Germanium crystals have been grown for the first time in space. It has been shown that solidification in space can provide six-fold improvement in macrosegregation and nearly two-fold improvement in microsegregation for crystal growth by the gradient freeze method. The influence of gravity on convective mixing has been quantified for solute redistribution in nearly unidirectional solidification and its role in macro and microsegregation is now better understood. A theoretical model based on the implications of the BPS thoery has been found to be consistent with the results obtained from the spreading resistance measurements. Additional detailed analysis and SR measurements are still in progress in order to further define the influence of gravity on microsegregation.

The results of this first experiment on solidification in space has indicated that quantitative data on the influence of gravity on solidification can be obtained. It is therefore recommended that further experiments be conducted to assess the magnitude of the improvement which can be achieved. It is critical for further experiments that the impurity doping level be sufficiently high that contamination not obscure the results.

ACKNOWLEDGMENT

The authors are appreciative to NASA for the opportunity to participate in such a fundamental study in crystal growth in space. They wish to thank Marshall Space Flight Center for performing the ground-base experiments and to Westinghouse Electric Corporation for providing the Multipurpose Electric Furnace. They are grateful to Mr. Roy Byrd for making the spreading resistance measurements.

REFERENCES

1. See for example : P. R. Camp, J. Appl. Phys. 25, 459 (1954); J. C. Brice, P.A.C. Whiffin, Brit J. Appl. Phys. 18, 581 (1967); A. F. Witt, M. Lichtensteiger, H. C. Gatos, J. Electrochem. Soc., 1119, (Aug. 1973); and the references contained in them.

2. See for example : J. W. Faust, Jr., H. F. John, S. O'Hara, Metallurgy of Sem. Mat'l, J. Schroeder, Ed., 181-189 (1962); H. F. John, J. W. Faust, Jr., R. Stickler, IEEE Trans. on Parta, Materials and Packaging, Vol. PMP-2, No. 3.

3. See for example: Fluid Mechanics, Landau & Lifshitz, Pergamon Press (1959), pp 8-9; W. R. Wilcox, L. D. Fullmer, Jr., of Appl. Phys., 36, 2201 (1965).

4. K. M. Kim, A. F. Witt, H. C. Gatos, Jr., Mat. Sci., 6, 1036 (1971).

5. Transport Processes in Unidirectional Crystal Growth, Chang Eun Chang, Ph.D. Thesis, USC (June 1973).

6. For detailed specifications see : NASA Report, "Data Package for Cartridge For the Multipurpose Electric Furnace System", Section IV, Nov. 1972.

7. See Ref. 6.

8. For detailed temperature information, see the report by R. G. Steindensticker, "Prototype Cartridge Test Report : SKYLAB EXP. M559", Nov. 1972, Westinghouse Electric Corp.

9. k_o = 0.087 see : F.A. Trumbore, Bell System Tech J., 39, 669 (1959); Transistor Technology, Vol. 1, Bell Labs, D. Van Nostrand Co., 1958.

10. Zone Melting, (2nd ed.), W. G. Pfann, Wiley & Sons, 1966.

11. Ting L. Chu, "Physical Phenomena Related to Crystal Growth in the Space Environment,"NASA Report NAS1-11869 (Nov. 1972).

12. J. A. Burton, R. C. Prim, W. P. Slichter, Jr. of Chem. Phys. 21, 1987 (1953).

13. The Art and Science of Growing Crystals, Gilman, Ed., Wiley & Sons, Chapter 15,; R. L. Parker, Solid State Phys. 25, 151 (1970).

14. See ref. 10.

15. V. G. Smith, W. A. Tiller, J. W. Rutter, Can. Jr. of Phys., 33, 723 (1955).

TABLE I Ga Doped Ge ko = 0.087

		SPACE 2-C	GROUND 4-C (HOR)	GROUND 5-C (VERT)
Center	k_e (int)	0.23	0.12	0.10
	k_e (slope)	~1.0 @ g = 0 to 0.25 ~.27 0.25 < g < 0.35	~1.0 0 < g < 0.26 ~.32 0.26 < g < 0.4	N.A.
Edge	k_e (int)	0.17	0.15	0.115
	k_e (slope)	0.7 @ g = 0 to .0.25 @ 0.25 < g < .4	1.0 @ g = 0	N.A.
Surface	k_e (int)	0.16	0.115	No meas.
	k_e (slope)	0.33 0 < g < 0.4	0.315 0 < g < 0.4	No meas.
Macroseg. (radial)	$\Delta\rho/\rho$ bulk	3% (25 μm)	15.3% (25 μm)	21.5% (25 μm)
Microseg. (radial)	$\Delta\rho/\rho$ surface	0.8% (25 μm)	6.4% (25 μm)	No meas (25 μm)
	$\Delta\rho/\rho$ σ_ρ/ρ bulk	2.4% (25 μm) 0.4% (5 μm)	4.2% (25 μm) 1.6% (5 μm)	1.4% (25 μm) 2.2% (5 μm)
Interface Shape		Initially convex toward melt	Irregular initially	No meas.
Contaminants (Emission Spect. melt end, Atm/cc)		Ga 1.6×10^{18} (2×10^{17}) Mn 0.5×10^{18} Fe 0.4×10^{18} Cu 0.55×10^{18} to 5.5×10^{18}	Ga 9.2×10^{17} (2×10^{17}) Mn 2.8×10^{17} Fe 6.4×10^{17} Cu 0.55×10^{17} to 5.5×10^{17}	No meas.

TABLE II Sb DOPED Ge ko = 0.005

	SPACE 3A	GROUND 1A (HOR)	GROUND 4A (VERT)
Contaminants (Emission Spect. of Melt End) Atom/cc	Sb "P" 3.3×10^{15} (0.4×10^{15}) Contaminants in solid 4×10^{15} Mn 2.1×10^{17} Fe 7×10^{17} Cu 5×10^{15}	Sb "P" 3.3×10^{15} (0.4×10^{15}) Contaminants in solid 4×10^{15} Mn 0.6×10^{17} Fe N.D. Cu 0.55×10^{17}	Sb "P" (0.4×10^{15}) No Meas.
Center k_{eff} (int)	2.2 (Seg. behavior does not follow phys. law)	2.6	No sharp interface
Macrosegregation $\Delta\rho/\rho$	31%	29%	No meas.
Microsegregation $\Delta\rho/\rho$	1%	1%	No meas.

TABLE III B DOPED Ge ko = 20

	SPACE 4B	GROUND 2B (HOR)	GROUND 1B (VERT)
Contaminants Emission Spect. of Melt End Atom/cc	B "P" 8×10^{15} (2×10^{15}) Contaminants in solid Mn 6×10^{18} Cr 9.3×10^{18} Fe 4.35×10^{17} Cu 5.5×10^{17}	B "P" 6×10^{15} (2×10^{15}) Contaminants in solid Mn 9×10^{18} Cr N.D. Fe 6.4×10^{17} Cu 5.5×10^{17}	B No meas.
Center k_{eff} (int)	0.54 follow seg. behavior by assuming only diffusion	0.1 follows seg. behavior by assuming only diffusion	0.52 follows seg. behavior by assuming only diffusion
Macrosegregation @ 0.5 cm	13%	42%	75%
Microsegregation @ 0.5 cm	0.5%	0.9%	2.0%

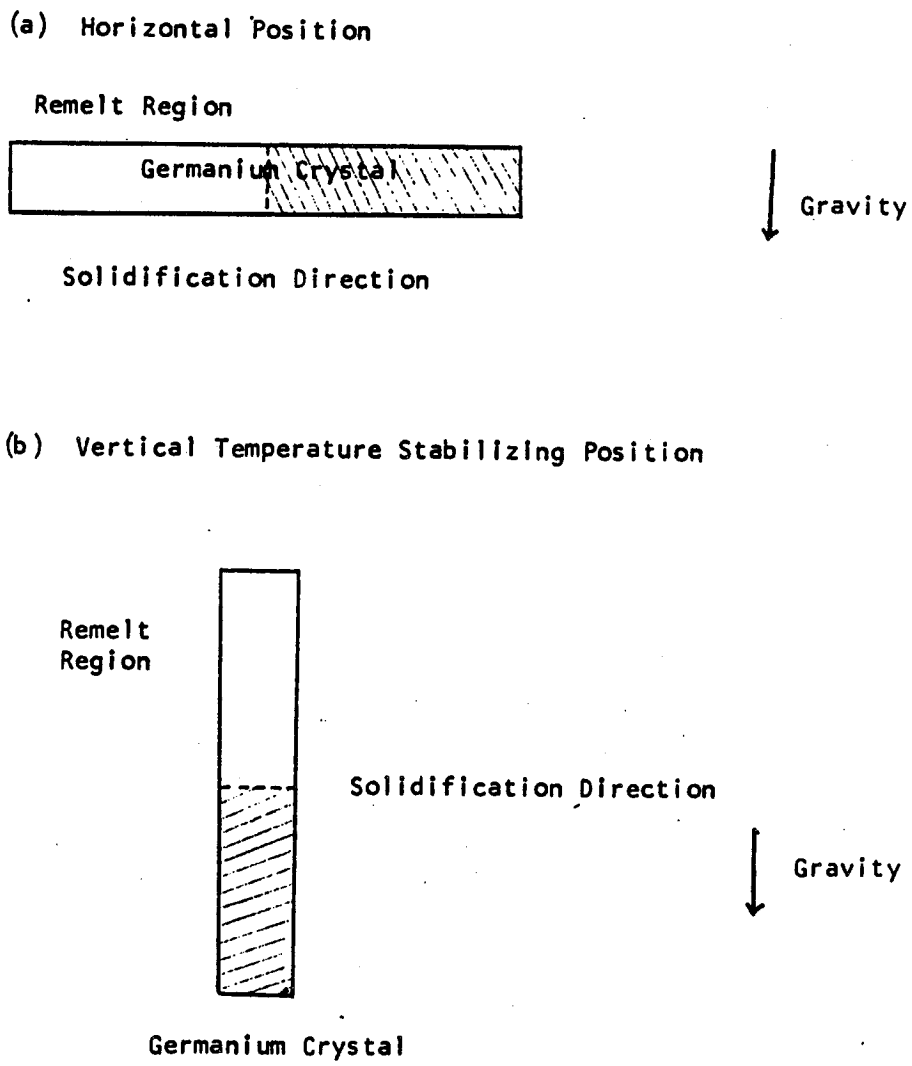

Figure 1. Horizontal (a) and Vertical (b) crystal growth orientations for terrestially grown Ge crystals. No orientational preference was distinguished for space grown crystals.

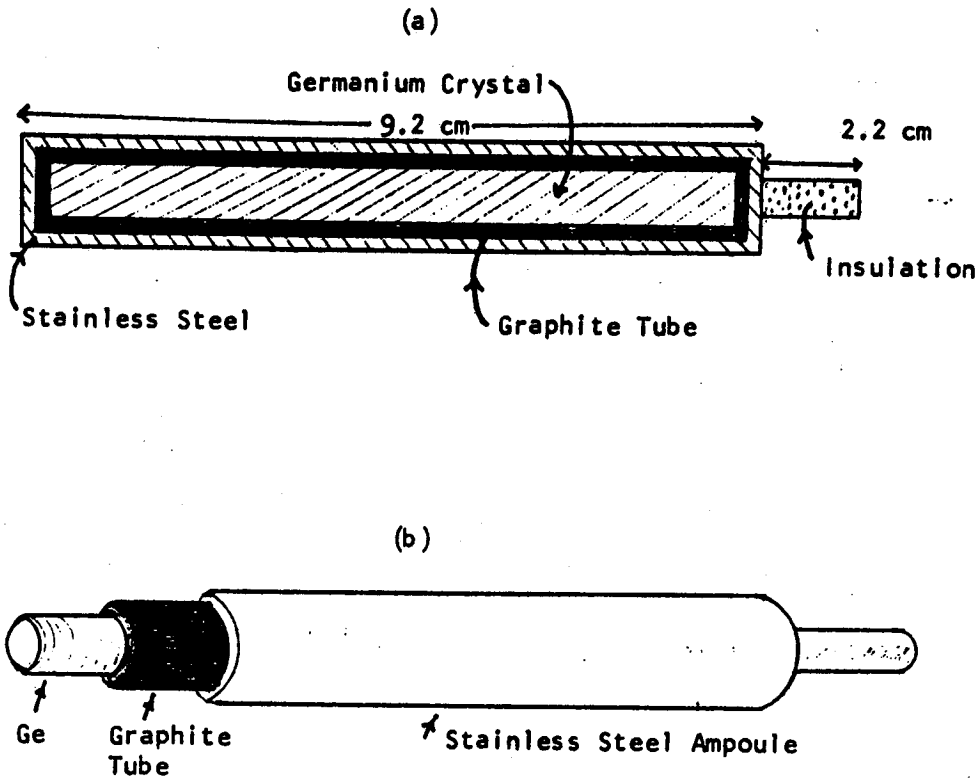

Figure 2. Stainless steel ampoule assembly for all germanium crystals. (a) Inside view (b) Cross-sectional view.

(a) Cartridge Design

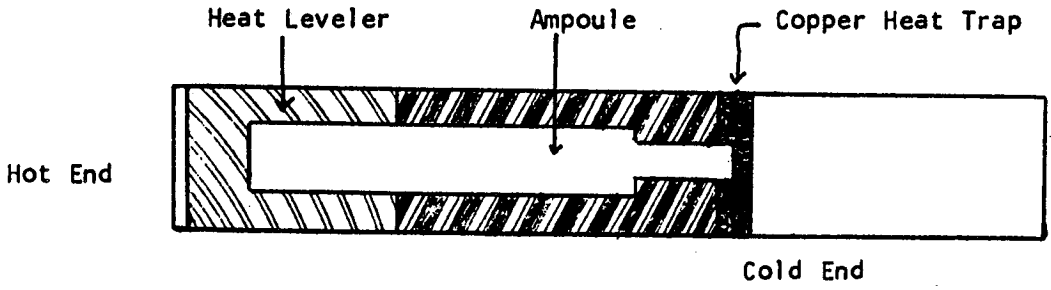

(b) Calculated Ampoule Temperature

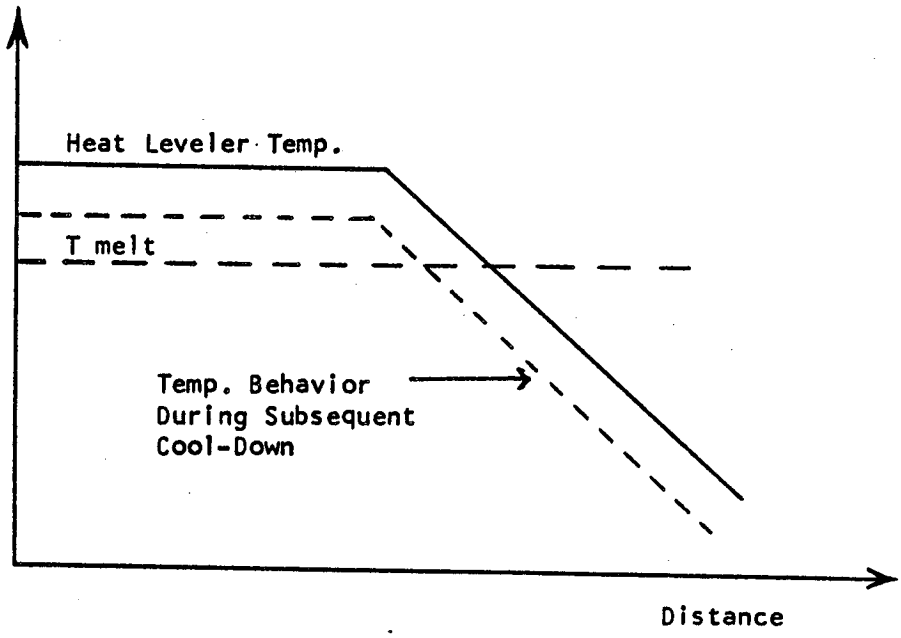

Figure 3. (a) Schematic diagram of cartridge
(b) Ampoule temperature profile. Solid line denote temp. profile during the 2 hr. soak period. Dotted line shows a typical profile during the cool-down cycle.

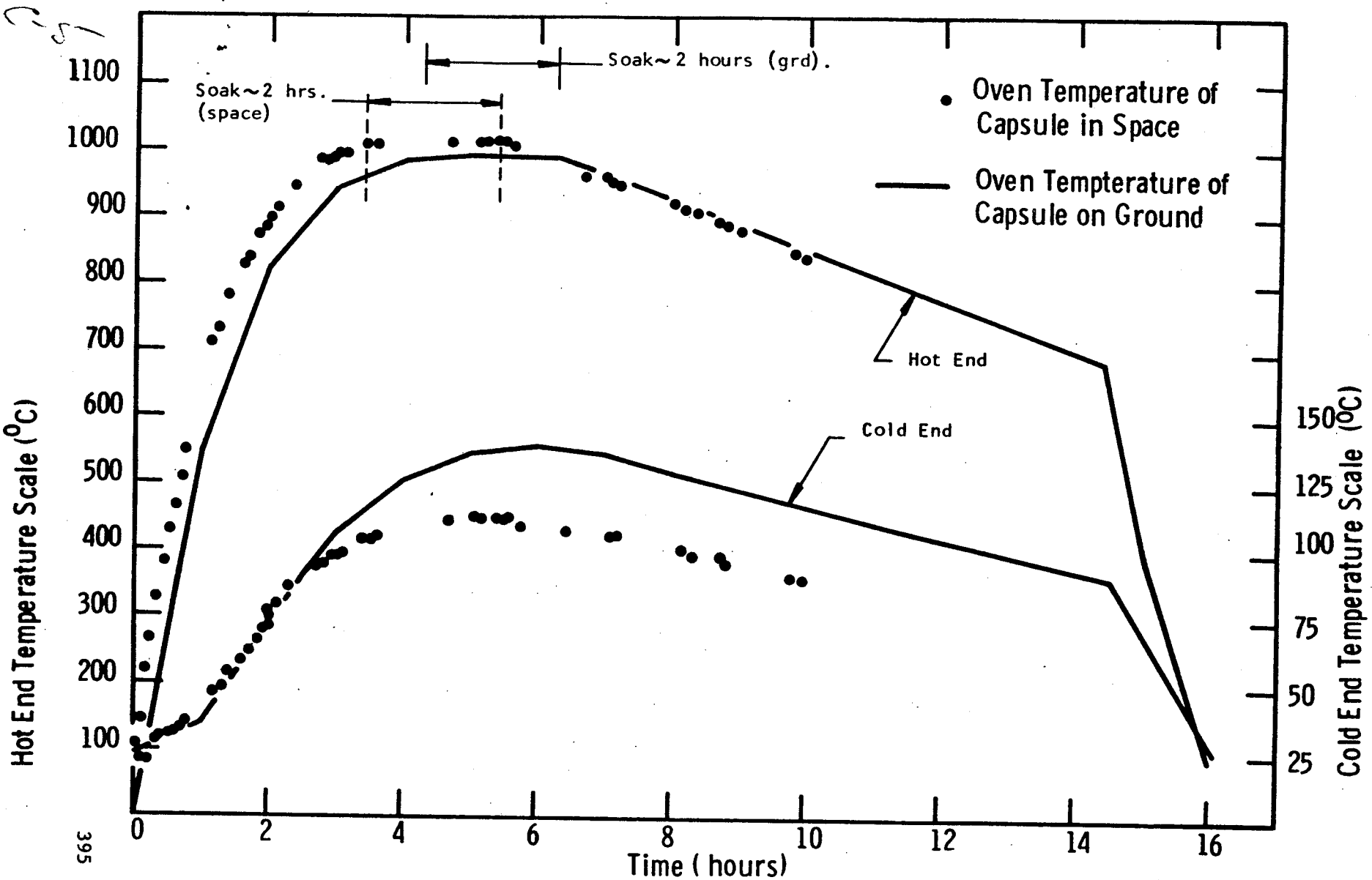

Figure 4. Temperature Profile of Westinghouse Furnace in Space and on Ground

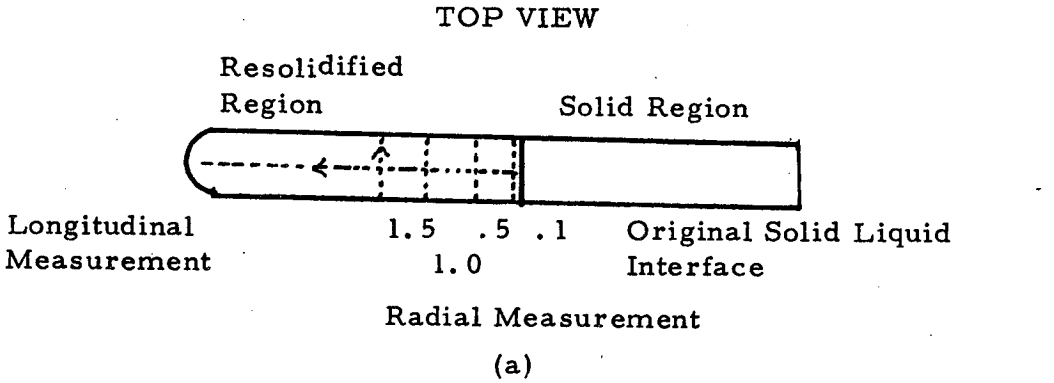

(a)

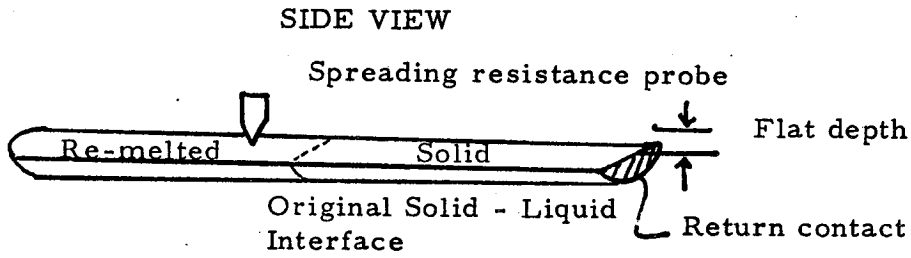

(b)

Figure 5. (a) A top view of the germanium crystal. The dotted lines with arrows indicate the path and direction taken by the spreading resistance probes.

(b) The side view indicates the one-point spreading resistance probe with the flat depth indicated. All crystals are about 0.3 inches in diameter.

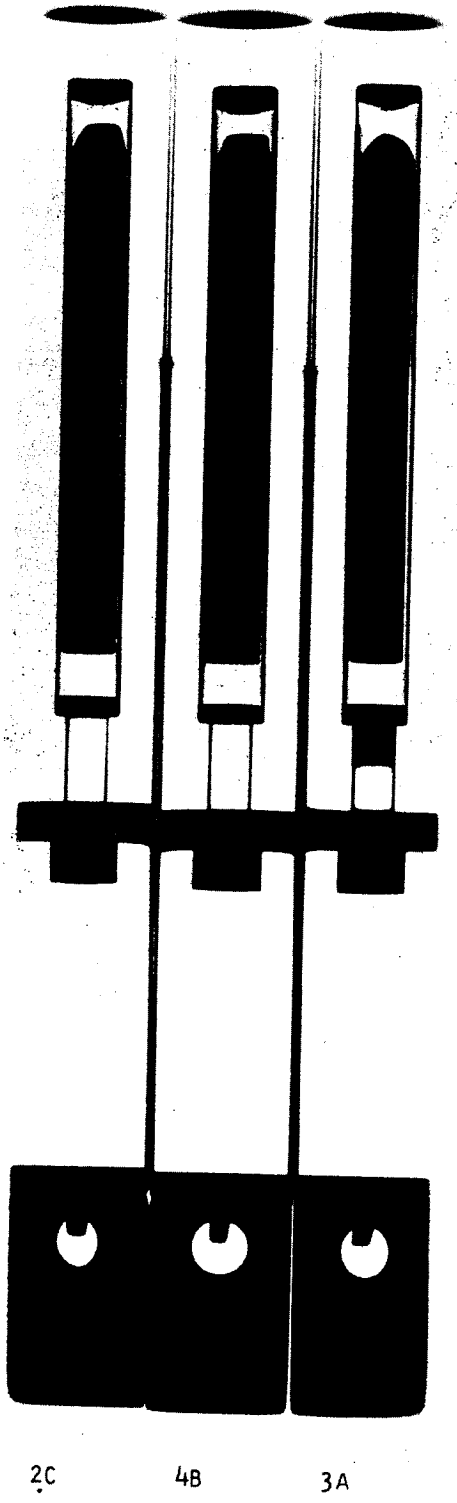

Figure 6. X-ray photographs of germanium capsules after solidification.

Figure 7. X-ray photographs of ampoules after solidification in space.

Figure 8. Gallium doped germanium crystal (Sample 2C) resolidified in space (region to the right of the sharp interface line).

Figure 9. Antimony doped germanium crystal (Sample 3A) resolidified in space (region to the right of the sharp interface line).

Figure 10. Boron doped germanium crystal (Sample 4B) resolidified in space (region to the right of the sharp interface line).

Figure 11. Berg Barrett X-ray topograph of space grown Ge crystals doped with Ga (2C), B (4B), and Sb (3A). Topographs are of shallow flats taken in longitudinal direction, confirming single crystalline and low dislocation growth.

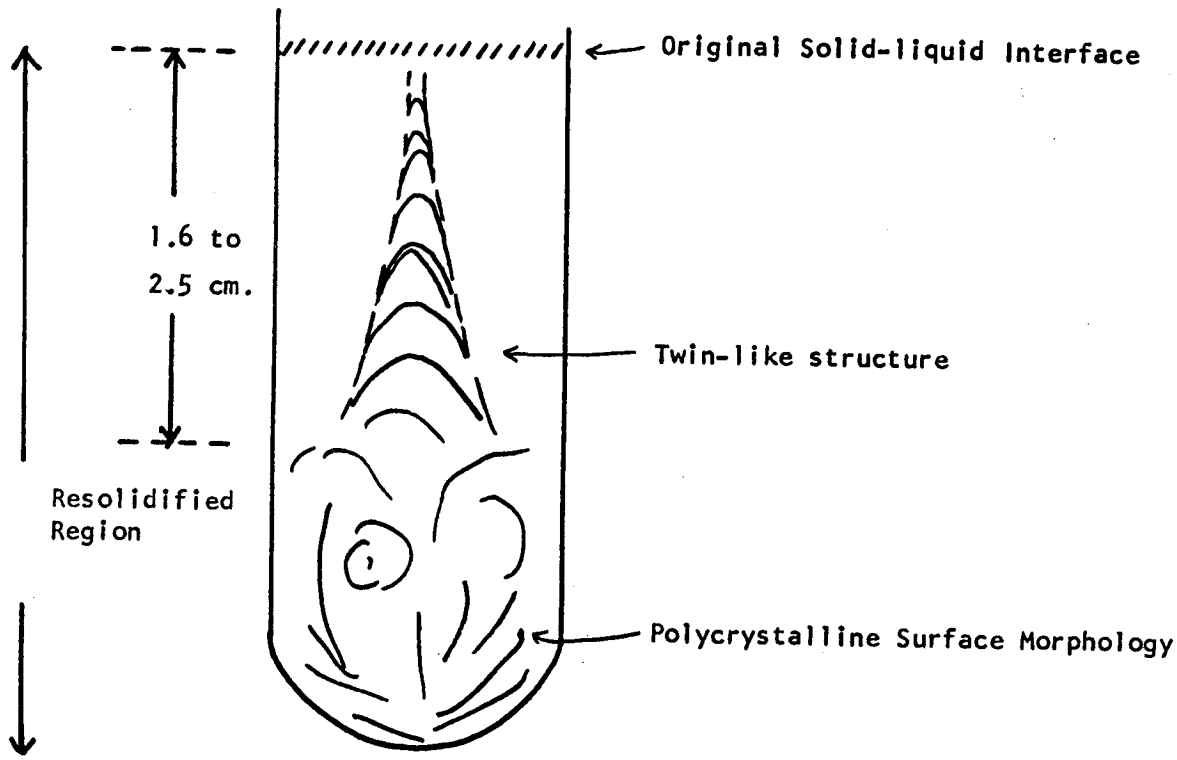

Figure 12. Pictorial illustration of the three distinct surface morphological structures observed before spreading resistance measurements.

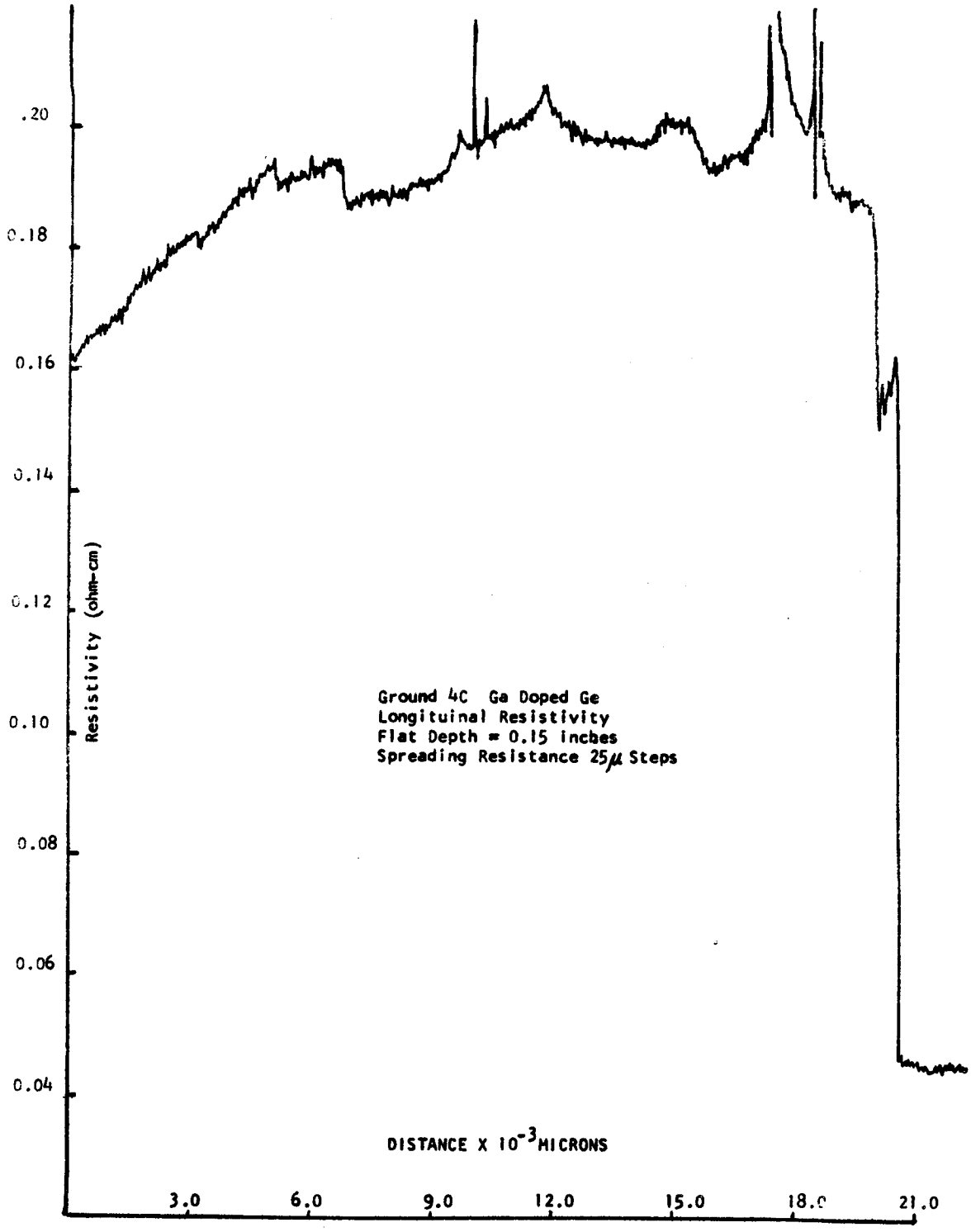

Figure 13. Axial measurements of longitudinal resistivity profile for terrestrially grown Ga doped Ge crystal 4-C in the horizontal position.

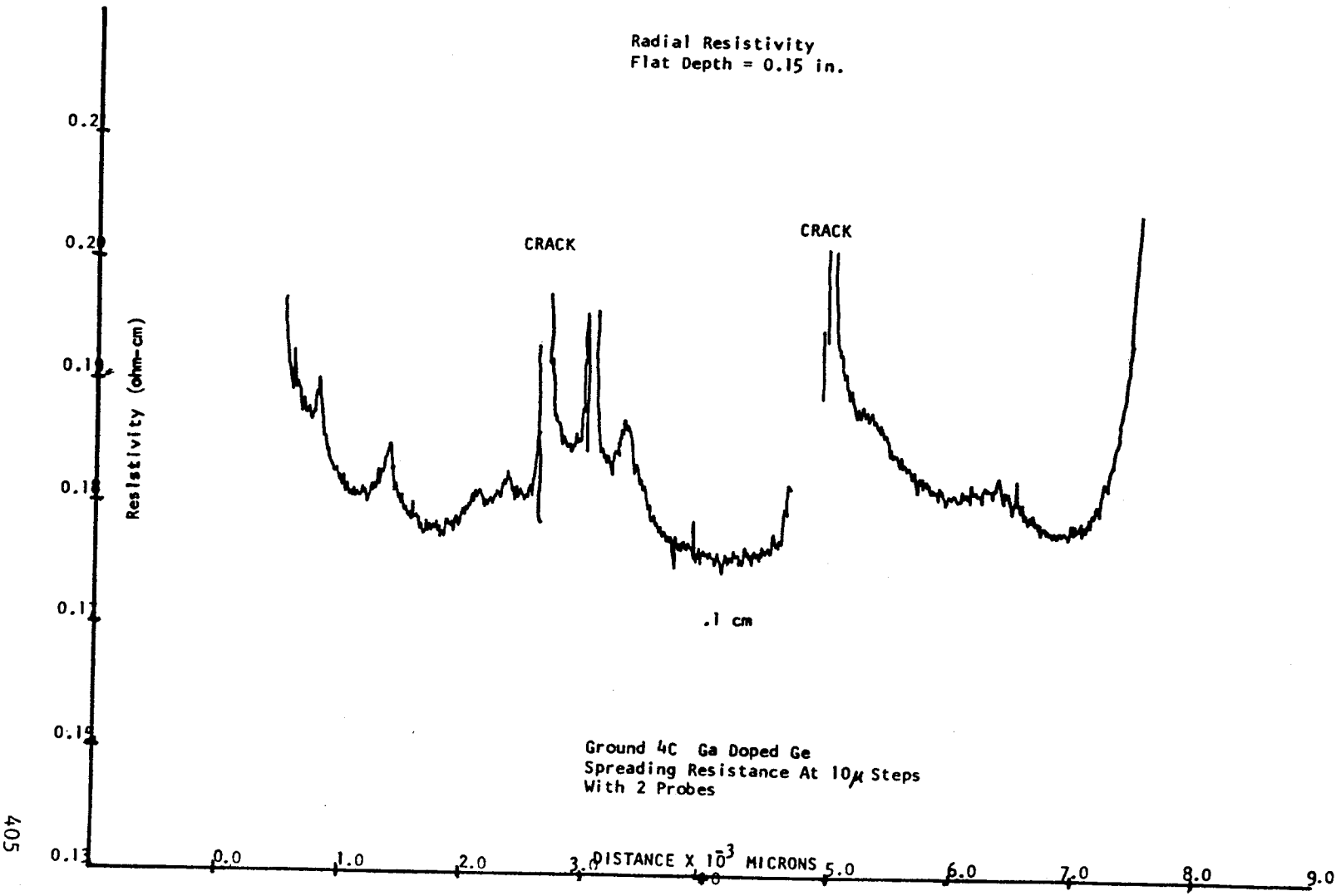

Figure 14. Radial resistivity profile in the bulk for 4-C at 0.1 cm from original solid-liquid interface.

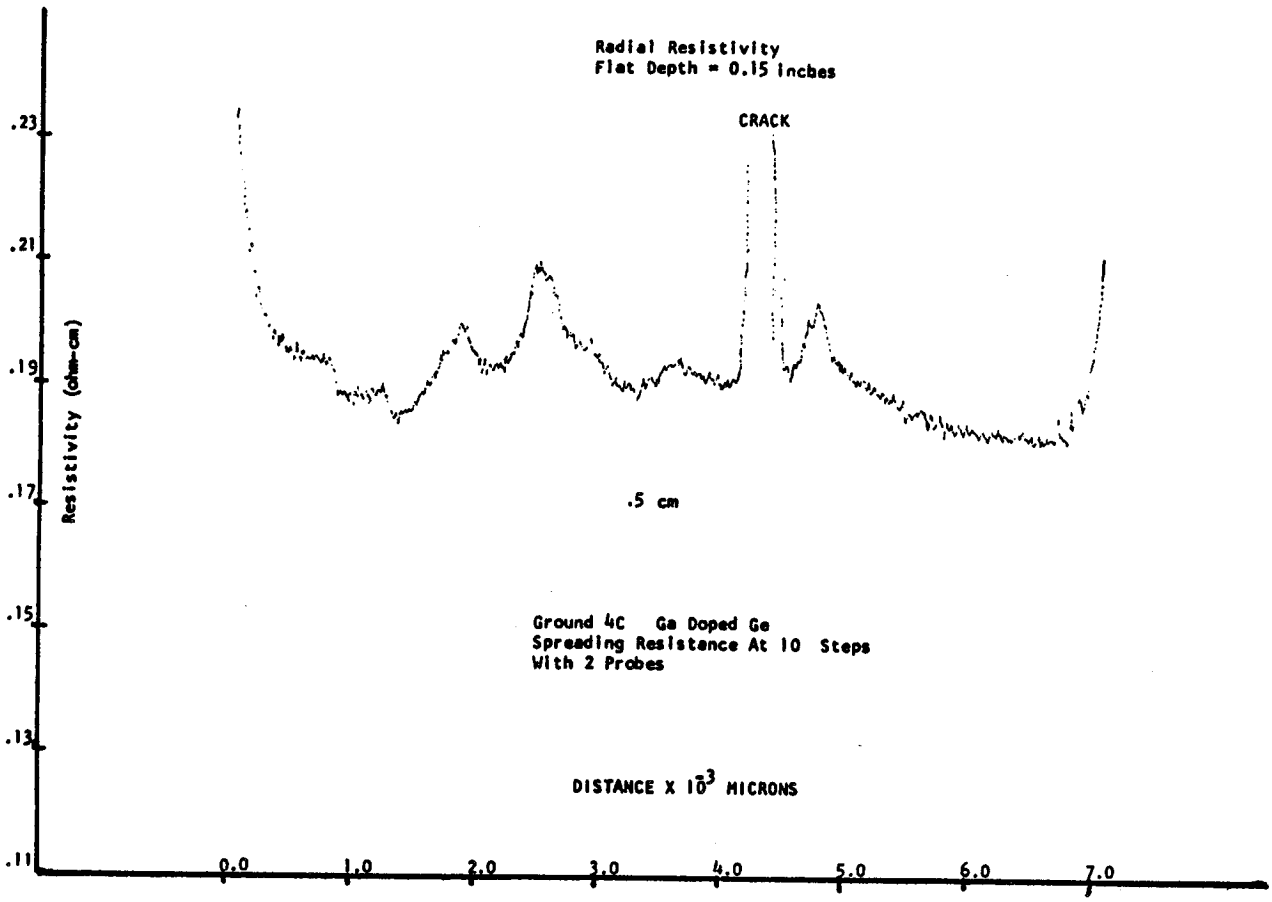

Figure 15. Radial resistivity profile in the bulk for the terrestrial crystal 4-C measured at 0.5 cm from the original solid-liquid interface.

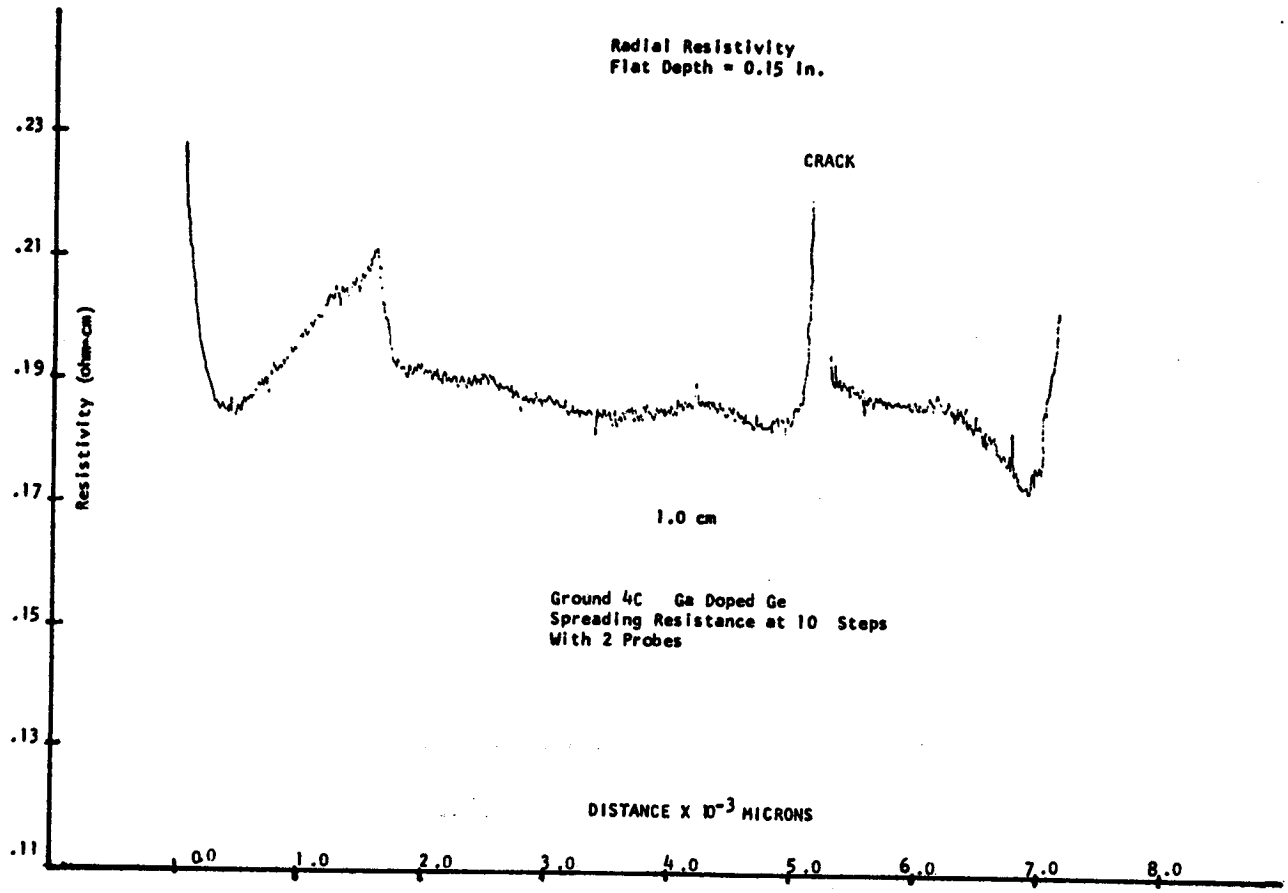

Figure 16. Radial resistivity profile in the bulk for the terrestrial crystal 4-C measured at 1.0 cm from the original solid-liquid interface.

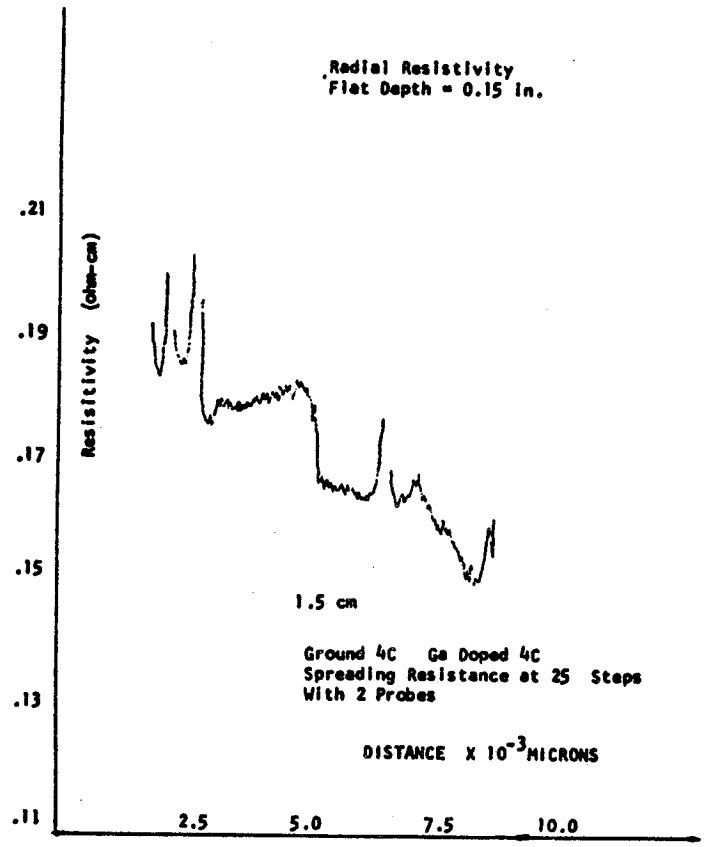

Figure 17. Radial resistivity profile in the bulk for the terrestrial crystal 4-C measured at 1.5 cm from the original solid-liquid interface.

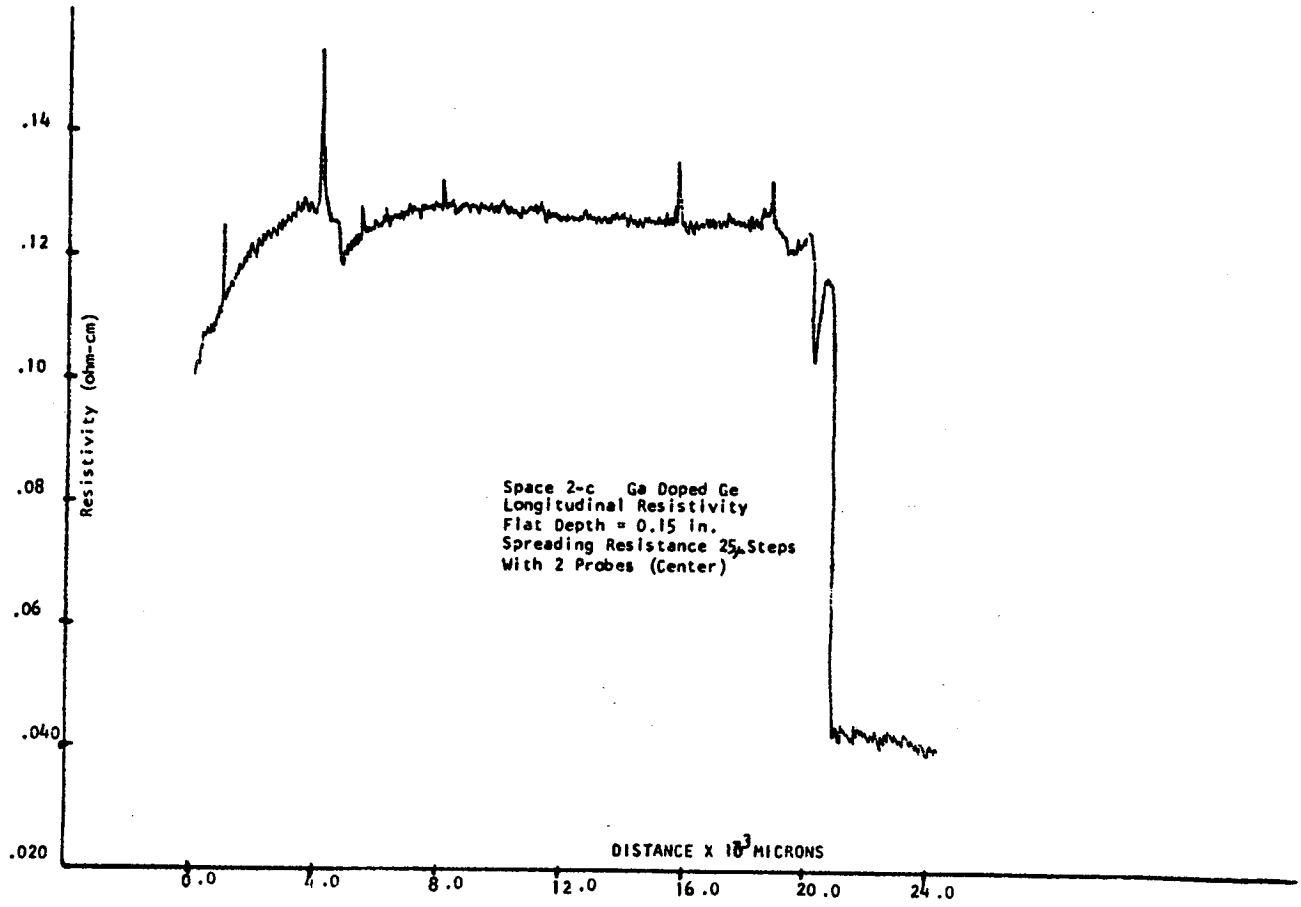

Figure 18. Axial measurements of longitudinal resistivity profile for space grown Ga doped Ge crystal 2-C.

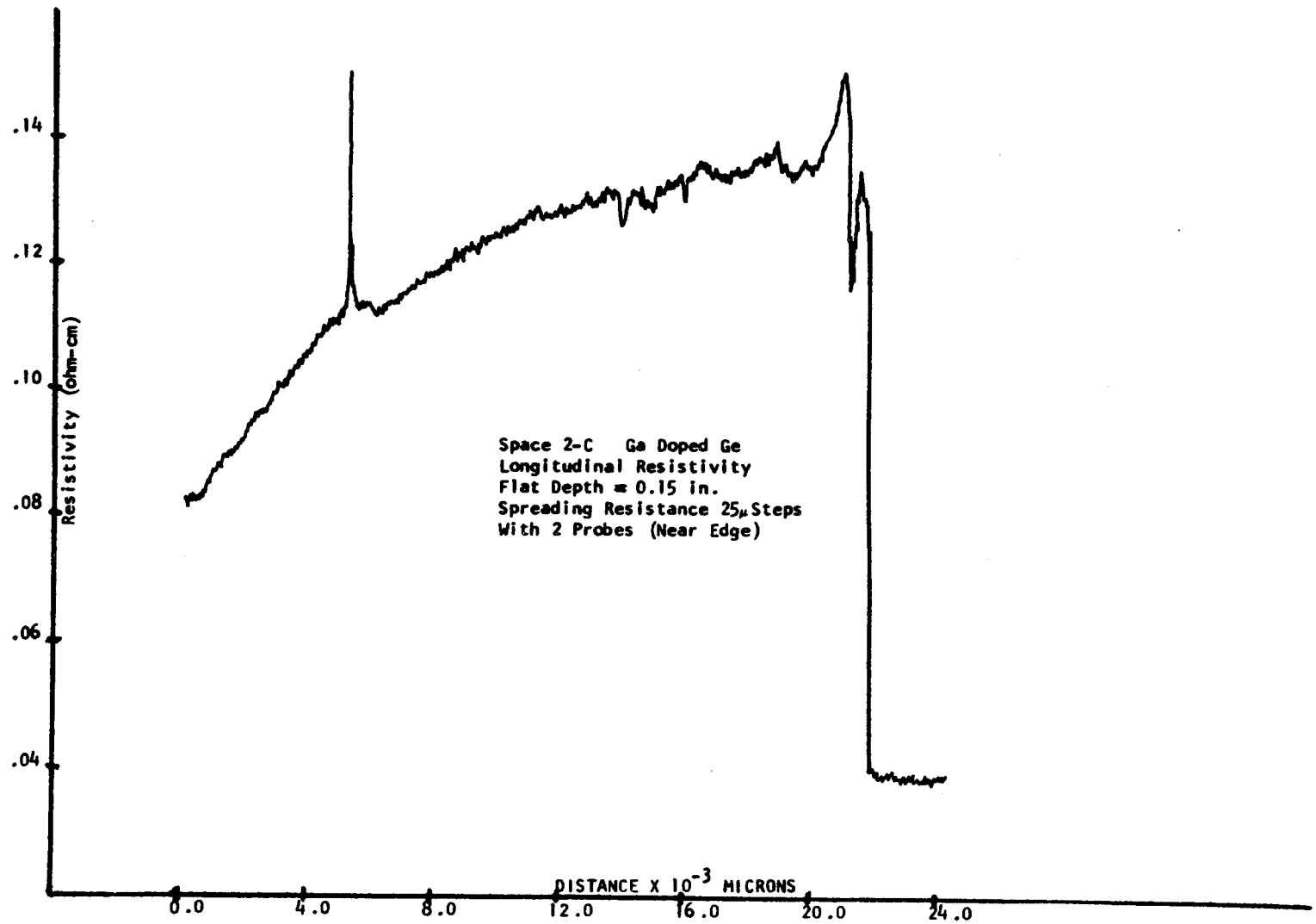

Figure 19. Longitudinal resistivity measurements of space grown Ga doped Ge crystal 2-C made 300 μm from the edge of the flat.

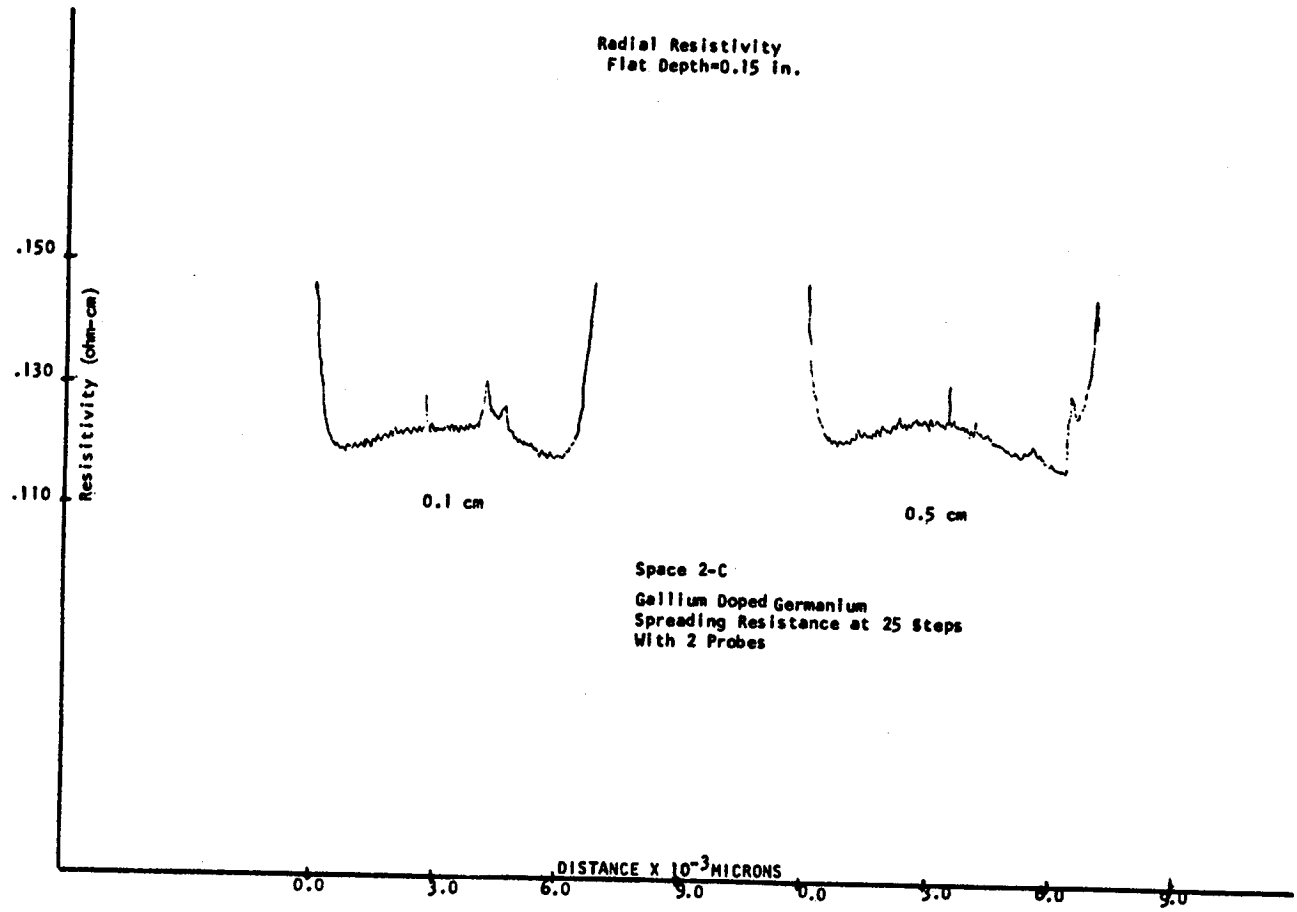

Figure 20. Radial resistivity profiles in the bulk for space crystal 2-C measured at 0.1 cm and 0.5 cm from the original solid-liquid interface.

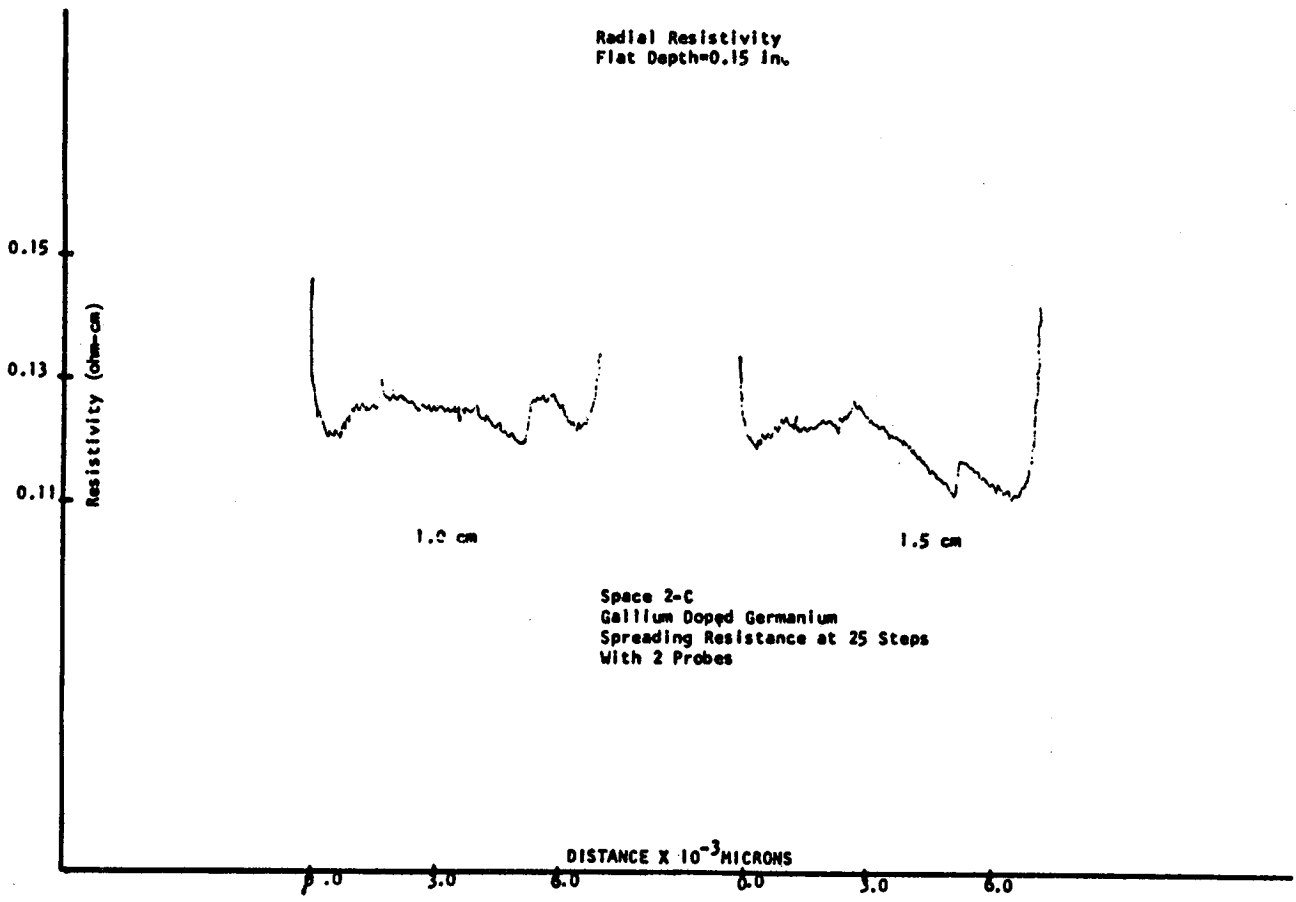

Figure 21. Radial resistivity profiles in the bulk for space crystal 2-C measured at 1.0 cm and 1.5 cm from the original solid-liquid interface.

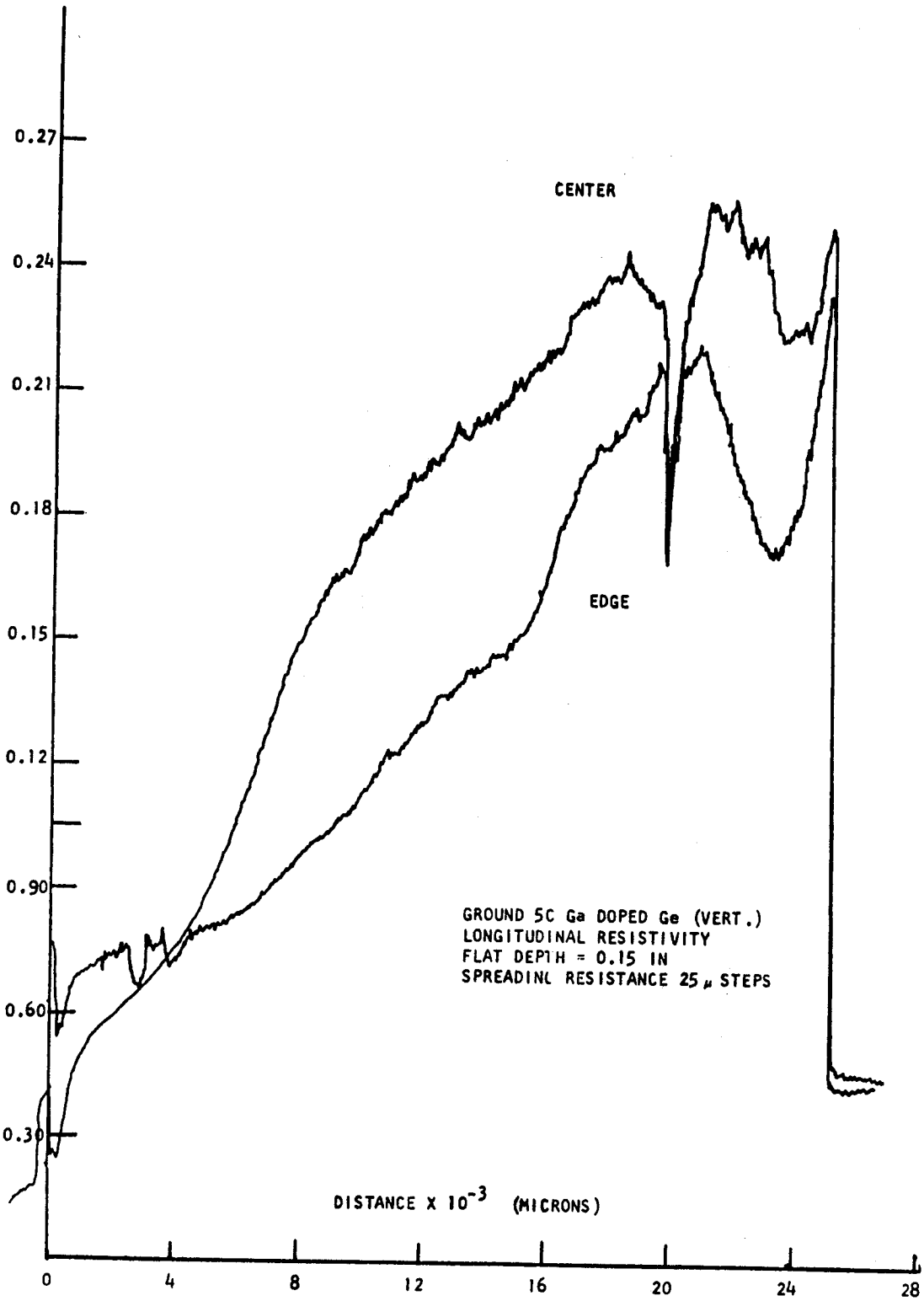

Figure 22. Axial and edge SR resistivity measurements for the terrestrially grown Ga doped Ge crystal 5-C in the vertical temperature stabilizing position. The edge measurement was made at 400 μm from the flat edge. The sharp dips in both curves are attributed to a sudden freezing phenomenon.

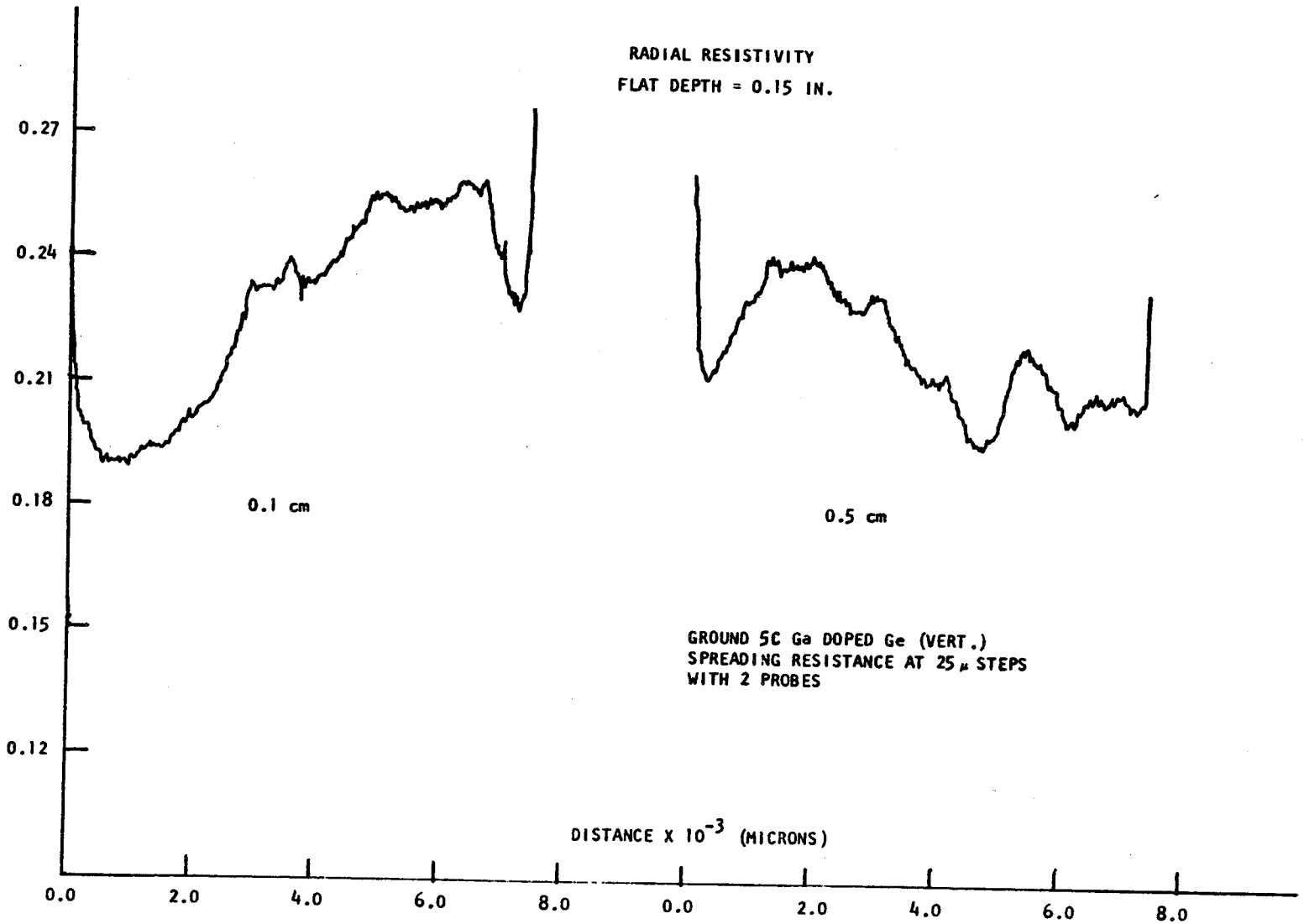

Figure 23. Radial resistivity profiles in the bulk for the horizontal crystal 5-C measured across the flat at 0.1 cm and 0.5 cm from the original solid-liquid interface. The switch in the resistivity minimum from the left to the right side of the 0.1 cm and 0.5 cm radial slices is indicative of changes in interface curvatures during resolidification.

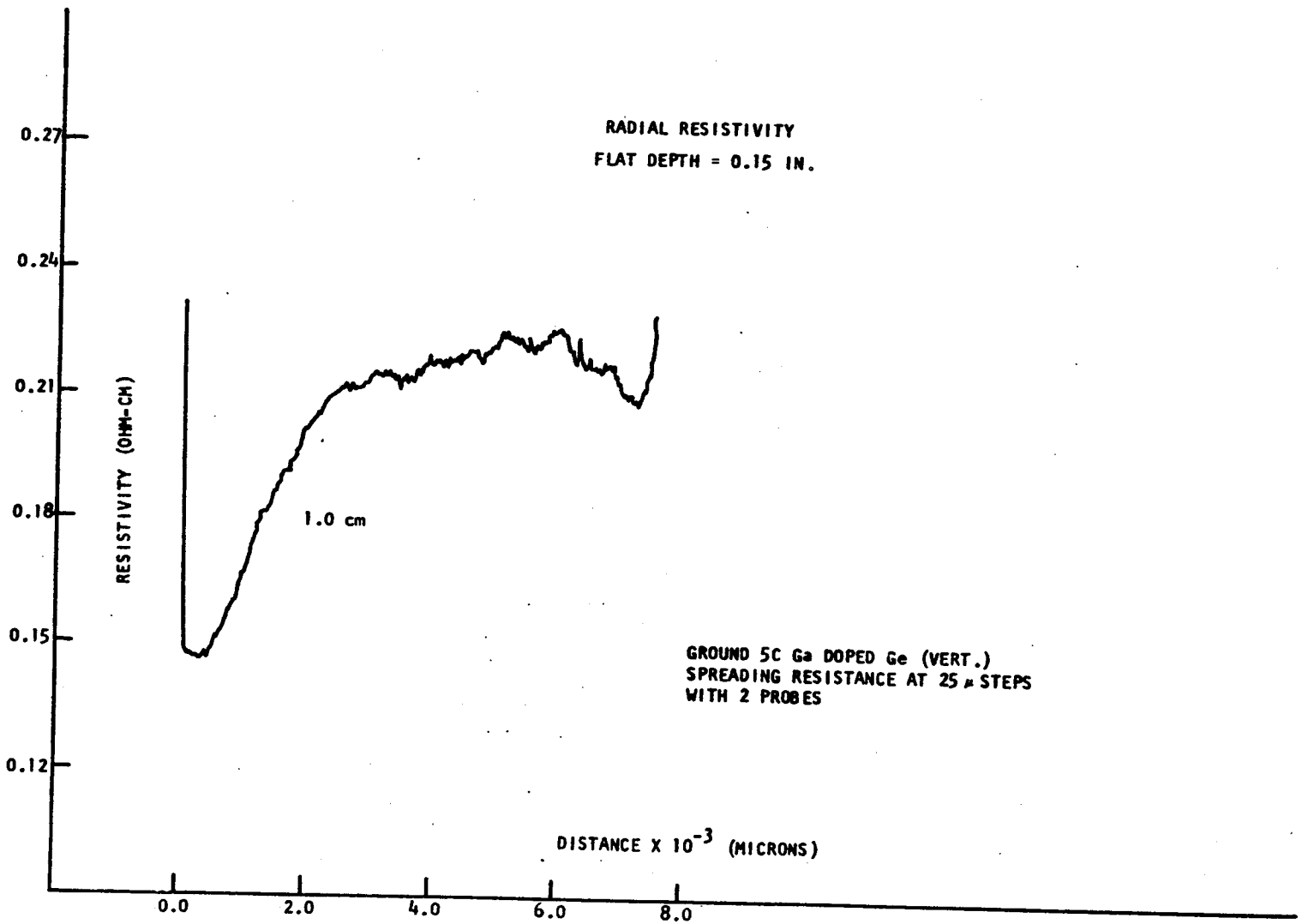

Figure 24. Radial resistivity profile in the bulk for 5-C made at 1.0 cm from original solid-liquid interface.

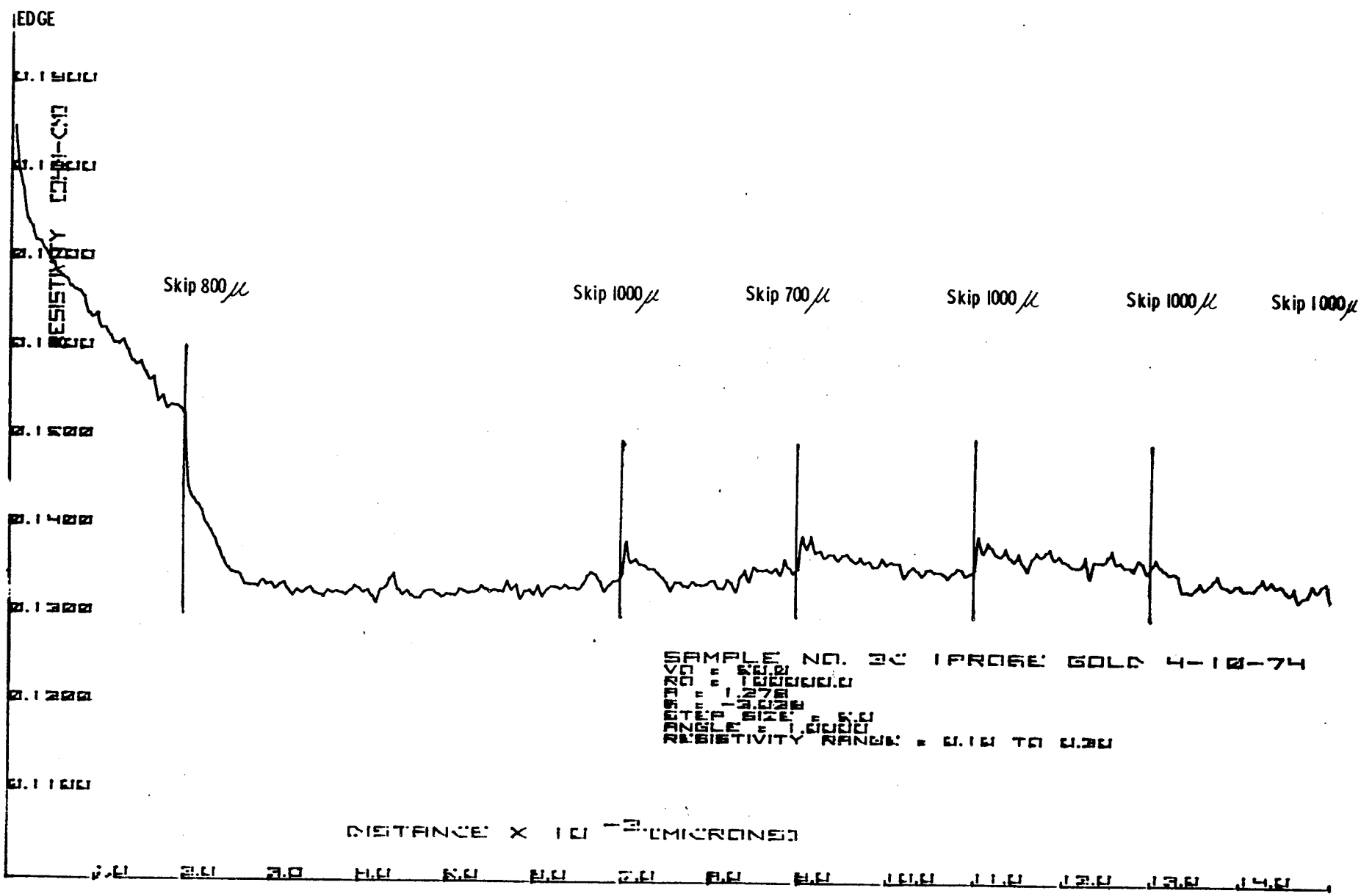

Figure 25. Detailed radial resistivity measurements for space crystal 2-C made at 0.5 cm. from original solid-liquid interface and 5 μm step intervals with one-probe SR.

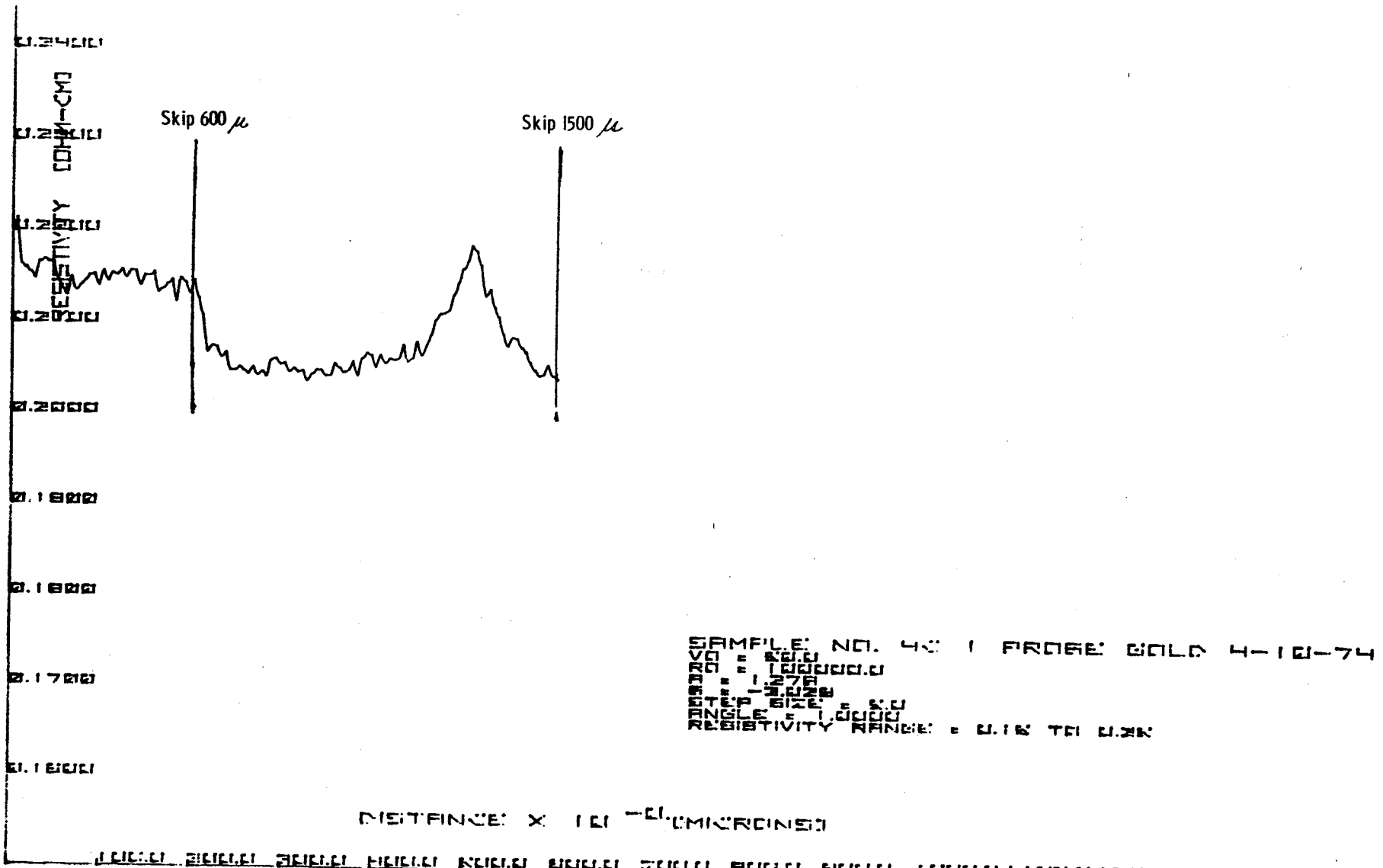

Figure 26. Detailed radial resistivity measurements for horizontally grown terrestrial crystal 4-C made at 0.5 cm from the original solid-liquid interface and at 5 μm step intervals with one-probe SR.

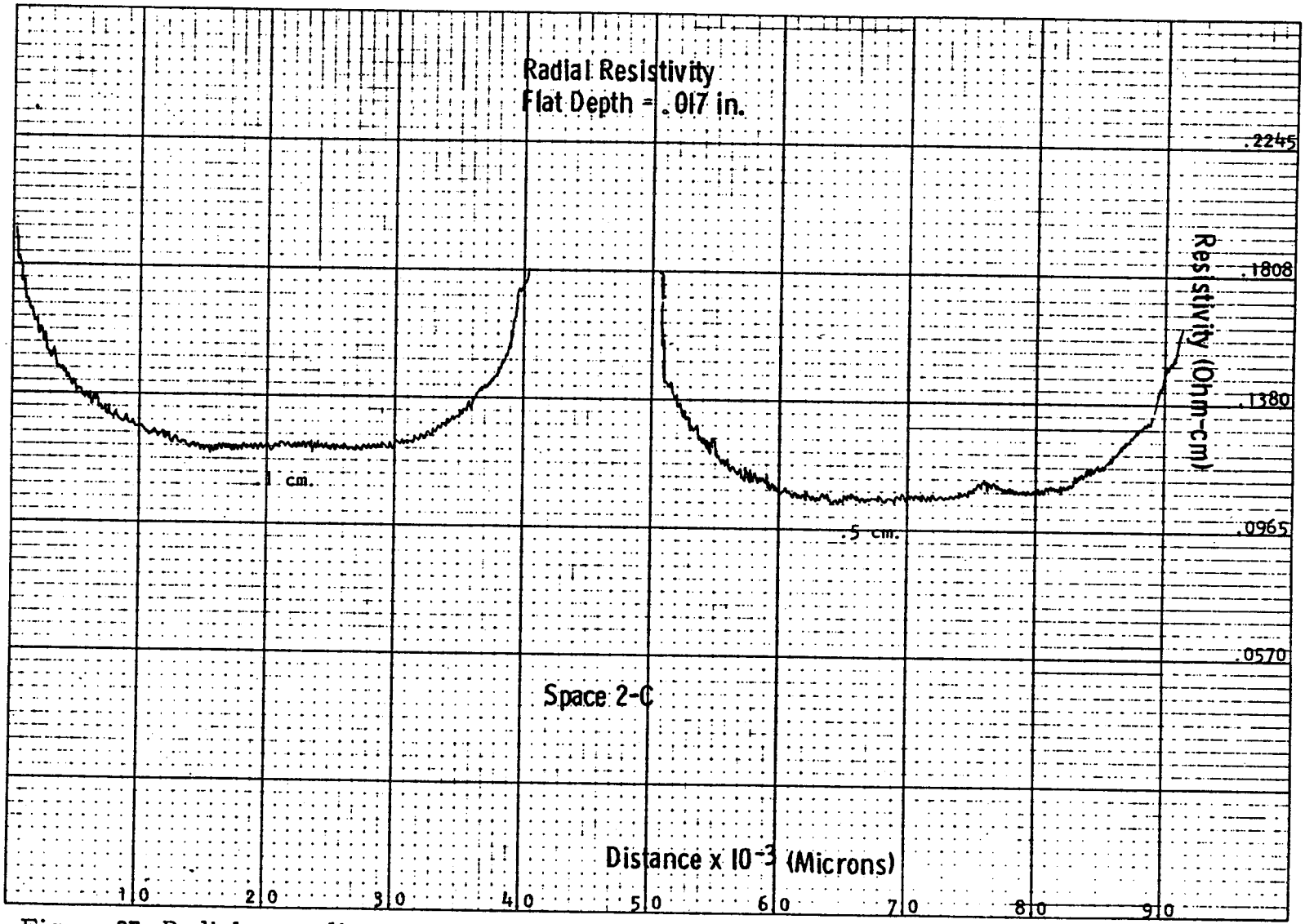

Figure 27. Radial spreading resistance profiles at distances of .1 cm and .5 cm away from the interface for space crystal 2-C. See Fig. 1 for the path of measurement.

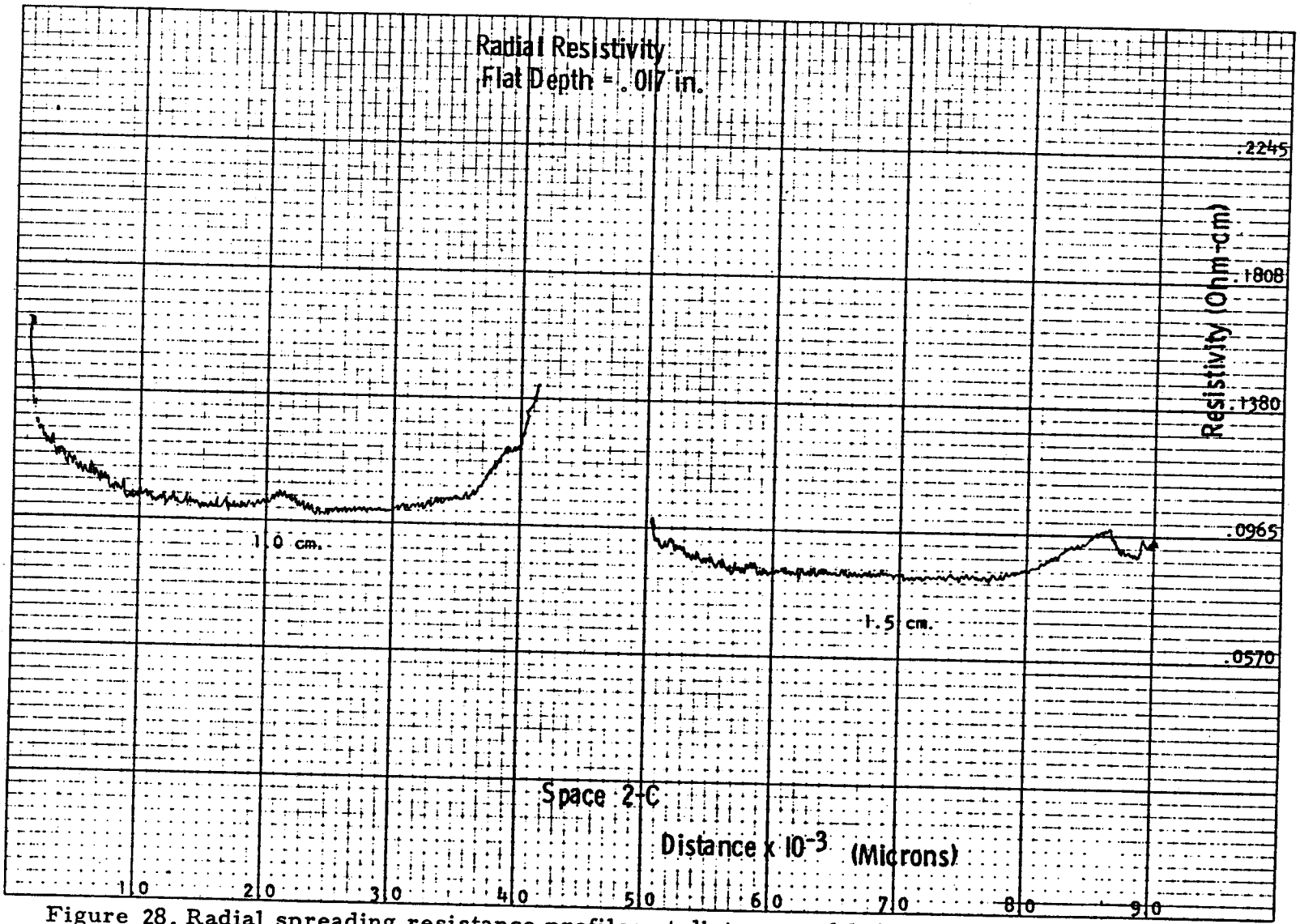

Figure 28. Radial spreading resistance profiles at distances of 1.0 cm and 1.5 cm away from the interface for space crystal 2-C. See Figure 1 for the path of measurement.

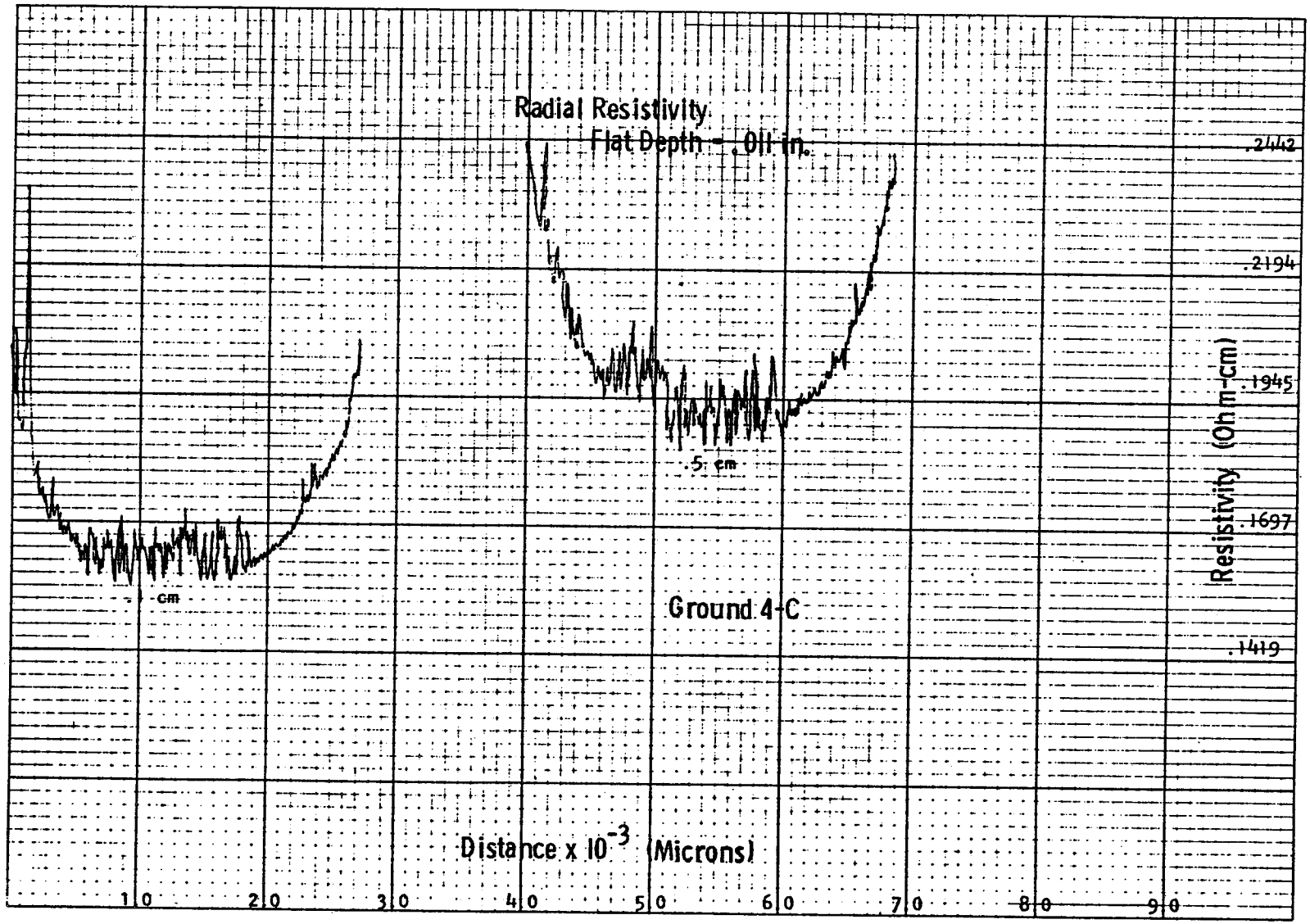

Figure 29. Radial spreading resistance profiles at distances of .1 cm and .5 cm away from the interface for ground crystal 4-C. See Figure 1 for the path of measurement.

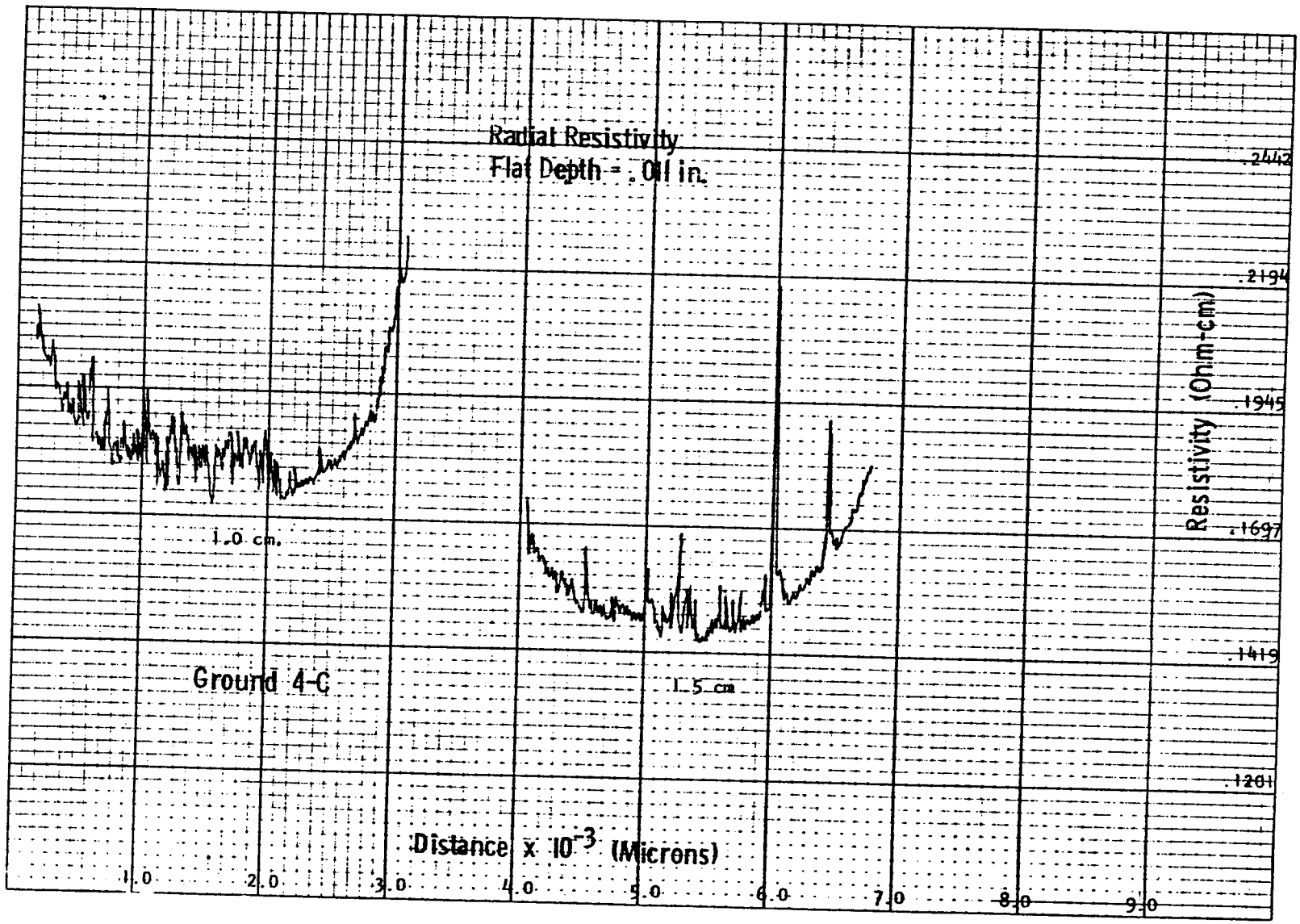

Figure 30. Radial spreading resistance profiles at distances of 1.0 and 1.5 cm away from the interface for ground crystal 4-C. See Figure 1 for the path of measurement.

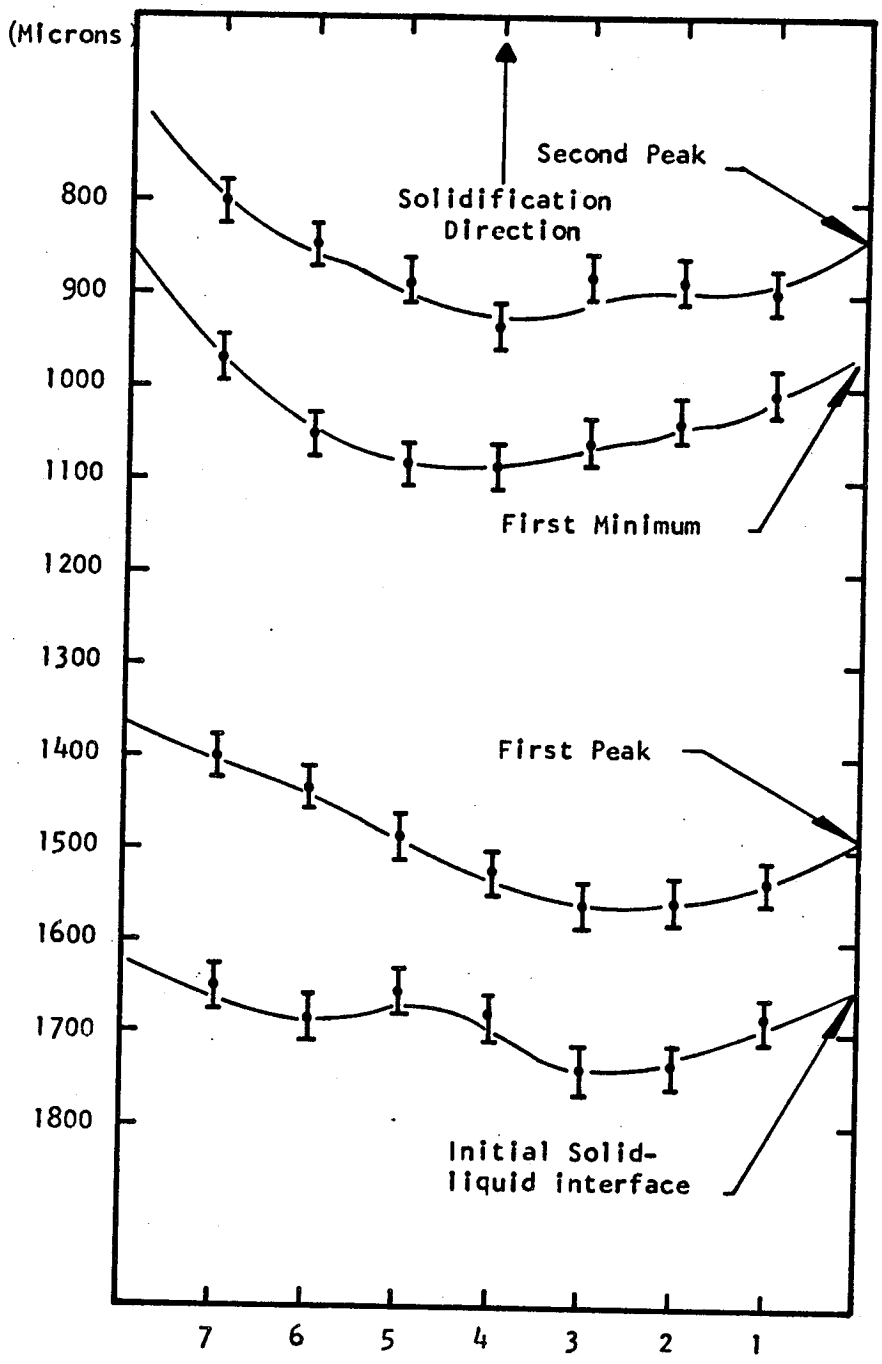

Figure 31. Probable interface shapes during the first 2.8 minutes of resolidification for the space crystal 2-C deduced from detailed SR measurements.

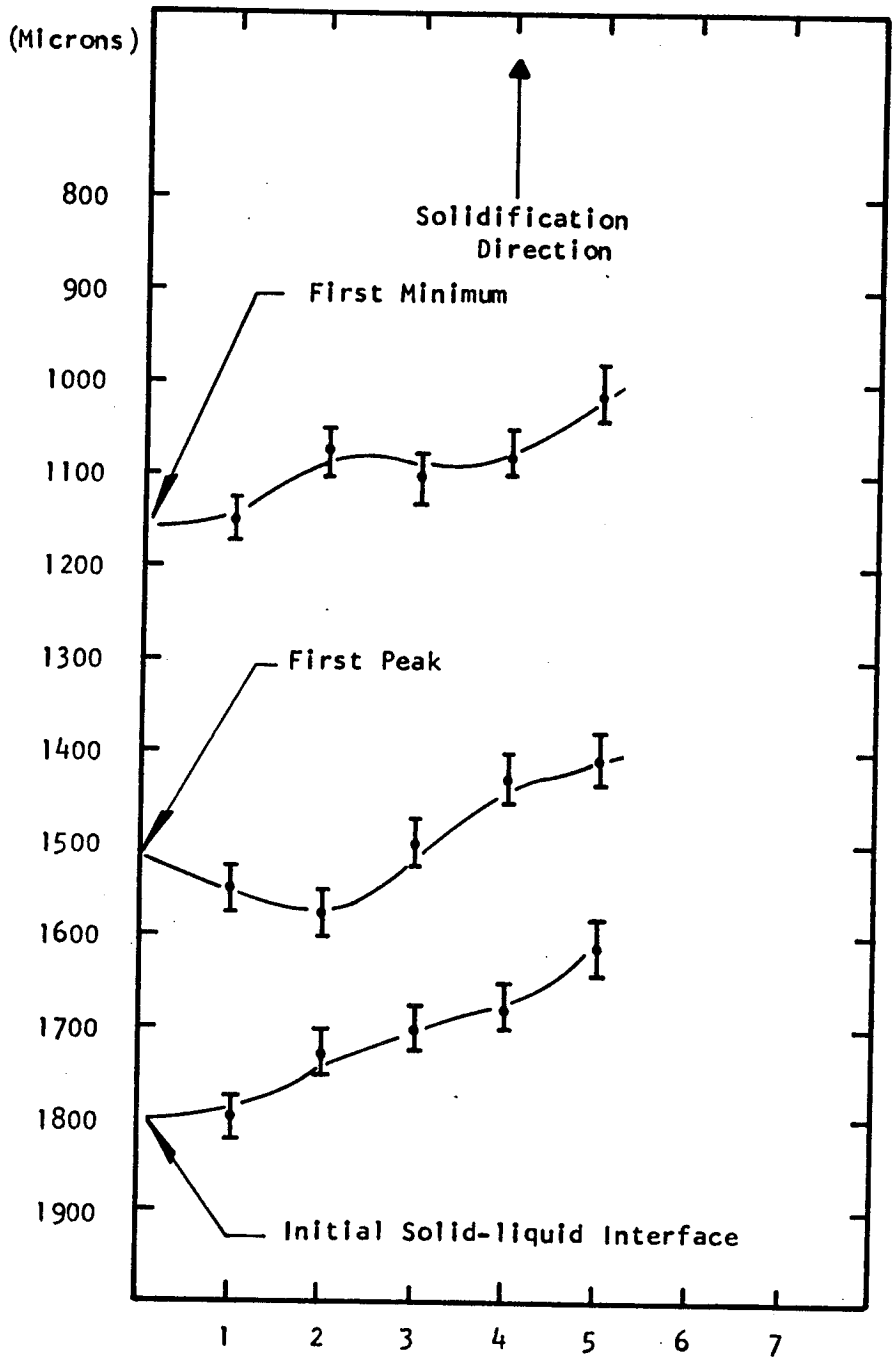

Figure 32. Probable interface shapes during the first 2.1 minutes of resolidification for the terrestially grown crystal 4-C deduced from detailed SR measurements.

(a) Temperature Profile of the Furnace in the Gradient Freeze Technique

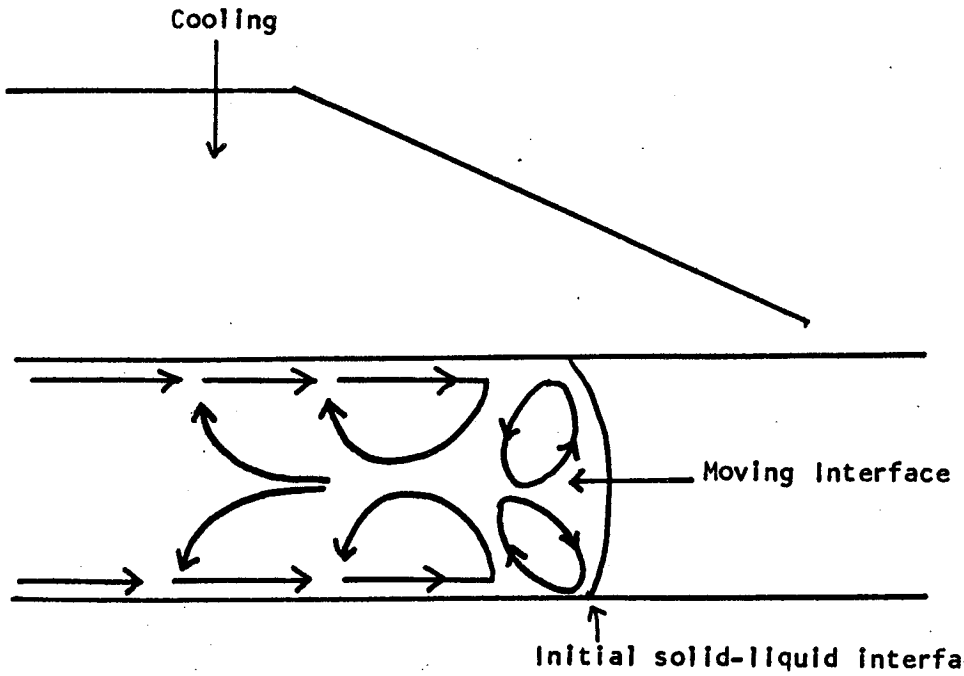

Figure 33. (a) Proposed convective mixing model advanced to explain the results of the SKYLAB experiment. The lines denote thermal convective currents in the melt during solidification in space. These currents will be complicated somewhat for solidification on earth, but the general contours should remain the same.

(b)

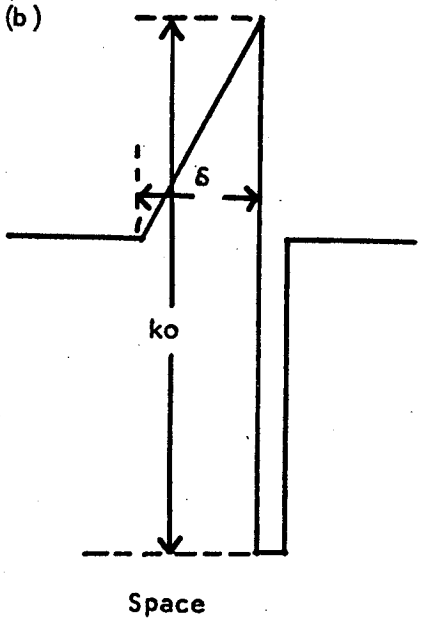

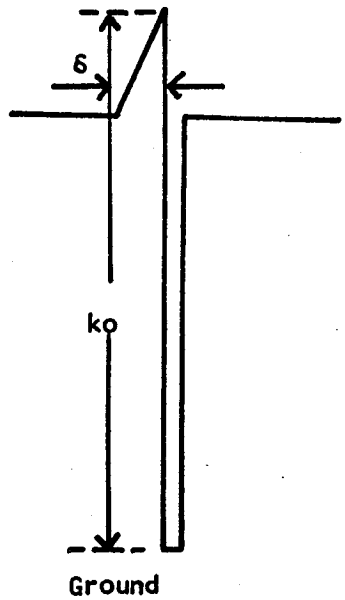

N74 29900

M558 RADIOACTIVE TRACER DIFFUSION

by

A. O. Ukanwa
Howard University
Washington, D.C. 20001

SUMMARY

The M558 Skylab Experiment was performed in Skylab III in 1973 with two objectives in mind. First, the experimental self-diffusion coefficients for liquid zinc were to be determined in a convection-free environment. Secondly, the reduction in convective mixing in earth gravity by going into the zero-gravity environment of space was to be estimated. The experiment was designed to utilize high temperatures and linear thermal gradients provided by the M518 Multipurpose Electric Furnace, and the radioactivity of zinc-65 of 245-day half-life to investigate self-diffusion in liquid zinc. At the time of fabrication in October, 1972, radioactivity level in each ampoule was 20 microcurie.

The Principal Investigator for the study was Dr. Anthony O. Ukanwa, formerly of Space Sciences Laboratory, Marshall Space Flight Center, Alabama. Mr. Tommy C. Bannister, also of MSFC, was Scientific Monitor. Fabrication of experiment zinc ampoules and radioactivity counting were contracted to Oak Ridge National Laboratory, Tennessee, where excellent monitoring facilities exist.

The ampoules were encased in cartridges by Westinghouse Astronuclear Laboratory, Pennsylvania to meet thermal conditions prescribed by the Principal Investigator. Skylab samples had temperature gradient of 45°C/cm over a length of 4.68 cm (1.84 in.) and midway temperature of 550°C.

The distribution of zinc-65 tracer, after melting, maintaining at soak temperature for 1 hour of soak time and then resolidifying, was obtained by sample sectioning. The concentration of activity of each section (microcurie/gram) was plotted against positions along the sample axial and radial position. Experimental data and theoretical results from solution of Fick's law of diffusion in one dimension were compared. Samples tested on earth showed very rapid diffusion. Diffusion coefficient in unit gravity was 50 times the zero-gravity diffusion coefficient of Skylab. This order of difference was attributable to unit gravity convective velocity of only 4.16×10^{-4} cm/sec in magnitude. The convection-free diffusion coefficient of Skylab was found to be $D = 9.17 \times 10^{-4} \exp(-5{,}160/RT)$ cm^2/sec for the temperature range from 693°K (420°C) to 973°K (700°C). The diffusion coefficient at 550°C was found to be 4.28×10^{-5} cm^2/sec.

INTRODUCTION

This paper presents the laboratory and theoretical results of radioactive tracer zinc diffusion from NASA Skylab-III experiment M558. The M558 study was made by Dr. Anthony O. Ukanwa, formerly of Space Sciences Laboratory, Marshall Space Flight Center (MSFC), Alabama as Principal Investigator between August, 1972 and November, 1973. The experiment was designed to investigate the self-diffusion of radioactive liquid zinc-65 in non-radioactive liquid zinc by utilizing high temperatures and linear thermal gradients provided by the M518 Multipurpose Electric Furnace. Fabrication of zinc samples, their encapsulation in tantalum tubes, selected ground tests, sample sectioning and tracer radioactivity counting were conducted at Oak Ridge National Laboratory (ORNL), Tennessee under sub-contract because of the excellent radiation counting facility there. The ORNL portion of this work was performed by E. H. Kobisk and D. N. Braski of the Isotopes Division, ORNL.

The zinc-tantalum ampoules fabricated by ORNL were encased in cartridges by Westinghouse Astronuclear Laboratory (WANL), Pennsylvania according to M518 furnace specifications and temperature conditions prescribed by the Principal Investigator. The cartridge performance was verified in tests in prototypes of the M518 furnace. Further ground base heat tests were made at MSFC. The ground base samples were sectioned and counted for radioactivity at ORNL. Three Skylab flight samples were also sectioned and counted at ORNL. The results of these ground base and flight tests are the ingredients of this paper.

Radioactive zinc-65 (^{65}Zn) is an isotope of normal zinc with a half-life of 245 days. This is the key in data retention after the performance of M558 experiments in Skylab until data analysis months later. It was estimated that a period of 20 months (2.5 half-lives for zinc-65) might elapse between time of fabrication of experiment ampoules and their return from Skylab for analysis. Thus a sufficient amount of radioactivity to ensure good data acquisition had to be incorporated into the ampoules. On the other hand, the radiation level had to be kept low enough to ensure the safety of the Skylab crew. A compromise radioactivity level of 20 microcurie per ampoule at time of fabrication was decided upon.

The approach in this paper is as follows. First, a brief description of the zinc sample, ampoule and cartridge fabrication is made. Secondly, a brief theoretical analysis is given. Thirdly, the ground base and Skylab flight results are presented. Finally, an assessment is made of how closely the two objectives of the M558 experiment have been realized, these objectives being the determination of experimental diffusion coefficients for liquid zinc in a convection-free environment and the estimation of the degree of reduction of convection in zero-gravity from its value in earth gravity.

Further details of the M558 Radioactive Tracer Diffusion Experiment may be found in the references cited in this paper.

FABRICATION

The materials used to fabricate the M558 hardware include high-purity zinc (99.99%), ATJ carbon, tantalum tubing, tantalum bar, graphite plug, stainless steel and Fiber Frax insulator. The vendors and chemical analyses for these materials are listed in Appendix A.

Zinc Specimens

Polishing and Irradiation

Zinc bar specimens in ½-in.-diameter ingots were cold drawn into bars of 5/16-in. diameter, and then machined to 0.286 in. diam and cut into 1.592-, 0.796-, and 0.250- in. lengths. One 1.592-in.-long rod bonded to a 0.250-in. pellet on one end was called an A-type specimen , while two 0.796-in.-long bars bonded to a 0.250-in. pellet in the center comprised a B-type specimen (Fig. 1). Before the bars were bonded, all the mating surfaces were polished to a mirror finish and the 0.25-in. pellets were irradiated in a reactor.

All of the 0.250-in. pellets were irradiated in the Bulk Shielding Reactor (BSR) at ORNL on October 5, 1972. They were subjected to a fluence of 1.5×10^{12} n/(cm^2.sec) thermal neutrons and a fluence of 7.0×10^{7} n/(cm^2.sec) fast neutrons. The irradiation produced zinc-65 in the pellets to an activity level of approximately 20 microcurie per pellet. Zn-65 decays to ^{65}Cu by two branches as shown schematically in Fig. 2. Slightly over half of the zinc-65 decay (50.6%) involves electron-capture process to an excited ^{65}Cu* state at 1.1155MeV. Decay of the ^{65}Cu* to stable ^{65}Cu produces gamma radiation of 1.1155 MeV energy. The other branch involves electron capture (48.0%) and positron emission (1.4%) with a 0.331-MeV energy as decay occurs directly to the stable ^{65}Cu. The electron capture also leads to subsequent atomic reactions producing X-rays and Auger electrons.

Joining Zinc Specimens

After investigating numerous joining techniques, a rather unique method of cold welding the zinc-65 pellets to the zinc bar (see Fig. 1) was developed. The equipment needed to conduct the process included a 5-ton capacity hydraulic press and a hardened steel die with a 0.286-in.-diam ram (zinc specification). To join A-type specimens (Fig. 1a), the mating surfaces of a 1.592-in.-long bar and zinc-65 pellet were first lightly abraded on 600-grit emery paper. The two pieces were

then etched for 1 to 2 min in an acid solution containing one part concentrated HCl and three parts distilled water. The zinc bar was then inserted in the die on top of the bottom ram with the abraded surface facing upwards. A glass eye dropper was used to place a drop of acid solution on this surface. The zinc-65 pellet was then inserted in the die, followed by the upper ram, and the entire assembly was placed in the hydraulic press. A load of 1500 to 1700 lb (23,400 to 26,600 psi in compression at the zinc interface) was sufficient to produce a cold-welding bond between the zinc bar and zinc-65 pellet. However, this force also caused substantial plastic flow of the zinc in the die body making removal of the bonded specimen difficult. Loads of 2000 lb or more were sometimes needed to eject the specimens, which invariably resulted in specimen breakage. This problem was solved by immersing the die in a cold bath of dry ice and acetone for 5 min. Since the thermal contraction of zinc was twice that of the steel die, it was possible to eject the zinc specimen with loads of 100 lb or less, and specimen failure seldom occurred. It should be pointed out that this entire procedure was carried out using techniques and a special hood designed for handling radioactive materials. The purpose for using acid in the joining process was to dissolve the oxide film from the interface, thus permitting the cold welding of two clean surfaces. The acid itself was not incorporated into the zinc specimen, but was forced out of the interface at low compressive load. Continued loading forced the zinc to expand and fill the die cavity which in turn expelled the acid from the die along paths between the zinc specimen and die walls. The B-type specimens were joined in a similar manner, except that two bonding operations were needed. First a zinc-65 pellet was bonded to a 0.796-in.-long zinc bar (see Fig. 1b) and ejected after cooling the die in the dry ice-acetone bath. Then the remaining surface of the zinc-65 was lightly abraded on 600-grit emery paper and the entire sample was etched in the hydrochloric acid solution (1 HCl:3 H_2O) for 2 to 4 min. Extra etching was sometimes needed to reduce the diameter of the zinc specimen so that it could be easily reinserted into the die. Finally, the second 0.796-in.-long zinc bar was bonded to the other half with the zinc-65 pellet using a load of 1700 to 1900 lb. The increased pressure was found to be necessary to compensate for the increase in mechanical properties of the first pellet due to work hardening. Moreover, if the second bond failed upon ejection from the die, it was necessary to repeat the second bonding procedure using a 1900 to 2100 lb load.

After the zinc specimens were joined, they were rinsed in methyl alcohol, dried in air, and chemically cleaned for 15 sec in a solution contining 40 g Cr_2O_3, 3 g Na_2SO_4, and 200 ml H_2O. The specimens were then rinsed for several minutes in an ultrasonic bath of methyl alcohol, dried in air, and weighed on a precision Mettler microbalance. The weights of the zinc specimens are listed in Table 1.

TABLE I

Zinc Cylinder Data

Capsule Number	A-6	A-7	B-5	A-0
Zn Wt Before Melting (g)	13.5846	13.6367	13.5613	13.6432
Zn Wt After Melting (g)	13.5807	13.6349	13.3650	13.6344
Zn Wt After Sectioning (g)	13.1595	13.2675	13.0177	12.8173
% Wt Loss to Sectioning	3.1	2.7	2.7	5.9
Activity After Melt (μCi)	8.34	7.75	7.32	19.64
Activity After Section (μCi)	7.66	6.699	6.223	17.834
Date Activity Measured	10/16/73	10/16/73	10/16/73	12/21/72
% Activity Loss to Section	8.1	13.5	15.	9.2
Where Melted	Skylab	Skylab	Skylab	MSFC
Diffusion Time (hr)	1.2	1.75	2.85	1.2

Ampoule Fabrication

The components of a flight ampoule consisted of two solid tantalum end plugs, a tantalum tube, a carbon tube, two carbon end caps, and the zinc specimen as shown in Fig. 3. The zinc specimen was placed in the carbon tube with end caps, which, in turn, was fitted inside the tantalum tube. The tantalum end plugs were welded in argon to the tantalum tube, producing a sealed specimen capsule. The capsules were permanently labeled at one end by vibratory marking or engraving according to the scheme depicted in Fig. 3. The first letter on the label was either an "A" or "B" and defined the type of zinc specimen contained. Type "A" capsules followed by an even number (0, 2, 4, etc.) had the specimen oriented with the zinc-65 pellet near the labeled end, while type "A" capsules followed by odd numbers (1, 3, 5, etc.) had the zinc-65 pellet oriented away from the labeled end. Flight instructions stated that the capsules were to be placed in the gradient furnace such that their labeled ends were in the colder zone of the furnace. Westinghouse Astronuclear Laboratory (WANL) incorporated these instructions into the assembly of the M558 cartridges.

Cleaning, Welding and Leak Checking of Ampoules

The carbon tubes and end caps were cleaned by heating at 850°C for 1-½ hr under a hydrogen atmosphere. Tantalum tubes and end plugs were degreased for 15 min in an ultrasonic bath containing trichloroethylene, followed by a 15-min rinse in an ultrasonic bath of ethyl alcohol. The cleaning treatment for the zinc specimen was described in the previous section.

The tantalum capsules were welded manually by the tungsten-inert-gas (TIG) process in an inert gas glove box. Capsules were loaded into the glove box and fixed vertically in a mechanical chuck, which was mounted to a motorized turntable to allow rotation of the specimen. Copper chill blocks were placed around the tantalum tube to help dissipate heat from the welding process. The glove box was then evacuated to 5×10^{-6} Torr and backfilled with argon. Both tantalum end caps were subsequently TIG welded at conditions of approximately 12 V and 100 A dc using pure tantalum filler wire. The weld metal was subsequently centerless ground flush with the tube and end caps.

The welded capsules were leak tested by immersion in a bath of ethylene glycol at approximately 100°C. The emission of tiny bubbles from any spot on the capsule indicated the presence and location of leaks in the capsule. Several capsules were found to have leaks in the weld zone and were rewelded. Subsequent leak tests show the repaired capsules to be tight.

X-Ray Radiographs of Tantalum Capsules

Seven B-type capsules, B-9 through B-15, were radiographed to check the bond lines. This test was initiated after Westinghouse found the specimens in capsules B-1, B-3, B-4, and B-5 of

TABLE II

Flight Sets and Ground Test Capsules

1. Capsules sent to Westinghouse 10-13-72

Flight Set	Capsule Numbers
I	A-0, A-1, B-1
II	A-2, A-3, B-2
III	A-4, A-5, B-3
IV	A-6, A-7, B-4
V	A-8, A-9, B-5

2. Revised sets due to substitution of B-1, B-3, B-4, B-5, with B-12, B-13, B-14, and B-15 sent to Westinghouse 10-31-72

Flight Set	Capsule Numbers
I	A-0*, A-1*, B-13*
II	A-2*, A-3*, B-14*
III	A-4, A-5, B-15
IV	A-6**, A-7**, B-2
V	A-8, A-9, B-12

3. Ground Test Capsules (ORNL)

A-11*, A-13*, A-15*
A-12*, A-14*, A-16
B-1, B-3, B-4, B-5**, B-6*, B-7*, B-8*, B-9, B-10*, B-11

*Capsule has been involved in a ground test as of 1-31-73

**Skylab flight samples

the original five flight sets to exhibit suspicious or faulty bond lines as shown by x-ray radiography. All of the A-type specimens and sample B-1 were satisfactory. X-ray radiographs were taken at ORNL with a Norelco 300 x-ray unit at 300 kV and 10 mA for 2 min, using a tube-to-object distance of 55 in. Since the radiographs showed that capsules B-12, B-13, B-14 and B-15 contained zinc specimens with satisfactory bonds, these capsules were substituted in the flight sets for B-1, B-3, B-4 and B-5 (see Table 2).

Cartridge Fabrication

Details of fabrication of M558 prototype, ground base and Skylab flight cartridges are in Reference 1. A sketch of a prototype cartridge used at WANL to calibrate thermal characteristics of the M558 ampoules is shown in Fig. 4. The cartridge was 7.94-in. long (20.1 cm). Cartridge temperatures were measured with thermocouples located as shown in the figure. Additional cartridges were built at ORNL to WANL specifications for additional ground base tests (Fig. 5) in a prototype of the M518 furnace, also assembled according to WANL specifications. A cartridge consisted essentially of a stainless steel tubing with graphite end plugs and Fiber Frax insulation. The cartridge encapsulated the zinc-tantalum ampoules in such a way as to give linear temperature gradients in the zinc under conditions of steady-state, high temperature soak.

THEORETICAL ANALYSIS

The theory of liquid metal diffusion is still not well understood. Whereas a lot of work has been done in solid diffusion, there is very little in the literature on diffusion in liquid metals. The principal investigator is aware of only two published experimental works in the literature on self-diffusion in liquid zinc and both works used Zn-65 as tracer isotope. Reference 2 lists the values obtained in these two experiments for the self-diffusion of liquid zinc as $D = D_o e^{-Q/RT}$ with one researcher giving the following values: $D_o = 8.2 \times 10^{-4}$ cm^2/sec; $Q = 5.09$ kcal/mole, and the other researcher giving the following: $D_o = 1.2 \times 10^{-3}$ cm^2/sec; $Q = 5.6$ kcal/mole.

Reference 2 also high-lighted the uncertainty in the data available on diffusion in liquid metals. As late as 1967, there were published data for only eleven liquid metals, excluding alloy systems. Some of the data are of indifferent quality. Reference 2 showed that most of the data could yield straight lines in the plots of log D versus 1/T, D versus $T^{\frac{1}{2}}$, D versus T or D versus T^2, making it almost impossible to tell whether D depends directly on T, $T^{\frac{1}{2}}$, T^2, or $e^{-Q/RT}$. However, the activated equation $D = D_o e^{-Q/RT}$ is the usual form adopted as an extension of the solid phase diffusion coefficient. For

zinc, the liquid diffusion coefficient is about 1,500 times the solid diffusion coefficient. Thus liquid zinc will self-diffuse a distance in 1 hour that will take 1,500 hours for solid zinc to self-diffuse.

Differential Equation for Diffusion

The equation for one-dimensional diffusion of zinc-65 along the axis x of a column of liquid zinc of total length L, in the absence of convection is given by:

$$\partial C/\partial t = \partial/\partial X(D\partial C/\partial X) \qquad (1)$$

where t = time for diffusion

C = concentration of diffusing zinc-65

$D = D_o e^{-Q/RT}$ = coefficient of self-diffusion

The boundary conditions are:

$$\partial C/\partial X = 0 \quad , \quad X = 0 \quad t > 0 \quad X = L \qquad (2)$$

Initial conditions are as follows:

For A (even)-type zinc sample

$$t \leq 0, \; C = C_o \; , \quad 0 \leq X \leq h$$
$$C = 0, \quad h \leq X \leq L \qquad (3)$$

where h = thickness of radioactive zinc-65 pellet.

For A (odd)-type zinc sample

$$C = 0 \qquad 0 \leq X \leq L-h$$
$$C = C_o \qquad L-h < X \leq L \qquad (4)$$

For B-type zinc sample

$$C = 0, \quad 0 \leq X \leq 1/2(L-h)$$
$$1/2(L+h) \leq X \leq L \qquad (5)$$
$$C = C_o \quad 1/2(L-h) \leq X \leq 1/2(L+h)$$

At a constant temperature, the diffusion coefficient is constant and Eq. 1 becomes

$$\partial C/\partial t = D \frac{\partial^2 C}{\partial X^2} \qquad (6)$$

with the same initial and boundary conditions as before.

The dimensionless forms of Eq. 1 and Eq. 6 are:

$$\frac{\partial \bar{C}}{\partial \Theta} = \frac{\partial}{\partial \bar{X}}\left(\frac{D}{\bar{D}}\frac{\partial \bar{C}}{\partial \bar{X}}\right) = \frac{\partial}{\partial \bar{X}}\left(\frac{\partial C}{\partial \bar{X}} \exp -\frac{Q}{R}(1/T - 1/\bar{T})\right) \qquad (7)$$

$$\frac{\partial \bar{C}}{\partial \Theta} = \frac{\partial^2 \bar{C}}{\partial \bar{X}^2} \qquad (8)$$

where $\bar{X} = X/L$, $\bar{C} = C/C_0$, $\Theta = \bar{D}t/L^2$, $\bar{D} = D_0 \exp(-\frac{Q}{R\bar{T}})$, $\bar{T}$ = average temperature of sample.

Boundary and initial conditions are also transformed. The A(even)-type conditions become

$$\Theta \leq 0 \quad \bar{C} = 1 \;,\; 0 \leq \bar{X} \leq h/L$$
$$\bar{C} = 0 \;,\; h/L \leq X \leq 1 \qquad (9)$$

The conditions for the A(odd)-type, and B-types are similarly changed.

Solution of Diffusion Equations

The analytical solutions for Eq. 6 and Eq. 8 were obtained. For initial conditions of Eq. 3 and Eq. 9, the solution is

$$C/C_0 = h/L + \frac{2}{\pi}\sum_{n=1}^{\infty}\frac{1}{n}\,\mathrm{SIN}\frac{n\pi h}{L}\,\mathrm{COS}\,\frac{n\pi X}{L}\,e^{-(n^2\pi^2 \bar{D}t/L^2)} \qquad (10)$$

Eq. 7 and Eq. 8 were also solved by finite difference method with a Univac 1108 computer program using $\bar{X}$ increments of 0.02 (0.037-in. average) and Θ increments of 1.645×10^{-4}. In solving Eq. 7, the value of 5 kcal/g-mole was assumed, while $\bar{T}$ was the average temperature of the zinc sample. The analytical and computer solutions for the constant temperature problem of Eq. 8 checked each other out. Fig. 6 through Fig. 8 show plots of some of the theoretical results on concentration-position coordinates with Θ as parameter. These graphs show that zinc-65 diffused more towards the hotter end of a temperature gradient.

These results also indicated that the zinc-65 concentration would reach 99.5% of its steady-state uniform value by $\Theta = Dt/L^2 = 0.538$ for the A-type samples and in $\frac{1}{4}$ of that time for the B-type samples. Using published literature value of $4.8 \times 10^{-5} cm^2/sec$ for D at 550°C for liquid zinc, these times would correspond to [2]:

$$t = 2.65 \times 10^5 \text{ SEC } (73.5 \text{ hr}) \quad \text{for A-type}$$
$$18.38 \text{ hr} \quad \text{for B-type} \qquad (11)$$

for uniform distribution over length L = 4.86 cm (1.842 in.).

Diffusion with Convection

An equation of the type

$$\frac{\partial C}{\partial t} + V\frac{\partial C}{\partial X} = D\frac{\partial^2 C}{\partial X^2} \qquad (12)$$

may be postulated for diffusion with convection. The boundary conditions would be

$$D\frac{\partial C}{\partial X} = VC \quad , \quad X = 0$$
$$X = L \qquad (13)$$

The initial conditions would be the same as for diffusion without convection. In Eq. 12, V is the magnitude of effective convective currents which arise due to temperature or surface tension perturbations in gravity. The solution for Eq. 12 would be

$$C = F(X) + \sum_n^{\infty} G_n(X) \cdot exp - D\left(\frac{n^2\pi^2}{L^2} + \frac{V^2}{4D^2}\right)t \qquad (14)$$

By comparing exponential terms of Eq. 14 with the exponential terms of the pure diffusion solution, we estimate an effective diffusion coefficient D_e such that

$$D_e = D\left(1 + \frac{P_e^2}{4\pi^2}\right) \qquad (15)$$

where $P_e = VL/D$ = Peclet number

D = coeff. of diffusion without convection

Thus Eq. 15 facilitates the estimation of effective convective velocity.

PROCEDURE

Zinc samples were melted in the M518 furnace under steady heat leveler soak temperatures for specified soak times. A set of three ground base samples were melted at soak temperature of 775°C at MSFC for soak time of 2 hours. After analysis showed that concentration distribution was uniform for 2 hour soak, another set of 3 cartridges was tested at 775°C and 1 hour soak time (Table I). Three samples A-6, A-7 and B-5 were melted in Skylab at the same soak temperature of 775°C and soak time of 1 hour. Fig. 9 is a plot of temperatures in liquid zinc samples used in prototype, ground base, and Skylab melt tests. The temperature histories of the tested samples are given in Fig. 10.

Physical Measurements

Zinc cylinders were removed from the tantalum capsules by cutting the tubes near the weld closures. This was accomplished using a lathe and a small metal-cutting saw. After removal, the zinc cylinders from Skylab were photographed using a Polaroid MP-3 camera and Type 52 sheet film. The length and average diameter of each zinc cylinder was measured using a direct reading caliper, while the weight was determined using a Mettler M-5 microbalance. The total zinc-65 activity in each cylinder was measured in a gross ionization chamber at ORNL.

Precise Sectioning

To determine the axial zinc-65 distribution in the three Skylab samples A-6, A-7, and B-5, after melting in space, each was machined into approximately 0.040-in. thick transverse sections which were accurately indexed. An Edelstaal Unimat jeweler's lathe with an ultrasharp tool bit was used to cut the transverse sections into shavings which were quantitatively collected and heat sealed in preweighed plastic envelopes. Each envelope containing the zinc shavings were subsequently reweighed to determine the zinc section weight (by difference). Every sixth or seventh section was machined and packaged in a manner to permit analysis of zinc-65 concentration as a function of radial distance. This was accomplished by machining a transverse section into three approximately equal parts (by weight) accurately indexed between the outer surface and the axis of the zinc cylinder. The first radial portion of the section to be machined off was designated an "outer" (O) radial section, followed by "middle" (M) and "inner" (I) radial sections. The combined activity of the O-M-I sections was equivalent to a whole section and could be plotted as such. In terms of zinc-65 concentration, the combined radiointensities of the O, M, and I sections were divided by their total weight.

Gamma-Counting

The gamma intensity from each envelope of zinc shavings

was measured using a low-level gamma-ray spectrometer that was also employed for the ground-tested samples reported in Reference 3. This system utilizes two opposed 5 x 4 in. NaI detectors, which, for small samples, provided essentially a 4 -geometry. The system also included a Nuclear Data 4420 mini-computer system which permited rapid data collection, analysis, and storage. Once the zinc-65 radiation intensity for a particular sample section was determined (in Ci), it needed only to be divided by the weight of that section (in grams) to produce a value of the relative zinc-65 concentration. Values of zinc-65 concentration were finally plotted as a function of section location on the zinc cylinder.

RESULTS

Ground base samples became shorter and thicker after melting because of the filling of space provided for expansion. As Table I reveals, the Skylab samples A-6, A-7, and B-5 had no appreciable dimensional changes on melting. The Skylab cylinders showed unique wrinkled surfaces 4 probably caused by solidification shrinkage and/or a surface effect occurring during heating. Earth samples had pipes or depressions on the top surface as a result of solidification, but no surface wrinkles. The wrinkles in the Skylab samples might be due to more rapid heat removal at selective sites along the cylinder. For instance, during cooling, certain portions of the cylinder would touch the walls of the carbon sleeve, thus possibly conducting heat away more rapidly in those areas. Wrinkles occurred in those parts of the zinc cylinders located in the hot end of the furnace, as it turned out. All of the samples showed weight loss that was probably due to a slight amount of zinc vaporization. Table I also indicates how much zinc was lost in the sectioning process. Material loss in itself did not affect the precision of the analysis because the data was normalized on a concentration basis.

Linear temperature profiles in zinc samples are shown in Table III. Table III, Fig. 9 and Fig. 10 describe the

TABLE III

	Prototype		Ground Base & Skylab
Heat Leveler temperature (Hot-1) °C	766	809	775
Hot cartridge temperature °C	683.5	726.5	700
Cold cartridge temperature °C	410.5	432.5	415
Temperature Gradient °C/cm	43	46.4	45
°C/in.	109.4	117.5	114
Hot End of Zinc (avg.) °C	641	680	656
Cold End of Zinc (avg.) °C	440	446	463
Average Zinc Length Before Melting- cm	4.675	4.675	4.675
in.	1.842	1.842	1.842

temperature history of the samples. The rate of solidification was calculated from prototype furnace results and was given by

Reference 1 as

$$ds/dt = 7.3 \times 10^{-4} + 10.55 \times 10^{-8}t \text{ cm/sec} \qquad (16)$$

Integrated form of Eq. 16 is

$$s = 7.3 \times 10^{-4}t + 5.278 \times 10^{-8}t^2 \text{ cm} \qquad (17)$$

By means of Eq. 17, Table II , Fig. 9 and Fig. 10, the effective diffusion time for each sample was estimated, the results being listed in Table I.

Distribution of Zinc-65

All ground base samples with soak times of 1 hour or more yielded uniform zinc-65 distribution. Such a distribution was predicted from pure diffusion mechanism to occur after a diffusion time of 73.5 hours for the A-type cylinder or 18.38 hours for the B-type cylinder. However, the uniform concentration was present in earth samples after a diffusion time less than 3 hours. The results of ground base tests of A-0, A-1, and B-13 at MSFC are shown in Fig. 11 through Fig. 13, respectively. Results of A-2, A-3 after 2-hour soak also showed uniform concentration. Sample A-0 (Fig. 12) is anomalous under 1-hour soak time. This anomaly can only be explained by a small , unmelted portion remaining. Only A-0 showed this incomplete melting. Fig. 14 also shows that sample A-13 melted at ORNL for 10 minutes soak time, had also uniform distribution. The rapid distribution of zinc-65 would be due to combined convection-diffusion effect. Radial sections of ground base samples A-0, A-1, A-2, A-3, B-13, and A-13 were uniform in concentration.

Sample A-14 was rapidly melted and solidified in about 30 minutes with about 1 minute soak time at ORNL. Effective diffusion time was obtained from a temperature-time data measured by a thermocouple located half-way from the end of zinc sample. It was found to be 360 seconds (0.1 hour). Fig. 15 shows that a concentration gradient does indeed exist. The curve shows plateaus from movement of melt fronts and convection. Radial sectioning confirmed presence of convection by showing that concentrations in the inner core were almost two times that of the outer core concentration. Thus convection profiles , much like parabolas with maxima at the axis and minima at the walls, were present. A match of theoretical curves with experimental data in Fig. 15 gave a diffusion coefficient of 2.16×10^{-5} cm^2/sec.

Zinc-65 distribution in the Skylab samples A-6, A-7 and B-5 are plotted in Fig. 16 through Fig. 18, respectively. The smooth "textbook" zinc-65 concentration gradient supports the observation that liquid metal diffusion was the main mechanism

of transport. The plot of experimental data for each of the Skylab samples was matched to a remarkable degree with a plot from the solution of the pure diffusion equation under linear temperature conditons (Eq. 1). Effective diffusion times were calculated from the sum of soak time plus average time in liquid phase during heat up and cool down. Table IV summarizes the resultant average diffusion times and coefficients. A-6 had the least effective diffusion time because its zinc-65 pellet was the last to melt and the first to solidify. A-7 had the longest diffusion time because its zinc-65 pellet was in the liquid phase the longest.

The average diffusion coefficient obtained from Skylab samples at 550°C was $D = 4.28 \times 10^{-5}$ cm^2/sec. The best available earth value for D is given in Reference 2 as $D = 4.8(10^{-5})$cm^2/sec at 550°C. The Skylab coefficient may be taken as convection-free and used to estimate magnitude of convective velocity from earth results using Eq. 15. The velocity in A-14 test was found in this way to be 4.16×10^{-4} cm/sec. Thus convective velocities this small can seriously influence diffusion of impurities in liquid zinc.

TABLE IV

Diffusion Results

$D = D_o \exp -(Q/RT)$

	Skylab			Ground Base	
	A-6	A-7	B-5	A-14	Lit 2
Diff. time (hr)	1.2	1.75	2.85	0.1	
$10^5 D$ (550°C) cm^2/sec	4.26	4.3	4.28	216.	4.8
$10^4 V$ (convective) cm/sec				4.16	0.2
D_o cm^2/sec	9.17×10^{-4}				10^{-3}
Q kcal/mol	5.16				5.0

When experimentally determined concentrations and corresponding locations were applied to plots of theoretical concentrations versus dimensionless time (Dt/L^2) with X/L as parameter, values of D versus temperature were obtained. This was made possible because temperature was linear with position. Plot of ln D versus 1/T for samples A-6, A-7 and B-5 yielded the straight line shown in Fig. 19. From this line, the equation for self-diffusion coefficient in zinc in the absence of convection was found to be

$$D = 9.17(10^{-4})e^{-5,160/RT} \text{cm}^2/\text{sec} \qquad (18)$$

$$693^\circ\text{K} < T < 973^\circ\text{K}$$

$$(420^\circ\text{C}) \qquad (700^\circ\text{C})$$

This should be compared to earth value given in Reference 2

for careful experiments in capillary tubes:

$$D = 10^{-3}e^{-5000/RT} cm^2/sec.$$

The radial zinc-65 distribution for the Skylab samples are shown in Fig. 20 to Fig. 22. The samples showed rather uniform radial concentrations except near or within the original zin-65 pellet. The sharp gradients in the outer surfaces in these later regions suggest that surface diffusion, capillary attraction or some sort of surface phenomena may have influenced the movement of the zinc-65.

CONCLUSIONS

The skylab samples had unique wrinkled surfaces after melting in space which may have been caused by solidification shrinkage and/or surface perturbations induced by the samples contacting the carbon liner walls of the tantalum capsule.

The length and diameter of the Skylab samples were little changed after melting in space, whereas gravity affected the final dimensions of the zinc cylinders melted on earth.

A one-hour soak time in the prescribed thermal gradient produced well-defined axial zinc-65 concentration gradients in samples melted in space. These gradients were well modoled by the one dimensional unsteady-state Fick's law of diffusion equation in the absence of convective currents. Zinc-65 concentrations in samples melted in unit gravity were homogeneous. The marked decrease in zinc-65 movement in liquid zinc in the near-zero gravity of space was apparently caused by the absence of gravity-induced convective mixing. The relatively uniform radial zinc-65 distribution observed in the Skylab samples also indicated that convective mixing was negligible in space.

An equation was determined for self-diffusion coefficient in liquid zinc in the temperature range from zinc normal melt point (420°C) to 700°C.

$$D = D_o \exp-(Q/RT) \text{ where}$$

$$D_o = 9.17 \times 10^{-4} \text{ cm}^2/\text{sec}$$

$$Q = 5.16 \text{ kcal/mole}$$

$$T = {}^oK$$

In addition, an average diffusion coefficient was found to be $D = 4.28 \times 10^{-5}$ cm^2/sec at 550°C.

It was determined that only an effective convective velocity of magnitude 4.16×10^{-4} cm/sec was needed to produce a 50 times increase in the value of the mass diffusivity for liquid zinc. Thus slight but persistent perturbations can have very

significant effects on the speed of distribution of impurities in liquid zinc and liquid metals.

Radioactive isotopes can be successfully used for experiments in space to study liquid metal diffusion.

Complications arising from convection in liquids during mass transfer on earth may be avoided or minimized by utilizing the zero-g environment of space.

ACKNOWLEDGMENTS

The author appreciates and acknowledges the careful work in ampoule fabrication, precise sectioning and radioactivity counting done by E. H. Kobisk and D. N. Braski of Isotopes Division, Oak Ridge National Laboratory. The author also recognizes the important support of Tommy Bannister of Space Sciences Laboratory, MSFC, and his many suggestions as Scientific Monitor of the M558 Experiment.

REFERENCES

1. Westinghouse Astronuclear Laboratory, Data Package for the Multipurpose Electric Furnace System, Vol. I, Section III "Experiment M-558 Cartridges," WANL-TME-2831, Contract NAS8-28271, Pittsburgh, Penn 15236, Nov. 1972

2. Nachtrieb, N. H., "Self-diffusion in Liquid Metals," The Properties of Liquid Metals: International Conference at Brookhaven National Lab, Upton, N. Y., 1966, Edited by P. O. Adams, H. A. Davies & S. U. Epstein

3. Braski, D. N., O'Donnell, F. R., Kobisk, E. H., "Progress Report on Specimen Fabrication and Ground Tests for NASA Skylab Experiment M-558," ORNL TM-4152, Oak Ridge, Tenn., April 1973

4. Braski, D. N. and Kobisk, E. H., "Radioactive Tracer Analysis of Flight Samples from Skylab Experiment M-558," Contract No. W-74-5-eng-26, ORNL, Oak Ridge, Tenn.

5. Leymonie, C., Radioactive Tracers in Physical Metallurgy, John Wiley & Sons, Inc., N. Y., 1963

6. Jost, W., Diffusion in Solids, Liquids, Gases, 3rd edition, Academic Press, Inc., N. Y., 1960

7. Jenkins, E. N., An Introduction to Radioactivity, Butterworths, London, 1964

8. Crank, J., The Mathematics of Diffusion, The Clarendon Press, Oxford, 1956

9. Curtiss, Leon F., Measurements of Radioactivity, National Bureau of Standards Circular 476, Washington, D.C., Oct. 15, 1949

10. Wahl, A. C., editor: Radioactivity Applied to Chemistry, John Wiley & Sons, N. Y., 1951

11. Bird, R. B., Stewart, E. E., and Lightfoot, E. N., Transport Phenomena, John Wiley & Sons, N. Y., 1960

APPENDIX A

Materials Analyses

I. Zinc

Vendor: Ventron Corporation, Alfa Products
Analysis: ORNL - Spectrographic

Element	Amount (wt. ppm)	Element	Amount (wt. ppm)
Al	0.3	P	<0.05
B	<0.05	Pb	<0.7
Ba	<0.05	Si	<0.9
Ca	<0.2	Sn	<0.05
Cr	<0.1	Ta	3.0
Cu	<0.5	Ti	<0.1
Fe	0.1	W	<0.1
K	<0.05	Cl	<0.1
Li	<0.05	*C	42
Mg	<0.1	*N	<1
Mn	<0.1	*O	46
Mo	<0.05	*S	22
Na	<0.05	Zn	Balance
Ni	<0.2		

*By vacuum fusion.

II. Carbon

Vendor: Union Carbide
Analysis: ORNL - Spectrographic

Element	Amount (wt. ppm)	Element	Amount (wt. ppm)
Al	7	Ni	<0.8
B	1	P	3
Ba	30	Rb	1
Ca	3000	Si	140
Cr	4	Sr	70
Cu	0.8	V	0.4
Fe	5	Zn	<20
K	10	S	<20
Mg	2	C	Balance

III. Tantalum Tubing (3/8-in. o.d. x 0.020 in. wall)

Vendor: Fansteel Metals
Analysis: Vendor

Element	Amount (ppm)	Element	Amount (ppm)
C	12	Mn	<10
O	43	Ca	<10
N	16	Al	<10
H	<5	Cu	<10
W	100	Sn	<10
Cb	230	Cr	<10
Zr	<10	V	<10
Mo	<10	Co	<10
Ti	<10	Mg	<10
Fe	<10	Pb	<10
Ni	<10	Ta	Balance
Si	<10		

IV. Tantalum Bar (3/8-in. diam)

Vendor: Teledyne - Wah Chang Albany
Ingot Analysis: By Vendor - Heat No. G00503

Element	Top (ppm)	Bottom (ppm)	Element	Top (ppm)	Bottom (ppm)
Al	<20	<20	N	22	42
C	<30	30	Ni	<10	<10
Cb	649	614	O	<50	<50
Cr	<10	<10	Si	<10	17
Cu	4	5	Ti	<10	<10
Fe	<15	<15	V	<10	<10
H	< 5	< 5	W	40	33
Mo	50	40	Zr	<50	<50
Co	< 5	< 5	Ta	Balance	Balance

APPENDIX B

Nomenclature

C	Concentration	uCi/gm
D	Coefficient of diffusion	cm^2/sec
h	Thickness of radioactive pellet	cm (in.)
L	Length of zinc sample	cm (in.)
Q	Activation energy for diffusion	cal/mol
R	Gas constant	1.987 cal/(mol-^oK)
s	Thickness of solid formed	cm (in.)
t	Diffusion time	sec
T	Temperature	^oK (^oC)
V	Velocity due to convection	cm/sec^{-1}
x	Position coordinate	cm (in.)
	Dimensionless	Dt/L^2

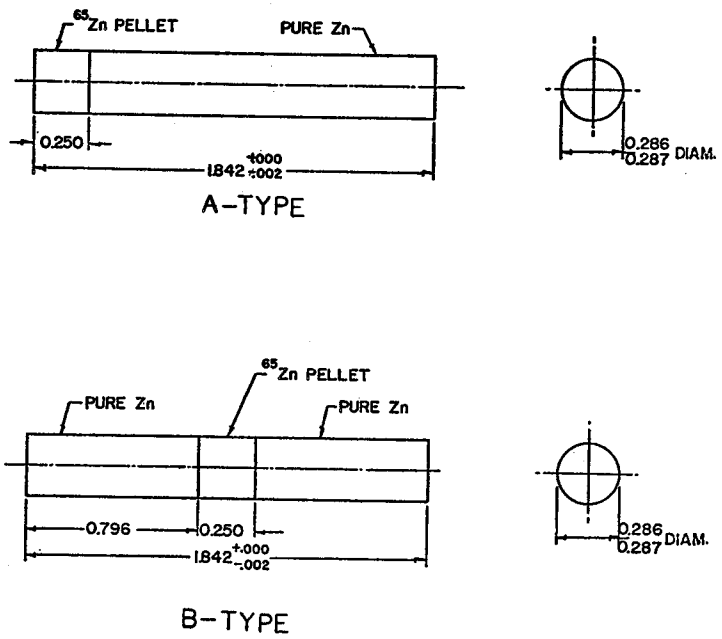

FIGURE 1 M558 ZINC SAMPLE

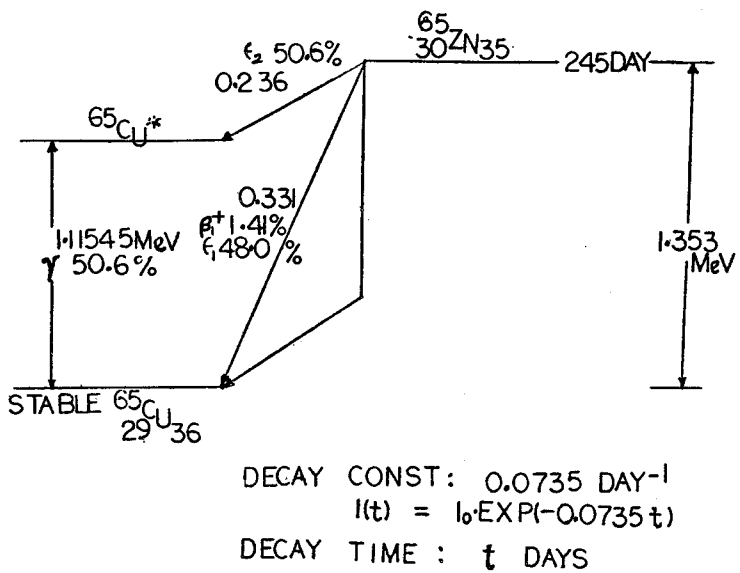

FIGURE 2 · ^{65}ZN RADIOACTIVE DECAY

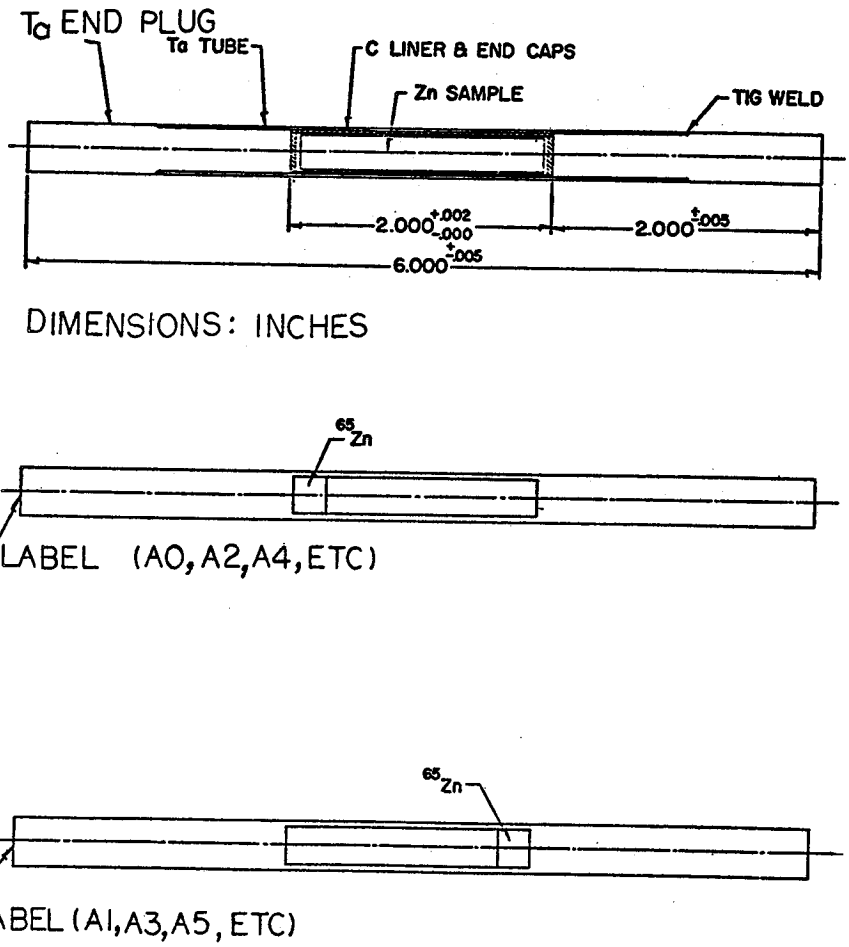

FIGURE 3 M558 AMPOULE CONFIGURATION

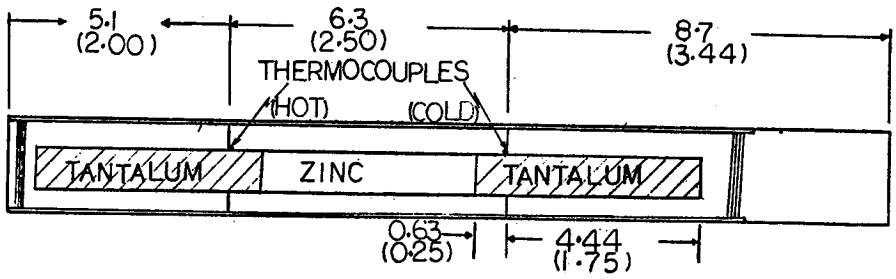

FIGURE 4 M558 PROTOTYPE CARTRIDGE

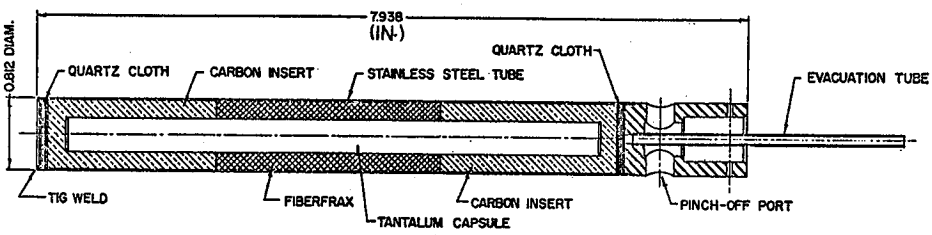

FIGURE 5 M558 CARTRIDGE

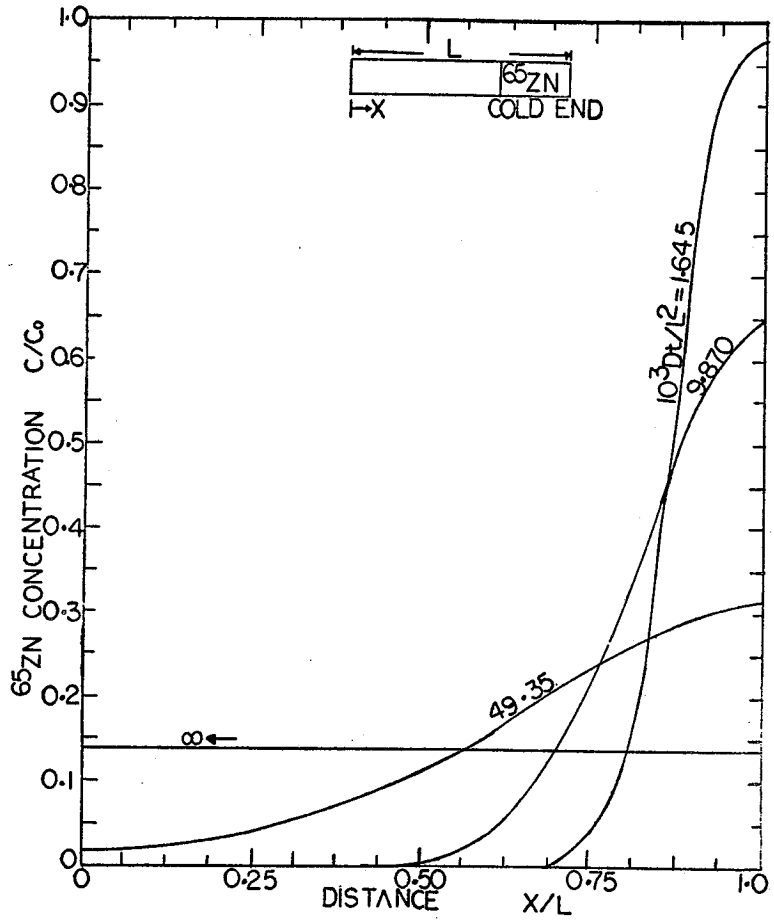

FIGURE 6 THEORETICAL ^{65}ZN DISTRIBUTION IN AO, A6-TYPE SAMPLE

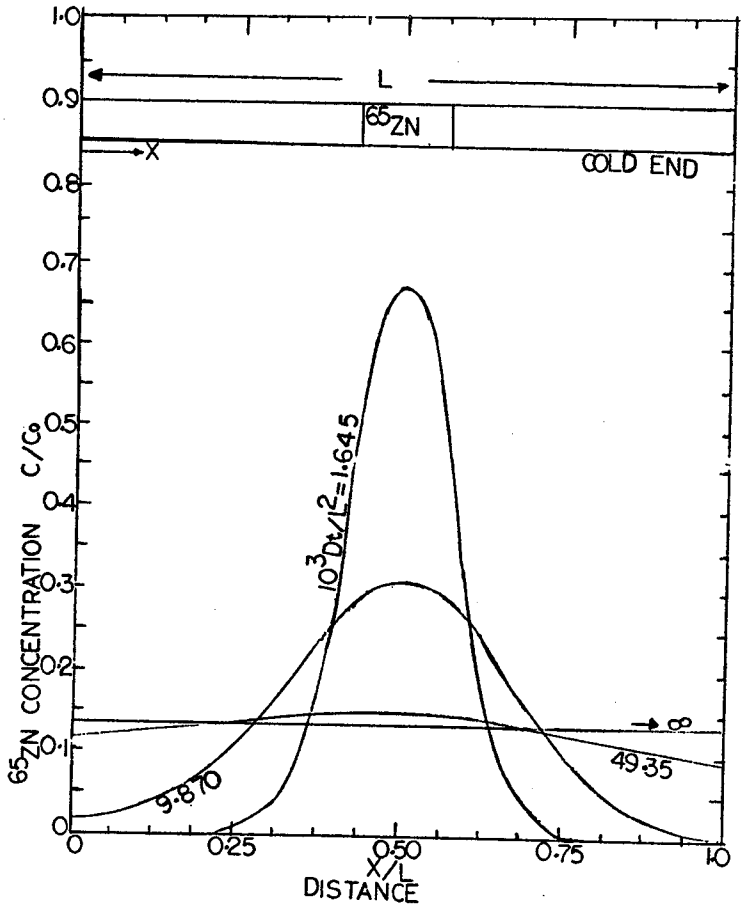

FIGURE 7 THEORETICAL ^{65}ZN DISTRIBUTION IN B-TYPE SAMPLE

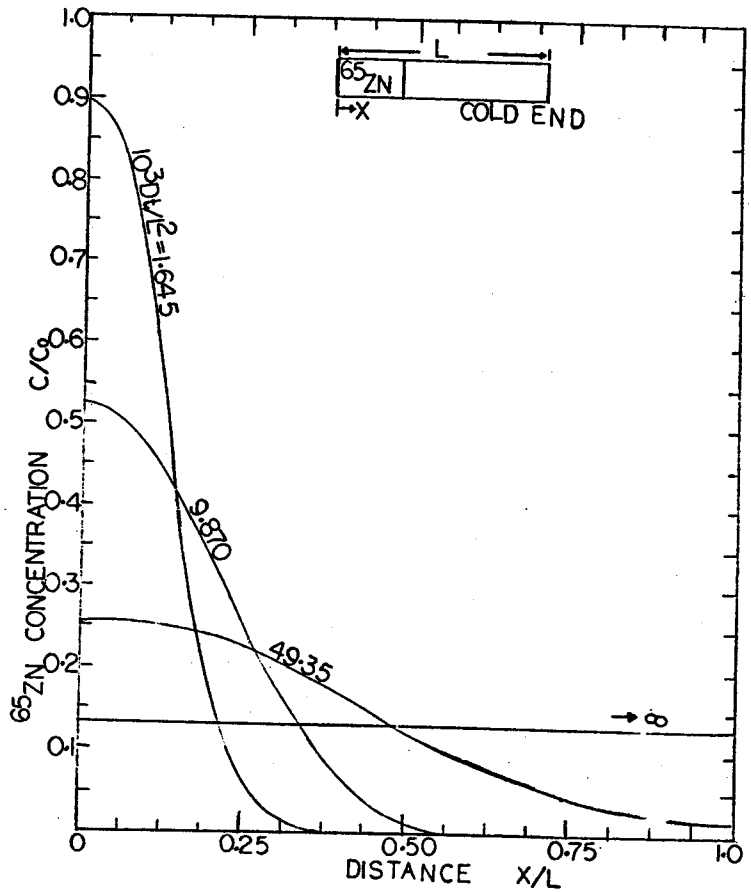

FIGURE 8 THEORETICAL ^{65}ZN DISTRIBUTION IN A1-TYPE SAMPLE

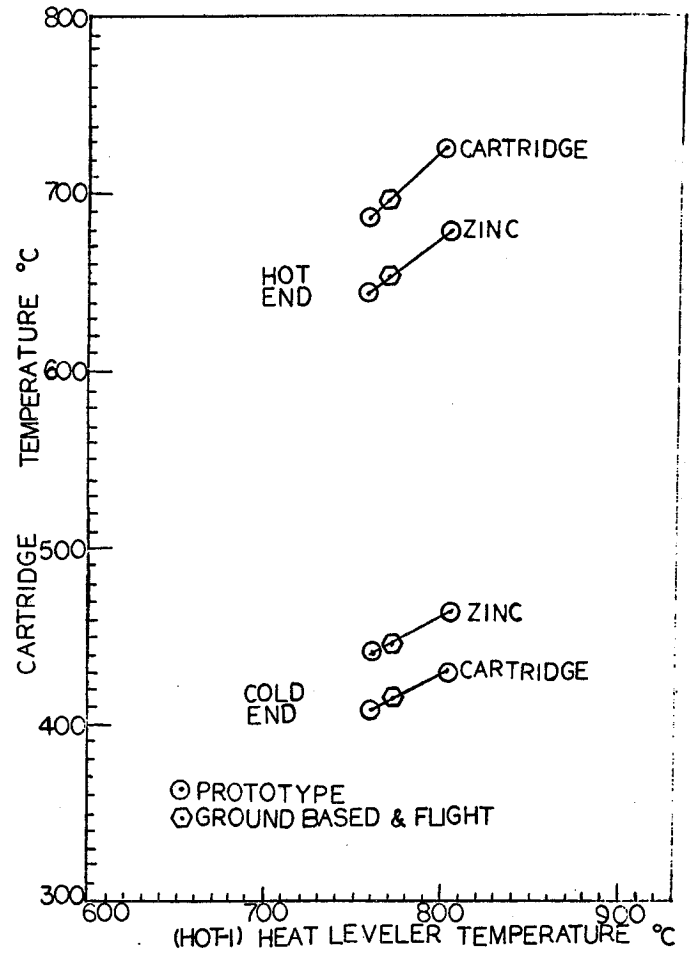

FIGURE 9 M558 CARTRIDGE STEADY STATE TEMPERATURE

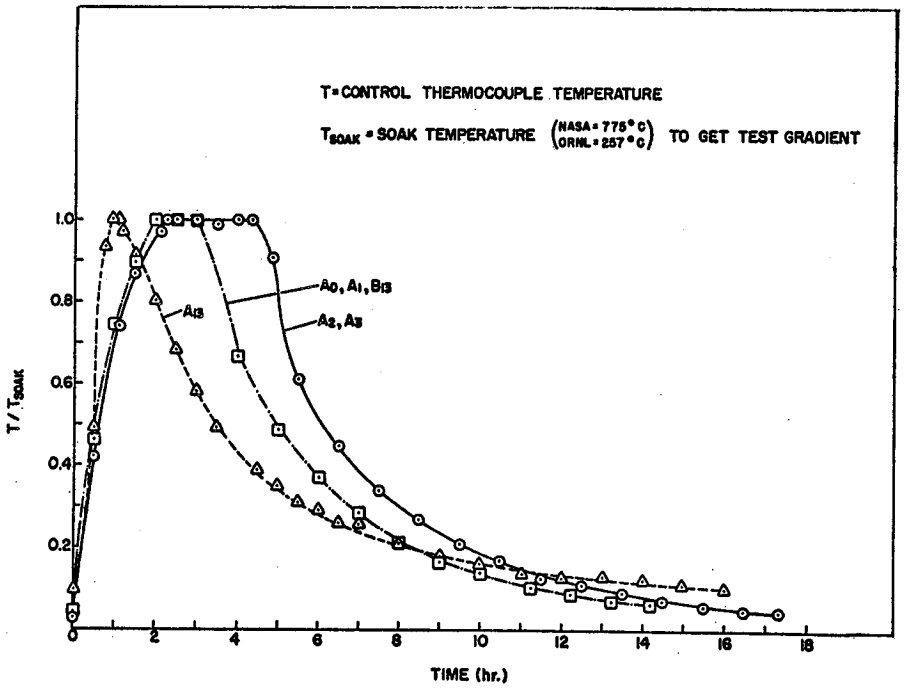

FIGURE 10 M558 GROUND-BASED SAMPLE TEMPERATURE

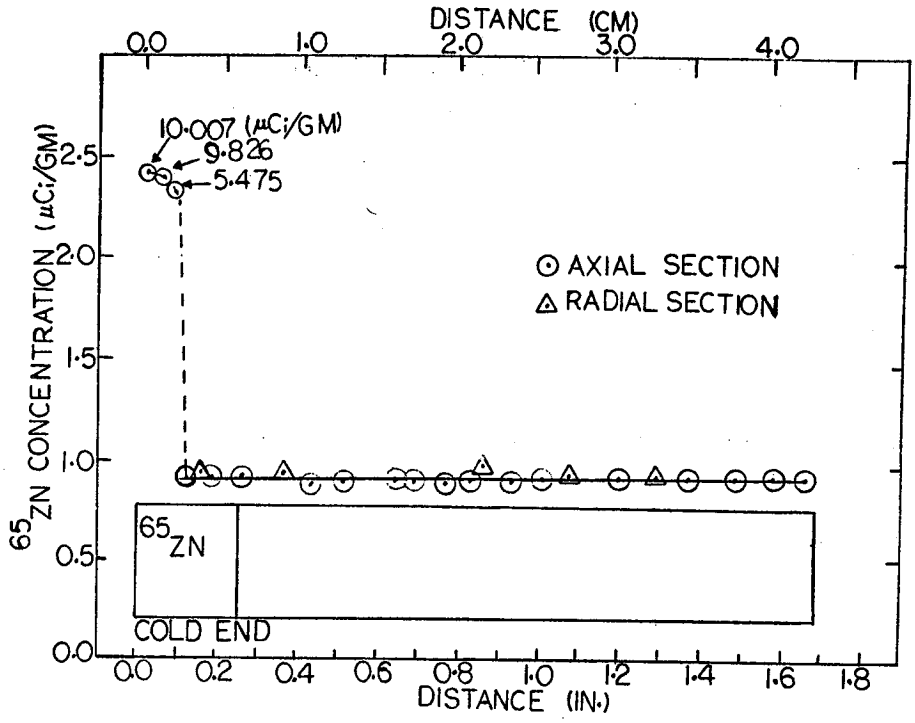

FIGURE 11 M558 GROUND BASED SAMPLE A-0

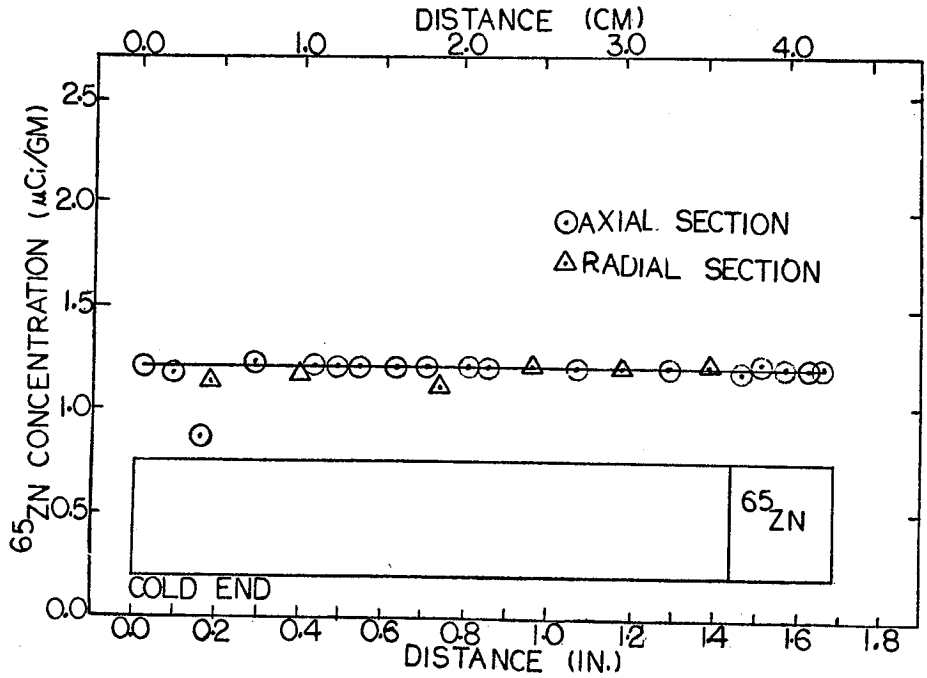

FIGURE 12 M558 GROUND BASED SAMPLE A-1

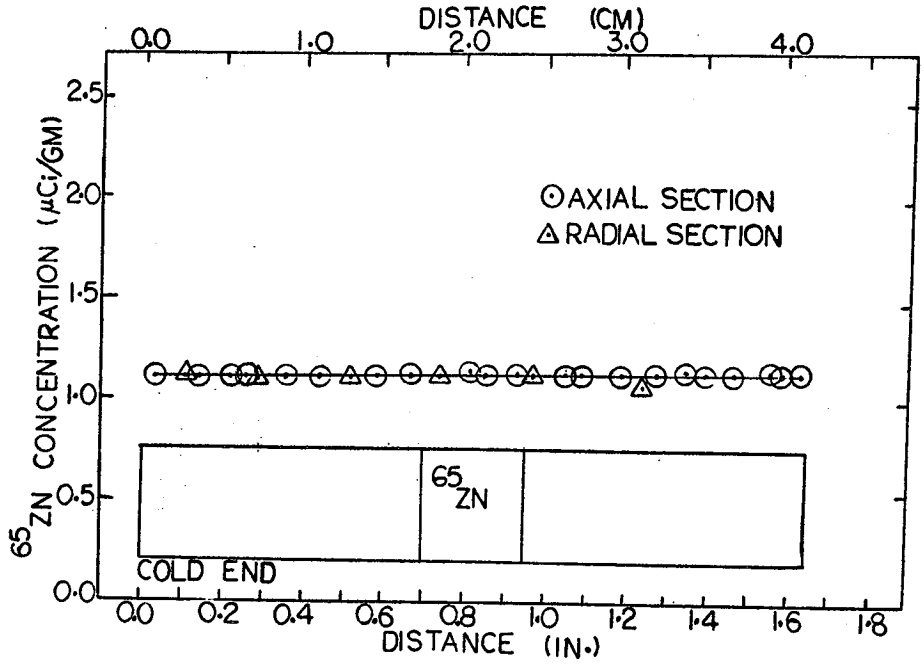

FIGURE 13 M558 GROUND BASED SAMPLE B-13

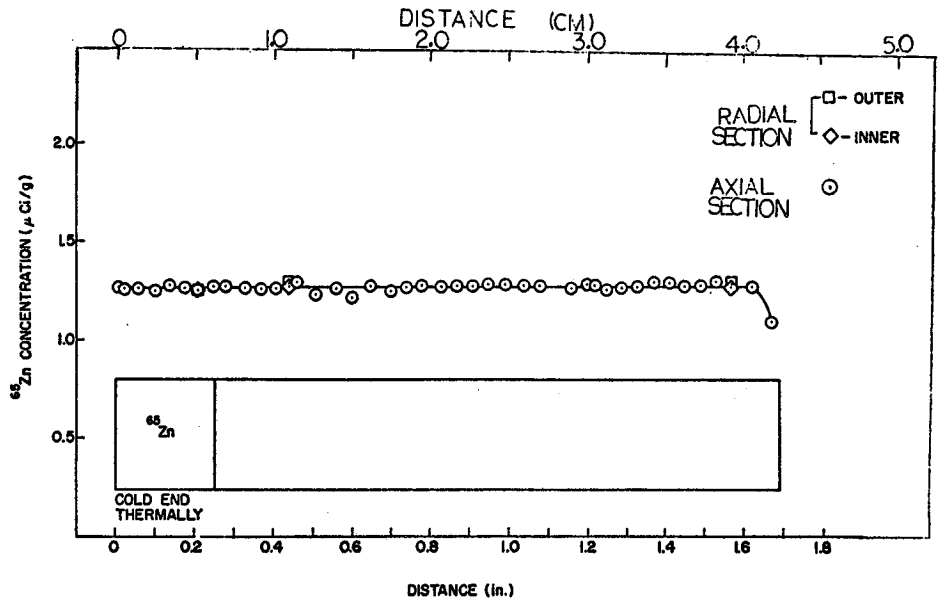

FIGURE 14 M558 GROUND BASED SAMPLE A-13

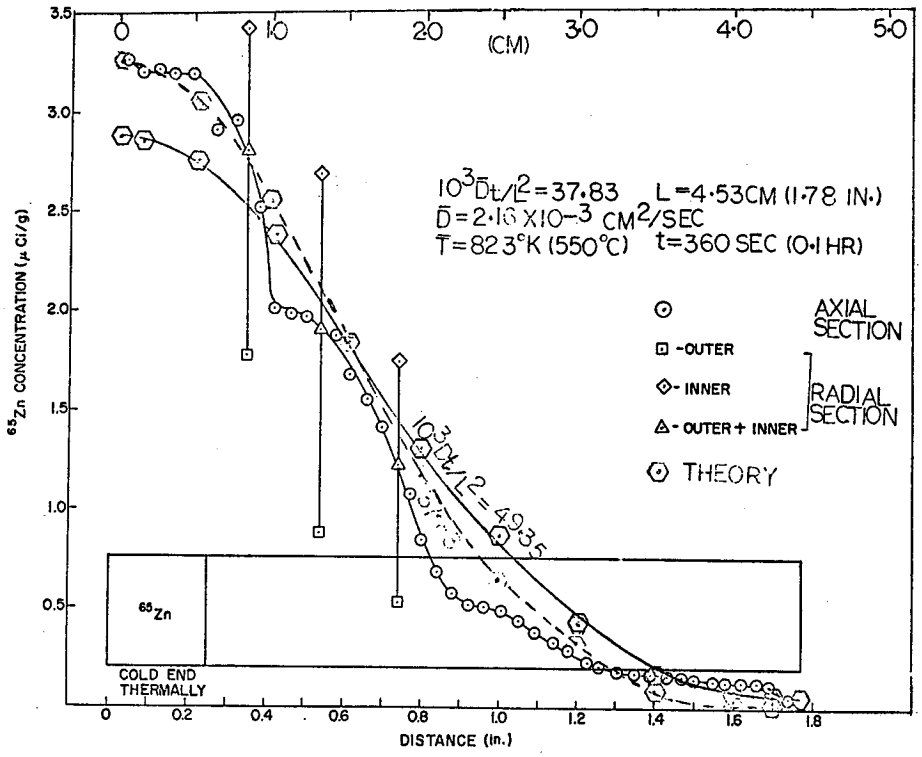

FIGURE 15 M558 GROUND BASED SAMPLE A-14

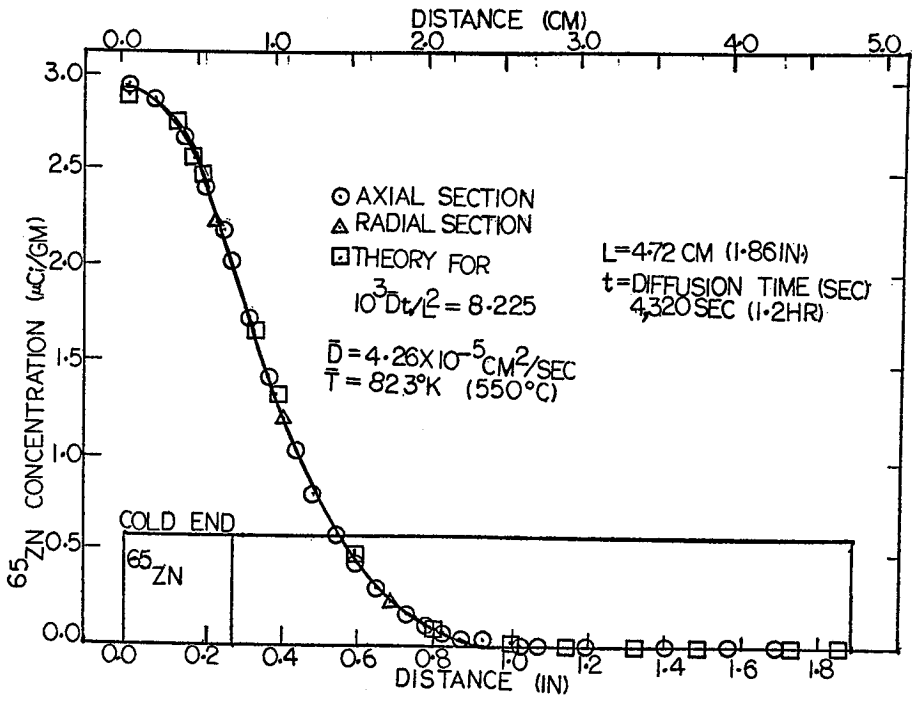

FIGURE 16 M558 FLIGHT SAMPLE A-6

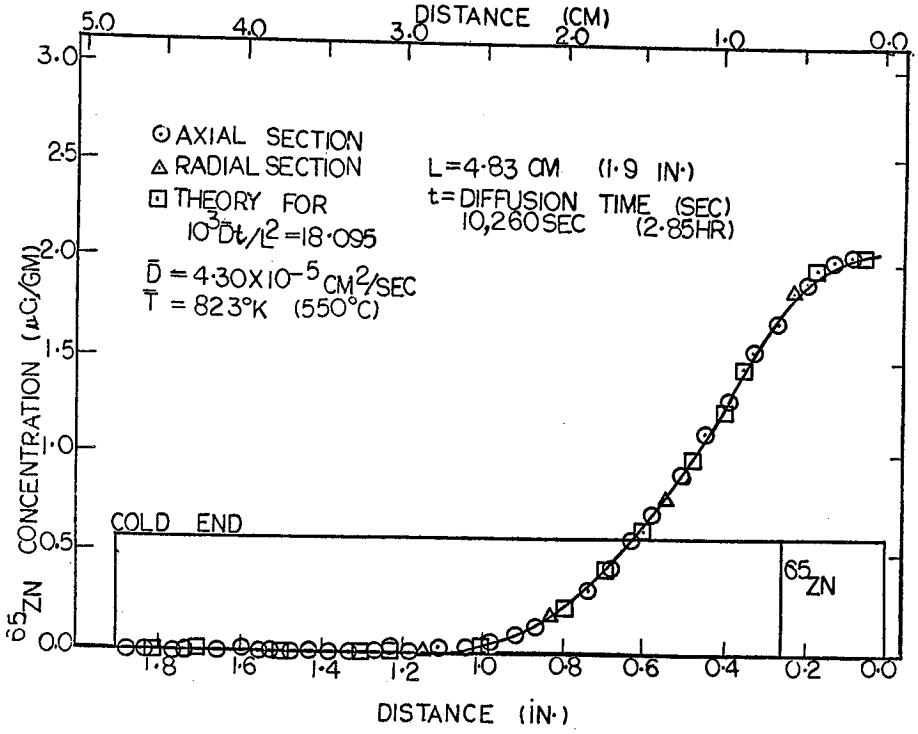

FIGURE 17 M558 FLIGHT SAMPLE A-7

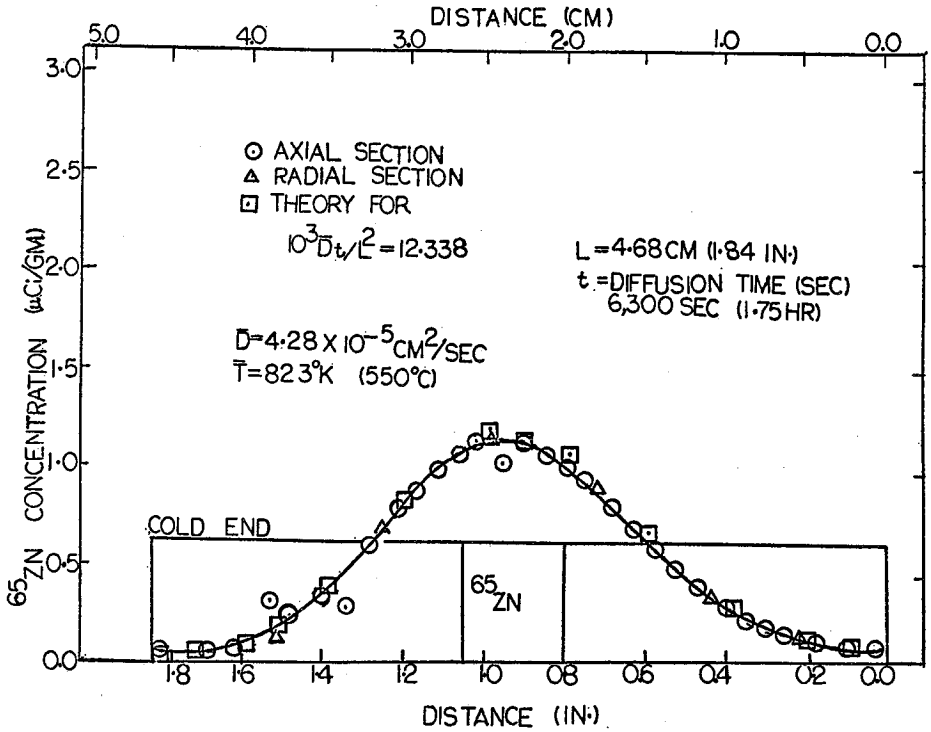

FIGURE 18 M558 FLIGHT SAMPLE B-5

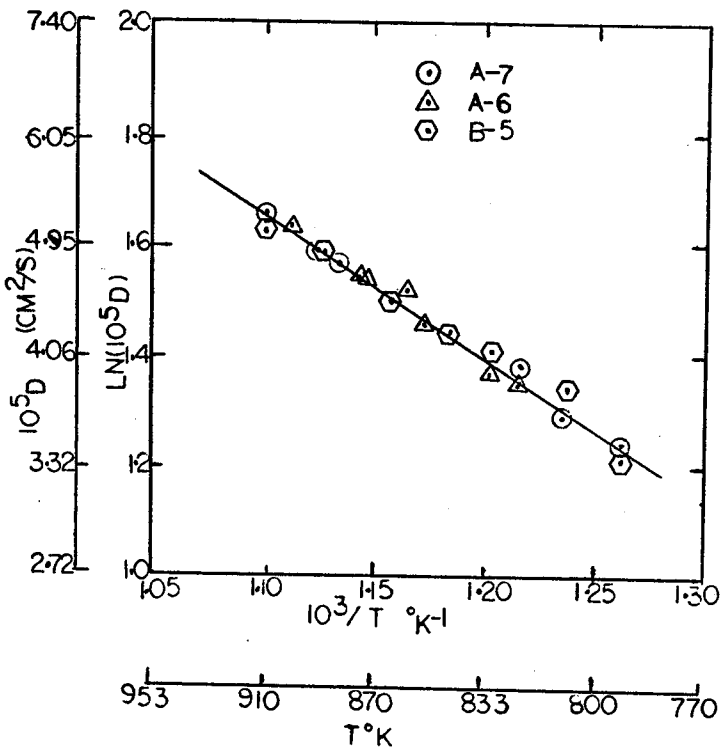

FIGURE 19 M558 SKYLAB DIFFUSION RESULTS

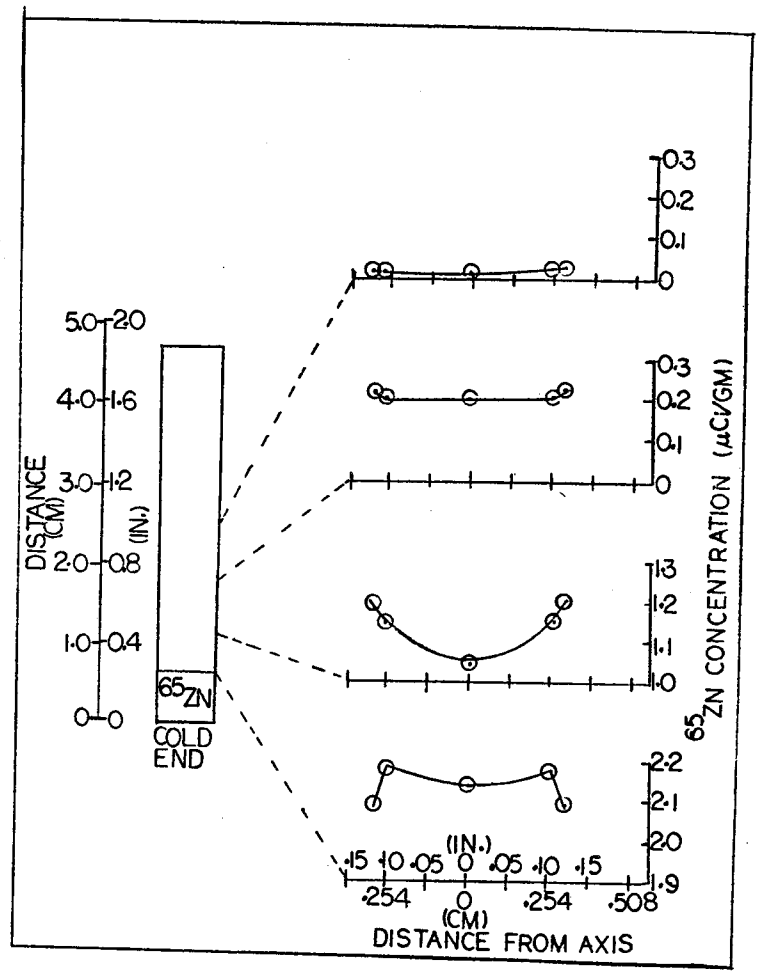

FIGURE 20 M558 FLIGHT SAMPLE A-6 RADIAL ^{65}ZN DISTRIBUTION

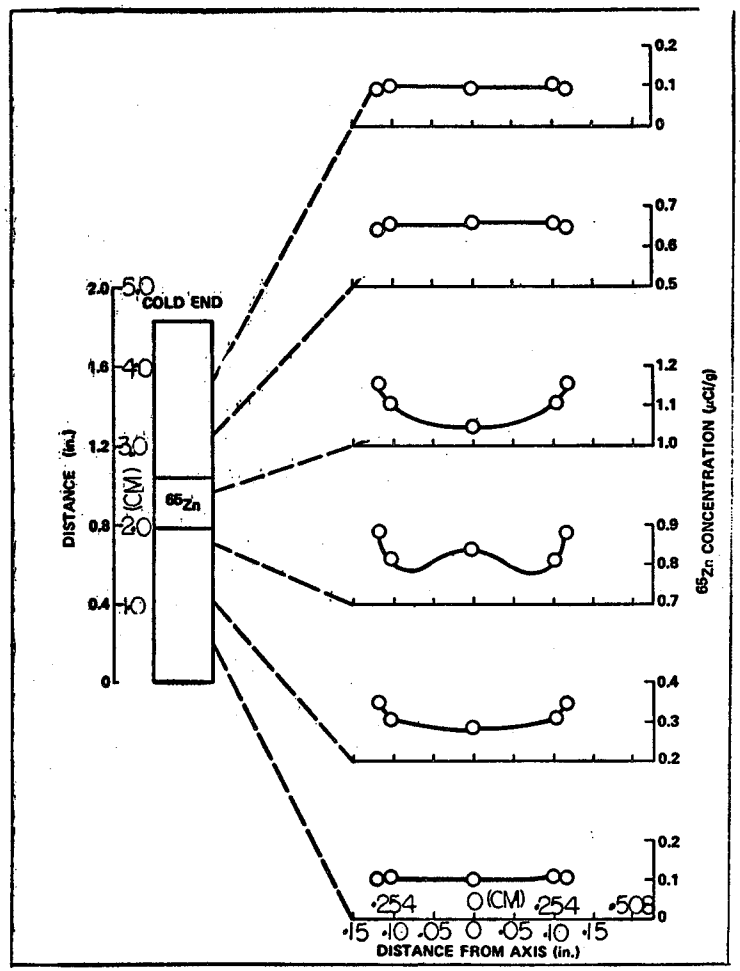

FIGURE 21 M558 FLIGHT SAMPLE B5
RADIAL ^{65}Zn DISTRIBUTION

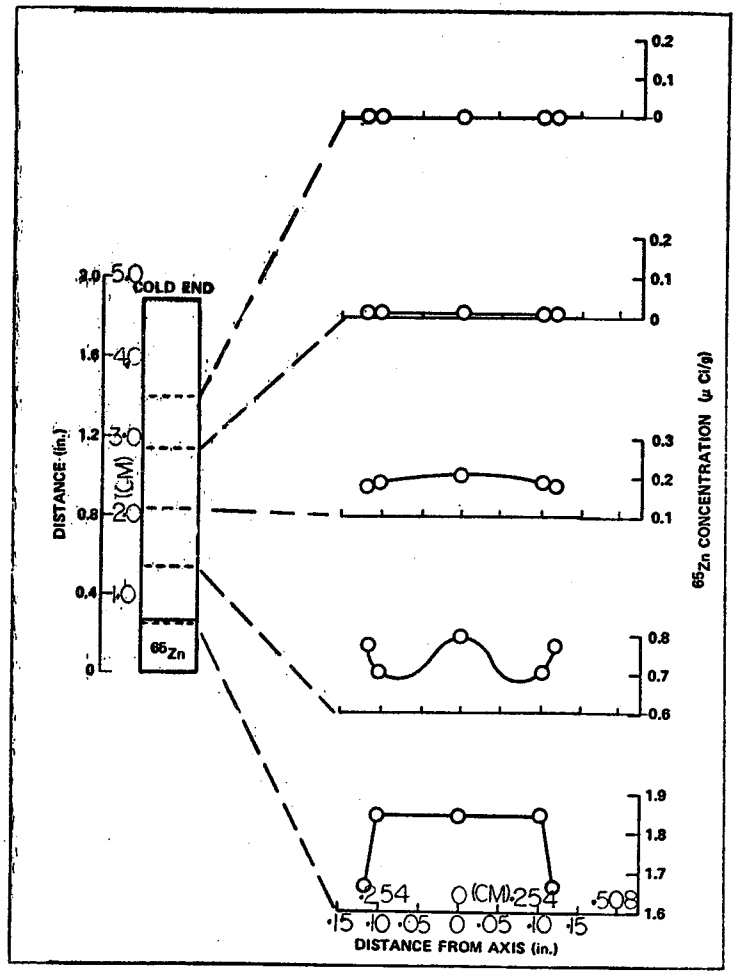

FIGURE 22 M558 FLIGHT SAMPLE A-7
RADIAL ^{65}Zn DISTRIBUTION

SKYLLAB EXPERIMENT M566 COPPER-ALUMINUM EUTECTIC

By

Earl A. Hasemeyer*, Charles V. Lovoy, L. L. Lacy
George C. Marshall Space Flight Center
Marshall Space Flight Center, Alabama 35812

SUMMARY

The experimental hardware in Skylab flights 3 and 4 functioned satisfactorily to process three specimens in the low gravity of a Space environment. The multi-purpose Electric Furnace melted portions of three copper-aluminum specimens in each flight, held them at a soaking temperature, then re-solidified the molten portions at a controlled rate. Non-destructive evaluations including electrical resistivity, have been completed. Preliminary data from quantitative metallography indicate that the aligned eutectic in specimens processed in Skylab 3 and 4 have fewer defects than ground-based specimens, specifically an improvement of 12% in average defect spacing and a decrease of 20% in the average fault density.

*Paper presented by Earl A. Hasemeyer.

INTRODUCTION

Directionally solidified eutectics as prepared in a one-g environment, almost always exhibit termination faults, mismatch surfaces and other defects. These growth imperfections limit their strength when used as structural composites and prevent their use for non-structural applications such as Micro Capacitors. The formation of a mismatch surface in an aligned eutectic involves an increase in net surface area. [1] The appearance of terminations allows lamellae to maintain their parallel growth but there is no compensation for the excess surface and increased energy at the mismatch surfaces. Because of the incomplete explanation for occurrence of all such defects in lamellar eutectics, it appeared reasonable [2] that an experiment in the orbiting Skylab would show that an improved structure could be grown in the absence of gravity induced thermal convection. The growth of a eutectic composite of aligned lamellae in low gravity should also provide new insights into the parameters affecting their solidification. The $CuAl_2$ eutectic (67% Wgt Aluminum-33% Wgt Copper) was selected as a model system on the basis of its moderate eutectic temperature and the extensive background of solidification information available with which zero-g results may be compared.

This paper will describe the hardware and results of our non-destructive evaluation and quantitative metallography.

Experimental Description

Specimens and Hardware Design

Single-grained specimens for this experiment were prepared by directional solidification. The initial castings were made from master heats of zone-refined aluminum and spectrographic copper. [3]

The design of the M566 cartridge is similar to others used in the M518 Multipurpose Electric Furnace. [4] The copper-aluminum eutectic specimen is 6.25 mm in diameter and 12.7 mm in length.

The cartridge assembly for each specimen was designed so that the molten eutectic alloy would contact graphite only. The following heating and cooling parameters were selected for ground-based tests and the Skylab experiment:

Peak Temperature - 867°C in the heated portion of furnace
- 790°C in the specimen
Soak Time at Peak Temperature - 1 hour
Solidification Rate - 2.4°C/min.
Average Thermal Gradient - 45°C/cm.

Due to a malfunction of the control thermocouple in the furnace in Skylab 3, the peak temperature did not exceed 844°C.

Three additional specimens were processed in Skylab 4, at the desired temperature of 867°C.

Results of Non-destructive Evaluation

Photography and Radiography

Each specimen from Skylab 3 shows a reduced diameter or hour glass shape in the regrowth region (Fig. 1). This hour glass shape was not present on ground based specimens. The cause of this reduction in diameter is not exactly known but is considered to be due to a combination of instability of the column of molten metal and surface tension restraints during solidification. Specimens from Skylab 4 had very slight diameter reduction only.

Resistivity

Electrical resistivity in directionally solidified specimens of aluminum-$CuAl_2$ eutectic is anisotropic. [5] The expected range of variations of resistivity as a function of orientation angle is shown in Fig. 2. When aligned lamellae are parallel to the direction of resistivity measurement, (Θ of 90°), resistivity will vary from 3.78 to 4.04 micro ohm-centimeter. When lamellae are perpendicular to the direction of resistivity measurement, (Θ of O°) resistivity will vary from 4.47 to 4.60 micro ohm-centimeter. Conventional techniques for measuring resistivity were not sufficiently accurate. Resistivity therefore was measured by a new technique using decay of eddy currents. Variations of resistivity values measured locally on a ground-based specimen and a Skylab 4 specimen are shown in Fig. 3. The resistivities at the hot ends of both specimens are comparable. Resistivities measured at the remelt interfaces of both specimens are also comparable. The increase in resistivity near the surface deformity is considered to be due to disruption of the aligned lamellae near this portion.

Quantitative Metallography

The lamellar width (λ) is the spacing for one pair of lamellae, expressed in microns or micro-meters. (Fig. 4)

The fault density (N_A) is the number of terminations and other defects such as kinks in an area of $(100\,\lambda)^2$. The average length of mismatch line is normalized for an area of $(100\,\lambda)^2$ and is expressed in $Cm/(100\,\lambda)^2$. The average defect spacing between mismatch lines is expressed in lamellar widths.

Results and Discussion

As shown in Fig. 5, the fault density [6] or the number of terminations and defects for a standard area in the Skylab 4 specimen is 20% fewer than the ground based specimens. The Skylab 3 specimen has a much higher fault density than either the ground-based or Skylab 4 specimen because of the surface irregularities and dis-orientation of the microstructure.

As shown in Fig. 6, the differences in average length of mismatch lines [6] and [7] are very slight. Again, one of the Skylab 3 specimens is much worse than ground-based specimens.

As shown in Fig. 7, the average defect spacing favors the Skylab 4 specimens. Please note that the data from Georgia Tech [7] shows their S/L 4 specimen to be best, while the University of Connecticut data [6] show their S/L 4 specimen to be the best. Some variation in counting techniques of such complex micro structures should be expected. In each instance the advantage is 12 to 13% for the S/L 4 specimen.

Figures 8, 9 and 10 show transverse sections of a typical ground-based specimen and Skylab processed specimens at similar distances from the remelt interface. A study of them will confirm that the Skylab 4 specimen has larger areas free from defects and therefore fewer defects. The magnification is approximately 500X on each but is varied slightly to facilitate visual comparison over normalized areas of $(100\,\bar{\lambda})^2$.

CONCLUSION

Quantitative metallography shows that specimens processed in the zero gravity of S/L 4 are superior to ground-based specimens on two characteristics:

The defect spacing in lamellar widths is 12% better.
The fault density is 20% less.

REFERENCES

1. L. M. Hogan, R. W. Kraft, and F. D. Lemkey, "Eutectic Grains" in Advances in Materials Research, Interscience Publishers, New York, Vol. 5, 1971, p. 182.

2. A. E. Wechsler, et al, "Sphere Forming and Composite Casting in Zero-G", Final Report on contract NAS8-21402, Arthur D. Little, Inc., Cambridge, Mass., Jan. 7, 1970, p. 94, 99.

3. F. D. George, "Preparation of Single Grain Eutectics for the M566 Experiment", Mod. 2 Report, contract NAS8-28724, United Aircraft Research Laboratories, East Hartford, Conn., Dec. 15, 1972, p. 2.

4. "Data Package for Cartridges for the Multipurpose Electric Furnace System, M518", WANL-TME-2831, Volume II, November 1972, Westinghouse Astronuclear Laboratory, P. O. Box 10864, Pittsburgh, Pennsylvania 15236, (Contract NAS8-28271).

5. L. L. Lacy, "Preliminary Report on the Physical Properties of Al-Cu Eutectic Samples Processed on Skylab 4", MISC-SSL-74-2 Space Sciences Laboratory, MSFC, April 2, 1974.

6. Theo. Z. Kattamis, Unpublished data, contract NAS8-28734, University of Connecticut, April 1974.

7. John L. Brown, Jim Hubbard and James Thompson, Monthly Progress Letter No. 19, contract NAS8-28735, Georgia Institute of Technology, April 15, 1974.

8. Jim Hubbard, Unpublished photos, contract NAS8-28735, Georgia Institute of Technology, April 1974.

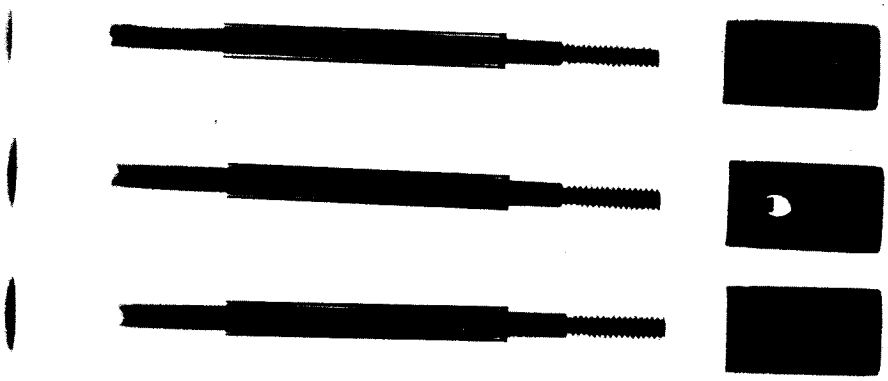

FIGURE 1. RADIOGRAPH OF COPPER-ALUMINUM EUTECTIC SPECIMENS IN CARTRIDGES FROM SKYLAB 4.

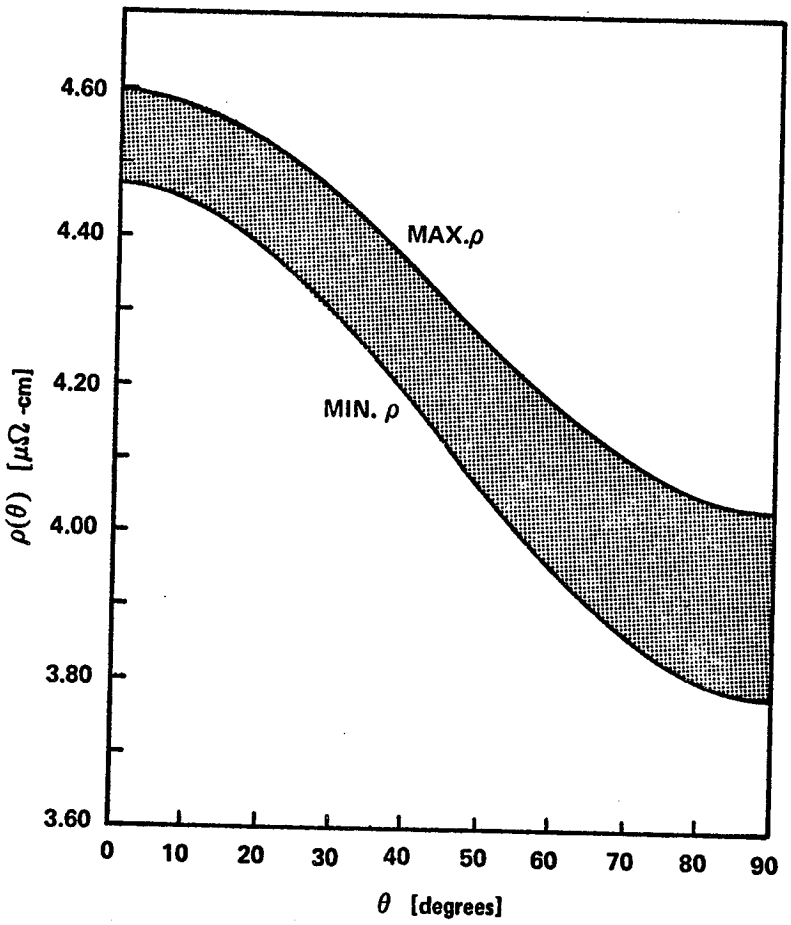

FIGURE 2. THE MAXIMUM AND MINIMUM VALUES OF ELECTRICAL RESISTIVITY FOR DIRECTIONALLY SOLIDIFIED Al-Cu EUTECTIC AS A FUNCTION OF ORIENTATION ANGLE.

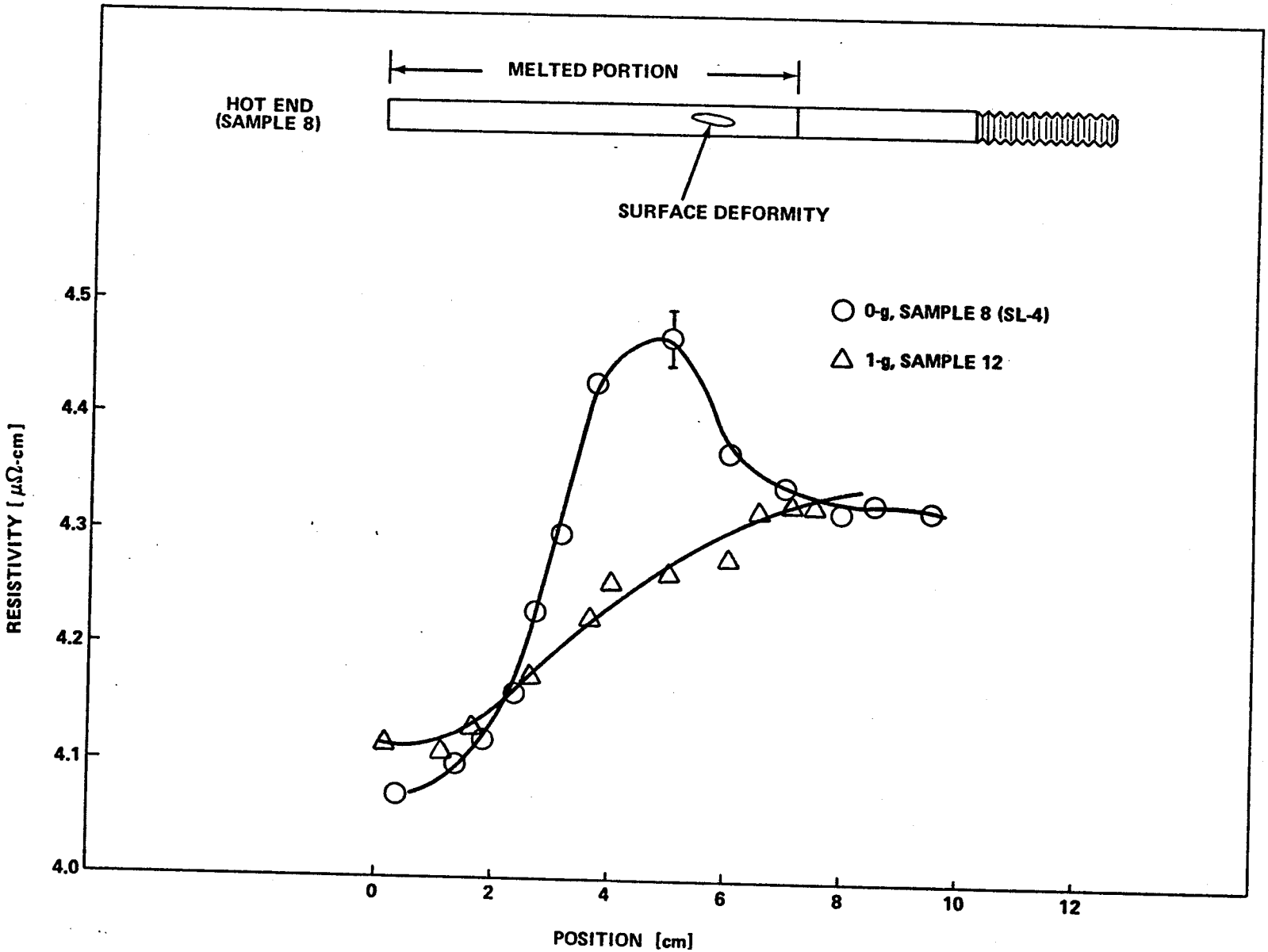

FIGURE 3. LOCAL RESISTIVITY OF SAMPLES M566-8 AND M566-12 [5]

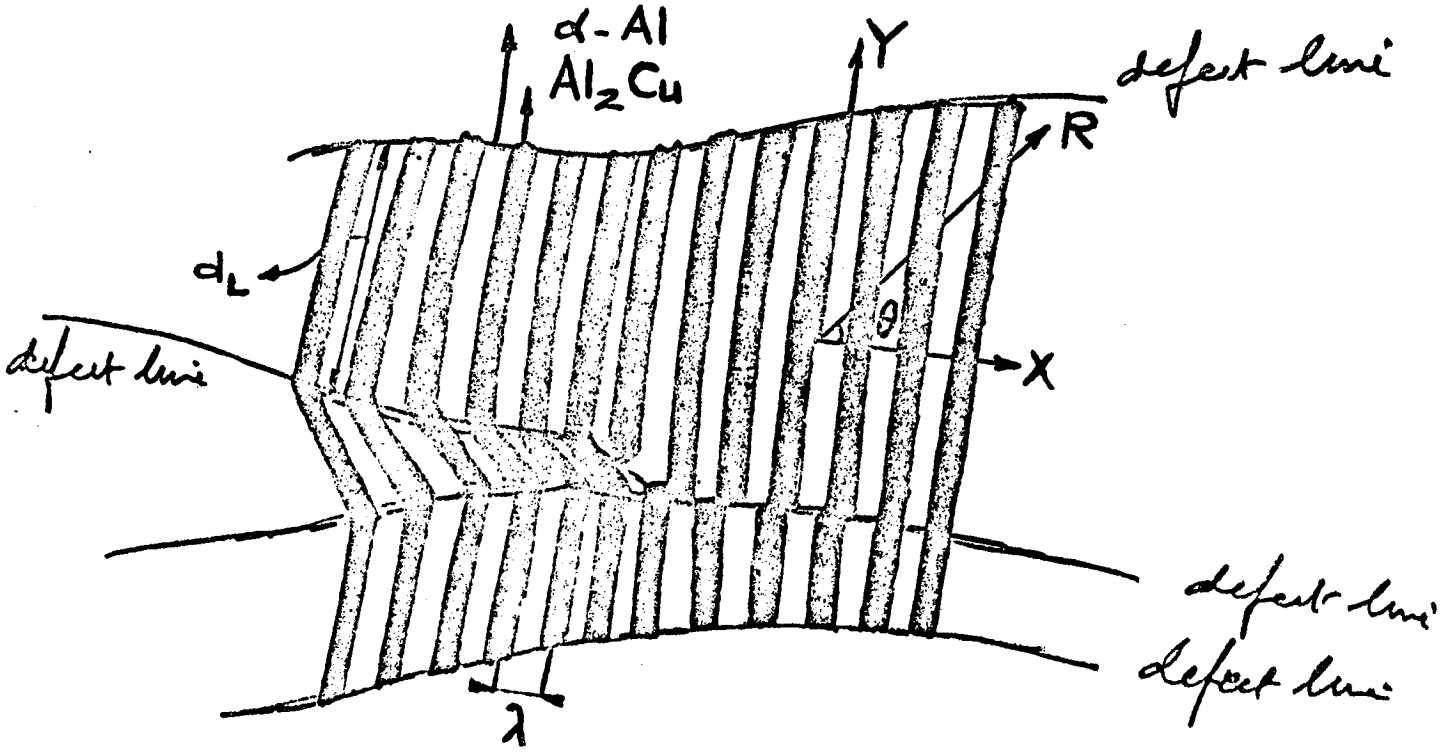

FIGURE 4. SCHEMATIC REPRESENTATION OF A TRANSVERSE SECTION IN DIRECTIONALLY SOLIDIFIED Aℓ-Cu EUTECTIC ALLOY [6]

QUANTITATIVE METALLOGRAPHY

SPECIMEN	NUMBER OF TERMINATIONS AND DEFECTS IN ($100\lambda^2$) AREA
M566-7 S/L 4	925
M566-11 GROUND	1150
M566-15 GROUND	1150
M566-5 S/L 3	2000

FIGURE 5. M566 COPPER-ALUMINUM EUTECTIC

QUANTITATIVE METALLOGRAPHY

SPECIMEN	AVERAGE LENGTH OF MISMATCH LINE, ($CM/(100\lambda)^2$
M566-15 GROUND	0.364 (C)
M566-7 S/L 4	0.380 (C)
M566-9 S/L 4	0.540 (T)
M566-11 GROUND	0.550 (C)
M566-6 S/L 3	0.584 (T)
M566-10 GROUND	0.668 (T)
M566-5 S/L 3	0.935 (C)

FIGURE 6. M566 COPPER-ALUMINUM EUTECTIC

HALIDE EUTECTIC GROWTH

By

A.S. Yue* and J.G. Yu
University of California
Los Angeles, California 90024

SUMMARY

Fiberlike NaCl-NaF eutectic mixtures have been produced on earth and in space by the directional solidification technique. It was found that continuous and discontinuous NaF fibers were embedded in a NaCl matrix from ingots grown in space and on earth, respectively. The production of continuous fibers in a eutectic mixture was attributed to the absence of convection current in the liquid during solidification.

Macroscopic and microscopic examinations on longitudinal and transverse sections of space-grown and earth-grown ingots were made. It was found that during the major portion of the space solidification process, the NaF fibers were aligned with the ingot axis. However, they were normal to it during the very beginning of the solidification process. This indicated that the direction of heat flow was perpendicular to the ingot axis. The best microstructures were obtained from ingots grown in space. These microstructures were compared with those produced on earth with and without convection current in the liquid during growth.

Optical transmittance measurements of transverse and longitudinal sections of the space-grown and earth-grown ingots were carried out with a polarizer in a Perkin Elmer Spectrometer. It was found that for a given sample thickness, the highest percentage of transmittance was obtained from ingots grown in space. The effect of sample thickness on transmittance was investigated. It was found that the thinner the sample, the higher the transmittance over a range of wavelengths, in agreement with the general optical property of transparent materials exposed to electromagnetic waves.

INTRODUCTION

When certain binary eutectic mixtures solidify, one of the two phases can form fibers or platelets in a matrix of the second phase. For example, when a eutectic liquid of NaCl and NaF solidifies, fibers of NaF form in a matrix of NaCl.

Fiberlike and platelike eutectics produced on earth are limited in perfection by the presence of a banded structure,[1,2] discontinuity, [3] and faults [4,5] due, at least in part, to vibration and convection currents in the melt during solidification. The presence of these defects renders the solid-state eutectic devices inefficient and useless [6].

*Paper presented by - A.S. Yue

If the solidification process is performed in a space environment, where there is no vibration and convection current in the melt, there is reason to believe that continuous fiberlike eutectic microstructures can be produced. The electric, thermomagnetic, optical, and superconducting characteristics of such fibers will be strongly anisotropic, and this will make possible various exciting device applications.

The purposes of this paper are (1) to prepare, in a space experiment, fiberlike NaCl-NaF eutectic with continuous NaF fibers embedded in a NaCl matrix and to examine the eutectic microstructure, and (2) to measure the relevant optical properties of the space-grown and earth-grown eutectics. Explanations of the differences in properties are given in terms of the scattering and absorption characteristic of the materials.

EXPERIMENTAL PROCEDURE

Experimental studies have been carried out at UCLA to acquire all possible knowledge of the solidification process of the eutectic mixture involved, short of doing the space experiments themselves. Calculations and design of equipment have been followed by a program of solidifications at various rates and with various temperature gradients at the interface.

The objective of the earth-based studies is to maximize the likelihood of success of the space experiments.

Ingots of NaCl-NaF eutectics, 0.31 inch in diameter and 2.5 inches long have been grown unidirectionally on earth and in the Skylab in a multipurpose furnace at one freezing rate and a steep temperature gradient.

RESULTS AND DISCUSSION

The experimental results are divided into three parts: The first part concerns the macroscopic and microscopic examinations of the samples that were grown in Skylab 3 and samples that were grown on earth. The second part concerns the preparation of continuous NaF fibers embedded in a NaCl matrix. The third part concerns the optical property of the NaCl-NaF eutectic. Comparison of the experimental results between the earth-grown and space-grown samples will be discussed in terms of scattering and absorption characteristic of the eutectic.

A. Macroscopic and Microscopic Examinations of Microstructures

Figure 1 is a macro-photograph showing the appearance of the three ampoules after the Skylab experiments. The surfaces of the stainless steel cylinders and the copper tubings (right side of Fig. 1) were in perfect condition, indicating that there was no reaction between the ampoules and the cartridges. Remelting of the silver solder was not detected at the joint binding the stainless steel cylinder and the copper tubing together.

Figure 2 is a macro-photograph of the three samples taken out of the ampoules by grinding off the welded ends of each cylinder. Careful inspection on the surface of the sample revealed no reaction between the the NaCl-NaF eutectic and graphite container. In sample M564-10, two transverse fractured

surfaces of the ingot occurred, both close to the head and tail portions of the sample as revealed in Fig. 2. However, the fracture did not interrupt the growth pattern of the ingot.

Figure 3 is a macro-photograph showing the solid-liquid interface, columnar grains of the solidified portion of the sample (on the right of the interface), and the unsolidified portion of the sample (on the left of the interface). An enlarged portion of the solid-liquid interface is given in Fig. 4 which shows that at the beginning of the solidification process, the NaF fibers were grown in the direction perpendicular to the growth direction. This indicates that the direction of heat extraction during the onset of solidification is normal to the growth direction in contrast to what was originally designed. This was tentatively attributed to improper insulation design. However, in a distance not far away from the initial solid-liquid interface (about 0.12 cm), the NaF fibers began to align toward the growth direction.

A representative photomicrograph of perfect and continuous fibers is given in Fig. 5 which shows that the NaF fibers are regularly spaced and parallel to the growth axis. When the NaCl-NaF eutectic was grown on earth with convection currents, the resulting eutectic microstructure is represented by Fig. 6 which shows that the solidified NaF fibers are randomly embedded in the NaCl matrix along the longitudinal section of the ingot. When the same eutectic was solidified vertically with very little convection current in the liquid during growth, the NaF fibers as revealed by Fig. 7 are regularly distributed along the ingot axis. However, these fibers are partially discontinuous.

A photomicrograph of the transverse section of the Skylab-grown sample is shown in Fig. 8 which reveals the shapes of the fibers which are preferentially rectangular. A scanning electron photomicrograph of the shapes of fibers is given in Fig. 9 which is the perspective view of the rectangular NaF fibers, sticking out of the continuous NaCl matrix.

Single-grain eutectic has not been produced in the presence of microgravity in space as evidenced in Fig. 10 which is a transverse section of sample M564-10. Many grains and subgrains are present throughout the whole cross-section. However, the fibers are aligned very regularly and parallel to the growth direction. Evidence in supporting the above statement is given in Fig. 11a which is a picture taken from Sample M564-6 which was grown in space. A filtered light from a Bausch & Lomb microscope was shone at the tail end of the sample. Due to good alignment of NaF fibers along the sample axis, light was transmitted from the tail end to the melted solid-liquid interface which is about 1.4 cm away from the "head" of the sample. Light was not transmitted through the unmelted portion of the sample because that portion of the ingot was grown on earth and the fibers did not line up with the sample axis. Note the homogeneity of the sample as revealed in Fig. 11a. Fig. 11b is a portion of a NaCl-NaF eutectic sample grown vertically on earth in a prototype furnace with very little convection current in the melt during growth. Light was completely transmitted from one end to the other, indicating that the NaF fibers are aligned in the direction of the growth axis. However, many striations appeared on the surface of the cylindrical sample, indicating the presence of non-homogeneity in the sample. In the absence of gravity (or in a

microgravity environment), a non-homogeneous crystal can be transformed to a homogeneous one if it is grown in a space environment. Fig. 11c is a picture taken from a sample grown in an induction furnace at UCLA. An attempt was made to shine a light at one end of the sample but it did not travel very far because the NaF fibers were not aligned in the direction of the light. However, when light was shone on the side of the sample as indicated by the white spot in Fig. 11c, transmittance of light occurred in the direction perpendicular to the sample axis, indicating that the fibers are also perpendicular to the sample axis. Banded microstructure was evidenced in Fig. 11c in agreement with our original prediction.

B. Sodium Flouride Fibers

In a zero-gravity environment, there is no convection current in the liquid during solidification and there is no difficulty in mixing two liquid phases of different densities. Furthermore, vibration levels in space will be far lower than those on earth. Consequently, a continuous fiber eutectic mixture can be produced in a space environment, and microstructure sensitive to convection currents and vibration can develop undisturbed.

Fig. 12a is a macrophotograph of a space-grown ingot (M564-11) which has been immersed in methane alcohol for five weeks. The surface of the undissolved portion of the ingot is encased with a skeleton of NaF fibers. An enlarged portion of the ingot containing the unsolidified portion, the curved solid-liquid interface and the solidified portion is given in Fig. 12b. Notice that on the right-hand side of the interface, the undissolved portion of the eutectic ingot reveals the presence of directional grains along the ingot axis. However, the grain directionality was not evident in the unsolidified portion of the ingot, indicating that the fibers are short and randomly distributed. Figure 13a proves that the growth of fibers was originated at the solid-liquid interface. Figure 13b is a picture of the end cross-section of the unsolidified portion of the ingot, showing that the short NaF fibers are perpendicular to the cylindrical surface of the ingot.

C. Optical Property

Image transmission properties similar to those of fiber optic materials were obtained with an NaCl-NaF eutectic [7]. Moreover, this eutectic was found to be far-field infrared transmitting medium for wavelengths longer than the inter-fiber distance. Since the NaCl-NaF eutectic used for optical measurement has discontinuous NaF fibers embedded in the NaCl matrix, far better results will be obtained if the same eutectic can be produced in space with continuous fibers.

Figure 14 is a plot of transmittance versus wave number, k ($40 \times 10^2 cm^{-1}$ to $4 \times 10^2 cm^{-1}$) for NaCl, NaF and NaCl-NaF eutectics, prepared at UCLA, reported previously, and grown in the Skylab. The eutectic sample thicknesses taken from the transverse sections of the ingots were 0.107 in. The transmittance of NaCl drops off abruptly at $k = 7 \times 10^2 cm^{-1}$ and that of NaF at $k = 10 \times 10^2 cm^{-1}$ because the former has a higher refractive index (1.54) than the latter (1.31). Due to the optiaal mode of lattice vibration, the transmittance of NaCl and NaF approach zero at $k = 4.5 \times 10^2 cm^{-1}$ and $6.8 \times 10^2 cm^{-1}$, respectively. For the NaCl-NaF eutectic grown at UCLA where there were

convection currents present in the liquid during growth, the transmittance was about 10% over a narrow range of wave numbers as indicated in Fig. 14. When the same eutectic was grown in space (M564-6) where there were no convection currents in the liquid during growth, the transmittance was increased to 65% over a much larger range of wave numbers. This was attributed to the achievement of producing continuous NaF fibers embedded in a continuous NaCl matrix so that the losses due to reflection and refraction of light within the eutectic specimen have been greatly reduced. The shape of the transmission curve for the NaCl-NaF eutectic is of great interest. At $k > 30 \times 10^2 cm^{-1}$, the transmittances of the two eutectics approach zero while those of NaCl and NaF remain at 95%. The explanation is that the interfacial atoms at the fiber-matrix interface are mismatched. When incident light is directed at the surface of a eutectic sample, a fraction of the incident light transmitted through the eutectic sample will decrease due to scattering. This observation is in agreement with the fact that the higher the wavenumber (or the shorter the wavelength) the higher the scattering. The scattering effect of the space-grown sample is not as severe as that of the earth-grown sample (B.D.G.) because the NaF fibers in the former are continuous while those in the latter are discontinuous. The decrease in transmittance for wave numbers less than $8.0 \times 10^2 cm^{-1}$ was attributed to absorption by the NaF fibers.

The effect of thickness on the transmission curve is given in Fig. 15 which indicates that the thinner the sample, the higher is the transmittance for a fixed wave number. This observation is in agreement with Lambert's law of absorption. The basic principle from which the law was derived is that the fraction of radiation absorbed in passing through a thin layer of matter is proportional to the thickness of the layer and the absorption coefficient which depends upon the nature of the absorbing matter and the wave length of the radiation. Expressed mathematically, where I_o is the intensity of incident radiation upon a thin layer of matter and I is the intensity of the radiation that passes through the matter, one obtains

$$\frac{I_o - I}{I_o} = \frac{\Delta I}{I_o} = - \mu_\ell \Delta X \qquad (1)$$

where ΔX is the thickness of the matter and $\mu\ell$ is the linear absorption coefficient for the particular material and wavelength concerned. The negative sign arises because ΔI is a mathematical symbol for the increase in intensity I of the radiation as it passes through the layer of matter.

The effect of surface condition on the transmission curve for both the transverse and longitudinal sections of the NaCl-NaF eutectic, grown vertically on earth is given in Figs. 16 and 17 respectively. The data indicated the intensity of the transmitted light decreased with etching over the whole range of wave number. This can be explained by the fact that etching resulted in the roughening of the sample surfaces. When a light is shone on a rough surface, the intensity of the transmitted light decreases as the degree of roughness increases, in agreement with experimental observations. However, there was an absorption band at $k \simeq 10 \times 10^2 cm^{-1}$ for both cases after etching. This was tentatively attributed to the presence of impurities in these specimens.

CONCLUSIONS

The following conclusions can be drawn from this investigation:

1. Continuous NaF fibers have been produced in the Skylab experiments. The success in producing continuous fibers is due to the absence of convection current in the liquid during solidification.
2. Larger transmittance over a wider wavelength was obtained from the Skylab-grown ingots. This is due to excellent alignment of NaF fibers embedded in the NaCl matrix.

ACKNOWLEDGMENT

The authors would like to thank Messrs B.K. Yue, D. Silkey and N.M. Akdas for their work on the preparation of the ampoules and metallography of the samples.

REFERENCES

1. A.S. Yue and J.B. Clark: Trans. TMS-AIME, 1961.
2. F.D. Lemkey and E.R. Thompson: Met. Trans., 1971, Vol. 2, p. 1537.
3. F.W. Crossman and A.S. Yue: Met. Trans., 1971, Vol. e, p. 1545.
4. A.S. Yue: Trans. TMS-AIME, 1962, Vol. 224, p. 1010.
5. R.W. Kraff and D.L. Albright: Trans. TMS-AIME, 1961, Vol. 221, p. 95.
6. H. Weiss: Met. Trans., 1971, Vol. 2, p. 1513.
7. J.A. Batt, F.C. Douglas, F.S. Galasso, Ceramic Bulletin, 1969, Vol. 48, No. 6, p. 622.

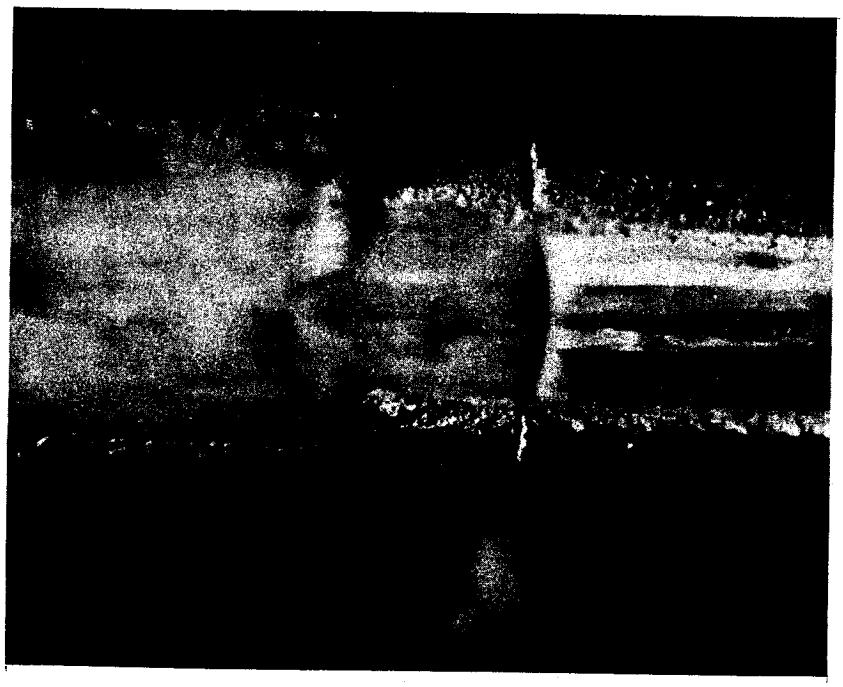

FIGURE 3. MACROGRAPH SHOWING THE SOLID-LIQUID INTERFACE OF THE SKYLAB GROWN NaCl-NaF EUTECTIC (6.5X)

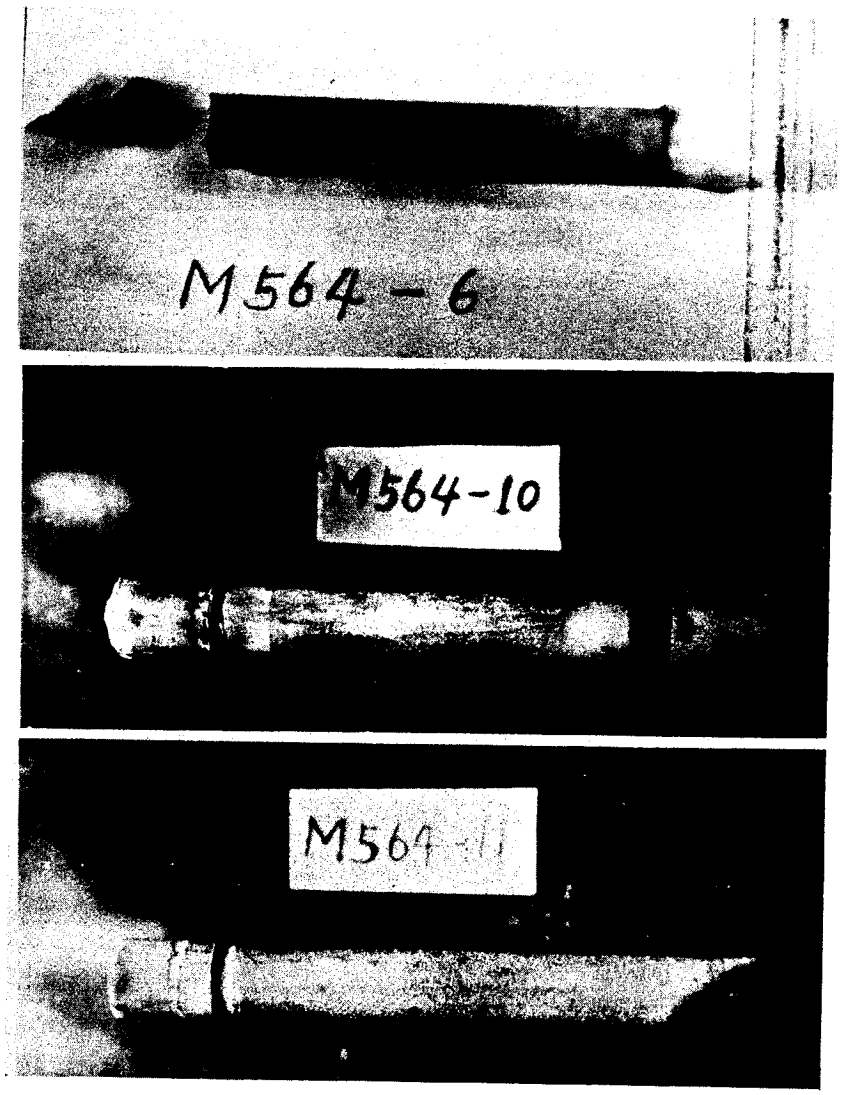

FIGURE 2. MACRO-PHOTOGRAPH OF THE NaCl-NaF EUTECTIC GROWN IN THE SKYLAB

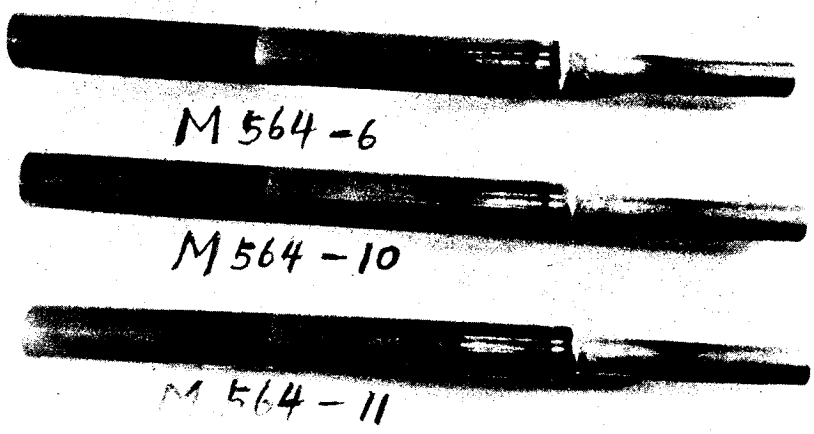

FIGURE 1. PHOTOMACROGRAPH OF THREE AMPOULES (0.8X)

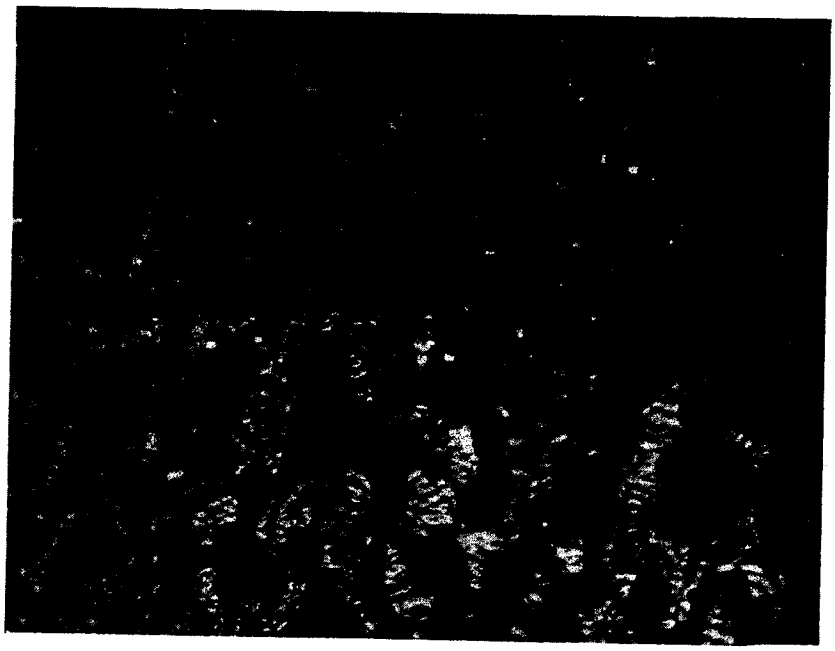

FIGURE 4. ENLARGED PORTION OF THE SOLID-LIQUID INTERFACE (410X)

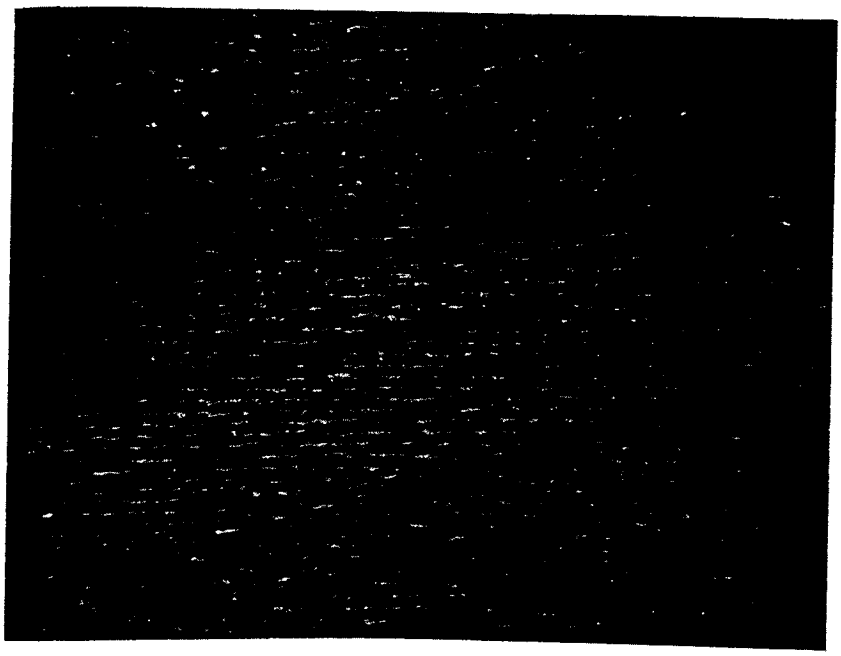

FIGURE 5. PHOTOMICROGRAPHS OF THE LONGITUDINAL SECTION OF THE NaCl-NaF EUTECTIC SHOWING CONTINUOUS NaF FIBERS (135X)

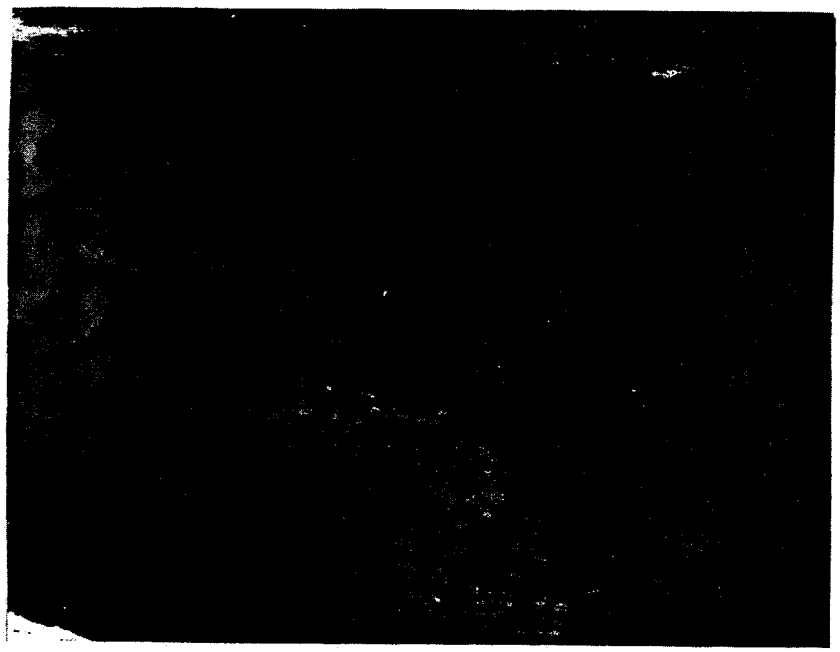

FIGURE 6. PHOTOMICROGRAPHS OF THE LONGITUDINAL SECTION OF NaCl-NaF EUTECTIC SHOWING DISCONTINUOUS NaF FIBERS (1500X)

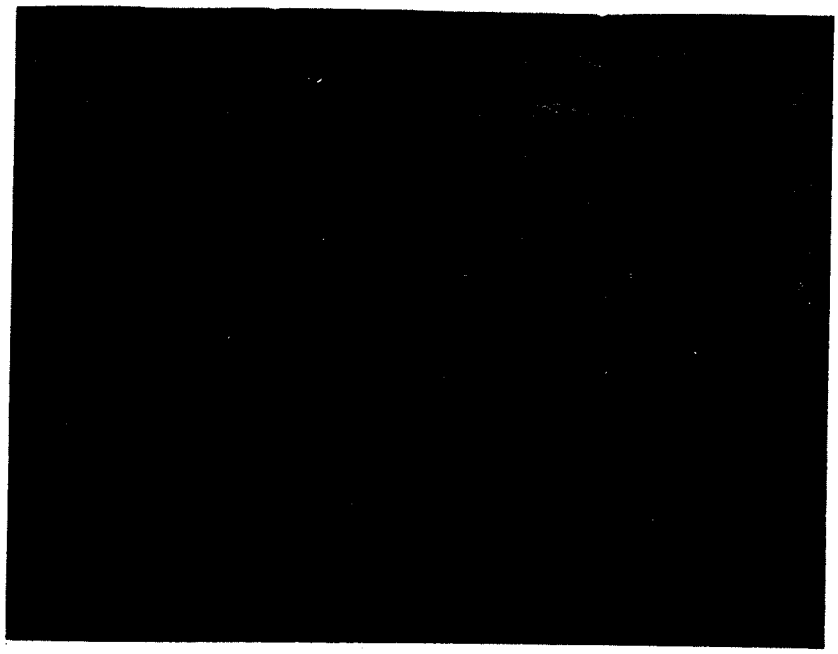

FIGURE 7. PHOTOMICROGRAPH OF LONGITUDINAL SECTION OF NaCl–NaF EUTECTIC SHOWING SOME DISCONTINUOUS NaF FIBERS (1500X)

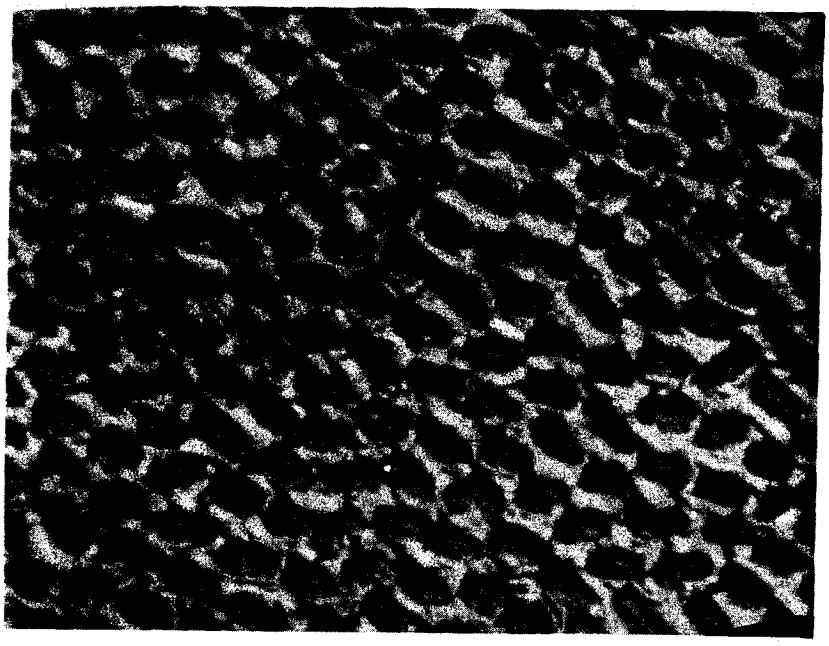

FIGURE 8. PHOTOMICROGRAPH OF THE TRANSVERSE SECTION SHOWING SHAPES OF NaF FIBERS (1500X)

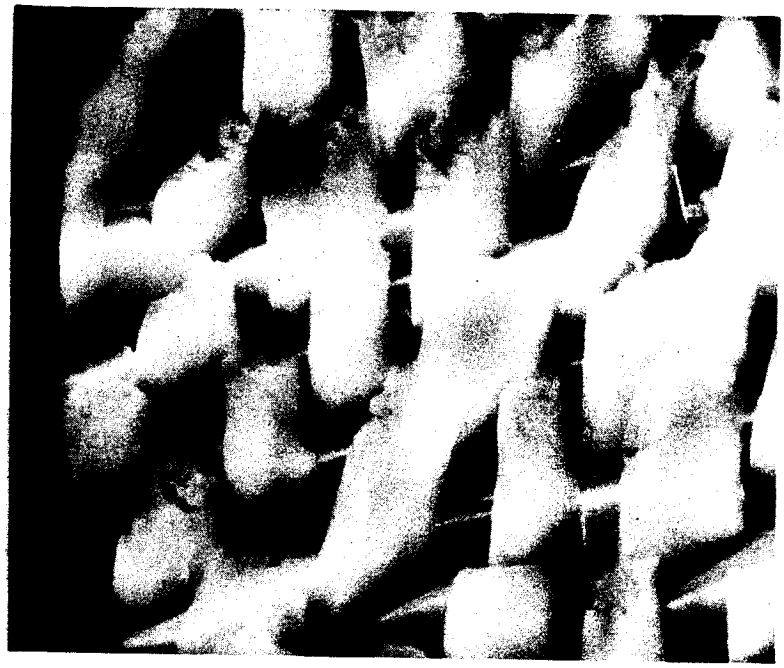

FIGURE 9. SCANNING ELECTRON PHOTOMICROGRAPH SHOWING THE NaF FIBERS (2100X)

FIGURE 10. MACROPHOTOGRAPH OF THE TRANSVERSE SECTION OF THE NaCl-NaF EUTECTIC, SHOWING GRAINS AND SUBGRAINS (9X)

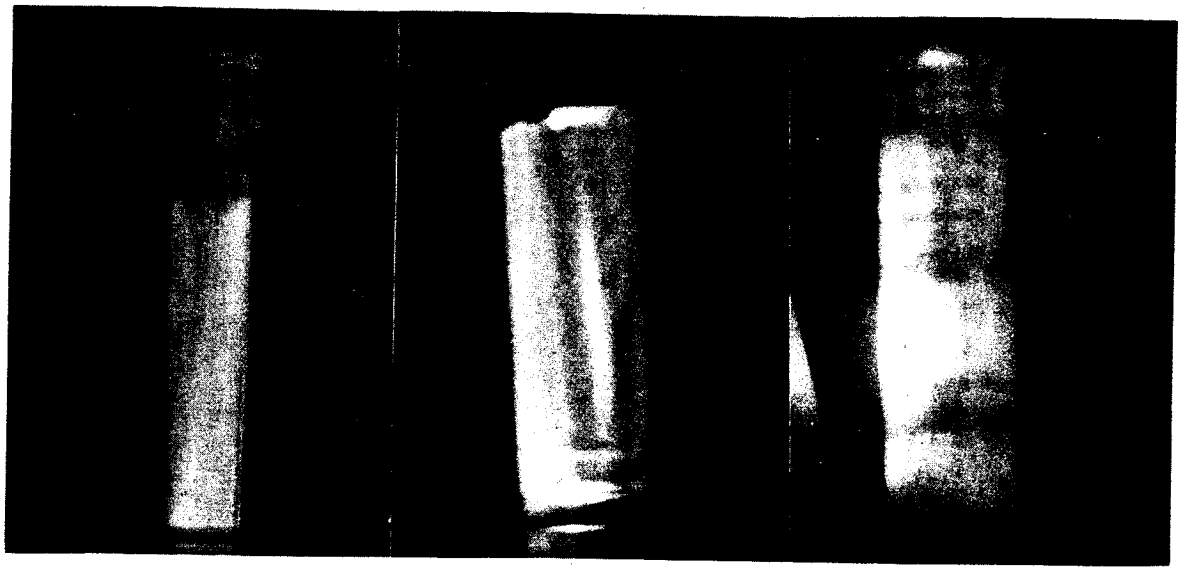

(a) (b) (c)

FIGURE 11. MACROPHOTOGRAPHS OF SKYLAB-GROWN (a), NASA-GROWN (b), AND EARTH-GROWN (c) NaCl-NaF EUTECTIC

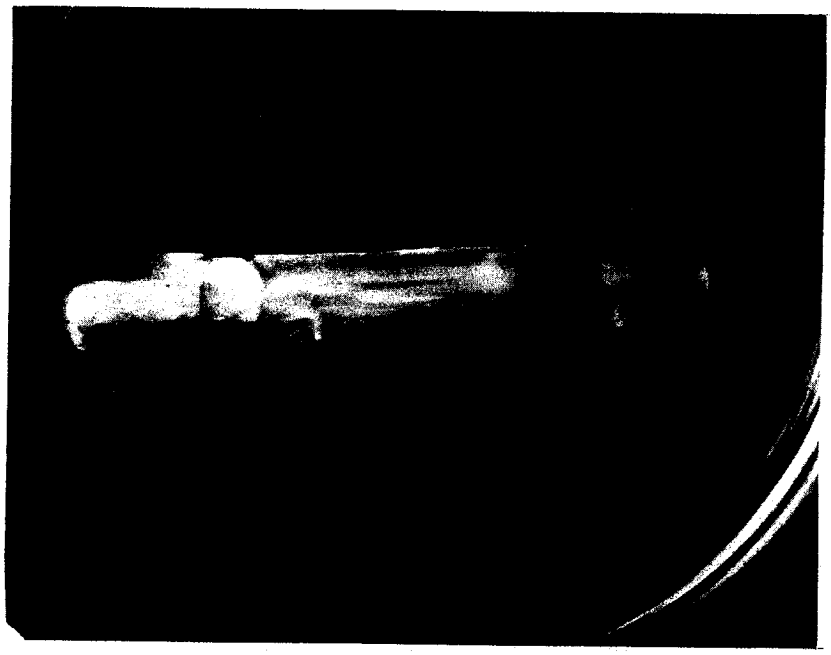

12a

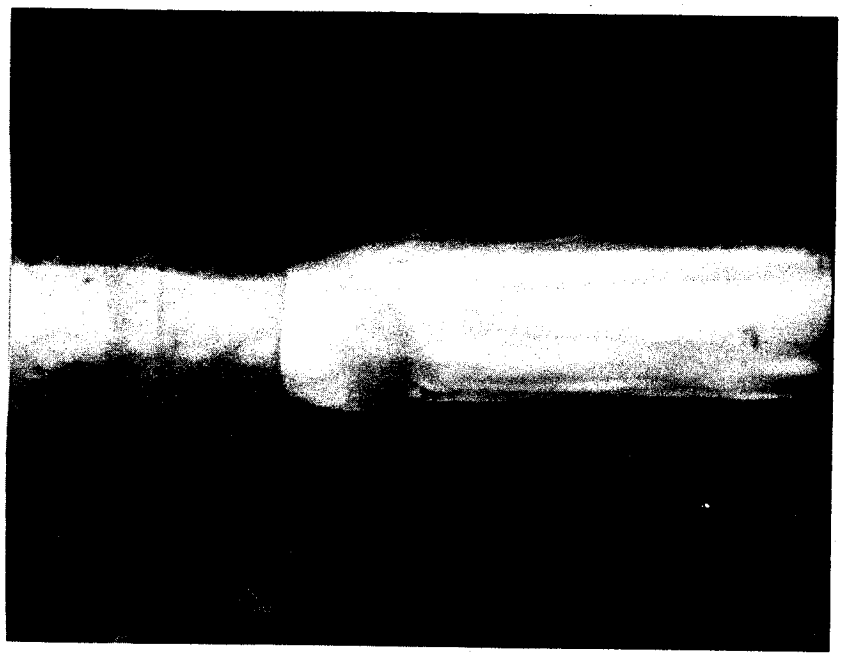

12b

FIGURE 12. SKYLAB GROWN INGOTS (M564-11) ENCASED WITH NaF FIBERS ETCHED OUT FROM NaCl-NaF EUTECTIC. (a) 2X AND (b) 4.3X

13a

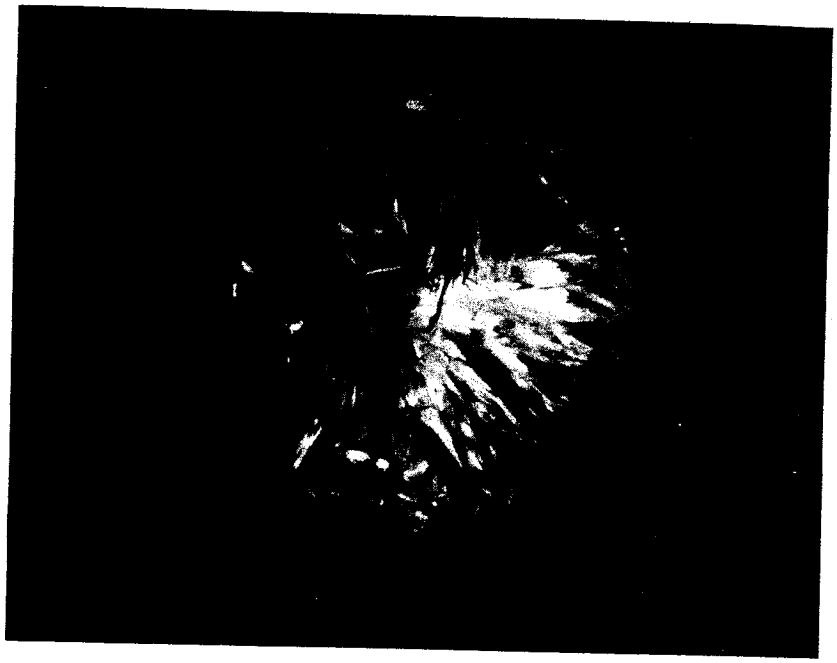

13b

FIGURE 13. (a) NaF FIBERS GROWN FROM THE SOLID-LIQUID INTERFACE.
(b) DISCONTINUOUS AND RANDOMLY ORIENTED FIBERS OF THE END INGOT.

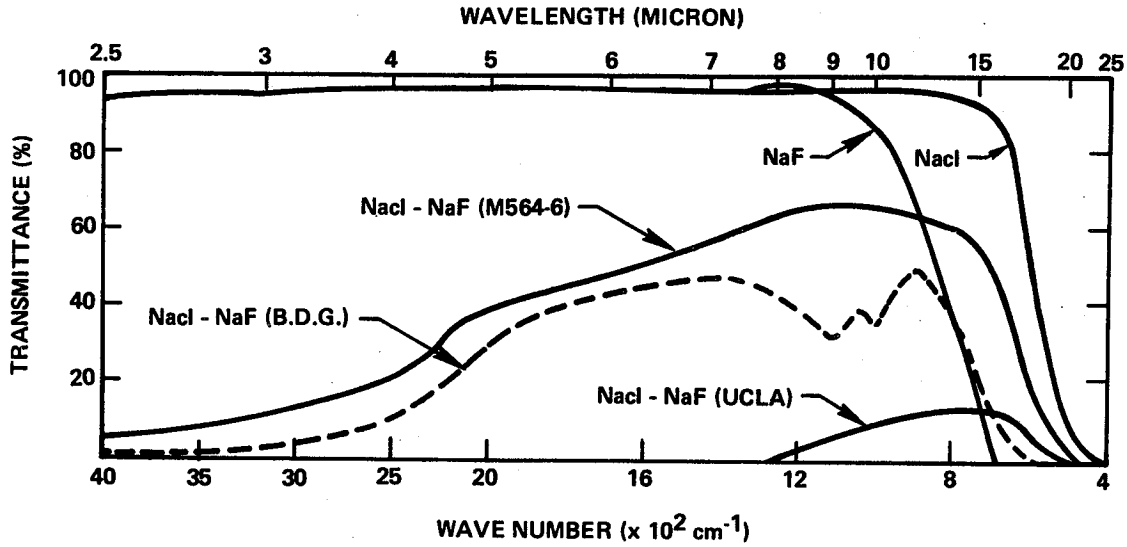

FIGURE 14. FAR-FIELD INFRARED TRANSMISSION CURVE FOR NaCl-NaF EUTECTICS GROWN ON EARTH AND IN SPACE. SAMPLE THICKNESS=0.107 in.

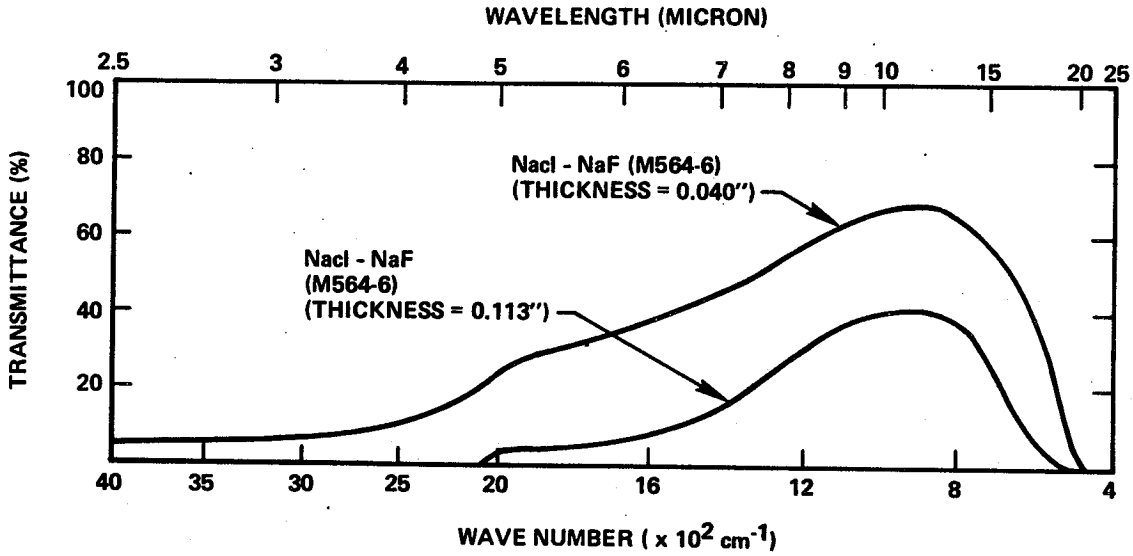

FIGURE 15. FAR-FIELD INFRARED TRANSMITTANCE CURVE FOR NaCl-NaF EUTECTICS OF DIFFERENT THICKNESS.

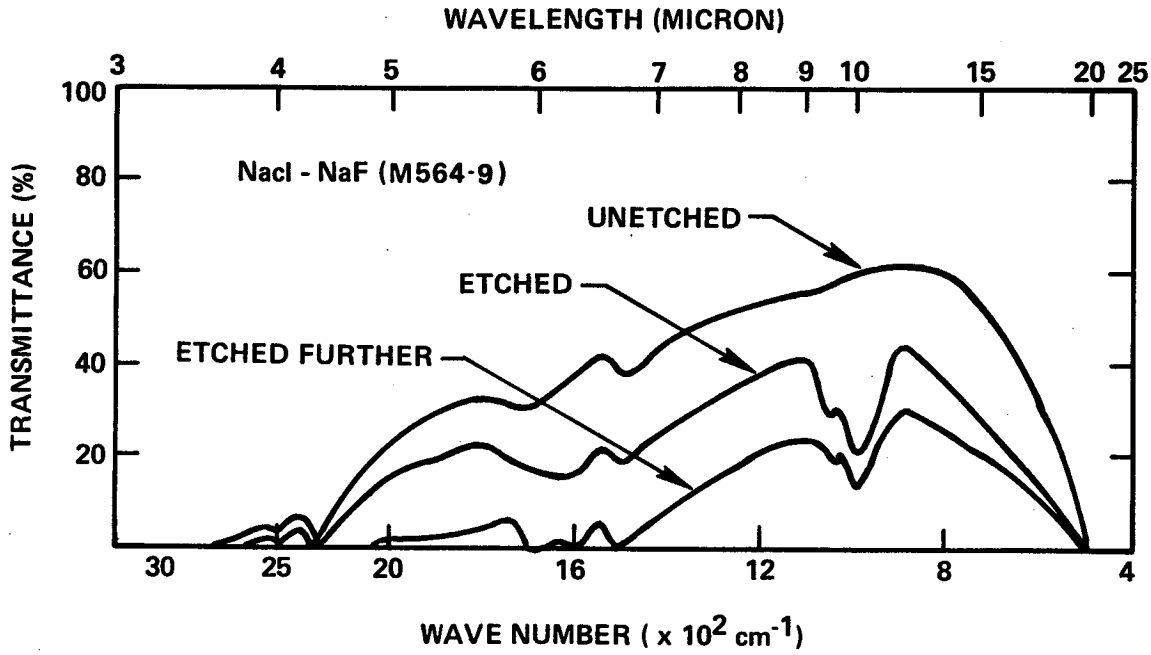

FIGURE 16. EFFECT OF SURFACE CONDITION ON FAR-FIELD INFRARED TRANSMITTANCE CURVE OF THE TRANSVERSE-SECTION SAMPLE. (THICKNESS = 0.035 ")

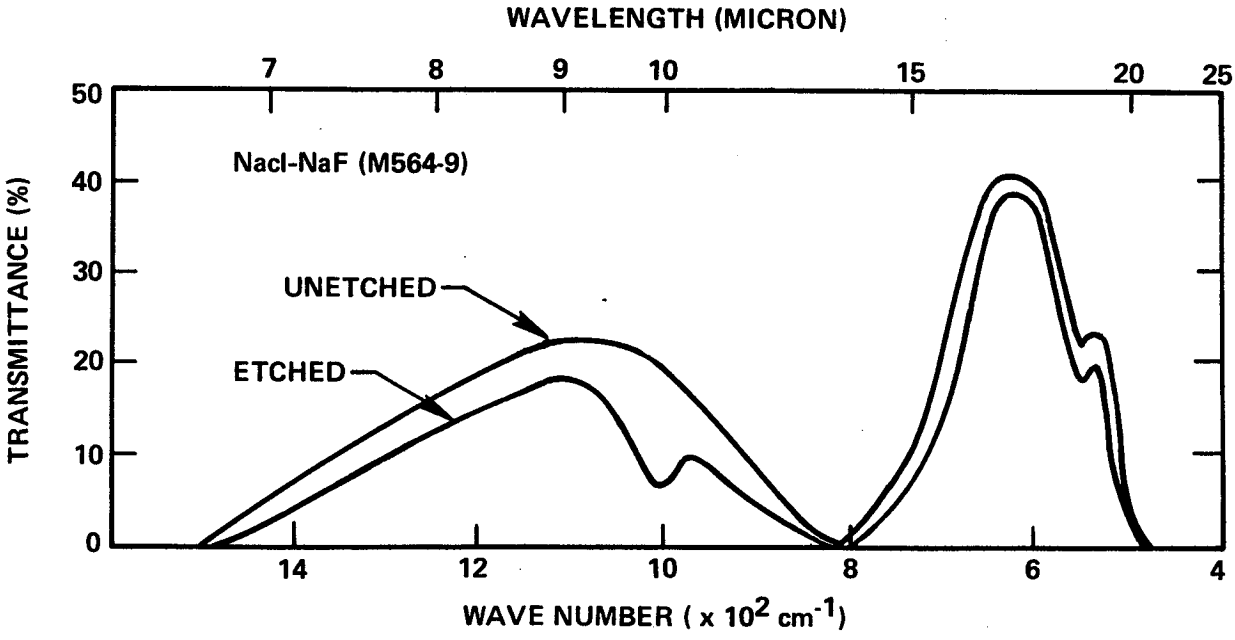

FIGURE 17. EFFECT OF SURFACE CONDITION ON FAR-FIELD INFRARED TRANSMITTANCE CURVE OF THE LONGITUDINAL-SECTION SAMPLE. (THICKNESS = 0.024")

SCIENCE DEMONSTRATIONS ON SKYLAB IN THE MATERIAL PROCESSING AREA

By

Tommy C. Bannister
Space Sciences Laboratory
Marshall Space Flight Center, Alabama 35812

SUMMARY

Twelve science demonstrations were accomplished on Skylab missions III and IV. These activities were defined in response to crew requests for time-gap fillers and were designed to be accomplished using onboard equipment. Nine of the demonstrations were in the area of materials science and space processing. They are described, and preliminary results are given. These nine science demonstrations are: Diffusion in Liquids, Ice Melting, Liquid Floating Zone, Immiscible Liquids, Liquid Films, Rochelle Salt Growth, Deposition of Silver Crystals, Fluid Mechanics Series, and Charged Particle Mobility.

INTRODUCTION

This paper discusses nine Marshall Space Flight Center (MSFC) science demonstrations in space processing (Table I) that were performed on Skylab missions III and IV. The objective of these demonstrations was to serve as time-gap fillers that would provide scientific data to be used for educational and scientific purposes. Each demonstration is briefly described, and a few results are discussed.

Most of the science demonstrations were performed on the last Skylab mission and used TV recording to obtain data. Therefore, the final reports from the investigators are not expected for a few months. For a written summary of the Skylab science demonstrations, see Skylab Science Demonstrations, a paper by Simon Ostrach which was presented at the March 1974 meeting of ESRO in Frascati, Italy [1], or NASA Technical Memorandum TM X-64835 entitled Skylab III and IV Science Demonstrations Preliminary Report [2].

TABLE I. SCIENCE DEMONSTRATIONS ON MATERIALS PROCESSING IN SPACE

	Demonstration	SL-3	SL-4
(No number)	Diffusion in Liquids	X	
(No number)	Ice Melting	X	
TV101	Liquid Floating Zone		X
TV102	Immiscible Liquids		X
TV103	Liquid Films		X
TV105	Rochelle Salt Growth		X
TV106	Deposition of Silver Crystals		X
TV107	Fluid Mechanics		X
TV117	Charged Particle Mobility		X

SKYLAB III SCIENCE DEMONSTRATIONS

The first Skylab III demonstration was Diffusion in Liquids. Ms. Barbara Facemire of the Space Sciences Laboratory at MSFC was the investigator for this experiment. For Diffusion in Liquids, a 5-inch long by 0.75-inch diameter plastic forceps tube holder was used for the test tube. Pilot Jack Lousma injected the tube three-fourths full of water with a hypodermic syringe (Figure 1). A concentrated solution of instant tea (about 7 times normal drinking tea) was carefully placed on top of the water in the tube. The diffusion of the tea into the water was periodically photographed over a period of three days. The tea diffused a length of 0.75 inch in 45 hours. The final diffusion front was parabolically shaped, somewhat like a bullet, with very little diffusion occurring near the tube wall. This shape has so far been attributed to static charges on the forceps tube. This demonstration shows how slow pure diffusion processes without gravity-induced convection will be in space.

The second demonstration on Skylab III, Ice Melting, was performed also by Pilot Lousma. The investigators were Dr. Lewis Lacy of the Space Sciences Laboratory and Dr. Guenther Otto of the University of Alabama in Huntsville. In this demonstration a cylinder of ice was frozen on a cue tip in a pill dispenser bottle that was 2.5 inches long by 1 inch diameter. After

remaining in the freezer for one day, the ice was removed from the pill bottle and mounted in front of the 35-mm camera. Periodic photographs of the ice melting were made. The rate of ice melting in zero gravity without buoyancy convection and the shape of the liquid on the unmelted ice portion were determined. The shape of the water went from cylindrical to ellipsoidal to circular in 4 hours (Figure 2). This demonstration illustrates how surface tension shapes liquid globules, altering the heat flow paths during melting.

Pilot Lousma had some free time after the ice melting demonstration was completed. It was decided to observe the effects of changing the surface tension of the globule with the addition of soap solution (Figure 3). Grape juice was added to the water globule for contrast. No distortion of the globule occurred when the soap was added. The soap diffused on the surface faster than inertial reaction because of surface tension gradients. Later, air was added to the interior of the globule. The cluster of air bubbles reached a critical size after which additional injections resulted in air bubbles popping out of the globule.

SKYLAB IV SCIENCE DEMONSTRATIONS

Because somewhat more time was available for planning the Skylab IV demonstrations, a science demonstration kit was flown to provide some critical hardware for use in these demonstrations. Even so, most of the hardware used was onboard hardware. The Skylab IV demonstrations were assigned numbers.

Demonstration TV101, Liquid Floating Zone, was proposed by Dr. John Carruthers of Bell Research Laboratories, Murray Hill, New Jersey. It was performed and recorded on TV video by Science Pilot Ed Gibson. This demonstration (Figure 4) simulates an important method of growing crystals and was done to define the stability of the liquid zone under a steady rotation rate of about 30 rpm as well as to obtain data on the instability modes and convection patterns. This information is important in the utilization of this technique for growing crystals both on the ground and in space in the planned Space Laboratory. Figure 4 is a schematic of the setup, while Figure 5 shows the setup in the Skylab mockup.

Demonstration TV102, Immiscible Liquids, was performed by Pilot William Pogue. The investigators were Dr. Lewis Lacy of the Space Sciences Laboratory and Dr. Guenther Otto of the University of Alabama in Huntsville. The objective of this demonstration was to photograph the coalescence of finely dispersed immiscible liquids. This demonstration visually defines some of the fluid dynamic aspects of the solidified immiscibles

done on Skylab experiment M518. A metal clip containing three vials (2.5 by 0.5 inch) was flown in the science demonstration kit (Figure 6). Krytox and dyed water were used in the three vials containing 25, 50, and 75 percent water, respectively. The recoalescence of the fluids was rather fast (10 sec) on the ground (Figure 7). However, the emulsion appeared to remain stably mixed for up to 10 hours in space. This is shown on the film of the experiment.

Demonstration TV103, Liquid Films, utilized shaped strips of onboard safety wire (Figure 8) to create thin films of pure water and water containing a small amount of shower soap. The investigator for this demonstration was Wesley Darbro of the Space Sciences Laboratory. Commander Gerry Carr recorded this demonstration on TV video. He was able to obtain soap films that lasted longer than on the ground, but they did burst after 3 or 4 minutes. Commander Carr was able to obtain a sizeable pure water film during his practice runs (approximately 1 by 6 by 1/16 inch). The solidification of films from liquids which we are not able to accomplish on the ground appears feasible in space.

The next demonstration was TV105, Rochelle Salt Growth. The investigator was Dr. I. Miyagawa of the University of Alabama, Tuscaloosa. Pilot Pogue also performed this demonstration. A 4-inch food can was filled with saturated Rochelle salt solution, 8 gm of Rochelle salt powder, and a 22-gm Rochelle salt seed crystal. The can contained a see-through membrane under the pull-top lid. Pilot Pogue removed the pull-top lid in space, placed the can in the food heating tray (Figure 9), and then heated the solution until three-fourths of the seed crystal dissolved (at approximately 160° F). The can was removed, wrapped in several towels for insulation, and stowed. During storage in zero g, the seed crystal slowly regrew as the can cooled back down to cabin temperature over a period of two days, after which the towels were removed. Two weeks later, Pogue removed the seed crystal from the solution to observe the results in space. The solution contained many small Rochelle salt crystals that had nucleated from solution. Pogue described the solution as "slushy" and the nucleated crystals which he saw as being "mica-like." The seed crystal (Figure 10), which was returned to earth, had regrown in the form of a plate about 1.5 inches on each side and about 0.25 inch thick. The crystal was broken into three parts during handling in space. The seed crystal is polycrystalline, containing at least five crystals. A striking feature of this crystal is the existence of 0.1-mm diameter cavities, many of which are a centimeter in length. Cavities having a geometry such as that seen in the space-grown crystals have not been seen in crystals grown on earth. The five or more component crystals are oriented with the axes

parallel. On earth the orientation of such crystals is usually random. A small part of the crystal is almost completely free of defects and appears extremely good optically. Measurements are being made at the University of Alabama, Tuscaloosa, on the ferroelectric hysteresis of selected parts of the crystal. It has been previously shown that the shape of the hysteresis curve yields the quality of Rochelle salt crystals (which are ferroelectric).

Demonstration TV106, Deposition of Silver Crystals, was also performed by Pilot Pogue. The investigator was Dr. P. Grodzka of Lockheed Missiles and Space Company, Huntsville. For this demonstration, a vial (2.5 by 0.5 inch) of dilute silver nitrate solution was flown in the science demonstration kit (Figure 11). In space, Pogue placed a scored copper wire in the vial. A slow chemical reaction between the copper and the solution produces silver crystals. On the ground these crystals are normally tree-shaped polycrystalline dendrites; in space long dendrites were formed which had small arms that could be described as "elongated" dendrite structures. As shown in the electron microscopic photograph (Figure 12), the earth-grown and space-grown silver crystals have a different microstructure (Figure 13). The microstructure of the space-grown material is composed of small crystallites that are more faceted and polygonal. (The space-grown material is also physically more powdery). Dr. Grodzka believes such new shapes may have application as new catalysts.

Demonstration TV107, Fluid Mechanics Series, consisted of several fluid demonstrations grouped under one heading. The investigators were Ms. Barbara Facemire and Mr. O. Vaughan of MSFC; Dr. S. Bourgeois of Lockheed Missiles and Space Company, Huntsville, Alabama; and Dr. T. Frost of the General Electric Company, Valley Forge, Pennsylvania. Both Science Pilot Ed Gibson and Pilot Pogue recorded this demonstration on TV video. It was essentially a series of tests (Figure 14) to obtain data on fluid oscillation times, dampening times, rotational instability, wetting characteristics, internal vortice, and fluid flow patterns. Over 2 hours of excellent data were obtained.

The last demonstration was TV117, Charged Particle Mobility. The primary investigator for this demonstration was Dr. Milan Bier of the Veterans Administration Hospital in Tucson, Arizona. Co-investigators were Dr. R. Snyder and Mr. S. Hall of Astronautics Laboratory at MSFC. Science Pilot Ed Gibson performed this demonstration. The objective was to study the movement of charged biological particles suspended in a solution in space. A pair of special test cells was fabricated at the

Veterans Hospital under the direction of Dr. Bier. These two cylindrical test cells had fluid cavities connected to each cell end. These components were mounted in a flight package at MSFC (Figure 15). An electrode was in each cavity, and a manually operated gate was installed at the cell entrance of the cavity containing the test specimen. The cavity of cell No. 1 contained human blood, while the cavity of cell No. 2 contained two proteins. Two buffer solutions were used in each cell to obtain a uniform diffusion front when the cell was operated. Twenty-eight volts were applied to the electrodes, and the gate was opened. The blood components moved down the cell under the influence of the electrical field (Figure 16). On the initial run in space, the front had a tendency to remain flat but was distorted by the presence of bubbles in the cell. Subsequently, Gibson reversed the potential, and the blood went back into the cavity. The crew was instructed real time to tap the unit in such a way that the bubbles moved to the opposite end. The experiment was then repeated (Figure 17). The blood migrated down the cell and showed a somewhat bullet-shaped front (the two buffer solutions on this run were now mixed). Unfortunately, the protein in cell No. 2 was exposed to ambient temperatures in the Command Module for approximately three weeks, which caused deterioration of the protein. No data were obtained from cell No. 2.

REFERENCES

1. Ostrach, Simon: Skylab Science Demonstrations. Presented at ESRO Space Processing Symposium, Frascati, Italy, March 25-27, 1974.

2. Bannister, Tommy C.: Skylab III and IV Science Demonstrations Preliminary Report. NASA Technical Memorandum TM X-68435, March 1974.

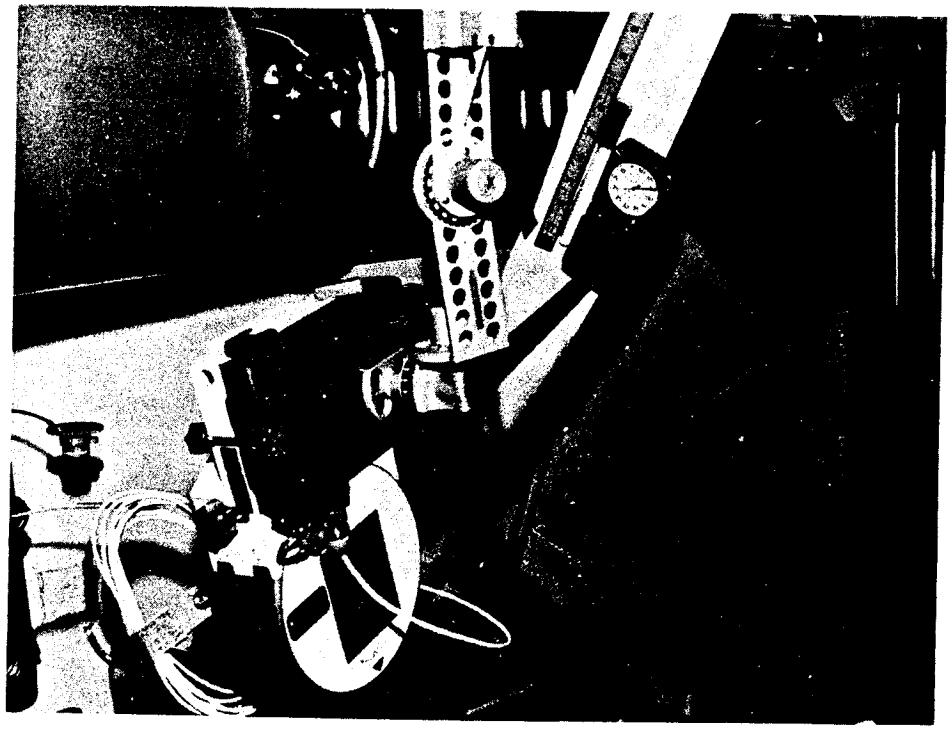

FIGURE 1. SKYLAB III SCIENCE DEMONSTRATION
DIFFUSION IN LIQUIDS.

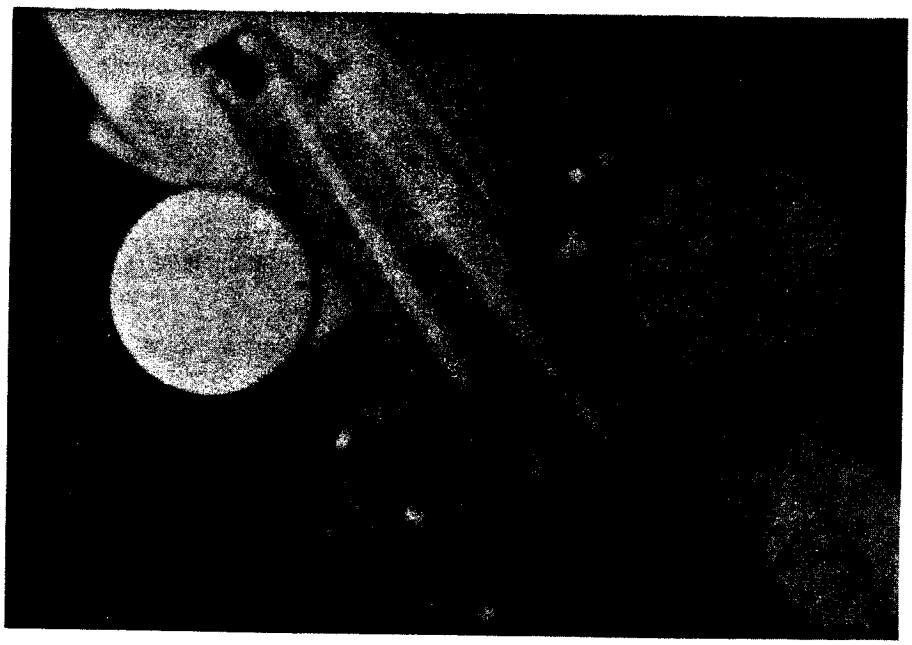

FIGURE 2. SKYLAB III SCIENCE DEMONSTRATIONS
DIFFUSION IN LIQUIDS AND ICE MELTING.

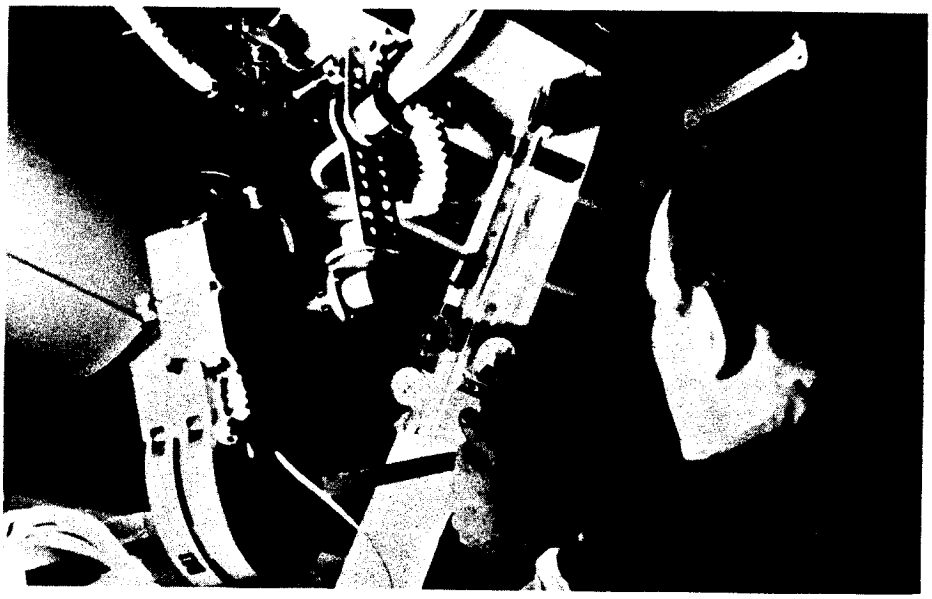

FIGURE 3. SKYLAB III SCIENCE DEMONSTRATION OF SURFACE TENSION EFFECTS.

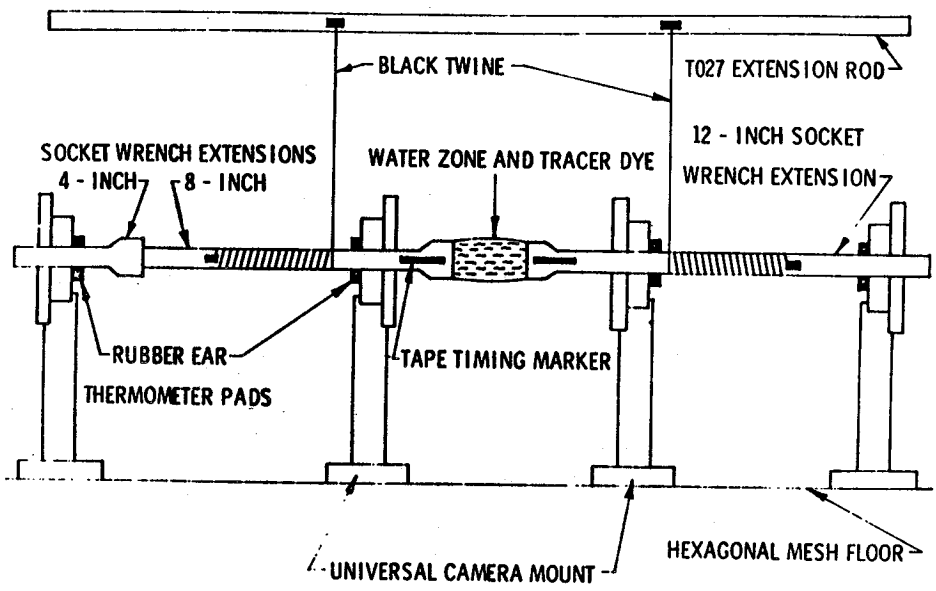

FIGURE 4. SCHEMATIC OF SKYLAB IV SCIENCE DEMONSTRATION TV101, LIQUID FLOATING ZONE.

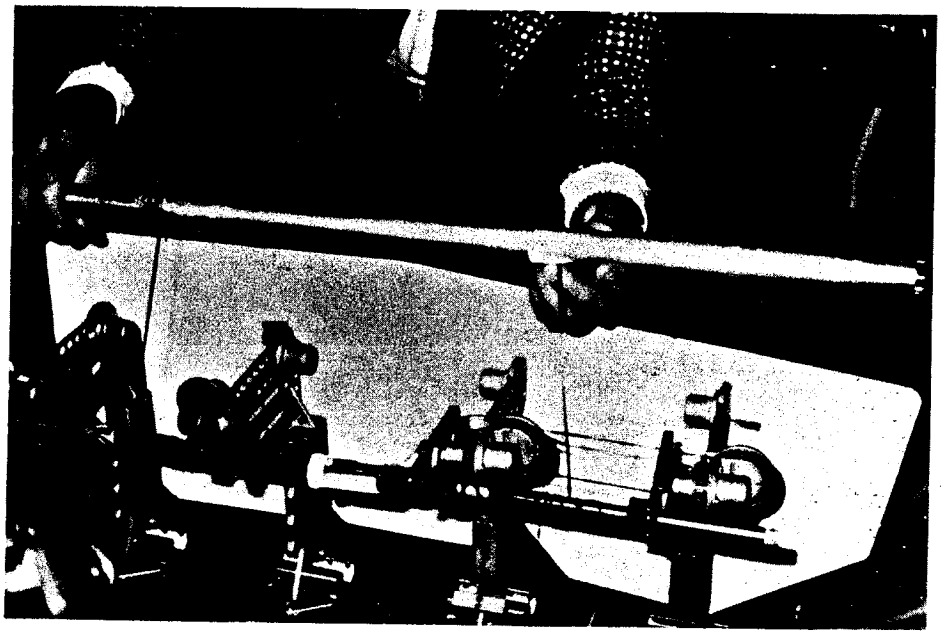

FIGURE 5. SKYLAB IV SCIENCE DEMONSTRATION TV101, LIQUID FLOATING ZONE.

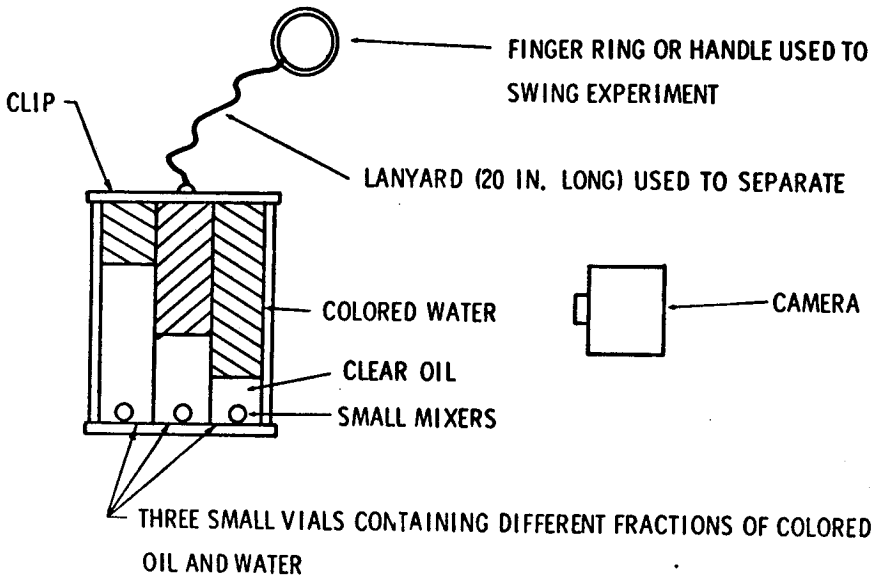

FIGURE 6. SKYLAB IV SCIENCE DEMONSTRATION TV102, IMMISCIBLE LIQUIDS.

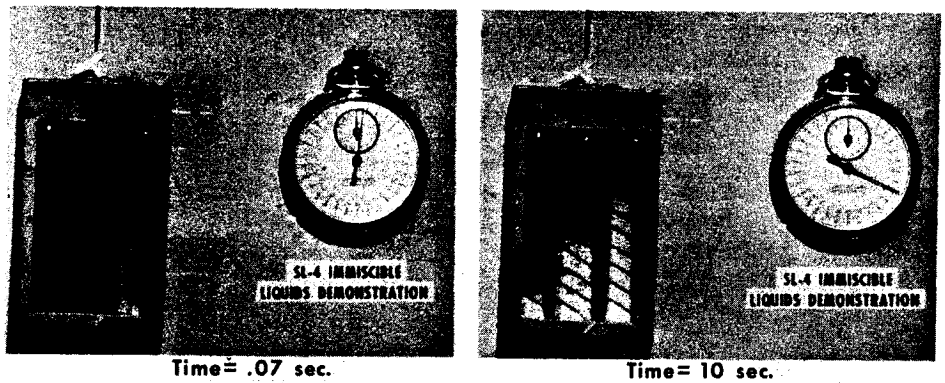

FIGURE 7. SKYLAB IV SCIENCE DEMONSTRATION TV102, IMMISCIBLE LIQUIDS, GROUND-BASED DATA.

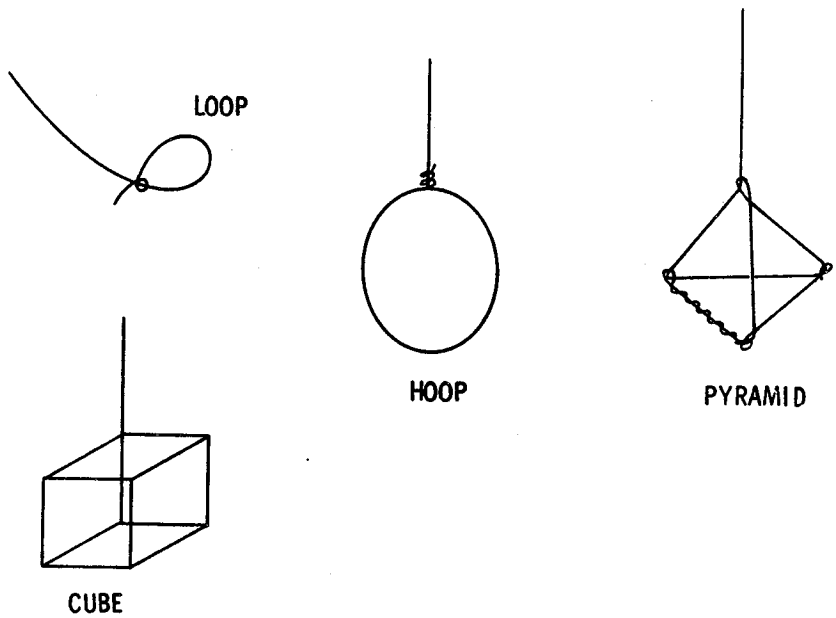

FIGURE 8. SKYLAB IV SCIENCE DEMONSTRATION TV103, LIQUID FILMS.

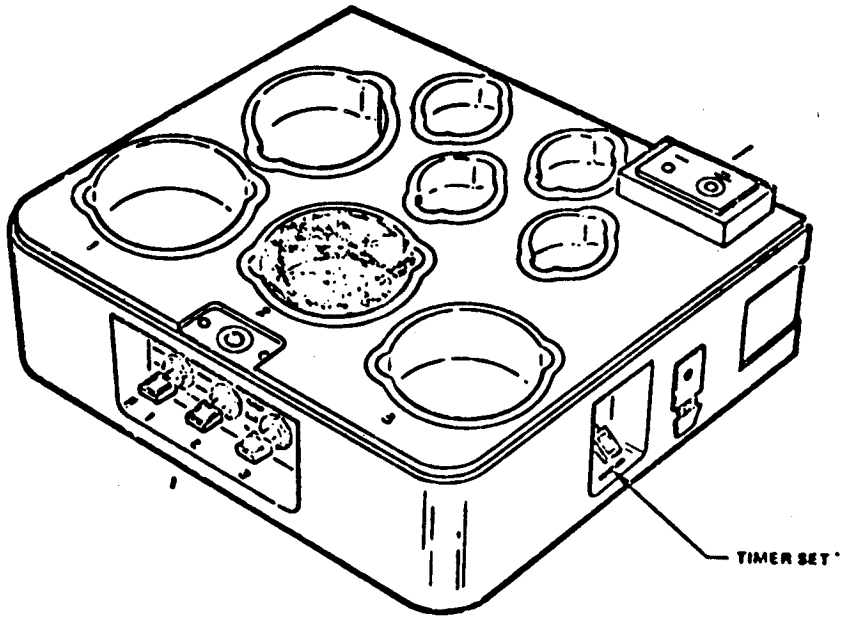

SPARE FOOD TRAY
- o S/N 4909
- o CAVITY 2 OPERATES AT 159° F

FIGURE 9. SKYLAB IV SCIENCE DEMONSTRATION TV105, ROCHELLE SALT GROWTH

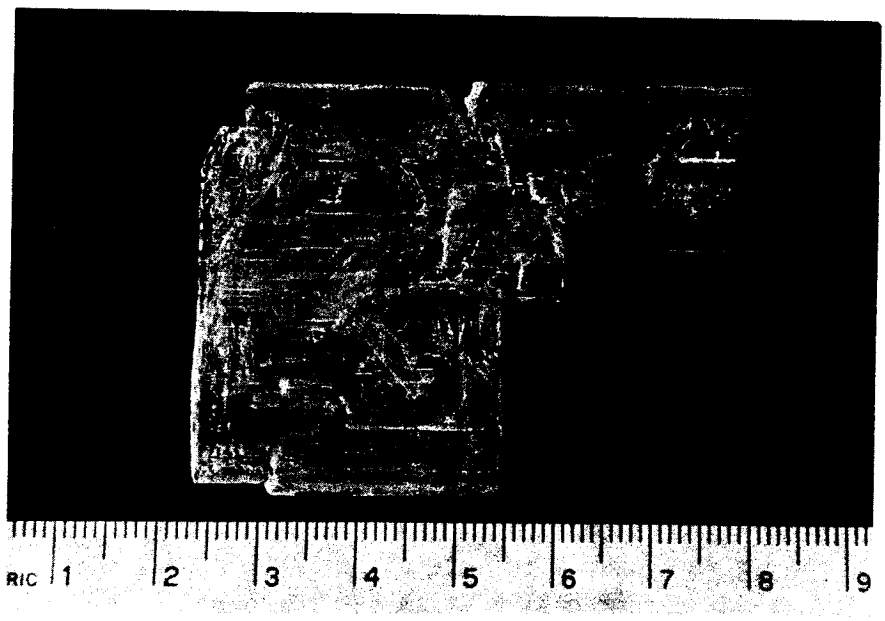

FIGURE 10. SKYLAB IV SCIENCE DEMONSTRATION TV105, ROCHELLE SALT GROWTH.

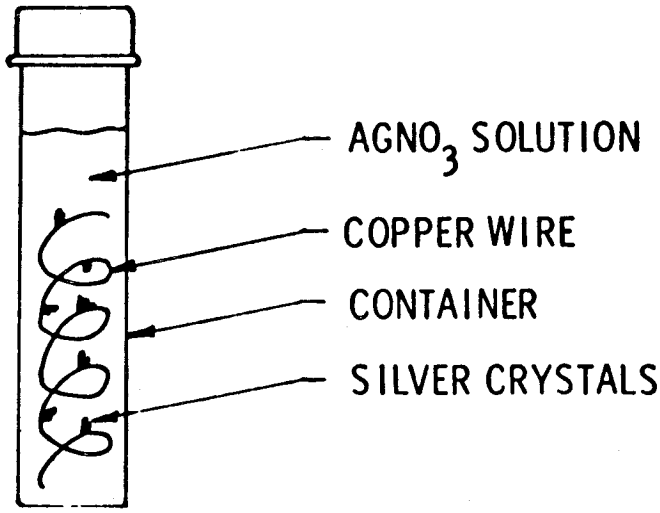

FIGURE 11. SKYLAB IV SCIENCE DEMONSTRATION TV106, DEPOSITION OF SILVER CRYSTALS.

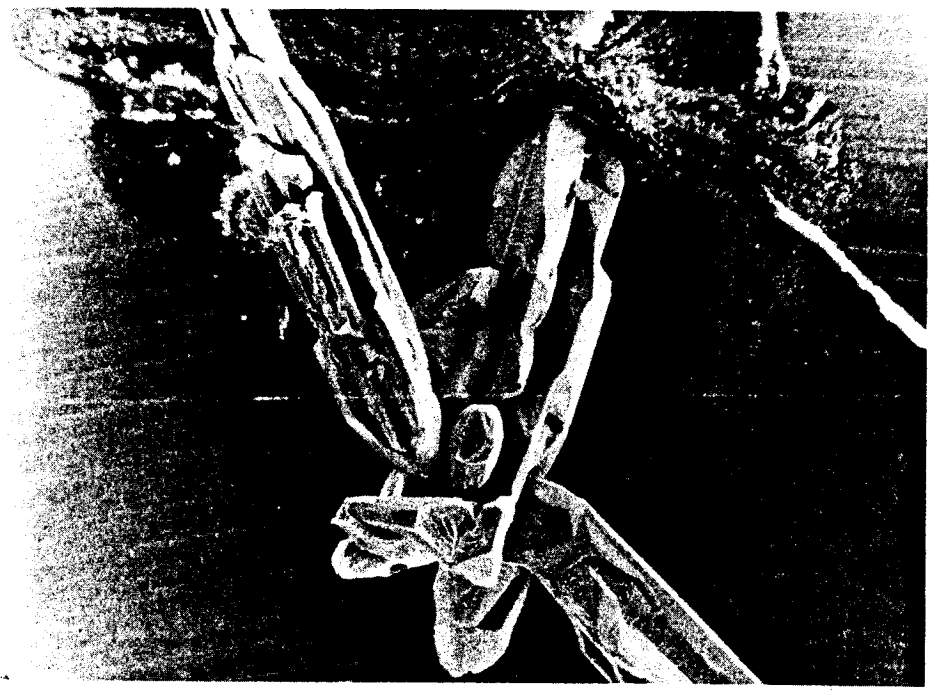

FIGURE 12. SKYLAB IV SCIENCE DEMONSTRATION TV106, DEPOSITION OF SILVER CRYSTALS, EARTH-GROWN (300X).

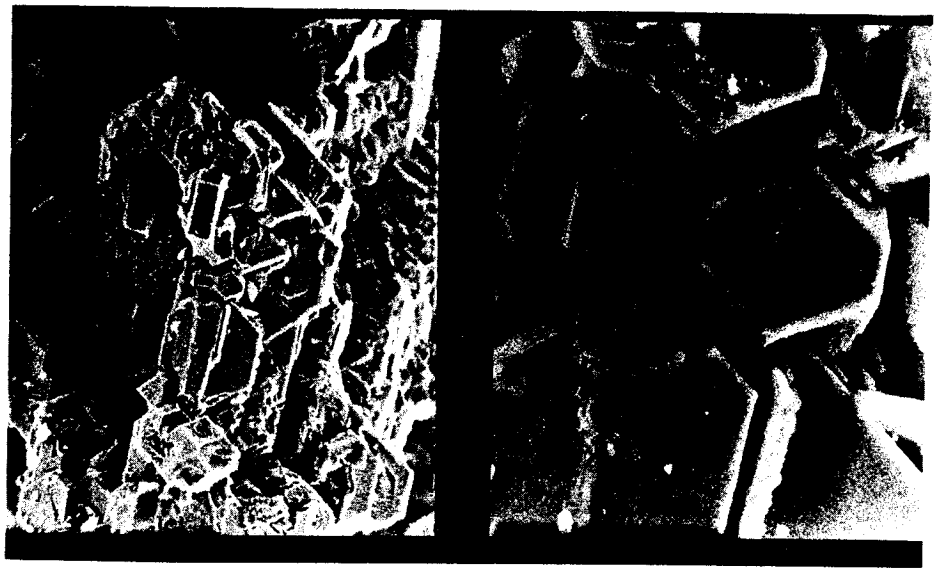

FIGURE 13. SKYLAB IV SCIENCE DEMONSTRATION TV106, DEPOSITION OF SILVER CRYSTALS, SPACE-GROWN.

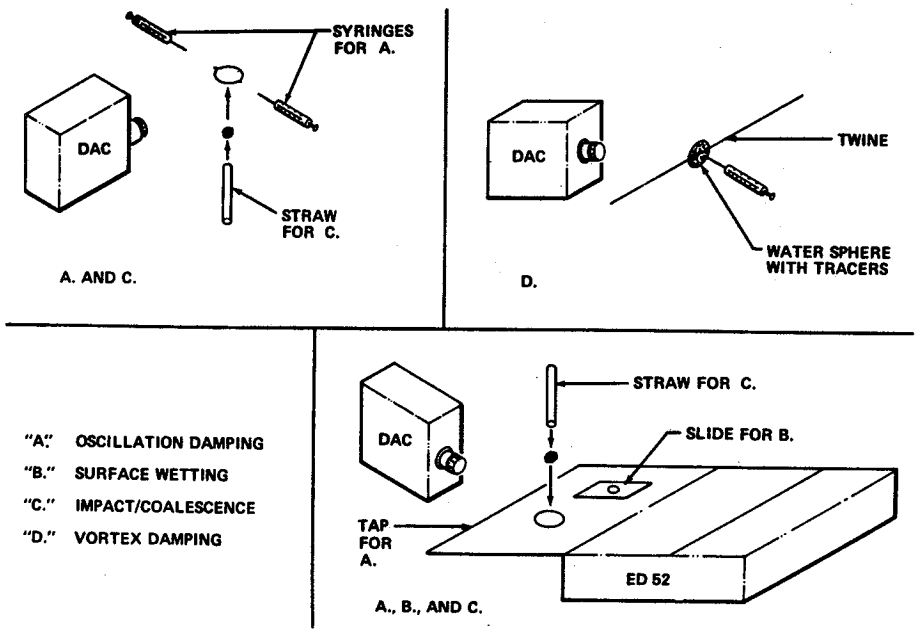

FIGURE 14. SKYLAB IV SCIENCE DEMONSTRATION TV107, FLUID MECHANICS SERIES.

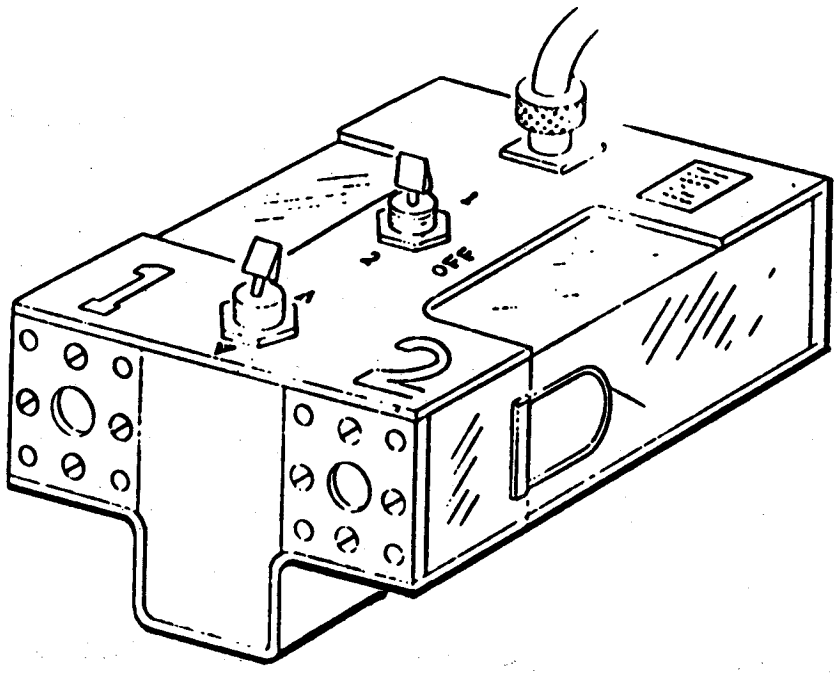

FIGURE 15. SKYLAB IV SCIENCE DEMONSTRATION TV117, CHARGED PARTICLE MOBILITY.

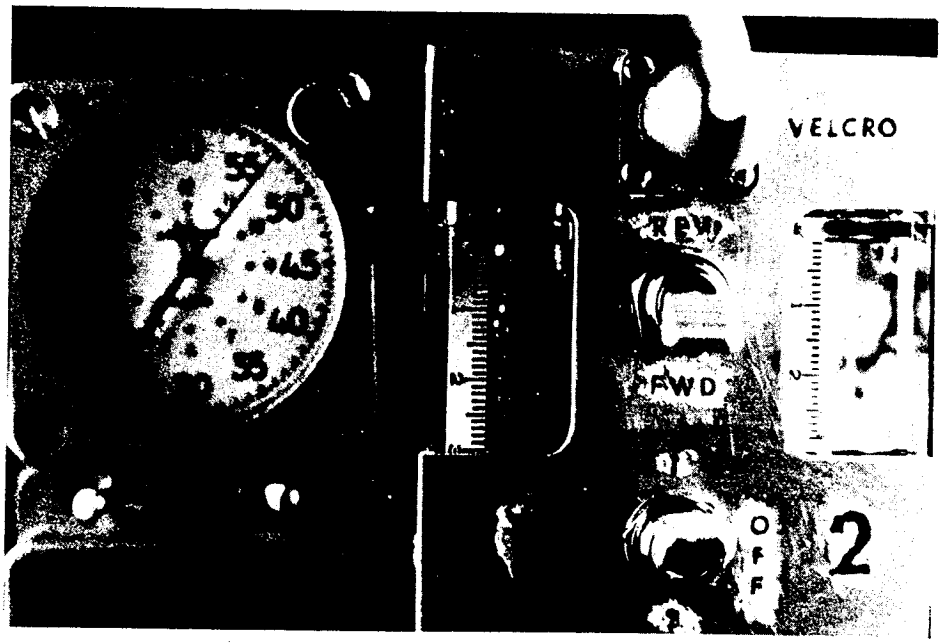

FIGURE 16. SKYLAB IV SCIENCE DEMONSTRATION TV117, CHARGED PARTICLE MOBILITY.

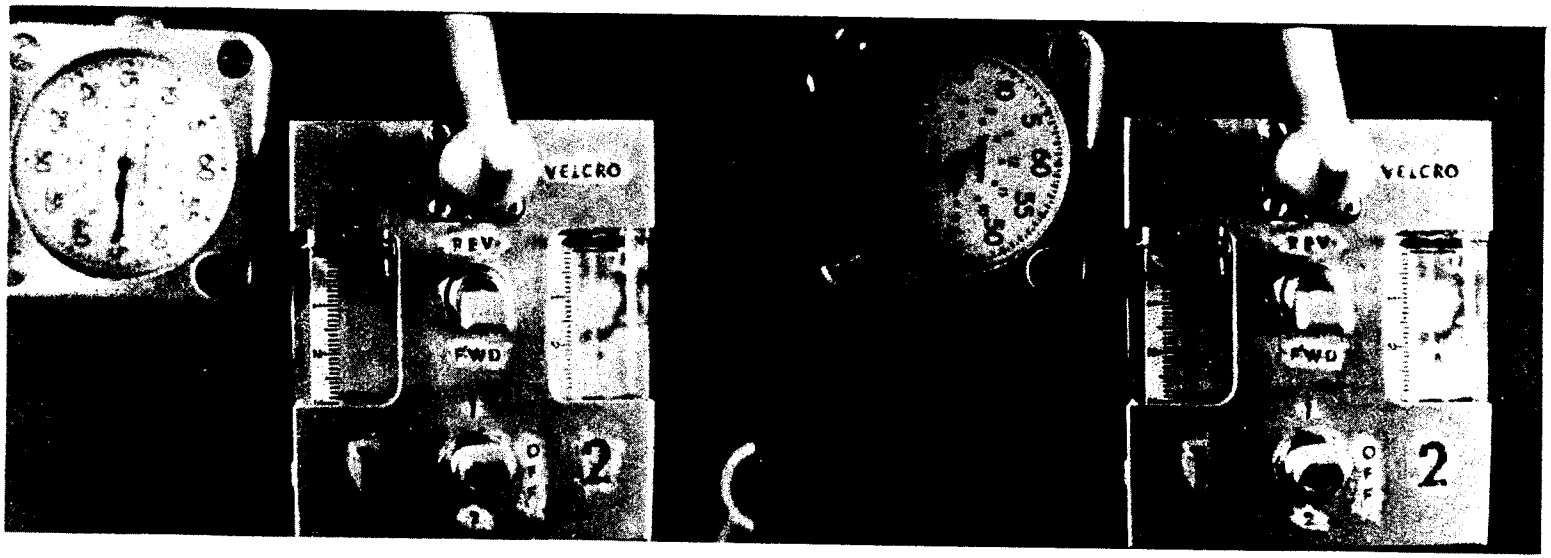

FIGURE 17. SKYLAB IV SCIENCE DEMONSTRATION TV117,
CHARGED PARTICLE MOBILITY.

N74 29904

MATERIALS PROCESSING UNDER ZERO GRAVITY, AN ASSESSMENT AFTER SKYLAB

By

Ernst Stuhlinger
George C. Marshall Space Flight Center
Marshall Space Flight Center, Alabama 35812

Skylab will live in the history of space flight as the turning point between two eras. The first era had belonged to the development of space flight techniques, and to the exploration of some of our neighbors in space. The next era will belong to the utilization of our space flight capabilities for science, for communications, for Earth observations, and for materials processing under weightlessness.

Yesterday's sessions dealt with the program in zero-gravity materials processing which was performed on Skylab, and with the very encouraging results of this first round of experiments. In today's presentations, the lessons learned from this first materials program will be discussed, as well as plans for further experiments under zero-gravity on rockets and satellites of the future.

For several hundred years, man has already carried on a modest, but successful program of zero-gravity materials processing. By allowing a finely dispersed spray of molten lead to solidify while the droplets are falling freely, tiny spheres can be produced as they are needed by bird and rabbit hunters for gunshot. Surface tension, without competitive

gravitational forces, makes the droplets assume spherical shapes while they are exposed for about a second of time to a state of zero-gravity.

There is no apparent need at the present time for better gunshot. However, there are other good reasons why the processing of materials under zero-gravity conditions is moving rapidly into the frontline of interest and effort of materials experts. First, in many instances our modern materials technology has reached limits of improvement which are clearly set by the effects of gravitational forces. Second, the achievements of the space flight program are now providing opportunities of performing experiments under nearly complete weightlessness for extended periods of time. Third, materials processing experiments on Skylab have yielded results in several fields of zero-gravity materials processing which are extremely encouraging.

A need for better materials seems to arise whenever high strength, or high thermal resistivity, or high precision, or high sensitivity, or high efficiency of a system is required. Some examples are listed in Table 1. Of particular interest are semiconductor materials which should be purer, larger, and of greater homogeneity than those which we have today. Better semiconductors would mean substantial progress in large computers, television systems, power generation and conversion, communication equipment, electric automobiles, and many other technical systems. Metals,

alloys, and plastics of higher strength are needed for high temperature turbine blades, for structural and functional elements of nuclear reactors, for artificial human organs, for oil drilling equipment, for precision tool machines. High purity glasses with large coefficients of refraction, and other optical materials with special features, are required for power lasers. If a powerful laser bean is generated in a crystal or transmitted through an optical element, even a minute bit of impurity leads to local absorption of radiative energy which may cause the explosive destruction of the system. Alloys and compounds of certain metals which do not form under normal conditions are of great interest because some of these new substances may include superconductors which become superconducting at temperatures above that of liquid hydrogen. Such superconductors would be of extreme importance for the transmission of electric power at minimal losses.

It would be wrong, however, to look at materials processing experiments only from the viewpoint of immediate applications. Materials science is a genuine science with all the challenge of potential new insights into the secrets of nature, a quality which has always distinguished true science. In following the lure of research and discovery, the scientist does not know at the outset where his work will take him, and what its results will be. He knows, however, that this work will make him wiser,

and that it will help eventually to make life better and easier for many others. In this effort to gain more fundamental knowledge of the world that surrounds him, man follows a law to which he has been subject since his early beginnings. The materials scientist, in studying the behavior of materials under the pure and almost abstract conditions of weightlessness, follows that very same law.

Forces of gravity influence a variety of processes which occur in liquids and gases. The internal structures of solids are not much affected by the presence or absence of gravitational forces; however, substantial effects of weightlessness are realized when diffusion, convection, sedimentation and heat conduction occur, when liquids solidify, or when crystals form from a liquid or gaseous phase. Some of these processes are listed in Table 2.

A number of materials processing studies under zero-gravity were made during past years by pioneers of materials sciences in laboratory free fall experiments, in drop towers, during short parabolic airplane flights, and on sounding rockets. The real opportunity for zero-gravity experimentation arrived with Project Skylab. A Materials Science and Manufacturing Program was established as part of this project; Principal Investigators were selected, and no less than 14 different experiments were performed on the three Skylab missions in a facility shown in Fig. 1.

Details of these experiments and of their results were the subject of yesterday's presentations. For those who took part in the Skylab Materials Program, the results are highly gratifying. However, we feel that the positive results of the materials program on Skylab should not be a reason for celebration and complacency. Primarily, this success represents an obligation, even a kind of mandate, to continue the good work. The Skylab experiments were exploratory at best. Dimensions, thermal conditions, concentrations, time histories, and other parameters were not at all optimized, simply because of lack of sufficient knowledge. The fact that the experiments did yield such impressive results indicates that the experimenters used good judgment and had a fair share of luck, but it also proves that zero-gravity materials processing is indeed an extremely promising and fruitful field for further endeavor. We have just cracked the door into a new world of science and technology full of potential success, and we feel that we must continue to make our way into this new world.

Skylab experiments proved very drastically that presence or absence of gravitational forces makes a substantial and even decisive difference in a number of material processes. Fig. 2 shows cross-sections through weld grooves in a piece of stainless steel. In the zero-gravity sample, the transition zone between the weld and the bulk material looks quite

different, and in fact much better, than in the ground-produced sample. An example of a space-grown single crystal of indium-antimonide is shown in Fig. 3. Careful study of this crystal has indicated that a far higher degree of purity, homogeneity, and freedom from lattice defects has been achieved in this crystal than in any Earth-grown crystals of similar composition. Another example of a single crystal, grown out of the vapor phase under zero-gravity conditions, is illustrated in Fig. 4. This germanium-selenium crystal has a length of about 20 millimeters. It is completely smooth and homogeneous throughout. If grown on Earth under similar conditions, germanium-selenium crystals remain small, and they assume shapes which indicate a high degree of stress and inhomogeneity, as illustrated in Fig. 5. A particularly impressive example of the disturbing influence of gravity is shown in Fig. 6. The upper part of this sample is a tellurium-doped crystal of indium-antimonide, manufactured under Earth conditions. The striations indicate the layered deposition of the tellurium dopant, caused by an interplay of diffusion, convection and sedimentation between the dopant and the bulk material during solidification. Needless to say that this local variation of the dopant concentration is extremely undesirable when a part of this crystal is to be prepared for use as a semiconductor element in an electronic apparatus. The lower part of this sample was melted under zero-gravity conditions.

After remaining some time in the molten stage, it was allowed to resolidify, still under zero-gravity. During that process, the striations disappeared completely, at least within the resolution of this microphotograph. Elimination of gravitational forces removed the disturbance of diffusion by convection and sedimentation, with the result that the dopant distributed in a completely homogeneous fashion throughout the sample. For materials scientists and for solid state physicists, this picture is equivalent to a bold dream that has come true. A similar feeling may be aroused in the minds of superconductivity experts when they see the picture in Fig. 7. Two metals of very different densities, gold and germanium, were mixed and melted together under zero-gravity conditions. In a ground-based laboratory, the two metals would immediately separate because of the difference in their densities, gold accumulating at the bottom and germanium floating on top. For this reason, an alloy cannot be obtained on Earth if the two are melted together in a container. In the Skylab experiment, the two did alloy; in fact, they formed a fine dispersion, as shown in the microphotograph of Fig. 8. Several places were found in this specimen where a gold-germanium compound had formed, a substance that had not been known from bulk samples heretofore. This compound even shows superconductivity! Admittedly, it becomes superconducting at a very low temperature, 1.7° K, but from all previous

experiences a higher transition temperature cannot be expected of a binary compound of this kind. Still, the result of this gold-germanium experiment proves that superconductors can be produced in space that cannot be manufactured on Earth.

Encouraged by these very positive results on Skylab, the program planners for materials science made plans to accommodate a set of zero-gravity materials processing experiments on the next manned space system, the Apollo-Soyuz Test Project. These experiments, listed in Table 3, are still of an exploratory nature, although they are utilizing the experience and the results gained from the Skylab experiments. A big leap for zero-gravity materials science and technology will come with the Shuttle-borne Spacelab in the early eighties. A broad program of materials processing work is being prepared for Spacelab, as shown in the Table.

This program, in contrast to the programs on Skylab and the Apollo-Soyuz Test Project, will not be limited to a few flights; it will continuously evolve through the years, and it will include exploratory experiments, purely scientific investigations, pilot projects for manufacturing of useful quantities of materials, and eventually even production runs for larger quantities. Instruments and facilities can be accommodated within the Spacelab capsule where scientists and engineers can personally tend to

the experiments, and also on the open Pallet where automated systems will be mounted. Fig. 9 shows the Shuttle with its large payload bay. A sketch of the Spacelab and the adjacent pallet is shown in Fig. 10. Some tentative figures for the quantities of materials that can be processed on the Shuttle are listed in Table 4. These figures show that the capabilities of the Shuttle for zero-gravity production runs are not all unrealistic for such very special materials as semiconductors, high temperature alloys, glasses for lasers and infrared optics, superconductors, and biomedical vaccines. Yearly quantities required of these materials range from a few hundred to several thousand kilograms per year. At least for a number of years, the Shuttle will be adequate to provide the zero-gravity facility for such a program.

In conclusion, it may be appropriate to quote a statement by Professor Goldberg, astronomer and Director of the Kitt Peak Observatory, who participated in the solar physics program of Skylab. When the Skylab Project had come to its end, he said: "When it all began, many of us were doubtful whether this combination of men and instruments in an orbiting station would lead to a success. Now, we are convinced, and we are deeply impressed. In fact, Skylab has made sincere believers out of us."

It seems that a very similar statement can be made for those who have participated in the materials processing program carried out under weightlessness on the orbiting Skylab, and who are looking forward now to an expanding program on future spacecraft.

TABLE 1 SPECIFIC MATERIALS TO BE PRODUCED UNDER WEIGHTLESSNESS

MATERIALS	USES
ALLOYS OF HIGH YIELD STRENGTH AND HEAT RESISTANCE	TURBINE BLADES, REACTOR COMPONENTS, STRUCTURAL ELEMENTS
GLASSES OF HIGH REFRACTIVE INDICES AND HIGH PURITY	OPTICAL INSTRUMENTS, LASERS, FIBER OPTICS
SEMICONDUCTORS OF GREAT HOMOGENEITY AND LARGE SIZE	ELECTRONIC SYSTEMS, COMPUTERS, LASERS, POWER CONVERSION
SUPER CONDUCTORS WITH TRANSITION TEMPERATURES ABOVE 20°K	ELECTRIC POWER GENERATION AND TRANSMISSION
BIOMEDICAL SUBSTANCES OF HIGH PURITY	VACCINES, SERA, BIOLOGICAL AND MEDICAL RESEARCH

TABLE 2 GRAVITATIONAL FORCES INFLUENCING MATERIALS PROCESSING

- CONVECTION
- DIFFUSION
- TURBULENCE
- BUOYANCY
- HEAT CONDUCTION
- LAYERING
- SEGREGATION
- LATTICE DEFECTS
- BUBBLE EFFECTS
- CRYSTAL GROWTH

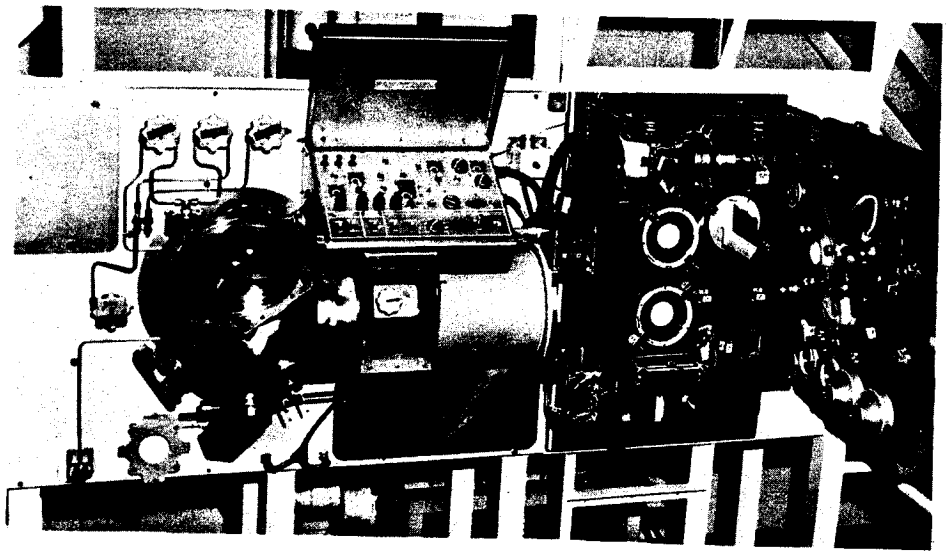

FIGURE 1 M512 SPACE PROCESSING FACILITY ON SKYLAB

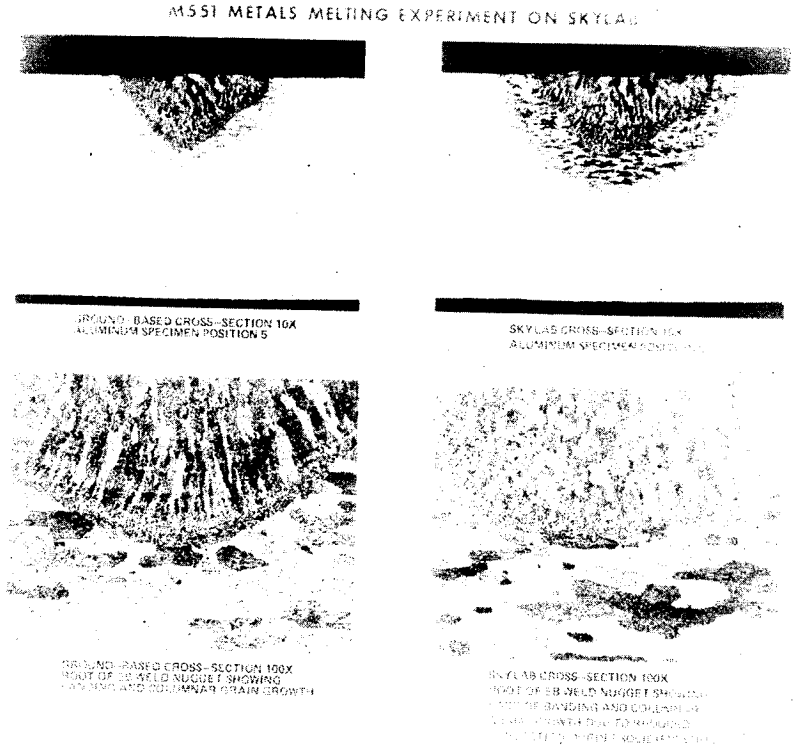

FIGURE 2 CROSS-SECTIONS THROUGH MELT GROOVE OF STAINLESS STEEL DISC

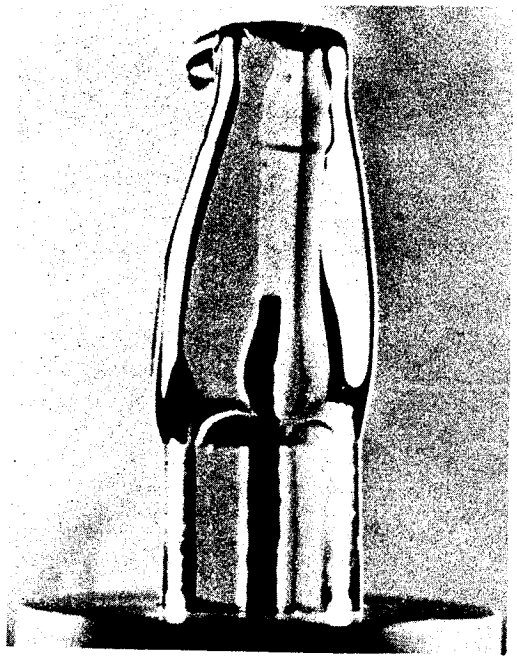

FIGURE 3 INDIUM-ANTIMONIDE CRYSTAL, RECRYSTALLIZED UNDER ZERO-GRAVITY

FIGURE 4 SPACE-GROWN (ZERO-GRAVITY) GERMANIUM-SELENIUM CRYSTALS

FIGURE 5 GERMANIUM-SELENIUM CRYSTALS, GROWN UNDER GROUND CONDITIONS

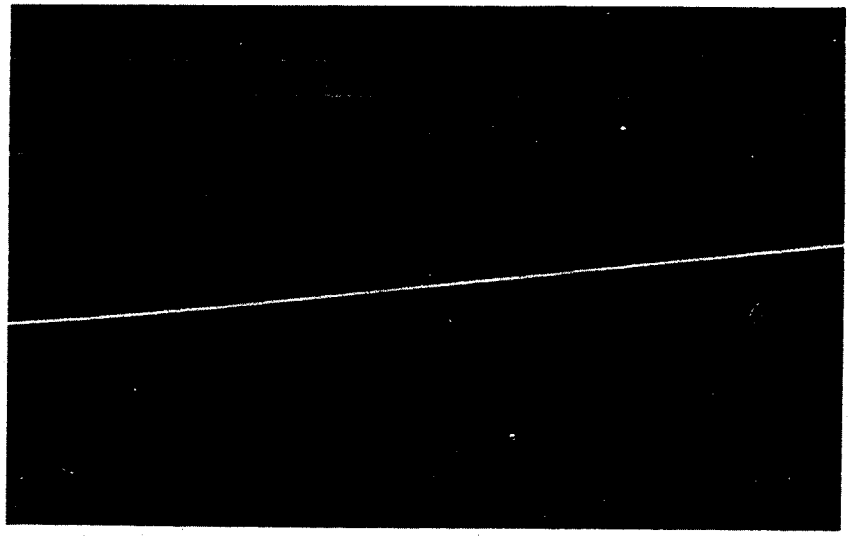

SEGMENT OF THE INITIAL REGROWTH INTERFACE OF TELLURIUM-DOPED InSb CRYSTAL. DOPANT INHOMOGENEITIES ARE SEEN IN THE EARTH-GROWN (UPPER) SECTION; NO DOPANT INHOMOGENEITIES ARE SEEN IN THE SPACE GROWN (LOWER) SECTION; 125X.

FIGURE 6 EARTH- AND SPACE-GROWN INDIUM-ANTIMONIDE CRYSTAL, DOPED WITH TELLURIUM

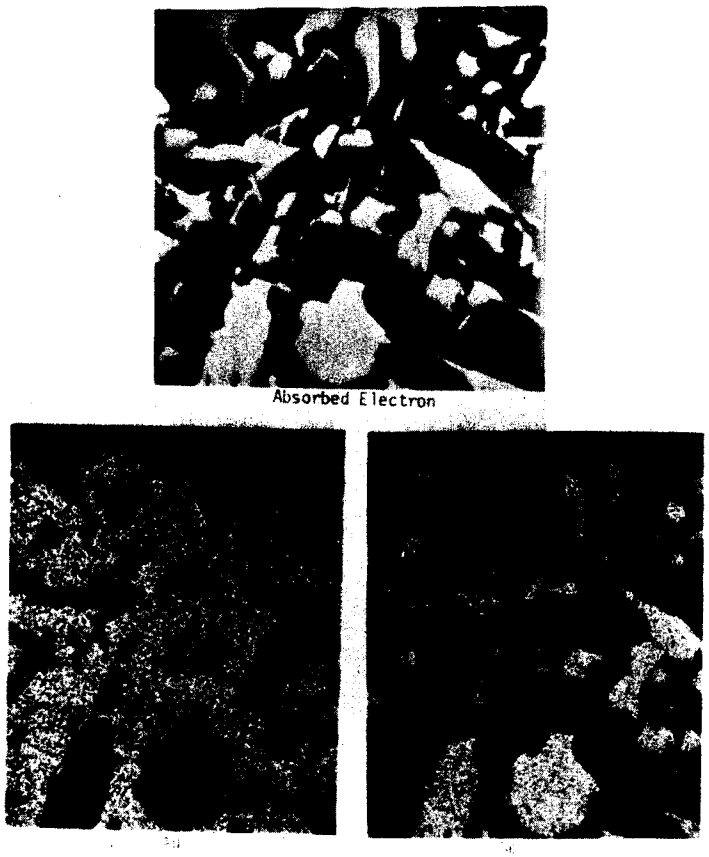

FIGURE 7 CROSS-SECTIONS THROUGH GOLD-GERMANIUM MIXTURE, MELTED AND SOLIDIFIED UNDER ZERO-GRAVITY

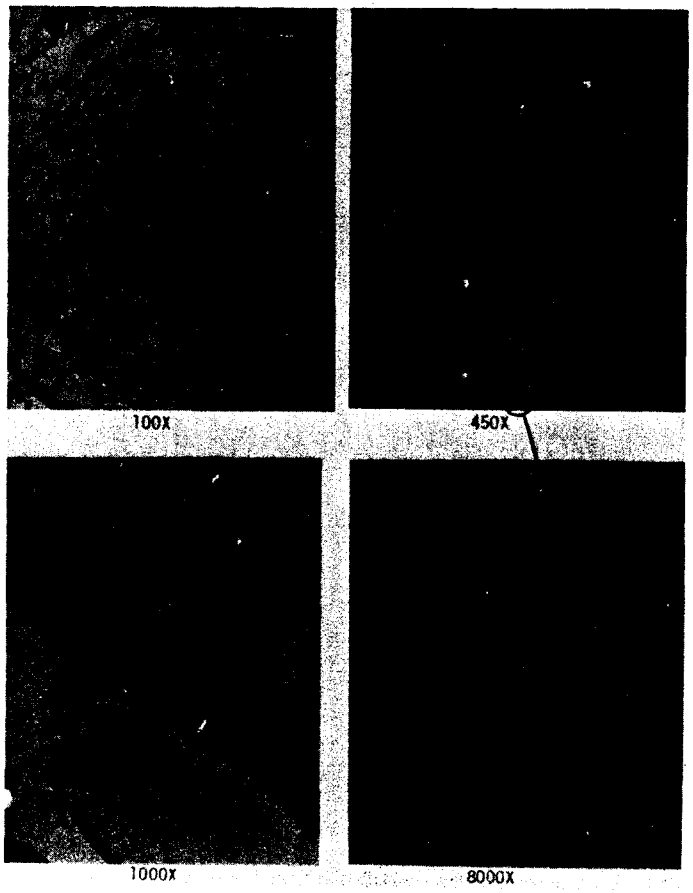

FIGURE 8 CROSS-SECTION THROUGH SPACE-PROCESSED GOLD-GERMANIUM MIXTURE, SHOWING NEW COMPOUND

	SKYLAB	APOLLO-SOYUZ	SPACELAB
METAL MELTING AND SOLIDIFICATION	X	X	X
METAL WELDING AND BRAZING	X		?
METAL MIXTURES, ALLOYS, COMPOUNDS	X	X	X
COMPOSITE MATERIALS	X	X	X
SEMICONDUCTORS (CRYSTALS)	X	X	X
SEMICONDUCTORS (DOPING)	X	X	X
SUPERCONDUCTORS	X		X
GLASSES			X
BIOMEDICAL SUBSTANCES		X	X

FIGURE 9 ZERO-GRAVITY EXPERIMENTS ON PAST AND FUTURE SPACECRAFT

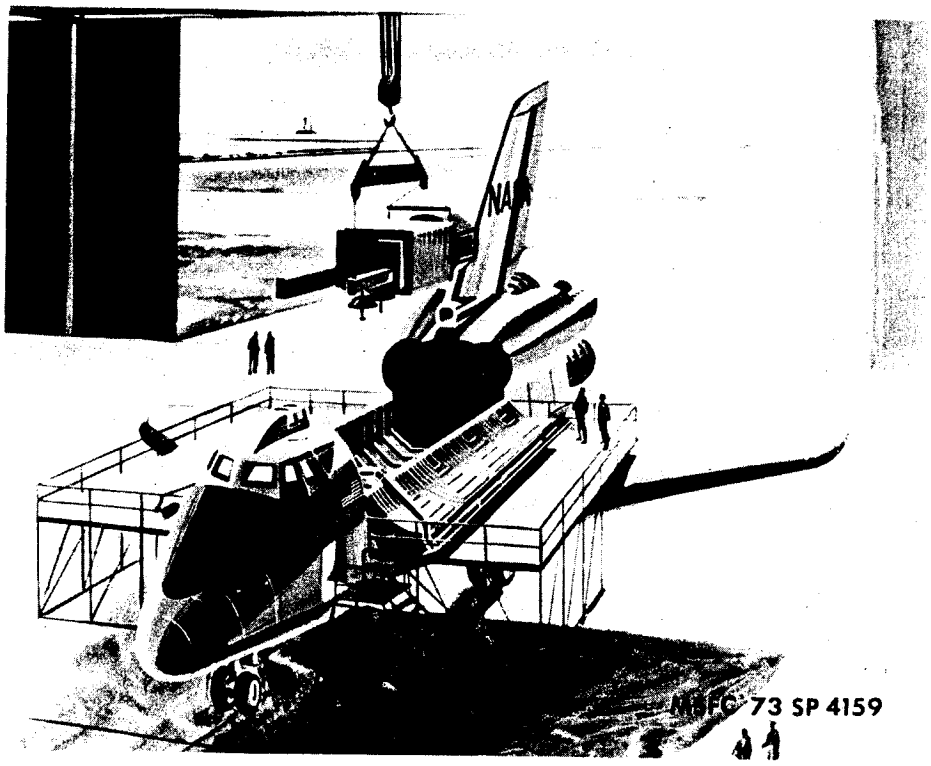

FIGURE 10 INSTALLING PAYLOAD IN SPACE SHUTTLE CARGO BAY

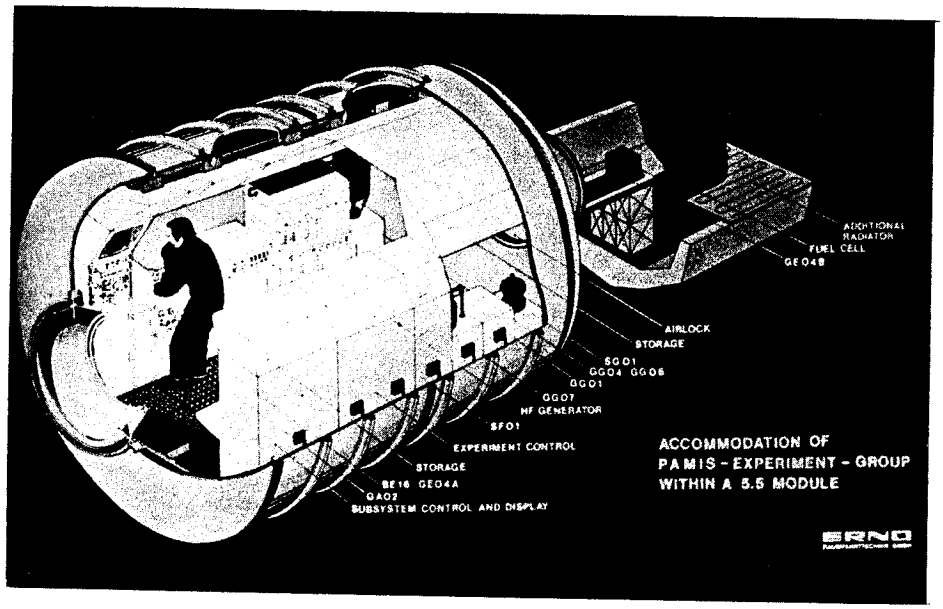

FIGURE 11 SPACELAB AND PALLET MODULES (ERNO CONCEPT)

TWO–WAY PAYLOAD FOR SHUTTLE (PRODUCTION FACILITY AND MATERIAL)	5 000	TO	9 000 KG
PRODUCTION QUANTITY PER FLIGHT	100	TO	2 000 KG
PRODUCTION QUANTITY PER YEAR			
WITH 1 FLIGHT PER MONTH	1 200	TO	2 400 KG
WITH 2 FLIGHTS PER WEEK	10 000	TO	200 000 KG

FIGURE 12 MATERIALS PROCESSING IN SPACE, PRODUCTION QUANTITIES OBTAINABLE ON SPACELAB